Floodplain Woodland Hydrodynamics

A thesis submitted to Cardiff University
in candidature for the degree of

Doctor of Philosophy

by

Patricia Anne Xavier

Division of Civil and Structural Engineering
Cardiff School of Engineering
Cardiff University
United Kingdom

September 2009

ProQuest LLC
789 East Eisenhower Parkway
P.O. Box 1346
Ann Arbor, MI 48106-1346

Contents

Declaration

This work has not previously been accepted in substance for any degree and is not concurrently submitted in candidature for any other higher degree.

Signed:..... (Candidate) Date:10/05/10

Statement 1

This thesis is being submitted in partial fulfillment of the requirements for the degree of .....

Signed:..... (Candidate) Date:10/05/10

Statement 2

This thesis is the results of my own independent work/investigation, except where otherwise stated. Other sources are acknowledged by explicit references.

Signed:..... (Candidate) Date:10/05/10

Statement 3

I hereby give consent for my thesis, if accepted, to be available for photocopying, inter-library loan and for the title and summary to be made available to outside organisations.

Signed:..... (Candidate) Date:10/05/10

Abstract

Floodplain woodlands are valuable environments, providing a diverse habitat for many riparian and land-based species. It is now recognised that the continual loss of floodplain woodland has impoverished the national biodiversity of riparian environments, and measures have been brought in both nationally and through the European Commission to halt the decline. This has however, highlighted a deficiency that has existed for many years in the field of river hydraulics. The representation of complex riparian vegetation environments within river models remains an area not adequately addressed. This research presents experimental investigations into floodplain woodland vegetation, with a view to improving the representation of these vegetations within numerical models.

Floodplain woodland hydrodynamics were explored with scaled-down (1:8) staggered arrays of single stem and multi-stem model trees at planting densities of 8.8, 19.8 and 80.6 plants per m^{-2}. The planting densities investigated correspond to the recommended planting densities cited by the Forestry Commission UK. Roughness factors, including Manning's n, the Darcy-Weisbach friction factor f and the bulk drag coefficient $\overline{C_d}$ were computed for the different model tree and planting density combinations. Velocity measurements within the arrays were investigated, and a study to determine the optimum sampling strategy was carried out to obtain representative velocity and turbulent kinetic energy measurements within the model tree arrays. The optimum sampling locations for streamwise velocity appeared to be clustered around 0.3 s and 0.7 s, where s is the lateral or longitudinal spacing between the model trees, while for turbulent kinetic energy the optimum location was 0.5 s. Full scale drag force versus velocity tests of floodplain woodland trees were carried out and a drag area parameter $C_dA.U_0$ derived. The trees experienced little to no bending at low velocities, with force varying linearly with the square of velocity, while considerable deflection was observed at higher velocities, with force varying linearly with the velocity. Physical parameters including height, diameter, mass and volume of the wood are compared against the drag area parameter, with mass and volume showing a stronger correlation than height or diameter. The increase in the drag area parameter due to the presence of foliage was also investigated. The numerical incorporation of floodplain woodland vegetation is presented with respect to two-dimensional depth-averaged numerical modelling. A reach of the River Laver in North Yorkshire, England was modelled to assess the hydraulic impact of the conversion of arable land to floodplain woodland.

Symbol	Description
A	Cross-sectional flow area
A_p	Projected area to flow direction
AR	Aspect Ratio
β	Momentum correction factor
b	Width
C	Chezy factor
C_d	Drag coefficient
C'_d	Drag-area parameter
C_dA	Drag-area parameter
C_w	Fluid resistance coefficient
d_v	Diameter of obstacle in flow field
ϵ	Depth-averaged turbulent eddy viscosity
E	Modulus of Elasticity
EAI	Element area index
EI	Flexural rigidity
ϕ	Solid volume fraction
f	Coriolis parameter
f	Darcy-Weisbach friction factor
F	Drag force
F_b	Drag force due to bed shear
F_γ	Stiffness force
F_d	Drag force due to obstacle in flow field
F_w	Force due to the self-weight of water
F_x	Drag force in x direction
F_y	Drag force in y direction
F_z	Drag force in x direction
Fd	Flooding and drying depth
g	Gravitational acceleration
h	Height
h_v	Height of obstacle in flow field
H	Total energy head
H	Total water depth
H_f	Head loss due to friction
$HF\Delta T$	Half time step
k_s	Roughness height
λ_a	Percentage plan area
l	Length
L_c	Lateral cover
LAI	Leaf area index

Symbol	Description
m	Percentage mass
M	Mass
M_x	Moment in x direction
M_y	Moment in y direction
M_z	Moment in z direction
n	Manning's n
μ	Fluid viscosity
$\hat{\mu}$	Sample mean
N	Number of events
N	Number of obstacles per m^3
N_r	Number of obstacles in the cross-streamwise direction
ν	Kinematic viscosity
P	Wetted perimeter
p	Streamwise discharge per unit width
p	Pressure
p_a	Atmospheric pressure
P	Porosity
q	Lateral discharge per unit width
ρ	Fluid density
ρ_a	Density of air
R	Hydraulic radius
Re	Reynold's number
σ	Basal-frontal silhouette
$\hat{\sigma}$	Sample variance
S_0	Bed slope
S_h	Height-spacing ratio
s_x	Spacing between objects along streamwise direction
s_y	Spacing between objects along cross-streamwise direction
τ	Shear stress
τ_w	Boundary shear stress
T	Time step
ΔT	Timestep
TKE	Turbulent kinetic energy
U	Streamwise velocity
U_0	Free-stream velocity
$\overline{U}$	Mean-area streamwise velocity
V	Lateral velocity

Symbol	Description
$\overline{V}$	Mean-area lateral velocity
W	Vertical velocity
υ	Fluid viscosity
$\overline{W}$	Mean-area vertical velocity
X, x	Streamwise direction
y	Flow depth
Y, y	Cross-streamwise direction
ζ	Water surface elevation
Z, z	Vertical direction

1

The Role of Floodplain Woodland in Flood Risk Management

1.1 Introduction

Worldwide, flooding affects many people and costs lives, often in the most deprived areas of the world. Settling on floodplains has enormous advantages, such as easy water access and fertile land, as is evident from the very high densities of human settlement in, for example, the Netherlands and Bangladesh. In the EU, the sharing of the wide range of experiences across member states has led to integration of approaches in recent years. The FP6 funded project FLOODSITE (Kiljn et al. 2008) and the ICE Learning to Live with Rivers (Fleming et al. 2001) are examples where recent best practice has been collated.

EU Directive *2007/60/EC* on the assessment and management of flood risks entered into force on 26 November 2007. The Directive requires EU Member States to identify all water courses and coast lines at risk from flooding and to map the extent of potential floods and identify assets and humans at risk in these areas. The Directive also requires Member States to take *adequate and coordinated measures to reduce this flood risk* (EC 2007). In the UK, the events of Boscastle and Carlisle

are highlighting more than ever the gaps in the national flood infrastructure, and the risks associated with poor flood management. The dangers of building on floodplains are well understood and under the Welsh Assembly Planning Guidance TAN 15 (PPG 25 in England), Local Planning Authorities are now advised to consult the Environment Agency if land is at risk of flood before development is planned. However, the very real risk of inundation remains for approximately 2.2 million existing and new UK homes. In 2007, 9% of new dwellings were constructed on land at high risk of flooding (NationalStatistics 2009). Disaster mitigation by removing existing occupants of floodplains and wetlands limits the potential of these lands for socio-economic development. Methods are then needed to protect effectively existing properties from the effects of flooding, (Fleming et al. 2001).

The activity of humans on floodplains has a direct impact on rivers. The recent increase in flood risk to many UK and other European towns and cities comes from a number of sources. Firstly, the increase in impervious surfaces replacing grassland routes rainfall to drains and the rivers more quickly, so the rate of rise in river levels is more rapid. Secondly, the demand for land means that natural floodplains are often built upon, and protected with, flood defences, so the natural storage potential of a river reach is reduced. Thirdly, due to the existence of rising global temperatures, the UK and the rest of Europe are seeing an increase in extreme weather patterns, so the incidence of high rainfall and flooding is rising.

Flooding is unpredictable, but inevitable, and the risk of flooding can be managed. The classic method of flood alleviation in recent times has been through a site specific 'flood defence' approach - blocking the water in the river channel and routing excess water more quickly downstream. This often had the effect of simply displacing problems from the site in question to other regions along the reach.

In recent years there has been a switch from 'flood defence' to 'flood risk management', a whole systems approach to flooding. This has been assisted by the introduction of catchment-based approaches to managing flooding. The approach encourages a look at river systems as a whole, and includes aspects of water quality, biodiversity and benefits to communities in terms of quality of life. The Flood Risk Management Research Consortium (FRMRC1/ FRMRC2) applies state-of-the-art modelling techniques to flood forecasting and modelling. Land use and its consequences for flood risk management is a key component of the ongoing research (FRMRC 2009).

Under EC legislation (Water Framework Directive (2000/60/EC), Floods Directive (20070/60/EC), the potential now exists with which to start reintroducing natural

and artificial floodplains for additional flood storage as part of wider flood risk management schemes. In England and Wales, Catchment Flood Management Plans (CFMPs) identify integrated, local flood risk management policies that balance environmental, social and economic needs over the long term i.e. 50-100 years (Wales 2009). CFMPs allow a catchment scale approach to flood risk management to be adopted, building in the evolution of flood risk in the future, and the needs of the communities served by the catchment.
The aim of this research, in particular, is to represent more accurately typical UK floodplain woodland in a depth-integrated hydrodynamic model. This will provide a tool for improving predicted inundation levels in such areas and help determine the potential flood storage benefits of constructed floodplain woodland.

1.2 Thesis Aims

This thesis investigates the hydrodynamics of floodplain woodland vegetation, and aims to improve the representation of floodplain woodland genera within numerical models. River modelling is a useful tool in determining river dynamics, particularly in the prediction of high flow events. However, the modelling of overland flows, such as occur during flood events, is hampered by a lack of data relating to the hydrodynamics of vegetated flows. At a time when the wide-ranging benefits of river restoration and reforestation is increasingly recognised, it is critical that numerical modelling keeps pace with improvements in the numerical representation of real vegetation. Currently, within numerical models, floodplain woodland is represented by using a hydraulic roughness coefficient, although little guidance is given as to the magnitude of this roughness factor.
The achieve this, the study has been split into two parts, experimental data collection and numerical modelling of vegetated flows. The research presented will broaden the available database of hydraulic roughness of floodplain woodland vegetation and provide a tool for numerical modellers. The specific thesis aims can be summarised as the following:

- Determination of roughness coefficients (Manning's n, Darcy-Weisbach friction factor f and the drag coefficient C_d) for single stem (dowels) and multi-stem (*Cornus sanguinea* saplings) model trees at three planting densities at a geometrically scaled-down factor of 1:8

- Sample and compare the three dimensional velocity and turbulence field

around the model tree arrays, and explore the difference in hydrodynamics between single stem and multi-stem arrays

- Determine the optimum point source sampling locations for streamwise velocity and turbulent kinetic energy within the single stem and multi-stem model tree arrays

- Present force-velocity data from full-scale drag force tests on submerged saplings up to a free stream velocity of 4 m/s, and determine the drag area parameter (C_dA) for the individual trees

- Link recorded physical characteristics of the full-scale trees to the drag area parameter (C_dA), moving towards a model for resistance parameterisation from field measurements

- Incorporation of the drag-area parameter (C_dA) within the depth-averaged finite difference numerical model DIVAST

- Use the obtained drag-area parameters (C_dA) to represent the potential flood attenuation effect of reintroducing floodplain woodland to the River Laver in North Yorkshire

1.3 Context and Global Perspective

1.3.1 Forests and Water

Through interception, forests regulate the flow of precipitation to streams. There are several well documented case studies of deforested areas experiencing an increase in flooding and periods of drought. Experiences within the developing world were collated by Bradshaw et al. (2007) to provide a consistent empirical link between deforestation and flood frequency, with a particularly strong link being established between flood duration and forest cover.

Floodplain woodlands have been shown to affect the morphology of a channel. Previous research has indicated that reaches of small streams with forested riparian zones are commonly wider than adjacent reaches with non-forest vegetation (McBride et al. 2007). There is a also a greater presence of large woody vegetation within woodland streams. Wide, shallow rivers with assorted large woody debris are ideal habitats for many invertebrates and fish (Hughes 2003) and vegetation can

create secondary circulation patterns and coherent flow structures (Li & Shen 1973, Lopez et al. 1995, Dunn 1996).
Through the filtration effects of woodlands, water quality from forested areas is freer from agricultural pollutants. This is a key benefit of smaller strategically placed riparian buffer zones, where smaller strips of woodlands separate agricultural land from the river zone, filtering out of the pollutants before the run-off reaches the stream (Hughes 2003). Research activities in Pontbren, mid-Wales, including those by Henshaw & Thorne (2007) are currently investigating the performance of such buffer strips.

1.3.2 Floodplain Woodland Economic and Environmental Dynamics

The natural environment is an ever-evolving interplay between different forces of nature. Woodlands are in a constant state of flux; to talk of a floodplain woodland is to define a specific point in time and space in a complex eco-system. For an individual woodland, intermerging areas are regenerating and degenerating simultaneously, both due to local changes of flora and fauna and influences from the meso-scale environment, such as wider catchment-scale changes affecting run-off and consequent flood peaks. Global climatic trends are another significant factor affecting the frequency of precipitation. Anthropogenic influence is an additional factor, and in the densely populated United Kingdom it is certainly the dominant one at present, having commenced with the first stages of human agricultural cultivation during the Bronze and Iron Ages.
Ecological systems can be represented by mathematical models to simulate carbon capture, transpiration and biomass productivity. Water resources and woodland processes are so closely interlinked that it is common to define forest ecosystems in terms of catchments. Linking an ecological model of riparian woodland growth with a hydraulic model of river processes and hydrology is beyond the scope of this research. It is however, necessary to reach a broad understanding of woodland processes to understand the context of floodplain woodland.

1.3.3 Climatic Effects on Floodplain Woodland

The UK lies on the peri-glacial boundary, and the repeated encroachment and retreat of polar ice between interglacial periods have impoverished the diversity of woodland species (Starr 2005). Only towards Southern Europe could tree species survive to recolonise northern areas during interglacial periods (Cousens 1974). The Alps, and

then the separation of the UK from mainland Europe approximately 7500 years ago, provided physical barriers to this recolonisation. Thus many species considered exotic to the UK today existed in equivalent climates during previous inter-glacial periods. This increases the possibility that new species may be identified and introduced to UK floodplain woodlands in the future, so a broad scale and flexible approach to the modelling requirements of floodplain woodlands is necessary.

1.3.4 Ecological Succession

Rather than a static eco-system at its ecological climax, floodplain woodlands exist as an intermediate stage in a sere i.e. a system of advancing ecological succession. One sere may last for hundreds of years. In the case of floodplain woodlands, this temporal succession is both allogenic i.e. changes induced by factors external to the ecosystem such as frequent flooding and deposition of sediment on the floodplain, and autogenic i.e. changes in the eco-system from successive species. Figure 1.1 is obtained from Cousens (1974) and illustrates the hydrosere as observed at Sweat Mere in Shropshire, where continuous advancing seral stages can be identified. At each stage dominant plants create the conditions that reduce their chances of survival. From the initial stages of the plant genera *Typha* and *Carex*, the nutrient capital is enriched from repeated growth and decay of these plants, allowing successive species of more nutrient intensive plants to exist, which then out compete and replace the pioneer species as dominant (Chapman & Reiss 1999). In a progressive succession system, floodplain woodlands exist at the early-intermediate stage, with predominant species of the genera *Salix* and *Alnus* which thrive in a saturated soil environment.

Retrogressive succession could occur on a floodplain woodland that was subject to increasing frequency and severity of flooding. Thus the order of succession in Figure 1.1 is reversed, with the increased soil saturation from advancing groundwater levels leaching nutrients from the soil, and restricting growth of late sere species of the genera *Alnus*, and *Betula*, which require a higher soil nutrient status.

An understanding of progressive and retrogressive succession can be a useful tool for modellers of riparian systems in assessing changes in woodlands, i.e. should anthropogenic activity be discontinued on arable land adjacent to rivers (with no major changes in the climate or hydrology), the land may revert to woodland due to progressive succession.

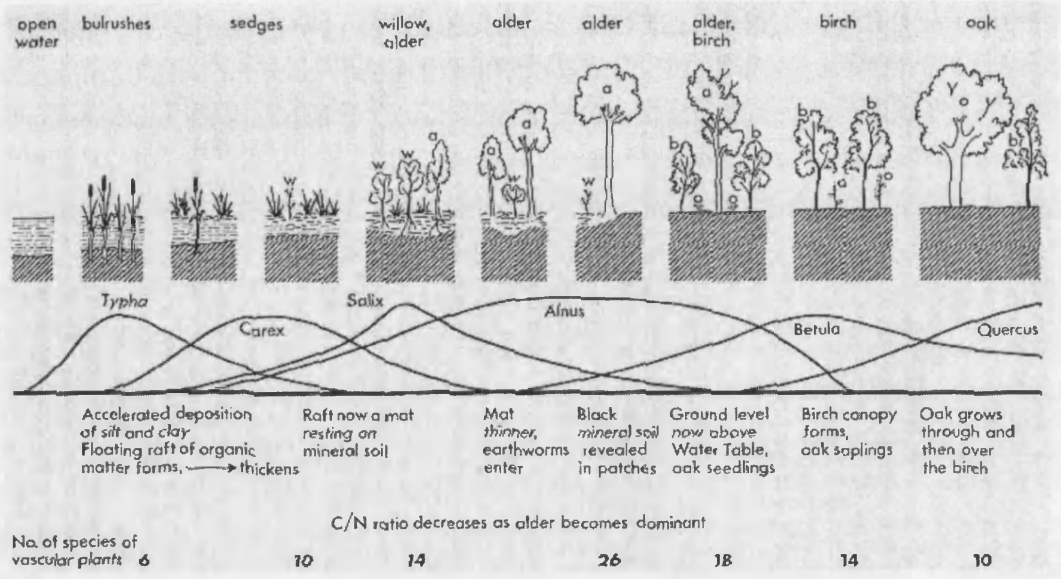

Figure 1.1: Temporal Succession in a Hydrosere, Cousens (1974)

1.3.5 Floodplain Woodlands Today

While the effects of climate and the competing nature of plants have shaped the composition of woodlands for millennia, anthropogenic activity has been a major influencing force on current UK woodlands during the Holocene (Roberts 1998), with woodland resources necessary for iron production, and fertile land needed for agricultural production (Tansley 1949). For more on the history of floodplain woodlands in relation to anthropology, the reader is referred to Cousens (1974).

Today, in those areas where wood is cultivated for fuel and construction, coppicing is the preferential management technique (Starr 2005). In coppice rotation, young tree stems are repeatedly cut to near ground level. Multiple new shoots appear at the base of the tree which could then be harvested. Coppicing keeps the wood in a constant juvenile stage, with prolific production of timber good for both burning and building. Coppiced woodlands provided a rich variety of habitats for biodiversity as the coppice stands vary in age (Fuller & Warren 1993).

Many existing floodplain woodlands contain trees that exhibited evidence of historical coppicing, some with uncoppiced multiple stems, or others as a single stem but presenting a clear coppice stool (Cousens 1974).

Woodlands are now recognised as a valuable natural asset. Protected areas in Europe expanded from 195 million hectares in 1990 to 234 million hectares in (UN 2008). However, the destruction of forests and woodlands continues (estimated at 13 million hectares per year between 1990 and 2005, (UN 2006)), due to both large scale clearance for agriculture and development, and smaller scale, but widespread subsistence farming. Sustainable Forest Management (SFM) has emerged in recent years to focus on forest management that recognises the three pillars of sustainability, with co-existing environmental, social and economic benefits. There is now a consistent international policy movement towards protecting and reinstating forest cover. At the United Nations Forum on Forests in 2006 (UN 2006), it was agreed to: reverse the loss of forest cover worldwide; enhance forest based benefits; increase the area of protected and sustainably managed forests and reverse the decline in official economic development assistance for SFM.

Climate Change is an immediate threat to the standard of life for humanity, and it is recognised that the rise in atmospheric carbon is linked to overall global temperature increases. The concentration of CO_2 has risen from pre-Industrial Revolution levels of 280ppm, to 380ppm in recent times, and human induced activities have resulted in a 70% increase between 1970 and 2004 alone (IPCC 2007). Forests play a key role

in the carbon cycle (Dresner et al. 2006), with the IPCC (2007) identifying three strategies where biological approaches can be used to curb CO_2 increase:

- Conservation: conserving woodlands as an existing C pool;
- Sequestration: increasing the existing pool and extracting CO_2 from the atmosphere; and
- Substitution: substituting biological products for fossil fuels or energy intensive products.

In addition to the increasing role in providing biomass for renewable energy, the forests of Europe are also valued as a carbon sink. Across Europe, current land use, changes in land-use and existing and new forestry reduce the continent's net emissions by almost 6 %, with forests probably accounting for almost all of this reduction (UN 2009).

As well as contributing to the global CO_2 cycle, forests experience feedback effects from the current increase in CO_2. In the UK and much of Northern Europe, it is predicted that warmer and wetter winters will occur. As the leaf size and in-leaf period of broadleaf species increase, interception losses and transpiration rates are expected to increase (Stern 2005).

The role of forests and floodplain woodlands in maintaining water quality will be a major factor, as the predicted increase in temperature and rainfall intensity will affect the transport, retention and in-stream processing of nutrients.

Planting densities for woodland based on Forestry Commission UK guidance are are listed in Table 1.1.

Planting Grid	Description
1.0 m x 1.0 m	This spacing is preferred for withies, a type of willow coppiced and used for weaving material and equates to 10,000 trees per hectare
2.1 m x 2.1 m	This is the normal minimum spacing for larger woodlands where timber production is an objective. This equates to 2,250 trees per hectare. To grow quality timber, planting at greater density is favoured. For example, a spacing of 2.1 m x 1.5 m will increase density yet still allow access for maintenance between rows
2.5 m x 2.5 m	This may be random within rows and/or random. It is preferred if a more natural appearance is desired or if wildlife and conservation are prime objectives. This variable spacing also allows space for natural regeneration to supplement the planted trees. To ensure successful creation of new native woodland a density of 1,600 trees per hectare should be achieved
3.0 m x 3.0 m	This spacing is acceptable for small woods and in cases where the prime objective is to create accessible community woodland. This equates to 1,100 trees per hectare
8.0 m x 8.0 m	This is an option often used for poplar plantations. The trees are carefully pruned and grown through to a single crop without thinning. This results in 156 trees per hectare
2.5 m x 2.5 m	This may be random within rows and/or random between rows. It is preferred if a more natural appearance is desired or if wildlife and conservation are prime objectives. This variable spacing also allows space for natural regeneration to supplement the planted trees. To ensure successful creation of new native woodland a density of 1,600 trees per hectare should be achieved

Table 1.1: Planting densities. Table taken from Rodwell & Patterson (1994)

1.3.6 Value of Floodplain Woodland

The valuation of woodland resources has stood in the way of their recognition as essential natural assets (Gibson et al. 2002). If a pile of chopped wood and cleared land for arable or pasture is more valuable to the landowner, there is no incentive to preserve it for the more intangible benefits of wider society. The underlying reasons for the destruction of forests are because the true value, incorporating the long-term environmental, social and economic value, is not recognised at the local level (Lindberg et al. 1997). Brazil is a good example, where small scale subsistence farming accounted for 30% of deforestation between 2000 and 2005.
Some ways of combating deforestation include *agroforestry*, *payment for environmental services* and *stewardship*.

1.3.6.1 Agroforestry

In Mexico, the Scolel Tê land use and agroforestry project aims to make woodlands a viable financial asset for the landowner. Scolel Tê manages a trust fund which helps farmers to develop forested land, (Dresner et al. 2006).

1.3.6.2 Payment for Environmental Services

Payment for Environmental Services (PES) is a system whereby landowners are paid for the environmental benefit of maintaining forested land. In Costa Rica, landowners maintain buffer strips of forest in riparian zones in exchange for a small stipend paid for by downstream water users, who have smaller water treatment costs due to the decreased suspended sediment load and lower levels of contamination from agricultural fertilizers and pesticides. In New York, concerns about the effect of upstream farming practices in the Catskill/ Deleware watershed on the water quality delivery to New York City prompted a Watershed Protection and Partnership Programme, working with a wide range of land owners to promote protection of water resources, including the maintenance of forests. Schemes embodying PES have contributed to an increase in forest cover from 21% to 51% between 1977 and 2005 (Stern 2005).

1.3.6.3 Environmental Stewardship

Natural England Environmental Stewardship scheme (Natural England 2008, EnvironmentAgency 2009) is a grant scheme available to landowners to create areas of

beneficial biodiversity such as woodland. The scheme may be a channel through which the maintenance and creation of floodplain woodland could becomes an economic incentive to landowners. Currently flood alleviation benefits of floodplain woodland are recognised in terms of attenuation of surface run-off and groundwater storage. Less understood is the effect of the presence of floodplain woodland and the impedance to a flood wave. If an economic benefit to downstream users can be quantified, it may become possible to reward landowners who convert or maintain floodplain woodland, with extra subsidies under the Natural England Environmental Stewardship scheme.

1.4 Floodplain Woodlands

The nature of the vegetation on a floodplain will affect its role in flood alleviation. A football field on a floodplain away from the main streamline of flow may simply act as a reservoir for flood storage. Floodplain woodlands in particular could add to the biodiversity, as well as alleviate flooding, although the storage volume may be reduced in the case of dense vegetation. On smaller upland reaches, there is the potential that floodplain woodlands could create online storage of floodwaters due to the increased hydraulic resistance from the vegetation and instream debris.
Floodplain woodland in the UK refers to woodlands dominated by tree stands in wet ground which is often flooded. Classification in the EU habitats directive denotes this form of habitat as Alluvial Forest with dominant species of *Alnus glutinosa* (Alder) and *Fraxinus excelsior* (Ash). These are woods that have developed on fertile floodplains, subjected to periodic inundation. The term does not apply to trees simply growing along the banks of a river, unless the trees form part of a wider woodland habitat. For reference, latin and common names of dominant species in UK floodplain woodland are listed in Table 1.2.
Since man first settled, anthropogenic activities have left very little virgin floodplain woodland, with the majority having been deforested and used for construction or agriculture. What remains is now fragmented. Within Europe, only 90 % of original floodplain forests still exist (Hughes 2003).

Genus	Species	Common name
Alnus	glutinosa	Alder
Betula	pubescens	Birch
Carex		Sedge
Corylus	avellana	Hazel
Craetagus	monogyna	Hawthorn
Filipendula	ulmaria	Meadowsweet
Fraxinus	excelsior	Ash
Galium	palustre	Marsh Bedstraw
Lysimachia	nemorum	Yellow Pimpernel
Phragmites	australis	Common Reed
Populus	nigira	Poplar
Quercus		Oak
Salix	cinera, pentandra, fragilis	Willow
Typha		
Urtica	dioica	Common Nettle

Table 1.2: Latin and common names of floodplain woodland species, NVC (2004)

1.5 A Profile of Floodplain Woodland

Floodplain woodland is defined in the National Vegetation Classification List (NVC 2004). The classifications that relate to *wet woodland* are listed in Table 1.3. In a typical floodplain woodland, the canopy is dominated by the genera *Fraxinus*, *Quercus*, *Betula* and *Alnus*. The understory includes the genera *Corylus* and *Craetagus*. Ground flora includes wet woodland genera *Carex* and *Filipendula*. There is often a history of *Corylus* coppicing in accessible woodlands.

Class No.	Dominant Species	Sub-Species
W1	*Salix cinerea*	*Galium palustre*
W2	*Salix cinerea*	*Betula pubescens - Phragmites. Australis*
W3	*Salix pentandra*	*Carex rostrata*
W4	*Betula pubescens*	*Molinia caerulea*
W5	*Alnus glutinosa*	*Carex paniculata*
W6	*Alnus glutinosa*	*Urtica dioica*
W7	*Alnus glutinosa*	*Fraxinus excelsior - Lysimachia. Nemorum*

Table 1.3: NVC List of Wet Woodland Categories

This research will focus on the hydraulic impact of woody shrubs and trees. The hydraulic effect of sedges and other groundcover species can be drawn from existing work (Jarvela 2002, Wilson et al. 2003). Among all floodplain woodland vegetation, woody plants exhibit the highest degree of structural rigidity. When inundated, woody plants produce a markedly different response from the more flexible sedges and other low canopy species. Woodland genera exhibit a variety of growth habits, some with a single stem, and other with multiple stems, perhaps due to coppicing or environmental factors. Common genera among floodplain woodland species are *Alnus* and *Salix*. These are the genera to be simulated in hydrodynamically scaled-down arrays in Chapters 3 and 4. Saplings of *Alnus* and *Salix* are also used in the full scale drag force tests carried out in Chapter 5.

1.5.1 Floodplain Woodland Tree Species

1.5.1.1 Alnus glutinosa (Common Alder)

The most common species of *Alnus glutinosa* is the Black Alder. It is widespread throughout Europe, and is a defining genus in wet woodland areas (NVC 2004). The annual rate of growth can be up to 90 cm a year when the tree is young, and *Alnus glutinosa* can grow to a height of 20-30 m and will live for up to 150 years

(Featherstone 2009). Multi-stemmed specimens occur often, with at least two or three main stands common. *Alnus glutinosa* is deciduous, with new leaves opening in April. The leaves can grow to 10 cm in diameter and are shed in Autumn, the bark of young trees is smooth, but becomes fissured and rougher textured in older specimens (Featherstone 2009).

Figure 1.2: An *Alnus* forest from Groß Wasserburg in Unterspreewald (2006), photographed by Botaurus-stellaris (2008)

1.5.1.2 Salix (Willow)

The genus *Salix* covers approximately 400 deciduous species from shrubs to small trees and creeping plants with certain species favouring floodplain woodland, in particular *Salix alba* and *Salix fragilis* (Mabberley 1997). A consistent feature of *Salix* is the tendency of certain species to form multiple stems (Fuller & Warren 1993). *Salix* is flexible, and when stems are young, deforms significantly when subject to external loading (Record 1914). Table 1.4 presents common varieties of *Salix* that show a preference for floodplain woodland.

Latin Name	Common Name
Salix cinerea	Grey Willow
Salix caprea	Goat Willow
Salix pentandra	Bay Willow
Salix viminalis	Common Osier
Salix alba	White Willow
Salix fragilis	Crack Willow
Salix purpurea	Purple Willow

Table 1.4: Common Floodplain Woodland species of *Salix* (Newsholme 1992)

Figure 1.3: *Salix fragilis* infesting a Tasmanian river channel, Rudman (2008)

Willow has many uses. *Salix* contains salicylic acid, the precursor to aspirin. Willow wood is also used in the manufacture of many household items and furniture. In addition tannin, fibre, paper, rope and string, can be produced from the wood. Willow is also used in basket weaving, wattle fences and wattle and daub (Newsholme 1992).

Willow is grown for biomass or biofuel in forestry systems, as a consequence of its high energy in to energy out ratio, large carbon mitigation potential and fast growth (Aylott et al. 2008). Large scale projects to support the development of *Salix* as an energy crop have been established, such as the Willow Biomass Project in the US and the Energy Coppice Project in the UK (ForestResearch 2003). In the University of Natural Resources and Applied life Sciences, Austria, *Salix* are investigated for hydraulic resistance in ongoing studies using the Wienfluss channel (Wilson, Yagci, Rauch & Stoesser 2003, Rauch et al. 2005). However, in Australia, *Salix* is considered an invasive weed in river channels and routinely removed, as seen in Figure 1.3 (CRC 2003).

1.6 Thesis Layout

A thorough exploration of the current theories behind vegetated flows is set out in *Chapter 2 Theory of Vegetated Flows*. The experimental programme, covered in *Chapters 3*, *4*, and *5* was designed to investigate a range of real and simulated, full scale and scaled-down floodplain woodland species. *Chapter 3 Hydrodynamics of Scaled Single Stem and Multi-stem Tree Arrays* presents bulk resistance results from three planting densities of scaled-down woodland arrays of single stemmed and multi-stemmed tree species. Comparisons are made between the single and multi-stemmed plants, and between the different planting densities investigated. The

results are also upscaled to prototype floodplain woodland scale. *Chapter 4 Velocity and Turbulence Measurements of Scaled Single Stem and Multi-stem Tree Arrays* presents point velocity and turbulence data from the arrays tested in *Chapter 3.* The focus in the data sampling for *Chapter 4* was to obtain a high density grid of measurements to characterise as fully as possible, the hydrodynamics of the flow field around the vegetation. This allowed a study into selective sampling of the arrays, with the intention of obtaining the optimal measurement grid for the vegetated flows investigated, making the fewest measurements but obtaining the most representative overall sample in terms of flow field velocity and turbulence. *Chapter 5 Drag Force Tests on Full Scale Trees* presents data collected as part of the European Hydralab III programme, in conjunction with BOKU and Universitaet Braunschweig. Twenty two specimens of *Alnus*, *Salix* and *Populus* were attached to a load cell, and the drag force measured under velocities from 0.125 m/s to 4 m/s.

The numerical modelling of vegetated flows is a useful tool. However, reducing the complexity of the natural environment to a few parameters within a numerical model requires a clear understanding of the physical phenomena involved. *Chapter 6 Numerical Modelling of Floodplain Woodland Vegetation* introduces the modelling of vegetated flows, using the experimental data gathered in *Chapter 3* and *Chapter 5* within the two-dimensional (depth-averaged) finite difference numerical model DIVAST. *Chapter 6* also presents a study into the flood alleviation effects of a floodplain woodland. A study is carried out into the hydrodynamics of floodplain woodland reintroduction over a stretch of the River Laver in North Yorkshire.

2

Review of Vegetated Flows Literature

2.1 Characterising Vegetated Flows

2.1.1 Introduction

This chapter will present relevant past and current theory on the hydrodynamics of vegetated flows, with particular reference to the determination of vegetative hydrodynamic resistance. Hydraulic roughness representation will be discussed in terms of Manning's n, the Darcy-Weisbach friction factor and the cylindrical drag coefficient. The variation in hydrodynamics at different locations around rigid emergent cylindrical arrays is investigated. Experiments investigating the drag force characteristics of trees under aero- and hydrodynamic loading are also presented.

2.2 Introducing Vegetated Flows

2.2.1 Hydraulic Scales of Plant-Flow Interaction

In experimental hydraulics, measurement parameters are selected depending on the scale of processes under investigation. For some invertebrate communities that live on the surface of in-stream vegetation and in the crevices and undersides of stones,

the hydraulic conditions on the surface of the plants is of paramount importance. In a study of overland sediment deposition on a floodplain woodland, the shear stress in the overland flow water column, particularly in the vicinity of area of dense vegetation, needs to be determined. In contrast, regarding flooding within a river system, determination of the attenuation of a flood through reaches with different vegetation conditions requires only the overall hydraulic resistive effect of the vegetation to be known. Clearly, for the last example, knowledge of the stem scale conditions for every plant in the river basin community is not necessary.

In reality, hydraulic processes from surface scale to stem scale through to reach and river basin scale operate on a continuous spectrum of increasing complexity, with individual effects from the stem scale contributing to large scale effects. The concept of dividing this spectrum into a series of *scales* is a useful tool, if care is taken to adopt the appropriate degree of approximation. Figure 2.1 presents an example of the range of scales that may be considered. At the *Boundary Scale*, surface processes such as the nature of the boundary layer can be considered. *Stem Scale* processes are appropriate for a cylindrical element of a plant. At the *Plant Scale*, a plant may be represented by a combination of many stems, however, due to hydraulic interaction effects between the different elements, the total resistance of the plant may not equal the combined resistive effect of the individual cylindrical elements that compose the plant. At the *Homogeneous Community Scale*, many plants of the same age and species, which each exhibit similar characteristic hydraulic resistivity, are combined. Again, due to hydraulic interaction, the total resistance of the community may not equal the sum of the resistance of the individual plants. At the *Heterogeneous Community Scale*, plants of different species and ages interact. At the *Reach Scale*, wider effects, including river channel dynamics and the effect of vegetation distribution may be taken into account.

With relation to hydraulic modelling, high resolution modellers of vegetated flows such as DNS (Direct Numerical Simulation)and LES (Large Eddy Simulation) may wish to model *Boundary Scale* and *Stem Scale* processes. This could be relevant in the modelling of gas exchange processes at the surface of the plants, and the determination of advective and diffusive characteristics, which may impact on sediment and nutrient transport. At a much larger scale, river modellers who wish to model the overall hydraulic resistance of a river channel may only need to be aware of the reach scale processes.

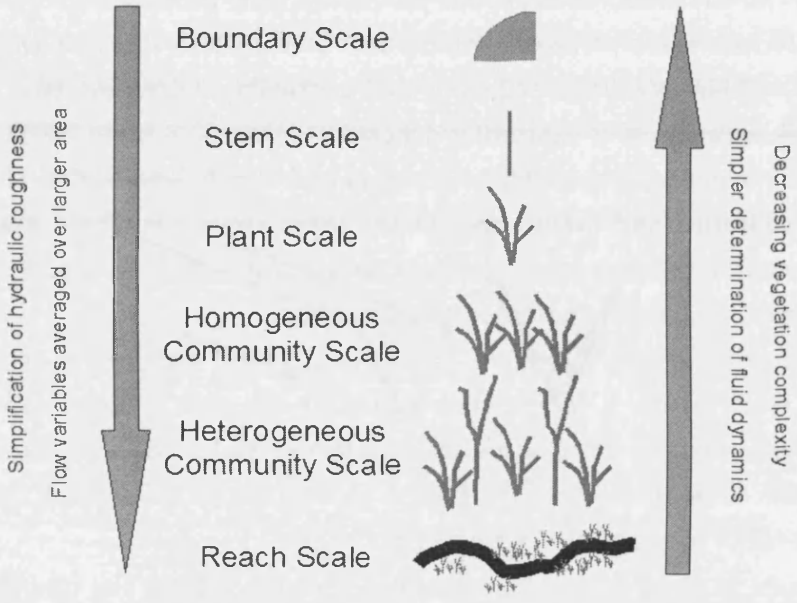

Figure 2.1: Scales of Vegetation Hydraulics

2.2.2 Boundary layer theory

2.2.3 Introducing Hydraulic Roughness

The infinite variability of the natural environment is the ever present challenge for hydrodynamic modellers. Ensuring that the governing hydrodynamic forces are represented with sufficient accuracy, whilst working within time and computational constraints, is a balance that requires an appreciation of the fundamental processes involved.

The term vegetated flows covers a wide range of eco-hydraulic conditions. Vegetation is present in many water bodies, and in many cases, has a dominant effect on flow conditions. At the smallest scale, the stem-scale flow processes that occur among reed beds reduce shear stresses within the water column close to the bed (Nepf et al. 1997). This can affect sediment and particulate transport surrounding the vegetation, encouraging or inhibiting deposition (Defina & Bixio 2005). Enhanced clarity of the water aids sunlight penetration and the decomposition of potentially dangerous coliforms and pollutants. Lower shear stress conditions also provide a protective environment for young fish and invertebrates that live amongst the reeds, as well as providing a source of food (Kadlec 1990).

At a larger stem scale, mangrove forests and other varieties of in-stream and floodplain trees create a larger obstruction to the flow. Floodplain woodland vegetation can promote attenuation of flood flows (Anderson et al. 2006, Musleh & Cruise 2006). Mangrove forests have been proven to protect against the otherwise destructive effect of tsunamis (Struve et al. 2003).

Any reduction in shear stress and enhanced turbulence from the interaction of the water with any emergent vegetation e.g. reeds, algae, bushes or trees, also causes a reduction in the mean-area velocity and thus the kinetic energy of the water column local to the plant (Nepf et al. 1997). Some of this lost kinetic energy is transferred to the plant and stored as elastic potential energy within the plant, or dissipated by the motion of the vegetation, transferred through bending and shearing motion to the ground through the root structure. The rest of the lost energy in the water column is converted from mean kinetic energy to turbulent kinetic energy, through the formation of eddy cascades, which eventually dissipate as heat energy at the smallest scale (Schlichting 2000). In the conversion from mean kinetic energy to turbulent kinetic energy, a local increase in the potential energy, i.e. a rise in the water surface level, must occur to maintain the total energy. Should the vegetation extend to cover the entire channel, the local water level across the reach

will rise slightly (in comparison to the same reach in an unvegetated condition) and conveyance through the channel will be retarded (Chow 1959). In fluid dynamics terminology, the 'hydraulic roughness' of the channel is said to increase. There are several empirically derived models characterising the hydraulic roughness of vegetation that are to be explored in this chapter.

Hydraulic roughness of vegetation can be determined from a variety of approaches. Wilson et al. (2003) note that many early studies into the hydraulic resistance of vegetated flows concentrated on defining vegetation-flow relationships, or determining bulk roughness coefficients, rather than improving understanding of the fluid dynamics of vegetation (e.g. Ree (1958), Thompson & Robertson (1976)). This can be seen in the simplest and most commonly adopted approach, which accounts for vegetation hydraulic roughness by treating it as an extension of the channel bulk roughness. The channel is assigned a bulk roughness coefficient which accounts for the combined effects of channel shape, sinuosity, boundary skin friction and vegetation hydraulic roughness.

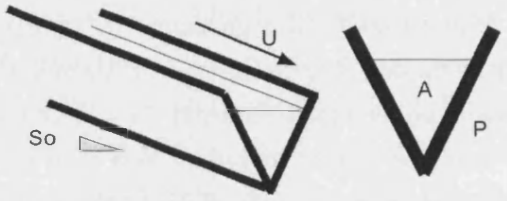

Figure 2.2: Control Volume of Fluid. U is the mean-area velocity, S_0 is the bed slope, A is the cross-sectional flow area and P is the wetted perimeter

One prevalent bulk roughness coefficient is the empirically derived Manning's n and associated Manning's equation found in standard hydraulics texts (Chow 1959, Massey 1997, Chadwick & Morfett 1999):

$$U = \frac{1}{n} R^{2/3} S_0^{1/2} \tag{2.1}$$

where U is the mean-area velocity, n is Manning's n, R is the hydraulic radius and S_0 is the channel slope. The hydraulic radius R is a term describing the efficiency of the flow area of the channel, defined as the ratio of flow area A to wetted perimeter P, where R is equal to A/P. Equation 2.1 is applicable only in uniform flow conditions. In a wide floodplain with a regularly shaped bed, where the depth to width ratio is equal to or exceeds 1:30, and in areas where the flow area of overbank flow is very large compared to the flow area of the channel, (2.1) can be expressed per unit

width of overland flow:

$$q = \frac{1}{n} y^{5/3} S_0^{1/2} \tag{2.2}$$

Where q is the discharge per unit width of flow, y is the flow depth and S_0 is the bed slope.

Vegetation often extends throughout the water column and therefore is not consistent with the model of boundary friction that is presented by Manning's n (Li & Shen 1973). Furthermore, the vegetation may not be uniformly spatially distributed throughout the cross-sectional area of flow or throughout the river reach.

In a heavily vegetated channel, the vegetation will have the dominant influence on the hydraulic roughness of the channel and therefore will have a dominant impact on the vegetation roughness coefficient. Values for Manning's n can be found in standard hydraulics texts, based on channel boundary material (Massey 1997) or a compound Manning's n can be computed for factors including channel shape, sinuosity, boundary skin friction and vegetation hydraulic roughness. The Roughness Adviser in ISIS provides the guidance in selection of values in Table 2.1. As it is an empirical model, determination of Manning's n requires flow and geometric data from the channel reach in order to calculate n. Manning's n was originally developed to describe rough, turbulent flow over surfaces having discrete, rigid, small-scale roughness elements (Smith et al. 1990). If the size of the roughness elements is small compared to the flow depth, the value of Manning's n will be constant for all flow depths for a given surface. The presence of vegetation however produces a relatively large obstruction to the flow, particularly if the vegetation extends throughout the water column. In this situation, assuming rough turbulent flow conditions are maintained, Manning's n becomes variable with depth (Smith et al. 1990, Kadlec 1990).

One-dimensional river modellers will choose values of Manning's n based on experience and knowledge of the physical appearance of the channel. For this reason, it is common to define a particular channel's Manning's n value through comparison with descriptions or photographs of channels for which Manning's n has already been deduced (Chow 1959). There is clearly a large margin of error in such an approach.

An improvement to the Manning's n equation is the use of the product of streamwise velocity U and hydraulic radius R, described in USDA (1947), Chow (1959). Relating Manning's n to UR (or Uy in wide channel flow) produces a series of

Tree Type	Descriptor	n	Lower	Upper
Small supple tree saplings e.g. willow		0.005	0.0001	0.050
Scattered brush and heavy weeds		0.050	0.035	0.070
Light Brush and trees	winter	0.050	0.035	0.060
Light Brush and trees	summer	0.060	0.040	0.080
Medium Brush and trees	winter	0.070	0.045	0.110
Medium Brush and trees	summer	0.100	0.070	0.160
Dense Willows	summer	0.150	0.110	0.200
Moderate to dense brush	depth below branches	0.065	0.050	0.100
Heavy stand of trees with some downed	depth below branches	0.100	0.080	0.120
Heavy stand of trees with some downed	depth above branches	0.150	0.100	0.200

Table 2.1: Roughness Adviser

standard $n - UR$ curves that recognise the dependence of n on flow depth and flow velocity. In a study with flexible vegetation, Ree (1958) showed that n decreased with increasing UR. These standard $n - UR$ curves have been related to both submerged (Ree 1958, Temple 1987) and emergent (Ree & R. 1977) flexible vegetation flow. Wilson (2007) combined new studies with the data from USDA (1947) and showed that while the $n-UR$ relationship is not consistent for vegetation types, it is unique for a grass type of a specific height. Smith et al. (1990) reports that $n - UR$ is not independent of slope, and Kouwen & Unny (1973) reports that the $n-UR$ method is not valid for slopes smaller than 5%. However, $n-UR$ curves give a consistant curved relationship throughout laminar to turbulent flow, giving an advantage to hydraulic modellers over Manning's n, which is applicable solely in fully rough turbulent flow Kadlec (1990).

Another approach proposed by Turner et al. (1978) is the discharge depth relationship:

$$q = ky^c \tag{2.3}$$

where q is the unit width discharge, y is the flow depth, and k and c coefficients obtained from log-log plots of field data. The coefficient k describes the geometry of the surface and is a function of the bed slope (S_0) and surface roughness (Turner et al. 1978). Equation 2.3 was further developed in Turner & Chanmeesri (1984) to expand k into the product of a coefficient a and the bed slope raised to a coefficient b:

$$q = aS_0^b y^c \tag{2.4}$$

where S_0 is the bed slope and y is the flow depth, a ans b are empirical parameters that relate to the vegetation type and flow conditions. Similar approaches were adopted in further studies including Smith et al. (1990), Kadlec (1990) and James et al. (2004). The presence of three coefficients a b and c in the discharge-depth relationship limits the applicability and requires a large database of coefficient values to be collated (Jordanova et al. 2006). Kadlec (1990) proposed that c is related to the variation in vegetation density and bed topography, while b should be equal to 1.0 when the stem Reynolds number (Re_d) is laminar, and equal to 0.5 when Re_d is turbulent. The Stem Reynolds number describes the wake characteristics of the stem, and is defined as follows:

$$Re_d = \frac{d\overline{U}}{\upsilon} \tag{2.5}$$

where Re_d is the stem Reynolds number, d is the stem diameter, $\overline{U}$ is the area-mean velocity and υ is the fluid viscosity. The Reynolds number (Re) is a ratio of inertial fluid forces ($\overline{U}$) to viscous fluid forces (υ), and governs the turbulence of the flow regime. The characteristic length used in the Reynolds number definition depends on the turbulent length scale of the processes being investigated (Schlichting 2000). Jarvela (2002) determined the friction factor f of a vegetated through consideration of head loss due to vegetation within a control volume. First, the gradually varied flow case was considered. By measuring the head loss H_f using Bernoulli's Equation (2.6), see Figure 2.3, and the Darcy Weisbach Equation 2.7, the friction factor could be obtained:

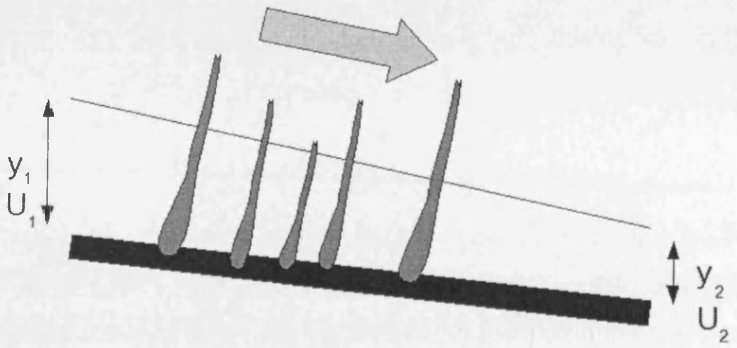

Figure 2.3: Bernoulli Control Volume

$$\beta\frac{\overline{U}_1^2}{2g} + y_1 = \beta\frac{\overline{U}_2^2}{2g} + y_2 + H_f \tag{2.6}$$

$$f = \frac{H_f}{l}\frac{8gR}{\overline{U}^2} \tag{2.7}$$

where $\overline{U}$ = mean-area flow velocity, g = gravitational acceleration, R = hydraulic radius of channel, β = the momentum coefficient, y_1 and y_2 are the flow depths at either end of the control volume, H_f is the head loss due to friction, l is the length of the control volume. In this case an average approach is adopted and turbulent conditions assumed. The friction factor can also be converted to the Manning's n roughness value, n, using:

$$f = 8gR^{-1/3}n^2 \tag{2.8}$$

The tradition of using friction factors to represent vegetation has a long history. The bulk roughness term f has an advantage over n in that it may be obtained from the roughness height of the surface (ks), therefore it is more sensitive to low velocity conditions than Manning's n, which will not work when applied to flows in the transitional and laminar phases of flow (Chow 1959).

Another approach to deduce the hydraulic roughness effect of vegetation may be made by using a direct physical dimension from the vegetation (Massey 1997, Righetti & Armanini 2002). The roughness height term ks, may be used to derive the Darcy-Weisbach friction factor f and the associated Chézy factor for pipe flow systems. Roughness height ks is a term representing a length scale of roughness and represented the roughness of the pipe walls. It has been adopted for use in open channel flow (Chadwick & Morfett 1999). Terms using roughness height ks can be preferable to the use of Manning's n, as the roughness is determined from a length scale and the flow regime, and therefore not purely empirically derived (Kouwen & Unny 1973).

Within the Darcy-Weisbach equation, the friction factor f is calculated iteratively depending on flow conditions. The flow condition is defined by the Reynolds number (Re) (Equation 2.5).

The Darcy-Weisbach friction factor can be found in either laminar flow (Equation 2.9), hydraulically smooth flow (Equation 2.10), transitional flow (Equation 2.11) or fully rough turbulent flow (Equation 2.12).

$$f = \frac{64}{Re} \tag{2.9}$$

$$f = \frac{0.316}{Re^{0.25}} \tag{2.10}$$

$$\frac{1}{\sqrt{f}} = -2log(\frac{k_s}{12R} + \frac{2.5}{R_e\sqrt{f}}) \tag{2.11}$$

$$\frac{1}{\sqrt{f}} = -2log(\frac{k_s}{12R}) \tag{2.12}$$

where f is the Darcy-Weisbach friction factor, k_s the roughness height, R is the hydraulic radius and Re is the Reynolds number.
The result is that the Darcy Weisbach equation, and the Chézy equation (2.13) may offer a different perspective to the problem of modelling transitional flows, an inherent obstacle to the modelling of vegetated flows with Manning's n.

$$\frac{C}{\sqrt{8g}} = \frac{1}{\sqrt{f}} \tag{2.13}$$

Kouwen & Unny (1973) carried out a series of laboratory experiments with flexible plastic strips (representing riparian vegetation) and determined that the Darcy-Weisbach friction factor f was a function of the relative roughness of the plants. Fathi-Maghadam & Kouwen (1997) carried out flume experiments with coniferous tree saplings and branches and showed that the friction factor f varied considerably with the mean flow velocity and flow depth, as a result of an increase in the submerged momentum absorbing area. The study was extended to include larger tree specimens in Kouwen & Fathi-Maghadam (2000), where the introduction of a Vegetation Index (accounting for shape, flexibility and biomass) provided a good correlation between the friction factor f and velocity.

2.3 Stem Scale Hydraulics

For larger floodplain woodland species, in particular shrubs and trees, stem scale processes are the principal mechanism that govern hydraulic resistance, and a bulk resistance approach becomes limited. As vegetation extends throughout the water column, resistance factors that a derived for boundary resistance become inadequate. Understanding stem-scale hydrodynamic processes is also vital in terms of establishing the impact of the flow on the ecology, i.e. the flow and wake structures generated at this scale directly affect the micro-organisms and macro-invertebrates that live and exist amongst submerged vegetation. A cascade of stem

scales will invariably co-exist for a common floodplain woodland genus such as *Salix*. Interaction effects introduce another dimension of complexity, as the wake generated by a main stem will be further interrupted by smaller twigs and branches of the plant.

2.3.1 Pressure Gradient Over a Curved Surface

As flow moves past a cylinder, the velocity and pressure gradients dictate the wake energy, and thus the energy dissipation potential of the object. Figure 2.4 illustrates the fluid motion. The boundary velocity u from point A will increase to a maximum at the widest part of the cylinder at point C. This corresponds with a negative pressure gradient. Past point C, there is a positive pressure gradient. This positive pressure gradient $(\partial p/\partial x)$ has a retarding effect on the fluid close to the boundary. A point of equilibrium is then reached at point D, where the oncoming fluid velocity u is fully canceled by the pressure gradient. This marks the separation point, where $(\partial u/\partial y)_{y=0} = 0$ at the surface. Beyond the separation point, the fluid breaks away to form a wake behind the cylinder. Here, the positive pressure gradient is stronger than the momentum of the fluid velocity u, and reverse flow occurs, where reverse flow is flow opposite in direction to the streamwise flow. The separation streamline indicated in Figure 2.4 demarcates the transition between streamwise and reverse flow.

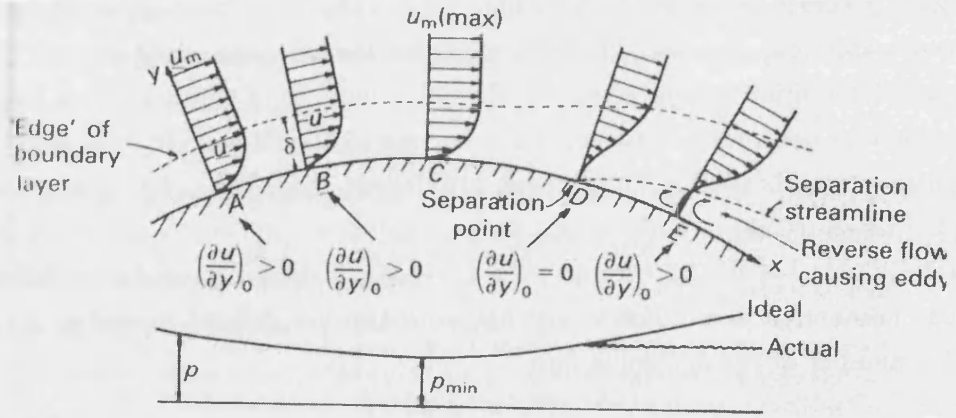

Figure 2.4: Boundary layer pressure and velocity gradient variation (Figure taken from Massey (1997))

2.3.2 Wake Variation with Stem Reynolds Number R_e

At the stem scale, flow past a single stem can be likened to two-dimensional flow around a cylinder (Li & Shen 1973, Petryk & Bosmajian 1975). The flow structure (and thus the hydraulic resistance exerted) at the stem scale are dominated by the form of the wake generated behind the cylinder (Massey 1997). The governing relationship between cylinder size and free stream velocity is the stem Reynolds number, Re_d. The Reynolds number is governed by the length scale of the largest eddy size. In open channel flow with no (or very few) obstructions, the dominant length scale is the flow depth, with flow structures circulating throughout the channel. In the case of emergent vegetated flows, these channel scale flow structures are disturbed and broken down by the presence of the vegetation. In vegetated flows the length scale is usually the diameter of the plant stem, in this case, d.
Figure 2.5 shows a cylindrical obstacle in a 2-D flow, and illustrates the boundary layer characteristics that are needed to describe the wake formation. Assuming a 2-D flow and no end effects, it is possible to identify three flow regimes, that may be defined by the separation characteristics of the cylinder boundary layer (Li & Shen 1973). Under sub-critical flow conditions, the boundary layer separates laminarly between 72 and 90 degrees from the point of stagnation (point B in Fig 2.5), forming a wide wake. At critical flow, the boundary layer separates laminarly, but quickly becomes turbulent, reattaching to the cylinder and then separating again at approximately 135 degrees. This is termed the 'laminar separation bubble'. The supercritical condition occurs when the Reynolds number of the boundary layer is so high that it becomes turbulent before leaving the cylinder. In this case, the boundary layer separation point is about 110 degrees from the point of stagnation (point C in Figure 2.5).
Figure 2.6 illustrates the pattern of wake formation behind a cylinder in different Reynolds number of flow. The wake characteristics are defined according to the Reynolds number of the oncoming flow.

- (a) $Re < 0.5$ Inertia effects are small, the flow pattern is close to ideal flow. The drag due to pressure variation due to shape around the cylinder is negligible and the profile drag is due almost entirely to skin friction.
- (b/c) $2 < Re < 30$ The boundary layer starts to separate. Fixed, symmetrical eddies form behind the cylinder.
- (d) $50 < Re < 200$ The eddies start to break away alternately, forming the von

Karman vortex street. The profile drag is increasingly dependent on pressure variations, with skin friction less influential.

- (e) $Re > 200$ A highly turbulent wake forms behind the cylinder, dissipating energy through turbulent eddy cascades.
- (f) $Re > 10^4$ As flow changes from laminar to turbulent, the separation point moves further back.

Understanding these flow structures resulting from the flow around a cylinder, assists the process of determining the resistance generated from cylindrically-shaped vegetation. It is the structure and change in state of the boundary layer that determines the point of separation and therefore the extent of the energy dissipating wake. The wake comes from the flow separation and the transformation of mean kinetic energy (MKE) to turbulent kinetic energy (TKE) and the energy dissipation through the generation of smaller and smaller eddies, down to the Kolmogorov length scale, when the kinetic energy is finally converted to heat energy through viscous dissipation between molecules.

2.3.3 Obtaining Drag Force of Cylinders

Kadlec (1990), following the approach by Li & Shen (1973) and Petryk & Bosmajian (1975), stated that the flow resistance due to vegetation is equal to the sum of the total drag force produced by the vegetation. The energy loss induced in the water column by the presence of vegetation can thus be represented within the momentum equation as a drag force sink term.
The total profile streamwise drag F exerted on a body of water by a cylinder is dependent on both the drag induced by boundary friction F_b and the energy-dissipation potential of the wake structure induced by the pressure distribution caused by the form (shape) of the obstacle F_d:

$$F = F_b + F_d \tag{2.14}$$

where F is total profile drag force, F_b is the drag force due to skin friction of the boundary and F_d is the streamwise drag force due to the form of the obstacle. The profile drag force of an object (F_d) can be defined by the dimensionless drag coefficient term (C_d):

$$F_d = \frac{1}{2}\rho C_d A U_0^2 \tag{2.15}$$

where ρ is the fluid density, C_d is the drag coefficient, A is the obstacle projected area in the streamwise direction of flow and U_0 is the free stream fluid velocity. Since both the boundary skin friction and the pressure drag caused by the form of the object are both functions of Reynolds number R_e, so too is the drag coefficient (C_d) (Chadwick & Morfett 1999). The thick line in Figure 2.7 illustrates the variation of C_d with R_e for an infinitely long cylinder in 2-D flow (Massey 1997). When the flow is highly laminar, with R_e below 0.5, the viscous (surface friction) forces predominate, the form drag has little influence as streamlines within the flow remain undisturbed around the object. In this case, C_d is inversely proportional to the free stream current (U_0). When Re_d is greater than 2 and less than 200, boundary separation occurs to an increasing degree, and consequently the form drag contributes more to the profile drag. When Re_d exceeds 200, the von Karman vortex street phenomenon is established (see Figure 2.6), with the form drag accounting for 90 % of the profile drag (Massey 1997). The drag reaches a minimum of approximately 0.9 when Re_d is approximately equal to 2000, and rises to 1.2 when Re_d exceeds 3×10^4. A drop in the drag coefficient occurs at a Reynold's number of approximately 2×10^5, due to the conversion of the boundary layer at the surface of the cylinder from a laminar to a fully turbulent layer.

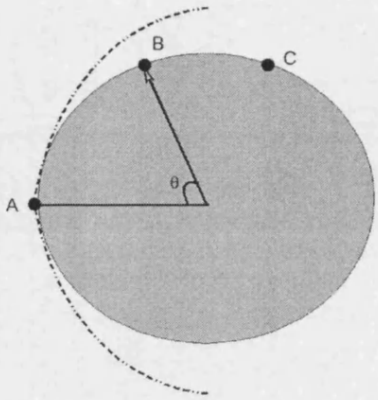

Figure 2.5: Boundary layer separation characteristics

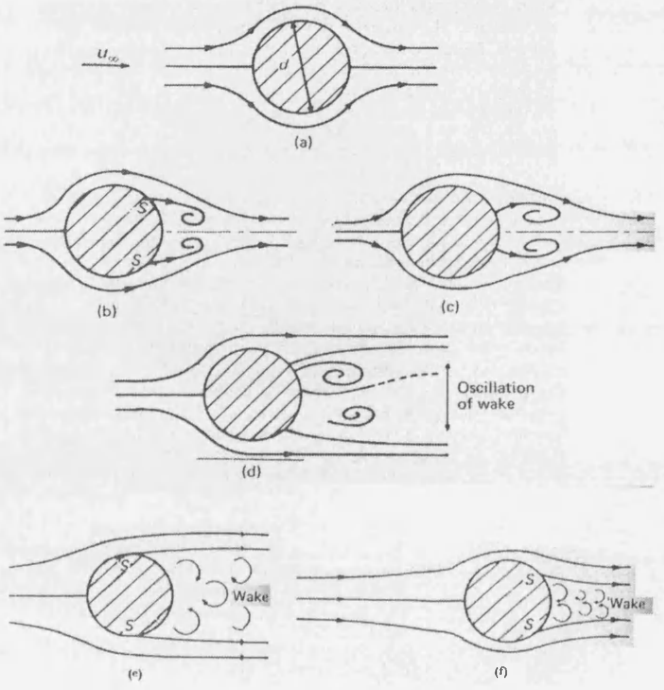

Figure 2.6: Wake characteristics with increasing Reynolds Number (Figures taken from Massey (1997))

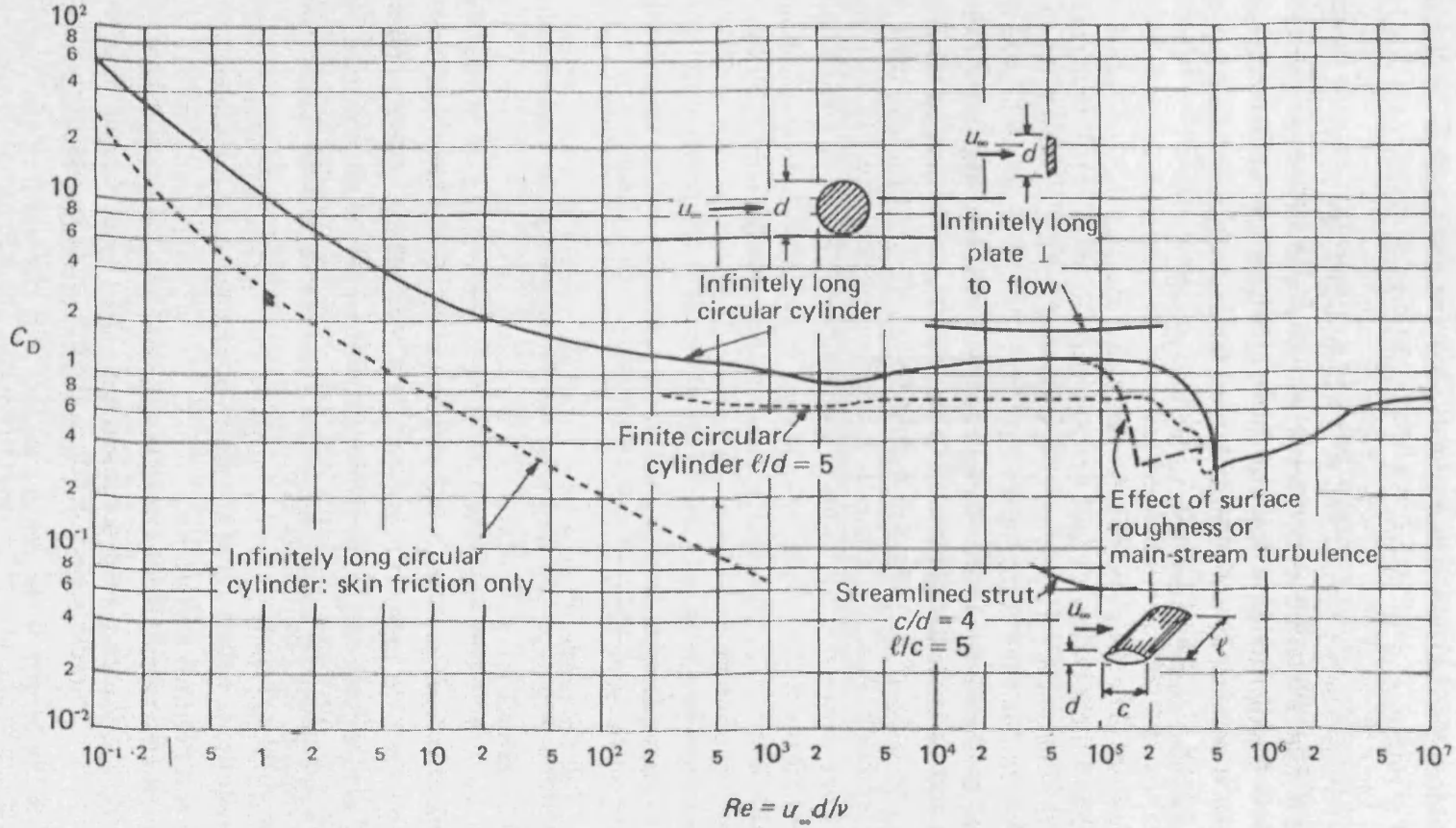

Figure 2.7: Variation of Cylinder Cd with Reynolds Number (Figure taken from Massey (1997))

2.3.4 Derivation of Drag Coefficient

By considering a control volume under uniform flow conditions an obstacle in the form of a cylinder, as in Figure 2.8, a formulation for calculating resistance from emergent cylinders (where emergent refers to a cylinder that extends throughout the entire water column) was developed by Petryk & Bosmajian (1975). By deriving the equation under uniform flow conditions, the pressure gradient caused by head difference is reduced to a negligible degree, leaving only the forces due to gravity, boundary shear and cylinder drag to be determined.

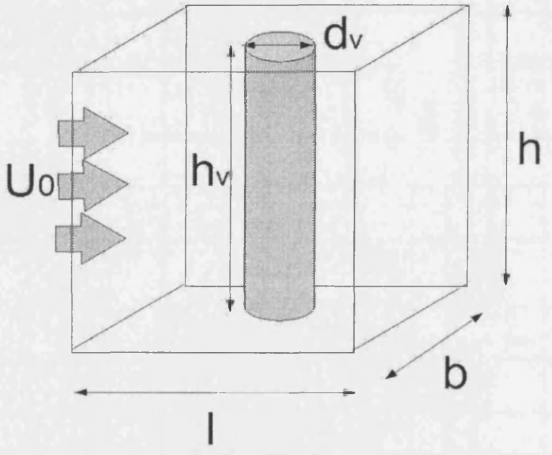

Figure 2.8: Control Volume with Cylinder

Since uniform flow is established, the net forces within the control volume must equal zero, given by:

$$F_w - F_b - F_d = 0 \tag{2.16}$$

where F_w is the force due to the self weight of the water in the streamwise direction, F_b is the boundary bed shear force and F_d is the drag force due to the physical presence of the cylinder.
The gravitational weight F_w of the water body defined by the dimensions length l, width b and height h is given by:

$$F_w = lbh\rho g S_0 \tag{2.17}$$

where l is the length of the control volume, b is the width of the control volume, h is the height of the control volume, ρ is the fluid density, g is the gravitational

acceleration and S_0 is the bed slope.
The total drag force on a single cylinder F_d can be determined from:

$$F_d = \frac{1}{2} C_d \rho U_0^2 h_v d_v \tag{2.18}$$

where C_d is the drag coefficient, ρ is the fluid density, U_0 is the free-stream streamwise velocity, h_v is the vegetation height and d_v is the vegetation diameter.
The boundary drag F_b is described as:

$$F_b = \tau_w bl \tag{2.19}$$

where F_b is the total boundary shear force and τ_w is the boundary shear force per unit area. The boundary shear force can be determined through the force-balance applied to an empty channel. In this way, the effects can be separated from the vegetation resistance.
By equating the gravitational weight of the water F_d with the drag force from the cylinder F_v and the boundary F_b, C_d can be determined from:

$$lbh\rho g S_0 - \frac{1}{2} C_d h_v d_v \rho U_0^2 - \tau_w bl = 0 \tag{2.20}$$

The relationship between the drag coefficient C_d of a cylinder and stem Reynolds number Re_d defined with the characteristic length equivalent to the stem diameter is presented in Figure 2.7.
Many authors note that in heavily vegetated conditions, boundary skin friction is negligible compared to the drag from the vegetation, and the third term in Equation 2.20 can be ignored (Wu et al. 1999, Nepf 1999, Righetti & Armanini 2002, Jarvela 2002). Thus for a given stem diameter and free stream velocity (assuming the fluid viscosity is kept constant - a reasonable assumption in riparian environments), and assuming the flow depth h is equal to the submerged length of vegetation h_v, the drag coefficient (C_d) for a single cylinder can be found from Equation 2.21.

$$C_d = \frac{2lbgS_0}{d_v U_0^2} \tag{2.21}$$

It should be remembered that these results apply to a theoretically infinite cylinder in a wide field of flow. White (1991) proposes the following formula to obtain C_d from Re for an isolated cylinder in infinite flow.

$$C_d \approx 10 Re_d^{-2/3}, 1 \leq Re_d \leq 105 \tag{2.22}$$

Introducing end effects promotes a more highly 3-D turbulence structure, as the pressure gradient will be reduced due to diversion around the end of the cylinder (Massey 1997). As the length reduces, for example, in the case of a submerged cylinder, flow will be diverted around the end of the cylinder, reducing pressure and thus reducing drag. The flow around the base of a cylindrical object is characterised by two flow structures, the horseshoe vortex and the leeward vortex, (Klebanoff 1955). The first is the 'Horseshoe' vortex: caused by the rotation of the incoming flow i.e. 3-D separation of the boundary layer due to the increased pressure gradient from the presence of the cylinder. The horseshoe vortex system is generated at the junction of a bluff body and a base plate and has been shown to vary with cylinder Reynolds number (Klebanoff 1955, Baker 1979, Sumer et al. 1997, Sahin et al. 2007). The second is the Leeward vortex caused by the separation of the boundary layer from the cylinder. Figure 2.9 illustrates the horseshoe vortex that forms round the cylinder and the leeward wake structure dissipating further energy. The horseshoe vortex may be the cause of the high velocity spike or bulge that is sometimes observed in near-bed measurements with rigid cylinders, as observed by Fairbanks (1998) and Schindler (2005).

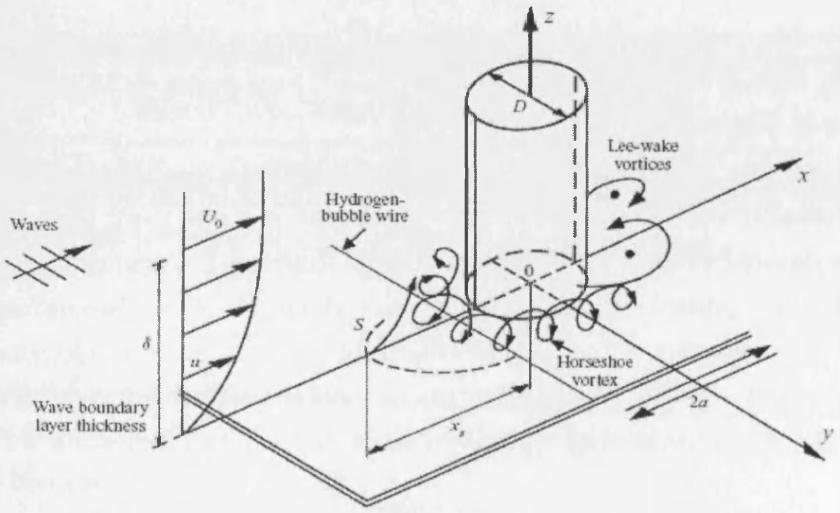

Figure 2.9: Horseshoe and leeward vortices Figure taken from Sumer et al. (1997)

2.4 Vegetation Arrays

2.4.1 Cylinder Hydraulics Applied to Plant Arrays

The analogy of a cylinder works well for individual plants but if an array of cylinders is wished to be considered, interaction effects of the cylinders must be taken into account (Li & Shen 1973, Petryk & Bosmajian 1975, Nepf 1999). It also becomes probable that morphological variability reduces the single cylinder analogy to an unrepresentative model, and alternative methods may need to be sought.

Using rigid cylinders is an appropriate model for groups of trees or reeds where the main stand is the dominant obstacle to the flow, and will not deform greatly under flow (Li & Shen 1973). For cylindrical species that grow in groups, a cylinder array can be considered. A cylinder array can be defined as sparse or dense. In a sparse distribution, cylinders are placed at a certain distance from each other in an array under fluid flow, and the total force exerted by that array will equal the sum of individual cylinder drag forces, as the wakes from the individual cylinders will not interact. In a dense distribution, the total force exerted by that array will be less than the sum of individual cylinder drag forces.

This reduction in drag is because the form of the wake dissipation structure, and thus the energy dissipation potential of a cylinder, is dependent on the upstream velocity. This upstream velocity is altered when an obstacle such as a second rigid cylinder is placed before the original cylinder, reducing the velocity.

As the average cylinder spacing decreases, the overall drag force will decrease due to the sheltering effect. The density of an array is therefore a key parameter and must be defined. The literature on vegetated flows contains different definitions of density and so it is useful to review the most common.

Various parameters have been used in the field of meteorology to describe the physical characteristics of vegetation. Dong et al. (2001) have summarised a number of the parameters and these are listed in Table 2.2, where d_v is the diameter of the vegetation, h_v is the height of the vegetation, s_x and s_y are the longitudinal and lateral spacing between elements and h is the flow depth.

The density definitions in Table 2.2, are commonly used in meteorological applications, where the vegetation can be approximated as a boundary layer in an atmospheric model. In many vegetated flows, including those through floodplain woodland, the vegetation may extend throughout the entire water column. In this case, flow depth h will be equivalent to average height of vegetation h_v. Researchers

Density Term	Symbol	Equation	Units
Aspect Ratio	AR	$\frac{d_v}{h_v}$	
Height-spacing Ratio	Sh	$\frac{hv}{s_y}$	
Basal-frontal silhouette	σ	$\frac{\pi d_v}{4h_v}$	
Lateral Cover	L_C	$\frac{h_v d_v}{s_x s_y}$	
Element Area Index	EAI	$\frac{h_v d_v}{s_x s_y h}$	m^{-1}
Porosity	P	$\frac{4 s_x s_y h / h_v}{\pi d_v^2}$	

Table 2.2: Density Definitions for Meterology

have parameterised densities of cylinder arrays in a number of ways (see Table 2.3).

Cited by	Term	Equation	Units
Stone & Shen (2002), James et al. (2004)	λ, λ_a	$\frac{\pi d_v^2}{4 s_x s_y}$	
Marshall (1970), Raupach (1992)	L_c	$\frac{d_v h_v}{s_x s_y}$	
Nepf (1999), Lopez et al. (1995)	$\mathbf{a}, EAI$	$\frac{d_v h_v}{s_x s_y h}$	m^{-1}
Tanino & Nepf (2008*b*)	ϕ	$\frac{\pi d_v^2 h_v}{4 s_x s_y h}$	

Table 2.3: Density Definitions for Vegetation Hydraulics

The first type of cylinder array density definition is the stem area concentration λ_a, used as a preferred definition by Stone & Shen (2002), which is the percentage plan area taken up by the dowels, regardless of the dowel height. In meteorological terms it is referred to as the *coverage* and applies to both emergent and submerged conditions. Stem area concentration (λ_a) is dimensionless:

$$\lambda_a = \frac{\pi d_v^2}{4 s_x s_y} \tag{2.23}$$

where λ_a is percentage coverage, d_v is the vegetation diameter, s_x is the longitudinal spacing and s_y is the lateral spacing.

The second density definition is the frontal projection per unit area, or lateral cover L_c, used commonly throughout the meteorological field.

$$L_c = \frac{d_v h_v}{s_x s_y} \tag{2.24}$$

where l is projected frontal area per unit ground area. This is the approach often adopted by meteorologists e.g. Raupach (1992), Finnigan (2000), and so comparison of drag coefficient results with vegetation hydraulics must take account of the different definitions of density used by researchers.

The projected frontal area per unit volume '**a**' density term is prevalent and equivalent to the meteorological value of Element Area Index, EAI. There are two definitions depending on whether conditions are emergent or submerged:

$$\mathbf{a} = \frac{d_v}{s^2} \tag{2.25}$$

$$\mathbf{a} = \frac{d_v h_v}{s^2 h} \tag{2.26}$$

where **a** is cylinder density per unit volume (EAI), d_v is stem diameter, h is the flow depth and s mean separation between the elements. Cylinder density per unit volume **a** is not non-dimensional, and has units L^{-1}. This unit, termed **a** in Nepf (1999) and is flexible for both submerged and emergent vegetation.

Nepf (1999) used the population density term $\mathbf{a}d$ to obtain a dimensionless parameter representing the fractional volume of flow domain occupied by plants. This is also the definition in the extensive studies into turbulence characteristics of vegetated flows in the research of Lopez & Garcia (2001*a*), Lopez et al. (1995).

The final definition is the solid volume fraction (ϕ) defined as:

$$\phi = \frac{\pi d_v^2 h_v}{4 s^2 h} \tag{2.27}$$

The term ϕ describes the portion of flow volume occupied by the plants, per plant, relative to the total control volume, per plant, and so the solid volume fraction is the reciprocal of the porosity parameter in Table 2.2.

The effect of density and spacing is now explored. In a sparse array, where wake interaction is negligible, the total drag of the cylinder array will equal the sum of the drag on each element in uninterrupted flow. In a dense array, where there is wake interaction, the drag of the cylinder array will be less that the sum of the drag on each cylinder. If a pair of cylinders in line is considered (Figure 2.10), the wake from behind Cylinder 1 reduces the oncoming velocity to Cylinder 2. Thus the drag induced is reduced by a proportional amount. This effect is termed sheltering and can contribute to a significant reduction in array drag, when compared to the combined drag of the individual elements if they were each placed in unobstructed flow (Li & Shen 1973, Petryk & Bosmajian 1975, Nepf 1999, Musleh & Cruise 2006).

Since the oncoming downstream velocity U_1 is less than the upstream velocity U_0, the drag coefficient C_{d1} will be less than C_{d2}. Thus for a line of cylinders, the overall drag force exerted by the cylinders will be less than the sum of the drag from

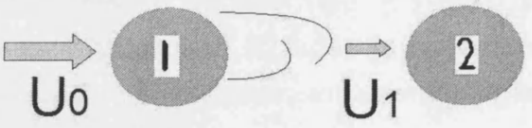

Figure 2.10: Sheltering effect on in-line cylinders

the same number of cylinders in uninterrupted flow. The relative drop in the drag force exerted is dependent on the oncoming wake structure and thus the upstream initial velocity. Depending on the separation distance of the two cylinders and the Reynolds number of the flow, the proportion of total drag force exerted by each cylinder will vary.

Li & Shen (1973) compared methods to determine the impact of a presence of a cylinder on downstream velocity, including that developed by Petryk (1969) to predict the change in array drag coefficient as a result of sheltering (Equation 2.28). Li & Shen (1973) coin the phrase *velocity defect* to describe the reduction in velocity behind the cylinder, and have proposed the following equation:

$$U_{0n} = U_{\infty}(x_n) + \sum_{i=1}^{m} u_i[(x_n - x_i), (z - z_i)] \tag{2.28}$$

where the coordinates of the ith cylinder are expressed as (x_i, z_i), U_{0n} is the cylinder approach velocity to the nth cylinder, U_{∞} is the initial cylinder approach velocity at the beginning of the array and $\sum_{i=1}^{m} u_i[(x_n - x_i), (z - z_i)]$ is the total velocity defect from m upstream cylinders. The velocity defect $\sum u_i$ that reduces the velocity from U_{∞} to U_{0n} is primarily dependent on the dimensions perpendicular to the flow direction, i.e. the principal diameter and the lateral spacing of elements.

The bulk drag coefficient per unit area for an array can be termed $\overline{C_d}$ to differentiate it from the drag due to a single element (Nepf 1999). The Force F_d of a cylinder array can be defined with respect to the bulk drag coefficient, $\overline{C_d}$ and vegetation density $\mathbf{a}$ in Equation 2.29.

$$F_d = \frac{1}{2}\rho\overline{C_d}\mathbf{a}U_0^2 \tag{2.29}$$

where F_d is the total drag force per unit mass exerted on the array, $\overline{C_d}$ is the bulk drag coefficient, $\mathbf{a}$ is the frontal projected area per unit volume of flow defined in Equation 2.26, and U_0 is the equivalent uniform velocity.

Bokaian & Geoola (1984) looked at the interactions of pairs of cylinders with both

lateral and longitudinal spacing. Nepf (1999) reported that the data obtained by Bokaian & Geoola (1984) agreed with that of Blevins (1994). The drag coefficient (C_d) for the downstream cylinder is shown to decrease as the lateral and longitudinal spacing decreases. The lateral spacing has a greater impact.

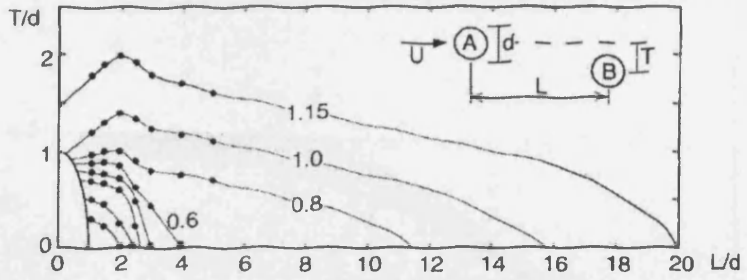

Figure 2.11: Variation of bulk drag coefficient with cylinder interactions, Blevins (1994), cited in Nepf (1999)

This disparity between the relative effect of longitudinal spacing (s_x) and lateral spacing (s_y) infers that vegetation arrays in different configurations but of the same density, e.g. either parallel, staggered or randomly distributed, have a different bulk drag coefficient and therefore a different hydraulic resistance. Musleh & Cruise (2006) carried out extensive laboratory tests on different staggered densities of cylinders and found similar results showing that lateral spacing and cylinder diameter have a more significant effect than longitudinal spacing on the hydraulic roughness. Their study determined that with a reduction in longitudinal spacing (s_x) of 50%, the friction factor (f) increases by a maximum of 67%, while a 50% reduction in lateral spacing (s_y) contributed to an increase in the friction factor (f) of 191%.

Figure 2.12 showed how the variation in the ratio of force on a plant in the middle of an array to the force on the plant furthest upstream, (F_i/F_0) varies for both staggered and parallel arrays (see Figure 2.12, where s is the spacing between elements and d is the cylinder diameter). It can be seen that as the spacing decreases, the force on the downstream plants in the staggered array remains relatively unaffected, in comparison to the downstream plants in the parallel array.

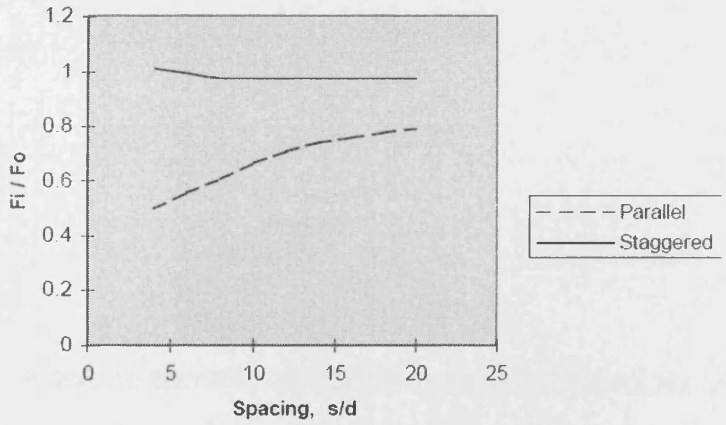

Figure 2.12: Effect of Parallel and Perpendicular Spacing on cylindrical elements, Li & Shen (1973). F_i is the force on a plant in the array under fully developed flow and F_0 is the drag force on the furthest upstream plant. This figure is taken from Fairbanks (1998)

Nepf (1999) developed a wake interference model based on data from Bokaian & Geoola (1984) to show the effect of arrangement on the bulk drag coefficient $\overline{C_d}$, plotted against data from other authors in Figure 2.14.

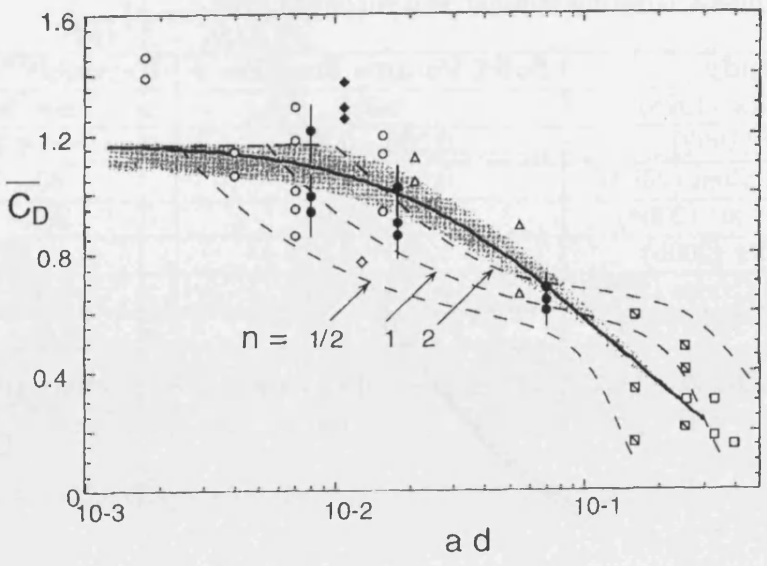

Figure 2.13: The effect of Parallel and Perpendicular alignment on Bulk Drag Coefficient $\overline{C_d}$. n is the ratio of longitudinal to lateral spacing, **a** is the project area per unit volume (See Equation 2.26) and d is the stem diameter. Figure is taken from Nepf (1999).

Tanino & Nepf (2008*b*) and Tanino & Nepf (2008*a*) investigated experimentally the drag in emergent cylinder arrays at high and low Reynolds numbers respectively. Tanino & Nepf (2008*a*) found that the dimensionless ratio of the mean drag per unit cylinder length F_{di} could be related to the product of the viscosity, υ, and $\overline{U}d_i$ to produce a linear dependency. Figure 2.14 presents investigated solid volume fractions against Reynolds number.

$$\frac{F_{di}}{\mu} = \alpha_0 + \alpha_1 Re_d \tag{2.30}$$

where F_{di} is the force per unit cylinder length, μ is the viscosity, α_0 is a constant and α_1 is the linear coefficient of the stem Reynolds number Re_d. Equation 2.30 is consistent with the formulation devised for packed columns by Ergun (1952).
A summary from different researchers investigating hydrodynamics of cylinder arrays is presented in Table 2.4, with the density of emergent cylinders tested listed against the stem Reynolds number of the experiments. The range of Reynolds numbers

expected in a woodland environment varies between a negligible Solid Volume Fraction (ϕ) in sparse tree arrangements, where sheltering effect is minimal, to larger densities in areas of dense multistemmed trees, for examples certain species of *Alnus* or *Salix*. A flood flow in a forest will clearly produce a large range of Stem Reynolds Numbers covering laminar and turbulent flow.

Study	**Solid Volume Fraction ϕ**	**Reynolds Number Re**
Fairbanks (1998)	0.016	not defined
Nepf (1999)	0.006 - 0.055	$\geq$ 200
Stone and Shen (2002)	0.006 - 0.061	83 - 7000
James et. al. (2004)	0.004 - 0.031	200 - 7000
Schindler (2005)	0.018 - 0.044	2500
Musleh and Cruise (2006)	0.005 - 0.045	500 - 2000
Tanino and Nepf (2008)	0.091 - 0.35	25 - 685

Table 2.4: Density and Reynolds numbers of experiments conducted with emergent arrays where ϕ is the percentage volume occupied by the cylinders

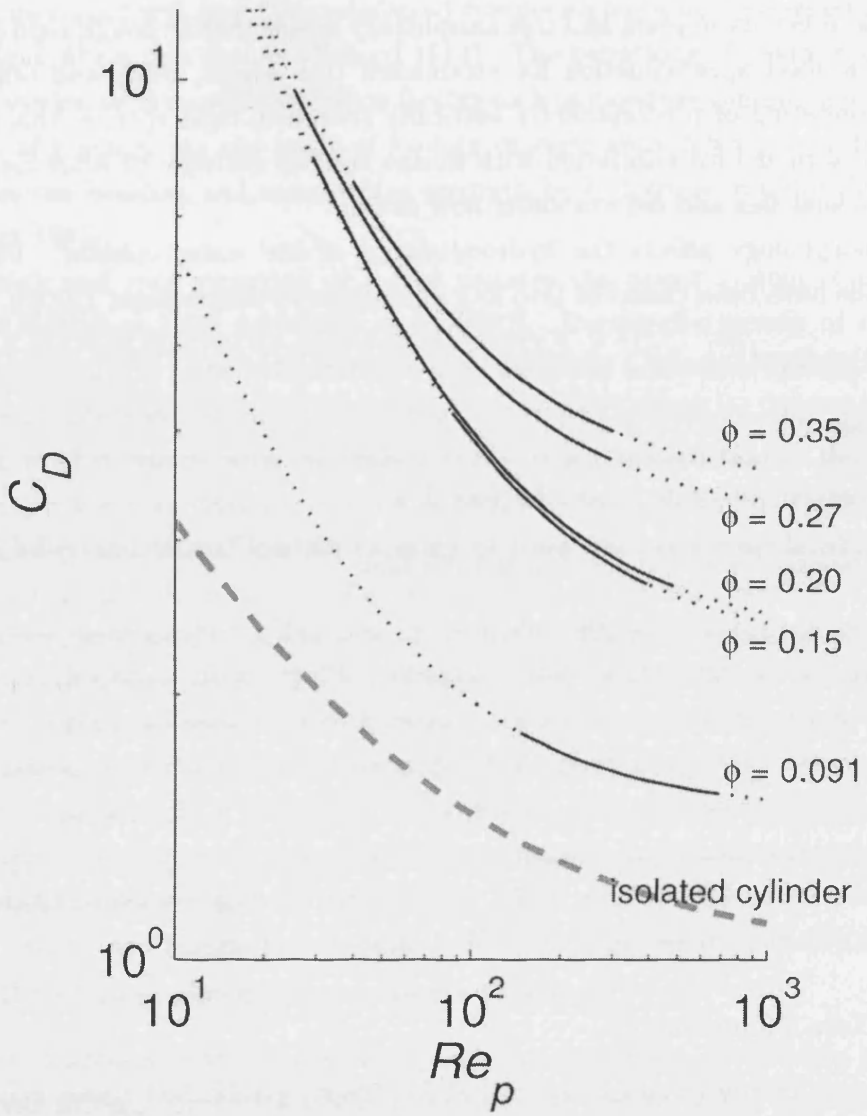

Figure 2.14: The effect of the solid volume fraction on the bulk drag coefficient $\overline{C_d}$ variation with Reynolds number. Re_p is the stem Reynold's number as calculated using the mean velocity modified by the porosity effect from the presence of the cylinders and calculated using the kinematic viscosity ν. Tanino & Nepf (2008*a*)

2.5 Tree Hydraulics

2.5.1 Introducing Hydraulics of Trees

The great diversity in plant and tree morphology means that although rigid cylinders may be a good approximation for established tree stands, reeds and other plant arrays consisting of predominantly vertically stemmed, rigid species, this may not be an ideal model for vegetation with foliage and/ or multiple or branching stems, or plants that flex and deform under flow action.
Plant morphology affects the hydrodynamics of the water column. Plant-flow conditions have been classified into four conditions by Ergenzinger (2005):

- Submerged
- Emergent
- Emerged with canopy and bottom flow
- Submerged with canopy and bottom flow

These flow conditions strongly influence the hydraulics and sediment and nutrient transport on the floodplain and riverbanks. Plants with uniformly distributed biomass under submerged conditions may lead to a decrease in velocity and shear stress near the bed (Li & Shen 1973). Emerged flow conditions commonly occur with woody vegetation genera. These trees often have a biomass distribution of rigid stem structures which generate wake flows and can cause scour. Bottom flow is the contraction of flow area under vegetation with large fronds and bare stems, these conditions increase the likelihood of local erosion around the plants.

2.5.2 Tree Biomechanics

While many plants (reed-like species at low flows, established trees) may deflect minimally under flow loading, many more species are susceptible to deflection from the force exerted by the water.
With limitations in the understanding of flow around complex flexible structures such as trees, the roughness parameters have been empirically rather than explicitly derived. As such, selecting roughness coefficients to characterise the resistance imposed by vegetation is still more akin to an empirical art than scientific procedure. Plant structures offer a particular challenge because of the myriad of shapes, structures and the mosaic of distribution in riparian corridors (Anderson et al. 2006).

A better understanding of the biomechanics of trees may lead to a more rigorously designed roughness parameter for hydraulic modelling. The mechanical properties of wood vary between and within species. Wood is anisotropic in its composition and can be considered as a fibre reinforced composite material comprised of tough longitudinal fibers in a matrix (Record 1914). The behaviour of wood in bending, tension, torsion or shear will depend on factors such as moisture content, age, density duration of loading. As the angle of loading changes away from perpendicular to the grain, the bending and compressive strength both decrease rapidly (Mattheck & Breloer 1995).

The branch and root structure of a tree dictates the upper system response to loading (McMahon 1975, Mattheck et al. 2003). During the growth of the tree, the root structure is principally influenced by the wind and water loading the tree experiences. Mechanistic models have been developed to look at wind loading on trees and predict failure rates (McMahon 1975). It is proposed that in the future a similar approach is adopted for analysis of hydrodynamic loading on trees.

The flexibility and lateral loading capacity of trees has been considered in wind-throw studies, and the results apply directly to hydrodynamic loading. The stem of standing trees can be considered as a flexible cantilever whose section size and properties varies with height. The main forces acting on the tree are the self weight of the tree plus the loading onto the side of the tree from wind or water loading. The canopy weight is assumed to act down the centre of mass. In the calculation of wind or water loading, a horizontal point load acting at the centre of mass of the canopy can be used. Trees tend to fail first under compression when subject to severe bending (Mattheck et al. 2003).

2.5.3 Direct Drag Force Measurements of Trees

The force exerted on a tree under aerodynamic or hydrodynamic loading has been determined through direct load cell or strain gauge measurement in a number of studies (Mayhead 1973, Fathi-Maghadam & Kouwen 1997, Oplatka 1998 *a*, Freeman et al. 2000, Kouwen & Fathi-Maghadam 2000, Armanini et al. 2005, Kane & Smiley 2006). Studies into the drag force and associated drag coefficient of trees have been carried out in both meteorological and hydraulic studies. Such studies are subject to a large margin of uncertainty due to natural variation. In one of the earliest studies of full scale tree drag force data, Mayhead (1973) presents the following caveats:

1. Failure to sample with regard to natural variation

2. Inaccurate determination of the frontal projected area of the tree (A_p), necessary for determination of the drag coefficient (see next section)

3. Obtaining trees suitable for test apparatus

4. Trees may vary in their drag coefficient according to the side presented to the wind, however testing form many sides is hindered as tree become distorted after exposure to a strong wind

5. Drying out of the foliage or wood, moisture content could affect flexibility and form

Multi-stemmed plants can be approximated to a continuous series of connected cylinders. This method was adopted by DeJong (2005) and illustrated in Figure 2.15.

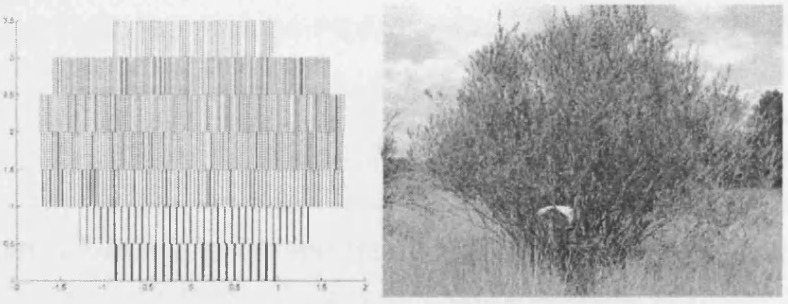

Figure 2.15: Idealisation of plant (after DeJong (2005))

Equation (2.31) presents the drag force equation.

$$F_d = \frac{1}{2}\rho A_p C_d U_0^2 \tag{2.31}$$

where F_d is the drag force exerted, ρ is the fluid density, A_p is the frontal projected area to flow, C_d is the form-dependent drag coefficient and U_0 is the free stream velocity.

Determining the drag coefficient (C_d) of a tree requires determination of the projected area (A_p). However, many species of tree are flexible and will deform and reconfigure under increasing fluid velocities, causing a reduction in the projected area under flow action. Moreover, the tree is not a single solid object, but a porous mass of branches and foliage, many of which may reconfigure into an increasingly dense streamlined mass at relatively higher velocities.

Determination of the appropriate definition of project area (A_p) to account for the heterogeneous wood and foliage components that form a tree has been the subject of much discussion Mayhead (1973), Vogel (1989), Fischenich & Dudley (2000), Kouwen & Fathi-Maghadam (2000). The drag coefficient (C_d) and the projected area term (A_p) work together to describe the physical form and profile drag characteristic of an object, termed here the drag area parameter (C_dA). In still air, individual branches have a typically solid, cylindrical form, however, even if the projected area is determined, perhaps through photographic methods, this is not enough to determine an appropriate drag coefficient.

A cylinder placed perpendicular to the flow field will have a form-dominant drag coefficient, as opposed to a cylinder placed at a parallel orientation to the flow field, which will have a skin friction-dominant drag coefficient (Massey 1997). Foliage that is streamlined in the fluid has a minimal projected area but can experience significant drag due to skin friction Vogel (1989), Wilson et al. (2005). Within Equation 2.31, the frontal projected area (A_p) term is only strictly relevant in form-dominant drag. For skin friction-dominant drag, the projected area term (A_p) is replaced with the surface area term (A_s).

A flexible, foliated tree exhibits branches at many orientations to the flow in still air, foliage that depending on type may be predominantly affected by skin friction drag, plus varying orientation of the wood and foliage under different fluid velocities (Vogel 1989). It is debatable which definition of the area (frontal projected (A_p) or surface (A_s)) to use. Vogel (1984) suggests frontal area projection for fully streamlined objects where dynamic pressure on the body is the largest force, while surface area should be applied to streamlined objects where drag is due to viscosity and shear. Fischenich & Dudley (2000) note that use of the frontal projected area and the surface area both present practical limitations due the permeable nature of trees. Some authors have adopted the leaf area index (LAI) in place of the area term (A_p), where LAI is the leaf area per unit volume:

$$LAI = \frac{A_{leaves}}{lbh} \tag{2.32}$$

where LAI is the leaf area index with dimension L^{-1}, A_{leaves} is the surface area of the leaves and lbh are the length, width and height respectively of a specified control volume. Fischenich & Dudley (2000) analysed data collected by Rahmeyer et al. (1995) and derived drag coefficients based on three definitions of area: frontal projected area, surface area and density.

The uncertainty of the contribution of foliage to the force exerted is addressed in many investigations (Freeman et al. 2000, Kane & Smiley 2006). Wilson et al. (2008) measured the drag force of two plant species, branches of *Pinus Sylvestrus* (Pine) and *Glechoma Hederaca* (Ivy) stipes, using a cantilever and strain gauge technique. In the flow visualisation that accompanied the study, it can be seen that the different morphology of the *Pinus Sylvestrus* and *Glechoma Hederaca* branches influence the streamlines of the flow. The streamline visualisation and the contribution of the foliage to the total drag force are presented in Figure 2.16.

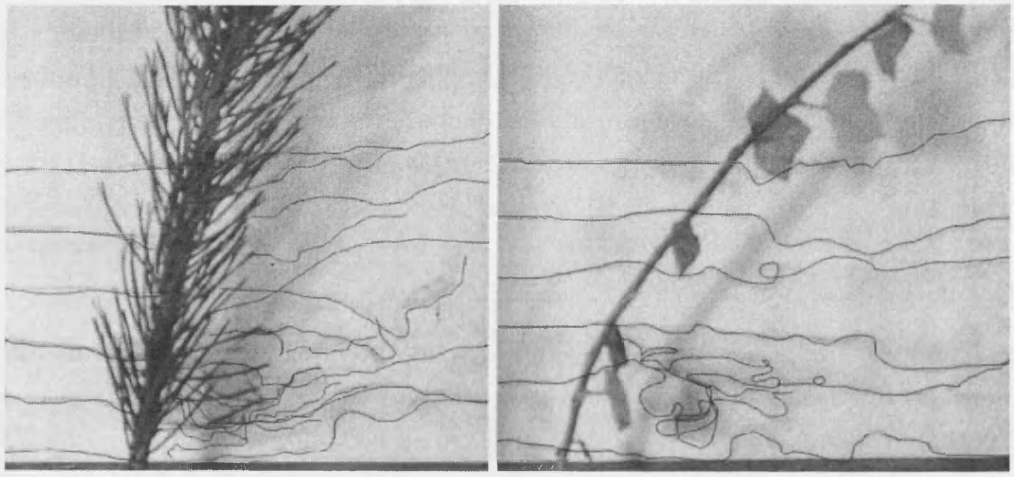

(a)

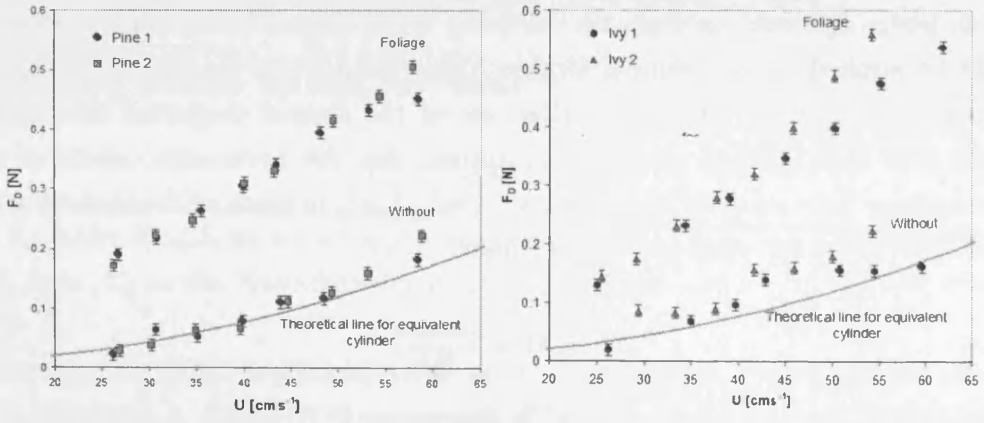

(b)

Figure 2.16: (a) Visualisation of streamlines through *Pinus Sylvestrus* (left) and *Glechoma Hederaca* (right), (b) Drag force against velocity for foliated and defoliated branches. Figures from Wilson et al. (2008)

Wilson et al. (2005) showed that the drag force exerted by the plant increased by a factor of 2 - 6 for the *Pinus* specimen and between 2 - 4 for the *Glechoma* specimen. Jarvela (2002) noted that the presence of foliage increased the friction factor by 2 or 3 times.

Several recent studies have looked at the hydrodynamic drag force characteristics of small scale woody vegetation. Fathi-Maghadam & Kouwen (1997) measured the drag force of 300 mm high pine and cedar saplings under flow action using load cells attached to a knife-edge table, noting that the variation of drag force with velocity was linear, rather than the squared relationship suggested by the classic drag force equation (2.31).Jarvela (2002) studied both rigid and flexible vegetation, noting that the friction factor increased with depth, but appeared independent of mean-area velocity.

2.5.4 Full-scale Tree Drag Force Studies

Raymer (1962) and Fraser (1962) tested individual young conifers between 5.8 and 8.5 m in height in a wind tunnel, measuring the horizontal drag force at wind velocities from 9.1 m/s to 38.3 m/s, at increments of approximately 1.5 m/s. Mayhead (1973) analysed the results and derived drag coefficients based on the full frontal area of the crown in still air, (see Figure 2.17). It can be seen that as the wind speed increases, there is a decrease in the drag coefficient (C_d) to compensate for the actual reduction in frontal projected area (A_p).

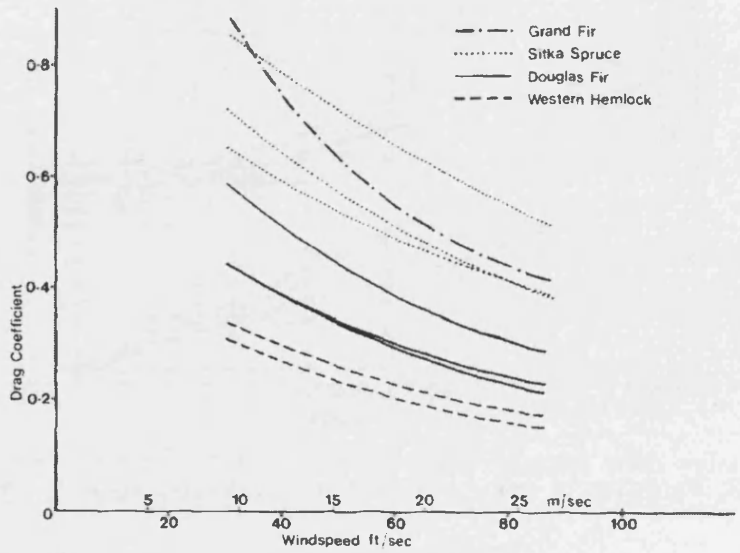

Figure 2.17: Variation of drag coefficient with velocity (Mayhead 1973)

Kouwen & Fathi-Maghadam (2000) mounted coniferous trees on a pick-up truck and tested drag force using a load cell at wind velocities from 10 to 100 km/h using a methodology to obtain the Darcy-Wesibach friction factor f presented in Fathi-Maghadam & Kouwen (1997).

Using a similar experimental methodology, Kane & Smiley (2006) drag-force tested 80 specimens of *Acer rubrum L.* (Red Maple) during September 2003. The trees had a mean height of 4 m and were tested by attaching the trees to to a steel sled with a mounted dynamometer in the bed of a pickup truck, and driving at up to 20 m/s. The authors measured the tree height and diameter, and crown height and width. The drag coefficient (C_d) was calculated from the force recorded on the dynamometer and the frontal projected area from the photographed trees in still air. The frontal projected area was then estimated from the crown measurements as either an ellipse, rectangle or triangle, and the drag coefficient estimated. None of the shapes accurately represented the measured frontal crown area. Kane & Smiley (2006) note that for the 80 foliated *Acer* specimens, the measured drag force was found to be proportional to the wind speed raised to the exponent 1.4. A limited set of six trees were stripped of foliage, and for these defoliated trees, the drag was proportional to wind speed raised to the power of 1.9. The individual and mean drag coefficient (C_d) computed is presented in Figure 2.18. There is a reduction in C_d with increasing velocity.

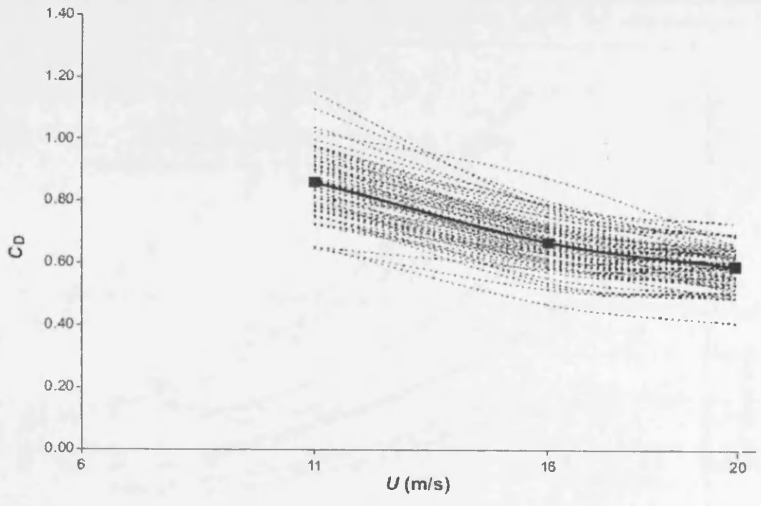

Figure 2.18: Variation of drag coefficient with velocity (Kane & Smiley 2006)

The shape and species of floodplain trees likely to be inundated are reduced when compared to the trees used in wind tunnel and open-air studies and due to this and

logistical reasons, in the field of hydrodynamics the trees tested have often been smaller in scale.

Oplatka (1998*a*) measured the drag force of 3 to 6 year old *Salix* trees between 1.8 m and 4.5 m in height. The *Salix* specimens were sourced from the region of Bern - Burgdorf in Switzerland, and the experiments were carried out during the month of July of 1995 and 1996. The trees were tested at velocities from 1 and 4 m/s at increments of 0.5 m/s, by attaching them to the base of an underwater frame in a 140 m towing tank and measuring the drag force and associated moment and lever arm of submerged and partially submerged trees at varying velocities (see Figure 2.19). Oplatka (1998*a*) also noted the apparently linear relationship between force and velocity. From the force and moment recorded, the lever arm and magnitude and direction of the resultant force on each tree could be determined. From the horizontal and vertical video cameras, the contraction of the *Salix* specimens could be observed and quantified. Figure 2.20 presents a schematic of the vertical and horizontal contraction, along with the contraction variation with velocity. Figures 2.20 (b) and (c) show that at low velocities, the rate of contraction is faster than at high velocities, when the tree is approaching its fully streamlined shape. Oplatka (1998*a*) reports that compared to the projected area when U_0 is zero, the area perpendicular to the flow reduces by a factor of 4 to 5 at a velocity of 1 m/s, and by a factor of 20 to 40 at a velocity of 4 m/s.

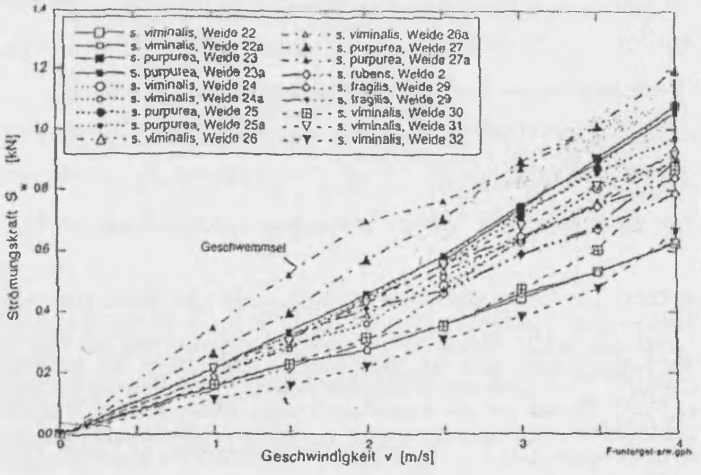

Figure 2.19: Variation of streamwise drag force (y-axis) with velocity (x-axis). Figure taken from Oplatka (1998*a*)

Armanini et al. (2005) measured the forces on partially and fully submerged upright *Salix alba* trees fixed to the base of a re-circulating flume via a force transducer.

The trees all had a height of at least 2.5 m. After testing, the top 1 m of the trees were pruned off to create a second group of smaller, and therefore more flexible, trees. Tree properties were measured, and included the height and diameter of the main trunk and the dimensions and positions of principal and second-order branches relative to the base. This enabled the variation in projected area with height to be obtained.

Armanini et al. (2005) note a clear difference in the variation of drag force with velocity for the semi-submerged original tall trees and the smaller cropped trees. While the tall trees exhibit a linear relationship with the square of velocity, the smaller trees only show a linear relationship with the square of velocity at low velocities, while at higher velocities, the smaller trees appear to vary directly with velocity.

All studies into the aero- or hydrodynamics of trees directly measured the drag force F for real trees at a range of velocities. The drag force equation (2.31) is specific to rigid bodies, and it has been shown that particularly for flexible species, Mayhead (1973), Fathi-Maghadam & Kouwen (1997) and Oplatka (1998*a*) report that the relationship recorded between drag force exerted (F) and free-stream velocity (U_0) varies linearly, as opposed to the expected squared relationship given in the classical formula (2.31). Vogel (1994) explains the ability of trees to reconfigure under increasing velocities as canopy shape becoming a function of velocity, as shown in the contraction of width and height in the results of Oplatka (1998*a*). This reduction in flow area is problematic in defining a drag relationship for non-rigid objects as the terms A_p and C_d in Equation 2.31 are both functions of velocity. Oplatka (1998*a*) proposed the use of the product of the drag coefficient and projected area given by:

$$C_d A = \frac{2}{\rho U_0^2 F_d} \tag{2.33}$$

where $C_d A$ is termed the drag area parameter, ρ is the fluid density, U_0 is the free stream velocity and F_d is the streamwise drag force exerted on the tree. An similar drag area parameter C_d' is presented in the research of Wu et al. (1999) in a study of the drag of simulated vegetation using a rubberised horsehair mattress. In the study, the drag area parameter C_d' was defined by:

$$C_d' = \lambda C_d \tag{2.34}$$

where C_d' is the drag area parameter, λ is the vegetal area coefficient representing the area fraction per unit length of channel (Wu et al. 1999). The drag area coefficient

(C_dA) was also used by Armanini et al. (2005).

Various approaches have been adopted to link the physical properties of the trees tested with the drag force exerted, however only a few researchers (Armanini et al. (2005), Kane & Smiley (2006)) record detailed physical properties of the tested trees. With a lack of precise information, there is as yet no direct link between measurable tree parameters and the drag force exerted. Freeman et al. (2000) and Kane & Smiley (2006) showed the variation in drag between leaved and unleaved plants, but do not include data on the amount of foliage or their physical properties. Some studies have recorded properties such as projected area in still air (Mayhead 1973, Kane & Smiley 2006) or photographs of dissected samples to determine the leaf area (Fathi-Maghadam & Kouwen 1997). Kane & Smiley (2006) took detailed measurements of mass, diameter and crown width and height and found that mass was more closely correlated with drag than diameter and height.

In determining the stiffness properties of flexible plants, several approaches have been adopted (Fathi-Maghadam & Kouwen 1997, Freeman et al. 2000). Freeman et al. (2000) measured the drag force of several small trees both with and without leaves through the use of a strain gauge attached to a platform with horizontal freedom of movement. The plant height, width, leaf size and stem height were all recorded along with branch and leaf numbers. Freeman et al. (2000) attempted to characterise the plant stiffness by determining the force necessary to bend the plant to a 45° angle. The plant stiffness for this condition was given by:.

$$E_s = \frac{F_{45}H^2}{3I} \tag{2.35}$$

where E_s is the modulus of elasticity, F_{45} is the force necessary to bend the plant to an angle of 45°, H is the height of the plant and I is the second moment of inertia for a circular shape.

Theoretically, a tree or plant stem with mass and elasticity may exhibit one or more resonance frequencies of vibration depending on the damping (McMahon 1975). Fathi-Maghadam & Kouwen (1997) applies linear beam theory to obtain the flexural rigidity EI, where E is the stiffness modulus and I is the second moment of inertia:

$$f_i = \frac{\lambda_i^2}{2\pi}\left(\frac{EI}{EI}\right)^{1/2} \tag{2.36}$$

where f_i is the resonance frequencies (i= 1, 2, 3,... n) with f_1 the base natural frequency, λ_i is a dimensionless parameter and a function of beam geometry, EI is

the flexural rigidity, m is the mass per unit length and l is the length.

2.6 Gaps in Existing Research to be Addressed in this Thesis

The past fifty years have seen a great deal of analysis with regard to both simulated and real vegetation, and a range of scaled and full-scale experiments. However, there remain a number of gaps which limit the potential of researchers within this field to connect with each other and with the wider multi-disciplinary field of river management. They are:

- No datasets were found that mimicked the multi-stem nature of rigid vegetation. Experiments investigated scaled tree arrays were invariably modelled with rigid cylinders
- Lack of a consistantly documented velocity measurement methodology in vegetated flume studies, limiting the possibility of reliable meta-analysis due to errors resulting from inaccurate point measurement locations
- An accurate, high-resolution dataset detailing the drag force variation with velocity of full-scale trees
- A consistant method linking physical plant parameters to roughness values, data that would be highly valuable to practitioners of river management
- Numerical modelling of floodplain woodland has not utilised roughness values derived from experimental data

This research will address these five major issues. The first point will be addressed in *Chapter 3* and *Chapter 4*, which present experimental data results and analysis into arrays of both rigid cylinders (to replicate the single stem condition) and *Cornus sanguinea* saplings (to replicate the multi-stem comdition). Comparision is made between the two types of model trees. The second point will be addressed in *Chapter 4*, where a study to find the optimum sampling locations is carried out. The third and fourth points are addressed in *Chapter 5* where the force is recorded for submerged trees at various velocities using a high precision dynamometer. The trees physical properties are recorded and related to the drag characteristics. The fifth point is addressed in *Chapter 6* where the drag parameters obtained from the real trees in *Chapter 5* are incorporated into the depth-averaged finite difference numerical model DIVAST.

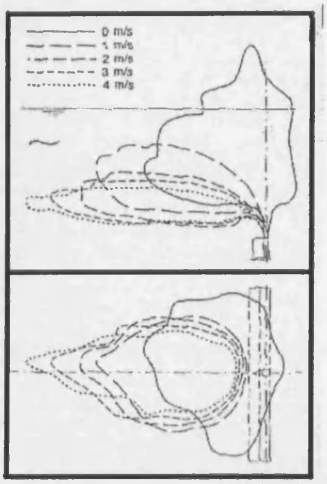

(a)

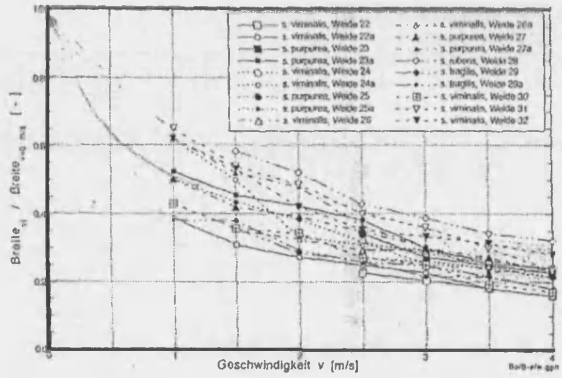

(b)

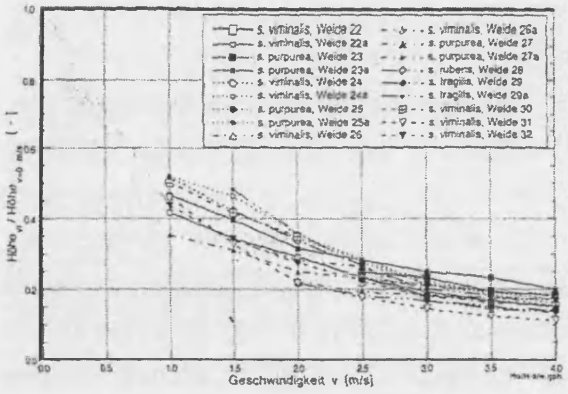

(c)

Figure 2.20: Contraction of trees under hydrodynamic loading. (a) schematic of contraction. (b) variation of normalised width (y-axis) against velocity (x-axis). (b) variation of normalised height (y-axis) against velocity (x-axis). Figures taken from Oplatka (1998*a*)

3

Hydrodynamics of Scaled Single Stem and Multi-stem Tree Arrays

3.1 Single Stem vs. Multi-stem

3.1.1 Introduction

The woody vegetation commonly found in floodplain woodland environments include groups of species of *Salix*, *Alnus*, *Corylus* and *Creatagus* (NVC 2004). These intermediate-sere plant genera grow in a range of shapes and sizes due local conditions such as neighbouring competing trees, soil conditions, light etc. (Starr 2005). Multiple dominant stems are common. The tendency to form multiple stems can be caused directly or indirectly due to man-made reasons such as coppicing or damage from livestock (Newsholme 1992). Small mammals such as rabbits or mice may feed upon the main stem of young saplings, causing an auxin driven response to grow multiple stems (Fuller & Warren 1993). At the other end of the tree life cycle, the trunk base of a single stand tree felled by wind or water may sprout several new stems if the root system is adequate.

Modelling the hydraulic resistance effect of tree groups, both single stem and multi-

stem, provides a challenge to hydrodynamic modellers, due to a lack of knowledge of the relevant hydraulic roughness parameters for woodland vegetation. In this chapter, the one-dimensional hydraulic resistance of model tree arrays of single and multi-stem plants at different planting densities are compared.

3.1.2 Scope of the Chapter

The aim of this Chapter is to fulfill Thesis Aim 1, to obtain the one-dimensional hydraulic resistance coefficients (Manning's n, friction factor f and bulk drag coefficient $\overline{C_d}$) for varying staggered densities of both single stem and multi-stem model tree arrays. The hydraulic resistance coefficients can be applied in one-dimensional and two-dimensional numerical models to simulate the effect of floodplain woodland vegetation in a river reach.

To facilitate this, one-dimensional stage discharge data is presented, in the form of rating curves, obtained from scaled tree array experiments. All experiments were carried out under uniform flow conditions. The experimental programme took place in the Cardiff University Hydraulics Laboratory. Two plant forms were investigated, single stem and multi-stem. The single stem, representative of established single stem tree stands, used wooden dowels, 25.4 mm in diameter. The multi-stemmed plants, representative of coppiced or multi-stemmed woodland varieties, used young saplings of *Cornus sanguinea*, (Dogwood).

The stage discharge data was analysed further, to develop commonly used bulk resistance coefficients of Manning's n and the friction factor (f) (Chow 1959). Both n and f employ the hydraulic radius (R), derived from the flow area divided by the wetted perimeter (P). However, when dealing with roughness elements that extend through the water column, and are not confined to the boundary, the correct derivation of the term R becomes less defined. New hydraulic radii are defined in Section 3.6.1 based on vegetation geometry, and then compared with the classic definition.

The $n-UR$ model (USDA 1947, Chow 1959, Temple 1987) is also investigated, with the measured data analysed with respect to $n-UR$ in Section 3.6.2.

The drag force exerted by the model tree arrays has also been determined. The bulk drag coefficient $\overline{C_d}$, a parameter linked to shape of projected area to oncoming flow and the Reynolds number (Re), has been calculated for both the single stem and multi-stem elements. Modification factors to account for the deviation of $\overline{C_d}$ away from the reported value for an infinite cylinder of $C_d = 1.0$ or 1.2 are also developed

	Model Spacing mm	N_m m^{-2}	Prototype Spacing mm	N_p m^{-2}
Low	310.5 x 180.0	17.89	2484 x 1440	0.28
Medium	210.0 x 120.0	39.68	1680 x 960	0.62
High	100.5 x 60.0	165.84	804 x 480	2.59

Table 3.1: Planting spacing and number of trees/ model trees per m^2 ($N_{m/p}$)

in Section 3.6.3.
In the final section of the Chapter, the experimental results are upscaled to floodplain woodland dimensions.

3.2 Methodology

3.2.1 Introducing the single stem and multi-stem models

The specimens under investigation were chosen to appropriately model emergent single stemmed and multi-stemmed tree species, where emergent refers to trees extending vertically throughout the entire water column and above the water surface. The diameter of trees is highly dependent on the planting density of trees. Planting densities for woodland based on Forestry Commission UK guidance are are listed in Table 1.1.
The three densities of model tree arrays to be investigated in the experimental programme were designed to cover a range of the higher density planting spacings at a physical scale of 1:8.
Single stemmed trees were represented by wooden dowels, 300 mm tall with a diameter of 25.4 mm, corresponding to a prototype diameter of $d = 203.2$ mm. Multi-stemmed trees were represented by *Cornus sanguinea* saplings with an average of five stems with diameters of 5 mm each, corresponding to a prototype diameter of $d = 40$ mm per stem. The coppiced young *Cornus* saplings were purchased from a local plant wholesaler in bundles during February 2007 (Figure 3.1). Until June 2007, the saplings were watered regularly. Because of the close spacing of the plants over this time period, some growth distortion occurred in the intervening months, with those plants on the outer edges of the bundles developing a wider spacing of stems. For the experiments, the location of plants was randomised to discourage clumping of under- or over-developed plants. Immediately before the experiments started, each specimen was pruned to a height of 300 mm and the basal stem trimmed manually with a pen-knife to fit the existing 5 mm threaded holes in

the base of the flume. The dowels were fitted with a basal brass screw to fit into the 5 mm threaded holes (for more on the construction of the dowel - flume set-up, see the original experimental study for dowel arrays in Westwater (2000)). Three of the prepared *Cornus* specimens used can be seen in Figure 3.2. Figure 3.3 presents the view of the three densities of the model tree arrays using the dowels and the *Cornus* saplings.

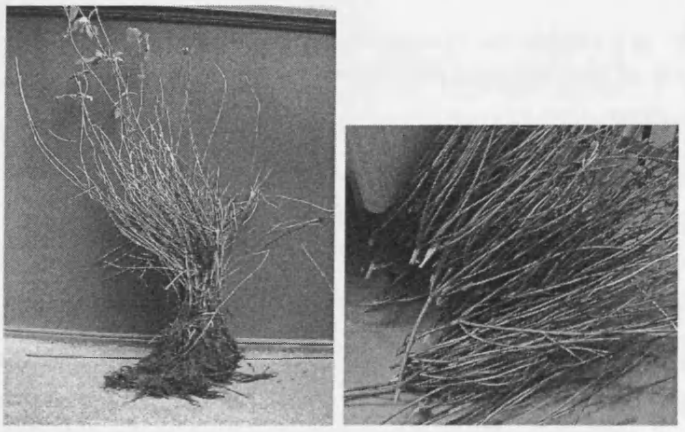

Figure 3.1: Cornus Sanguinea Saplings purchased in bundles (left) were individually pruned to fit into the flume (right)

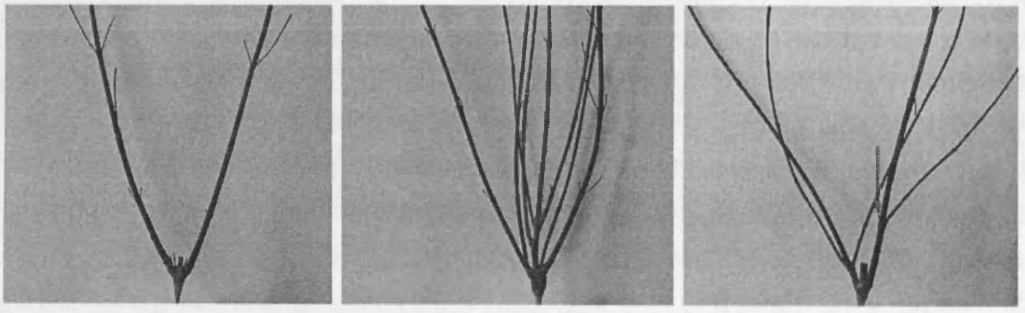

Figure 3.2: Prepared *Cornus* Sanguinea Specimens

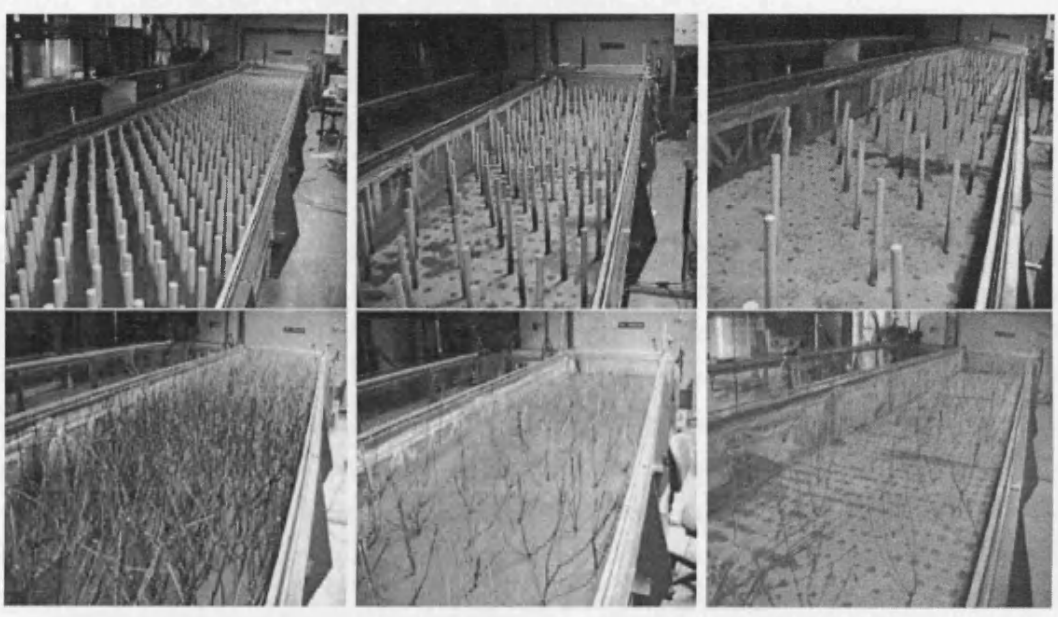

Figure 3.3: View along flume. Top row, left to right, single stem (dowel) high, medium and low density model tree arrays. Bottom row, left to right, multi-stem *Cornus* high, medium and low density model tree arrays

3.2.2 Variation of Dowel and *Cornus* Physical Properties With Submergence

To obtain the physical characteristics of the *Cornus sanguina* saplings, including the number of stems, projected area (where projected area is the frontal area of the sapling facing the oncoming flow) and plant volume, the saplings were photographed against a white background in a well lit room. The saplings were preferentially orientated to view all the stems. Photographs were taken at a set distance with a scale rule beside the specimen. Using the photographed scale, it was determined that 2.2 pixels composed each millimetre. A Matlab script was developed to crop the image to contain the 300mm height of plant that would be exposed to flow conditions within the flume. The image was then converted to binary using a threshold intensity of $I = 0.31$. Areas of *Cornus* were identified with a the binary value of 0, and black areas were identified with the binary value of 1. The threshold intensity was chosen based on visual inspection at a range of thresholds. Below a threshold of $I = 0.30$, shadows were incorrectly included in the binary conversion. The image was then cut into 30 one centimetre thick horizontal strips. By counting the number of white pixels in each horizontal strip (n_i, where i is the strip number), it was then possible to calculate the projected area at each height (A_{pi}, where i is the strip number). The variation of average projected area with height for a sample of 642 *Cornus* saplings is shown in Figure 3.4. The series of black dots at each centimetre interval by height represents the projected area at that height for each of the individual specimens photographed. It can be seen that there is a larger variance in the lower half of the plant compared to the upper half. There is an approximately linear distribution of cumulative area with height, presented in Figure 3.5.

The averaging convention adopted to describe the plant characteristics of mean stem diameter (d) etc. are as follows: depth-averaged (d_z), horizontally-averaged (d_{xy}), and plant-averaged (d_{xyz}).

The horizontally-averaged mean number of individual stems at centimetre intervals by height $\overline{n_{xy}}$ were identified by obtaining the mean number of binary boundaries within each horizontal strip of the 642 photographs using:

$$\overline{n_{xy}} = \frac{\overline{B_{xy}}}{2} \tag{3.1}$$

where $\overline{n_{xy}}$ is the mean number of stems in the horizontal plant between a distance k cm and $k-1$ cm from the ground and $\overline{B_{xy}}$ is the mean number of vertical binary boundaries (the interface between 1 and 0) from each strip. This procedure was validated by carrying out the procedure with a sample of 10 original images.

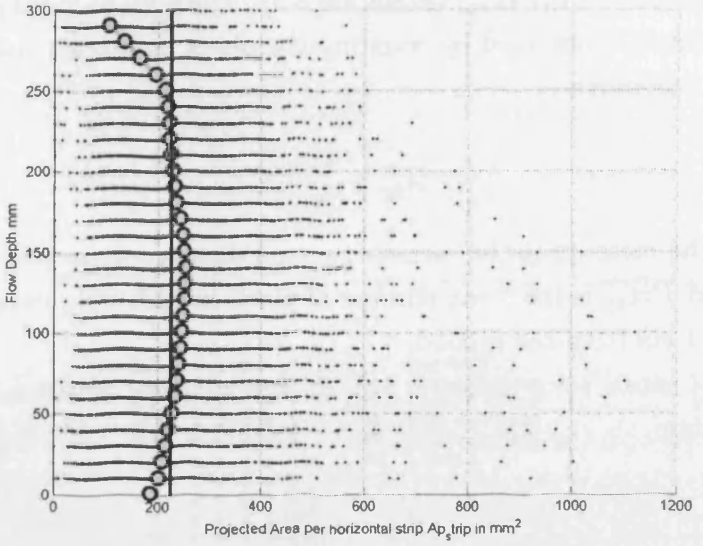

Figure 3.4: Average Projected Area of *Cornus Sanguinea* by height for a sample of 642 saplings (circles represent the mean value at each height, dots represent each sample). Projected area of a single dowel is indicated as a line for comparison.

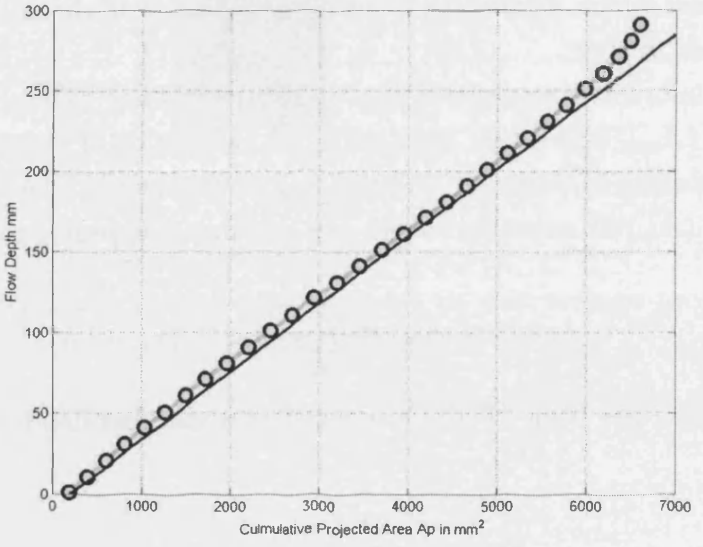

Figure 3.5: Average cumulative projected area by height per *Cornus* sapling for a sample of 642 saplings. Cumulative projected area of a single dowel is indicated as a line for comparison.

The mean projected area ($\overline{A}$) in mm^2 was calculated by determining the mean number of pixels per mm ($\overline{Pix_{xy}}$) (Equation 3.2). The pixel to millimetre conversion was 2.2 pixels mm^{-1}, obtained by counting the pixels on a scale rule adjacent to a photographed specimen:

$$\overline{A_{xy}} = \frac{\overline{Pix_{xy}}}{2.2^2} \tag{3.2}$$

where $\overline{A_{xy}}$ is the mean projected area between a distance k cm and $k-1$ cm from the ground and $\overline{Pix_{xy}}$ is the mean number of pixels in each strip between a distance k cm and $k-1$ cm from the ground.

The equivalent mean stem diameter $\overline{d_{xy}}$ in mm at each elevation could then be determined using:

$$\overline{d_{xy}} = \frac{\overline{A_{xy}}}{10\overline{n_{xy}}} \tag{3.3}$$

where 10 accounts for the 10 mm height of each strip. These data are listed in Table 3.2 and give the average diameter and number of stems for an idealised *Cornus sanguinea* specimen. This idealised plant takes the form shown in Figure 3.6. In Figure 3.6, the flow depth is depicted as 160 mm and using this information, the total projected area and volume of submerged plant can be determined from the Matlab program, which follows the following procedure. It should be noted that Figure 3.6 is not to scale.

The stem size information translates directly to stem volume ($\overline{Vol_{xy}}$) and projected area by depth (A_{xy}), values that are used in the calculation of hydraulic resistance parameters including Manning's n and the drag coefficient C_d. The mean projected area per plant ($\overline{A_{xy}}$) at a specified depth k is calculated according to:

$$\overline{A_{xyz}} = \sum_{k=1}^{k=z} A_{xy} \tag{3.4}$$

The mean volume per plant ($\overline{Vol_{xyz}}$) im mm^3 at a specified depth z is calculated according to:

$$\overline{Vol_{xyz}} = \sum_{k=1}^{k=z} 10 n_{xy} \frac{\pi d_{xy}^2}{4} \tag{3.5}$$

Which can be used to calculate the solid volume fraction.

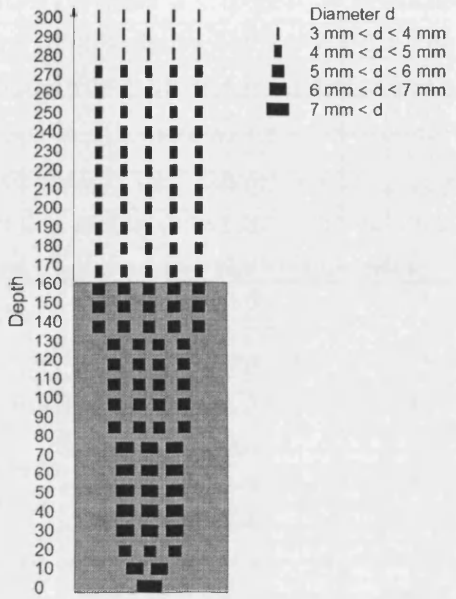

Figure 3.6: Idealised *Cornus* sapling based on the average properties of 642 specimens. The plant is shown submerged to depth 160 mm

Height k	Stems	Total Ap	Ap per stem	Volume	Stem d	Ap culm
k	n_{xy}	A_{xy}	$A_{xy}i$	Vol_{xy}	d_{xy}	Ap_{xyz}
cm	No.	mm^2	mm^2	mm^3	mm	mm^2
30	1.00	104.5	104.5	857.9	10.5	104.5
29	1.96	134.3	68.5	368.8	6.9	238.8
28	2.92	164.2	56.2	248.4	5.6	403.1
27	2.86	194.9	68.1	364.8	6.8	598.0
26	3.09	213.2	69.0	374.3	6.9	811.2
25	3.12	219.1	70.2	386.9	7.0	1030.3
24	3.24	220.8	68.2	365.4	6.8	1251.0
23	3.42	220.6	64.4	326.1	6.4	1471.6
22	3.85	223.8	58.1	265.0	5.8	1695.5
21	3.8	227.4	59.8	280.8	6.0	1922.9
20	3.96	230.8	58.2	266.2	5.8	2153.7
19	4.17	235.5	56.5	250.3	5.6	2389.1
18	4.3	242.5	56.4	249.5	5.6	2631.6
17	4.63	248.3	53.6	225.9	5.4	2879.9
16	4.77	251.1	52.7	218.0	5.3	3131.0
15	4.96	252.7	50.9	203.8	5.1	3383.7
14	5.05	252.1	49.9	195.6	5.0	3635.8
13	5.06	250.3	49.4	192.1	4.9	3886.1
12	5.15	248.2	48.2	182.2	4.8	4134.3
11	5.23	245.6	47.0	173.5	4.7	4379.9
10	5.33	242.6	45.5	162.4	4.5	4622.5
9	5.4	238.6	44.2	153.2	4.4	4861.1
8	5.44	236.2	43.4	147.8	4.3	5097.3
7	5.45	232.1	42.6	142.5	4.3	5329.3
6	5.36	226.3	42.2	139.7	4.2	5555.6
5	5.22	220.3	42.2	139.8	4.2	5775.9
4	5.18	214.3	41.4	134.5	4.1	5990.1
3	5.23	208.3	39.8	124.5	4.0	6198.5
2	5.15	201.9	39.2	120.7	3.9	6400.3
1	5.13	186.6	36.4	103.9	3.6	6586.9

Table 3.2: Mean stem diameter $\overline{d}$ and mean number of stems $\overline{n}$ by height increment k (cm) of multi-stemmed *Cornus* saplings

The six experimental set-ups investigated are outlined in Table 3.3 with spacing in the longitudinal (s_x) and lateral (s_y) dimensions, the solid volume fraction (ϕ) and the number of plants per m^2 (N) and the number plants in a row (N_r). The solid volume fraction (ϕ) is calculated according to Equation 3.6 and defined as the solid volume of plant per unit volume of fluid.

$$\phi_{xyz} = \frac{\overline{Vol_{xyz}}}{s_x s_y z} \times 100 \tag{3.6}$$

Figure 3.7 plots the mean projected area per plan m^2 against flow depth for the three model tree array densities in Table 3.1. It can be seen that the mean projected area of the low, medium and high density arrays of both the *Cornus* saplings and the dowels are similar in magnitude. In Figure 3.8 the mean solid volume fraction (ϕ) is plotted against the flow depth. The mean solid volume fraction (ϕ) of the *Cornus* saplings comes to approximately one quarter of the mean solid volume fraction (ϕ) of the dowel arrays of equal planting density. In the calculation of the drag coefficient, the mean projected area $\overline{A_{xyz}}$ and not the volume is the only parameter taking into account the physical shape of an obstacle to flow. At high Reynolds numbers and low array densities, this would suggest that the magnitude of obstruction resistance of the single stem and multi-stem arrays would be similar.

Exp Number	**Specimen**	**Density**	s_x **mm**	s_y **mm**	ϕ	**N** m^{-2}	N_r
E	none	n/a	n/a	n/a	0	0	0
D1	dowel	Low	0.315	0.180	0.455	8.8	3.5
D2	dowel	Medium	0.210	0.120	1.023	19.8	5.0
D3	dowel	High	0.105	0.060	4.091	80.6	10.0
V1	*Cornus*	Low	0.315	0.180	0.014	8.8	3.5
V2	*Cornus*	Medium	0.210	0.120	0.035	19.8	5.0
V3	*Cornus*	High	0.105	0.060	0.170	80.6	10.0

Table 3.3: Scaled Tree Experiments. s_x and s_y are longitudinal and lateral distances, ϕ is the solid volume fraction occupied by the type of plant per density, N is the number of model trees per m^2 and N_r is the number of model trees in each lateral row. The values of ϕ for the *Cornus* saplings was determined at a depth of $z = 20$ cm.

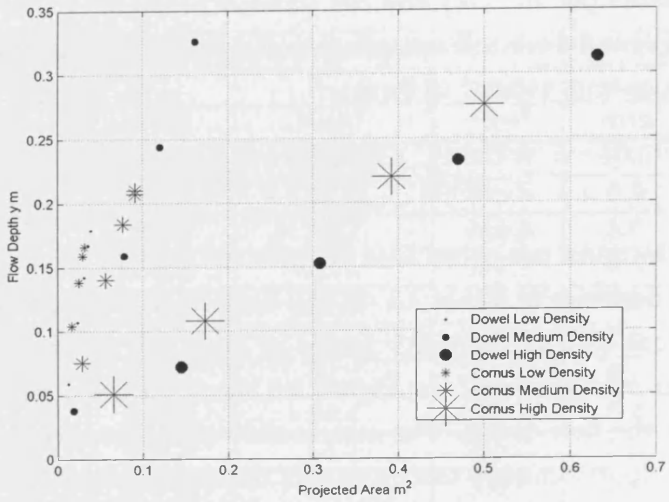

Figure 3.7: Variation of Projected Area (A_{xyz}) per m^2 plan area with flow depth

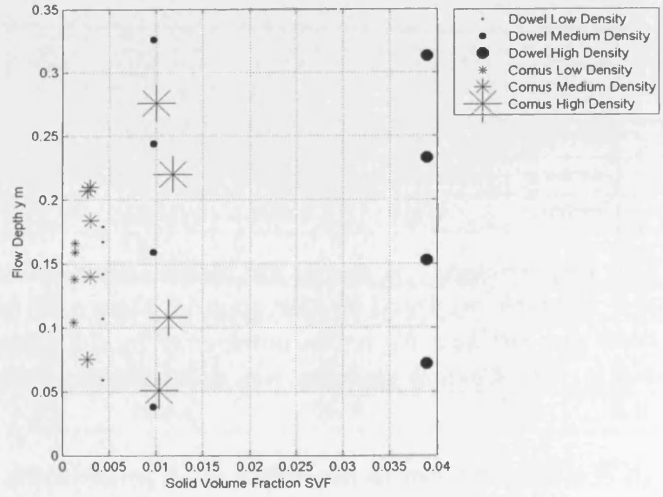

Figure 3.8: Solid Volume Fraction (ϕ) variation with flow depth

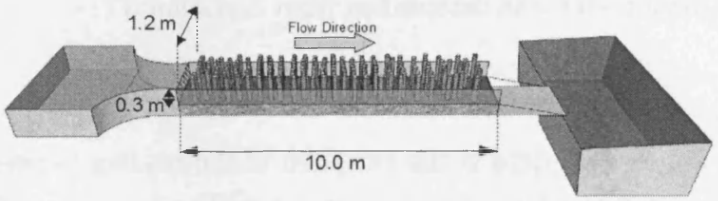

Figure 3.9: Schematic of flume

3.3 Experimental Setup

The experiments investigating the hydraulic characteristics of scaled tree arrays were carried out in the Cardiff University School of Engineering Hydraulics Laboratory. A schematic of the flume used is shown in Figure 3.9. The flume had dimensions 10 m long, 1.2 m wide and 0.3 m deep with an adjustable slope set at a slope of $S_0 = 0.001$ to represent a typical low-lying river gradient.

Water was fed into the flume from the reservoir beneath the flume via one of two pipes. For low flows the 50 mm pipe offered the highest accuracy up to approximately 6 l/s, while the 200 mm pipe could deliver flows from 10 l/s to above 60 l/s. A flowmeter monitored the discharge. The water surface elevation was controlled by a manually operated tailgate weir with an accuracy of 1 mm.

3.4 Experimental Procedure

3.4.1 Depth Measurements

A methodology was developed to minimise sources of error based on the experimental conditions. The 10 m flume had insufficient length to achieve fully developed flow. The boundary roughness was not an even value for the full length of the flume, due to bed undulations and the presence of the exposed holes drilled to accommodate the vegetation. Depth measurements were initially taken using a Vernier pointer gauge at discrete intervals along the length of the flume. Due to the high degree of error that was associated with this method, stilling wells were constructed to enable faster measurement time and to benefit from the damping effect of the manometer tubes (see Figure 3.10). To compare and calibrate the manometer, a series of experiments was carried out with measurements from both methods. The correction to the manometer was found by comparing the pointer gauge reading with the manometer reading under various flow conditions. The absolute error P_{error} between the pointer

gauge and the manometer was determined from Equation 3.7.

$$P_{error} = d_{manometer} - d_{pointer} \tag{3.7}$$

Each point in Figure 3.11 depicts the variation in the reading between the pointer gauge and the manometer for a flow measurement. The line of best fit was used to correct the flow depths obtained by the manometer.

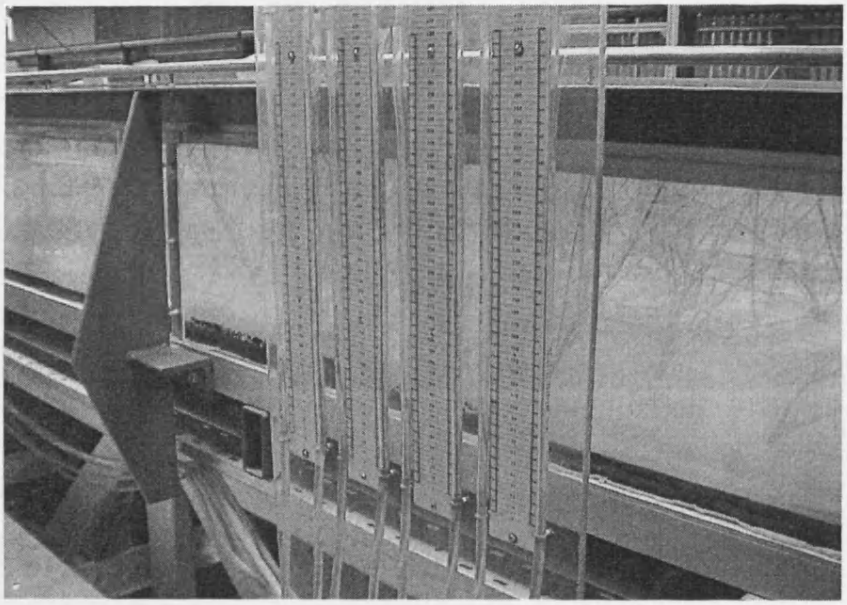

Figure 3.10: Manometer

The point gauge is subject to three principal sources of error:

- Small undulations in the bed
- Uneven carriage rail
- Water surface undulations

The variations in error in readings in Figure 3.11 are due to a combination of these three errors. The manometer has the benefit that it is unhindered by the uneven carriage rail. Local bed undulations will not adversely affect the reading, and the water surface oscillations are damped by the length of the manometer tube.

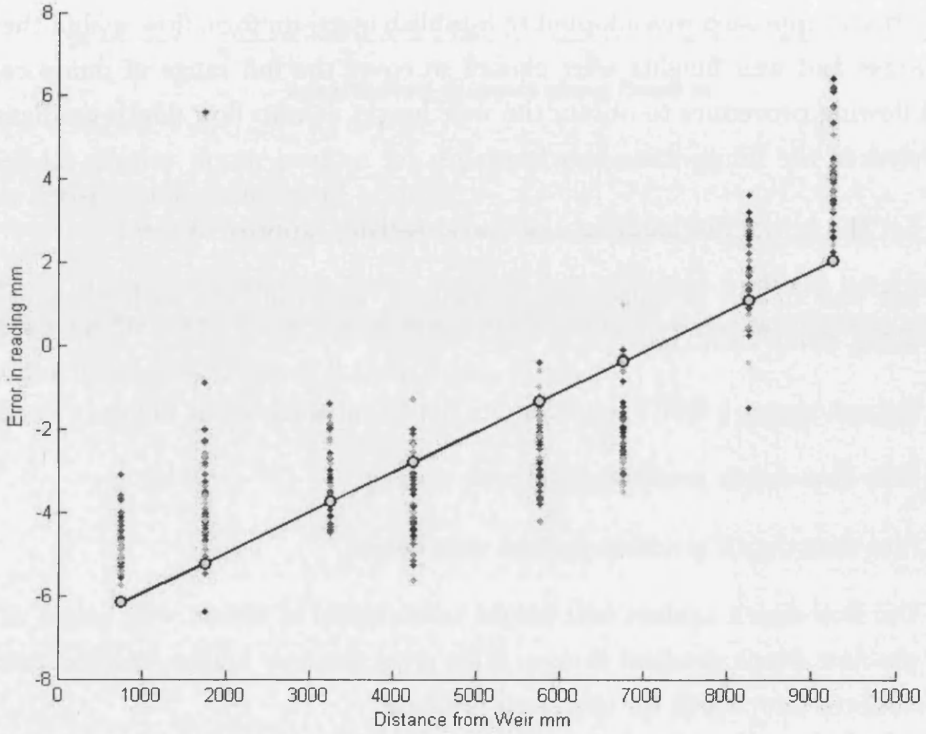

Figure 3.11: Gauge Correction. $P_{error} = d_{manometer}$-$d_{pointer}$. This gauge correction was carried out using the data obtained from the experiments to determine uniform flow, described in the following section, covering discharge from 3 l/s to 50 l/s.

3.4.2 Procedure for Establishment of Quasi-uniform Flow

Uniform flow occurs when there is no loss of flow depth along the length of a body of water. It will occur when the component of gravitational weight of water parallel to the flow direction is balanced by the frictional forces of the perimeter and any obstacles present in the water column. Ensuring uniform flow conditions exist allows precise derivation of the hydraulic resistance of the model tree arrays. The uneven base of the flume as seen in Figure 3.11 would not permit uniform flow to be established precisely, and so the flow conditions have been termed quasi-uniform.
A systematic approach was adopted to establish quasi-uniform flow within the flume. Discharges and weir heights were chosen to cover the full range of pump capacity. The following procedure to obtain the weir height at zero flow depth gradient along the length of the flume was carried out:

1. Set the initial discharge at the lowest setting (approx. 3 l/s)
2. Set weir height in increasing increments, recording the surface water profile along flume each time
3. Repeat stages 1 and 2 to maximum depth capacity of the flume ($z = 300\ mm$)
4. Plot flow depth profile against weir setting
5. Plot flow depth gradient against weir height
6. Use flow depth against weir height relationship to obtain weir height at which the flow depth gradient is zero. This gives the weir height, and the associated uniform flow depth for the given discharge

Flow depth measurements were taken along the length of the flume using either the pointer gauge or the manometer arrangement, as described above, to obtain the water surface profile and determine the flow depth gradient. While the discharge remained constant, the weir was then raised and after the water had settled, the water surface profile was measured again. The weir raising was repeated to the maximum flume depth capacity. At this point (Stage 3) the weir was reset to its lowest level, the discharge increased, and the process of weir raising and water surface profile measuring repeated. In Stage 4, the longitudinal flow depth gradient was plotted against each weir depth. An example of this can be seen in Figure 3.12 for the Medium Density dowel arrangements. It can be seen that as the weir height is increased, the flow depth gradient decreases and eventually becomes positive.

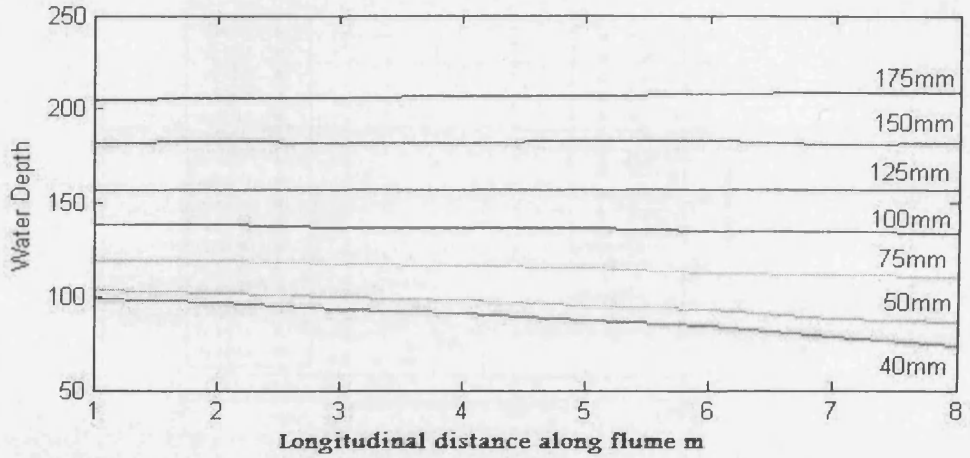

Figure 3.12: Water depth profiles for different weir settings for the dowel array, medium density and discharge $Q = 20l/s$

In Stage 5, the longitudinal flow depth gradient was obtained from the longitudinal flow depth profile. The longitudinal flow depth gradient was then plotted against weir height in Stage 6 (Figures 3.13 to 3.15).

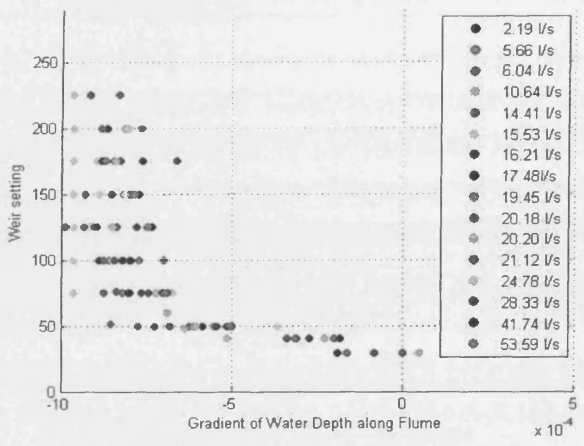

Figure 3.13: Empty Flume, nested curves of longitudinal flow depth gradient vs. weir height (h) for varying discharge (Q)

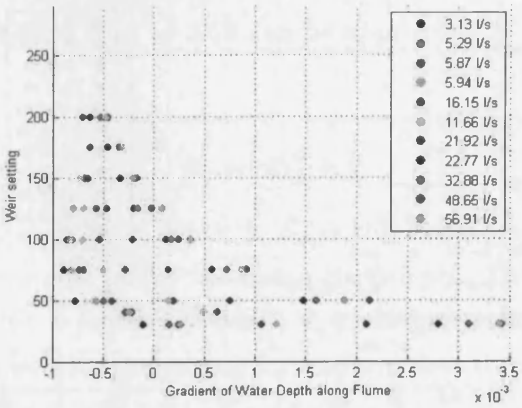

(a) Low density

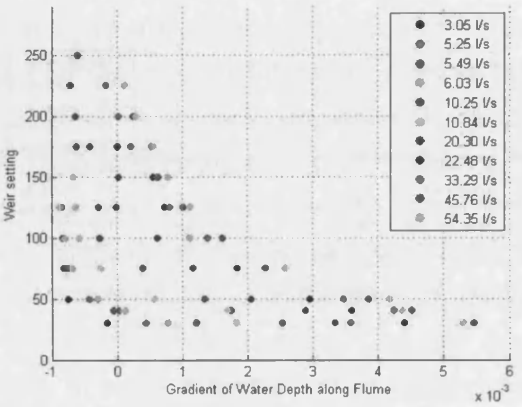

(b) Medium density

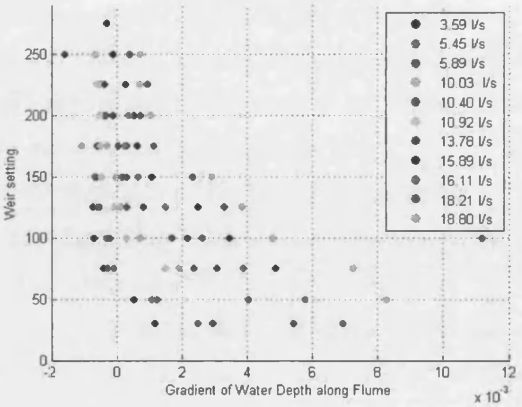

(c) High density

Figure 3.14: Dowel arrays, nested curves of longitudinal flow depth gradient vs. weir height (h_w) for varying discharge (Q)

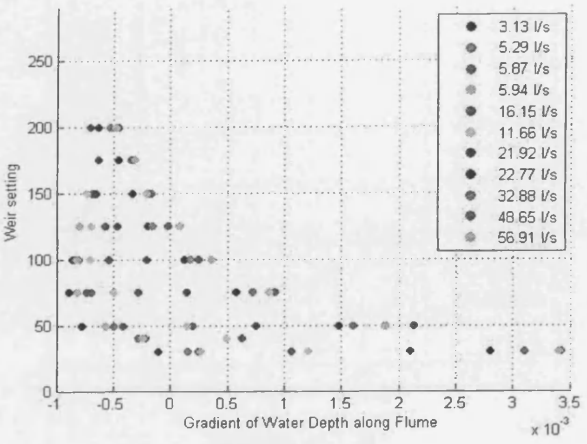

(a) Low density

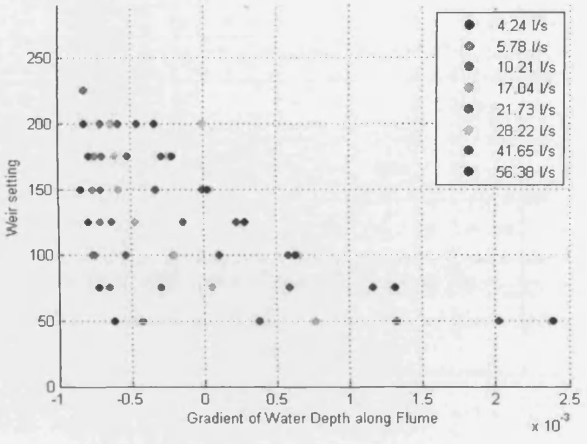

(b) Medium density

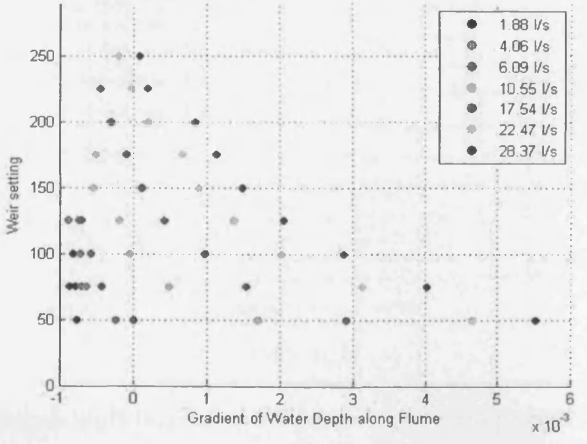

(c) High density

Figure 3.15: *Cornus* arrays, nested curves of longitudinal flow depth gradient vs. weir height (h) for varying discharge (Q)

Uniform flow occurs at the location of zero longitudinal flow depth gradient. Each curve presented in Figures 3.13 to 3.15 can be approximated to a power law curve of the form:

$$h_w = \alpha S_d^{\beta} + \gamma \tag{3.8}$$

Where h_w is the weir height at depth z, S_d is the longitudinal water depth slope and α, β and γ are variable power law curve coefficients. The Matlab curve fitting toolbox was used to fit a power law curve to each dataset in Figure 3.13 to 3.15, and this enabled the weir height setting for uniform flow to be determined.

3.5 Stage Discharge Relationships of Scaled Arrays

Figure 3.16 presents the stage discharge relationships obtained for each model tree array. Tabulated values for the measured data are given in Table 8 in the Appendix. There is a relatively large effect of increasing the density of both the single stem and multi-stem arrays. It is interesting to note the effects of equivalent densities of the multi-stem array of *Cornus sanguinea* and the single stem dowel array. For the low density of 8.8 $plants/m^2$, there is a close agreement between the two data. At the medium and high densities of 19.8 and 80.6 $plants/m^2$, the dowel array displays an increasingly higher hydraulic resistive effect than the *Cornus* array. This may be due to the difference in projected area and average diameter. For the multi-stemmed plant, the solid volume fraction (ϕ) throughout the height of the water column remains a fairly constant value (see Figure 3.8). However, as flow depth tends towards a maximum, there are more branches of lower diameter in the upper flow region. Although the results for the high density dowel and *Cornus* arrays are a linear best fit trend line, with more results at higher discharges it is expected that the overall shape of the stage-discharge graph would be of a similar form to the curved relationships shown for the low density arrays. The data fitted to the regression curves are presented in Tables 1 to 7 in the Appendix.

Power curve fitting, the standard fitting technique for open channel flow, gave poor agreement with the measured data. Polynomial relationships gave a better agreement for the range of data measured and the polynomial coefficients obtained to fit Equation 3.9 are given in Table 3.4. The fitted values are used to plot the following figures.

$$y = \alpha Q^2 + \beta Q + \gamma \tag{3.9}$$

	α	β	γ
Empty Flume	-0.046	4.053	2.160
Low Density dowel	-0.059	6.551	-0.961
Medium Density dowel	0	8.273	-4.689
High Density dowel D	0	16.04	-7.744
Low Density *Cornus*	-0.066	6.705	-3.706
Medium Density *Cornus*	-0.103	9.540	-9.864
High Density *Cornus*	0	11.25	-4.944

Table 3.4: Fitted Polynomial Curves for Stage Discharge Relationships

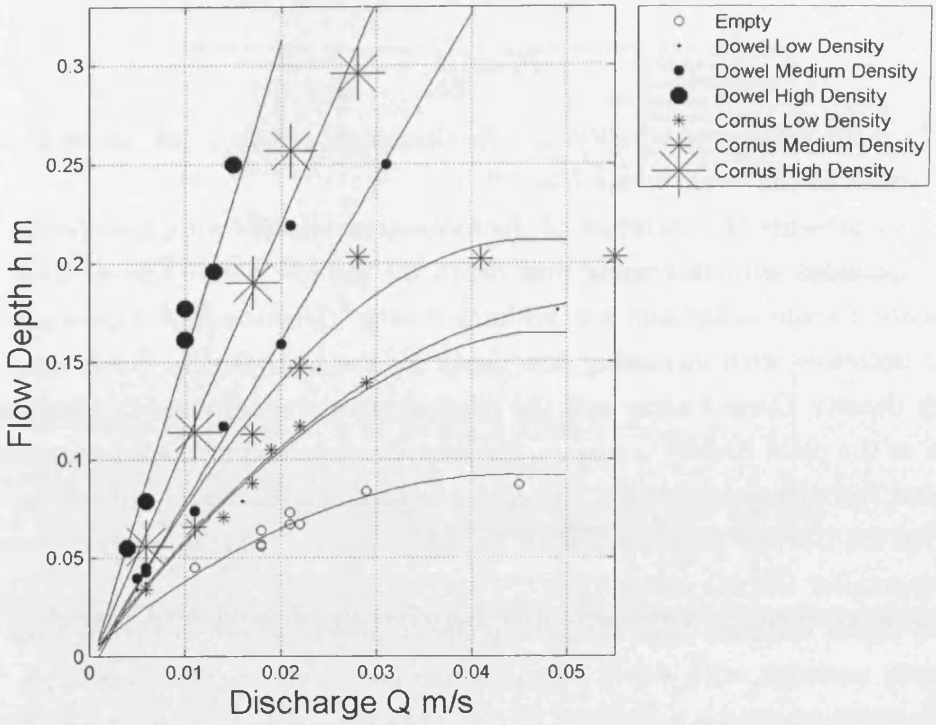

Figure 3.16: Stage (y) discharge (Q) relationship of scaled arrays

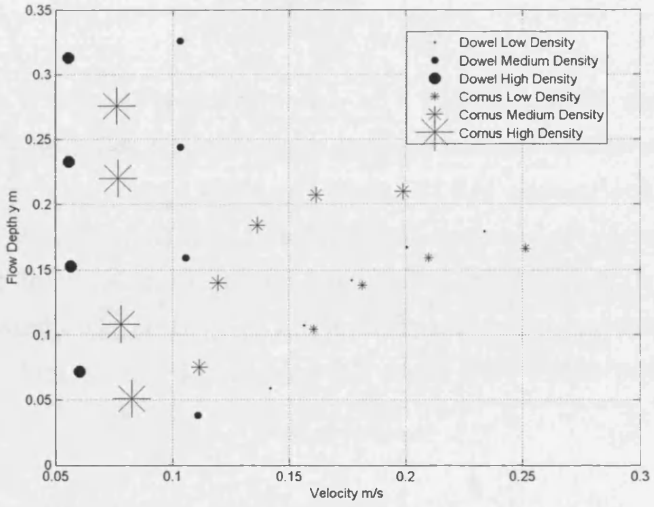

Figure 3.17: Flow depth variation with mean-area velocity

The mean-area velocity ($\overline{U}$) was calculated by modifying the flow area by the solid volume fraction (ϕ) using:

$$\overline{U_0} = \frac{Q}{\phi b z} \tag{3.10}$$

Where U_0 is the mean-area velocity, Q is the discharge, ϕ is the solid volume fraction, b is the width of the flume where $b = 1.2$.

Figure 3.17 presents the variation of the mean-area velocity with flow depth. The velocity increases with increasing flow depth for the low density dowel array and low density *Cornus* array and the medium density *Cornus* array. Conversely, the velocity decreases with increasing flow depth for the high density dowel array and the high density *Cornus* array and the medium density *dowel* array. This may be because as the plant density increases, the lateral component of the velocity and the associated turbulence increases. This happens to a greater degree with the dowels than with the *Cornus* arrays as fluid is forced round the dowel in a larger diversion than the smaller *Cornus* stems.

The flow depth variation with stem Reynolds number is shown in Figure 3.18. The flow depth variation with depth Reynolds number is shown in Figure 3.19. The stem Reynolds number is a function of the mean stem diameter (d), which itself is a function of flow depth (z). For each data point in Figure 3.18, the mean stem diameter d has been calculated based on the mean stem diameter in the Idealised Plant depicted in Figure 3.6, and the flow depth (z) according to Equation 3.11.

$$Re_d = \frac{\overline{U_0}}{\upsilon} \frac{\sum_{k=1}^{k_z} \overline{d_k}}{z} \tag{3.11}$$

By using the mean stem diameter d to define the flow regime, it can be seen that the experiments with the *Cornus* saplings experience a lower stem Reynolds number that the dowel experiments. All the stem Reynolds numbers fall within the vortex shedding zone, with Re_d greater than 200 and less than 2×10^5 (Massey 1997). Within this zone, pressure drag accounts for at least 90 % of the total profile drag. For comparisons where the flow depth is used as the characteristic length, the variation of flow depth with depth Reynolds number is presented in Figure 3.19.

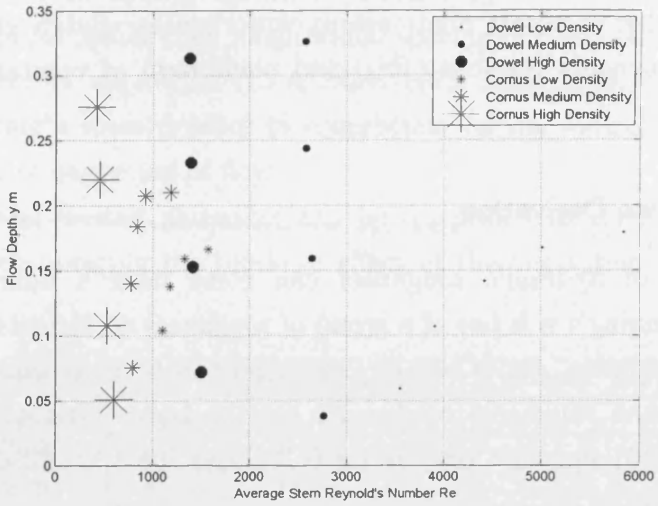

Figure 3.18: Flow depth variation with mean stem reynolds number

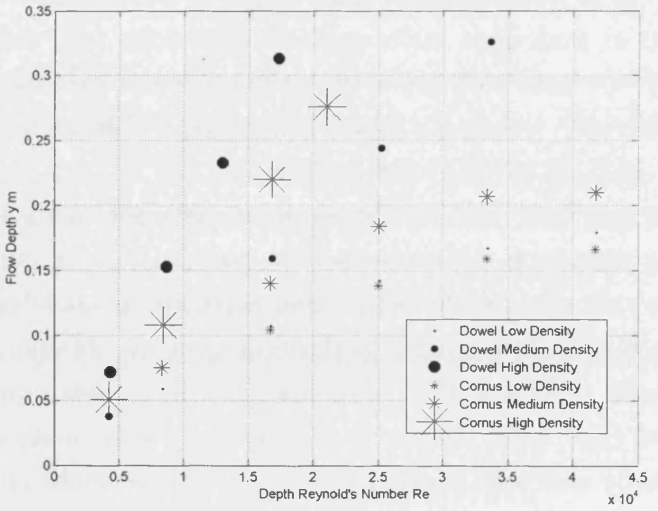

Figure 3.19: Flow depth variation with depth reynolds number

3.6 Determining Roughness of Single and Multistem Arrays

The single stem and multi-stem stage-discharge relationships in this study can be investigated further to obtain relationships exploring the relative effects of planting density, stem Reynolds Number (Re_d) and plant form of vegetation, on a water body.

3.6.1 Resistance Derivation

The derivation of hydraulic roughness can come from a number of different approaches. Manning's n is one of a group of roughness coefficients with which any type of fluid roughness, gravel bed or vegetation can be represented Chow (1959). Two other common roughness coefficients are the Darcy-Weisbach friction factor (f) (Equation 3.13) and the Chézy factor (C) (Equation 3.14) Chadwick & Morfett (1999), given here:

$$U = \frac{R^{\frac{2}{3}} x S^{\frac{1}{2}}}{n} \tag{3.12}$$

$$U^2 = \frac{8gRS}{f} \tag{3.13}$$

$$U = C\sqrt{RS} \tag{3.14}$$

Where n is Manning's n, R is the hydraulic radius, S is the bed slope, here equivalent to both S_0 the bed slope and S_f the friction slope due to the uniform flow condition, U is the velocity, g is the gravitational constant.

These commonly employed bulk roughness parameters are based in the determination of boundary roughness. Manning's n in particular is an empirically derived formula, with 'n' an absorption factor that accounts for the loss of streamwise kinetic energy head caused by resistive surfaces or elements. Manning's n values only apply in fully rough, turbulent flow. Manning's n will increase rapidly when depths approach the bed (Ree 1958, Turner & Chanmeesri 1984), making n a roughness factor that should be used with caution where shallow flow conditions exist. However due to the wide use of Manning's n in research and industry, Manning's n values have been calculated for the conditions investigated.

With the roughness extending up through the water column, it is conceptually uneasy to extend the parameters of cross-sectional flow area (A), wetted perimeter

(P) and consequently the hydraulic radius (R) to apply to a vegetated reach. Following the definition of wetted perimeter (P), it is logical to extend it to include the entire surface area of the vegetation. Studies by several authors have noted however, that lateral rather than longitudinal spacing of plant elements dominates the resistive effect of vegetation (Li & Shen 1973, Nepf 1999, Musleh & Cruise 2006). Thus it might seem prudent to concentrate on the wetted perimeter of the most constricted cross-section of flow.

The flow area and wetted perimeter can be quantified in three ways based on neglecting or incorporating the blockage effect of the vegetation, as described in Table 3.5.

Derivation	Area	Wetted Perimeter	Hydraulic Radius
Original	A_o	P_o	R_o
Bulk	A_b	P_b	R_b
Gap	A_g	P_g	R_g

Table 3.5: Definitions of Original, Bulk and Gap: Areas A, Wetted Perimeter P and Hydraulic Radius R

The three definitions of the cross-sectional flow area (A) and wetted perimeter (P) are presented in Equations 3.15 to 3.20. The *Original* cross-sectional flow area definition A_o uses the flume cross-sectional flow area A assuming no blockage effect. The *Original* wetted perimeter (P_o) uses the wetted perimeter of the flume. The *Bulk* flow area definition (A_b) assumes a blockage effect equivalent to the Solid Volume Fraction ϕ is applied to the flume cross-sectional flow area A. The *Bulk* wetted perimeter (P_b) is identical to the *Original* wetted perimeter. The *Gap* cross-sectional flow area definition (A_g) is the flow area at the point of greatest constriction i.e. laterally bisecting a row of model tree dowels or *Cornus*. The *Gap* wetted perimeter (P_g) is equivalent to the wetted perimeter at the point of greatest constriction, and includes the edges of the model trees in the calculation.

The definition of the *Original* cross-sectional flow area (A_o) and wetter perimeter (P_o) is given by:

$$A_o = bz \tag{3.15}$$

$$P_o = b + 2z \tag{3.16}$$

Where A_o is the *Original* cross-sectional flow area definition, b is the width of the

flume, z is the flow depth and P_o is the *Original* wetted perimeter.
The definition of the *Bulk* cross-sectional flow area A_b and wetted perimeter P_b is given by:

$$A_b = \phi b z \tag{3.17}$$

$$P_b = b + 2z \tag{3.18}$$

Where A_b is the *Bulk* cross-sectional flow area definition, ϕ is the solid volume fraction (a constant value for the dowel arrays, but a function of flow depth z for *Cornus* arrays, see Equations 3.5 and P_b is the *Bulk* wetted perimeter).
The definition of the *Gap* cross-sectional flow area A_g and the wetted perimeter P_g is given by:

$$A_g = [b - (N_r \overline{A_p z})]z \tag{3.19}$$

$$P_g = [b - (N_r \times d_1)] + 2z[N_r + 1] \tag{3.20}$$

Where A_g is the *Gap* cross-sectional flow area, $\overline{A_p z}$ is the projected area per model tree at flow depth z, given in Equation 3.4, N_r is the number of model trees in each lateral row, given in Table 3.3, P_g is the *Gap* wetted perimeter and $\overline{d_1}$ is the average diameter at the base of the model tree, defined from Equation 3.3.
These three definitions all have consequences for the mean-area velocity $\overline{U}$ and the stem Reynolds number Re, which is a function of mean-area velocity $\overline{U}$.
The derivation of the three variants of mean-area velocity $\overline{U}$: *Original* mean-area velocity $\overline{U_o}$, *Bulk* mean-area velocity $\overline{U_b}$ and *Gap* mean-area velocity $\overline{U_g}$ are given by:

$$\overline{U_o} = \frac{Q}{A_o} \tag{3.21}$$

$$\overline{U_b} = \frac{Q}{A_b} \tag{3.22}$$

$$\overline{U_g} = \frac{Q}{A_g} \tag{3.23}$$

$$\tag{3.24}$$

The derivation of the three variants of Reynolds number Re: *Original* Re_o, *Bulk*

Reynolds number Re_b and *Gap* Reynolds number Re_g are given by:

$$Re_o = \frac{\overline{U_o} d_z}{\upsilon} \tag{3.25}$$

$$Re_b = \frac{\overline{U_b} d_z}{\upsilon} \tag{3.26}$$

$$Re_g = \frac{\overline{U_g} d_z}{\upsilon} \tag{3.27}$$

$$\tag{3.28}$$

The hydraulic roughness coefficient Manning's n can then be computed taking into account each derivation to give the *Original* Manning's n_o, *Bulk* Manning's n_b and *Gap* Manning's n_g. The equations are presented and Figure 3.20 presents the variation of the blockage Manning's n_b with flow depth.

$$n_o = \frac{R_o^{2/3} S_0^{1/2}}{\overline{U_o}} \tag{3.29}$$

$$n_b = \frac{R_b^{2/3} S_0^{1/2}}{\overline{U_b}} \tag{3.30}$$

$$n_g = \frac{R_g^{2/3} S_0^{1/2}}{\overline{U_g}} \tag{3.31}$$

$$\tag{3.32}$$

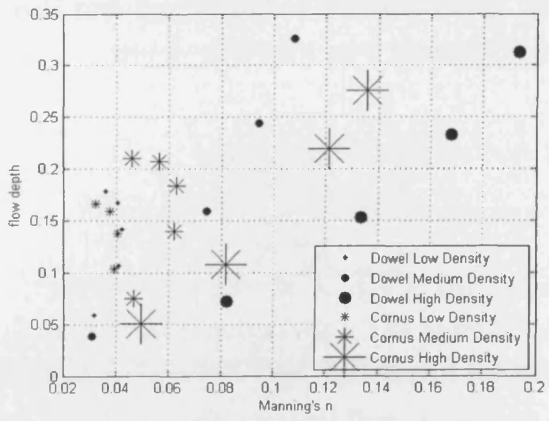

(a)

Figure 3.20: Variation Manning's n vs. flow depth (h). Dowel and *Cornus* with blockage derivation n_b

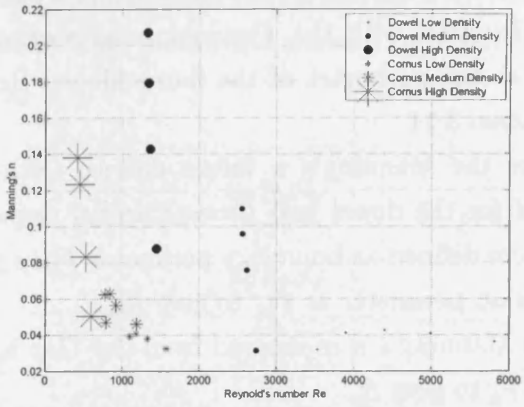

(a)

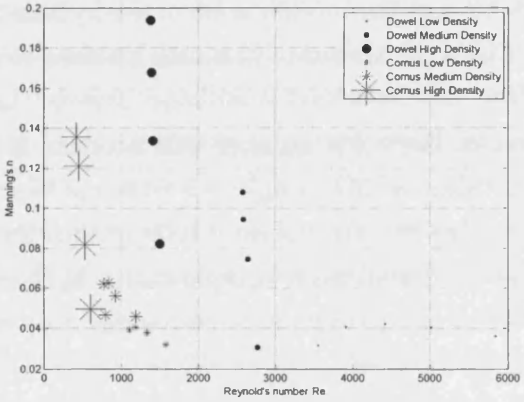

(b)

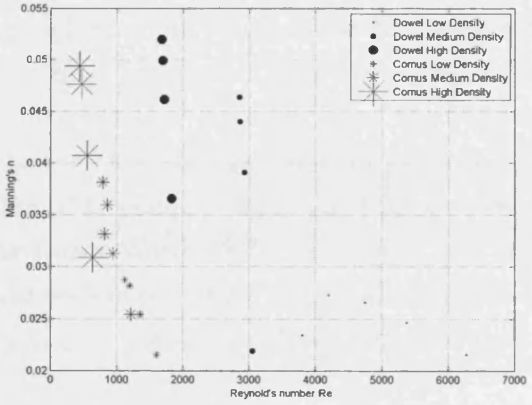

(c)

Figure 3.21: Variation Manning's n vs. Stem Reynolds number Re_d. dowel $d = 25mm$ and Cornus. (a) n derivation *Original*; (b) n derivation *Blockage*; (c) n derivation *Gap*

Figure 3.21 (a) shows the Manning's n relationship with Reynolds number of the stem $R_e stem.$ as calculated with the *Original* cross sectional flow area A_o and wetted perimeter P_o as the perimeter of the flume alone. Reynolds number Re is calculated from Equation 3.11

Figure 3.21 (b) shows the Manning's n values derived with the *Bulk* definitions of hydraulic radius R for the dowel and *Cornus* arrays respectively. The original wetted perimeter is here defined as boundary perimeter P_b to give R_b, the combined boundary and vegetation perimeter as P_{bv} to give R_{bv}.

Figure 3.21 (c) shows Manning's n as derived from the *Gap* hydraulic Radius, with the gap perimeter as P_g to give R_g.

With the change in hydraulic radius, the cross-sectional flow area A will also be affected and this in turn will affect the Reynolds number of flow. From the results in Figure 3.21, it can be seen that the modification of the hydraulic radius R within the Manning's equation reduces the spread of Manning's values to a smaller range. This may have some benefits. In the transitional zone between laminar and turbulent flow, a small reduction in Reynolds number will produce a large increase in the Manning's n roughness value, as Manning's n is only applicable in turbulent flows. However, it may be possible to extrapolate a relationship for the transitional and laminar ranges. The use of a modified hydraulic radius in the form of a bulk or gap R as described here, seems to produce more consistent results with a lower degree of associated error.

The hydraulic roughness coefficient the Darcy-Weisbach friction factor f can then be calculated from Equations 3.35, taking into account each derivation to give: *Original* f_o, *Bulk* f_b and *Gap* f_g.

$$f_o = \frac{8gR_oS_0}{\overline{U_o}^2} \tag{3.33}$$

$$f_b = \frac{8gR_bS_0}{\overline{U_b}^2} \tag{3.34}$$

$$f_g = \frac{8gR_gS_0}{\overline{U_g}^2} \tag{3.35}$$

The variation of the Darcy-Weisbach friction factor (f) with stem Reynolds number Re is presented in Figure 3.22. The friction factor f for all dowel and *Cornus* experiments are plotted against Reynolds number Re. The channel R is defined using P of the flume, and also modified R's for the *Gap* wetted perimeter and the *Bulk* wetted perimeter. The resulting f values could be further equated to the roughness length k_s. The use of the modified R values lends itself to the possibility of k_s becoming equivalent to a term related to the physical shape of the vegetation, incorporating both the density and plant form, in a similar way to defining a porosity value for a mesh.

Figure 3.22 presents the derivations of the Darcy-Weisbach friction factor (f) against the stem Reynolds number (Re_d). The contribution of the blockage effect is highlighted between Figures 3.22 (a) and (b). By deriving f without the blockage effect, the f for the low planting density dowel array remains almost constant, while both the medium and high planting density dowels experience a large reduction in f over a small increase in Re_d. The results for *Cornus* low, medium and high planting densities follow a similar pattern. Incorporating the blockage effect considerably reduces the friction factor by more that 50% for all arrays and plant types. This infers that the f value of blockage is high and that in order to obtain meaningful information using the Darcy-Weisbach friction factor (f) that the blockage area of the model trees should be ignored (see Figure 3.8). Using the obtained value of the friciton factor, it may also be possible to obtain the equivalent roughness length (k_s)

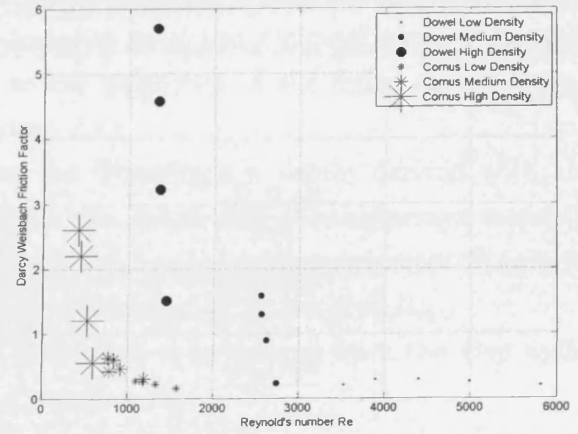

(a)

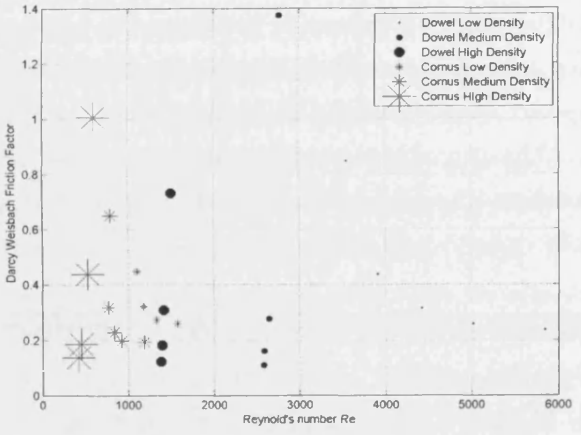

(b)

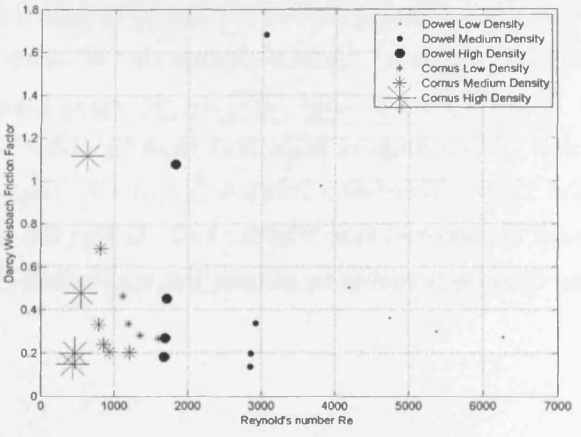

(c)

Figure 3.22: Variation of Darcy-Weisbach friction factor f vs. Stem Reynolds number Re_d. Top, f derived without blockage effect; Middle, f derived with blockage effect; Bottom, f derived using Gap hydraulic Radius

3.6.2 n-UR variation

The **n-UR method** (Ree 1958) links Manning's n to the product of mean-area velocity ($\overline{U}$) and hydraulic radius (R).

Figure 3.23 presents the calculated n-UR relationship, calculated using the *Original* hydraulic radius (R), the *Bulk* hydraulic radius (R_b) and the *Gap* hydraulic radius (R_g). There is very little difference between the first two plots, with Manning's n only slightly higher in Figure 3.23 (a). In both Figure 3.23(a) and (b), the low density dowel and *Cornus* arrays maintain a constant Manning's n number at approximately n=0.04. The medium density *Cornus* array increases slightly then decreases, with a peak n occurring at approximately n=0.062. The medium density dowel array and the high density dowel and *Cornus* arrays all display a linear increase of n with increasing UR, with the rate of increase in n directly related to the projected a. The values of Manning's n calculated are approximately 1/4 of the magnitude shown in (a) and (b). The low density dowel and *Cornus* results are further apart, with low density *Cornus* producing a higher n than the low density dowel array, and the high density dowel and *Cornus* arrays are more closely matched. This smaller variation in n means less associated error. It also suggests that the use of the *Gap* hydraulic radius allows improved comparison between plants of different form, but equal projected area.

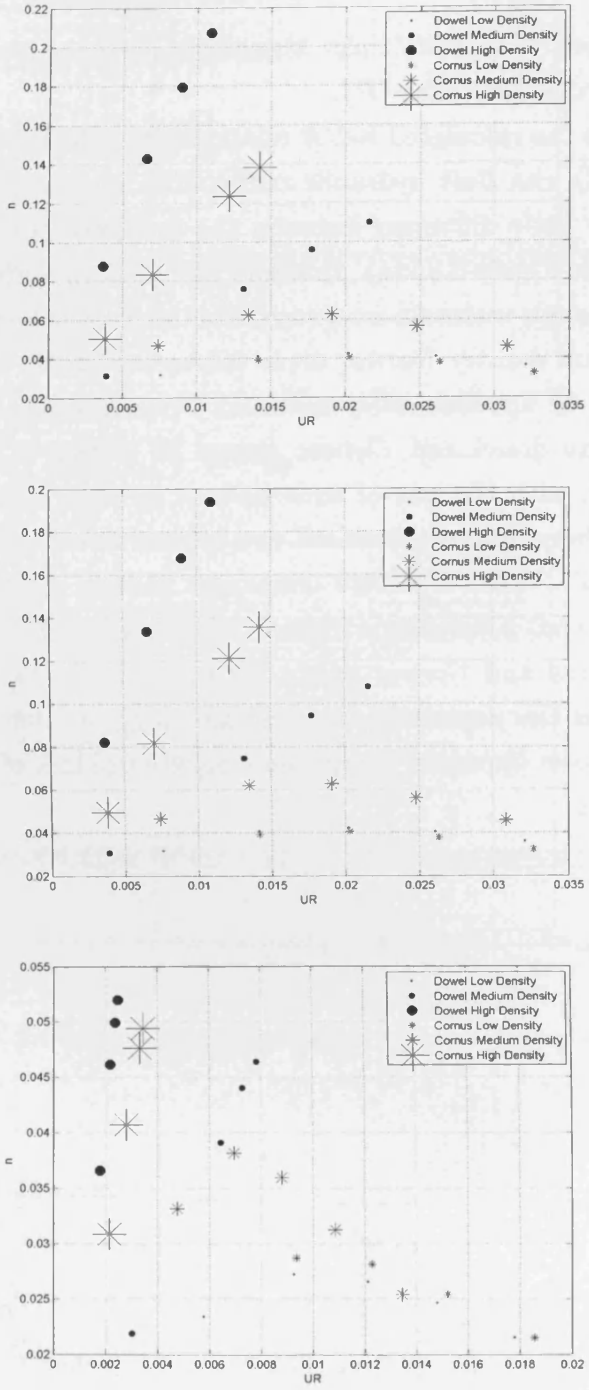

Figure 3.23: Variation of Manning's n with product of velocity and original hydraulic radius. Top, n derivation using R; Middle, derivation using R_b;Bottom, derivation using R_g

3.6.3 Drag Coefficient Derivations

As explained earlier, the bulk drag coefficient $\overline{C_d}$ (Nepf 1999) is calculated, see Chapter 2. The overbar in $\overline{C_d}$ signifies that it is not only form driven but also dependent on the spacing and morphology of the vegetative forms. The force balance approach is adopted, resolving the gravitational fluid weight (Equation 3.36) against the resistive force of the model tree arrays (Equation 3.37) and it is assumed that bed drag is negligible (Li & Shen 1973, Nepf et al. 1997). The standard drag force relationship (Equation 2.29 in Chapter 2, Massey (1997)) is modified through the inclusion of the solid volume fraction ϕ, whereby:

$$F_w = \rho g S_0 (1 - \phi) \tag{3.36}$$

$$F_v = \frac{\overline{C_d} A_p N \rho \overline{U_b^2}}{2} \tag{3.37}$$

Where F_w is the streamwise component of the weight of water, ρ is the fluid density, g is the gravitational acceleration, S is the slope of the flume, ϕ is the solid volume fraction of the plant array, F_v is the hydrodynamic force exerted on the dowels or *Cornus*, $\overline{C_d}$ is the bulk drag coefficient, A_p is the projected area of an individual model tree a function of flow depth z, N is the planting density of the model trees per m^2, $\overline{U_b}$ is the mean-area streamwise velocity.

By assuming gravitational fluid weight is equal to the drag resistance from the vegetation and rearranging, the following relationship is obtained:

$$\overline{C_d} = \frac{2 g S_0 (1 - \phi)}{A_p N \overline{U_b}^2} \tag{3.38}$$

Using this derivation, a range of $\overline{C_d}$ values can be computed from the experimental data. These values are presented in Figure 3.24, and far exceed commonly stated values of $C_d \simeq 1.0$ to 1.2 for an infinite cylinder in two-dimensional flow (Massey 1997).

The results of the bulk drag coefficient ($\overline{C_d}$) against the stem Reynolds number Re_d are presented in Figure 3.24. As the planting density of the dowel array increases, the Reynolds number of flow Re and the bulk drag coefficient ($\overline{C_d}$) both decrease. Although the stem Reynolds numbers do not coincide between different densities, inter-density comparison can be made as the flow regime is reasonably constant within this region (see Section 2.3.3 and Figure 2.7). It can be seen that for both

the dowel and *Cornus* arrays, the bulk drag coefficient($\overline{C_d}$) reduces as the density increases. This confirms the result of other authors that as the density increases, the overall array resistance decreases due to the effect of sheltering (Li & Shen 1973, Petryk & Bosmajian 1975, Nepf 1999, Tanino & Nepf 2008*b*) (see Section 2.4.1), however, the values of bulk drag coefficient ($\overline{C_d}$) obtained are greater than those seen in the literature, including the study by Nepf (1999). This is likely due to the larger dowel size to spacing ratio in the present study in comparison to other cited studies.

Note that there is the potential for bed friction effects to be significant at the lower densities, particularly for the *Cornus* low density array.

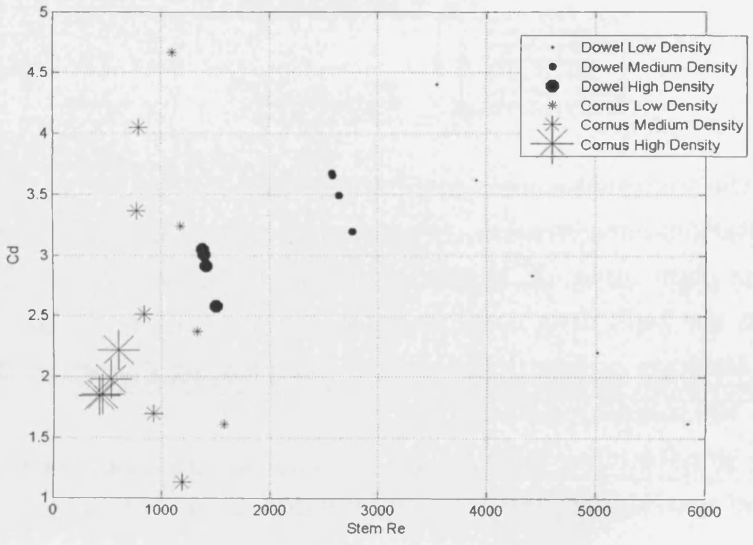

Figure 3.24: Bulk drag coefficient ($\overline{C_d}$) vs. stem Reynolds number (Re_d)

3.6.3.1 *Richter (1973) Modification*

To ensure wider application in a range of flow conditions, it is desirable to find a methodology to obtain the bulk drag coefficient ($\overline{C_d}$) of an array given the plant spacing and the characteristic diameter. The REEDFLO model described by Jordanova et al. (2006) also used a force-balance approach together with an empirical formula proposed by Richter (1973) to evaluate the Richter bulk drag coefficient for a group of cylinders. This is given by:

$$C_{de} = [1 + 1.9C_d(\frac{d}{a_y})]C_d \tag{3.39}$$

Where C_{de} is the Richter bulk drag coefficient, a_y is the lateral distance between stems and C_d is the drag coefficient for the isolated cylinder. To validate Equation 3.39, the Richter bulk drag coefficient ($\overline{C_{de}}$) values derived from the present study will be compared with the 'ideal' value documented for an infinite cylinder of $C_d = 1$ (Massey 1997). For the dowel arrays, this modification is straightforward as d and a_y can be obtained. For the *Cornus* saplings, the definition breaks down as there is ambiguity regarding the mean spacing between the multiple stems. As the bulk drag coefficient has been calculated using the projected area, it is questionable whether the spacing be taken as the average spacing between individual plants or all the individual stems. For the high density *Cornus* array, and to a similar extent the medium density *Cornus* array, the stem spacing approaches uniformity with stems of adjacent plants physically touching and interacting hydraulically. However, in the low density *Cornus* array, it is clear that the individual plants act more as stem clumps and are physically separated from each other. To overcome this problem, the average spacing has been calculated following Equation 3.40.

$$a_y a_x = \frac{s_x s_y}{n_z} \tag{3.40}$$

Where a_y is the lateral separation between stems, a_x is the longitudinal spacing between stems, s_x is the longitudinal spacing between the *Cornus* plants, s_y is the lateral spacing between the *Cornus* plants and n_z is the mean number of stems per *Cornus* at flow depth z.

To maintain similitude with the ratio of dowel Spacings of $s_x = 0.105$ and $s_y = 0.060$ for the high density dowel array $D3$, the *Cornus* spacings of s_x and s_y maintain the same longitudinal: lateral spacing ratio of 0.64 : 0.36. For Cornus, the data from $Q = 20\ l/s$ has been chosen for the calculation of the Richter bulk drag coefficient

$\overline{C_{de}}$. Table 3.6 and Table 3.7 show the computed Richter bulk drag coefficient ($\overline{C_{de}}$) against the bulk drag coefficient ($\overline{C_d}$) derived from the data for a discharge of 20 l/s. Although the Richter bulk drag coefficient ($\overline{C_{de}}$) does increase the standard values of $C_d \cong 1.0$ for a isolated cylinder in 2-D flow, the value of the Richter bulk drag coefficient ($\overline{C_{de}}$) increases with density, which is contrary to the findings within this thesis and those by other researchers, which show the computed bulk drag coefficient ($\overline{C_d}$) decreasing with increasing density.

	dowel			
Density	d	a_y	$\overline{C_{de}}$	$\overline{C_d}$
Low	0.025	0.180	1.260	3.620
Medium	0.025	0.120	1.396	3.495
High	0.025	0.060	1.792	3.046

Table 3.6: dowel C_{de} modification (assuming $C_d = 1.0$) using data from Q = 20 l/s

	Cornus			
Density	d	a_y	$\overline{C_{de}}$	$\overline{C_d}$
Low	0.006	0.116	1.103	4.667
Medium	0.007	0.078	1.147	3.360
High	0.007	0.039	1.267	1.851

Table 3.7: Cornus C_{de} modification (assuming $C_d = 1.0$) using data from $Q = 20$ l/s

3.6.3.2 Power relationships

An improvement to the Richter bulk drag coefficient ($\overline{C_{de}}$) is the power law equation proposed for vegetation arrays by Turner et al. (1978), and adopted by several later authors including Smith et al. (1990), Kadlec (1990), James et al. (2004) and Jordanova et al. (2006). The following formulation is proposed by Jordanova et al. (2006) for single plants:

$$\overline{C_{di}} = \alpha Re^{\beta} \tag{3.41}$$

Where $\overline{C_{di}}$ is here termed the Improved bulk drag coefficient, Re_b is the stem Reynolds number modified using the solid volume fraction (ϕ) and α and β are power law coefficients relating to the shape of the plants. Jordanova et al. (2006) applied Equation 3.41 in drag force studies into single reed stems with and without leaves. α and β are coefficients. Although the approach was proposed for single plants, this formula can be applied to the measured data of model tree arrays. The α and β coefficients fitted to the data are shown in Table 3.8 with R^2 values greater than 0.99. The curves are presented in Figure 3.25.

Density	α	β
dowel Low	5.537×10^7	-2
dowel Medium	2.447×10^7	-2
dowel High	0.584×10^7	-2
Cornus Low	2.950×10^{10}	-3.228
Cornus Medium	0.874×10^{10}	-3.244

Table 3.8: α and β coefficients for fitted dowel and *Cornus* data

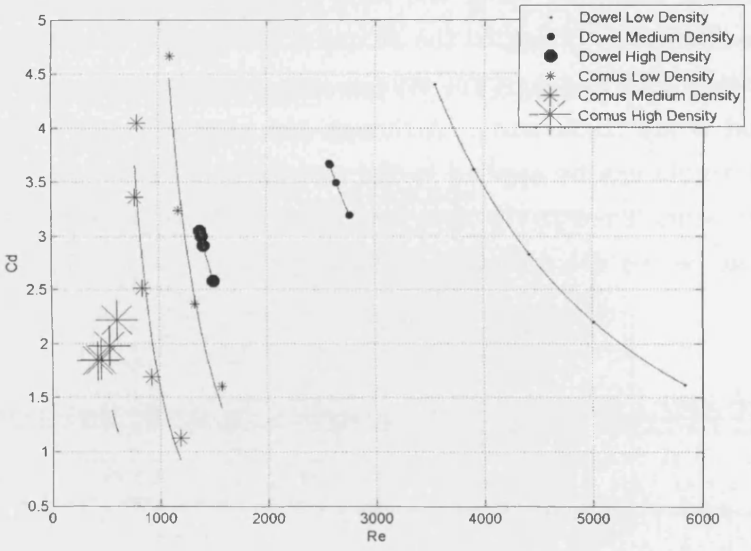

Figure 3.25: Fitted power curves to variation of the Improved bulk drag coefficient (C_{di}) vs. stem Reynolds number (Re_d). Dowel $d = 25mm$ and Cornus. $d = 9mm$

Looking at the coefficient values (with the exception of the results for high density *Cornus* array) in Table 3.8, it can be seen that the β coefficient has a constant value for the two different forms of single stem dowels and multi-stem *Cornus*, suggesting it is shape related. The α coefficient is then a term that is influenced by the spacing, and potentially also by the Reynolds number.
A simple procedure is proposed to determine the drag coefficient of non flexible single stem and multi-stemmed vegetation.

1. Photograph plant specimen (preferably in situ)
2. Determine average stem diameter and total projected area
3. Use Table 3.8 to obtain α and β coefficients based on spacing and form (single or multi-stemmed
4. Calculate Improved bulk drag coefficient $\overline{C_{di}}$ from Equation 3.41

Although clearly limited in scope to plant species that fit the forms of single vertical tree stands or multistemmed species that fit the growth pattern of *Cornus sanguinea*, this procedure and the tables of α and β coefficients has scope to be expanded to include other species.

3.7 Upscaling Results to Floodplain Woodland Scale

Field scale studies are subject to a high degree of uncertainty and logistical problems inherent in on-site data collection. Upscaling the results from the experiments of the model tree arrays presented in this Chapter gives a guide to the hydraulic resistance of field scale tree arrays. Geometric, kinematic and dynamic similitude need to be maintained in the scaling process for optimum scaling. However, not all processes scale at a similar rate. The dominant processes are identified and dimensional analysis applied according to the principle of dimensional homogeneity.
For free surface flows where flow is dictated by the ratio of inertial to gravitational forces and the friction due to kinetic viscosity is key, thus the two ratios of greatest relevance are the Reynolds number Re and the Froude number F_r ASCE (2000). This will allow the laboratory results obtained (model scale) be directly applied to the field situation (prototype scale).
Froudian length scaling of 1:8 provides field scale planting densities as recommended by Rodwell & Patterson (1994) for both forest farming (including biomass production) and broadleaf plantation densities. If a length scale ratio of 1:8 is chosen, the

diameter of the dowel will be equivalent to $d = 203.2$ mm, representing an established single stem tree, and the average projected diameter per multi-stem *Cornus* will be equivalent to 5 stems each of $d = 40$ mm. Table 3.9 contains the scaled values for the medium density planting density arrays of dowel and *Cornus* at the experimental discharge of 20 l/s. Note the large divergence of Reynolds number. This is an inherent problem with dimensional scaling. Full values of all dimensionalised stage discharge data are given in the Appendix in Table 11.

	h_m m	U_m m/s	Re_{dm}	h_p m	U_p m/s	Re_{dp}	Fr
D2	0.159	0.106	4770	1.272	0.212	42400	0.085
V2	0.140	0.120	840	1.120	0.240	9600	0.102

Table 3.9: Dowel and *Cornus* medium density scaling from Model (m) to Biomass Prototype Scale (p) (1:8) using data from Q = 20 l/s

With the *Cornus sangiunea* experiments, the average diameter of individual stems is approximately 5 mm. Flows within the *Cornus* canopy are closing towards the transition zone of turbulence ($Re_d < 200$). For flow conditions where the Reynolds number is above 200, the drag coefficient remains fairly constant as the drag is mainly reliant on the shape of the obstacle (Massey 1997). Through and below the transition zone into the laminar zone, the skin friction effect becomes increasingly more dominant, and the drag coefficient will increase with decreasing Reynolds number.

Figure 3.26 presents the projected area (A_{xyz}) per plan m^2 of ground at flow depth z. The projected area of the respective tree forms at the same density are almost equivalent. Figure 3.27 presents the variation of volume with flow depth. The volume of the dowel planting arrays are all significantly larger in magnitude than the *Cornus* arrays. This has consequences for a floodplain woodland intended for harvesting purposes such as biomass production.

Figure 3.28 presents the prototype scale variation in low depth y with Velocity m/s for velocities within the field-scale planting densities up to velocity $\overline{U} = 0.71$ m/s. For the high densities of single stem and multi-stem, a proportional similarity can be observed at all flow depths, and as the flow depth decreases, the velocity increases. In the medium density arrays, as the flow depth increases, there is a divergence in the respective velocities of the medium density single stem (dowel) array, and the medium density multi-stem (*Cornus*) array. The single stem array experiences a slight reduction in velocity with increasing flow depth, while the multi-stem array experiences rapidly increasing velocity, which appears to reach an asymptotic value

above a flow depth of 1.5 m. Within the low density arrays, as the flow depth increases, the velocity increases, although the rate of increase reduces, and the flow depth appears to reach an asymptotic value for both the single stem (dowel) and multi-stem (*Cornus*) arrays.

The two clear patterns suggests there is a fundamental difference in the flow regimes. It appears to relate to the Reynolds number of flow. The velocity is calculated from the mean-area velocity including the blockage effect from the presence of the vegetation. At the high density arrays, a relatively small range of velocities were recorded for a large range of discharges. Small changes in the velocity result in large changes in the flow depth, while in the low density arrays, an increase in flow depth is associated with an increase in velocity. Regarding the passage of a flood wave through an area planted at the high density, it follows that the high density array will have a proportionally bigger effect at retarding the mean velocity of a floodwave at a range of flood peak discharges, when compared to the low planting density. In terms of flood warning, this provides extra time to warn downstream landowners and communities.

Figure 3.29 presents the calculated values of bulk roughness coefficient the Darcy-Weisbach friction factor f, plotted against velocity, calculated by incorporating the blockage effect from the occupied volume of vegetation. The results illustrate the limitations of applying bulk roughness coefficients to vegetated flows. Assuming the validity of Froude scaling, f undergoes a rapid change in value for the high biomass planting densities, for both the single stem (dowel) and multi-stem (*Cornus*) arrays. Only at the low planting densities is a uniformly constant value found. f is seen to decrease slightly with increasing velocity.

Figure 3.30 presents the data for bulk drag coefficient ($\overline{C_d}$) against mean-area velocity ($\overline{U}$). As the velocity increases, the bulk drag coefficient ($\overline{C_d}$) decreases. Increasing the planting density reduces the velocity relative to the flow depth.

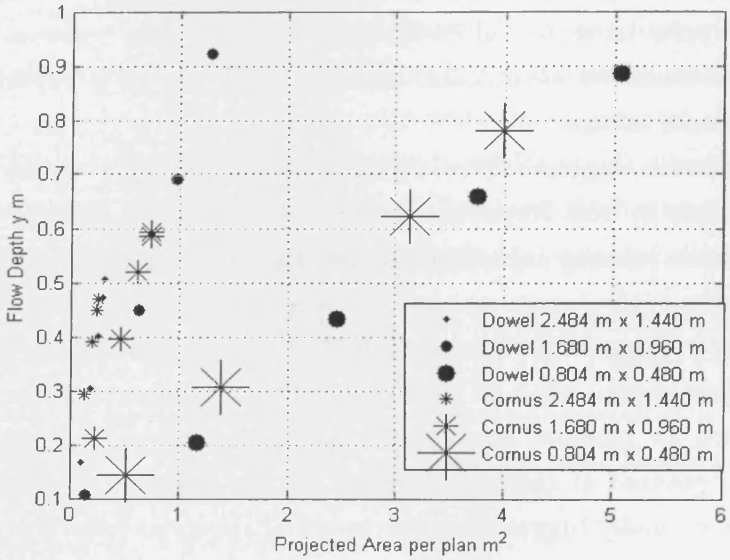

Figure 3.26: Model to Field Scale (1:8): Projected Area (A)

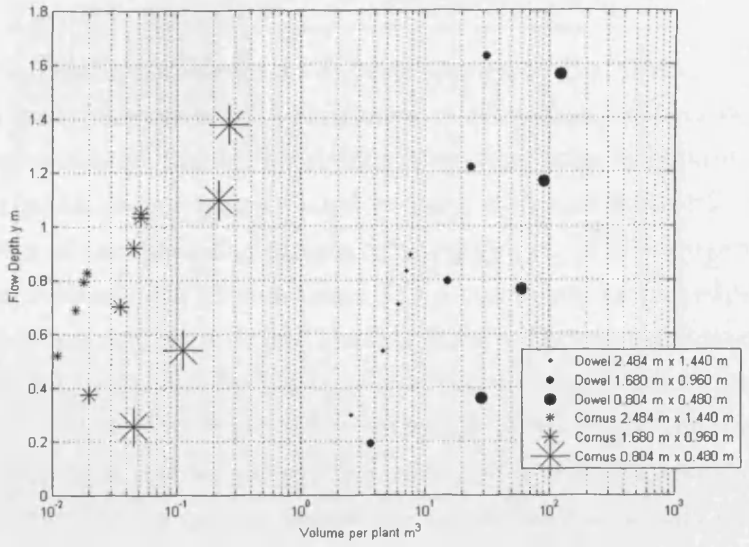

Figure 3.27: Model to Field Scale (1:8): Volume (Vol)

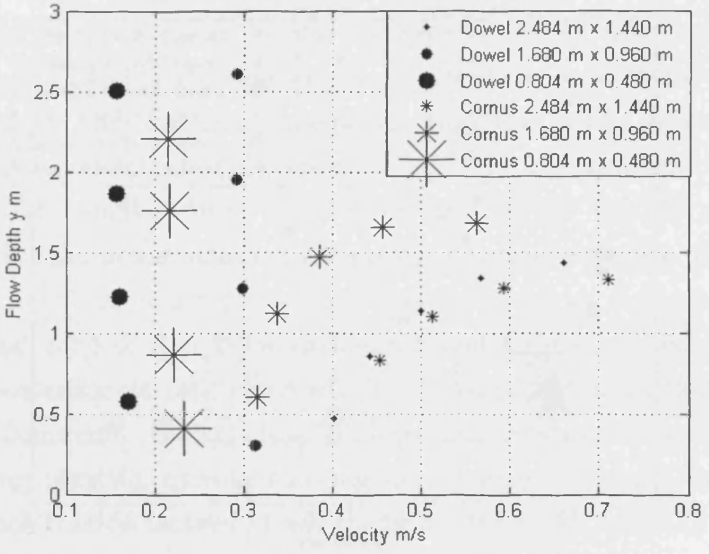

Figure 3.28: Model to Field Scale (1:8): Top, flow depth with velocity; Bottom, variation of projected area (A) with flow depth

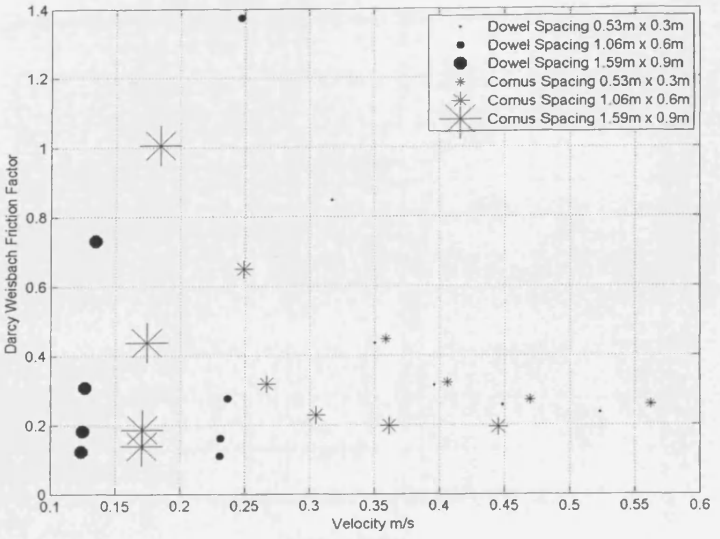

Figure 3.29: Model to Field Scale (1:8): Variation of f against average flow field velocity (U)

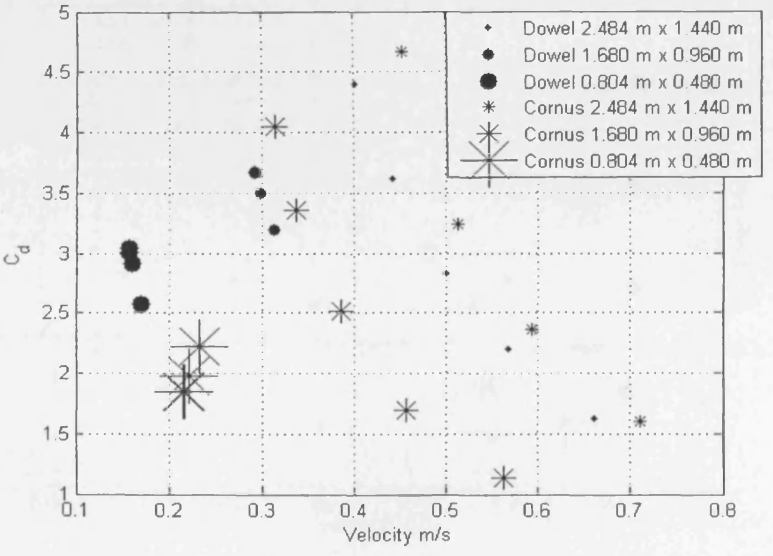

Figure 3.30: Model to Field Scale (1:8): Variation of drag coefficient (C_d) against velocity

3.8 Conclusions from Roughness Relationships and Derivations

A number of roughness derivations have been applied to the measured data. The aim of the study was to investigate roughness relationships, and move towards a generic and representative system for determining vegetative roughness. Applying bulk roughness values to vegetation should be done with care and with reference to the sophistication of the modelling system to be employed. While roughness factors such as the Darcy-Weishbach friction factor (f) is commonly employed to represent roughness in river studies, for low and shallow flows with tree roughness, the drag coefficient approach is more appropriate where vegetation extends throughout the water column (Petryk & Bosmajian 1975), although in this study, the magnitude of the bulk drag coefficient was found to be a function of flow depth and the Reynolds number. In the study of the *Cornus* arrays, the plants have been fully characterised in terms of projected area, diameter and volume, and this has enabled the drag coefficient to be calculated based on the average stem Reynolds number. Although the projected areas of the *Cornus* and dowel arrays are close in magnitude, the resistance effects are very different due to the differences in diameter and volume.
The present study has been hindered by a number of limitations including the uneven flume bed enabling only quasi-uniform flow to be established, and the presences of waves at higher velocities. Carrying out the experiments at uniform flow conditions limits the range of Reynolds numbers investigated for each model tree type and planting density. This has the consequence that the results based on Reynolds numbers are not comparable between densities. The experiments cover the range of stem Reynolds numbers from Re_d 400 to 1600 for the *Cornus* arrays and Re_d 1300 to 5900 for the dowel arrays. Care should be taken with the upscaled results, the range of Reynolds numbers for the *Cornus* arrays in particular fall towards the transitional zone of flow between laminar and turbulent flow (Massey 1997), although all experiments take place within the vortex-shedding zone of Re where form drag is dominant. General relationships and trends can however be derived, with increasing planting density showing an increase in roughness value for the Darcy-Weisbach friction factor (f) and the bulk drag coefficient ($\overline{C_d}$). In particular, the power relationship derived in Section (3.6.3.2) provides a simple framework within which to continue to explore drag coefficient relationships with stem Reynolds number.

4

Velocity and Turbulence Measurements of Scaled Single Stem and Multi-stem Tree Arrays

4.1 Flow Measurements in Model Tree Arrays

4.1.1 Introduction

Hydrodynamics of vegetated flows (where vegetation present in a water column) includes the study of velocity and turbulence profiles around plants under different hydrodynamic conditions. The sampling of vegetated flows in order to characterise the velocity and turbulence field can be carried out directly using rotating flow profilers, or preferably, by employing non-invasive point sourcing techniques, such as Laser Doppler Velocimetry (LDV) or Acoustic Doppler Velocimetry (ADV). However, the optimum sampling locations within simulated and real vegetative arrays is a subject not thoroughly explored in the hydraulics literature. Knowledge of the temporally and spatially averaged velocity statistics allows us to begin to understand the complex flow processes that govern vegetation-flow interactions.

Sediment transport, biological processes and the dispersion of materials within the water column are all directly related to the nature of the velocity field. Spatially-averaged measurements from arbitrarily selected locations may not fully represent the complete flow field. To be successful, sampling must be sensitive to field in both space and time. In a study into flow though simulated vegetation, Lopez & Garcia (2001*a*) noted that detailed descriptions of measurement locations and the spatial averaging procedure employed were lacking from the literature. Righetti & Armanini (2002) in a study investigating the hydraulic resistance of submerged vegetation noted that in many studies, local measurements have been implicitly considered as representative of the entire flow field. For example, in studies investigating simulated vegetative roughness with regularly spaced dowels using an ADV, Stone & Shen (2002) sampled in two locations, Fairbanks (1998) used six locations, Westwater (2000) used seven sampling locations and Poggi et al. (2004) used eleven locations. Fairbanks (1998) and Westwater (2000) give no specific justification for choosing their locations. Stone & Shen (2002) initially sampled at three locations, and found that an average of two of these matched the known channel average velocity. Poggi et al. (2004) concentrated measurements close to the dowels, where there is a higher spatial variability of velocity.

4.1.2 Scope of the Chapter

This Chapter investigates the velocity and turbulence characteristics around simulated and real tree arrays. The focus has been on obtaining a relatively large amount of point measurements, sampled using an ADV, in order to fully characterise the field of flow. In the first part of the Chapter, the full, depth averaged, and volume averaged results from the experiments are presented. The second part explores different sampling techniques to obtain the optimum representation of the flow field from between three and only a few sampling locations. The aim is to use the data collected to compare a selection of measurement locations (between three and eleven) against the whole flow field, with the view to obtaining an optimum sampling regime through comparison of partial and full flow field velocity and turbulent kinetic energy.

4.2 Sampling Methodology

In Chapter 3, staggered arrays of single stem model trees (25 mm diameter dowels) and multi-stemmed model trees (*Cornus* samplings) were arranged in three different

planting densities in the flume depicted in Figure 4.1.

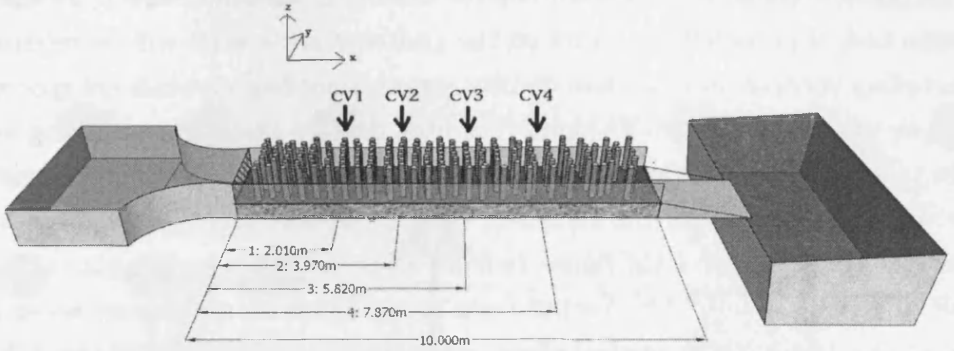

Figure 4.1: Schematic of Hydraulic Flume indicating locations of Sampling Control Volumes CV1, CV2, CV3 and CV4

Figure 4.2 indicates the sampling control volumes for the high density and medium density arrays investigated. Each model tree array/planting density combination was sampled at two flow depths. For the single stem dowel arrays, a single control volume ($CV3$) was sampled in each experiment at both a high flow depth and a low flow depth. The expected increased spatial heterogeneity of the flow field among the multi-stemmed *Cornus sanguinea* saplings required more than one control volume to be sampled. For the high flow depths, four control volumes were chosen for both the high and medium density model tree arrays ($CV1$, $CV2$, $CV3$ and $CV4$) . For the lower flow depth, two control volumes were selected ($CV2$ and $CV3$).
Uniform flow (where the flow depth is constant throughout the flume) was established at a range of discharges. From the combinations of flow depth and discharge that provided uniform flow conditions, the stage-discharge relationship for each model tree type and planting density was determined. The relationships obtained are presented in Chapter 3 Figure 3.16.
From the collected stage-discharge data, flows depths (and corresponding discharges) for each model tree type/ planting density combination were chosen for more detailed investigation using ADV sampling of velocity and turbulence. Only the medium and high density array set-ups were chosen for velocity measurement sampling, as the flow depth for the low density arrays proved too shallow for effective deployment of the Vectrino. A 200 Hz vertical plane Nortek Vectrino, on loan from Nortek UK,

was employed to sample the flow field within each control volume. A plan view of the measurement zone of each control volume is identified in Figure 4.3. Each intersection of perpendicular lines on the grid represents what will be referred to as a *sampling vertical.* For medium density arrays, sampling verticals are spaced every 2 cm in the horizontal (X-Y) plane. For high density arrays the sampling verticals were taken every 1 cm throughout the horizontal (X-Y) plane of measurements. In the vertical (Z) plane of the sampling vertical, measurements were taken at 2 cm intervals from the bed of the flume, to 5 cm below the water surface (the operational limit of the Vectrino). The Vectrino was mounted on an automated system which moved the device in the vertical plane. At each sampling vertical on the X-Y plane, the carriage was initially set to record the point velocity field near the bed. At each measurement location the flow field was recorded for a minimum of 45 s. Between each measurement location the carriage moved the Vectrino at a speed of 2 mm/s. This transition velocity was kept low to minimise disruption to the flow field under measurement.

Figure 4.1 is a schematic of the flume indicating the locations of the sample control volumes $CV1$, $CV2$, $CV3$ and $CV4$. In the physically uniform dowel model tree array, a single control volume $CV3$ was sampled at each model tree type/ planting density combination (Experiments $D2b-c$ and $D3d-c$), with the dowel orientation as depicted in Figure 4.2, with the downstream dowel on the right hand side. The variable growth patterns of the *Cornus* saplings introduced a greater degree of spatial heterogeneity within the flow field. Consequently, up to four control volumes were sampled at each *Cornus*/ planting density combination (Experiments $V2b-g$ and $V3b-g$). In control volumes $CV2$ and $CV3$, the *Cornus* plants are orientated as in Figure 4.2, with the downstream *Cornus* on the right hand side. In control volumes $CV1$ and $CV4$, the *Cornus* saplings are oppositely orientated, with the downstream *Cornus* sapling on the left hand side. Table 4.1 lists the flume settings and flow conditions for each measurement.

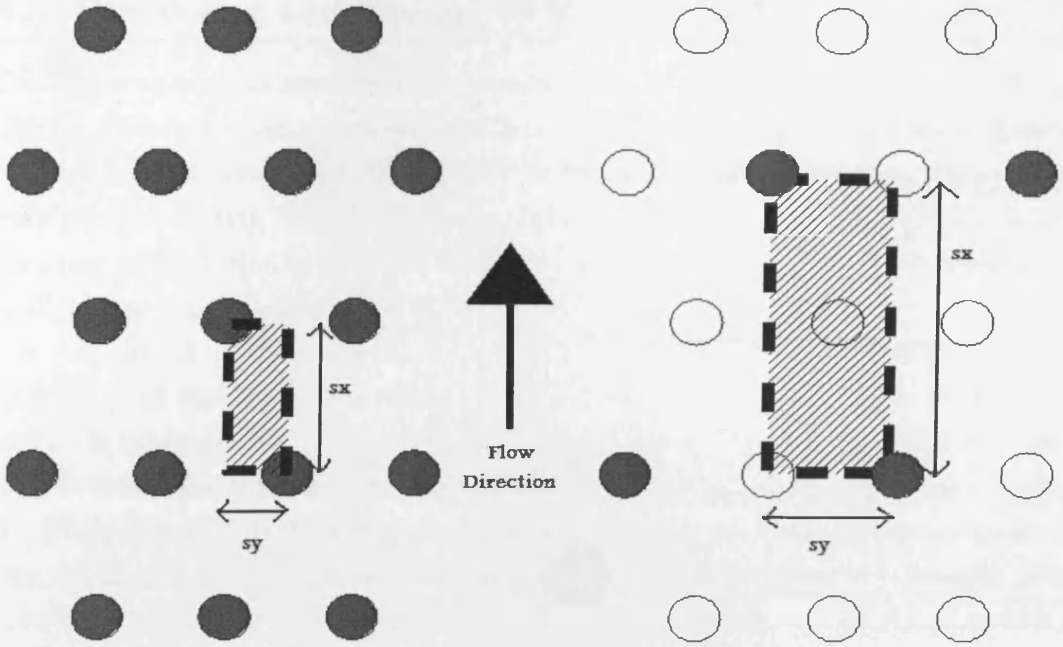

Figure 4.2: Plan view of high and medium density dowel arrays. Hatched area indicates typical sampling control volume

Exp.	Type	CV	Density	Depth	s_x	s_y	weir	depth	Q
					mm	mm	mm	mm	m^3/s
D2g	dowel	3	medium	low	0.210	0.120	115	135	0.017
D2d	dowel	3	medium	high	0.210	0.120	200	235	0.029
D3g	dowel	3	high	low	0.105	0.060	170	175	0.011
D3d	dowel	3	high	high	0.105	0.060	235	215	0.014
V2f	Cornus	2	medium	low	0.210	0.120	100	149	0.022
V2g	Cornus	3	medium	low	0.210	0.120	100	149	0.022
V2b	Cornus	1	medium	high	0.210	0.120	130	187	0.032
V2c	Cornus	2	medium	high	0.210	0.120	130	187	0.032
V2d	Cornus	3	medium	high	0.210	0.120	130	187	0.032
V2e	Cornus	4	medium	high	0.210	0.120	130	187	0.032
V3f	Cornus	2	high	low	0.105	0.060	160	195	0.018
V3g	Cornus	3	high	low	0.105	0.060	160	195	0.018
V3b	Cornus	1	high	high	0.105	0.060	230	275	0.025
V3c	Cornus	2	high	high	0.105	0.060	230	275	0.025
V3d	Cornus	3	high	high	0.105	0.060	230	275	0.025
V3e	Cornus	4	high	high	0.105	0.060	230	275	0.025

Table 4.1: Laboratory Settings for dowel Arrays and *Cornus* Arrays

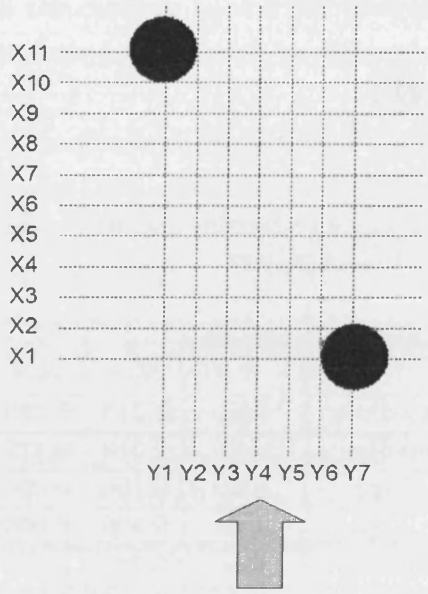

Figure 4.3: Plan view of the horizontal (X-Y) sampling plane indicating transect lines

4.3 Processing and filtering of Vectrino data

The Vectrino records instantaneous velocity data in three dimensions at a rate of 200 Hz. Measurements were taken for at least 45 s. The time series data collected requires pre-processing and checking before further analysis can occur. The results were processed using WinADV (version 2.025). As there was one data file for each sampling vertical, this required division into individual depths. Flags were employed to divide up the data file and give the output for each depth.

The correlation (COR) and signal to noise ratio (SNR) are indications of the uniformity of the signal and signal strength respectively. Data with poor COR and SNR values (COR < 70 and SNR < 5) are less likely to be representative. The results were filtered using three criteria: COR less than 70; SNR less than 7; and the Phase Space Threshold de-spiking method (Goring & Nikora 2002). Data at a flow depth of $z = 15$ *cm* above the base was highly distorted due to resonance. All data collected at $z = 15$ *cm* was removed and replaced with an interpolation from the flow depths above and below $z = 13$ *cm* and $z = 17$ *cm*.

4.4 Definition of Velocity and Turbulence Parameters

The components of velocity are the mean streamwise velocity (U), mean cross-streamwise velocity (V) and mean vertical velocity (W). The mean of the turbulent fluctuations of flow in the three dimensions are denoted as streamwise turbulence u', cross-streamwise turbulence v', and vertical turbulence w'. The turbulent kinetic energy is a measure of the kinetic energy of turbulent eddies in the flow per unit fluid mass, given by:

$$TKE = \frac{\overline{u'^2} + \overline{v'^2} + \overline{w'^2}}{2} \tag{4.1}$$

The velocity and turbulence measurements from the single stem dowel and multi-stem *Cornus* arrays can be averaged in space in the following manner. A depth averaged parameter will be denoted by $\overline{U}_z$, where:

$$\overline{U}_z = \frac{1}{n} \sum_{z=1}^{z_{max}} \overline{U}_{xyz} \tag{4.2}$$

Where the overbar represents the depth averaging, n is the number of layers over which the velocity is averaged. A horizontal-plane averaged variable will be denoted by $\overline{U}_{xy}$, where:

$$\overline{U}_{xy} = \frac{1}{n} \sum_{x,y=1}^{x,y_{max}} \overline{U}_{xyz} \tag{4.3}$$

A volume-averaged variable denoted by $\overline{U}_{xyz}$, where:

$$\overline{U}_{xyz} = \frac{1}{n} \sum_{x,y,z=1}^{x,y,z_{max}} \overline{U}_{xyz} \tag{4.4}$$

Equations 4.2 to 4.4 can be equally applied to the average turbulent fluctuations u' and the Turbulent Kinetic Energy TKE. The preferred averaging method is dependent on the end use of the data.

The depth-averaged parameter $\overline{U}_z$ is averaged over depth and is directly applicable to depth averaged 2-D numerical modelling of flow through vertically-regular obstacles (obstacles that do not change their shape over depth) extending throughout the water column. In this situation, there may be significant changes in the streamwise and lateral planes as flow is diverted around the obstacles, but mixing in the vertical plane is expected to be limited.

The horizontal-plane averaged parameter $\overline{U}_{xy}$ may be the most insightful if there is vertical irregularity in the obstacle through the depth, and there is reason to consider the variation in shear stress throughout the water column. Reasons for this could be the presence of a mobile bed, or the presence of organisms that are sensitive to areas of high shear stress. For example, a plant with a top-heavy biomass distribution will divert flow towards the lower part of the water column, potentially causing scour and disturbing benthic communities, but providing shelter for organisms which favour feeding amongst vegetation in free flowing water. Conversely, a plant with a bottom-heavy biomass distribution will divert flow towards the upper part of the water column, preventing scour and protecting bethic communities.

The volume averaged parameter $\overline{U}_{xyz}$ is useful to compare overall flow characteristics in the model tree type/ planting density combinations. Regarding modelling, $\overline{U}_{xyz}$ is applicable to models of sub-grid modelling of large flow areas, where each cell is larger than the scale of flow processes at plant level.

The number of measured vertical profiles taken varies between the experiments with dowels and the experiments with the multi-stem *Cornus* saplings. In the dowel arrays, 69 vertical profiles were sampled in each experiment, spaced 2 cm in the medium density arrays and spaced every 1 cm in the high density arrays. In the *Cornus* arrays, 77 vertical profiles were sampled in each experiment. The additional

profiles measured in the *Cornus* array could not physically be measured in the dowel arrays due to obstruction from the dowels. In this section, the velocity and turbulence measurements from the dowel and *Cornus* arrays are discussed in in terms of their volume-averaged ($\overline{U}_{xyz}$, u'_{xyz} and $\overline{TKE}_{xyz}$) depth-averaged ($\overline{U}_z$, $\overline{u'_z}$ and $\overline{TKE}_z$) and horizontally-averaged profile ($\overline{U}_{xy}$, $\overline{u'_{xy}}$ and $\overline{TKE}_{xy}$) parameters. Examining the depth-averaged and horizontally-averaged spatial averaging options gives an appreciation of the degree of heterogeneity of the flow field.

According to the stem Reynold's number, the wake pattern for both the medium and high density arrays lie within the vortex-shedding zone, as all the values of Re lie within the turbulent wake zone, therefore comparisons between the two densities are valid. Comparisons can thus be made within and between the dowel and *Cornus* flow field characteristics as depth and stem Reynolds number varies within the range of vortex shedding . Variations within the *Cornus* canopy, and variations in flow characteristics for different flow depths at the same point in the array can also be analysed.

4.4.1 Statistical Analysis

The aim is to find the sampling location or locations where taking measurements will consistently provide both good velocity and turbulence measurements. The optimal samples (those that provide the closest match to streamwise velocity and turbulent kinetic energy) will be compared using a range of techniques. The volume averaged values of Streamwise velocity (U) and Turbulent Kinetic Energy (TKE) will be compared against the full flow field volume averaged results. Comparing volume averaged values has a limitation in that the flow profile throughout the depth may not be adequately represented, therefore the 'fit' to the plan averaged vertical profile will also be computed.

To determine the optimal sampling regime, it is useful to obtain the statistical distribution of flow variables. Determining skewness, standard deviation of results and interquartile range from the array can give an indication as to how successful a random approach will be. Figures 4.4 and 4.5 display box plots indicating the distribution of streamwise velocity and turbulent kinetic energy for depth averaged data from sampled verticals.

The box itself represents the median value by the central line. The box limits are the upper and lower interquartile limits. The whiskers extend to include all data within 1.5 times the value of the interquartile limits. Data that are considered outliers are represented by crosses. There are two results from the box plots displayed that can inform sampling. The first is the majority of sampling volumes are negatively skewed. Secondly, the number of outliers is high. Sampling outliers would compromise the representativeness of any sampling strategy. Tabulated statistical values are given in Tables 4.2 and 4.3. Deviation is measured both using the standard deviation (Std) and the interquartile range (Iqr). Due to the high proportion of values classified numerically as outliers, the Iqr presents a more robust method of checking deviation. Skewness is a measurement of the asymmetry around the sample mean and kurtosis is a measurement of the proportion of outliers.

The distributions of streamwise velocity measurements are consistently negatively skewed around the mean, and heavily out lier prone in most instances for both the dowel and Cornus arrays. The results for the turbulent kinetic energy are positively skewed and also subject to outliers, however they vary independently. Thus while the velocity measurements may be accurately represented, the turbulent characteristics of the flow may not be. This may adversely affect results obtained. For example, Stone and Shen (2002) selected their sampling pattern based on matching recorded

velocity measurements with the streamwise averaged velocity. Figures 4.4 to 4.5 and Table 4.2 are based on the depth-averaged values. It is also necessary to accurately capture the vertical profile of flow characteristics. The shape of the plan-averaged vertical profile will provide information on depths of low and high flow areas, locations of shear stress, and at which flow depths turbulent flow structures are dominant. It is possible that although the depth-averaged values are well fitted, the shape of the sampled measurements will not reflect the plan averaged profile. For 2-D and 3-D numerical modelling, the accurate capture of flow variation throughout the depth is critical for calibration and validation of vegetated flows.

To give an indication of the fit of the the sampled profile to the full flow field results, the χ^2-test is applied. The χ^2-test is used to test homogeneity and goodness of fit between observed and expected results.

$$\chi^2 = 2\sum \frac{(O_i - E_i)^2}{E_i} \tag{4.5}$$

In Equation 4.5, i represents a flow depth, O_i is the observed variable at that depth and E_i is the expected variable at that depth, as calculated from the full sample. χ^2 therefore takes into account any deviation of the sampled profile from the full sample profile. Matching the streamwise velocity will be easier than matching turbulent kinetic energy. Any systematic or stochastic sampling regime with sampled values in outlier-prone flow regions will be at a high risk of unrepresentative results.

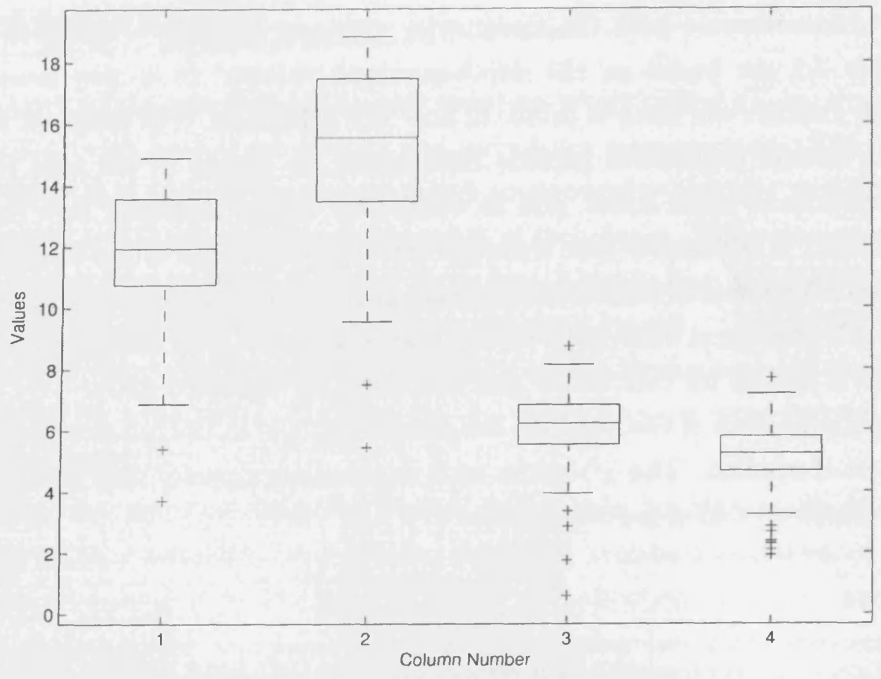

(a) From left: high density low depth, high density high depth, medium density high depth and medium density low depth

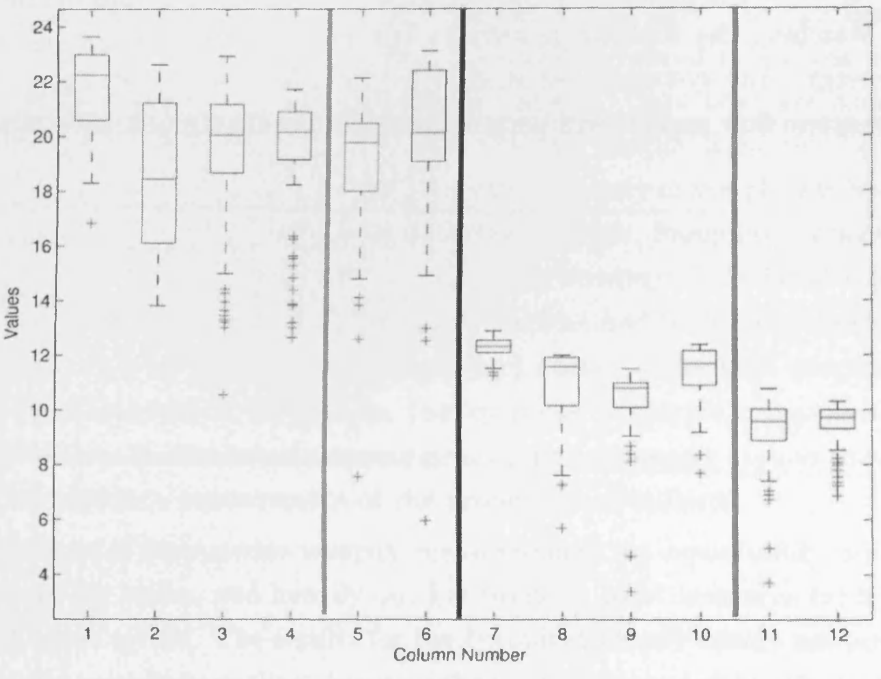

(b) Columns from left: high density high depth, high density low depth, medium density high depth and medium density low depth

Figure 4.4: Box Plots showing data median, interquartile range and outliers for streamwise velocities in Dowel and Cornus arrays. 'Values' refers to mean velocity

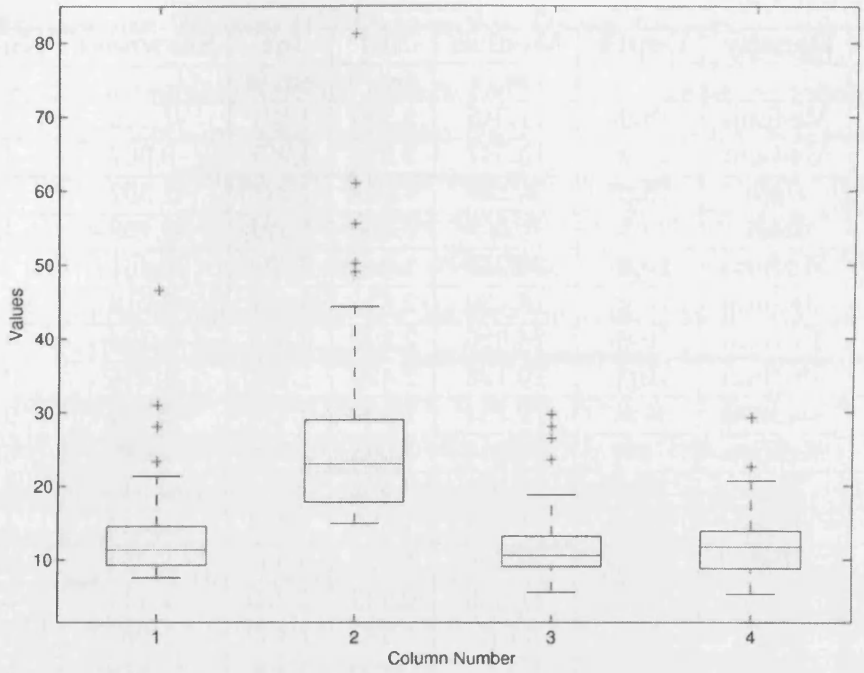

(a) From left: high density low depth, high density high depth, medium density high depth and medium density low depth

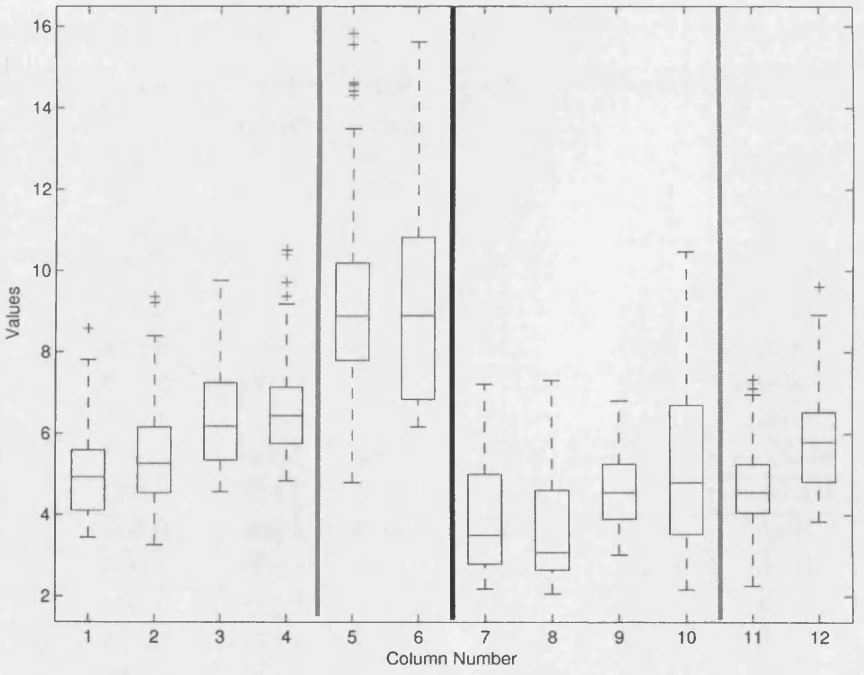

(b) Columns from left: high density high depth, high density low depth, medium density high depth and medium density low depth

Figure 4.5: Box Plots showing depth-averaged data median, interquartile range and outliers for turbulent kinetic energy in dowel and Cornus arrays. 'Values' refers to mean TKE

Exp.	Density	Depth	Median	Std	Iqr	Skewness	Kurtosis
			cm/s	cm/s	cm/s		
D2d	Medium	High	11.946	2.190	2.831	-1.330	5.286
D2g	Medium	Low	15.547	2.778	3.987	-0.967	4.117
D3d	High	High	6.226	1.379	1.275	-1.392	6.390
D3g	High	Low	5.235	1.200	1.121	-0.760	3.490
V2b	Medium	High	22.230	1.744	2.424	-0.461	2.189
V2c	Medium	High	18.439	2.615	5.107	-0.018	1.679
V2d	Medium	High	20.026	2.898	2.512	-1.124	3.558
V2e	Medium	High	20.138	2.420	1.744	-1.416	3.844
V2f	Medium	Low	19.754	2.399	2.477	-2.169	9.876
V2g	Medium	Low	20.114	3.008	3.308	-1.910	8.718
V3b	High	High	12.302	0.362	0.454	-0.515	3.156
V3c	High	High	11.556	1.395	1.759	-1.442	4.800
V3d	High	High	10.776	1.319	0.907	-3.451	16.977
V3e	High	High	11.676	0.943	1.259	-1.711	6.558
V3f	High	Low	9.572	1.283	1.132	-1.968	8.105
V3g	High	Low	9.721	0.809	0.705	-1.478	4.399

Table 4.2: Statistical volume averaged values for streamwise velocity

Exp.	Density	Depth	Median	Std	Iqr	Skewness	Kurtosis
			cm/s	cm/s	cm/s		
D2d	Medium	High	11.338	6.221	5.269	2.842	13.806
D2g	Medium	Low	23.055	12.168	11.129	2.147	8.588
D3d	High	High	10.579	4.840	4.123	1.808	6.876
D3g	High	Low	11.721	4.283	5.088	1.215	5.927
V2b	Medium	High	4.933	1.180	1.487	0.794	3.610
V2c	Medium	High	5.257	1.398	1.612	0.844	3.295
V2d	Medium	High	6.178	1.422	1.906	0.703	2.635
V2e	Medium	High	6.432	1.632	1.385	1.791	6.601
V2f	Medium	Low	8.881	2.264	2.396	1.182	4.063
V2g	Medium	Low	8.893	2.516	3.979	0.652	2.556
V3b	High	High	3.508	1.354	2.208	0.809	2.541
V3c	High	High	3.084	1.532	1.955	1.019	2.672
V3d	High	High	4.543	0.894	1.351	0.304	2.409
V3e	High	High	4.7925	2.010	3.174	0.571	2.483
V3f	High	Low	5.818	3.170	4.220	0.789	2.609
V3g	High	Low	6.410	2.097	1.593	1.443	4.385

Table 4.3: Statistical volume averaged values for Turbulent Kinetic Energy

4.4.2 Streamwise Velocity (U) Data within Dowel Arrays

The dowel depth-averaged velocity data normalised by volume-averaged velocity (U_{xyz}), with the depth-averaged horizontal plane (U, V) velocity vectors superimposed, are presented in Figure 4.6. A large degree of variation in streamwise velocity is visible. There is a clear difference in flow field between medium density (N = 19.8 m^{-2}) (a) and (b), and the high density (N = 80.6 m^{-2}) (c) and (d). There is a clearly defined area of high velocity flow between the dowels in the medium density (N = 19.8 m^{-2}) pair, although some sheltering is evident from the darker areas in line with the dowels. In contrast with this, the high density (N = 80.6 m^{-2}) pair display a much higher degree of sheltering, with the flow field indicated by the vectors, affected laterally and not just in the streamwise direction. The area of highest flow in all plots lies in the area laterally adjacent to each dowel.

Figure 4.7 presents all the normalised vertically sampled profiles. The distribution of streamwise velocities throughout the control volume can be seen. The diagrams give an indication of the spatial heterogeneity of the flow. Each thin line represents a sampled vertical (measurements taken along the vertical z plane). The thick line marked with circles represents the horizontally-averaged profile (U_{xy}), in which each plotted point is the mean value of all measurement points within its respective horizontal plane. The distribution of the vertical profiles does not follow a normal distribution - in all instances the mean value is slightly skewed higher than the median value.

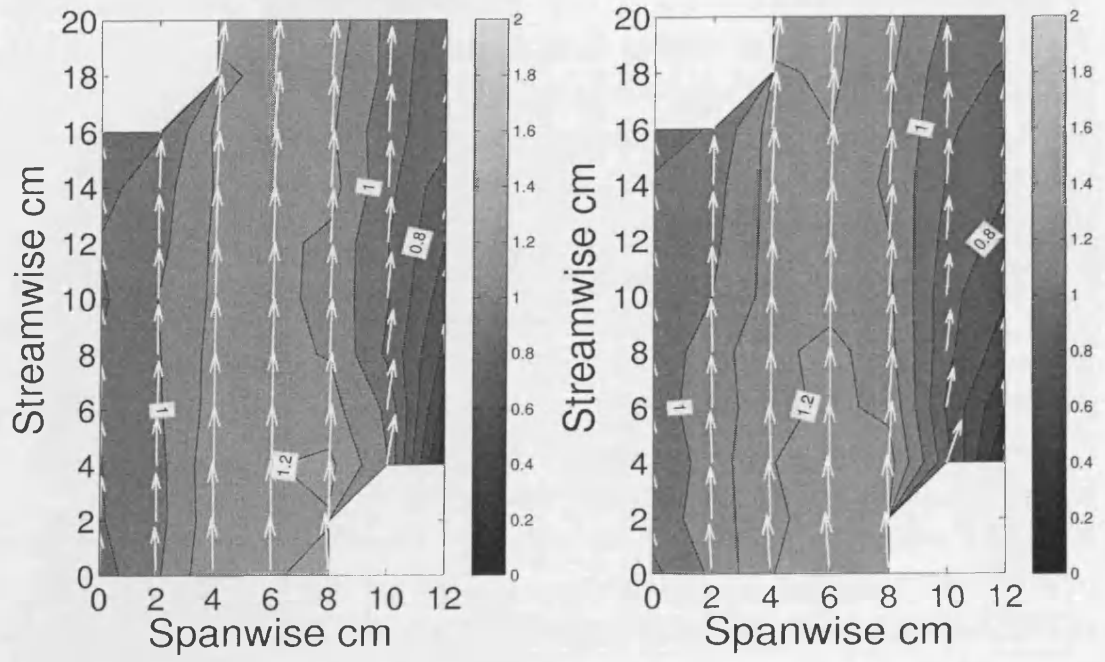

(a) Dowel, N=19.8 m^{-2}, low depth

(b) Dowel, N=19.8 m^{-2}, high depth

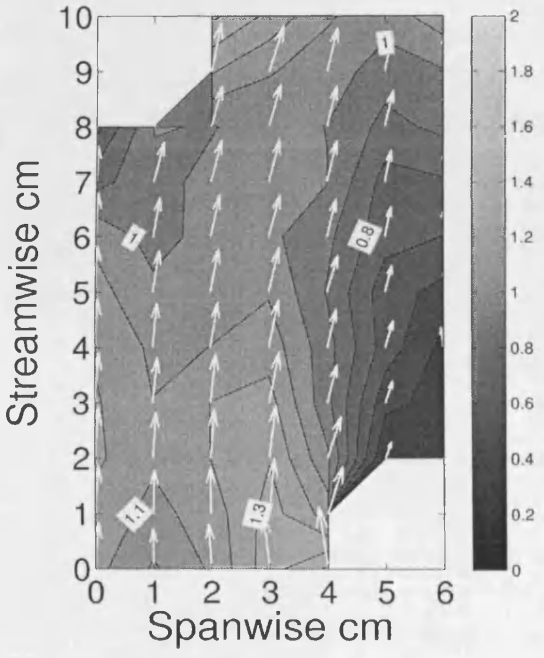

(c) Dowel, N=80.6 m^{-2}, low depth

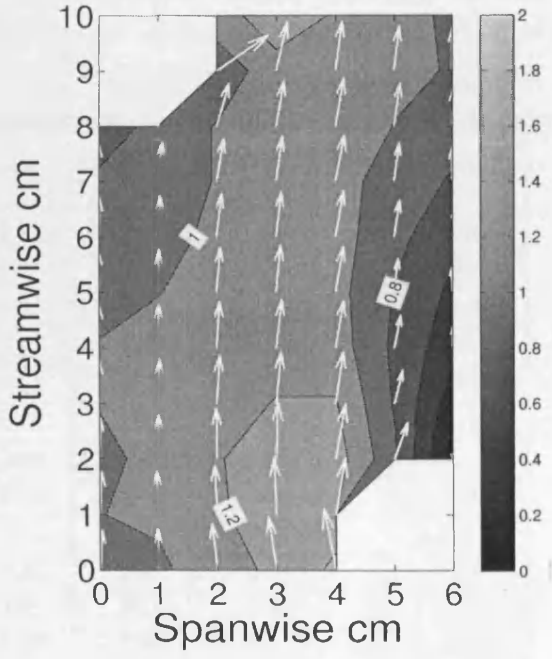

(d) Dowel, N=80.6 m^{-2}, high depth

Figure 4.6: Normalised depth-averaged streamwise velocity U_{xz}/U_{xyz} within dowel arrays

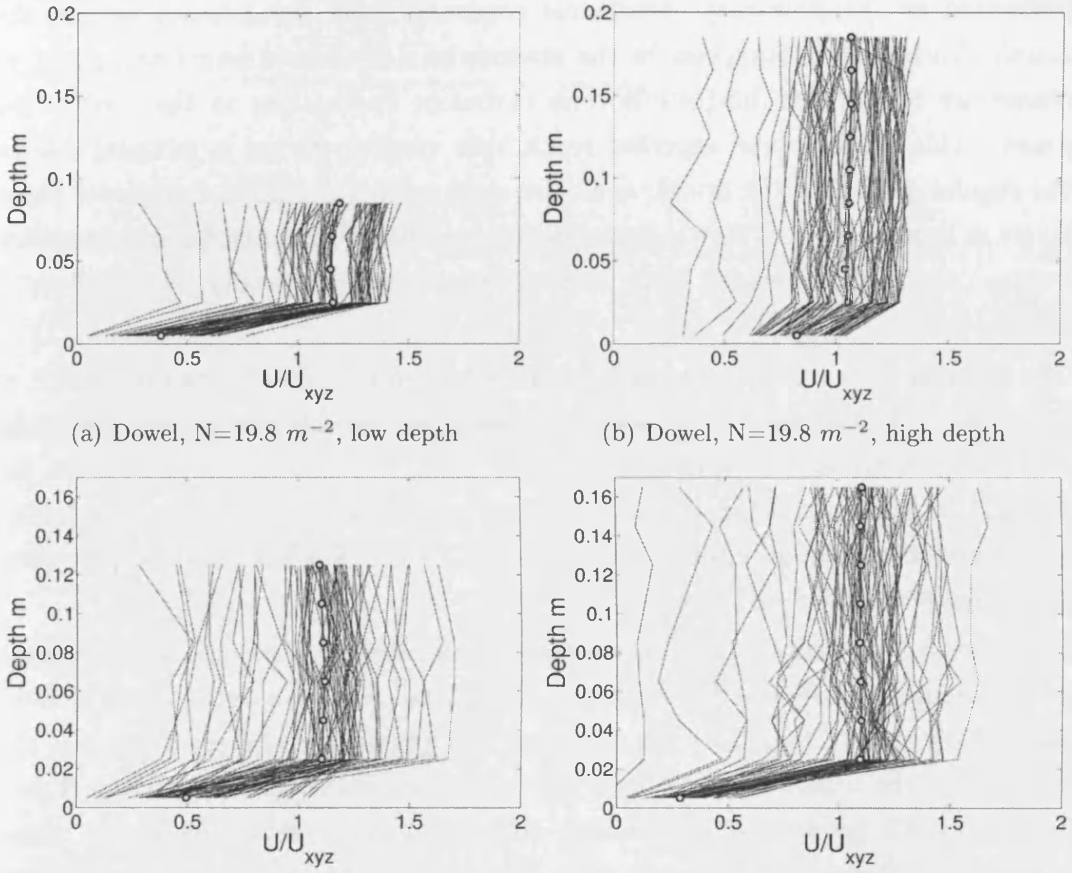

(a) Dowel, N=19.8 m^{-2}, low depth

(b) Dowel, N=19.8 m^{-2}, high depth

(c) Dowel, N=80.6 m^{-2}, low depth

(d) Dowel, N=80.6 m^{-2}, high depth

Figure 4.7: Vertical plots of normalised streamwise velocity (U/U_{xyz}) and horizontally-averaged velocity (U_{xy}/U_{xyz}) within dowel arrays. Thin lines are individual samples, thick line marked with circles is the horizontally-averaged profile U_z.

4.4.3 Turbulent Intensities (u', v' and w') and TKE within dowels

Figures 4.8, 4.9 and 4.10 present the normalised depth-averaged turbulent intensities for the streamwise, cross-streamwise and vertical planes for the data from the dowel experiments. In all three directions, the highest magnitude of turbulent intensity (indicated by contour values) and the highest rate of change of turbulence magnitude (indicated by the proximity of adjacent contours) occur immediately behind the dowel. Turbulent fluctuations in the streamwise and cross-streamwise (x and y) planes are of a higher magnitude than turbulent fluctuations in the vertical (z) plane. This confirms the expected result that vertical mixing is minimal due to the regular profile of the dowel, and that most mixing occurs in horizontal plane layers in dowel arrays. There is variation in the distribution of turbulence intensity between the medium density (N = 19.8 m^{-2}) and the high density (N = 80.6 m^{-2}) arrays.

The greatest streamwise turbulence intensity has approximately the same value of 1.5 u'/u'_{xyz}. In Figures 4.8 (a) and (b), presenting the medium density data, the area of lowest streamwise turbulent intensity (u') lies in the centerline between the dowels. In Figures 4.8 (c) and (d), presenting the high density data, the lowest streamwise turbulent intensity (u') lies in the lower left-hand corner of the plot, away from the presence of obstructions.

In Figures 4.9 (a) and (b), presenting the medium density data, the area of lowest cross-streamwise turbulent intensity (v') lies in the centerline between the dowels, and the division of high and low turbulence intensities can be split between the area behind the upstream dowel, and the area approaching the downstream dowel. In Figures 4.9 (c) and (d), presenting the high density data, the lowest cross-streamwise turbulent intensity (v') lies in the left-hand center of the plot, away from the obstructions, and the distribution of high cross-streamwise turbulent intensities is more complex, with two regions apparent, one immediately behind the dowel, and the other at the location of greatest constriction between adjacent dowels in the arrays.

The pattern of distribution of vertical turbulence intensity (w') follows a similar structure to the pattern seen in the cross-streamwise (v') data. In Figures 4.10 (a) and (b), presenting the medium density data, the area of lowest vertical turbulent intensity (w') lies in the centerline between the dowels and the area immediately before the downstream dowel. High and low turbulence intensities can be split into two vertical segments, the area behind the upstream dowel, and the area approaching

the downstream dowel. In Figures 4.10 (c) and (d), presenting the high density data, the lowest vertical turbulent intensity (w') lies in the top-left of the plot, in the area of flow approaching the downstream dowel.

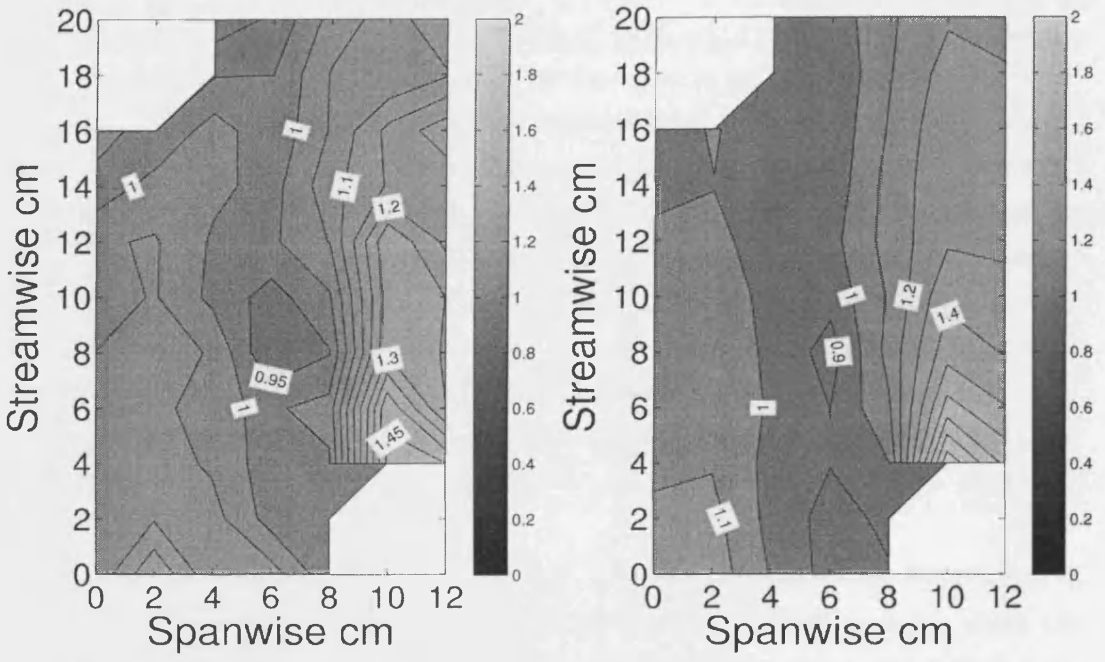

(a) Dowel, N=19.8 m^{-2}, low depth

(b) Dowel, N=19.8 m^{-2}, high depth

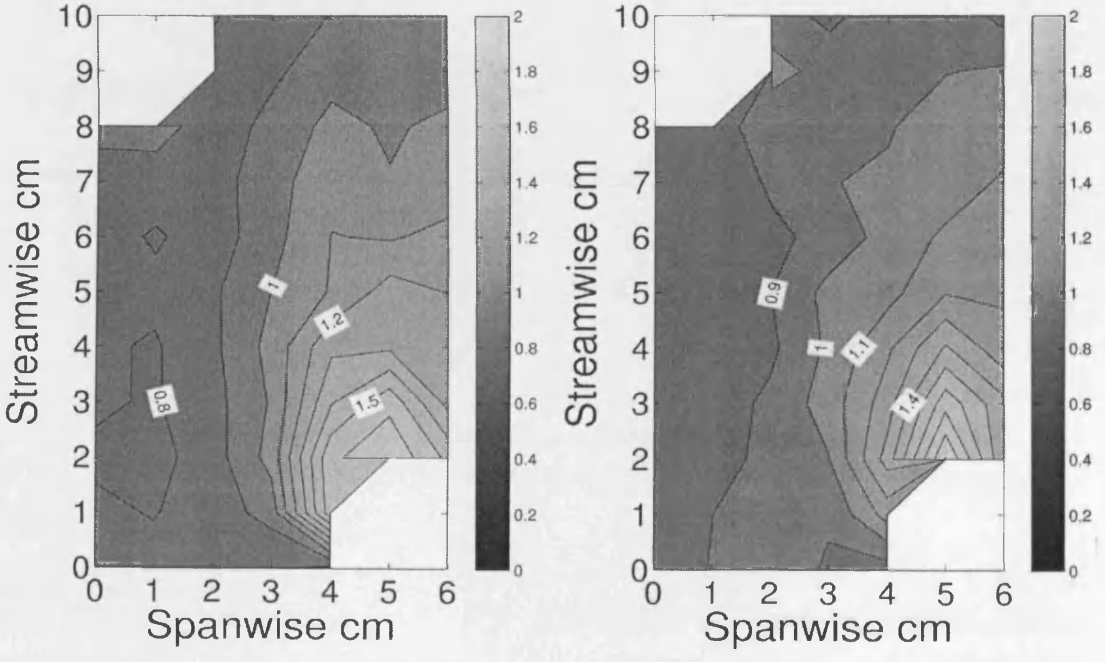

(c) Dowel, N=80.6 m^{-2}, low depth

(d) Dowel, N=80.6 m^{-2}, high depth

Figure 4.8: Depth-averaged streamwise turbulent intensity u' within dowel arrays

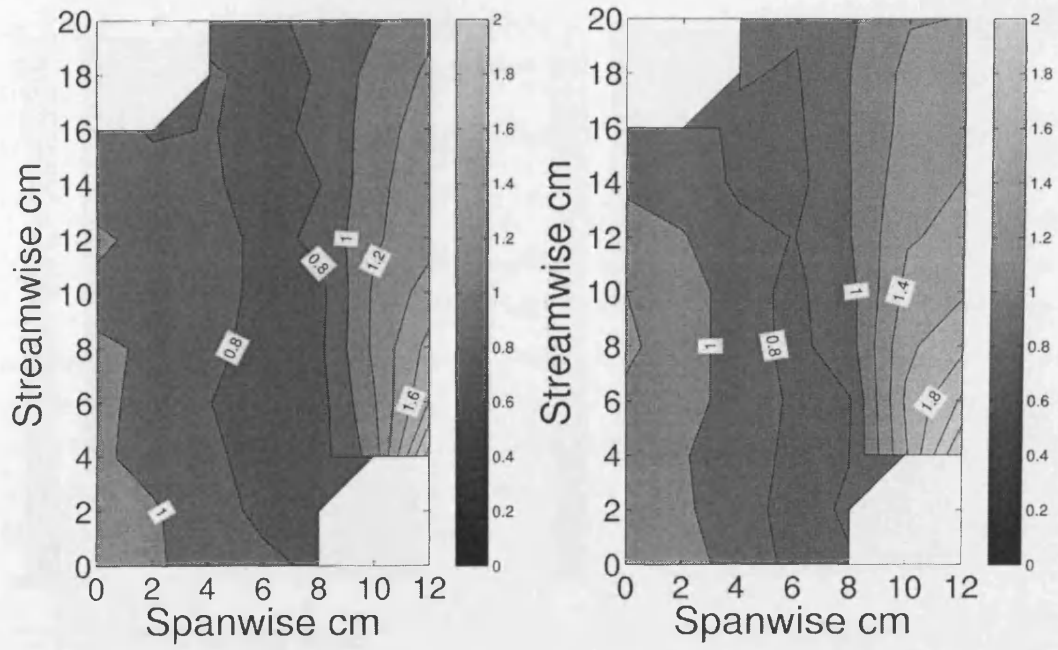

(a) Dowel, N=19.8 m^{-2}, low depth

(b) Dowel, N=19.8 m^{-2}, high depth

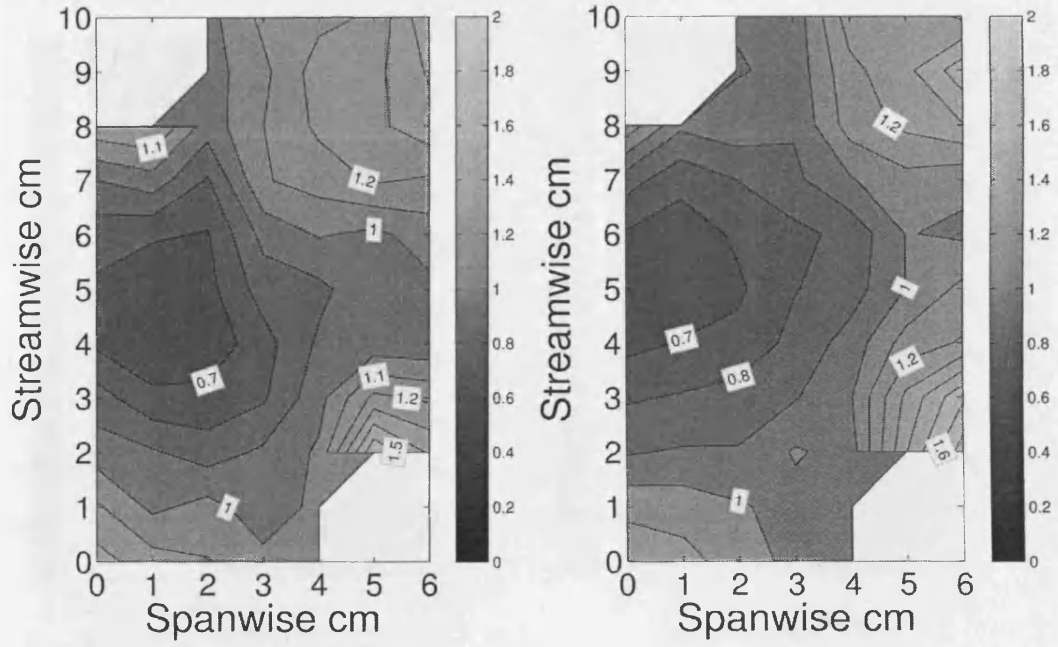

(c) Dowel, N=80.6 m^{-2}, low depth

(d) Dowel, N=80.6 m^{-2}, high depth

Figure 4.9: Depth-averaged cross-streamwise turbulent intensity v' within dowel arrays

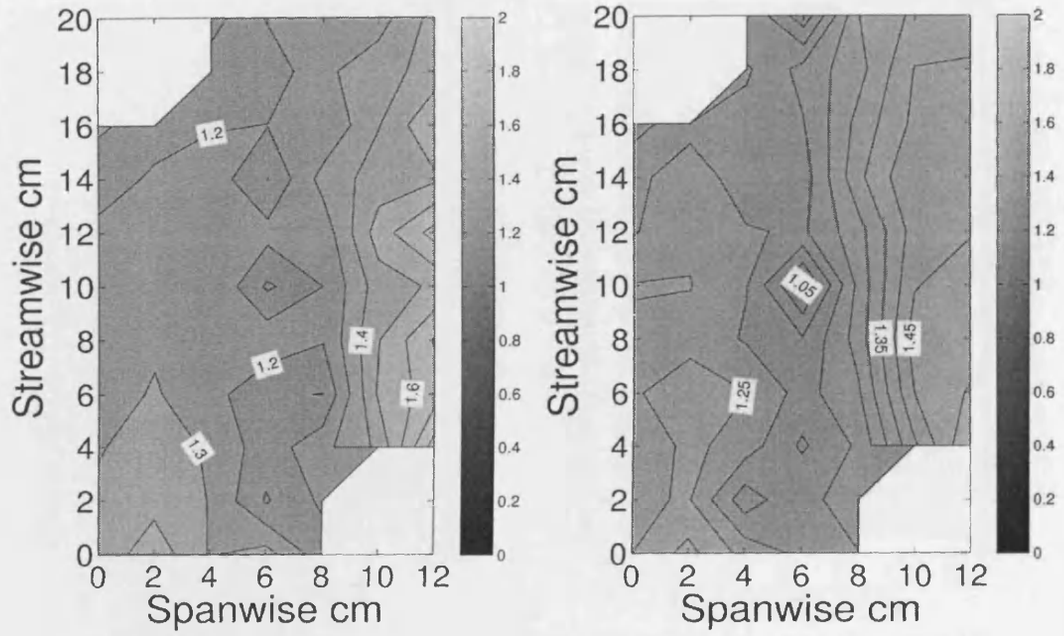

(a) Dowel, N=19.8 m^{-2}, low depth

(b) Dowel, N=19.8 m^{-2}, high depth

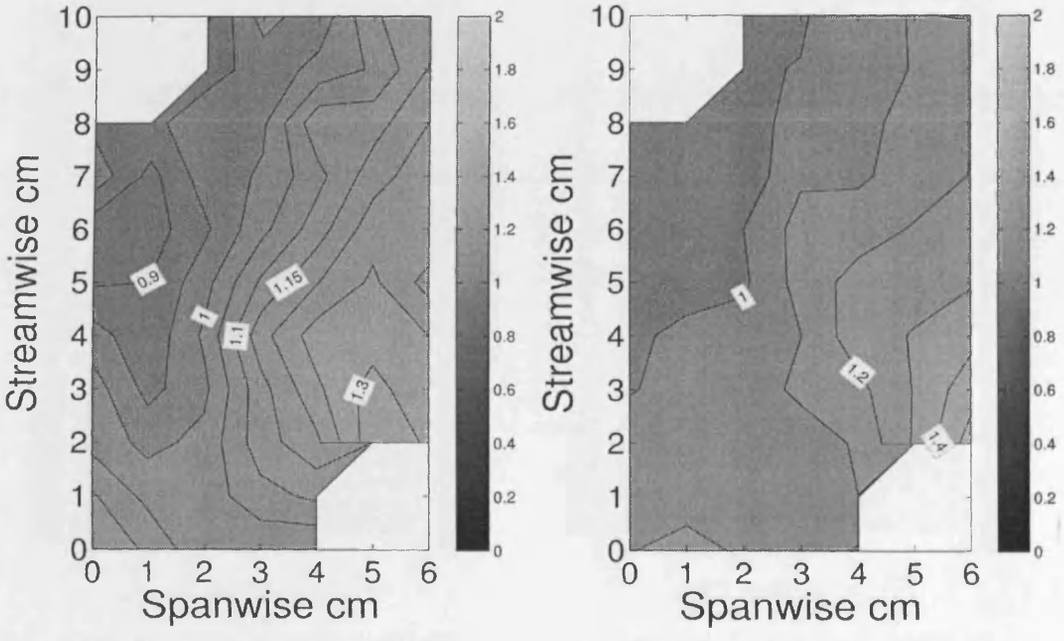

(c) Dowel, N=80.6 m^{-2}, low depth

(d) Dowel, N=80.6 m^{-2}, high depth

Figure 4.10: Depth-averaged vertical turbulent intensity w' within dowel arrays

The depth-averaged results in Figures 4.8, 4.9 and 4.10 plot the fluctuation averaged by depth. Figure 4.11 presents the vertical profiles of turbulent kinetic energy (TKE), where TKE is defined in Equation 4.6.

$$TKE = \frac{\overline{u'^2} + \overline{v'^2} + \overline{w'^2}}{2} \tag{4.6}$$

The TKE profile combines the effects of turbulent fluctuations in all three dimensions, weighting the contribution of each evenly and can be used to represent the nature of the turbulence variability within a water column. All the TKE plan-averaged profiles have an inclination towards higher turbulence values at the top of the water column, however the 1st profile $D2d$ has a more exaggerated increase than the others. Control volume $D2d$ has a higher stem Re_d than the other flow scenarios. It is also possible air entrainment was occurring, and this may have had an impact on the turbulence values recorded. The depth of $D2g$ is perhaps too shallow to see the full development of the velocity profile, but it can be seen from the high increase in TKE from the bed to a height of 85 mm above the bed that there is a definite trend of increasing intensity. In contrast, the results for the close spaced dowels display a more uniform TKE profile throughout the depth.

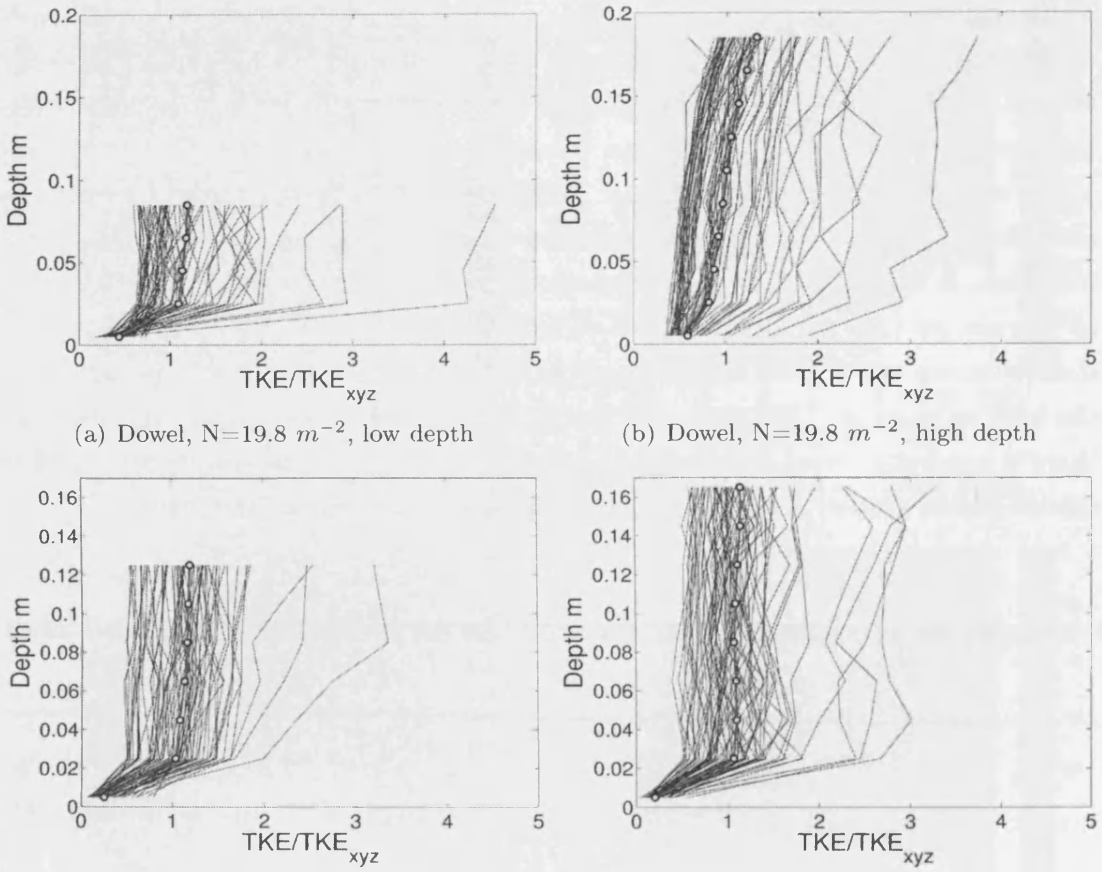

(a) Dowel, N=19.8 m^{-2}, low depth

(b) Dowel, N=19.8 m^{-2}, high depth

(c) Dowel, N=80.6 m^{-2}, low depth

(d) Dowel, N=80.6 m^{-2}, high depth

Figure 4.11: Thin lines are individually sampled vertical plots of normalised turbulent kinetic energy (TKE/TKE_{xyz}). Thick line marked with circles is the horizontally-averaged turbulent kinetic energy profile (TKE_{xy}/TKE_{xyz}) within dowel arrays

4.4.4 Streamwise Velocity (U) within *Cornus*

The random forms of the *Cornus* sanguinea saplings suggest that the flow field will display markedly less uniformity than the dowel experiments. The depth averaged streamwise velocity component (U) for data collected within control volume $CV3$ are shown in Figure 4.12, with the streamwise and cross-streamwise velocity vectors superimposed. In comparison with the normalised streamwise velocity data for the dowels in Figure 4.6, there is less variation away from the mean velocity and the flow field displays a higher degree of uniformity. The small and dispersed branches of the *Cornus* saplings encourage less lateral diversion of flow than needs to occur to negotiate the dowels. The variation among different locations in the canopy but under the same flow conditions is also to be expected, and can be seen in Figures 1 to 4 in the Appendix.

In the medium density array (N = 19.8 m^{-2}), the normalised streamwise velocity reaches a greater magnitude within the free stream area between the plants than in the high density array (N = 80.6 m^{-2}). The area behind the upstream plant show sheltering in all the plots, but to a smaller degree than seen in the plots of the dowel data. In Figures 4.12 (a), (b) and (d), streamlines are consistent in pointing downstream. The deviation observed in the streamlines of Figure 4.12 (c) may be due to a misaligned ADV probe.

Figure 4.13 presents the individual and horizontally-averaged streamwise velocity (U) profiles within the *Cornus* arrays. There is less variation in the velocity profiles than in the dowel profiles in Figure 4.7. The medium density (N = 19.8 m^{-2}) pair (a) and (b) both have horizontally-averaged profiles that display a slight bulge in the lower half of the plot. The high density (N = 80.6 m^{-2}) pair (c) and (d) both have a more pronounced velocity bulge in the lower half of the plot. Note that in (a), (b) and (c), the horizontally averaged profile has an 'S' shape, and this 'S' is also seen in the lower half of (d). Excepting the bottom measurement, there is a point of lowest velocity higher up. In the medium density pair (a) and (b), this low velocity occurs at a depth of 5 cm and 7 cm respectively. In the high density pair (c) and (d), the point of low velocity has shifted up to a depth of 9 cm for both plots. This low point of velocity may be a function of Reynolds number Re, which has a lower value for the high density pair. This could also be further related to the average stem size (see Figure 3.6).

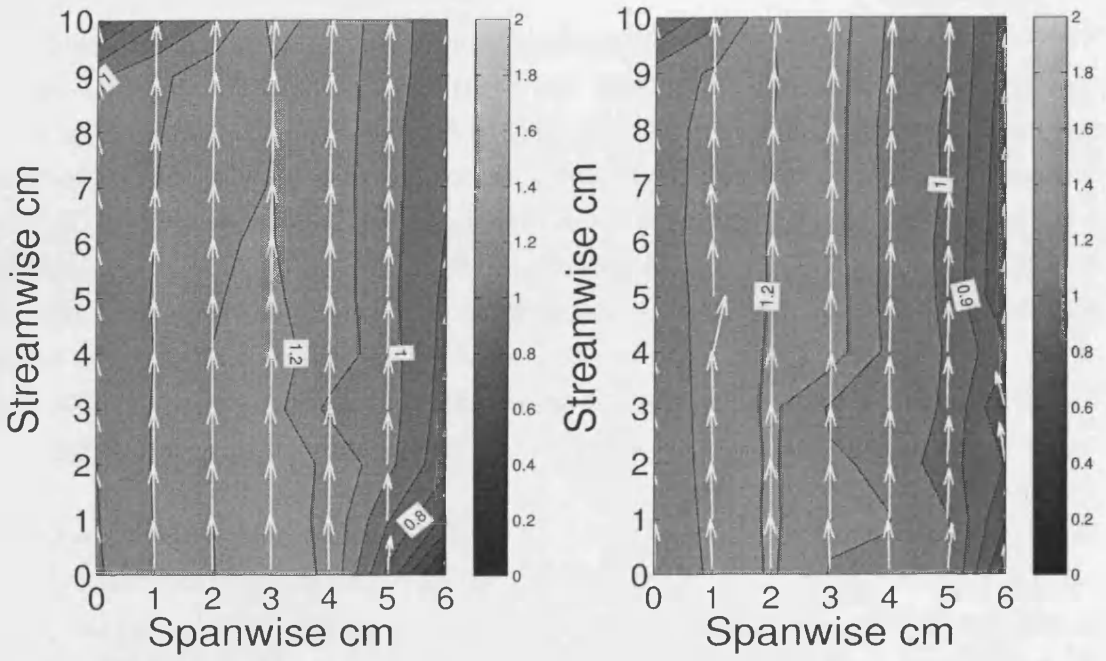

(a) *Cornus*, N=19.8 m^{-2}, low depth

(b) *Cornus*, N=19.8 m^{-2}, high depth

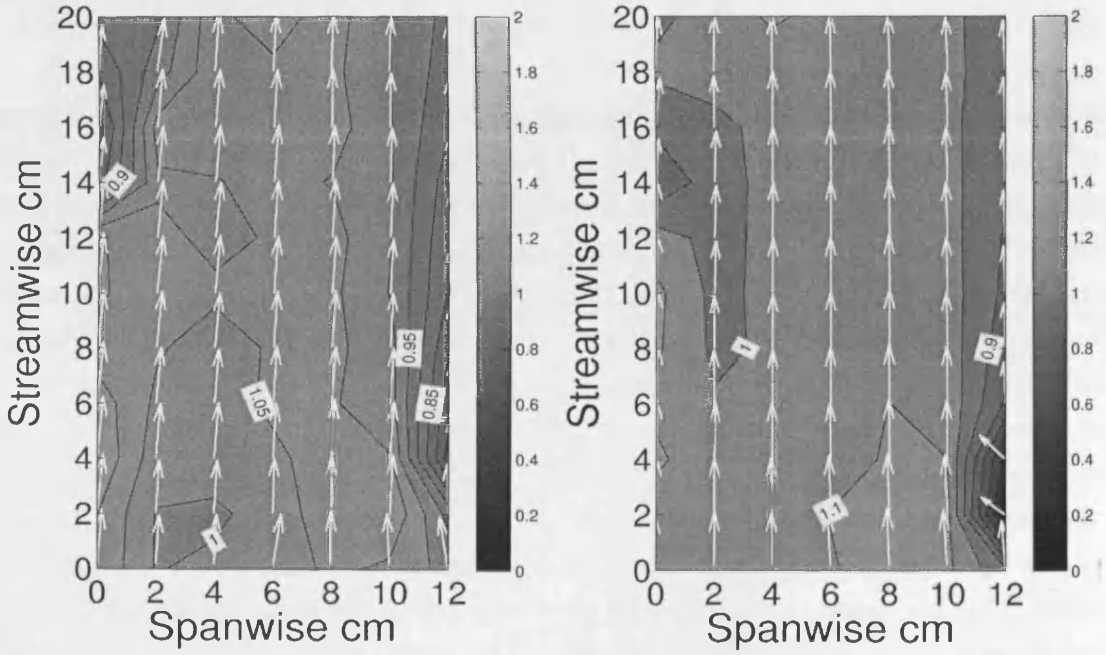

(c) *Cornus*, N=80.6 m^{-2}, low depth

(d) *Cornus*, N=80.6 m^{-2}, high depth

Figure 4.12: Normalised depth-averaged streamwise velocity U_{xy}/U_{xyz} within *Cornus* arrays

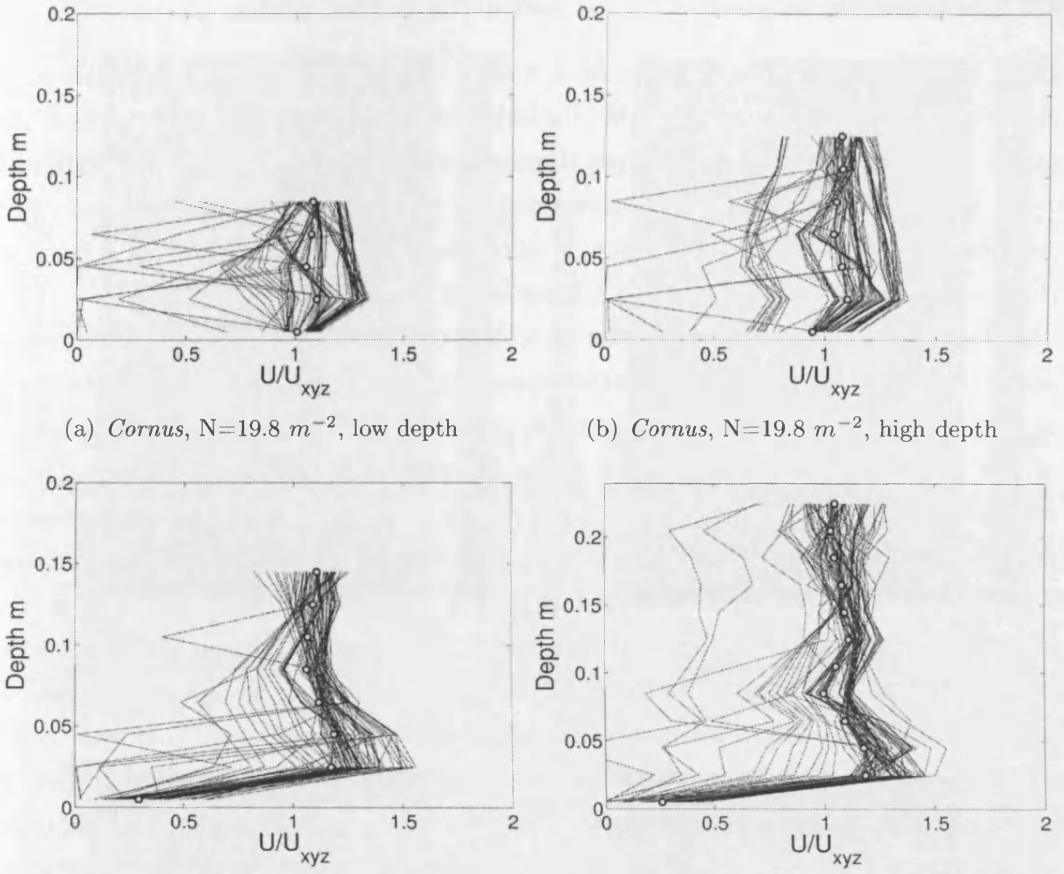

(a) *Cornus*, N=19.8 m^{-2}, low depth

(b) *Cornus*, N=19.8 m^{-2}, high depth

(c) *Cornus*, N=80.6 m^{-2}, low depth

(d) *Cornus*, N=80.6 m^{-2}, high depth

Figure 4.13: Thin lines are individually sampled vertical plots of normalised streamwise velocity (U/U_{xyz}) within *Cornus* arrays. Thick line marked with circles is the horizontally-averaged profile (U_{xy}/U_{xyz})

4.4.5 Turbulent Intensities (u', v' and w') and TKE within *Cornus*

Since the stems are in the order of 2 mm - 14 mm, the dominant length scale of turbulence is of this order, and the large eddies generated in flow around the dowel will not occur. At the same time, the channel scale eddies that normally occur in reach-scale flow will be disrupted by the presence of the saplings. The combined effect means that the flow is dominated by smaller scale flow structures (in comparison to the dowels) and a lower shear stress.

The fluctuating velocity components u', v' and w', for the *Cornus sanguinea* arrays are presented in Figures 9 to 20 in the Appendix, it can be seen that the turbulence field shows a markedly less uniform profile of turbulent fluctuations. In the locations of the plants, there are occasional peaks of turbulence, but their distribution is stochastic in nature. In contrast with the results from the dowels, there is turbulent activity of similar magnitude in all three dimensional planes, suggesting that the flow through the saplings is more uniformly 3-D than flow through the dowel arrays of equivalent density, which displays dominant turbulent activity in the streamwise (x) and lateral (y) planes. The Reynold's number of the flow though the saplings is in the range 700 - 1500, much lower than the Reynold's numbers of the dowel arrays which vary between 1300 to 3000. A lower Reynold's number means that flow is moving toward a more laminar state, which would involve a smaller, rather than more vigorous turbulent wake. Intuitively, this would involve less exchange between flow layers. It is plausible then that the multi-stemmed nature of the saplings - key features being the inclined and branching stems - encourages interaction of individual eddies coming off the various stems, and the consequential effect is to promote an increased degree of vertical mixing.

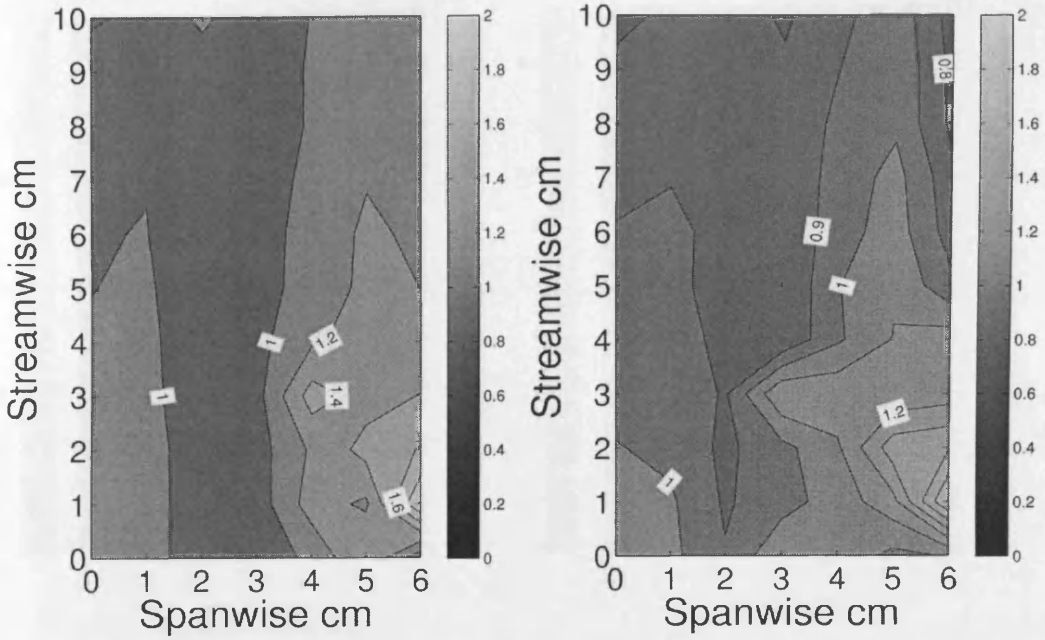

(a) *Cornus*, N=19.8 m^{-2}, low depth

(b) *Cornus*, N=19.8 m^{-2}, high depth

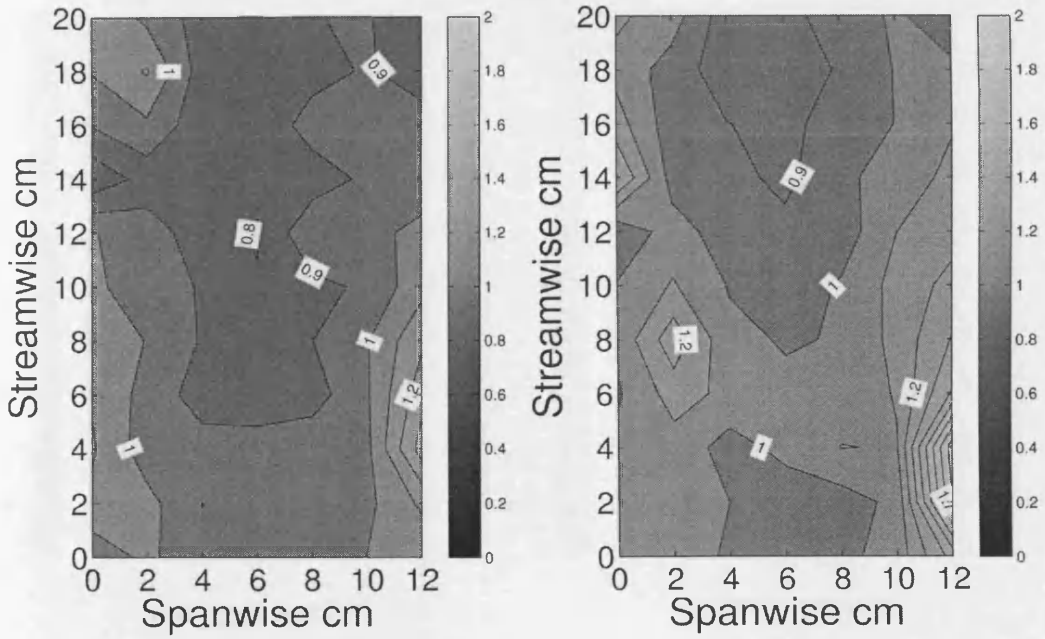

(c) *Cornus*, N=80.6 m^{-2}, low depth

(d) *Cornus*, N=80.6 m^{-2}, high depth

Figure 4.14: Normalised depth-averaged streamwise turbulent intensity u'_{xy}/u'_{xyz} within *Cornus* arrays

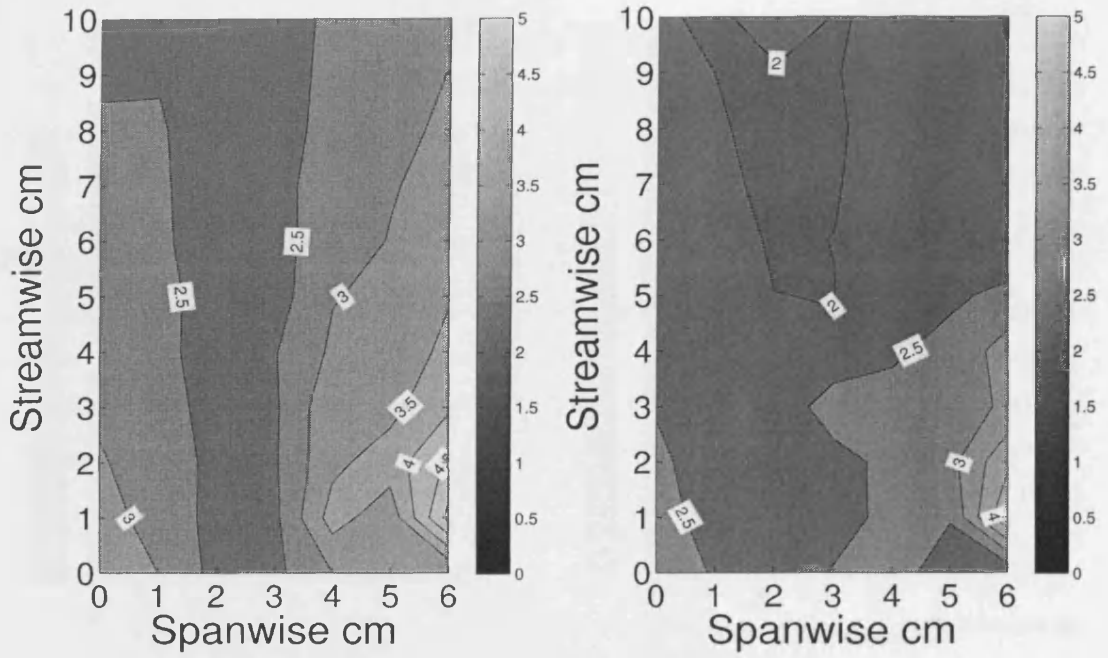

(a) *Cornus*, N=19.8 m^{-2}, low depth

(b) *Cornus*, N=19.8 m^{-2}, high depth

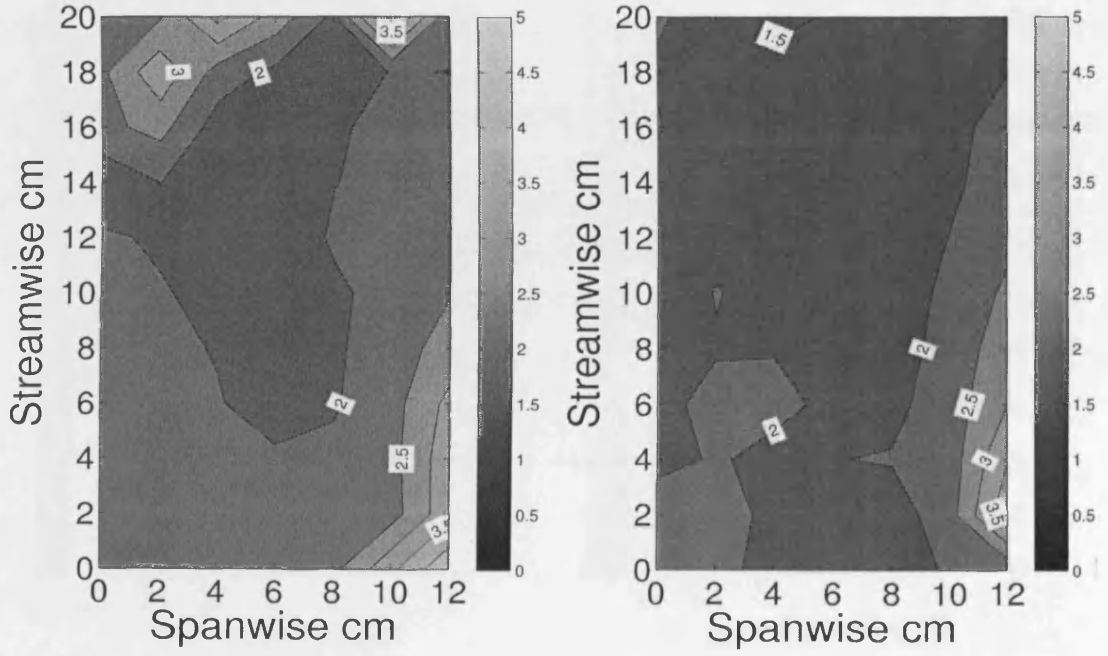

(c) *Cornus*, N=80.6 m^{-2}, low depth

(d) *Cornus*, N=80.6 m^{-2}, high depth

Figure 4.15: Normalised depth-averaged cross-streamwise turbulent intensity v'_{xy}/v'_{xyz} within *Cornus* arrays

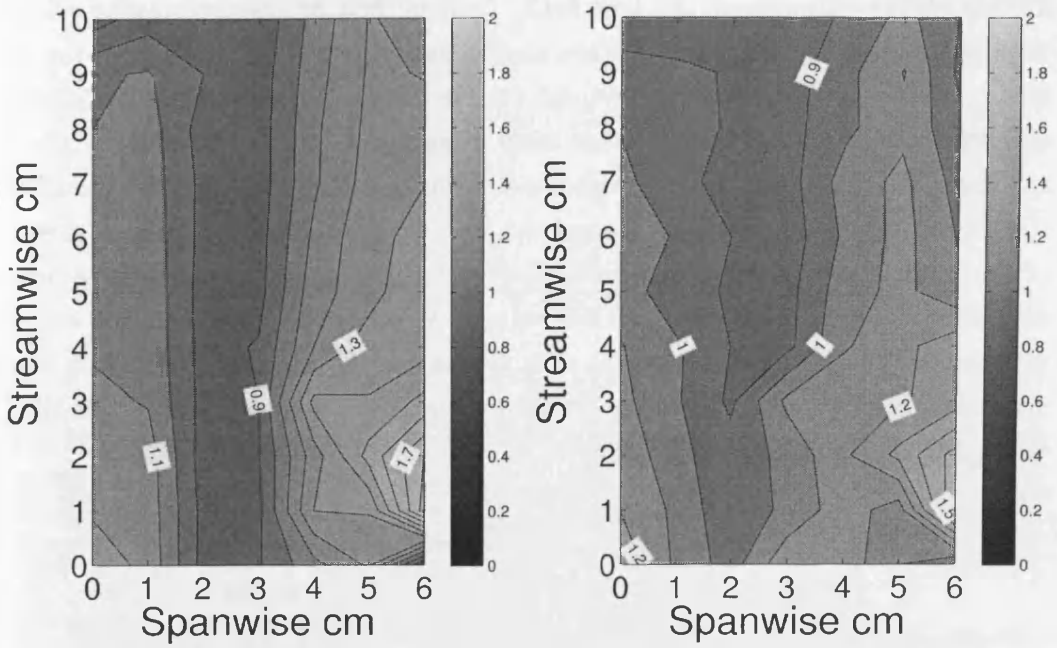

(a) *Cornus*, N=19.8 m^{-2}, low depth

(b) *Cornus*, N=19.8 m^{-2}, high depth

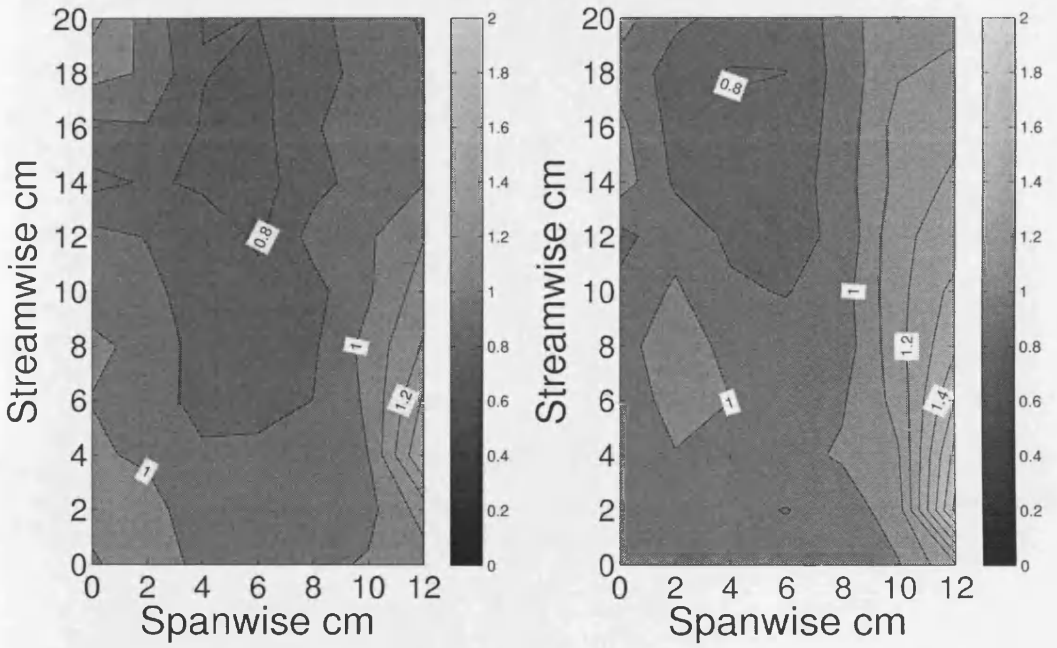

(c) *Cornus*, N=80.6 m^{-2}, low depth

(d) *Cornus*, N=80.6 m^{-2}, high depth

Figure 4.16: Normalised depth-averaged vertical turbulent intensity w'_{xy}/w'_{xyz} within *Cornus* arrays

The vertically-sampled profiles in Figure 4.17 give another picture of the turbulent kinetic energy throughout the flow field. Looking first at the streamwise velocity profiles, again it is clear that there is a smaller spatial variation throughout the flow field. However, the vertically sampled profiles show distinct differences between the flow characteristics of the single stem dowels and the multi-stemmed *Cornus* saplings. There are points of low velocity at seemingly random locations throughout the depth. These points occur around the location of the saplings and are a result of the probe having been placed immediately downstream of a stem. These points also coincide with areas of high TKE values. Many of the plan averaged velocity profiles for the saplings show a peak near the base of the water column. This would suggest that flow is preferentially diverted below the biomass center of the plant, where flow is relatively unobstructed.

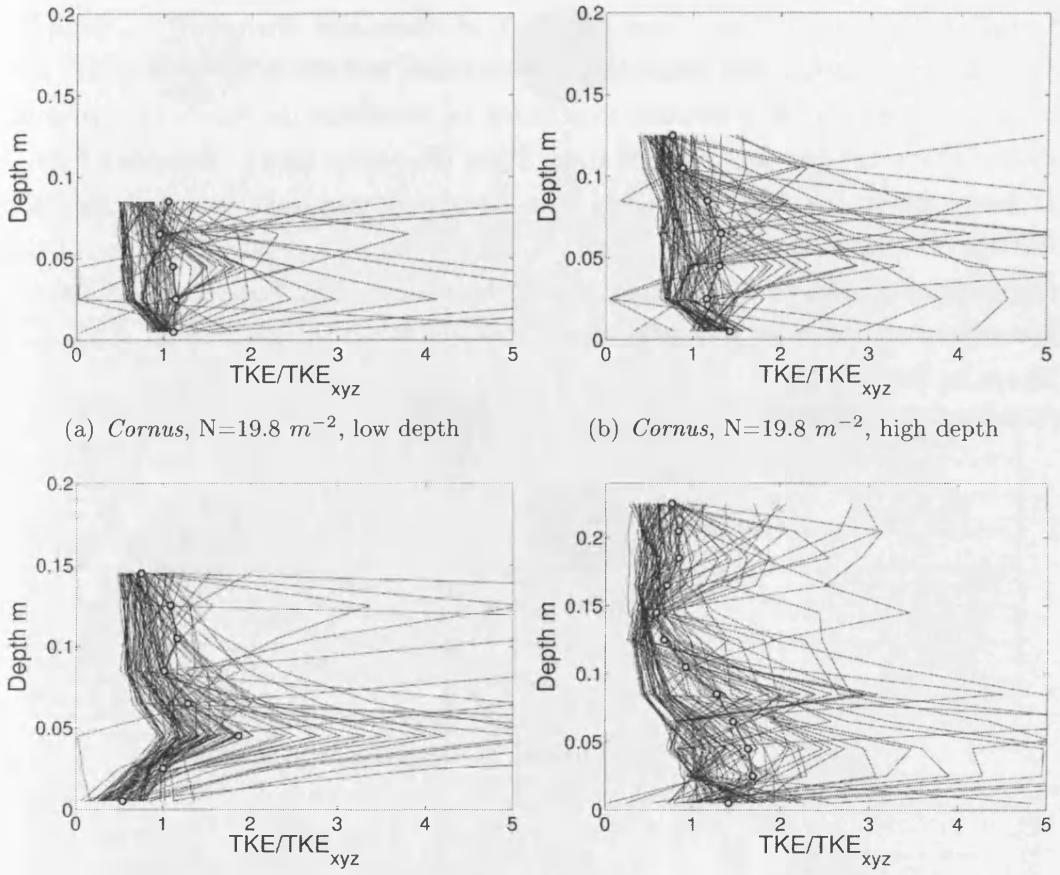

(a) *Cornus*, N=19.8 m^{-2}, low depth

(b) *Cornus*, N=19.8 m^{-2}, high depth

(c) *Cornus*, N=80.6 m^{-2}, low depth

(d) *Cornus*, N=80.6 m^{-2}, high depth

Figure 4.17: Thin lines are individually sampled vertical plots of normalised turbulent kinetic energy (TKE/TKE_{xyz}) within *Cornus* arrays. Thick line marked with circles is the horizontally-averaged profile (TKE_{xy}/TKE_{xyz})

4.5 Selective Sampling of Arrays

4.5.1 Sampling patterns inspired by the literature

Four sampling patterns have been selected to sample the flow field results. The sampling patterns chosen were inspired by authors investigating the flow resistance of emergent or submerged rigid rods. The patterns are shown in Figure 4.18. Sampling Pattern A comes from the work of Stone and Shen (2002). Sampling Pattern B was used in the laboratory investigations of Fairbanks (1998) where a set of measurements at six locations were taken to determine the flow and turbulence characteristics of flow around rigid rods. From Westwater (2001), Sampling Pattern C investigated the flow resistance from simulated mangrove forests. Sampling Pattern D places samples according to the degree of spatial variability of flow characteristics, similar in principle to a method adopted by Poggi et al. (2004).
For reference, the flow and array conditions employed in the original studies are shown in Table 4.4.

Author	**Stone and Shen**	**Fairbanks**	**Westwater**	**Poggi**
Year	**2002**	**1998**	**2001**	**2003**
Pattern	**A**	**B**	**C**	**D**
Re_d	80 - 7000	1000	2000	560 - 1000
Diameter mm	12.7/6.35/3.18	6.35	9/12/18/25	4
Depth mm	124	64.9	250	120
SAC m^{-1}	173 - 696	1000	100 - 367	67 - 1072
EAI m^2/m^3	1 - 6	6.3	2.2 - 6.1	0.3 - 4.23

Table 4.4: Flow Conditions for Original Experiments

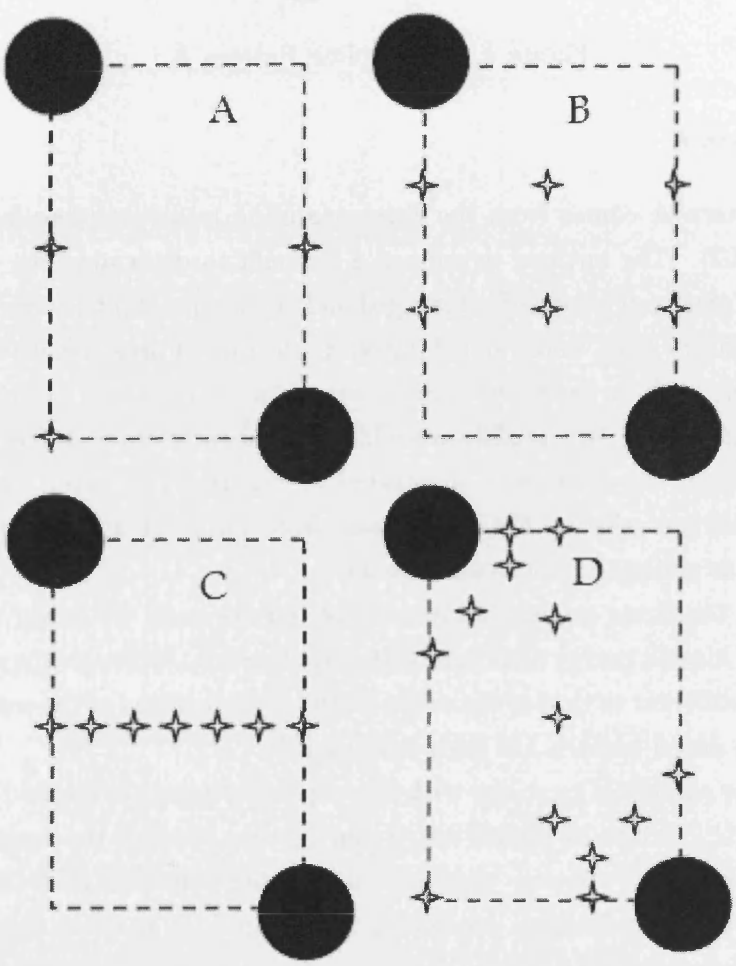

Figure 4.18: Sampling Patterns inspired by other authors

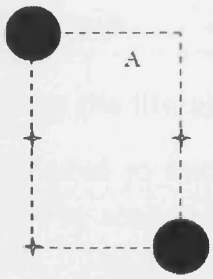

Figure 4.19: Sampling Pattern A

Sampling Pattern A

Sampling Pattern A comes from the three sampling locations identified by Stone and Shen (2002). The authors developed a formula to determine the variation of vegetative roughness of arrays of submerged and emergent cylinders. To validate the formula, laboratory tests were carried out at a selection of arrays densities and flow conditions. The authors expressed uncertainty as to the optimum location at which to measure, and so velocity profiles were initially taken at three different locations (placed relative to the cylinders), illustrated in Figure 4.19. After comparison to the channel average velocity, the mean result from the right and bottom locations were selected as giving the optimum velocity.

In this study, the three original locations selected are used to obtain the velocity and turbulent kinetic energy structure within each array. Although the spacing and dowel size are different to that of the original study, the location of the measurements relative to the dowel pattern has been maintained.

Comparing the sampling locations with the depth-averaged normalised streamwise velocity (U_{xz}/U_{xyz}) data in Figure 4.6, it can be seen that all the sampling points lie within area of low velocity, therefore, it was hypothesised that the Sampling Pattern A streamwise velocity prediction would produce a lower value than the volume averaged value (U_{xyz}).

Prediction of Streamwise Velocity (U) using Sampling Pattern A

Figures 4.20 and 4.21 present the streamwise velocity (U) data for the dowels and the control volume $CV3$ data for the *Cornus*. Full results for the remaining control volumes may be found in Figures 25 to 26 in the Appendix.

Sampled-averaged mean and χ^2 values for streamwise velocity (U) and turbulent kinetic energy (TKE) using Sampling Pattern A are listed in Tables 13 to 17 in the

Appendix.

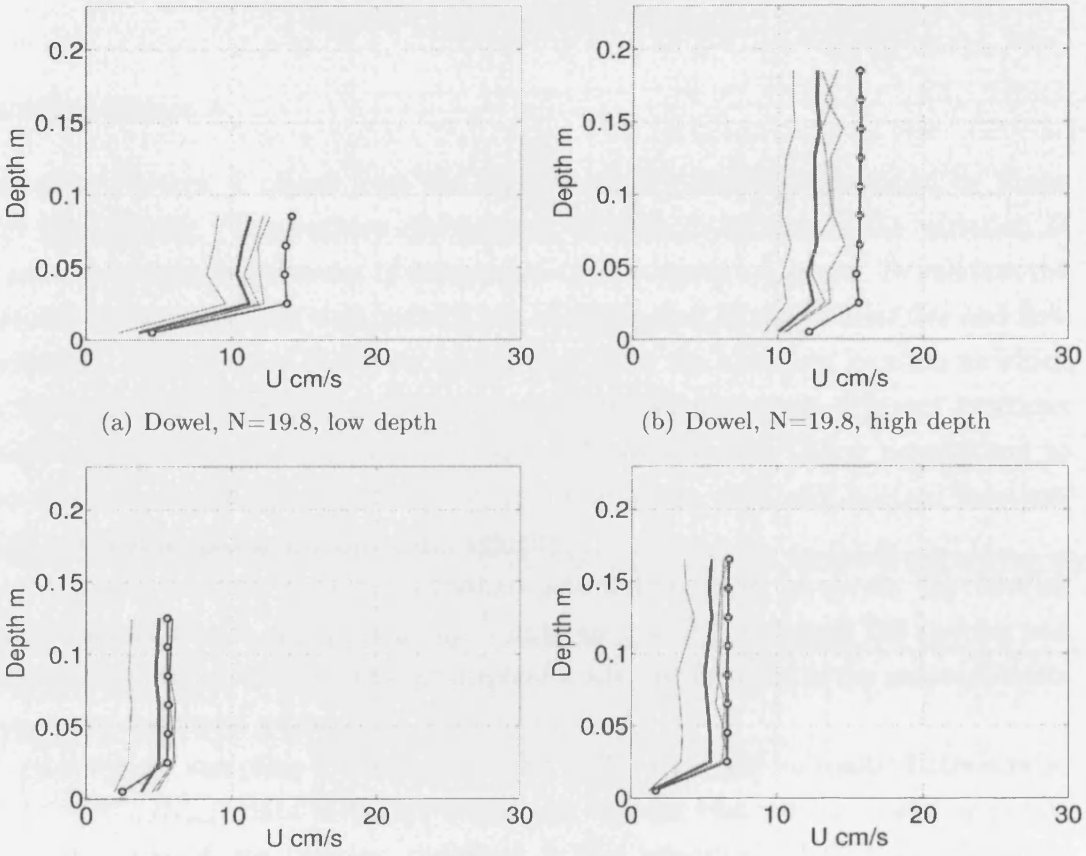

(a) Dowel, N=19.8, low depth

(b) Dowel, N=19.8, high depth

(c) Dowel, N=80.6, low depth

(d) Dowel, N=80.6, high depth

Figure 4.20: Sampled streamwise velocity U using Sampling Pattern A within dowel arrays.

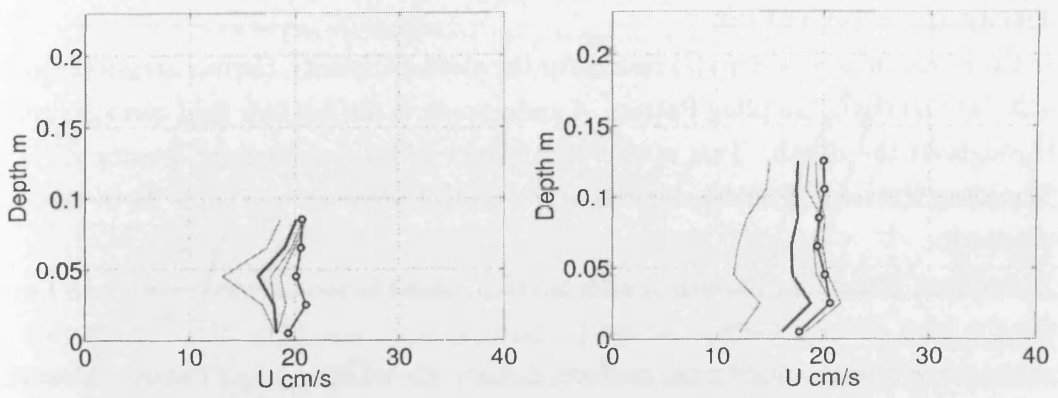

(a) *Cornus*, N=19.8, low depth

(b) *Cornus*, N=19.8, high depth

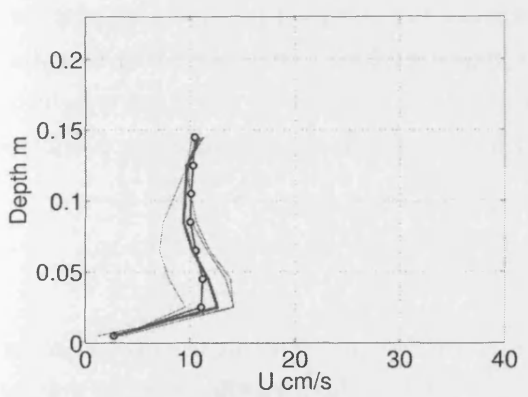

(c) *Cornus*, N=80.6, low depth

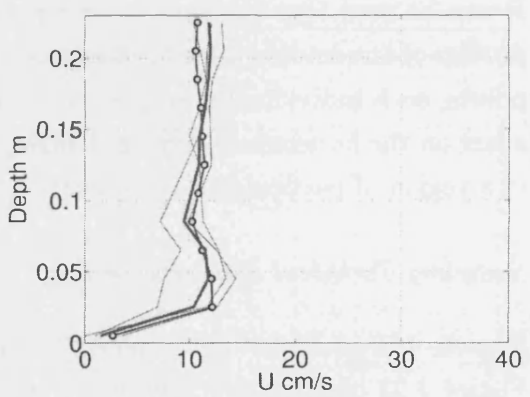

(d) *Cornus*, N=80.6, high depth

Figure 4.21: Sampled streamwise velocity U using Sampling Pattern A within *Cornus* arrays.

The streamwise velocity (U) data for the medium and high density dowel arrays are shown in Figure 4.20. The thin lines are the data included in the sampling pattern. The thick line is the Sampling Pattern A horizontally-averaged mean velocity (U_{xy}). The thick line marked with circles displays the plan averaged velocity from the full dataset. It can be seen that all the sampling verticals consistently underpredict the mean velocity to varying degrees. Sampling Pattern A predicts the absolute full flow field mean value better for the high density arrays (c) and (d) than the medium density arrays (a) and (b).

In the streamwise velocity (U) results for the medium density *Cornus* arrays (Figures 4.20 (a) and (b)), Sampling Pattern A underpredicts the full flow field average values throughout the depth. This is also seen in the additional medium density *Cornus* Sampling Pattern A results for the other control volumes in Figure 25 in the the Appendix.

In contrast, Sampling Pattern A appears to predict the streamwise velocity (U) well for the high density *Cornus* arrays (Figures 4.21 (c) and (d)). Good prediction is also achieved in the additional medium density *Cornus* Sampling Pattern A results for the other control volumes in Figure 26 in the Appendix.

It can be seen that the thick lines representing the sampled horizontally averaged profiles of streamwise velocity often have a jagged profile. Using only three sampling points, each individually sampled point contributes a relatively large 1/3 weighting effect on the horizontally-averaged value, which is significant if a sampling point lies in a region of particularly low velocity.

Sampling Turbulent Kinetic Energy

Figures 4.22 presents the Sampling Pattern A TKE predictions for the dowel arrays. Figure 4.23 presents the Sampling Pattern A TKE predictions for control volume $CV3$. Full results for the remaining control volumes may be found in Figures 27 to 28 in the Appendix.

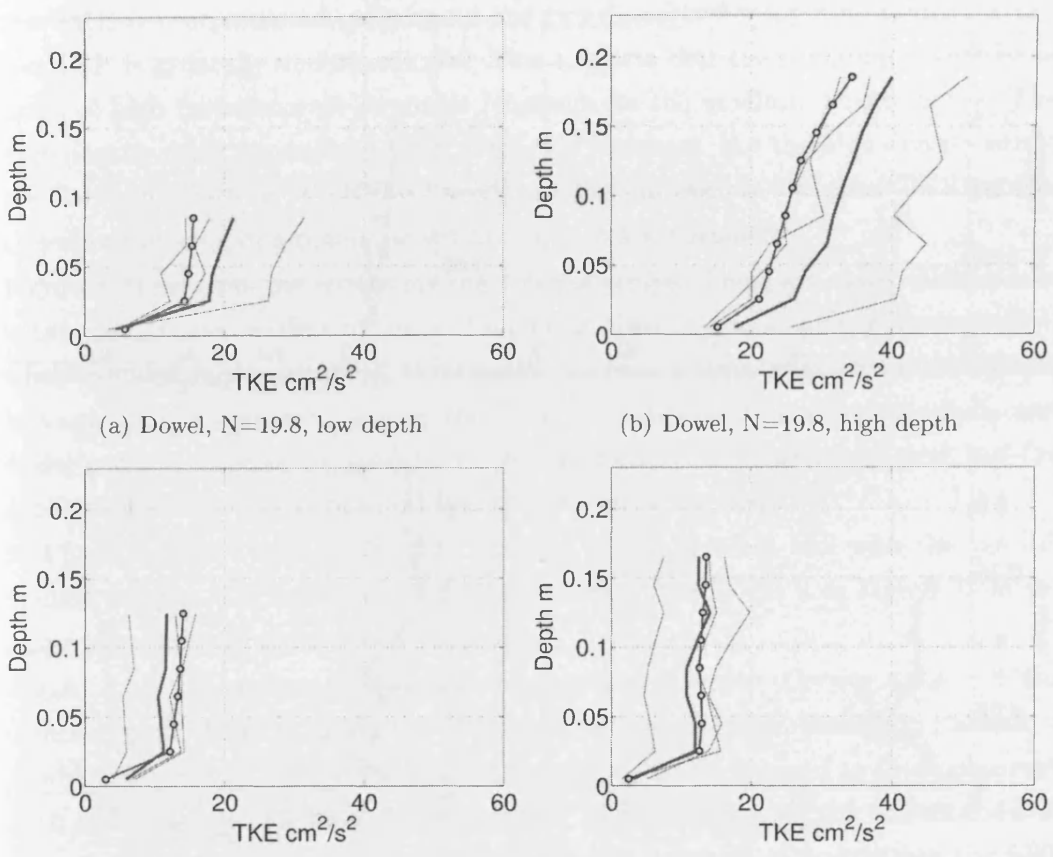

(a) Dowel, N=19.8, low depth

(b) Dowel, N=19.8, high depth

(c) Dowel, N=80.6, low depth

(d) Dowel, N=80.6, high depth

Figure 4.22: Sampled TKE using Sampling Pattern A within dowel arrays.

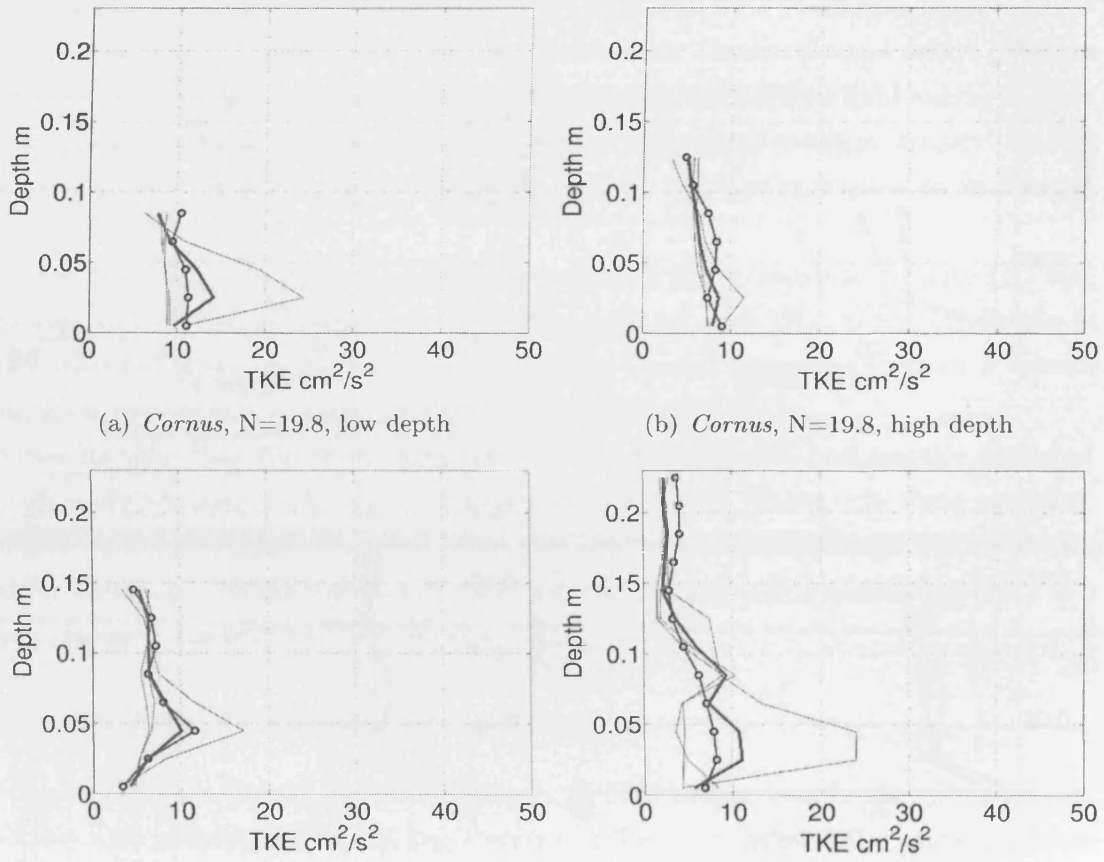

(a) *Cornus*, N=19.8, low depth

(b) *Cornus*, N=19.8, high depth

(c) *Cornus*, N=80.6, low depth

(d) *Cornus*, N=80.6, high depth

Figure 4.23: Sampled TKE using Sampling Pattern A within *Cornus* arrays.

The results for the Sampling Pattern A turbulent kinetic energy are shown in Figures 4.22. Note the individual sampling verticals lie well distributed around the averaged mean in all plots.

The thin, individual sampling verticals do not appear highly skewed, however the thick line, indicating the Sampling Pattern A averaged vertical profile, does not match the full sample averaged vertical profile thick line with circles. It is interesting to note that in the two datasets for the medium density array (4.22 (a) and (b)), the TKE is overpredicted, whereas in the two datasets for the high density array, the TKE is generally underpredicted. This suggests that the sampling points lie in areas of high turbulence at Reynolds Numbers for the medium density array. The high density array experiences lower Reynolds Numbers. For the high density array, the Sampling Pattern A TKE is lower than the full sample averaged TKE profile, therefore the sampling points lie within areas of low turbulence.

Figure 4.23 presents the results for the *Cornus* arrays. There are many sharp peaks within the dataset, indicating areas of high turbulence near the plants. As expected, when included in the sampling, these peaks can have a large influence on the sample averaged velocity profile. In (a), the TKE is over-predicted nearer the bed, and under-predicted nearer the surface. In (b), the mean value is well predicted, but the profile is distorted,particularly in the mid-section of the flow.

In Figure 4.23 (c), high density, the sampled profile matches well with the the full volume sample. The equivalent results for control volume $CV2$ in Figure 28 in the Appendix similarly shows good prediction.

Figure 4.23 (d) presents the results for the High Density *Cornus* array. When comparing all the data in Figures 27 and 28 in the appendix, Sampling Pattern A produces fewer high magnitude peaks using these data, compared to those observed with sampling the medium density data. This conforms to the expectation of lower turbulence, because of the lower Reynold's numbers of flow within the high density array. In (d), the TKE is overpredicted in the lower portion of flow, and underpredicted in the higher portion of flow.

Sampling Pattern A Review

Sampling Pattern A uses only three sampling verticals, the smallest number of sampling verticals of all four sampling patterns investigated. When sampling dowel data, all the sampled streamwise velocity profiles are under-predicted, with a larger error for the medium density array. When sampling the *Cornus* data, the medium

density streamwise velocity is underpredicted, but the high density streamwise velocity is well predicted. Since in both instances the prediction of streamwise velocity for medium density is worse than that for high density, it can be concluded that the sampling locations in Sampling Pattern A are more suited to arrays at staggered spacing of $s_x = 0.10$ and $s_y = 0.6$ than the lower density staggered spacings of $s_x = 0.20$ and $s_y = 0.12$.

The results for TKE are more variable. For the prediction of TKE in the dowels, TKE is over-predicted for the medium density array, and under-predicted for the high density. Looking at the thin lines, which indicate the three individual sampling verticals that make up Sampling Pattern A, it can be seen that areas of both high and low TKE are sampled. In most control volumes, the general shape of the TKE profile is reflected - the bulge near the bed in the medium density arrays is shown in the sampled profiles. Apart from obvious peaks, many points in the medium density sample are well matched to the full sample profile. In the high density arrays, fewer distortions by TKE peaks are observed and the predicted TKE profile is a better fit. Therefore, it can be concluded that Sampling Pattern A has improved prediction of mean streamwise velocity and TKE of arrays at the high density staggered density of spacing $s_x = 0.10$ and $s_y = 0.6$. Table 14 in the Appendix presents the full statistical mean error and error χ^2 values in all control volumes for Sampling Pattern A.

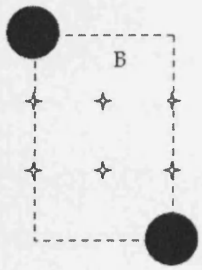

Figure 4.24: Sampling Pattern B

Sampling Pattern B

Sampling Pattern B is inspired by the selection of sampling points from the research of Fairbanks (1998). Fairbanks investigated the effect of rigid vegetation on velocity and turbulence structures. Acrylic dowels were used and tested under submerged, emergent and double layer conditions. An LDV sampling for 20 s at 75 Hz was employed to measure velocity and turbulence at six locations, shown in Figure 4.24. Measurements in the vertical plane were taken in steps of between 2.31 mm and 5.02mm. Within the study, it was noted that the mean velocity and turbulence intensity varied considerably depending on the measurement location. It was also observed that there was an inverse relationship between the mean velocity and turbulence intensity, with the the highest turbulence intensities occurring at the location of lowest mean velocity.
Within the data of Fairbanks (1998), a high velocity spike was seen at the base of the dowel, it was hypothesised that this was caused by the presence of a horseshoe vortex, within which momentum was transported to the central wake region behind the dowel.
Sampled-averaged mean and χ^2 values for streamwise velocity (U) and turbulent kinetic energy (TKE) using Sampling Pattern B are listed in Tables 13 to 17 in the Appendix.

Prediction of Streamwise Velocity Using Sampling Pattern B

Figures 4.25 and 4.26 present the data for the dowels and the results for control volume $CV3$ of the *Cornus* data respectively. The thin lines represent an individual streamwise velocity sample from Sampling Pattern B, the thick line is the horizontally-averaged profile for Sampling Pattern B, and the line with circle markers is the horizontally-averaged profile for the total control volume.

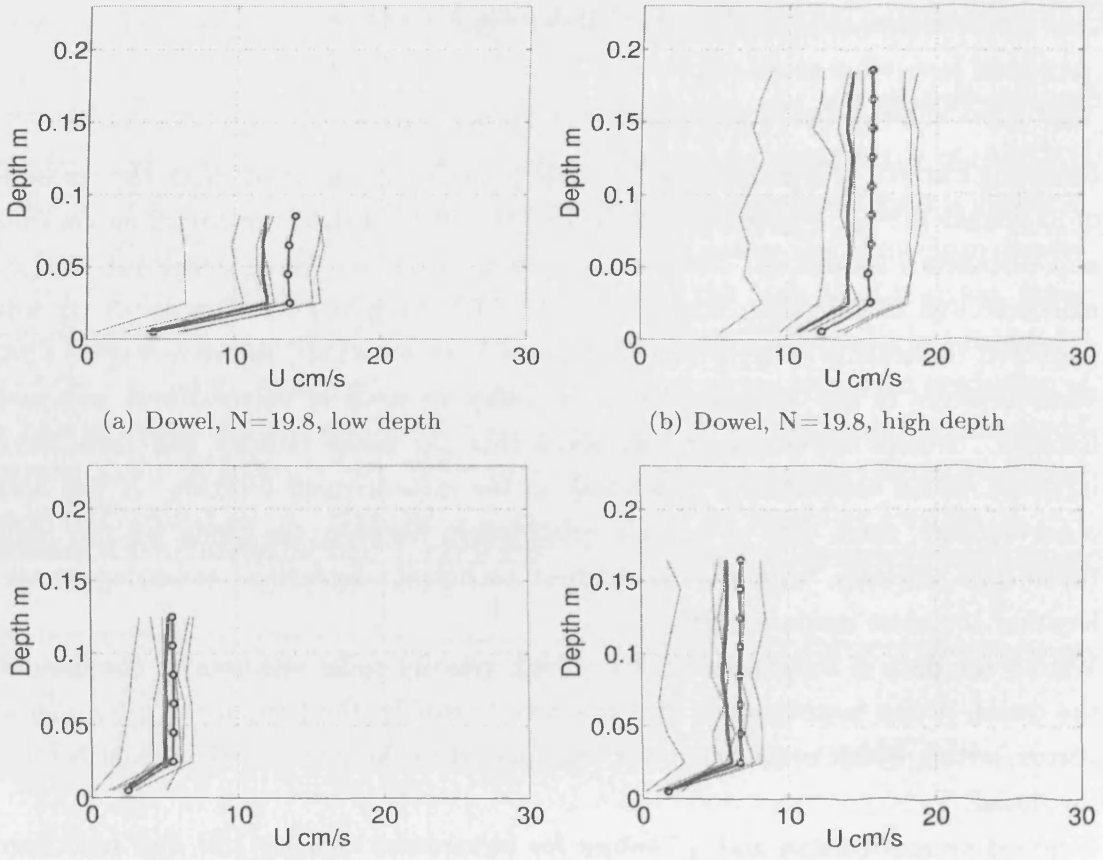

(a) Dowel, N=19.8, low depth

(b) Dowel, N=19.8, high depth

(c) Dowel, N=80.6, low depth

(d) Dowel, N=80.6, high depth

Figure 4.25: Sampled streamwise velocity U using Sampling Pattern B within dowel arrays

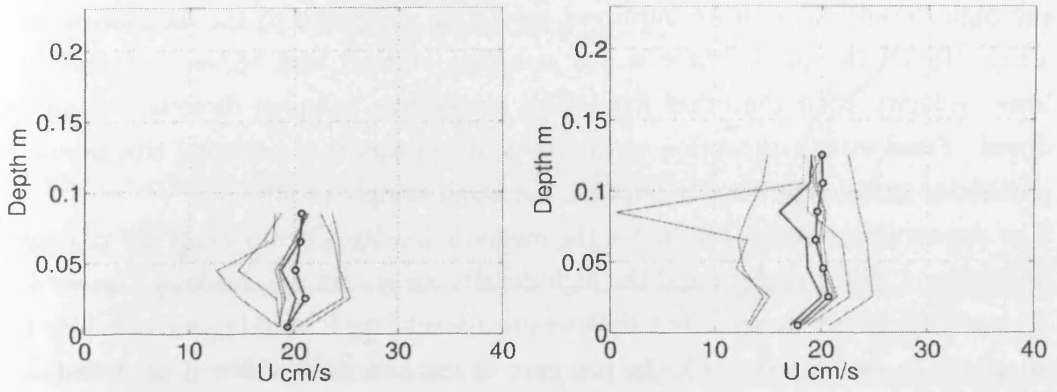

(a) *Cornus*, N=19.8, low depth

(b) *Cornus*, N=19.8, high depth

(c) *Cornus*, N=80.6, low depth

(d) *Cornus*, N=80.6, high depth

Figure 4.26: Sampled streamwise velocity U using Sampling Pattern B within dowel arrays

The streamwise velocity results for the dowel medium density are presented in Figures 4.25 (a) and (b) and the high density arrays are presented in Figures 4.25 (c) and (d). The thin lines, each representing an individual sampling vertical are widely spread, so it appears that the six sampling locations from Sampling Pattern B sample a wide range of high and low velocity areas of flow. All the Sampling Pattern B profiles in the dowel arrays underpredict the full volume horizontally-averaged velocity profile, indicated by the thick line with circles. The results for the high density array have improved prediction compared to the medium density array. In all the plots, there is one sampling vertical that shows a significantly lower velocity than the other five. This profile was sampled directly behind the dowel. From visual inspection of the plots, it appears that omitting this profile in particular would significantly improve the mean sample profile.

The streamwise velocity results for the medium density *Cornus* array are presented in Figures 4.26 (a) and (b) and the high density arrays are presented in Figures 4.26 (c) and (d). It can be seen that the streamwise velocity is mostly underpredicted in all plots. In (a), (c) and (d), the top part of the flow profile is well predicted, but the lower half is where the deviation away from the volume-averaged mean. This suggests that not only is the flow three-dimensional, but different flow structures exist at different levels, and using this sampling configuration, the turbulent structures away from the bed are well predicted, but those that exist nearer the bed are not.

Further results for prediction of velocity within the *Cornus* data using Sampling Pattern B are available in Figures 29 to 30 in the Appendix. In these extended results, note that in general, the medium density results are under-predicted while, overall, the high density *Cornus* results are well predicted.

Prediction of TKE Using Sampling Pattern B

In contrast to the streamwise velocity, the turbulent kinetic energy (TKE) is generally overpredicted in the dowel and *Cornus* arrays. Figures 4.27 and 4.28 present the results for TKE prediction using Sampling Pattern B within the dowel and *Cornus* arrays respectively.

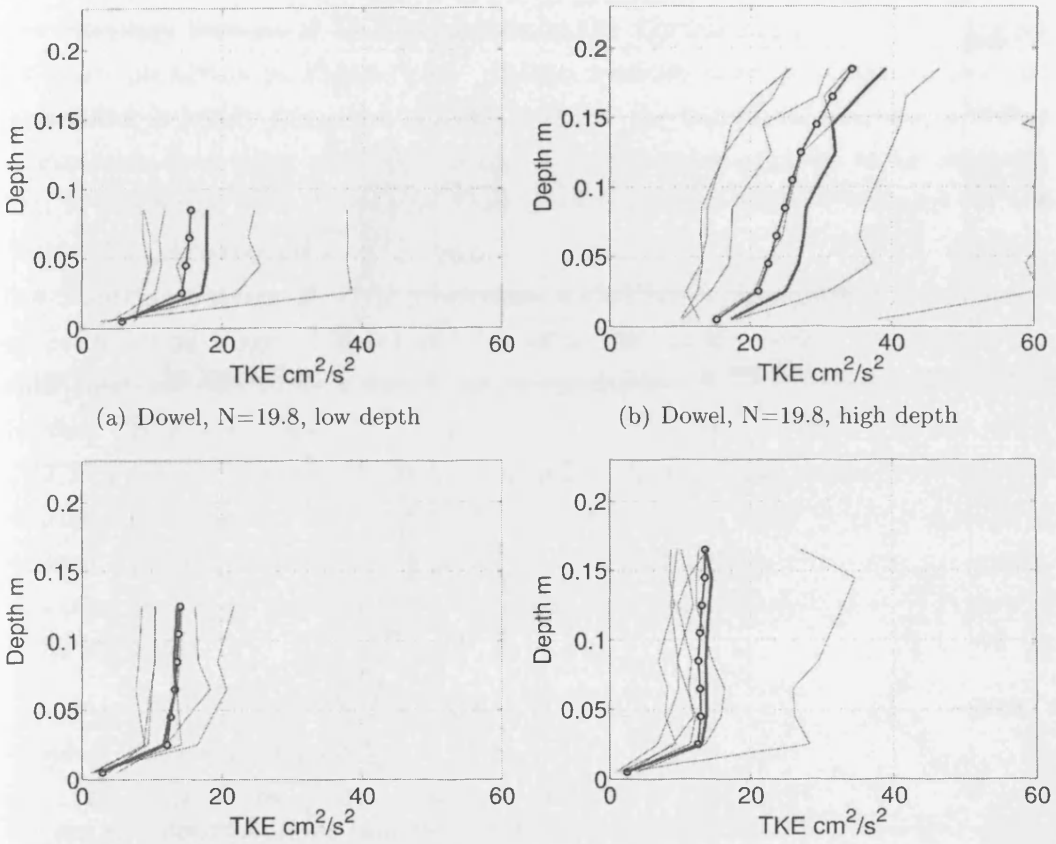

(a) Dowel, N=19.8, low depth

(b) Dowel, N=19.8, high depth

(c) Dowel, N=80.6, low depth

(d) Dowel, N=80.6, high depth

Figure 4.27: Sampled turbulent kinetic energy TKE using Sampling Pattern B within dowel arrays

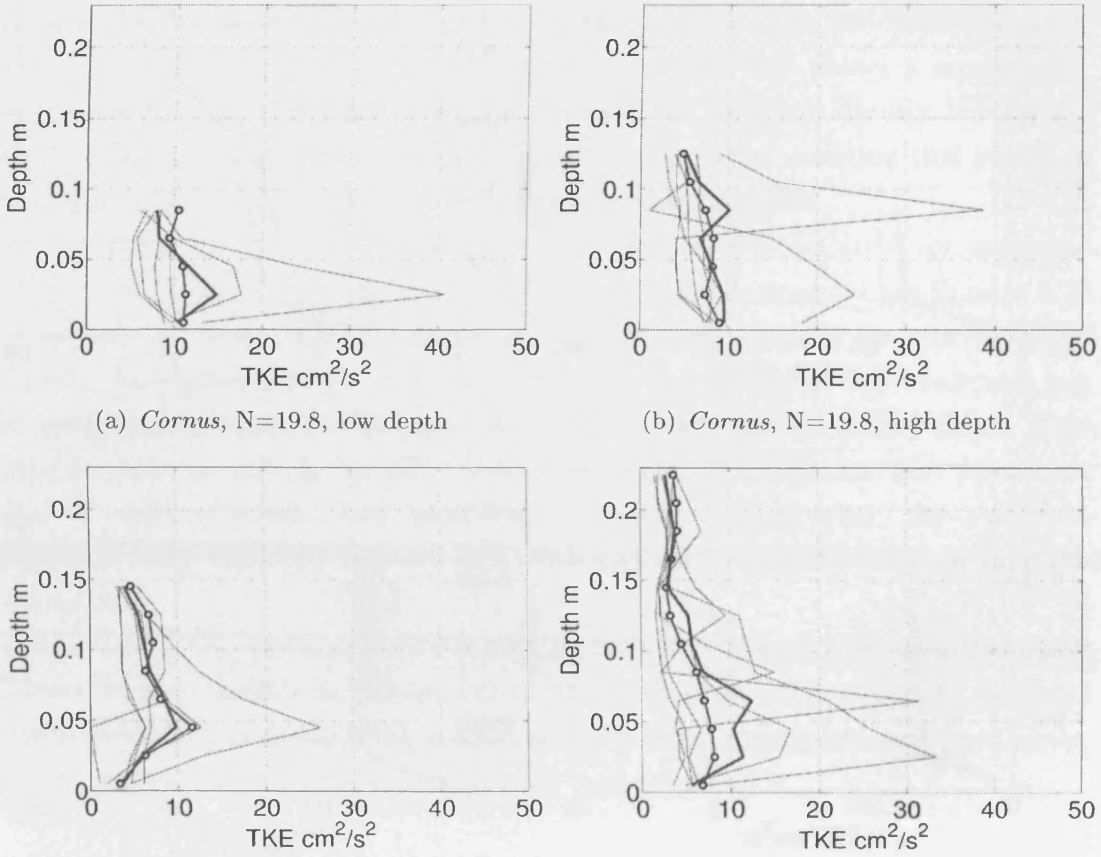

(a) *Cornus*, N=19.8, low depth

(b) *Cornus*, N=19.8, high depth

(c) *Cornus*, N=80.6, low depth

(d) *Cornus*, N=80.6, high depth

Figure 4.28: Sampled turbulent kinetic energy TKE using Sampling Pattern B within *Cornus* arrays

Figure 4.27 (a) and (b) present the results for the medium density dowel array. Sampling Pattern B overpredicts the TKE in both the low and high depth conditions. Note that if the sampling vertical with the highest TKE is omitted, the prediction would be improve. This is same sampling vertical that distorted the streamwise velocity (U) profile earlier, located immediately behind the dowel. In the high density dowel array, seen in (c) and (d), the agreement is much closer, particularly in (d).

The Sampling Pattern B TKE prediction in the *Cornus* arrays in control volume $CV3$ are presented in Figure 4.28. In the medium density plots (a) and (b), the profiles is highly distorted by local peaks in the individual samples, however, approximate agreement with the volume averaged value appears to be achieved. This is consistent with the results from control volumes $CV1$, $CV2$ and $CV4$ in Figure 31 in the Appendix

The Sampling Pattern B TKE predictions within the high density *Cornus* arrays are presented in Figure 4.28 (c) and (d). The TKE profile is well matched in (c), while there appears to be a significant overprediction of TKE in the lower half of the flow. However, inspection of the results for the other control volumes $CV1$, $CV2$ and $CV4$ in Figure 32 in the Appendix, show a close match with the full horizontally-averaged TKE profile. In Figure 4.28 (d), there is good agreement between the Sampling Pattern B profile and the full horizontally-averaged profile. This is supported by the result in $CV2$ under identical flow conditions in Figure 32 in the Appendix.

Sampling Pattern B Review

The six sampling locations that form Sampling Pattern B have mixed fortunes in terms of prediction of streamwise velocity U and turbulent kinetic energy TKE. For the dowels, generally, streamwise velocity U is underpredicted, whereas the TKE is overpredicted. The prediction is more accurate in the high density array for both the low and high flow depths.

In the medium density *Cornus* array, streamwise velocity U is mostly underpredicted, whereas TKE is generally overpredicted. In the high density *Cornus* array, U is well predicted, with only a few instances of underprediction, mostly in the lower portion of flow. The TKE prediction suffers from a few high and low TKE peaks, however the general agreement between the sampled TKE profile and the full TKE profile is well matched, and only in a few instances it can be seen that TKE is

overpredicted.

In both the streamwise velocity U and the turbulent kinetic energy TKE, the sampling point immediately upstream of the dowel has an unfair weight on the Sampling Pattern B averaged profile. This can be related to the statistical distributions explored in Section 4.4.1, where it can be seen that there are many statistical outliers with low velocity but high turbulent intensities. This suggests that in a measurement strategy with limited measurements, sampling in the wake of an obstacle will significantly skew the overall profile sampled.

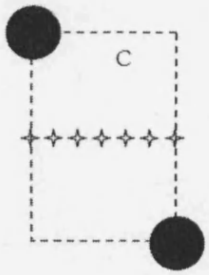

Figure 4.29: Sampling Pattern C

Sampling Pattern C

The measurements in Sampling Pattern C were those taken by Westwater (2000). A cross-streamwise transect bisecting the control volume was sampled, perpendicular to the direction of flow. Westwater compared dowel size and spacing effects on velocity throughout the canopy. Seven sampling points are taken to make Sampling Pattern C and can be seen in Figure 4.29.
Transect sampling is common if there is an automated sampling rig. Sampling in along a cross-streamwise plane is satisfying for the determination of streamwise velocity in an unobstructed steady and incompressible flow field where mass and momentum are conserved. With the simulated vegetated flows considered here,if the two-dimensional sampling plane is a representative section (as in this case), and if the sampling resolution is high enough, in theory the sampled averaged should produce a close match to the full horizontally-averaged profile. This is true for the regular shape of the dowels, but may not be adequate for the velocity field induced by the spatial heterogeneity of the *Cornus* saplings.
Sampled-averaged mean and χ^2 values for streamwise velocity (U) and turbulent kinetic energy (TKE) using Sampling Pattern C are listed in Tables 13 to 17 in the Appendix.

Prediction of Streamwise Velocity U using Sampling Pattern C

Figures 4.30 and 4.31 present the prediction of streamwise velocity U using Sampling Pattern C in the dowel and *Cornus* arrays respectively.

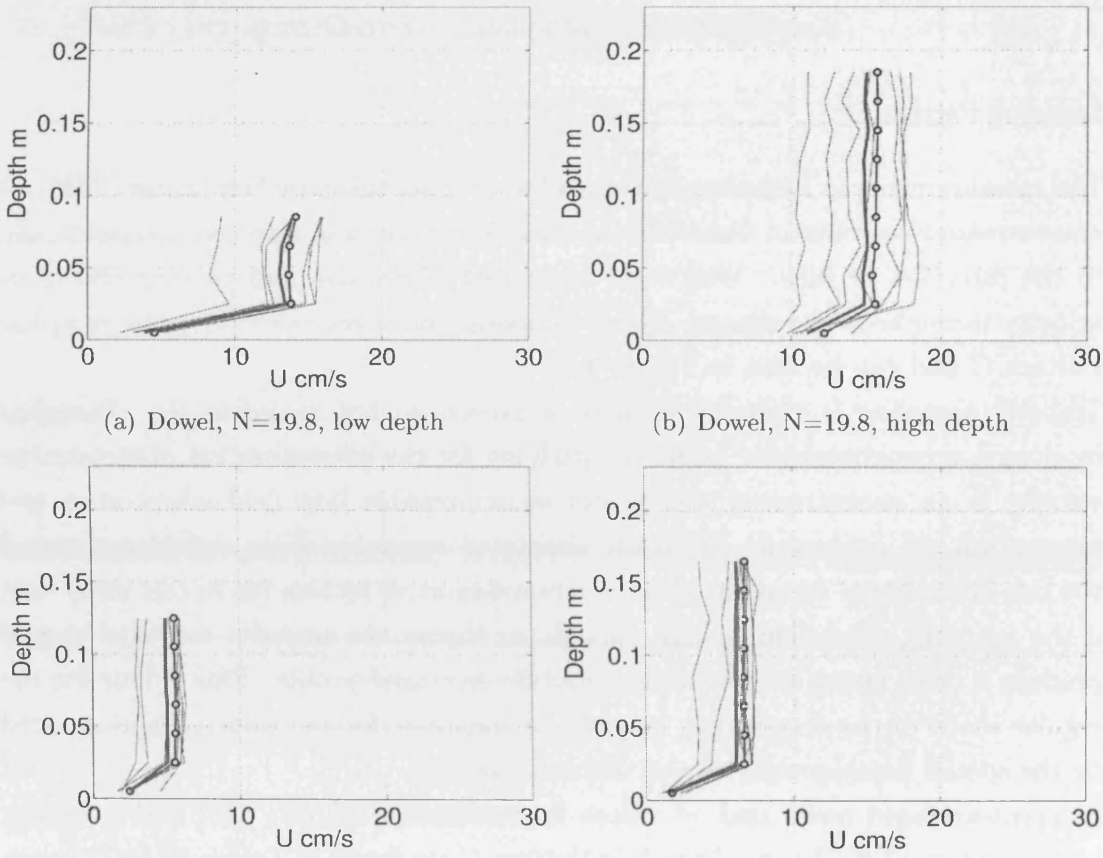

(a) Dowel, N=19.8, low depth

(b) Dowel, N=19.8, high depth

(c) Dowel, N=80.6, low depth

(d) Dowel, N=80.6, high depth

Figure 4.30: Sampled streamwise velocity U using Sampling Pattern B within dowel arrays

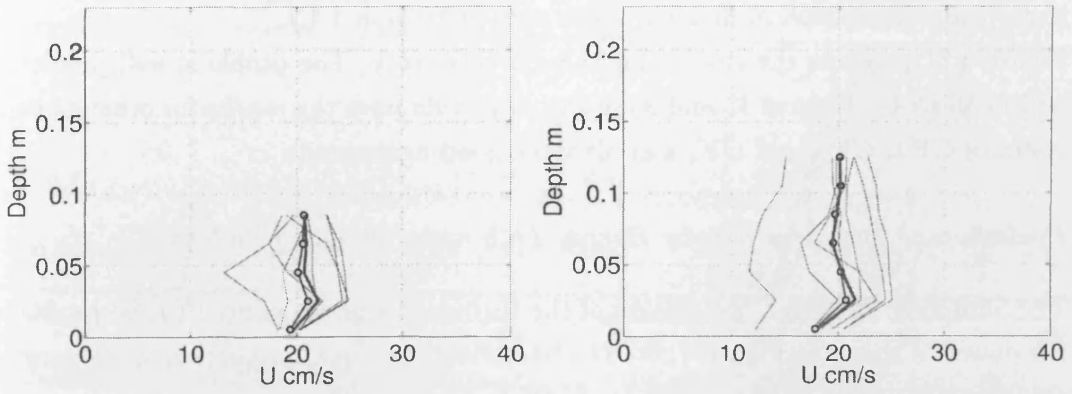

(a) *Cornus*, N=19.8, low depth

(b) *Cornus*, N=19.8, high depth

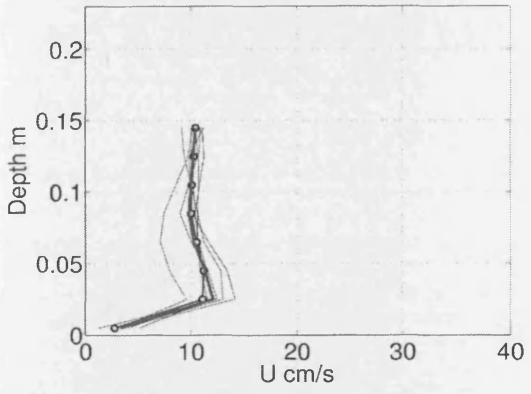

(c) *Cornus*, N=80.6, low depth

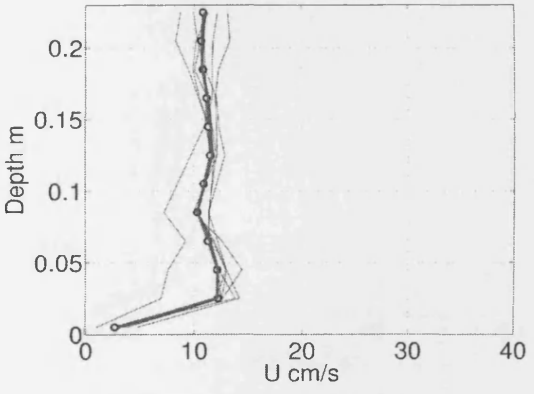

(d) *Cornus*, N=80.6, high depth

Figure 4.31: Sampled streamwise velocity U using Sampling Pattern B within *Cornus* arrays

In Figure 4.30, presenting the streamwise velocity within the dowel arrays, it can be seen that Sampling Pattern C consistently underpredicts the streamwise velocity in all plots. No improvement in the prediction of the high density array was observed when compared to the medium density array, as was seen with Sampling Patterns A and B. In all plots, the individual samples are well spread out around the Sampling Pattern B horizontally-averaged profile, but the high velocity profiles are bunched closely together, while the low velocity profiles are more spread out, reflecting the statistical distribution of flow variables seen in Section 4.4.1.
Figure 4.31 presents the results for the *Cornus* array. The profile is well predicted within all plots. Figures 33 and 34 in the Appendix have the results for other control volumes $CV1$, $CV2$ and CV, and all show good agreement.

Prediction of Turbulent Kinetic Energy TKE using Sampling Pattern C

The Sampling Pattern C prediction of the turbulent kinetic energy (TKE) profile in the dowels is shown in Figure 4.32. The Sampling Pattern C prediction of streamwise velocity (U) profile in the dowels is shown in Figure 4.33.

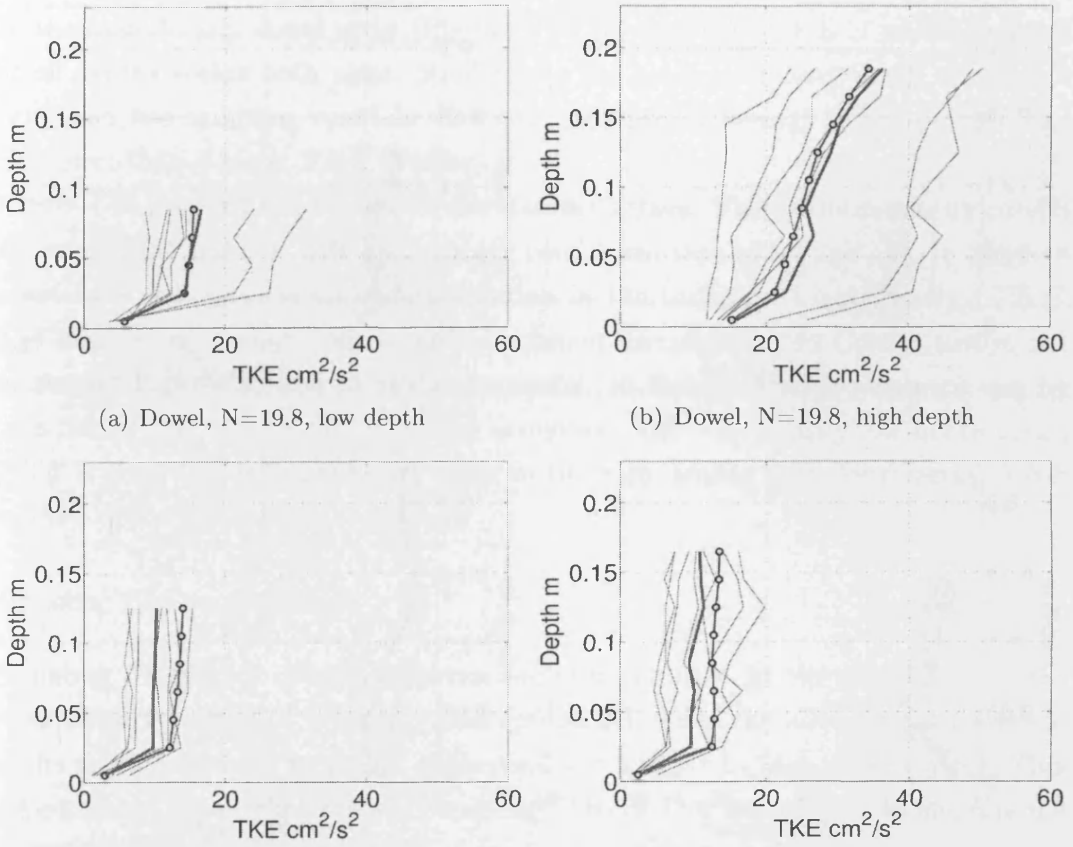

(a) Dowel, N=19.8, low depth

(b) Dowel, N=19.8, high depth

(c) Dowel, N=80.6, low depth

(d) Dowel, N=80.6, high depth

Figure 4.32: Sampled turbulent kinetic energy (TKE) using Sampling Pattern C within dowel arrays

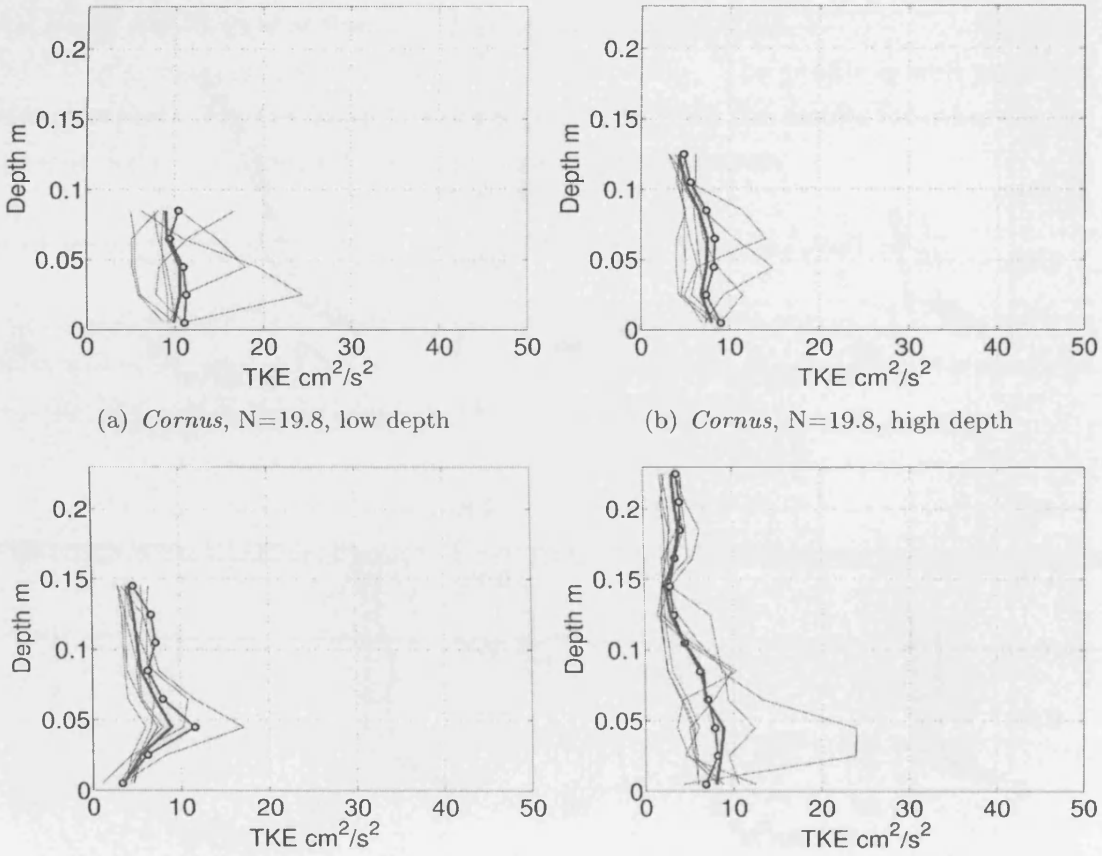

(a) *Cornus*, N=19.8, low depth

(b) *Cornus*, N=19.8, high depth

(c) *Cornus*, N=80.6, low depth

(d) *Cornus*, N=80.6, high depth

Figure 4.33: Sampled turbulent kinetic energy (TKE) using Sampling Pattern C within *Cornus* arrays

The TKE prediction within the medium density dowel array is presented in Figures 4.32 (a) and (b). It can be seen that at the low depth, there is good agreement between the Sampling Pattern C profile and the full horizontally-averaged profile, while at the high depth the TKE is overpredicted. Both (a) and (b) have two individual profiles of high TKE, which are the two sample points in the wake of the upstream dowel, located at the far right of the transect in Figure 4.29. Mostly, the other five profiles have a lower-than-average magnitude of TKE.
In the high density dowel array (Figures 4.32 (c) and (d)), TKE is underpredicted at all depths within both plots. Similarly to the medium density dowel array, plot (c) shows two sampling verticals with two higher-than-average TKE profiles, and five lower-than-average TKE profiles.
Figure 4.33 presents the results for the *Cornus* arrays. The medium density results are seen in (a) and (b). The high density results are seen in (c) and (d). In all plots apart from (d), there is an underprediction in the turbulent kinetic energy TKE. The full results from the other control volumes sampled in the *Cornus* arrays can be seen in Figures 33 and 33 in the Appendix. In these extended results, it can be seen that within both medium density arrays and the high density low depth array, TKE is generally underpredicted, while in the high density high depth array, TKE is often overpredicted.

Sampling Pattern C Review

Sampling Pattern C consists of seven sampling points. In the dowel arrays, the streamwise velocity (U) is slightly underpredicted, while the TKE is overpredicted in the medium density array and underpredicted within the high density array. This suggests that in sampling dowels, Sampling Pattern C is appropriate to measure the streamwise velocity (U), but large errors in the TKE can be found.
Overall,in the medium density *Cornus* array, both the streamwise velocity (U) and the turbulent kinetic energy (TKE) are closely predicted. In the high density *Cornus* array, the streamwise velocity (U) is again well predicted, but the turbulent kinetic energy profile is adversely affected by TKE peaks in the data.

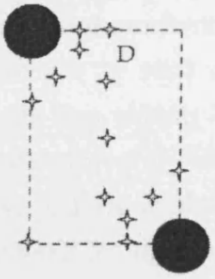

Figure 4.34: Sampling Pattern D

Sampling Pattern *D*

The pattern in Sampling Pattern D has been inspired by the research described in Poggi et al. (2004). More measurements are taken in areas that exhibit high spatial variability of flow characteristics. In the case of the staggered array, areas close to the plants will have the greatest variability, and so more measurements are taken in these areas, with fewer taken in the free flow regions away from the plants.
In a regular array, the general pattern of spatial variability can be determined approximately, as it is known for example that a low velocity, high wake forms behind the dowel. However there is a paradox inherent - if the flow field is being sampled to determine the velocity characteristics, a weighted sampling scheme assumes a knowledge of the velocity characteristics in the field.
Figure 4.34 presents the sample points for Sampling Pattern D.
Sampled-averaged mean and χ^2 values for streamwise velocity (U) and turbulent kinetic energy (TKE) using Sampling Pattern C are listed in Tables 13 to 17 in the Appendix.

Prediction of U using Sampling Pattern D

Figure 4.35 presents the Sampling Pattern 4 results for the dowel arrays, Figure 4.36 presents the Sampling Pattern 4 results for the *Cornus* array.

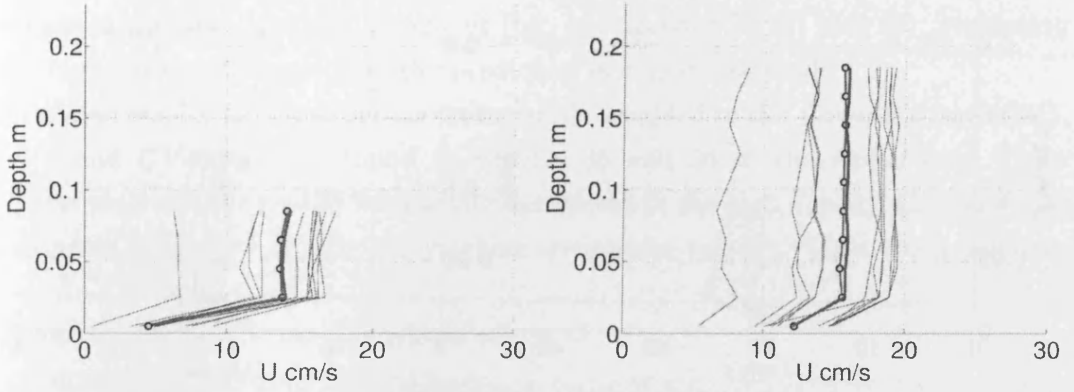

(a) Dowel, N=19.8, low depth

(b) Dowel, N=19.8, high depth

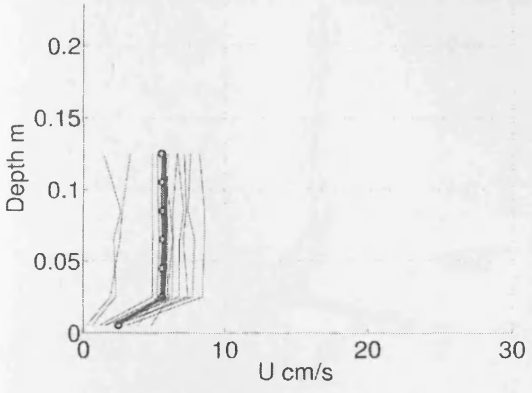

(c) Dowel, N=80.6, low depth

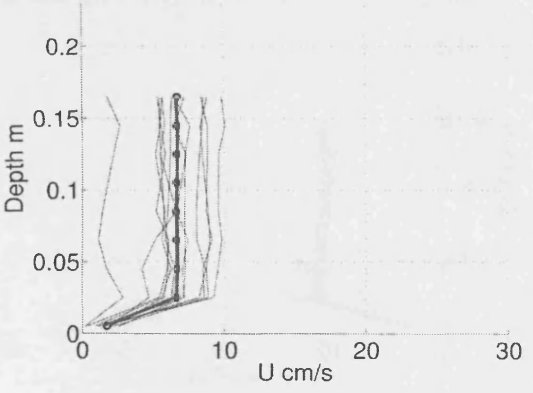

(d) Dowel, N=80.6, high depth

Figure 4.35: Sampled streamwise velocity (U) using Sampling Pattern C within *Cornus* arrays

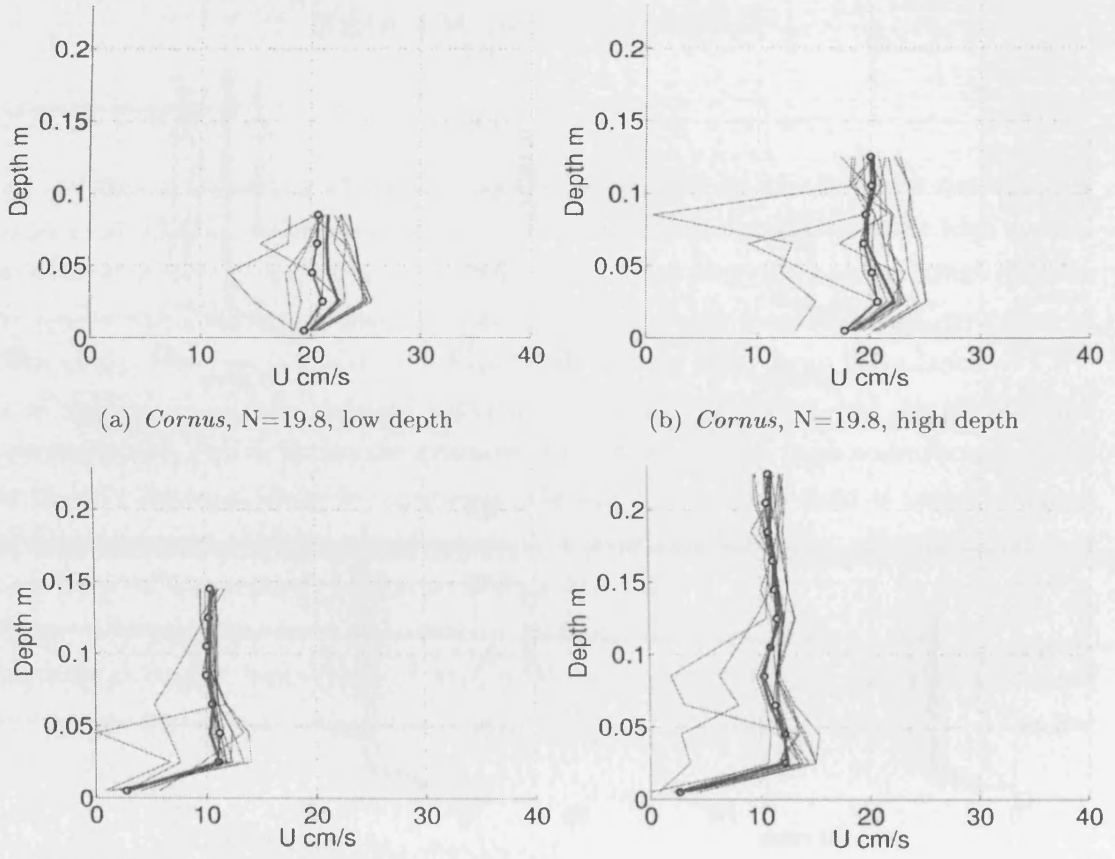

(a) *Cornus*, N=19.8, low depth

(b) *Cornus*, N=19.8, high depth

(c) *Cornus*, N=80.6, low depth

(d) *Cornus*, N=80.6, high depth

Figure 4.36: Sampled streamwise velocity (U) using Sampling Pattern C within *Cornus* arrays

The Sampling Pattern D streamwise velocity (U) predictions within the dowel arrays are presented in Figure 4.35. It can be seen that all the plots show a close prediction, although in each case, the streamwise velocity is slightly overpredicted to a similar magnitude. Unlike most of the other sampling schemes, there is no difference between the medium density and the high density arrays.

Figure 4.36 presents the results for the *Cornus* arrays. In (a), the Sampling Pattern D profile produces an overprediction in streamwise velocity. An overprediction also occurs in the lower portion of flow of (b). In Figures 4.36 (c) and (d), presenting the high density *Cornus* data, the prediction is closely matched.

Extended results for the other control volumes sampled in the *Cornus* arrays ($CV1$, $CV2$ and $CV4$) may be found in Figures 35 and 36 in the Appendix. These figures show similar results with better agreement in the high density *Cornus* array, compared to the low density array, where streamwise velocity (U) is over-predicted.

Prediction of TKE using Sampling Pattern D

Figure 4.37 presents the results for the medium and high density dowel arrays. Figure 4.38 presents the results for the medium and high density *Cornus* arrays.

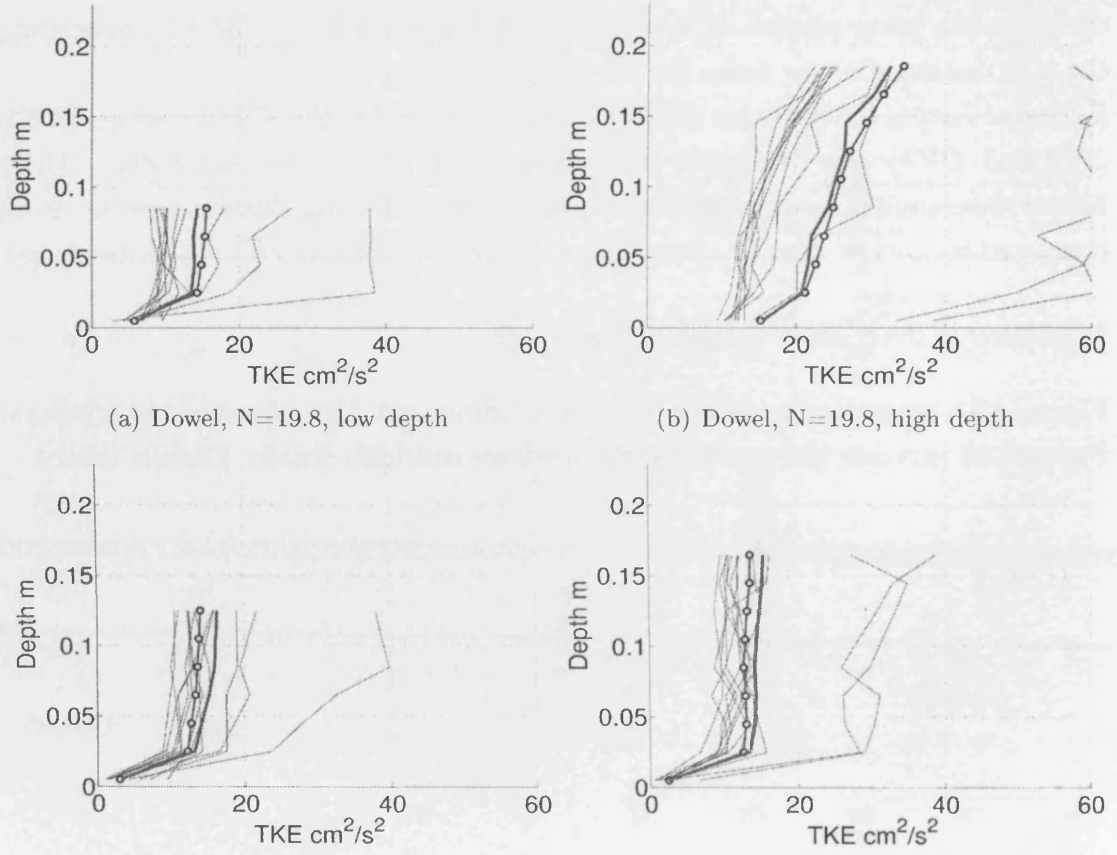

(a) Dowel, N=19.8, low depth

(b) Dowel, N=19.8, high depth

(c) Dowel, N=80.6, low depth

(d) Dowel, N=80.6, high depth

Figure 4.37: Sampled turbulent kinetic energy (TKE) using Sampling Pattern C within dowel arrays

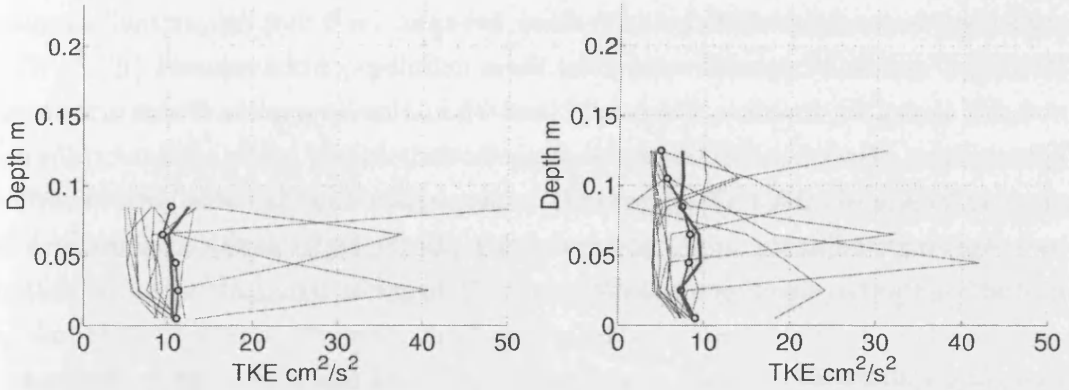

(a) *Cornus*, N=19.8, low depth

(b) *Cornus*, N=19.8, high depth

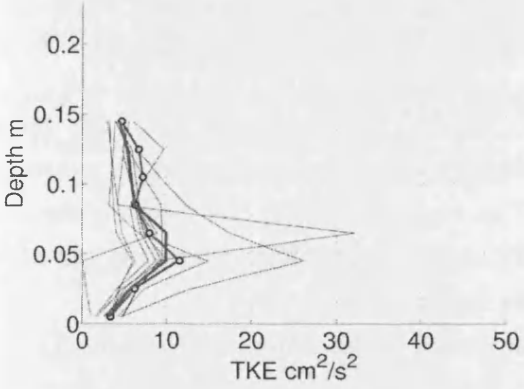

(c) *Cornus*, N=80.6, low depth

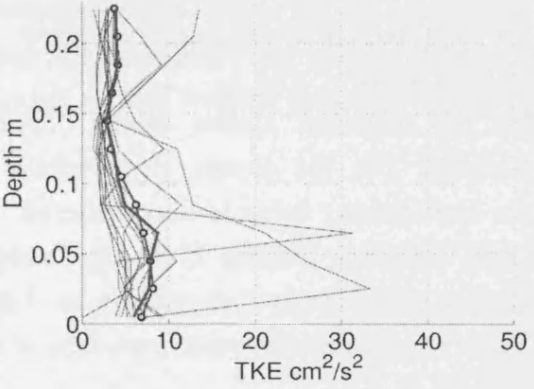

(d) *Cornus*, N=80.6, high depth

Figure 4.38: Sampled turbulent kinetic energy (TKE) using Sampling Pattern C within *Cornus* arrays

Figure 4.38 presents the results for the dowel arrays. In the medium density array plots (a) and (b), the TKE is underpredicted, whereas in the high density array (c) and (d), the TKE is overpredicted. The spread of the individual sampling verticals included in Sampling Pattern D shows that Sampling Pattern D includes many grouped sampling verticals and a few outliers with high TKE. These high value TKE values have a weighted effect on the average.
The results for TKE within the *Cornus* array are seen in Figure 4.38. Overall, the agreement is good, however there are many peaks in TKE that distort the Sampling Pattern D profile. Extended results for the remaining control volumes ($CV1$, $CV2$ and $CV4$) can be found in Figures 37 and 38 in the Appendix. These additional figures show extremely variable rates of prediction. In the medium density *Cornus* array in Figure 37, the TKE is generally underpredicted in the lower portion of flow and overpredicted in the upper portion of flow. In the high density *Cornus* array in Figure 37, there is much more variation.

Sampling Pattern D Review

Sampling Pattern D closely predicts the streamwise velocity (U) for the dowels and the high density *Cornus* array, however, U is overpredicted for the medium density *Cornus* array.
For the turbulent kinetic energy (TKE) results, the prediction rates are more variable. For the dowels, the medium density array is underpredicted, whereas the high density array is overpredicted. This suggests that in the medium density array, Sampling Pattern D does not sample areas of high TKE, whereas in the high density array, overly turbulent areas of flow are sampled.
Table 14 presents the statistical data of mean and χ^2 for Sampling Pattern D.

Analysis of the Spread of Error in Streamwise Velocity and Turbulent Kinetic Energy

The streamwise velocity (U) and turbulent kinetic energy (TKE) data in the previous section can be aggregated to determine the effectiveness of the Sampling Patterns A to D within a range of different flow scenarios. Analysing all the results together in a global dataset allows an overall comparison of the success of the respective methods to be made. Figure 4.39 presents the error in the sampled streamwise velocity (U) prediction for both the dowel and *Cornus* arrays. Each circle in the Figures represents the percentage error in the sampled streamwise velocity (U), when compared to the flow-field volume-averaged mean value (U_{xyz}). As

expected, due to the higher degree of flow field uniformity in the *Cornus* arrays, the sampling patterns are overall more successful at predicting mean U, when compared to the dowel arrays. Although the sample sizes are small, there is a general trend, with the increasing sample pattern number, and consequently number of samples, moving from a negative to a positive error.

Figure 4.40 presents the variation in turbulent kinetic energy (TKE) prediction for both the dowel and *Cornus* arrays. Once again, each circle represents the percentage error in the sampled TKE as compared to the full flow-field volume-averaged value (TKE_{xyz}). The spread of prediction error in the dowel arrays does not appear to improve with sampling pattern number within either the dowel or *Cornus* data.

Looking at this global dataset, it is apparent that to accurately capture the streamwise velocity (U) in a staggered dowel array, for the range of flow conditions and planting densities in this study, Sampling Pattern D should be the preferred option, while for staggered arrays of *Cornus* or similar plant form, Sampling Pattern C should be preferred. However, checking the error in TKE for both of these shows that errors of up to 14% and 18% may be expected.

It is unlikely that these sampling patterns form the optimum sampling strategy available. The sheer number of possible sampling combinations makes a definitive study including all possible combinations very intensive, however, a methodical and practical approach has been adopted to attempt to find realistic optimum sampling locations for the dataset.

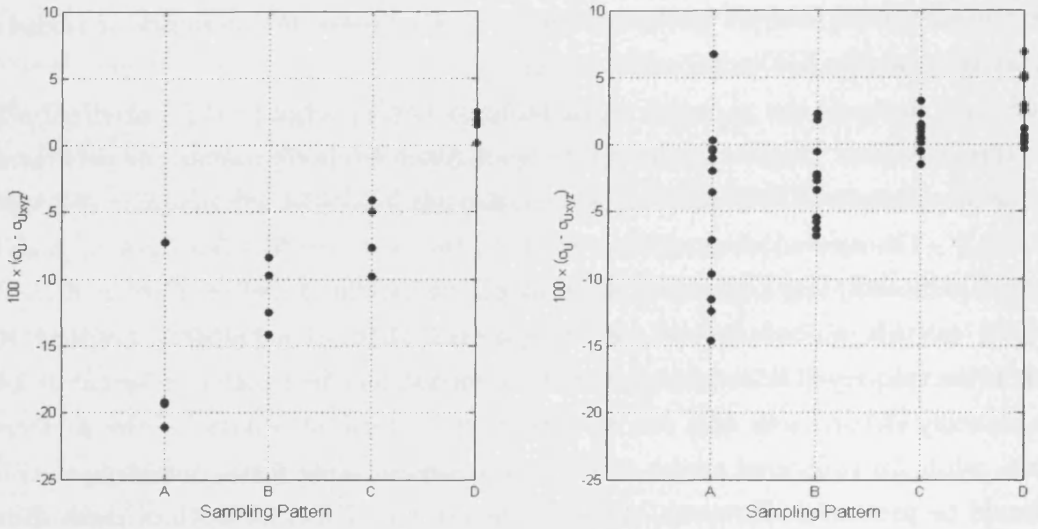

Figure 4.39: Error in sampled streamwise velocity mean (σ_U) for dowel and (local) *Cornus* arrays

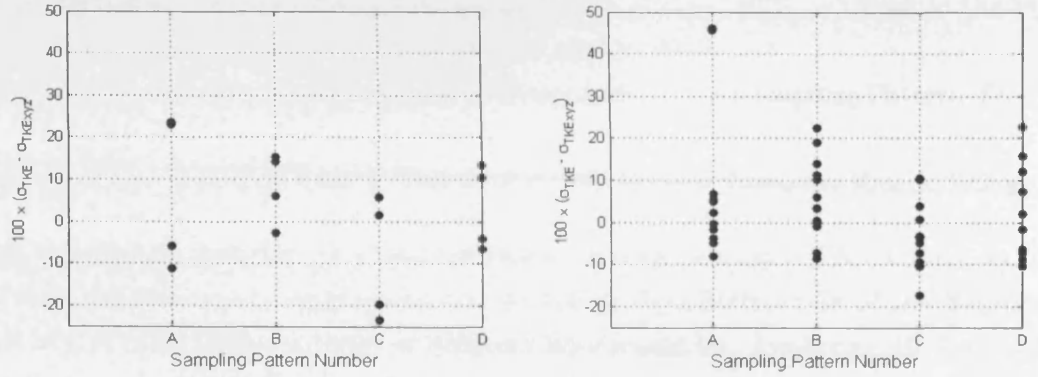

Figure 4.40: Error in sampled turbulent kinetic energy mean (σ_{TKE}) for dowel and (local) *Cornus* arrays

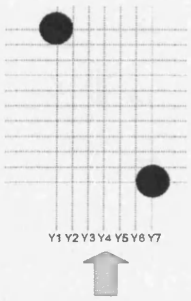

Figure 4.41: Sampling Transects Parallel to Flow Direction

4.5.2 Transect Sampling

Many experimental studies use mounted automated devices (ADV, LDV, laser etc.) to sample the flow characteristics of arrays, saving time and ensuring a greater degree of control and repeatability than can be achieved through manual adjustment. Such devices often move in one plane and so sample along pre-defined transect lines. To find the optimum location of sampling transects, the data collected will be resampled along streamwise and spanwise lines, and compared to the full sample mean. Results for the high density, dowel $D3g$ and *Cornus* $V3d$ arrays have been selected to show the full development of sampling in transect lines parallel to the principal flow direction. Streamwise velocity (U) and turbulent kinetic energy (TKE) are the variables to be compared to the profiles from the full sample.

Sampling Parallel to Flow Direction - Examples from Dowel and *Cornus* Arrays

Sampling parallel to the flow direction is likely to be highly biased. Since the wake structure from the dowels and *Cornus* specimens extends for some distance directly behind the obstacle, and transect sited in line with the plants will be highly influenced by their presence and are likely to show particularly low velocities and high, compared to the full sample mean values. Consequently, transects in line with the free flow stream should exhibit higher velocities and low TKE. It is proposed therefore, that at distances of approximately $1/3$ and $2/3$ between elements, the optimal sampling locations with representative (U) and (TKE) should be found. Figure 4.41 shows the sampling transects, labelled $Y1$ to $Y7$.
Streamwise velocity (U)and mean and χ^2 values for all transects sampled parallel

to the flow direction may be found in Table 18 in the Appendix.

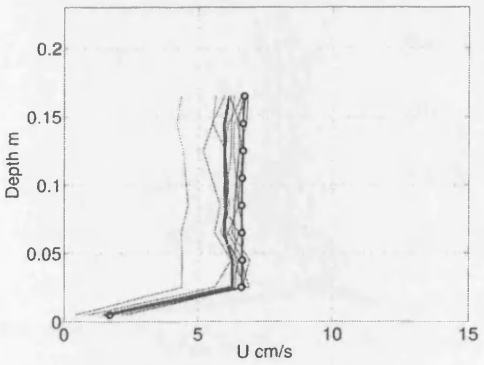

(a) dowel, N=80.6, high depth, Y1

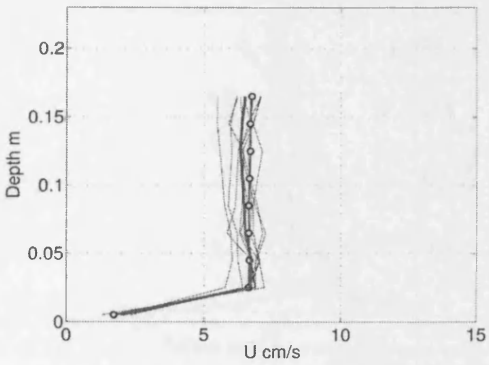

(b) dowel, N=80.6, high depth, Y2

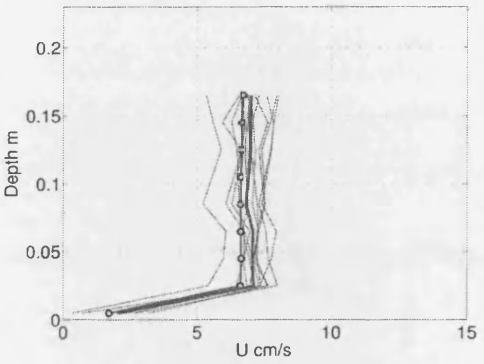

(c) dowel, N=80.6, high depth, Y3

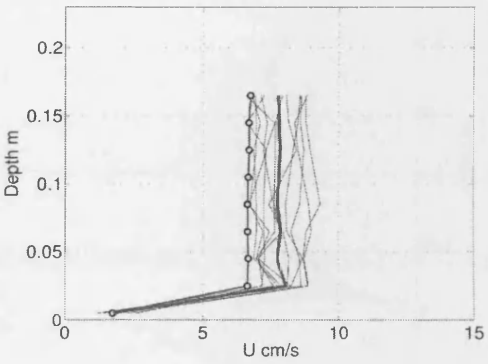

(d) dowel, N=80.6, high depth, Y4

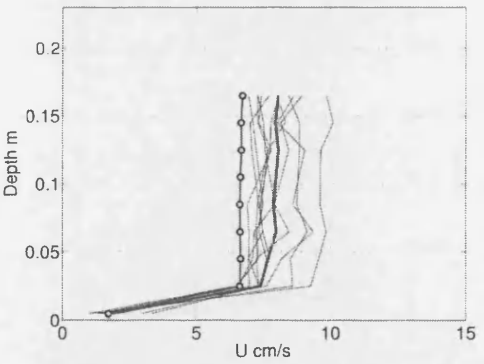

(e) dowel, N=80.6, high depth, Y5

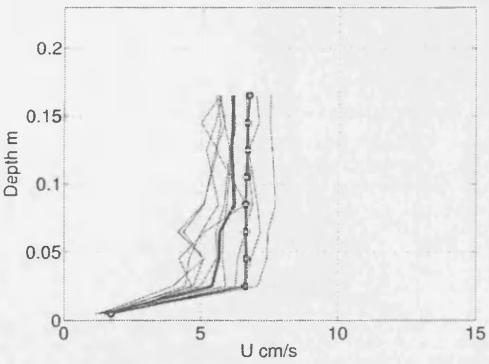

(f) dowel, N=80.6, high depth, Y6

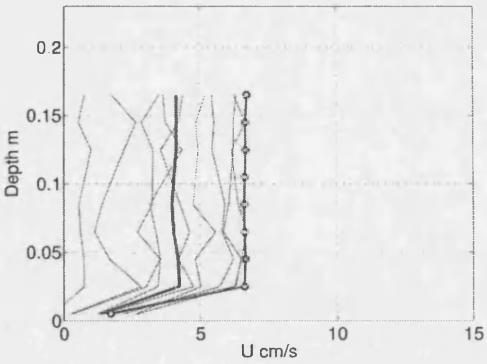

(g) dowel, N=80.6, high depth, Y7

Figure 4.42: Sampling streamwise velocity (U) parallel to flow direction in high density dowel array

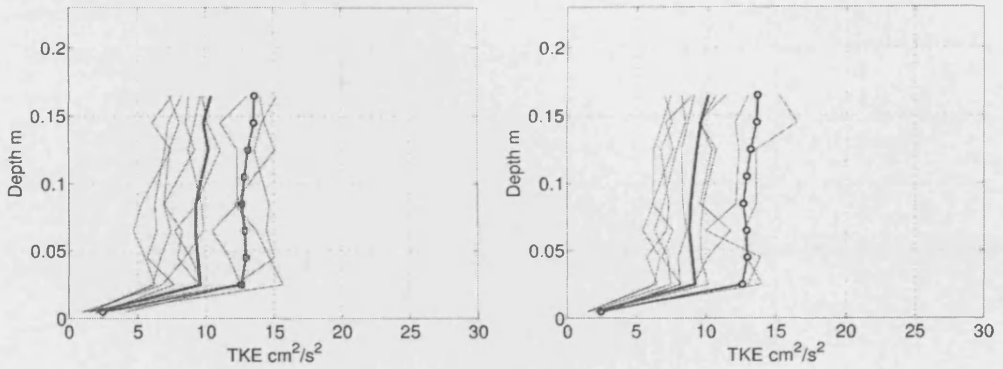

(a) dowel, N=80.6, Y1

(b) dowel, N=80.6, Y2

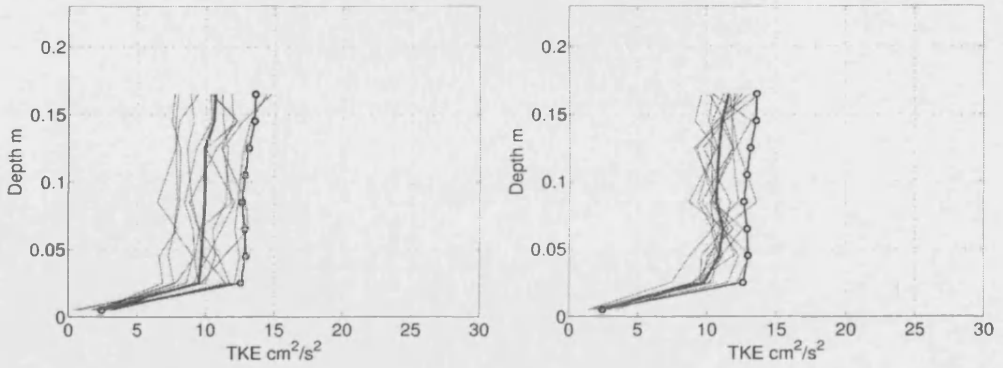

(c) dowel, N=80.6, Y3

(d) dowel, N=80.6, Y4

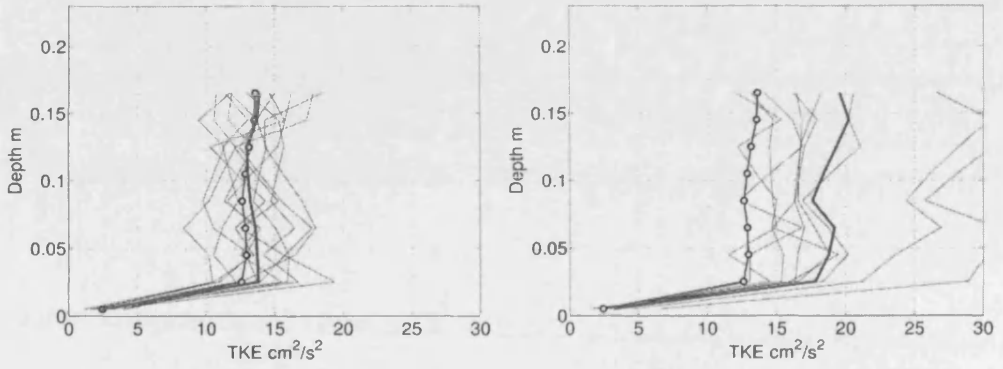

(e) dowel, N=80.6, Y5

(f) dowel, N=80.6, Y6

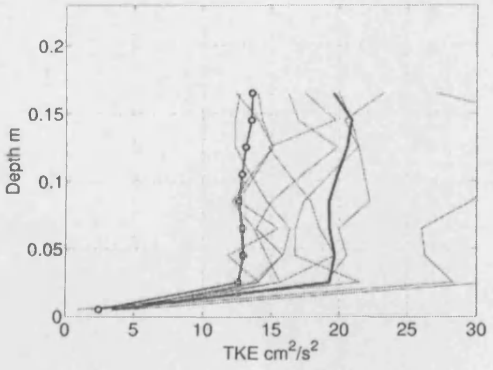

(g) dowel, N=80.6, Y7

Figure 4.43: Sampling turbulent kinetic energy (TKE) parallel to flow direction in high density dowel array

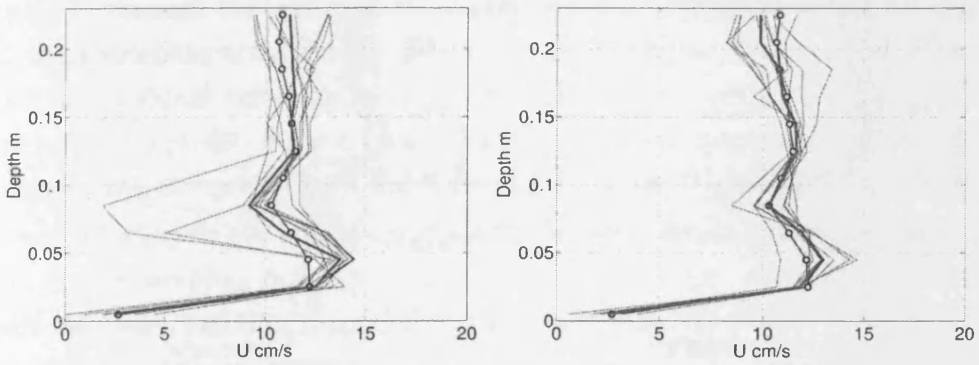

(a) *Cornus*, N=80.6, Y1

(b) *Cornus*, N=80.6, Y2

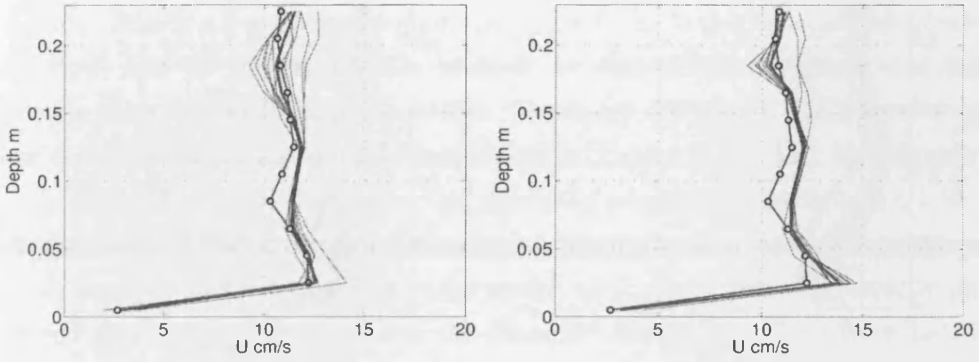

(c) *Cornus*, N=80.6, Y3

(d) *Cornus*, N=80.6, Y4

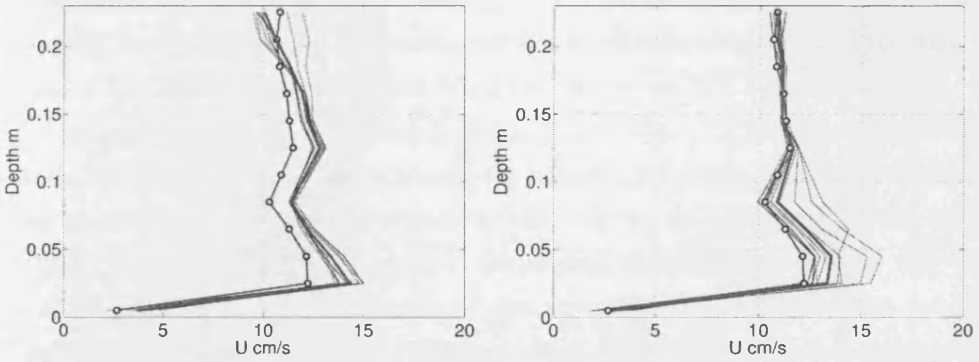

(e) *Cornus*, N=80.6, Y5

(f) *Cornus*, N=80.6, Y6

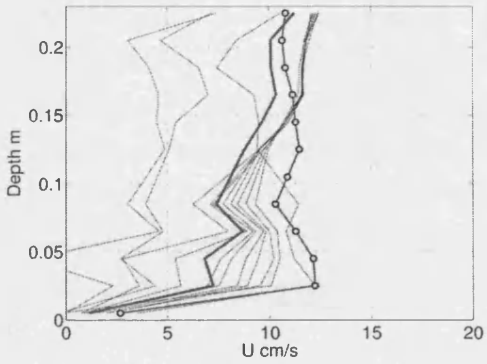

(g) *Cornus*, N=80.6, Y7

Figure 4.44: Sampling streamwise velocity (U) parallel to flow direction in high density *Cornus* array

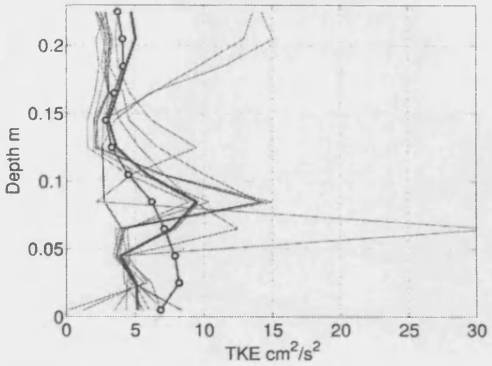

(a) *Cornus*, N=80.6, Y1

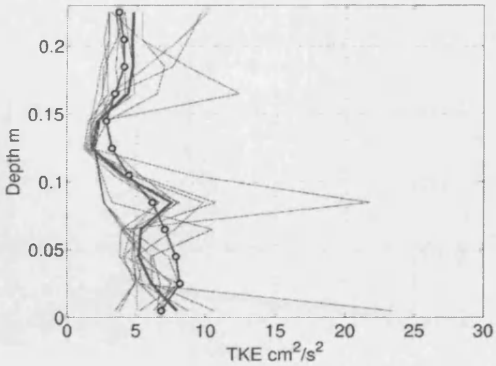

(b) *Cornus*, N=80.6, Y2

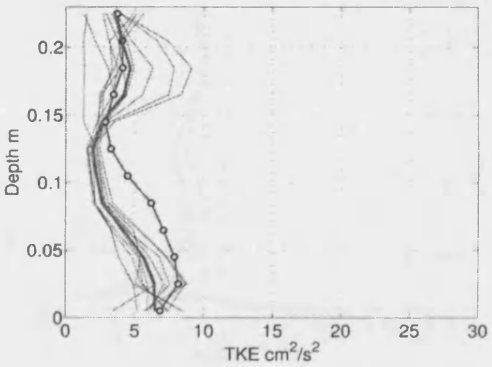

(c) *Cornus*, N=80.6, Y3

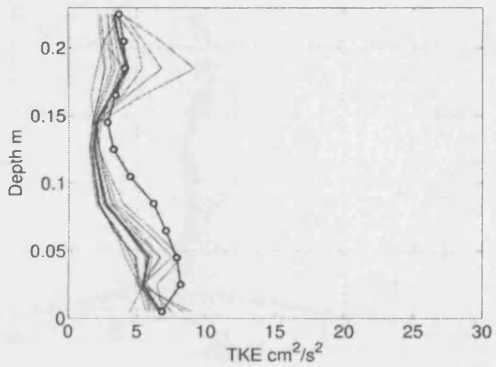

(d) *Cornus*, N=80.6, Y4

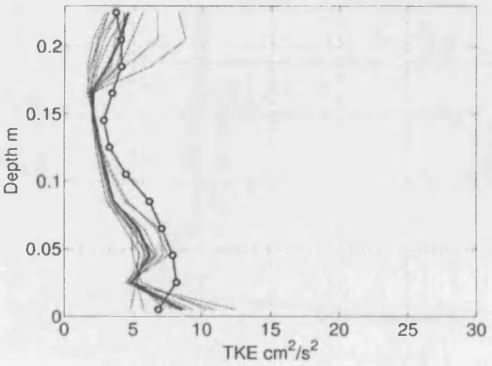

(e) *Cornus*, N=80.6, Y5

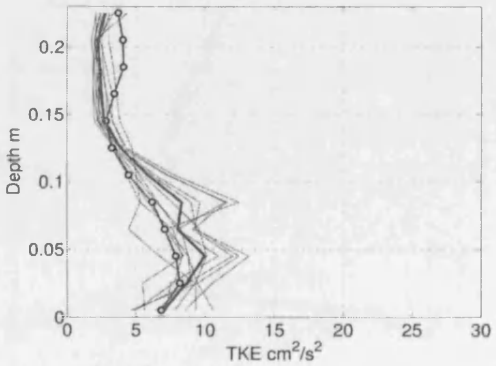

(f) *Cornus*, N=80.6, Y6

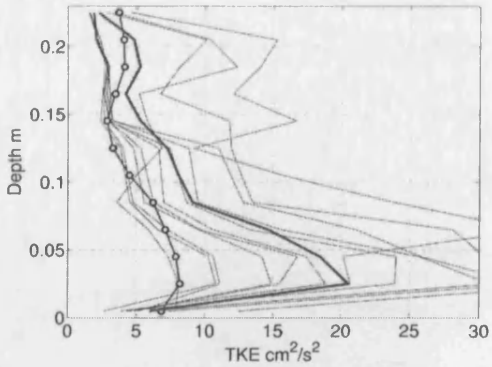

(g) *Cornus*, N=80.6, Y7

Figure 4.45: Sampling turbulent kinetic energy (TKE) parallel to flow direction in high density *Cornus* array

Figure 4.42 presents the predicted streamwise velocity(U) results in the dowel array *D3d*, using sampling transects *Y1* to *Y7*. In each subfigure, the thin lines represent the seven individual sampling verticals that comprise the transect. The thick line is the mean (U) profile of the transect, and the thick line marked with circles is the streamwise velocity profile from the full control volume (U_{xy}).

Transect *Y1* samples the points approaching the downstream dowel (refer to Figure 4.41). As the sampling points approach the dowel, the flow gets diverted laterally around the dowel, and the proportion of streamwise velocity reduces. Thus, sampling along this transect underpredicts the streamwise velocity (U). Transect *Y2* is similarly affected. Transects *Y3*, *Y4* and *Y5* sample in the flow space in between the dowels. This is a free stream region, throughout the flume there are no obstacles to the flow, and so the streamwise velocity predicted here exhibits at a higher magnitude than the the full sample profile. Transects *Y6* and *Y7* sample the region of flow directly behind the downstream dowel in Figure 4.41. The turbulent wake structure behind the dowel reduces the predicted streamwise velocity (U) to well below the profile obtained from the full sample. Thus, sampling transects progressing from left to right in the grid, U is underpredicted at the edges, and overpredicted in the middle. Thus, it follows that the optimum result will come from sampling points that lie between pairs $Y2$ and $Y3$, and $Y5$ and $Y6$.

The prediction of turbulent kinetic energy TKE in the high density, high depth dowel array, according to the transects parallel to the flow direction, are presented in Figure 4.43. The TKE prediction from the transects fall into two groups. The TKE is underpredicted in all transects from $Y1$ to $Y3$. These transects cover the region of flow approaching the downstream dowel in Figure 4.41, where the flow is more streamlined and comparatively unaffected by the presence of the dowels. Conversely, transects $Y5$ to $Y7$ sample the region immediately behind the dowel, where the highly turbulent conditions of the wake bias the results. The predicted TKE profile from these regions is therefore much higher than the full sample TKE profile.

The high density, high depth *Cornus* array was similarly sampled using transects parallel to the principal flow direction. Figure 4.44 presents the results for parallel sampling along Transects $Y1$ to $Y7$. In contrast to the single stem dowels, the *Cornus* array consists of multi-stem plants. The heterogeneous nature of the *Cornus* plants is documented in Section 3.2 on Page 77. Rather than concentrated areas of high and low turbulence, as exhibited by the dowel flow field, the streamwise velocity and turbulence conditions show less variation throughout the flow field. Transects

$Y1$ and $Y2$ lie in the approach to the downstream dowel of Figure 4.41 do not appear to significantly overpredict or underpredict the streamwise velocity. Transects $Y3$ to $Y6$ generally overpredict the streamwise velocity. Transect $Y7$, which lies directly behind the plant, underpredicts the streamwise velocity.

The prediction of turbulent kinetic energy (TKE) in the dowel array using parallel transects is presented in Figure 4.43. Transects $Y1$ and $Y2$ approximately match the overall $D3d$ global TKE Profile, although the magnitude at lower depths is variously overpredicted and underpredicted. Transects $Y3$ to $Y5$ underpredict the $D3d$ TKE profile, particularly at lower depths. Transects $Y6$ and $Y7$ overpredict the TKE profile in the lower portion of flow, but underpredict in the top region of flow.

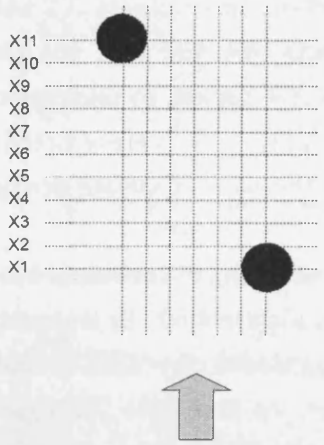

Figure 4.46: Sampling Transects Perpendicular to Flow Direction

Sampling Perpendicular to Flow Direction - Examples from Dowel and *Cornus* Arrays

Sampling velocity and turbulence perpendicular to the flow should cut through a greater variation of the flow field than sampling parallel, however, a similar bias is likely to exist. Transects which sample a portion of flow immediately behind a plant element will probably exhibit higher degrees of turbulence, than those not cutting through an area of flow affected by the plants.

The results for perpendicular sampling of streamwise velocity (U) in the high density dowel array are presented in Figure 4.47. In Transects $X1$ and $X2$, which sample the area of flow next to the downstream dowel, the streamwise velocity is overpredicted. In transects $X3$ to $X9$, the streamwise velocity is underpredicted. In Transects $X10$ and $X11$, the streamwise velocity is overpredicted. Transects $X3$ and $X10$ appear to produce the most accurate prediction of the global TKE Profile.

The results for perpendicular sampling of turbulent kinetic energy in the high density dowel array are presented in Figure 4.48. In transects $X1$ and $X2$, which sample the area of flow next to the downstream dowel, the TKE is underpredicted. In transects $X3$ and $X4$, the TKE is overpredicted. In transects $X5$ and $X8$, the the TKE is underpredicted. In transects $X9$ to $X11$, the TKE is overpredicted. transects $X1$ and $X11$ appear to produce the most accurate prediction of the D3d Global TKE Profile.

The results for perpendicular sampling of streamwise velocity (U) in the high density *Cornus* array are presented in Figure 4.49. In transect $X1$, which samples the area of flow next to the downstream dowel, the streamwise velocity is overpredicted. In transect $X2$, U is underpredicted. In transects $X2$ and $X3$, the streamwise velocity is underpredicted. In transects $X4$ and $X7$, the the streamwise velocity is well predicted. Transects $X8$ and $X9$ appear to underpredict U in the lower portion of flow. In transects $X10$ and $X11$, U is overpredicted in the lower portion of flow. Transects $X4$ to $X7$ produce the most accurate prediction of the D3d Global TKE Profile.

The results for perpendicular sampling of turbulent kinetic energy in the high density *Cornus* array are presented in Figure 4.50. In transects $X1$, which samples the area of flow next to the downstream dowel, the TKE is underpredicted near the bed and overpredicted near the surface. In transects $X2$ to $X5$, the TKE is overpredicted. In transects $X6$ and $X7$, the the TKE is generally well predicted. In transects $X8$ to $X11$, the TKE is underpredicted. Transects $X6$ and $X7$ appear to produce the most accurate prediction of the D3d global TKE Profile.

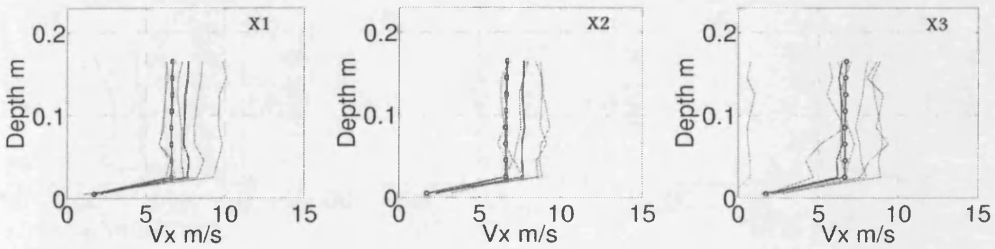

(a) dowel, N=80.6, X1 (b) dowel, N=80.6, X2 (c) dowel, N=80.6, X3

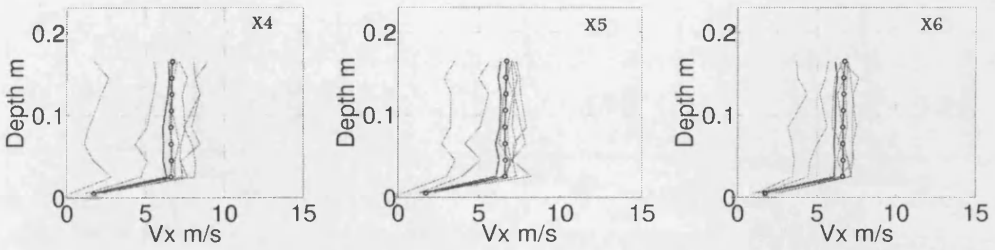

(d) dowel, N=80.6, X4 (e) dowel, N=80.6, X5 (f) dowel, N=80.6, X6

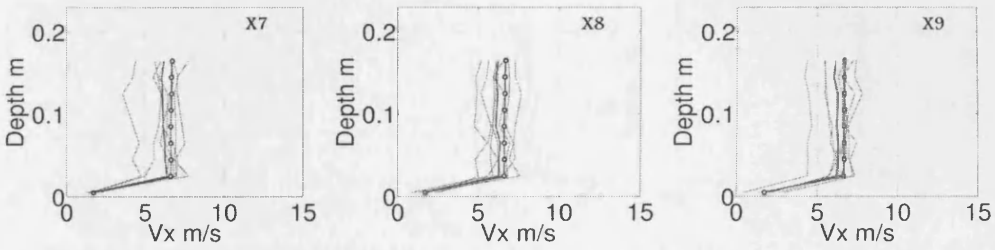

(g) dowel, N=80.6, X7 (h) dowel, N=80.6, X8 (i) dowel, N=80.6, X9

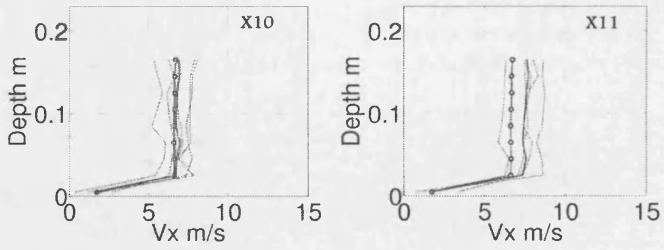

(j) dowel, N=80.6, X10 (k) dowel, N=80.6, X11

Figure 4.47: Sampling streamwise velocity (U) perpendicular to flow direction in high density dowel array

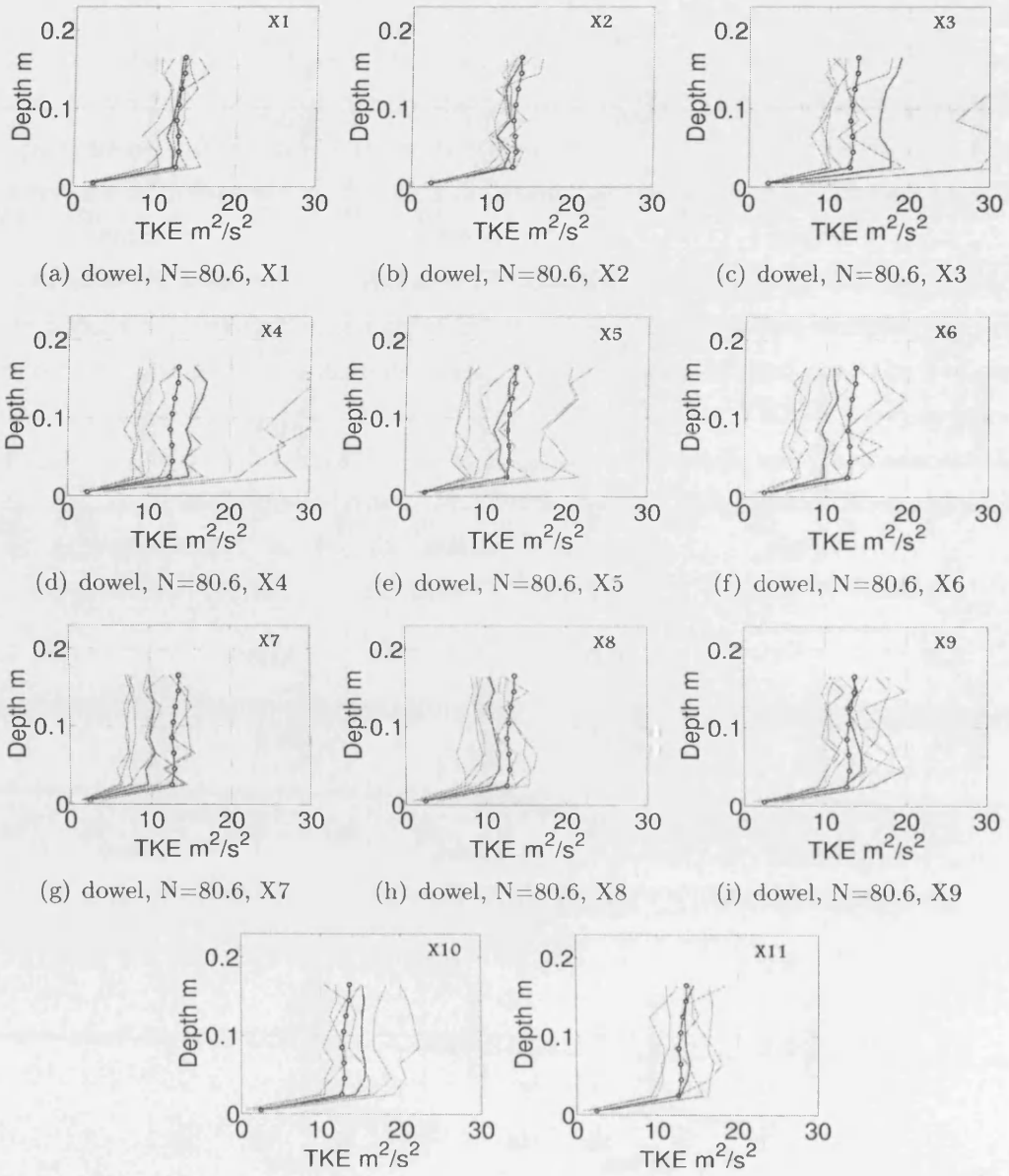

(a) dowel, N=80.6, X1 (b) dowel, N=80.6, X2 (c) dowel, N=80.6, X3

(d) dowel, N=80.6, X4 (e) dowel, N=80.6, X5 (f) dowel, N=80.6, X6

(g) dowel, N=80.6, X7 (h) dowel, N=80.6, X8 (i) dowel, N=80.6, X9

(j) dowel, N=80.6, X10 (k) dowel, N=80.6, X11

Figure 4.48: Sampling turbulent kinetic energy (TKE) perpendicular to flow direction in high density dowel array

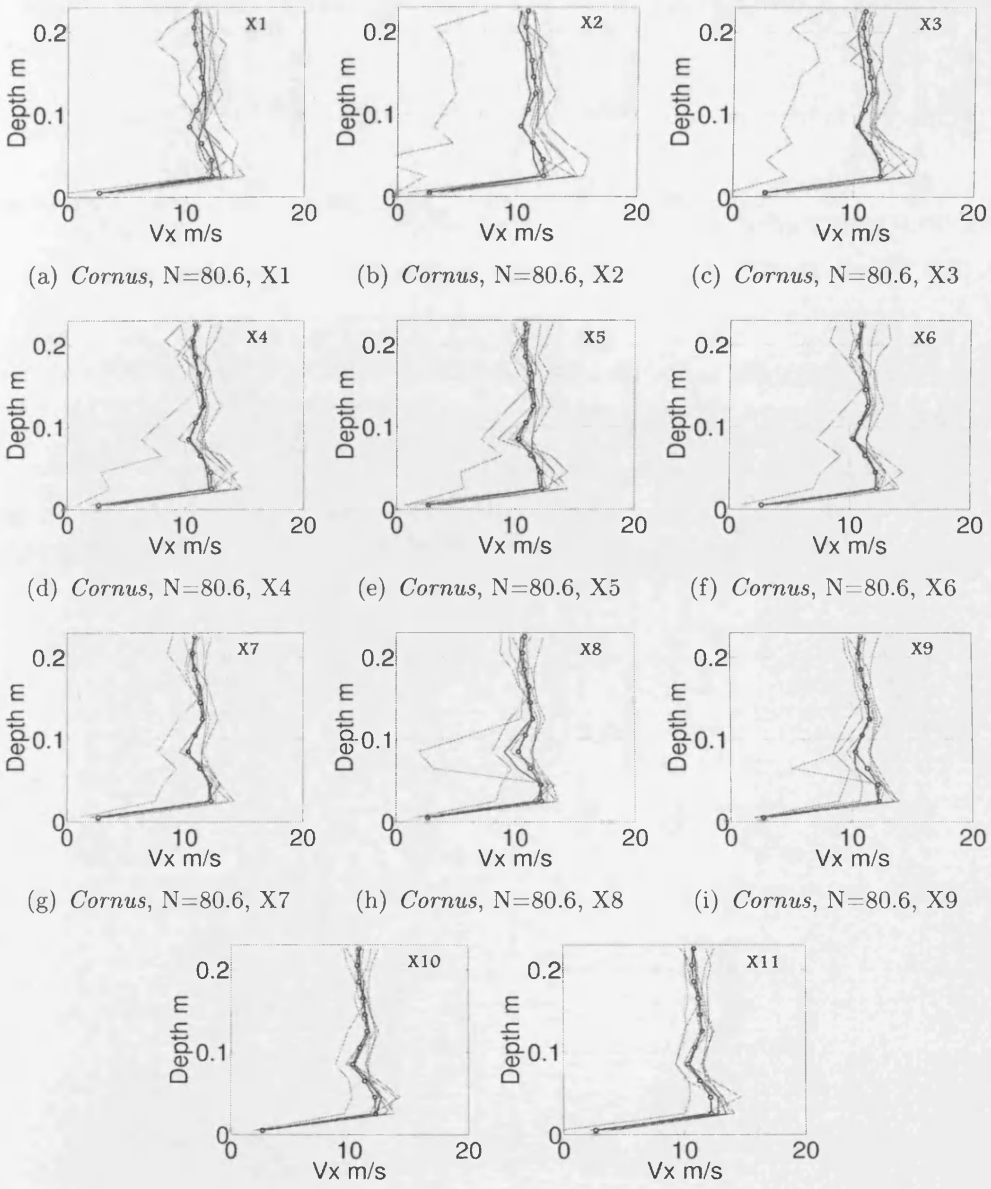

(a) *Cornus*, N=80.6, X1 (b) *Cornus*, N=80.6, X2 (c) *Cornus*, N=80.6, X3

(d) *Cornus*, N=80.6, X4 (e) *Cornus*, N=80.6, X5 (f) *Cornus*, N=80.6, X6

(g) *Cornus*, N=80.6, X7 (h) *Cornus*, N=80.6, X8 (i) *Cornus*, N=80.6, X9

(j) *Cornus*, N=80.6, X10 (k) *Cornus*, N=80.6, X11

Figure 4.49: Sampling streamwise velocity (U) perpendicular to flow direction in high density *Cornus* array

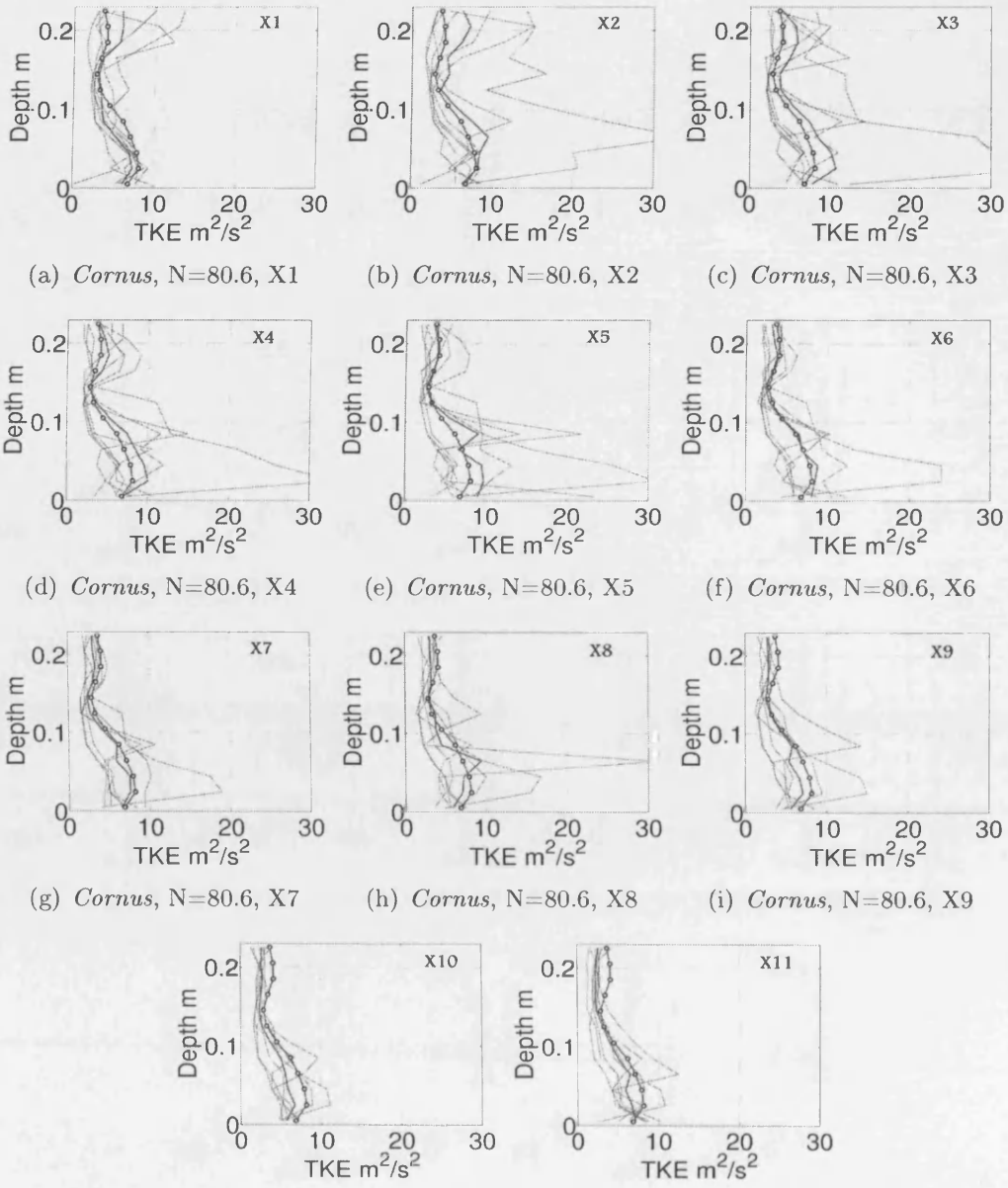

(a) *Cornus*, N=80.6, X1 (b) *Cornus*, N=80.6, X2 (c) *Cornus*, N=80.6, X3

(d) *Cornus*, N=80.6, X4 (e) *Cornus*, N=80.6, X5 (f) *Cornus*, N=80.6, X6

(g) *Cornus*, N=80.6, X7 (h) *Cornus*, N=80.6, X8 (i) *Cornus*, N=80.6, X9

(j) *Cornus*, N=80.6, X10 (k) *Cornus*, N=80.6, X11

Figure 4.50: Sampling turbulent kinetic energy (TKE) perpendicular to flow direction in high density *Cornus* array

Analysis of Error in Parallel and Perpendicular Sampling

An analysis of linear transect sampling both parallel and perpendicular to the flow direction has been carried out for all the dowel and *Cornus* Control Volumes sampled.

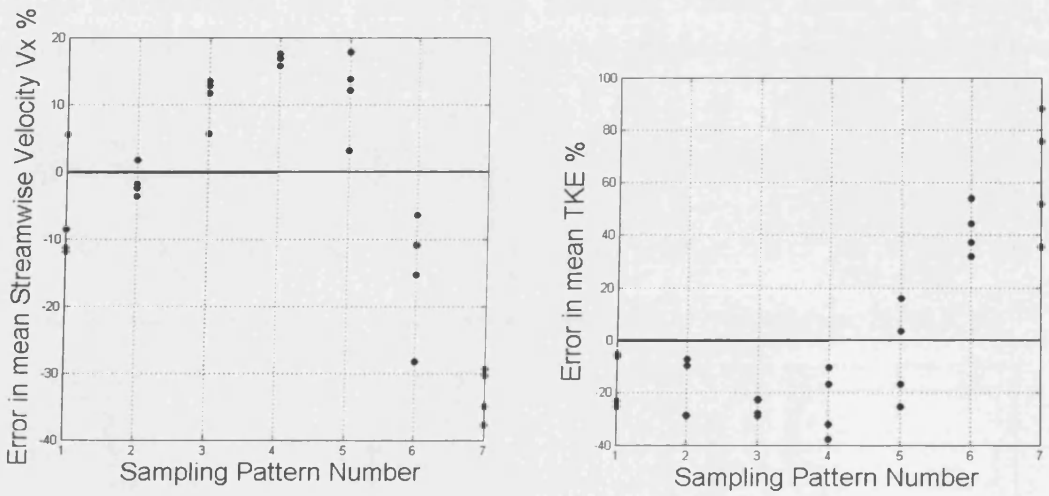

Figure 4.51: Parallel Transect Sampling in dowel arrays. Error in mean predicted U (left) and TKE (right)

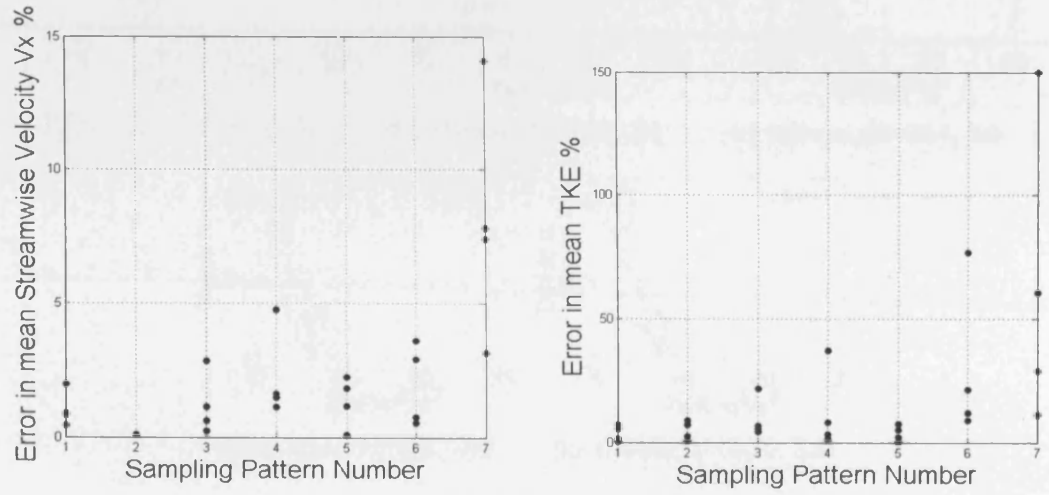

Figure 4.52: Parallel Transect Sampling in dowel arrays. χ^2 of U (left) and TKE (right)

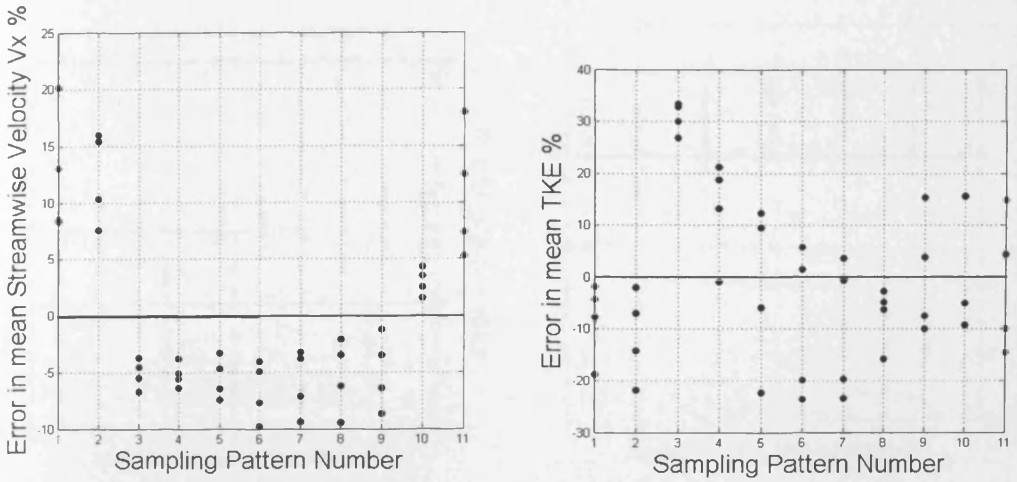

Figure 4.53: Perpendicular Transect Sampling in dowel arrays. Error in Mean predicted U (left) and TKE (right)

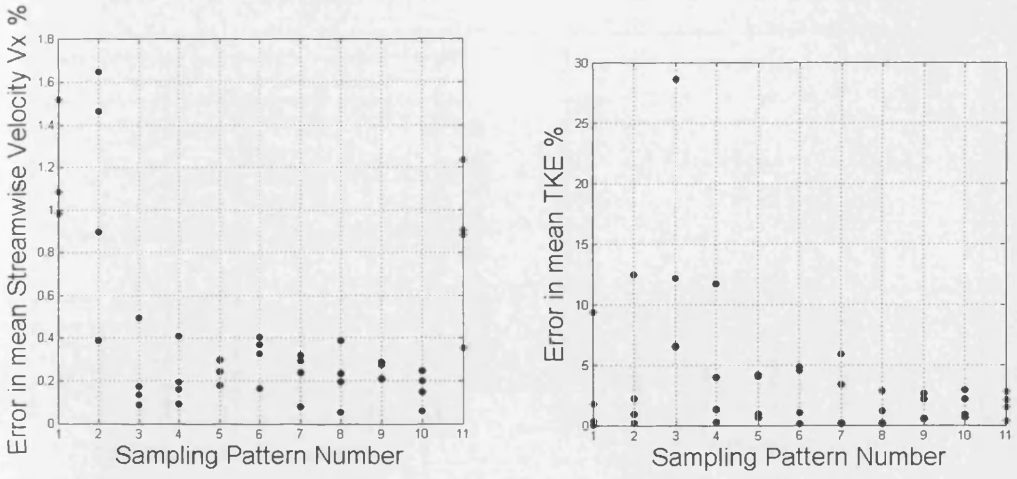

Figure 4.54: Perpendicular Transect Sampling in dowel arrays. χ^2 of U (left) and TKE (right)

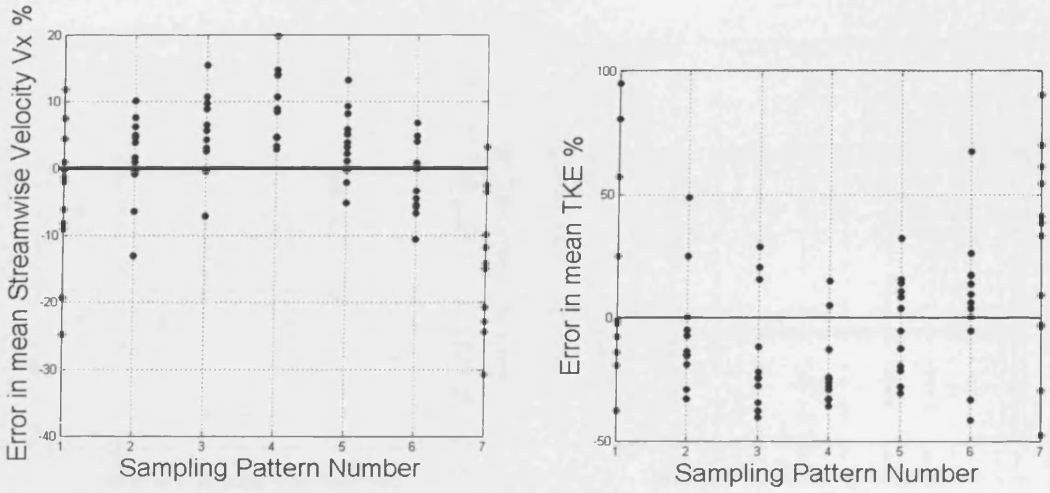

Figure 4.55: Parallel Transect Sampling in *Cornus* arrays. Error in Mean U (left) and TKE (right)

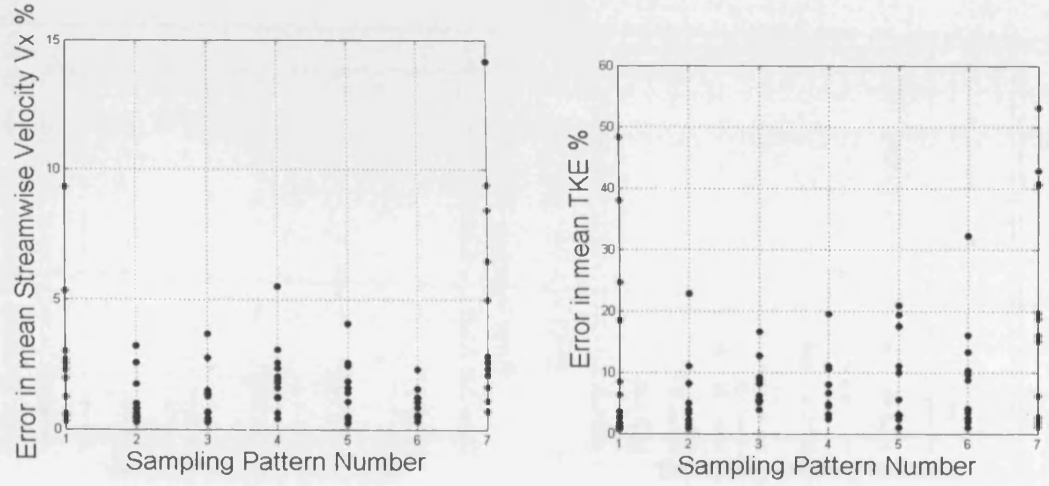

Figure 4.56: Parallel Transect Sampling in *Cornus* arrays. χ^2 of U (left) and TKE (right)

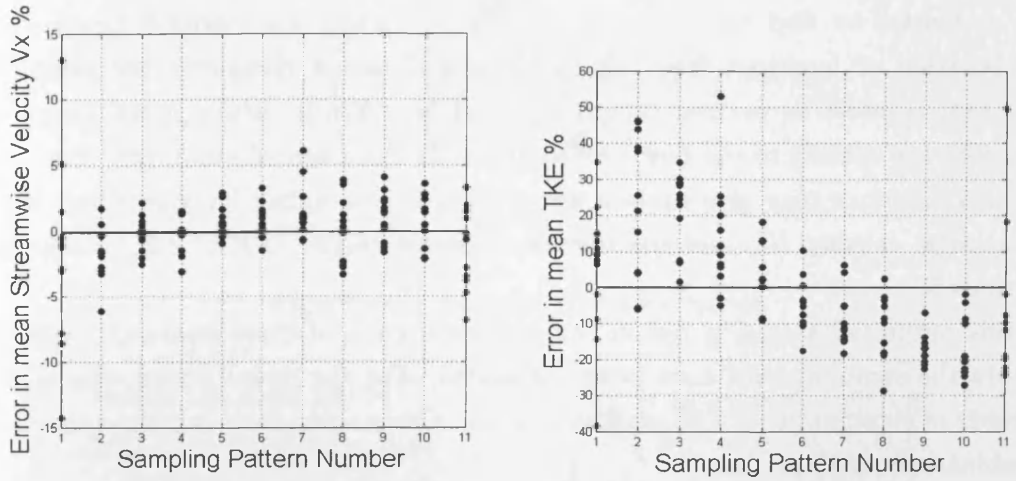

Figure 4.57: Perpendicular Transect Sampling in *Cornus* arrays. Error in Mean U (left) and TKE (right)

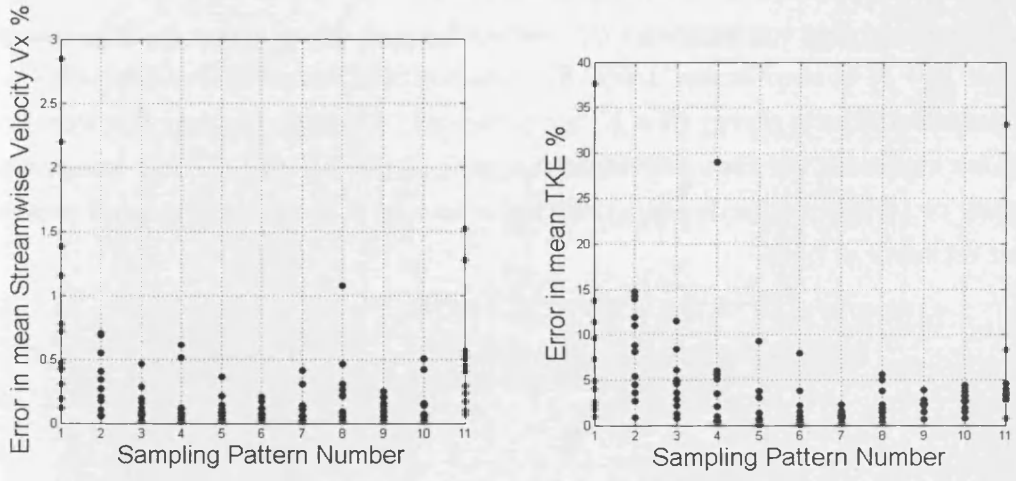

Figure 4.58: Perpendicular Transect Sampling in *Cornus* arrays. χ^2 of U (left) and TKE (right)

4.5.3 Optimised Sampling - Three Samples

Selecting the optimal sampling locations using systematic sampling patterns limits the potential to find the optimal location. Finding the optimal location or combination of locations from all the results obtained eliminates the sampling bias that transect or pattern sampling introduces. While these optimal sampling locations are specific to the flow conditions in the documented study, any recurring optimal locations may give an indication towards a sampling location where both streamwise velocity (U) and the turbulent kinetic energy (TKE) can be sampled accurately.

In this optimised sampling regime, every combination of three sampling locations within the sampling grid have been calculated. For the dowel arrays, this is the number of combinations of 69 profiles. For the *Cornus* arrays, this is the number of combinations of 77 profiles.

The optimal locations has been selected according to the sample mean error (σ_{O3}) which is the mean error of the streamwise velocity and turbulence, with each weighted evenly. The mean error is calculated using:

$$\sigma_{O3} = \sqrt{(\sigma_U - \sigma_{U_{xyz}})^2 + (\sigma_{TKE} - \sigma_{TKE_{xyz}})^2} \tag{4.7}$$

Where σ_{O3} is the combined mean error, σ_U is streamwise velocity mean error and σ_{TKE} is the turbulent kinetic energy mean error.

The three sampling combinations are plotted for each dowel arrays, and for control volume ($CV3$) of the *Cornus* array. Plots of both the streamwise velocity (U) and the turbulent kinetic energy (TKE) are presented. Although the sampling locations may not represent the best individual sampling combinations for either streamwise velocity or turbulent kinetic energy, they give an idea of locations which will provide a fair estimate of both.

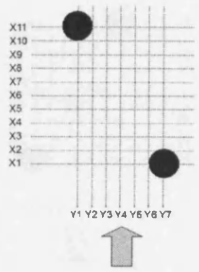

Figure 4.59: Sampling Grid Reference

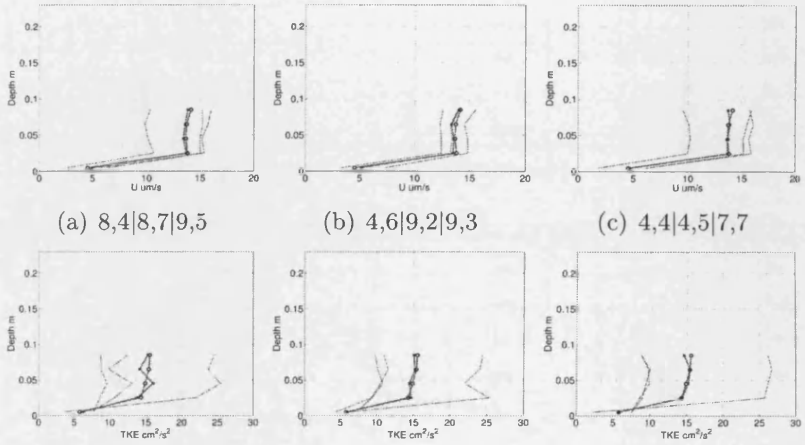

(a) 8,4|8,7|9,5 (b) 4,6|9,2|9,3 (c) 4,4|4,5|7,7

Figure 4.60: dowel array, low density low flow depth. Sampled streamwise velocity (U) (top row) and turbulent kinetic energy (TKE) (bottom row)

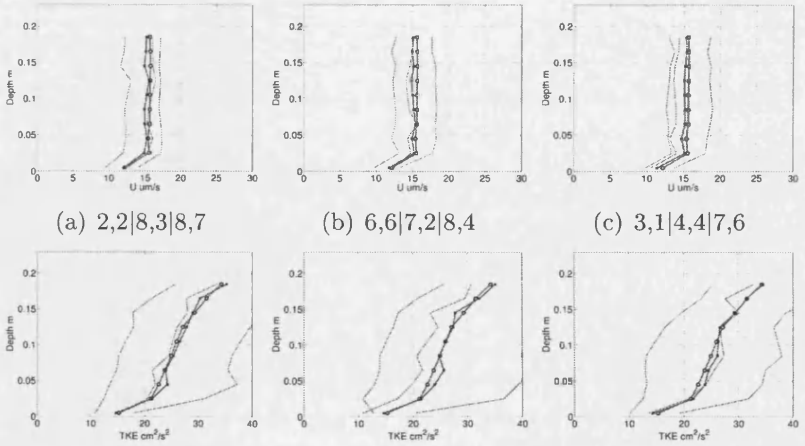

(a) 2,2|8,3|8,7 (b) 6,6|7,2|8,4 (c) 3,1|4,4|7,6

Figure 4.61: dowel array, low density high flow depth. Sampled streamwise velocity (U) (top row) and turbulent kinetic energy (TKE) (bottom row)

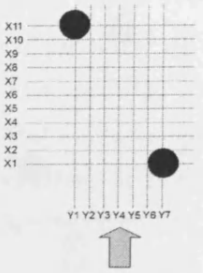

Figure 4.62: Sampling Grid Reference

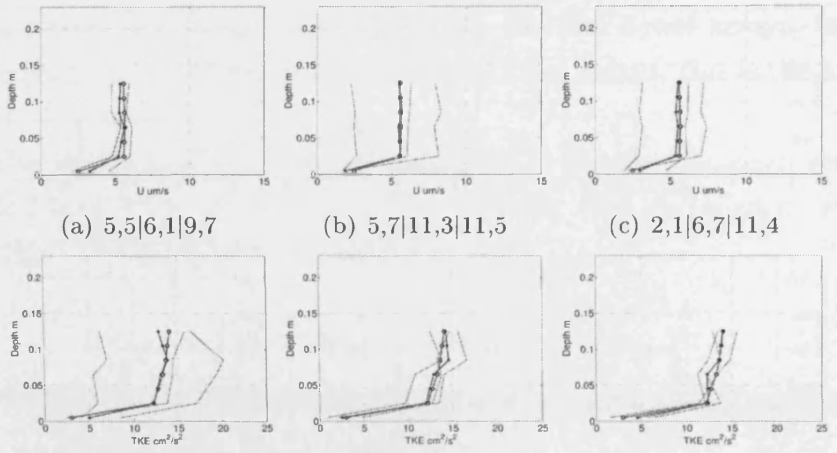

(a) 5,5|6,1|9,7 (b) 5,7|11,3|11,5 (c) 2,1|6,7|11,4

Figure 4.63: dowel array, high density low flow depth. Sampled streamwise velocity (U) (top row) and turbulent kinetic energy (TKE) (bottom row)

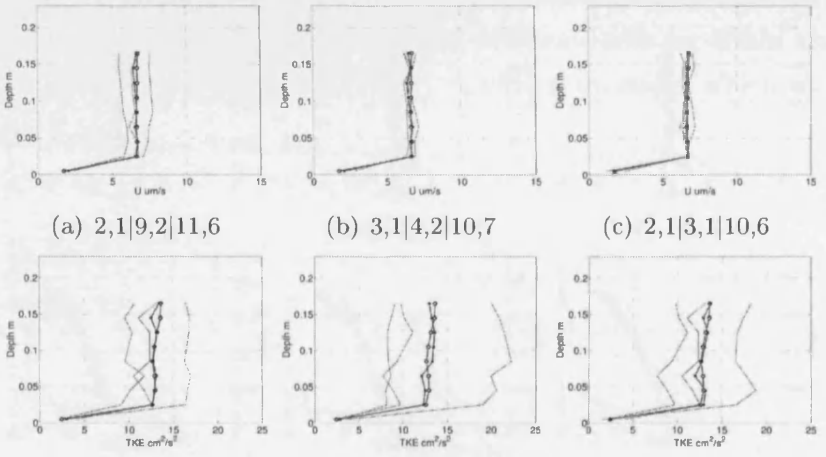

(a) 2,1|9,2|11,6 (b) 3,1|4,2|10,7 (c) 2,1|3,1|10,6

Figure 4.64: dowel array, high density high flow depth. Sampled streamwise velocity (U) (top row) and turbulent kinetic energy (TKE) (bottom row)

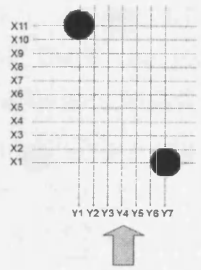

Figure 4.65: Sampling Grid Reference

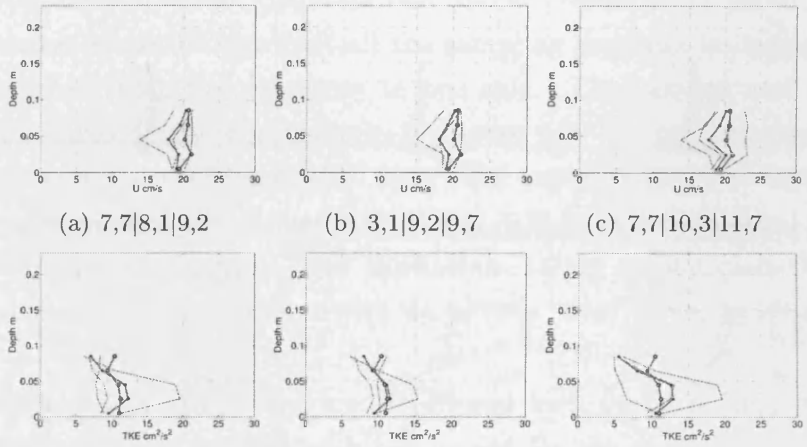

(a) 7,7|8,1|9,2 (b) 3,1|9,2|9,7 (c) 7,7|10,3|11,7

Figure 4.66: *Cornus* array, low density low flow depth. Sampled streamwise velocity (U) (top row) and turbulent kinetic energy (TKE) (bottom row))

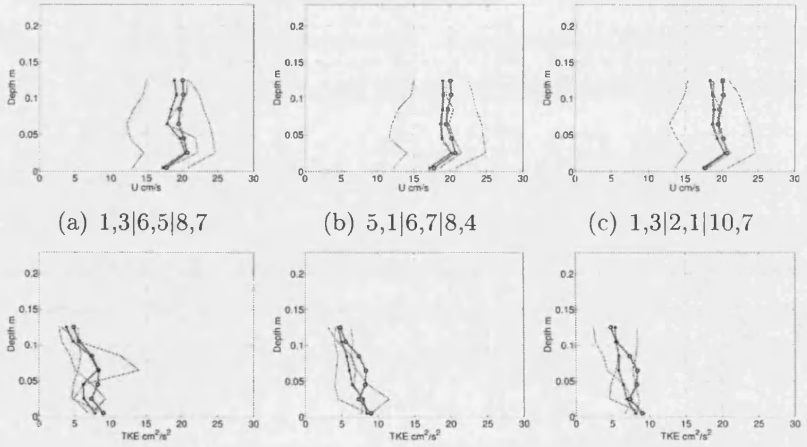

(a) 1,3|6,5|8,7 (b) 5,1|6,7|8,4 (c) 1,3|2,1|10,7

Figure 4.67: *Cornus* array, low density high flow depth. Sampled streamwise velocity (U) (top row) and turbulent kinetic energy (TKE) (bottom row)

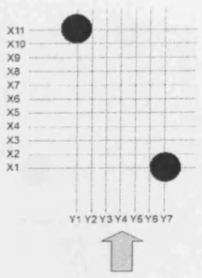

Figure 4.68: Sampling Grid Reference

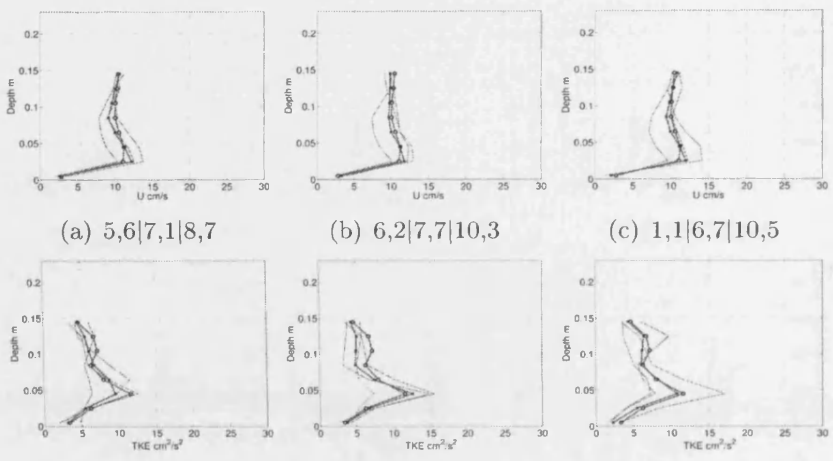

(a) 5,6|7,1|8,7 (b) 6,2|7,7|10,3 (c) 1,1|6,7|10,5

Figure 4.69: *Cornus* array, high density low flow depth. Sampled streamwise velocity (U) (top row) and turbulent kinetic energy (TKE) (bottom row)

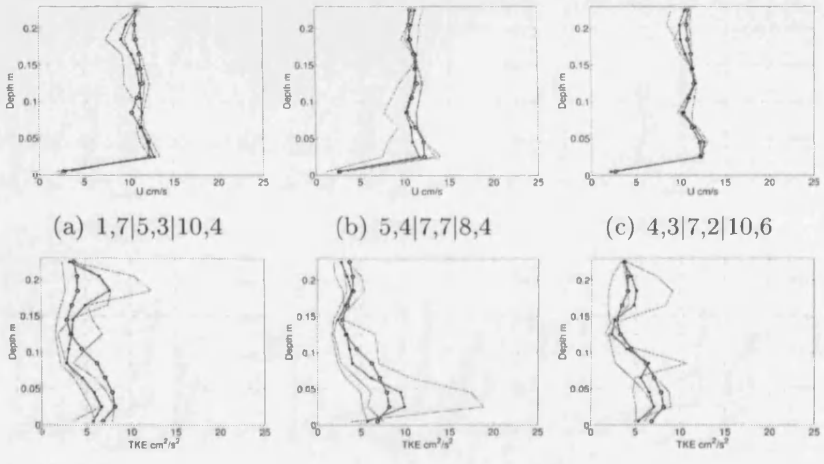

(a) 1,7|5,3|10,4 (b) 5,4|7,7|8,4 (c) 4,3|7,2|10,6

Figure 4.70: *Cornus* array, high density high flow depth. Sampled streamwise velocity (U) (top row) and turbulent kinetic energy (TKE) (bottom row)

Discussion of Three Sampling Locations Within dowel and *Cornus* Arrays

Figures 4.60 to 4.64 present the top three optimum three-sample strategy for the dowel arrays. Within the full flow field, the pattern of high and low streamwise velocity (U) and high and low turbulent kinetic energy (TKE) do not coincide. Therefore it is the aim to find a combination of locations that will combine enough of the diverse flow characteristics to reliably indicate combinations of sampling locations that will produce an accurate prediction for both streamwise velocity and turbulent kinetic energy.

Figures 4.60 and 4.61 present the low depth and high depth results for the medium density dowel array. Overall, there are two 'spread' distribution patterns evident. In the first case, it can be seen that all the sampling locations lie well distributed around the mean, with the pair close to one side. The velocity and turbulence values balance accordingly. For example, in Figure 4.60 (a), one low velocity/ high turbulence location at coordinates (8,7) has been sampled, and two high velocity/ low turbulence locations at coordinates (8,7) and (9,5) have been sampled to produce both averaged sample means in good agreement. In the second case, there is one sample on either side, and another with an already close value, as seen in Figure 4.60 (a).

Figures 4.60 and 4.61 present the low depth and high depth results for the high density dowel array. In contrast with the results for the medium array, many of the plots show groupings of locations with little deviation from the horizontally-averaged mean profile. An example of this can be seen in Figure 4.61 (b) top plot, where the streamwise velocity has been sampled in areas of similar velocity, but radically different turbulent kinetic energy. Significantly, there is no instance here where both the streamwise velocity and the turbulent kinetic energy both have these 'tight' sampling groupings.

Figures 4.66 to 4.70 present the top three three-sample strategy for the *Cornus* arrays. In Figures 4.66 and 4.67 presenting the medium density *Cornus* results, it is evident that accuracy in both the streamwise velocity and the turbulent kinetic energy have suffered. Note that the streamwise velocity is underpredicted by similar amounts in all the plots, while there is a greater variation in the sampled turbulent kinetic energy profile.

In Figures 4.69 and 4.70 presenting the high density *Cornus* results, it can be seen that the sampled streamwise velocity profiles are well matched to the full horizontally-averaged profile. There is more variation in the profile of turbulent

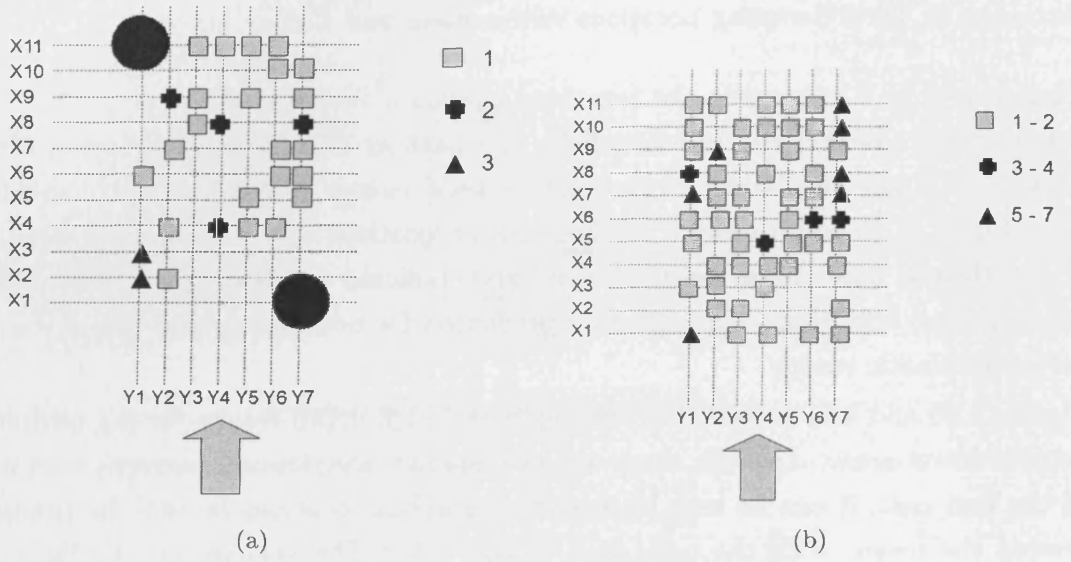

(a) (b)

Figure 4.71: Sampling grid dowel (a) and *Cornus* (b) location frequency in triple sampling

kinetic energy.

It can be seen that when sampling within the dowel array, good prediction of both the streamwise velocity and the turbulent kinetic energy can be achieved, while it seems to be harder to find good predictions of both within the *Cornus* array.

Analysis of the results may provide guidance to obtaining good sampling locations. Two methods are compared here. The frequency of each sampling location has been noted and plotted in Figure 4.71 for the dowels and *Cornus* respectively. This shows whether a coordinate has been used once, twice or three times. Only the top three combinations have been used to create the plot. No clear pattern in evident, this may be due to the small number of samples.

Alternatively, it may be more interesting to plot 'sampling triangles' in order to identify the optimum strategy, with each vertex a sampling point. Certain 'sampling triangle' shapes and orientations may be dominant. Figure 4.72 presents the sampling triangles from the data in Figures 4.60 to 4.70. The sampling triangles form a range of shapes with no immediately distinguishing pattern, with a variety of triangles long and inclined and others almost equilateral in shape. Some sampling patterns appear to be repeated throughout all plots. If the sampling grid is sub-divided into four quadrants, bisected by the central transects X6 and Y4, each triangle could be defined by the number of quadrants entered, and thus the rough sampling shape that appears most frequently.

Tables 4.5 and 4.6 present the global dataset results including both dowels and *Cornus* for triangles entering two quadrants and three quadrants respectively. Where a vertex lies on a boundary between two quadrants, the vertex location has been counted twice, once in each adjacent quadrant. It can be seen that within the location options for triangles entering two quadrants, most triangles are located diagonally across from the top right to the bottom left. For triangles entering three quadrants, most triangles are located across the top left and right and bottom left quadrants.

The consistency of the results suggests a good strategy for sampling may lie in a diagonal bisecting the control volume.

	Top left	Top right	Bottom left	Bottom right
Top left	0	4	0	2
Top right	-	1	8	2
Bottom left	-	-	0	0
Bottom right	-	-	-	0

Table 4.5: Global sampling triangles entering two quadrants only

		Top right	Bottom left	Bottom right
Top left	Top right	-	9	4
Top left	Bottom left	-	-	2
Top right	Bottom left	-	-	6

Table 4.6: Global sampling triangles entering three quadrants

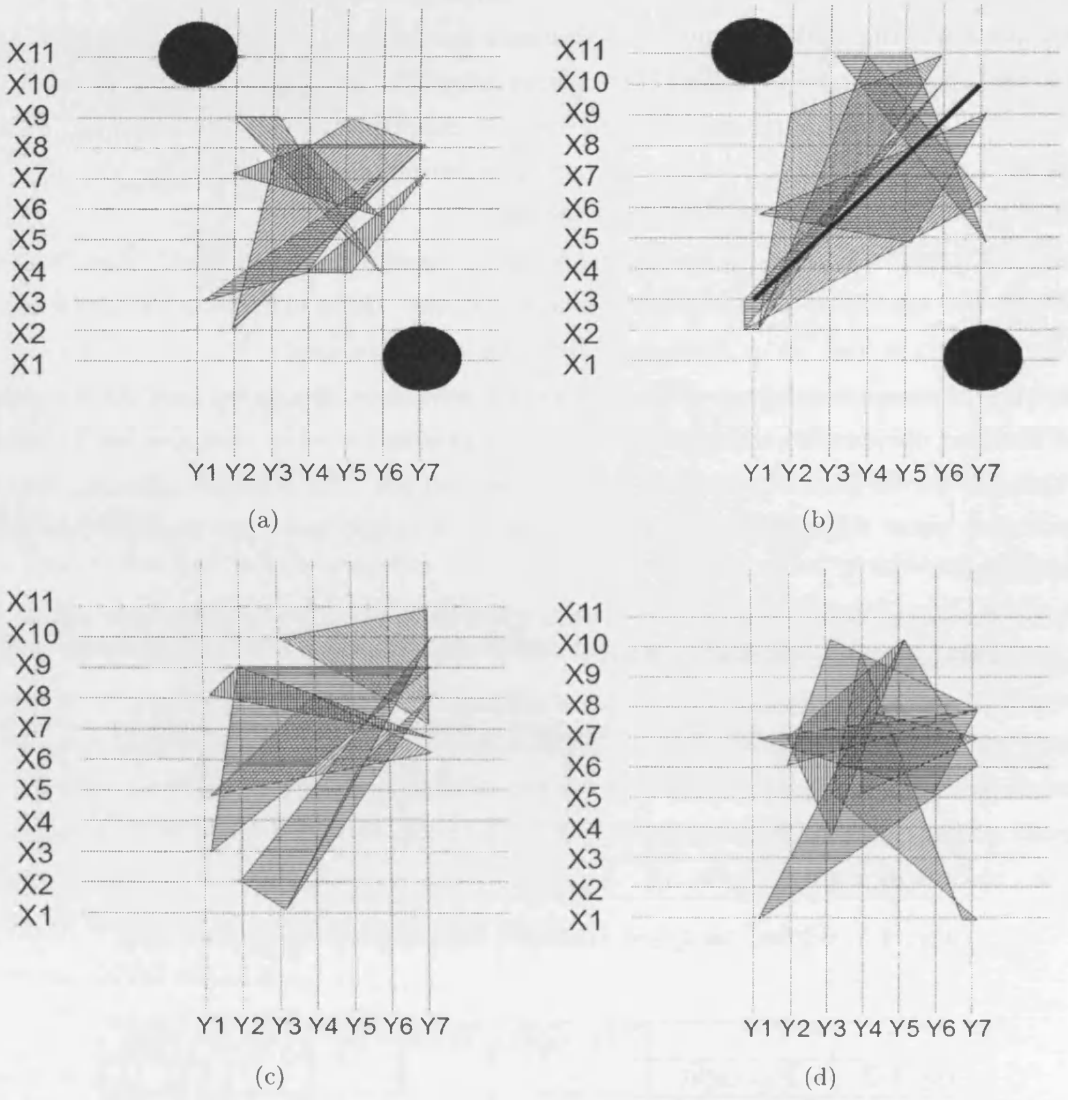

Figure 4.72: Sampling grid dowel medium density (a) and high density (b) and *Cornus* medium density (c) and high density (d) triple sampling triangles

5

Drag Force Tests on Full Scale Trees

5.1 Introduction

5.1.1 Hydrodynamics and Trees

This Chapter explains the experimental methodology and results obtained from direct drag force tests on twenty three fully submerged floodplain woodland trees of the *Salix*, *Alnus* and *Populus* genera. This work was carried out in collaboration with Braunschweig University (Germany) and the University of Natural Sciences (Austria). The facility used was the Canal de Experiencias Hidrodinámicas de El Pardo (CEHIPAR), located near Madrid, Spain.

Recent years have seen a new appreciation for floodplain woodland, and measures to reintroduce these diverse environments have been brought forward both nationally and internationally (Fleming et al. 2001, Dresner et al. 2006, IPCC 2007, Kiljn et al. 2008, EnvironmentAgency 2009). The biological diversity that makes floodplain woodland so treasured, is a very real problem when assessing the wider hydrodynamic impact on river systems. Numerical modelling is routinely employed to model the flood routing characteristics of rivers, and is a critical step in determining the flood alleviation potential of floodplain woodland. While scaled

experiments, explored in Chapters 3 and 4 can identify broad trends of vegetation array dynamics, it is experiments investigating real shrubs and trees that can help develop a true understanding of the processes, both biomechanic and hydrodynamic, that come into play in floodplain woodland environments.

From the earliest numerical river models, vegetation has been modelled as an extension of boundary skin friction using roughness factors such as Manning's n or the Chezy factor (Chow 1959). The limitation is that for vegetation that extends throughout the whole water column, roughness coefficients such Manning's n become a function of depth (Ree 1958, Smith et al. 1990). A more appropriate model is the inclusion of a hydrodynamic drag term (Wilson & Shaw 1977) which extends throughout the water column, and the value of which does not vary with depth for a particular type of vegetation. In the field of mangrove modelling, this has generally taken the form of the classical drag coefficient term (5.1), where the mangrove trees are assumed to behave as circular cylinders with a drag coefficient value (C_d) of 1.0.

$$F_d = \frac{1}{2} C_d N A_p U_0^2 \tag{5.1}$$

Where F_d is the drag force exerted on/ by the vegetation, C_d is the drag coefficient (in turbulent flows this relates to the shape of the obstacle), N is the number of trees, A_p is the projected area of an individual tree, and U_0 is the free stream velocity.

The two limitations of this method are the lack of an incorporation of the effect of sheltering which can reduce the drag coefficient of an individual by up to 60 % of the original value (Li & Shen 1973, Nepf 1999), and the inability to account for the representation of flexible and/ or foliated vegetation.

Several authors have determined the drag coefficient of flexing trees through direct measurement (Mayhead 1973, Fathi-Maghadam & Kouwen 1997, Oplatka 1998 *a*, Freeman et al. 2000, Armanini et al. 2005, Kane & Smiley 2006). All researchers note that the variation between force and velocity is linear. Oplatka (1998 *a*) proposed the use of the compound drag coefficient term ($C_d A$) to characterise the drag coefficient, due to the difficulty of determining the projected area (A_p) once the tree deflects:

$$C_d A = \frac{2F_x}{\rho U_0^2} \tag{5.2}$$

Section 5.2 explains the preparation and documentation of the plant properties. Section 5.3 presents results from a cylinder test. Section 5.4 presents the drag force data obtained. In Section 5.6, the drag data is linked to the plant properties and empirically derived relationships between the plant properties and velocity data are

defined.

5.1.2 Participants in Hydralab

Person	Institute	Responsibility
Catherine Wilson	CU	Project Leader
Jochen Aberle	UB	Drag forces measurement
Hans Peter Rauch	BOKU	Measurement of tree properties
Patricia Xavier	CU	Experimental work and force - velocity data analysis
Thomas Schoneboom	UB	Experimental work and drag force data post-processing
Walter Lammeranner	BOKU	Experimental work and determination of tree properties including bending stiffness
Clemens Weissteiner	BOKU	Video Analysis, tree properties post processing

Table 5.1: Participants in Hydralab III. (CU) Cardiff University, UK; (UB) Braunschweig University, Germany; (BOKU) University of Natural Resources and Applied Life Sciences, Austria

5.1.3 Project Background

This study mimics the methodology employed by Oplatka (1998*a*), who dragged *Salix purpurea L.* and *Salix viminalis L.* trees via a 140 m towing tank through water on a frame, and directly measured the drag force and moment exerted in three directions. The *Salix* specimens were sourced from the region of Bern - Burgdorf in Switzerland, and the experiments were carried out during July of 1995 and 1996. The maximum age of the *Salix* was 5 years, and the heights of the willows tested varied from 1.8 m to 4.5 m, with towing velocities ranged from 1 m/s to 4 m/s.
In the present study, twenty-two trees (including 13 *Salix* specimens)were tested by pulling them horizontally through a still body of water under different velocities, and the drag force and moment exerted was measured in three dimensions. The drag force - velocity relationships were principally examined to assess the impact of foliage on the drag force exerted. The deflection and reconfiguration of the trees at varying velocities was documented using underwater cameras.
Table 5.2 documents the range of tree properties and testing conditions in the study of Oplatka (1998*a*) versus the conditions in the present study. Figure 5.1 presents the different experimental set-ups. A key difference is that Oplatka mounted upright submerged specimens on a frame, to which a force tranducer was attached, while in the present study, the trees were submerged upside down and attached directly to the force transducer.

Trees	**Oplatka (1998*a*)**	**Present Study**
Species	*Salix purpurea L., Salix viminalis*	*Salix atrocinerea Brot., Salix alba*
Heights	1.8 m to 4.5 m	
Flume	**Oplatka (1998*a*)**	**Present Study**
Length	140 m	300 m
Width	4 m	30 m
Depth	1.9 m	10 m
Velocities	1 m/s to 4 m/s	0.125 m/s to 4 m/s

Table 5.2: Comparative experimental conditions between the study of *Oplatka* and the present study

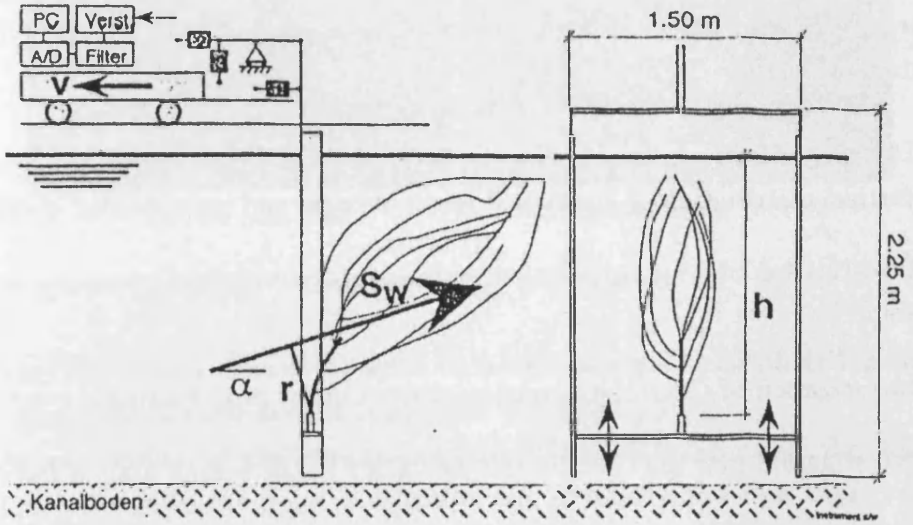

(a)

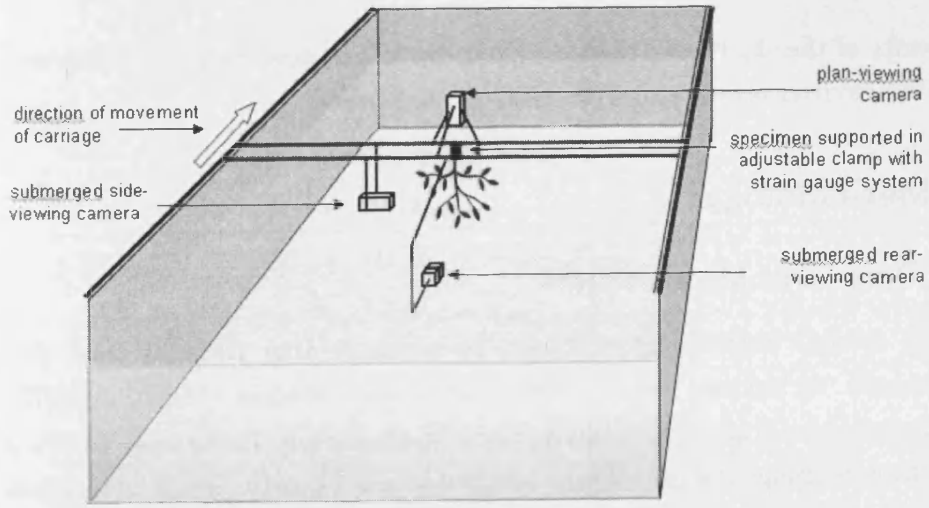

(b)

Figure 5.1: (a) Experimental set-up for the study of Oplatka (1998*a*), S_w is the resultant force, α is the resultant angle and r is the lever arm of the force. (b) Experimental set-up for present study

5.1.4 Hydralab Project Objectives

The principal objective of the Hydralab Project was to improve current approaches for the accurate prediction of flows in riparian floodplains, with a focus on common European woodland tree and shrub species. This was achieved through the following objectives:

1. Documentation of the tree properties including frontal projected area and vertical distribution of leaves and wood biomass and the modulus of elasticity
2. Investigation of a high-resolution, high accuracy drag force - velocity relationship
3. Investigation of the reconfiguration of trees under fluid loading
4. Investigation into the contribution of foliage to the overall drag of the tree
5. Development and formulation of physically-based formulae which quantify the hydraulic resistance of plants as a function of measurable characteristics

The results of the study will lead to improvements in numerical modelling tools for integrated environmental and hydraulic management.

5.2 Methodology

5.2.1 Drag Force Measurements

To date, several authors have chosen to measure drag force of trees directly. Measurement techniques vary, from wind tunnel studies (Mayhead 1973), to mounting trees on trucks (Kouwen & Fathi-Maghadam 2000, Kane & Smiley 2006) and hydraulic flume studies (Fathi-Maghadam & Kouwen 1997, Oplatka 1998*a*, Freeman et al. 2000).

5.2.2 Dynanometer

In the present study, a three-dimensional dynamometer was used to measure the forces and moments in three dimensions. The dynanometer rig can be seen in Figure 5.2 (a). The rig consisted of five load cells measuring forces in three dimensions. Two sensors each for the vertical and lateral directions and one for the longitudinal

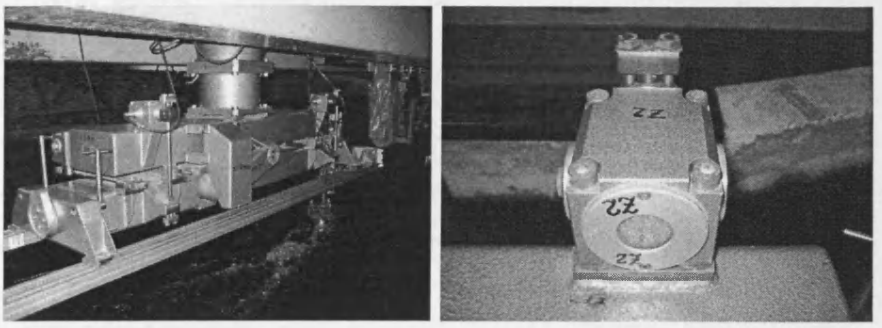

(a) View from side (b) Dynamometer Unit Z2

Figure 5.2: Dynamometer (a) and load cell unit (b)

direction. The sensors allowed both the force and moment to calculated in all three dimensions. One of these sensors is pictured in Figure 5.2 (b).
For the calculation of the resulting forces, CEHIPAR provided the following equations referred to the point of origin of the dynamometer (see Figures 5.3 (a) and (b) and Figure 5.4):

$$X = F_x cos\beta + (F_{y1} + F_{y2}4)\, sin\beta \tag{5.3}$$
$$Y = (F_{y1} + F_{y2})\, cos\beta - F_x sin\beta \tag{5.4}$$
$$Z = F_{z1} + F_{z2} + F_{z3} \tag{5.5}$$
$$M_x = 23\,(F_{z3} - F_{z1} - F_{z2}) \tag{5.6}$$
$$M_y = 60\,(F_{z1} - F_{z2} + F_{z3}) \tag{5.7}$$
$$M_z = 70\,(F_{y1} - F_{y2}) \tag{5.8}$$
$$\tag{5.9}$$

Where X, Y and Z are the recorded mass in kg aligned to the local axis of the dynamometer, F_x, F_y and F_z are the forces aligned to the axis of the basin, β is the correction angle between the x-axis of the basin and the orientation of the dynamometer.

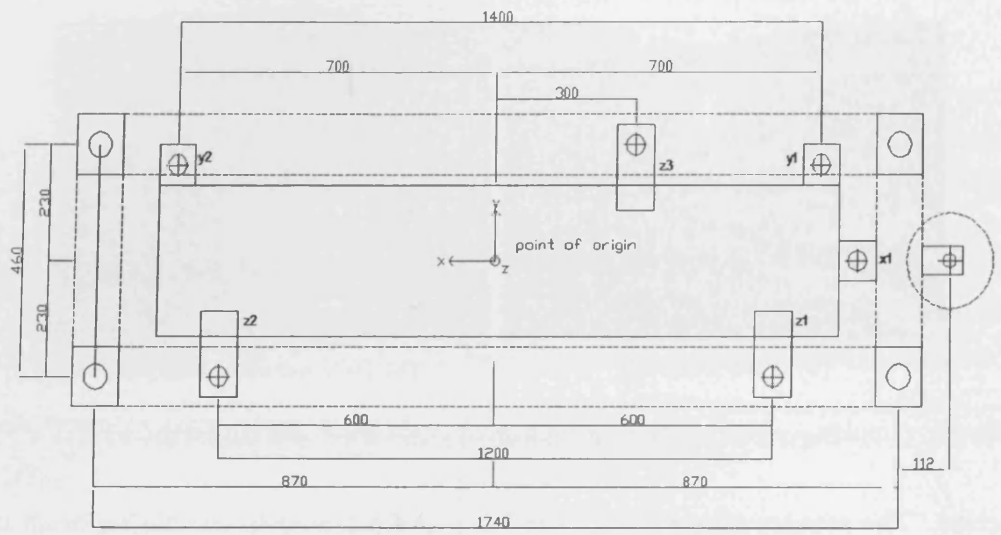

(a) Plan view from above

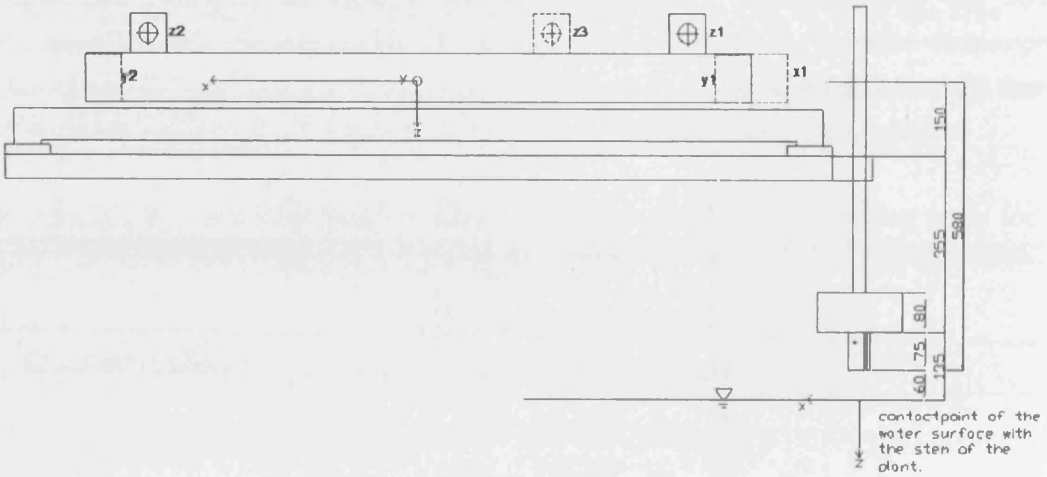

(b) Side elevation

Figure 5.3: Dynomometer Arrangement

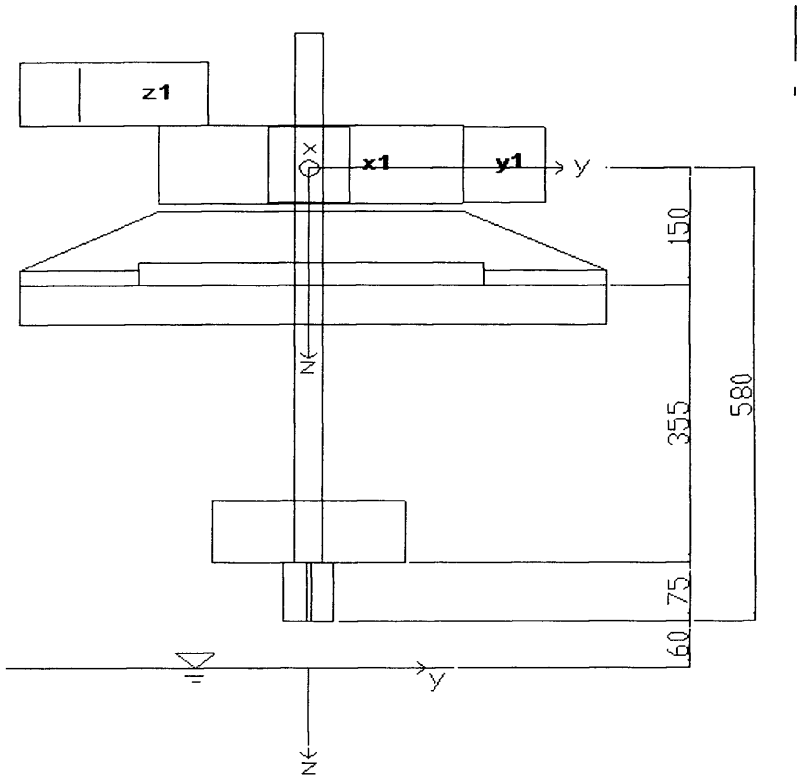

(a) Front elevation

Figure 5.4: Dynomometer

5.2.2.1 Amplifier and Software

- Measuring Amplifier und A/D-Converter: Hottinger Baldwin Messtechnik AB22A
- Slots: HBM ML30
- Software: MGC Plus Asstistant 3.3 Release 8

5.2.3 Procedure for Force Data Analysis

This analysis procedure was developed by Thomas Schonebaum from Technische Universitaet Braunschweig according to the following steps:

1. Determination of appropriate time segment for calculation of the mean values
2. Calculation of directional forces (Fx, Fy, Fz [N]) and moments ($M_{x,0}$, $M_{y,0}$, $M_{z,0}$, $M_{x,ws}$, $M_{y,ws}$, $M_{z,ws}$ [Nm]) from the raw data (X, $Y1$, $Y2$, $Z1$, $Z2$, $Z3$ [kg])
3. Calculation of resulting force $Fres_{xz}$ [N], lever arm $hres_{xz}$ [m], angle $alphares_{xz}$ [°], CdA (m_2)
4. Manual Determination of the ultimate point before acceleration of the carriage for each velocity and each run (t_{end})
5. Calculation of the mean values and statistical parameters of the forces F_x, F_y, F_z (N) and moments $M_{x,ws}$, $M_{y,ws}$, $M_{z,ws}$ (Nm) with the time segment defined in step 1 using a script in 'Diadem'. Calculation of a linear regression of the force F_x and F_z as indicator for a temporal decline of the forces
6. Saving the data, exporting the data to a Matlab-File and a PDF-file. Exporting the mean values and statistical parameters to Excel

5.2.4 Equations for the Calculation of Forces and Moments

For the drag force calculations on the trees, the angle β was set to zero. The following equations are based on the units N and Nm and are referred to the point of origin of the dynamometer (see Figure 5.3).

$$
\begin{aligned}
F_x &= 9.81x && (5.10)\\
F_y &= 9.81\,(y_1 + y_2) && (5.11)\\
F_z &= 9.81\,(z_1 + z_2 + z_3) && (5.12)\\
M_{x,0} &= 0.23 \cdot 9.81\,(z_3 - z_2 - z_1) && (5.13)\\
M_{y,0} &= 0.60 \cdot 9.81\,(z_1 - z_2 + 0.5z_3) && (5.14)\\
M_{z,0} &= 0.70 \cdot 9.81\,(y_2 - y_1) && (5.15)\\
& && (5.16)
\end{aligned}
$$

For the calculation of the moments on the plant, a new reference point is set to the contact point of the water surface with the stem of the plant (see Figure 5.3 (b)).

$$
\begin{aligned}
M_{x,ws} &= [0.23 \cdot 9.81\,(z_3 - z_2 - z_1)] + [0.64 \cdot 9.81\,(y_1 + y_2)] && (5.17)\\
M_{y,ws} &= 9.81\,[-(0.382z_1) - (0.682z_3) - (0.1.582z_2)] - [0.64 \cdot 9.81x] && (5.18)\\
M_{z,ws} &= [9.81\,(0.282y_1)] + [9.81\,(1.682y_2)] && (5.19)\\
& && (5.20)
\end{aligned}
$$

The equations above are valid for the direction 'forward'. For the calculation of the forces and moments in the 'backward' direction, Equations 5.16 to 5.20 have to be adapted with a factor of -1 in the x and y directions.

During a single forward or backward run, several velocities could be attained in series. Figure 5.5 shows the recorded time series data of Forces Fx, Fy and Fz exerted on the Dynanometer by tree $S1$, during a forward run, at velocities 0.25 m/s to 1.75 m/s. Figure 5.6 presents the equivalent moments Mx, My and Mz. It can be seen that the force at the transition point between velocities shows a peak at the point of transition, before reducing slowly. The actual change in carriage velocity takes place over a time period in the order of a few seconds. It is clear, however, the force exerted on the dynanometer continues to change for a much longer period, and particularly at high velocities, there is a significant temporal decline of force. In order to ensure that representative force and moment values are derived from the time series dataset, statistical analysis was carried out to find the optimum time segment to use.

The calculation of the cumulative average and standard deviation started with the

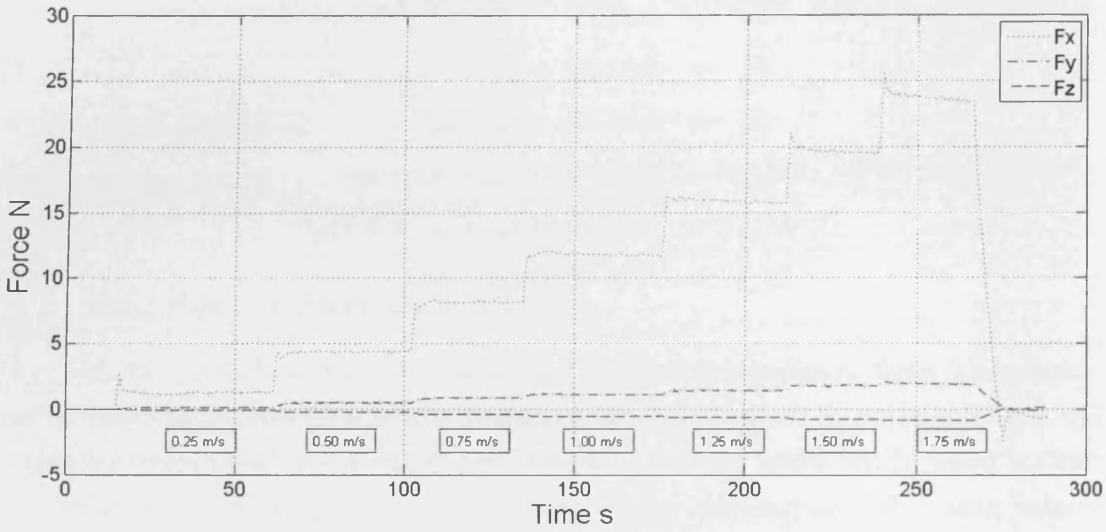

Figure 5.5: Forces Fx Fy and Fx (N) against time (s) for multiple velocities between 0.25 m/s and 1.75 m/s

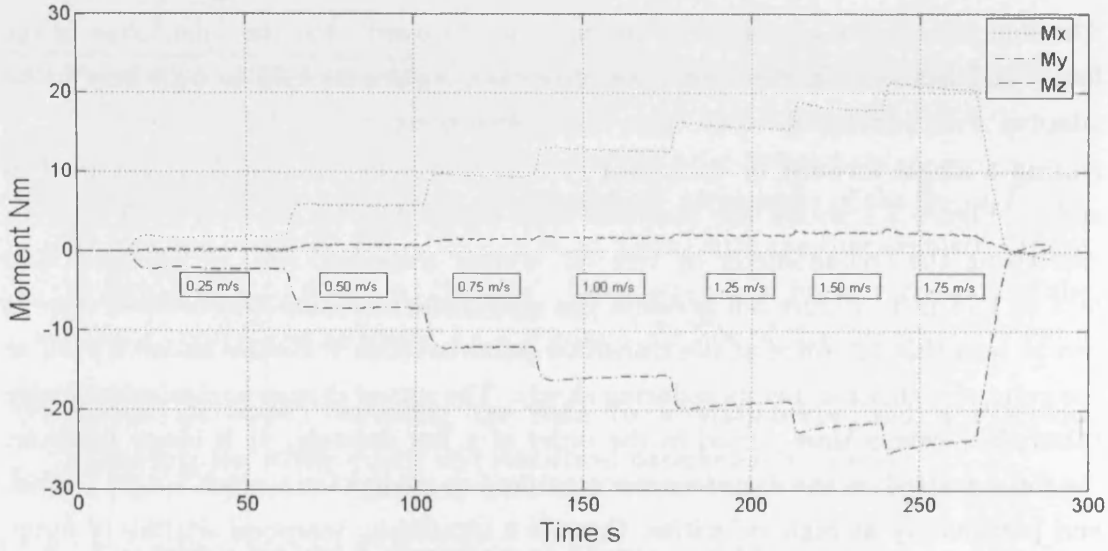

Figure 5.6: Moments Mx My and Mz (Nm) against time (s) for multiple velocities between 0.25 m/s and 1.75 m/s

last point in the timeline of the measurement and ended with the first data point (backward calculation). Figures 5.7 (a) to (b) shows that the cumulative average is stable after approximately 8 seconds for velocity U = 0.25 m/s, after approximately 6 seconds for U = 1.25 m/s and after approximately 5 s for U = 3.50 m/s.

Assuming seven different velocities are tested in one run and a maximum number of data points of 3000 at a data rate of 10 Hz are collected, approximately 40 seconds are available for every run. Considering acceleration, deceleration and a stabilization of the trees, approximately 30 seconds is the maximum theoretical time segment for averaging. Considering the variations in measuring time due to the manual handling of the dynamometer wagon in the backward direction, the available time segment is probably less than 30 seconds. The lower limit was calculated from Salix 11. To account for the different trees with and without leaves and their different vibration characteristics the time segment should be chosen higher than the lower limit. On the basis of these considerations, the time segment for averaging was set to 20 seconds, bounded at each end of one velocity-time measurement series by t_{start} where t_{start} = t_{end} - 20 s and t_{end}.

The device was calibrated to measure forces in 3 dimensions to an accuracy of 1 gram, when the loading exceeded 100g. At smaller loads the accuracy is unknown so every attempt was made to ensure measurements taken exceeded 100g.

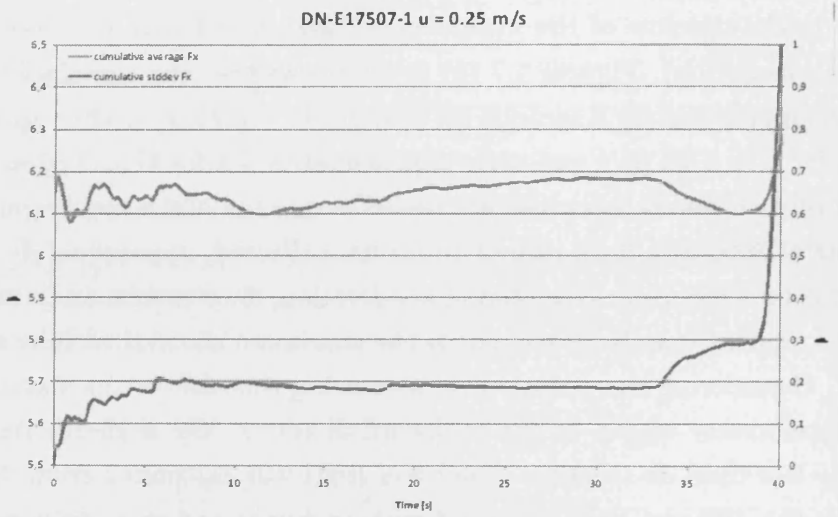

(a)

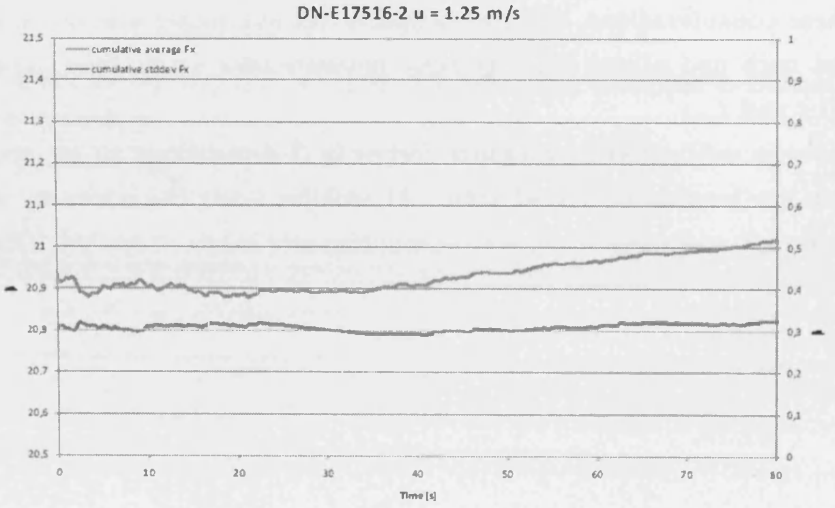

(b)

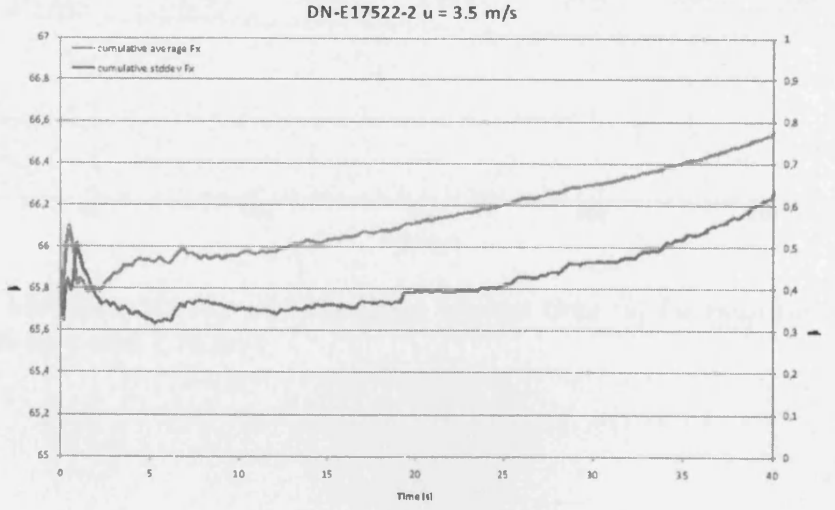

(c)

Figure 5.7: Temporal decline of measured forces

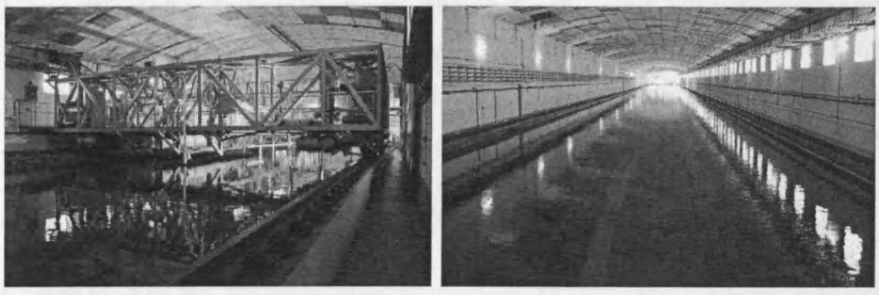

(a) (b)

Figure 5.8: Images taken from the CEHIPAR facility, El Pardo, Madrid

5.2.5 Experimental Procedure

5.2.5.1 The CEHIPAR Facility

The experiments were carried out during March and April 2008 under the Hydralab grant scheme (Ad van Os, 2005) at the CEHIPAR ship canal facility in El Pardo, Madrid. A figure of the basin facility is shown in Figure 5.8 (a). The canal was 300 m in length x 30 m wide x 6 m deep. The view along the canal can be seen in Figure 5.8 (b). The dynanometer was suspended beneath a carriage above the canal. The carriage moved along the canal on railings and the speed could be controlled to an accuracy of 1 mm/s. The carriage also housed the operations room. Within the operations room the velocity of the carriage was controlled, and the forces on the dynanometer monitored in real time. Underwater digital video recordings from the side of the tree and behind the rig were also taken and monitored in real time aboard the carriage. The carriage was bi-directional and could move and take measurements in both directions along the channel by rotating the tree at each end.

5.2.5.2 Tree Sourcing

To ensure the trees selected were appropriate specimens to replicate floodplain woodland, the trees were sourced from a nearby floodplain woodland site that was undergoing routine maintenance, rather than a nursery. Species of *Salix*, *Alnus* and *Populus* were collected at the beginning of the programme and mid-way through the programme. Trees were selected for testing to cover a broad range of growth habits (Weissteiner et. al., 2009). The time from being cut to arrival at the facility did not exceed five hours. Upon arrival at the facility, the trees were stored inside with the main stem submerged in the water of the canal. From visual inspection,

trees remained fresh for approximately two weeks before showing signs of decay. As the testing period extended from mid March to mid April, a range of stages of leaf development were captured, from emerging leaf buds, to more fully developed leaves in the later tests.

5.2.5.3 Test Procedure

From the 30+ collected specimens, test trees were selected based on obtaining a tree with a height between 2m and 5m, with an even distribution of side branches and foliage. The tree properties for each specimen can be found in the appendix. Each selected tree was tested according to the following procedure:

1. Specimen height and stem diameter measured. The height of each tree was recorded, then the specimen was marked at quarter sections by height. The diameter of the main stem at the base, 1st quartile, mid height and 3rd quartile were recorded.

2. The tree was photographed to capture the projected area at 0° and 90°, and from above to capture the plan view (Figure 5.9).

3. A bending stiffness test was carried out (see Figure 5.11).

4. The foliated tree was mounted in the dynanometer by attaching a brass cylinder fitted securely to the stem, with a brass screw if necessary 5.10 (b). The tree was tested in incremental velocities to a maximum of 4 m/s. Several velocities could be reached during one run of the carriage along the canal. At the far end of the canal, the tree was rotated, and tested under the same velocities in the return direction. F_x, F_y, F_z and M_x, M_y, M_z were recorded continuously throughout runs in both directions.

5. Once testing with the foliated tree was completed, the tree was defoliated. The fresh leaf mass and volume in quarter sections of height were recorded (see Figure 5.10 (c)). The leaf masses were recorded using a scale with an accuracy of 0.1 g, and the volume by immersing the leaves in a known volume of water and recording the displacement of the water. The leaves were then placed in a warm oven to dry.

6. The defoliated tree was re-mounted in the dynometer and re-tested at identical velocities.

7. After testing, the tree branches were cut into quarter sections and the fresh mass and volume of branches in each section were recorded. The branches were placed in a warm oven to dry.

8. After drying for at least 24 hours, the dried leaf and branch masses were obtained using a scale with accuracy 0.1 g.

It was observed that the trees appeared to show signs of inelastic deformation during testing. To ensure comparable results, the trees were tested to a maximum velocity of 1.0 m/s while in the foliated condition to avoid causing permanent deformation to the specimen and therefore obtaining potentially misleading results when comparing the foliated and defoliated conditions. The physical properties of the wood and leaves were recorded both when fresh and dry. The tree properties and drag force results for each tree are presented in Section 5.4
The tree properties and drag force results for each tree are presented in Section 5.4.

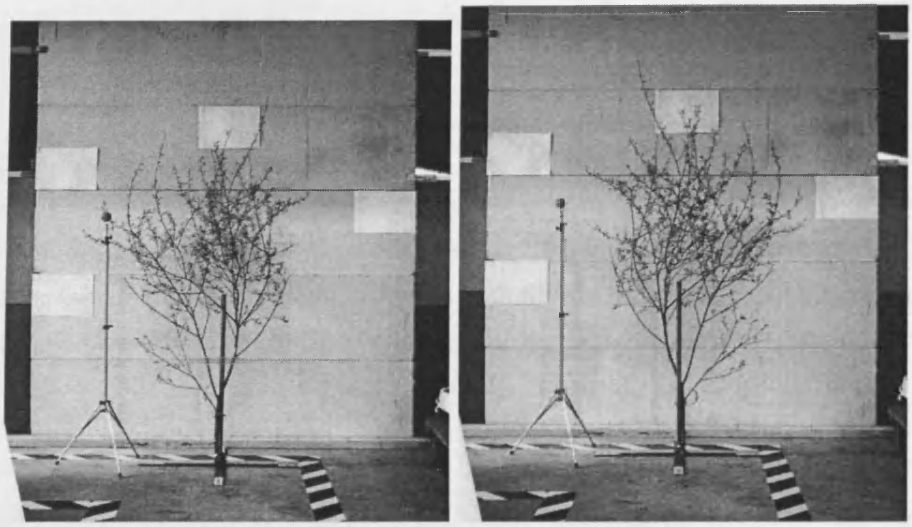

(a) (b)

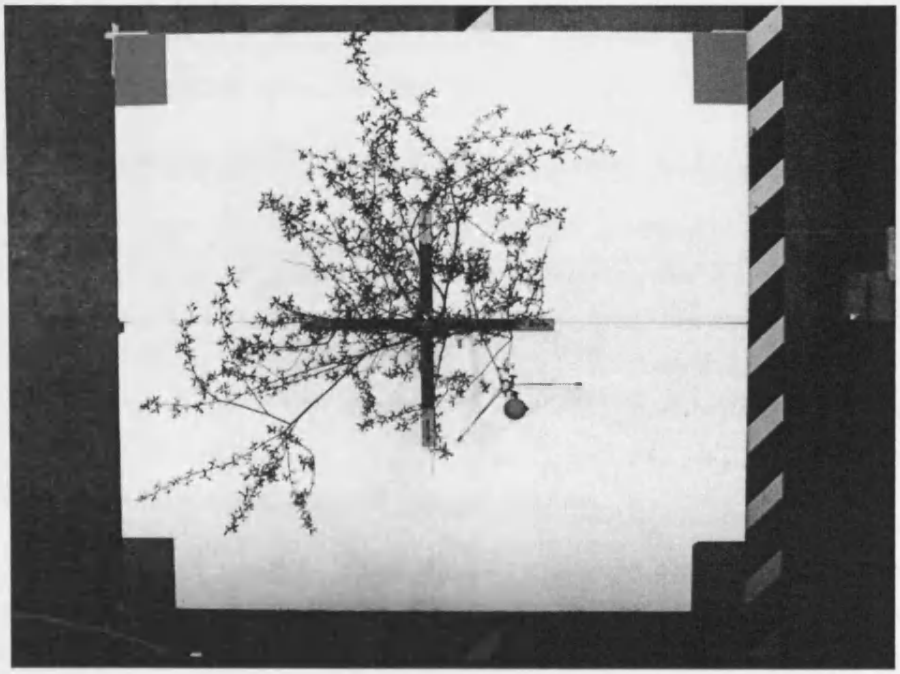

(c)

Figure 5.9: Salix 4 photographed at (a) 0° to flow direction (frontal projection area A_p), (b) 90° to flow direction and (c) plan view

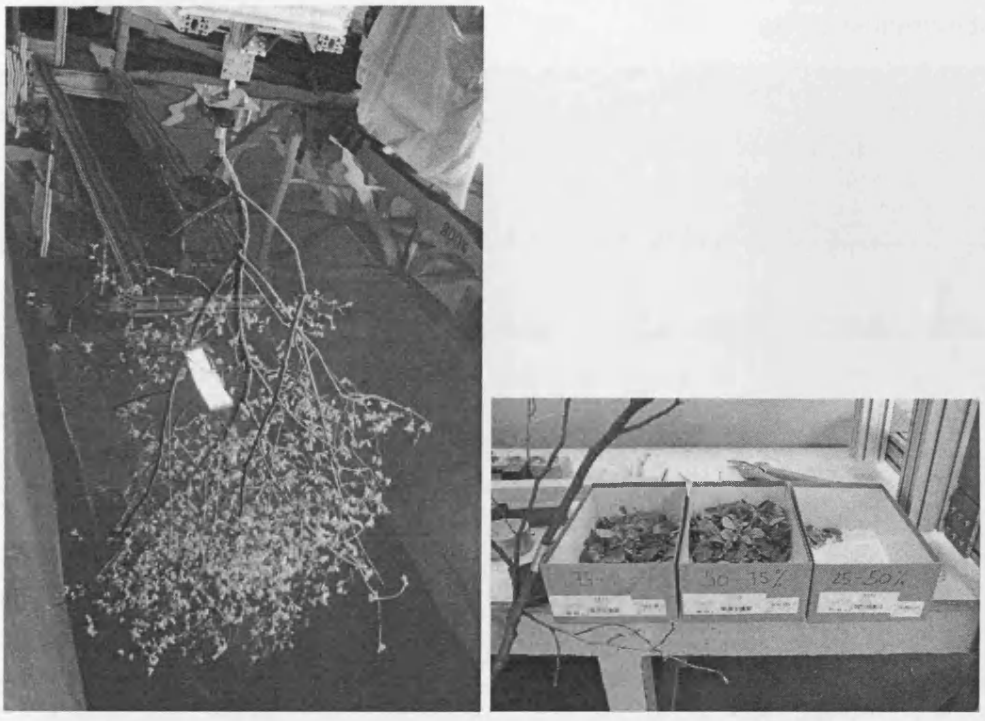

(a) (b)

Figure 5.10: (a) Tree submerged in canal, (b) leaves divided prior to mass and volume measurement

5.2.5.4 *Bending Stiffness Determination*

A bending stiffness test on the tree specimens was carried out. Due to time limitations, the properties of all the trees could not be determined. Each tree was initially fixed with a pair of G-clamps to lie in a horizontal position off the edge of a secure table. Masses from 0.2 kg to a maximum of 13 kg were attached to the tree at the 1st quartile height or the mid-height point, as in Figure 5.11. The observed bending was recorded as the vertical deflection at the point of loading.
By equating the tree to a cantilever, an estimate for the tree bending stiffness could be determined given:

$$E = \frac{PL^3}{3\delta I} \tag{5.21}$$

$$I = \frac{\pi r^4}{4} \tag{5.22}$$

Where E is the stiffness modules, P is the load applied to the tree, L is the distance from the point of load to the secured base of the tree, δ is the vertical deflection, I is the second moment of area of the section of the tree, r is the diameter at the mid point between the secured base and the applied load. Equation 5.21 is developed for small deflections of uniform cantilever beams of linear elasticity where $(\frac{dy}{dx})^2 << 1$. This approach is limited for two reasons. The trees are not uniform throughout the width or length as younger wood in the outer cambium and higher parts of the tree are more flexible. At higher loads, particularly those loads fixed to the mid-height, the deflections are also of a high magnitude relative to the length. Therefore the modulus of elasticity (E) obtained is averaged from the modulus of elasticity values derived from various loads attached to the first quartile (25 %) of the height, as in Equation 5.23.

$$\overline{E_{25}} = \frac{E_{25}^{0.2} + E_{25}^{0.5} + E_{25}^{1.0} + E_{25}^{2.0} + E_{25}^{3.0} + E_{25}^{6.0}}{n_{masses}} \tag{5.23}$$

Where $\overline{E_{25}}$ is the average modulus of stiffness for the tree, E_{25}^{mass} is the modulus of stiffness, the superscript $mass$ refers to the applied mass in kg and the subscript 25 refers to location of the applied mass in terms of the percentile height from the base, n_{masses} is the number of individual modulii of elasticity that have been determined for a single tree.

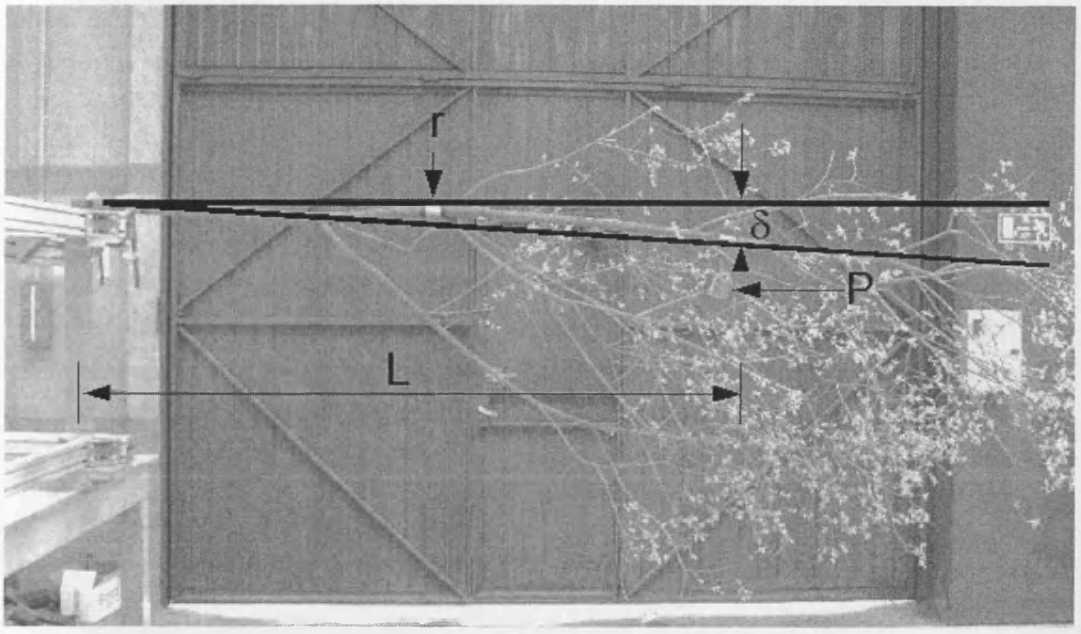

Figure 5.11: Bending Stiffness test on Salix specimen. Mass P attached at mid height at distance L

5.3 Cylinder Test

In order to have a baseline with which to compare the results from the trees, and to test the load cell, experiments were first carried out with a rigid cylinder of a similar diameter and height to the trees. The solid steel cylinder of diameter (d) of 0.03 m and a submerged length (l) of 2.0 m was attached securely to the load cell and tests were carried out at a range of velocities from 0.125 m/s to 5 m/s. The measured force versus velocity results from these tests can be seen in Figure 5.12.

The force versus velocity relationship appears to be quadratic up to a velocity of 1.4 m/s. Between a velocity 1.4 m/s and 2.25 m/s, there is a bulge in the graph that appears. During this, the force exerted on the load cell rises dramatically and the cylinder was observed to vibrate. Using the cylinder's diameter of d = 0.03 m as the characteristic length, the Reynold's number of flow in this region is between 42000 and 67500. The C_d - Re relationship in Figure 2.7 shows a dip in the relationship, but this occurs at the higher Re value of approximately $100,000$, when the boundary layer changes from laminar to turbulent. This bulge may therefore be attributed to a resonance in the frequency of shedded vortices. At higher velocities, the rate of increase of force with respect to velocity decreases. On the recorded underwater image, the cylinder is seen to deflect slightly at these higher velocities. A large amount of air entrainment along the downstream side of the cylinder was also observed. Figure 5.13 presents the drag coefficient (C_d) versus velocity and Reynold's number. C_d is calculated from the drag force equation given by:

$$C_d = \frac{2F}{\rho A_p U_0^2} \tag{5.24}$$

Where C_d is the drag coefficient, F is the streamwise force experienced by the load cell, ρ is the density of water, A_p is the projected area of the cylinder at zero velocity and U is the Streamwise velocity. It can be seen in Figure 5.13 that the drag coefficient value (C_d) value is in the range 1.0 to 1.2 at low velocities. There is a peak in Cd at a Reynolds number of $50,000$, and a general decrease after that point. Note that at higher velocities, the derivation of C_d is not strictly accurate, due to the bending of the cylinder, reducing the projected area A_p, please note that the projected area used in this calculation has been set to the original value.

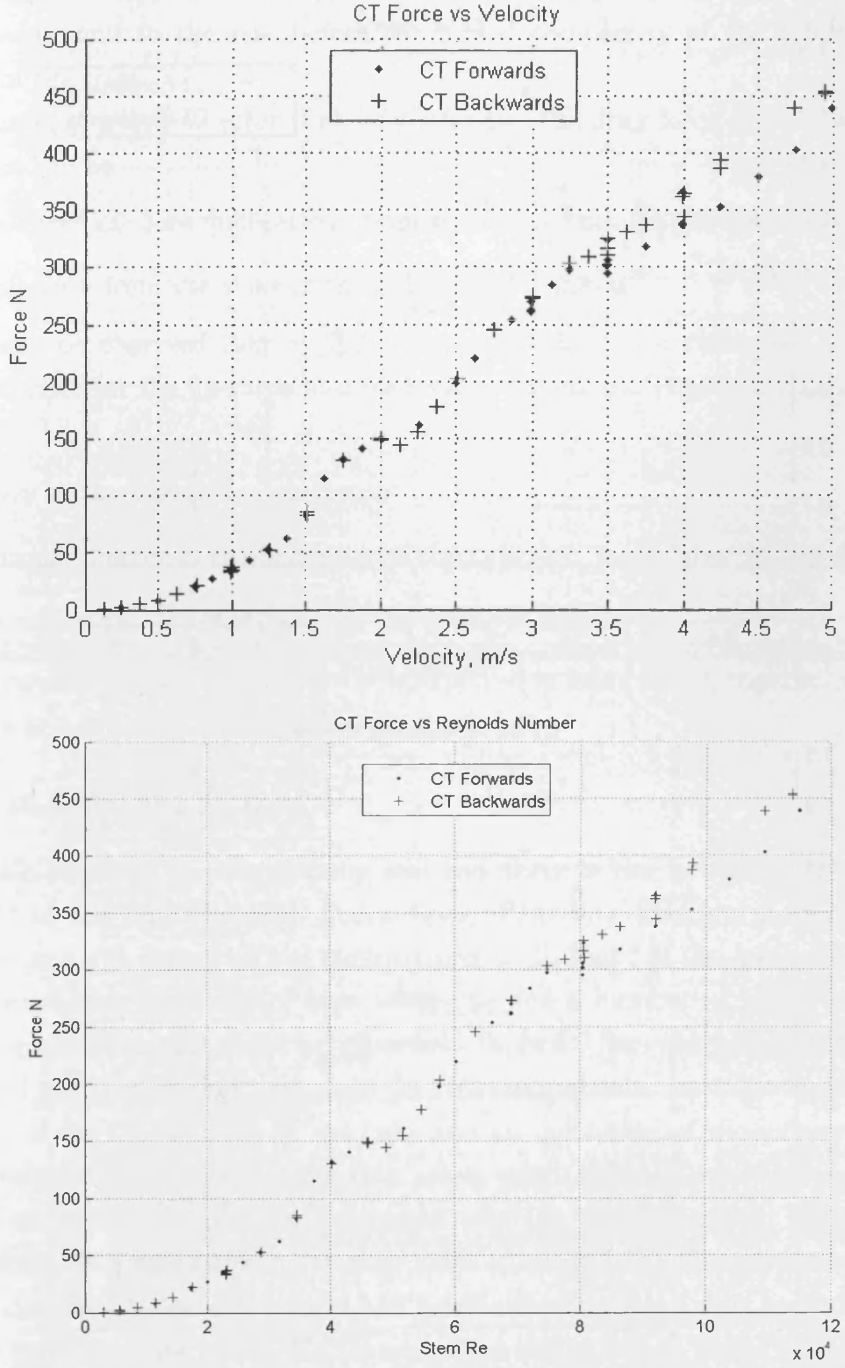

Figure 5.12: Plot of (a) drag force in N against velocity m/s and (b) Reynold's number, from cylinder test, where cylinder characteristic length (diameter) is $d = 0.030$ m

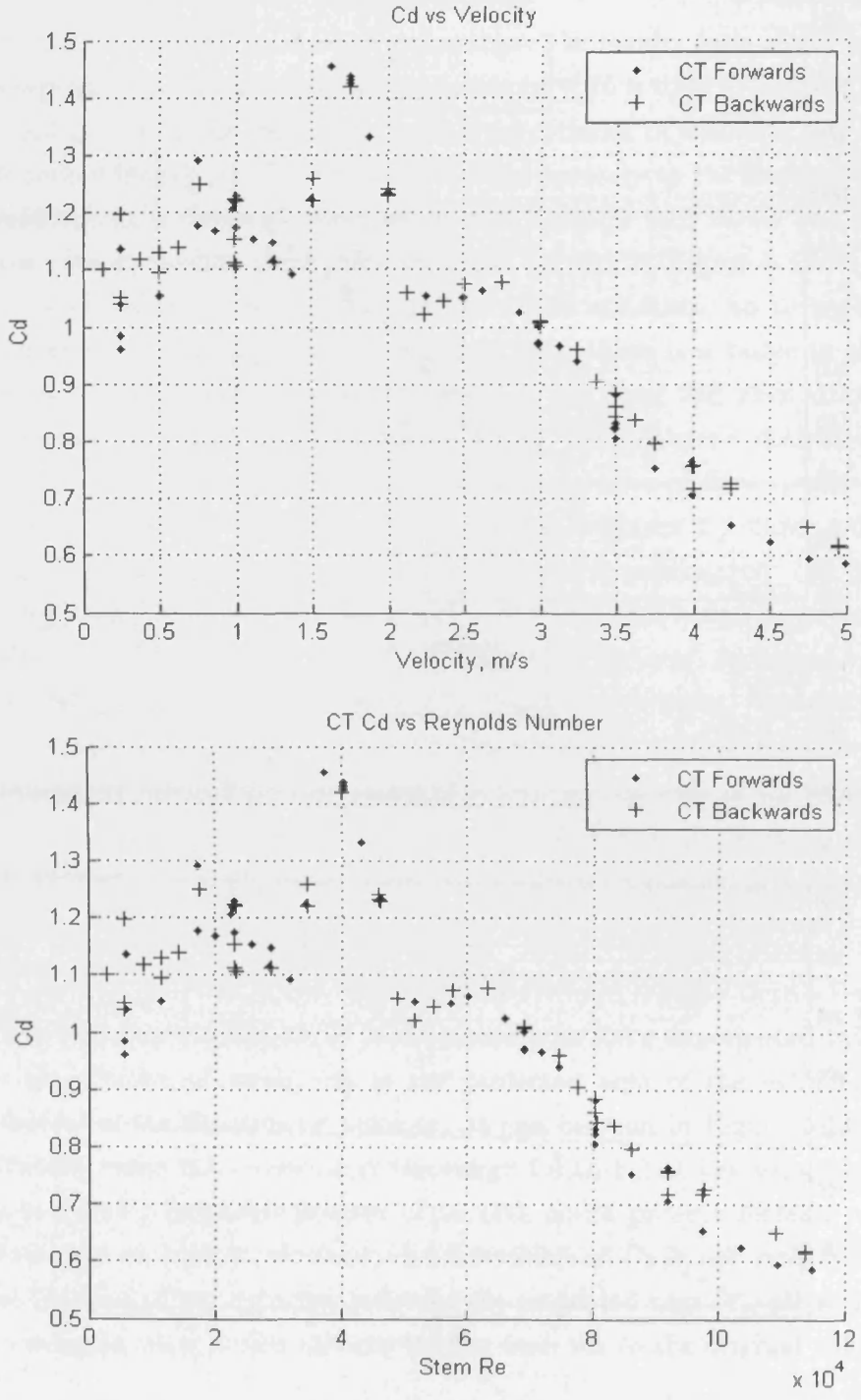

Figure 5.13: Plot of (a) bulk drag coefficient CdA against velocity m/s and (b) Re, from cylinder test, $d = 0.030m$

The cylinder test provided an opportunity to investigate potential sources of error that could occur in the test before the added complexity of the inhomogeneous nature of the trees.
The sources of potential error that may influence the drag force data collected were considered to be:

- Inherent random fluctuations from turbulent fluctuations in the basin
- Influence from the wake of the submerged cameras

It can also be observed that at higher velocities there is a difference between the recorded force for the forwards and backwards directions. Potential reasons for this could be:

- Bias in the load cell arrangement
- Inconsistencies in the fastening of the cylinder: more 'give' in one direction
- Dimensional inconsistencies of the cylinder itself

These potential sources of error are now explored in more detail, together with plans for error mitigation, where possible.

5.3.1 Repeatability of Tests

The basin of water is never entirely still and there is the potential for error from the random and unpredicatable fluctuations in the flow field and from the moving carriage that will impact on the measurements. To find out the range of error that can be expected, a number of tests were repeated a number of times to ascertain the margin of error that could be expected. Table 5.3 lists the test number and the measured parameters that were used for this comparison. In order to determine a measure of the repeatability of the tests and an indication of the inherent random fluctuations of the testing system, the mean value of the measured drag force for force tests was determined, and for each test the deviation from the mean was determined. The equivalent percentage error is also listed. This gives a measure of how an individual test defers from the mean values from all four tests. These are limited measurements but it can be seen from the values in Table 5.3 that except for one measurement at a velocity of 1.75 m/s, the absolute error remains within 1 N. It follows that as the force experienced by the cylinder increases, the percentage relative error will reduce. In order to ensure repeatablity, all tests were taken in both the forward and backward direction along the canal.

Test	F/B	Velocity	Force	Deviation	Deviation %
		m/s	N	N	%
080327.1409CT0250F	F	0.250	1.804	0.164	-8.34
080327.1435CT0250F	F	0.250	2.167	-0.199	10.09
080327.1409CT0250B	B	0.250	1.971	-0.003	0.125
080327.1435CT0250B	B	0.250	1.932	0.037	-1.868
			mean	**1.968**	
080327.1409CT1000F	F	1.000	36.090	0.706	-1.919
080327.1435CT1000F	F	1.000	37.129	-0.333	0.906
080327.1409CT1000B	B	1.000	37.345	-0.549	1.493
080327.1435CT1000B	B	1.000	36.619	0.176	-0.480
			mean	**36.796**	
080327.1409CT1750F	F	1.750	132.051	-1.047	0.799
080327.1435CT1750F	F	1.750	131.414	-0.409	0.313
080327.1409CT1750B	B	1.750	130.386	0.718	-0.548
080327.1435CT1750B	B	1.750	130.366	0.738	-0.563
			mean	**131.004**	

Table 5.3: Cylinder Test data. F refers to a forward run, B refers to a backward run

5.3.2 Camera Wake Influence

The submerged cameras (positions documented in Figure 5.1 (b)) have the potential to adversely affect the results, particularly during the backwards run where due to the positions of cameras Camera B and Camera C, there is greater chance of wake interaction with the cylinder ,which would reduce the force experienced by the cylinder. Efforts were taken to reduce this effect by submerging Cameras B and C just below the water surface, and both were mounted on a streamlined body to minimise resistance. As Camera A was sited at a distance of 5 m perpendicular to the streamline, influence was assumed to be negligible. As wake influence will increase with velocity, relatively high velocity values of 3.5 m/s and 4 m/s were chosen for comparison.

Test	**F/B**	**Velocity**	**No camera**	**With camera**	**Error**	**Error**
		m/s	N	N	N	%
CT3500F	F	3.500	31.166	30.804	-0.362	-1.16
CT4000F	F	4.000	34.421	34.504	0.083	2.40
CT3500B	B	3.500	33.158	32.254	-0.904	-2.66
CT4000B	B	4.000	37.952	36.952	0.330	-0.75

Table 5.4: Cylinder Test Results with and without cameras submerged

Table 5.4 lists the variation of drag force measurements at velocities of 3.5m/s and 4m/s with and without all cameras submerged. The results are also shown pictorially in Figure 5.14 for comparison.

It can be seen that there is an error in the force recorded up to 2.5% for both velocities. To avoid any bias introduced due to the presence of the cameras, Camera B was used only in the Forward direction when it lay behind the tree, and removed when the tree was tested in the Backward direction.

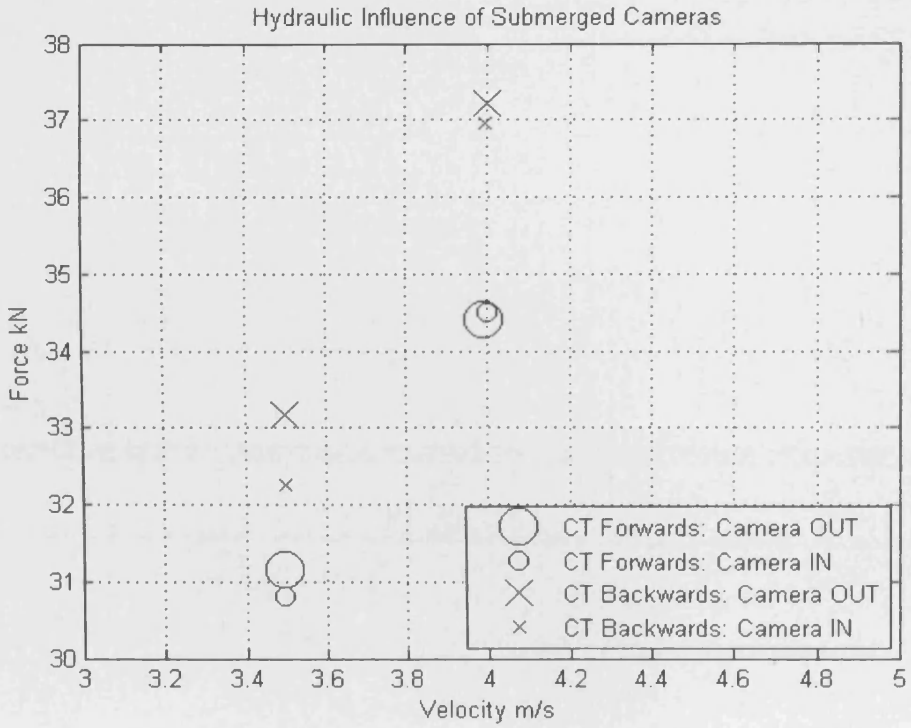

Figure 5.14: Impact of camera submergence on drag force measured

5.4 Results from Drag Force Tests

5.4.1 Drag Force Specimens

Species of *Salix*, *Alnus* and *Populus* were tested. Trees were tested in leaved and unleaved condition. Some trees were also sub-divided into branches and tested with and without leaves.

In total, thirteen *Salix*, five *Alnus* and four *Populus* trees were tested. Due to time restrictions, *Salix* 13 was not tested. As shown in Table 5.5, most trees were tested both with and without leaves. A few trees, which exhibited multi-stem characteristics, were selected for subdivision into branches, which were then tested individually with and without leaves.

One *Alnus* tree, A3, was a particularly straight specimen. For A3, the branches were stripped off and the stem only tested. The stem was then halved and the lower 50% of the stem was tested.

No	Tree	With Leaves	Without Leaves	Sub-branches	Stem Only
S1	*Salix*	✓	✓		
S2	*Salix*	✓	✓		
S3	*Salix*	✓	✓		
S4	*Salix*	✓	✓		
S5	*Salix*	✓		✓	
S5B1	*Salix*	✓	✓	✓	
S5B2	*Salix*	✓	✓	✓	
S6	*Salix*	✓		✓	
S6B1	*Salix*	✓	✓	✓	
S6B2	*Salix*	✓	✓	✓	
S7	*Salix*	✓		✓	
S7B1	*Salix*	✓	✓	✓	
S7B2	*Salix*	✓	✓	✓	
S7B3	*Salix*	✓	✓	✓	
S8	*Salix*	✓	✓		
S9	*Salix*	✓	✓		
S10	*Salix*	✓	✓		
S11	*Salix*	✓	✓		
S12	*Salix*	✓	✓		
S14	*Salix*	✓			
A1	*Alnus*	✓	✓		
A2	*Alnus*	✓			✓
A2B1	*Alnus*	✓	✓		✓
A2B2	*Alnus*	✓	✓		✓
A3	*Alnus*	✓	✓		✓
A4	*Alnus*	✓	✓		
A5	*Alnus*	✓	✓		
P1	*Populus*	✓			
P2	*Populus*	✓		✓	
P2B1	*Populus*	✓	✓	✓	
P2B2	*Populus*	✓	✓	✓	
P3	*Populus*	✓	✓	✓	
P4	*Populus*	✓			
P4B1	*Populus*	✓	✓		
P4B2	*Populus*	✓	✓		

Table 5.5: Tree Specimens and Investigations

5.4.2 Salix Properties and Drag Force Data

Salix is a common floodplain woodland species with many species suited to floodplain woodland environments. The species in the experiments were *Salix atrocinerea Brot.* and *Salix alba.* In particular, *Salix alba* has been used in the hydrodynamic investigations of Armanini et al. (2005).

The study investigated tree type, size and branching patterns. Each tree had the physical properties of height and main stem diameter recorded. Photographs were taken of the tree were taken, and the bending stiffness determined. While still with leaves, the tree was then attached to the dynanometer, and the drag force exerted on the dynanometer measured at increasing velocities. The tree was then defoliated, with the leaf mass and volume recorded. The defoliated tree was then reattached to the dynanometer and re-tested, this time to higher velocities.

Tree S14 was tested with progressive defoliation, with leaves and branches removed in quartiles, the results are not explored further here. Trees S5, S6 and S7 were divided into sub-branches after the initial test, and each sub-branch was tested with leaves, before being defoliated and retested without leaves.

The heights are presented in Figure 5.15. The trees had a mean height of 3.170 m. The tallest tree tested was $S12$ with a height of 4.1 m. The smallest whole tree tested was $S4$ with a height of 2.0 m. The stem diameters of the Salix trees and main sub branches investigated are presented in Figure 5.16. There is an approximately linear reduction in the mean diameter from the base to the 3rd quartile of height and the average basal diameter was 30.85 mm. The tree heights and diameters are listed in Table 37 in the Appendix.

The fresh wood and foliage mass are presented in Figure 5.17. Both the fresh and dry mass of *Salix* trees $S5$ to $S12$ were recorded and the mean ratio of fresh to dry wood was found to be 0.470. Only the fresh mass was recorded for *Salix* trees 1 to 4, so an estimate dry mass has been calculated using the fresh to dry wood ratio. Tree $S3$ has the greatest wood mass of 5.45 kg, however, most of the trees have a fresh wood mass below 3 kg. Tree $S5$ has the greatest foliage mass of 0.612 kg, the leaf mass of $S14$ was not recorded. The fresh wood and foliage volume are presented in Figure 5.18. As expected, the pattern of wood volume follows that of the wood and foliage mass. The wood volume of $S3$ and $S4$ were not recorded and the leaf volume of $S4$ and $S14$ were not recorded. The fresh and dry masses, volume and fresh and dry densities of the leaves and branches are recorded in Table 38 and Table 39 in the Appendix.

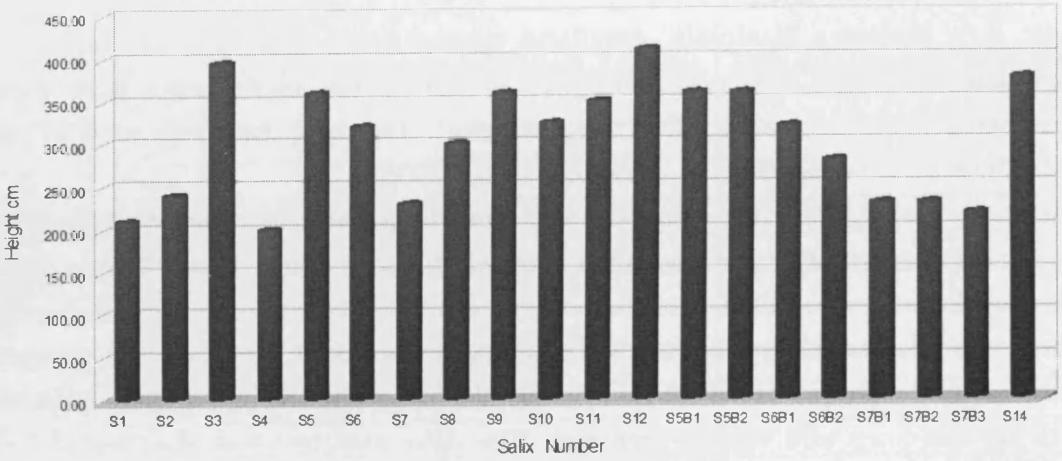

Figure 5.15: Salix Heights

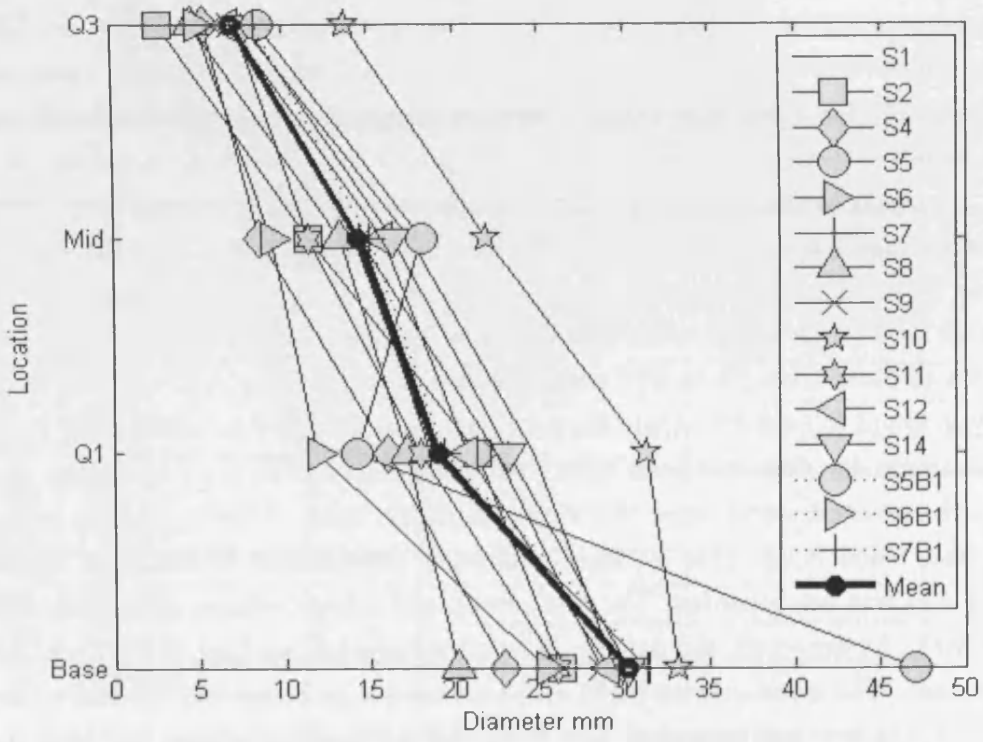

Figure 5.16: Salix Stem Diameter at Base, Quartile 1, Mid and Quartile 3 heights

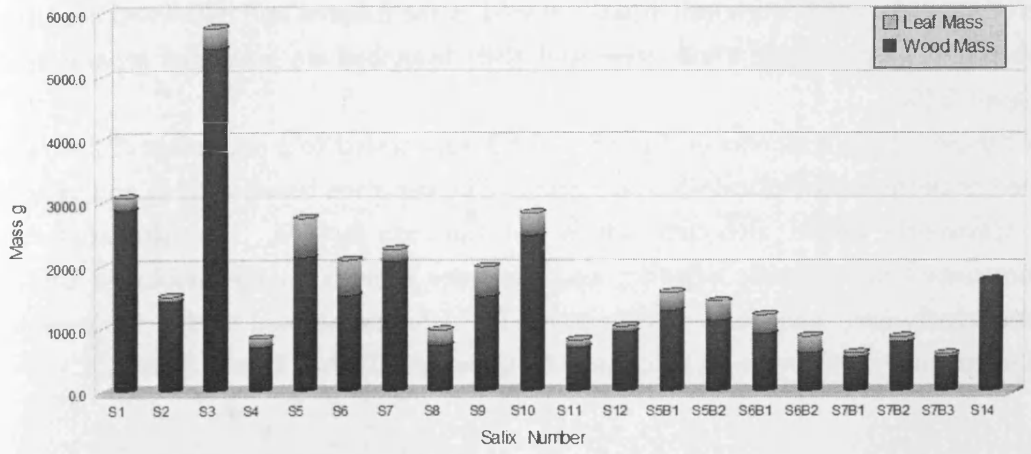

Figure 5.17: Salix Wood and Leaf Mass

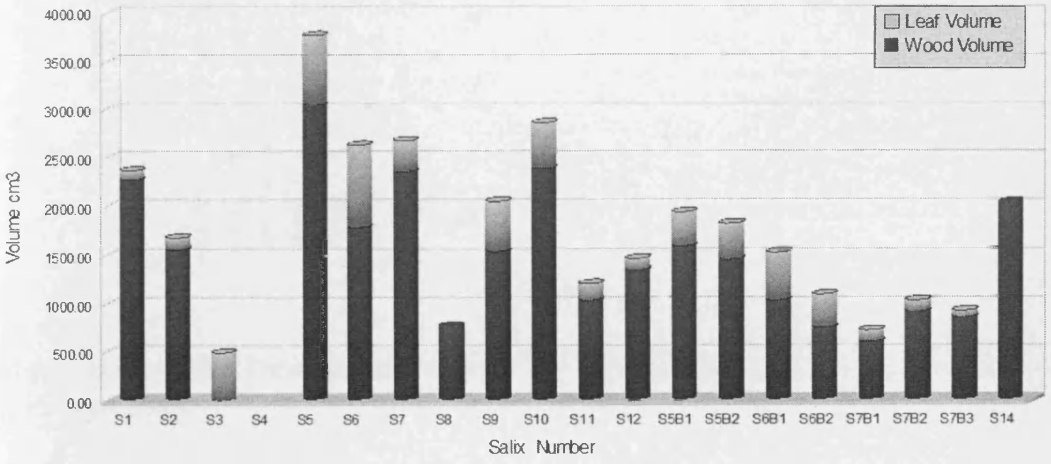

Figure 5.18: Salix Wood and Leaf Volume

Figure 5.19 (a) presents the streamwise drag force against the velocity for the foliated trees and (b) presents the streamwise drag force against the velocity for the defoliated trees. Trees $S5$, $S6$ and $S7$ were tested in the foliated condition, then subdivided into branches which were individually tested in the foliated and defoliated condition (the results from these whole trees and their branches are presented separately in Figure 5.19).

In Figure 5.19 (a), all except $S1$, $S8$ and $S9$ were tested to a maximum of 2 m/s, to prevent permanent deformation occurring. The variation between force and velocity is apparently linear, although this is not the case for $S9$. The defoliated trees were tested to a greater velocity, and the force exerted on the defoliated trees is consistently less than the foliated trees. The results obtained compare reasonably in magnitude to those from the study by Oplatka (1998*a*), Figure 5.20.

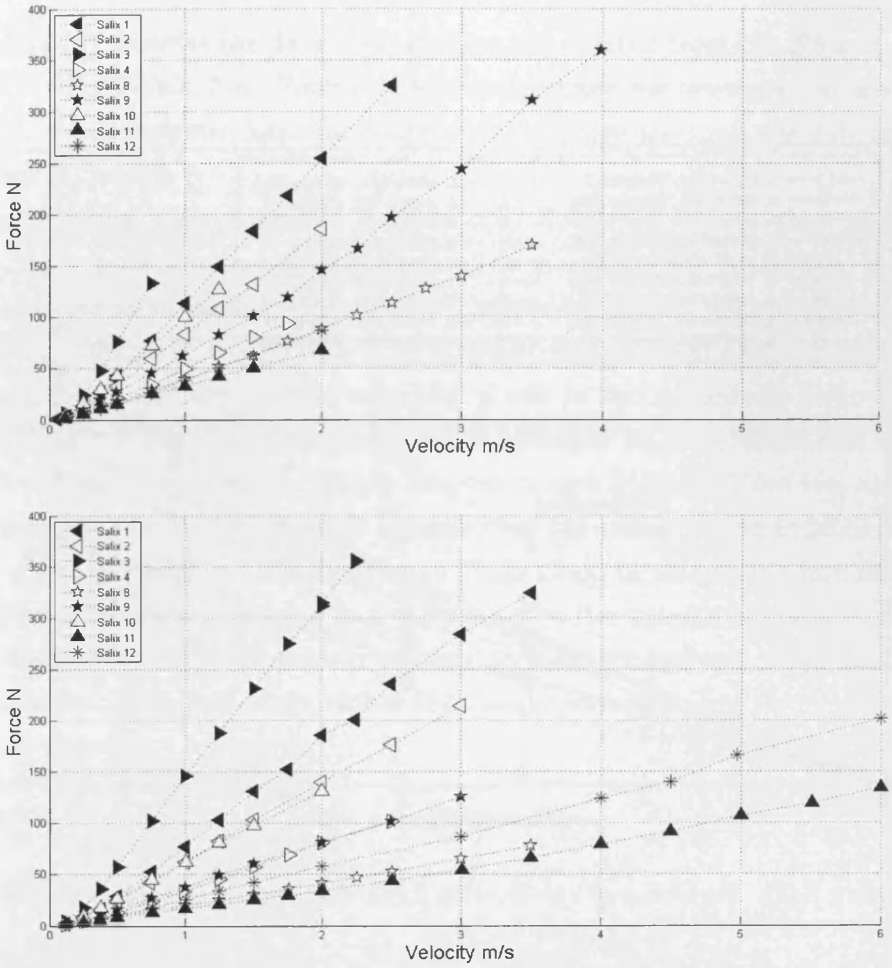

Figure 5.19: *Salix* Force versus Velocity for full-scale trees (a) foliated trees, (b) defoliated trees

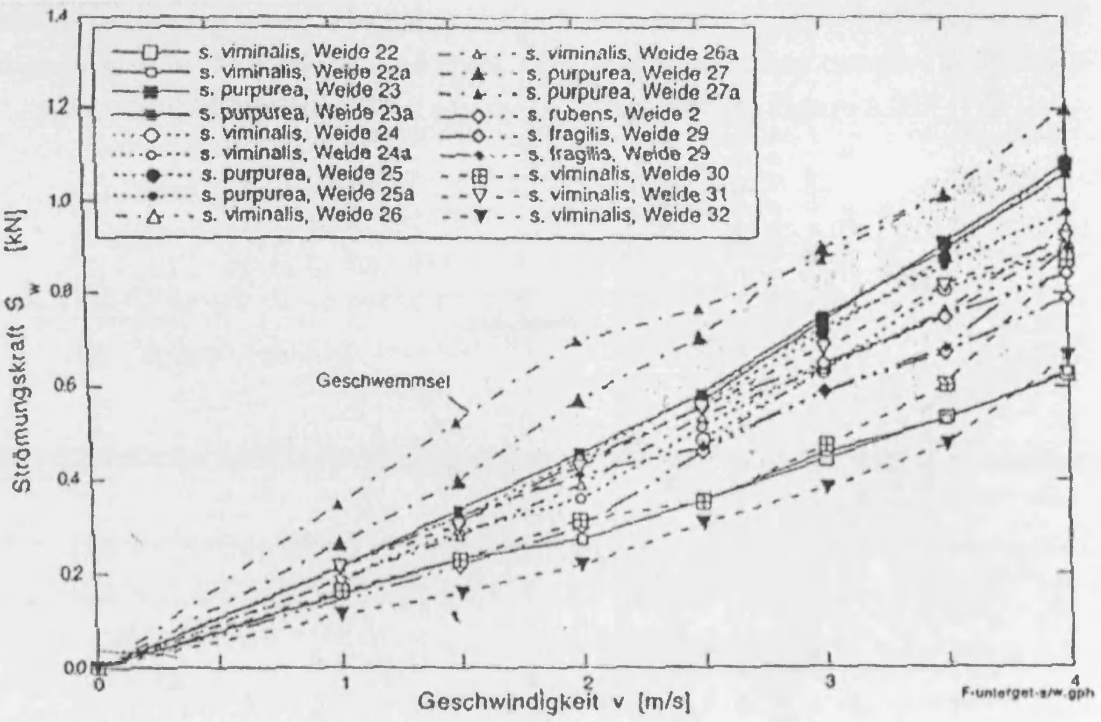

Figure 5.20: Variation of streamwise force with velocity (Oplatka 1998 *a*)

Tree	Whole	B1	B2	B3	$\sum B$	%
Salix 5	116.656	58.399	56.971		115.370	-1.1
Salix 6	85.340	52.900	31.850		84.750	-0.7
Salix 7	93.830	27.560	37.970	26.370	91.900	-2.1

Table 5.6: Whole and sub-branches of Salix trees $S5$, $S6$ and $S7$, force (N) measured at a streamwise velocity of 1 m/s

Figure 5.21 (a) presents the data measured for the foliated trees $S5$, $S6$ and $S7$ and their foliated sub-branches. Comparisons can be made for the data. At a velocity of 1 m/s, the streamwise force measured for the whole tree and the sub branches are shown in Table 5.7.

Although dealing with a limited sample set, Table 5.6 shows that measuring individual component branches compares well to measuring the entire tree, although there is a consistent underestimation in the combined force from the branches compared to the whole tree. There is an inherent limitation in drawing conclusions from the above data. Orientation may play a role in the streamwise force exerted, and the orientation of the sub branches while attached to the original tree will not be the same as the orientation during the sub-branch testing. However, assuming this orientation effect is negligible, it appears that the sum of the individual parts of the tree come to less than the original tree. This could be due to the fact that once streamlined, the tree is behaving as a porous body, the density of which is directly related to the leaf and wood mass present, with a denser leaf and wood mass body behaving more like a bluff body, rather than a porous body.

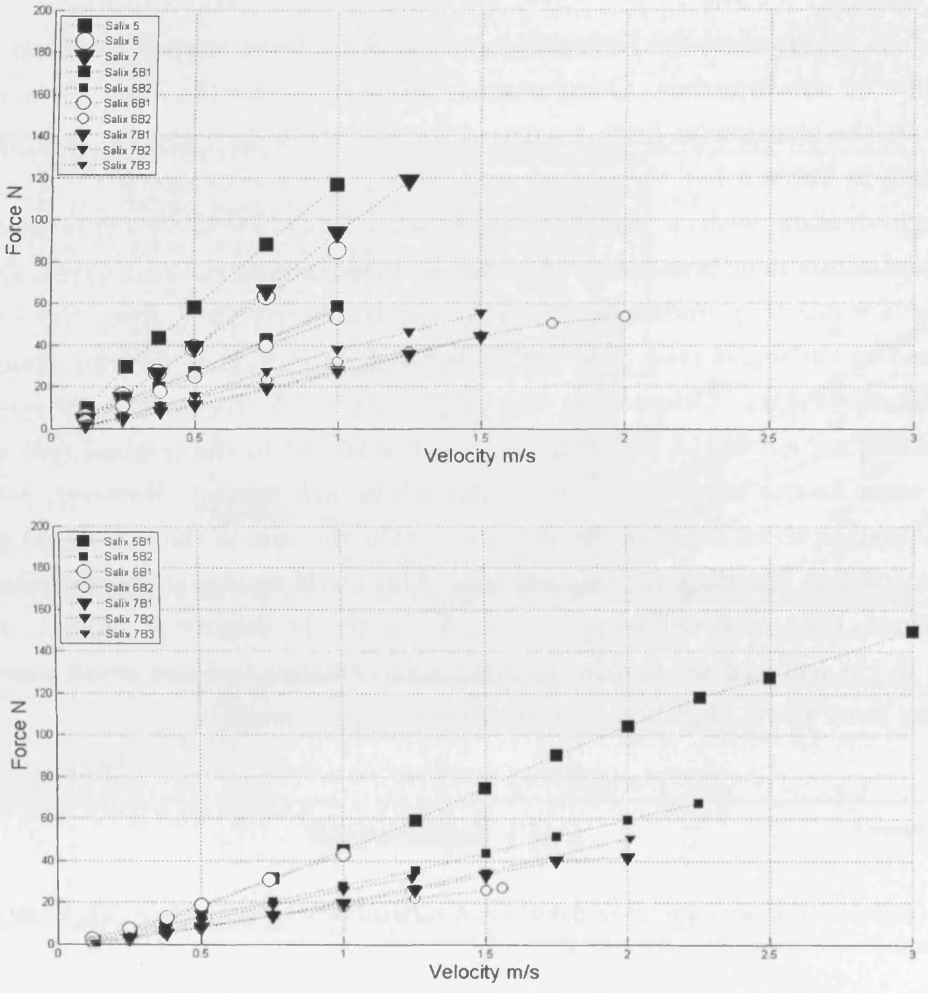

Figure 5.21: *Salix* Force versus Velocity for sub-branches (a) foliated trees, (b) defoliated trees

5.4.3 *Alnus* Drag Force Data

Alnus glutinosa is a common floodplain woodland variety, highly tolerant of wet conditions. In the UK, *Alnus* is designated as a defining species of wet woodland. The *Alnus* study investigated tree type, size and contribution from branches with a total of five original trees labeled A1 to A5. Each tree had the physical properties of height and main stem diameter recorded. Photographs were taken of the tree, and the bending stiffness determined. While foliated, the tree was then attached to the dynanometer, and the drag force exerted on the dynanometer measured at increasing velocities. The tree was then defoliated, with the foliage mass and volume recorded. The defoliated tree was then reattached to the dynanometer and re-tested, this time to higher velocities.

Tree $A2$ was tested in sub-branches, although the force-velocity data is not presented here. Tree $A3$ was a particularly straight specimen. After the initial testing with and without leaves, all the side branches were removed to leave just the main stem and the tree was retested. Following the test on the main stem, the stem was halved and the lower 50% of the main stem was reattached to the dynanometer and re-tested. The data from this part of the study is not presented here.

The heights of the *Alnus* specimens tested are presented in Figure 5.22. The trees had an average height of 2.57 m, with the largest tree ($A2$) having a height of 3.6 m, and the smallest tree ($A5$) with a height of 1.8 m. The diameters are presented in Figure 5.23. The trees had an average basal diameter of 35.4 mm and the variation of diameter with height measured at quartiles was approximately linear.

The fresh wood and foliage mass of the *Alnus* are presented in Figure 5.24. The fresh and dry wood mass of $A2$, $A3$ and $A4$ were recorded to give a ratio of fresh to dry wood of 0.503. Only the fresh wood mass of $A1$ and $A5$ were recorded, and an estimate for the dry mass obtained by applying the ratio. It can be noted that although $A4$ and $A5$ have a difference in height of 0.6 m, the masses are almost identical. The foliage mass of the *Alnus* is approximately equal for $A1$ and $A4$.

The fresh wood and foliage volume of the *Alnus* are presented in Figure 5.25. The wood volume for *Alnus* 2 was not recorded and the foliage volume for $A3$ and $A3$ were not recorded.

The heights and stem diameters of the *Alnus* trees are listed in Table 40 in the Appendix. The fresh and dry masses, volume and fresh and dry densities of the leaves and branches are recorded in Table 41 and Table 42 in the Appendix.

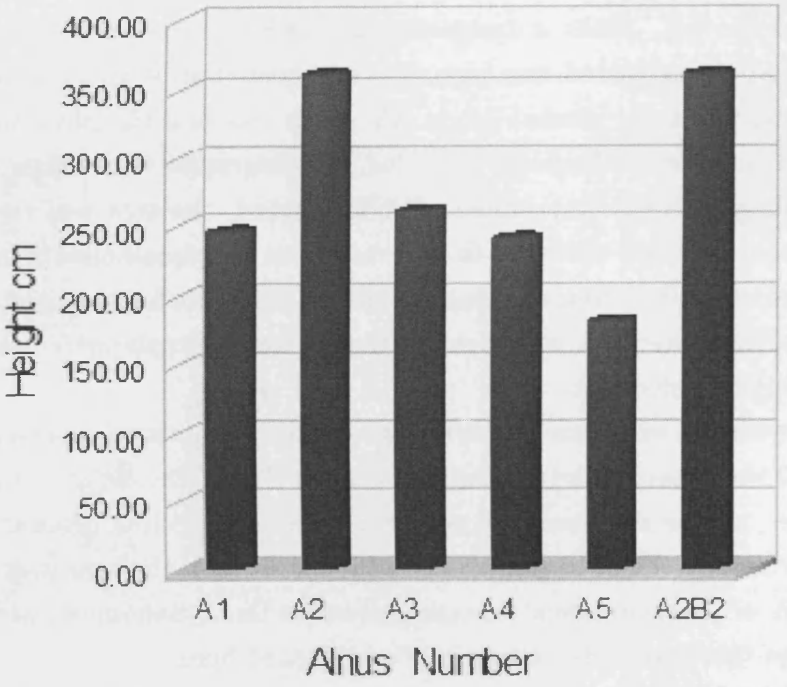

Figure 5.22: *Alnus* Heights

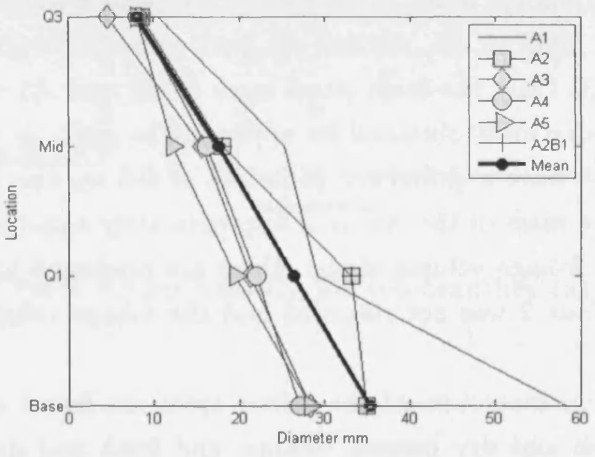

Figure 5.23: *Alnus* Stem Diameter at Base, Quartile 1, Mid and Quartile 3 heights

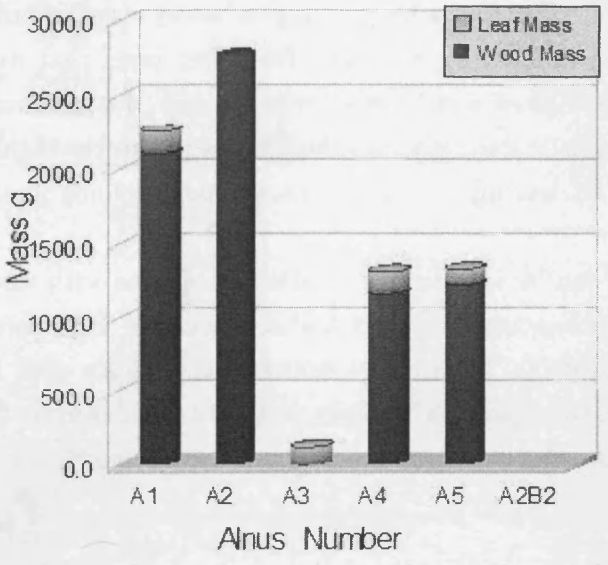

Figure 5.24: *Alnus* Wood and Leaf Mass

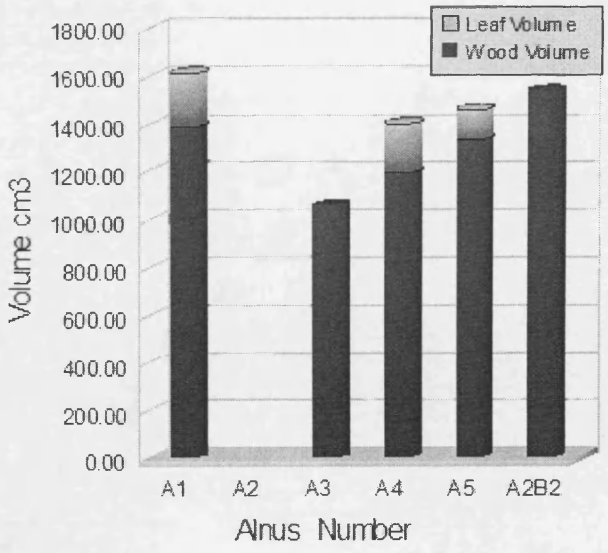

Figure 5.25: *Alnus* Wood and Leaf Volume

The force-velocity results are shown in Figure 5.26. All five *Alnus* were tested in the foliated condition, but only the results for $A1$, $A4$ and $A5$ were recorded in the defoliated condition. The tree with the largest wood mass, volume and height $A2$, also exerts the largest force by velocity. The three trees that were tested in both the foliated and defoliated conditions ($A1$, $A4$ and $A5$) all produce very similar force - velocity results at low velocities, but $A5$ produces the highest force at higher velocities, despite $A1$ having the largest wood mass, volume and height out of the three trees.

At low velocities it can be seen that the variation of force with velocity is not linear, but the relationship becomes linear at higher velocities. This corresponds with the results of Armanini et al. (2005) who noted that in tests with larger trees, force varied linearly with the square of velocity, but with smaller more flexible trees, force varied linearly with velocity. The experiments here appear to cover both regimes for single plants.

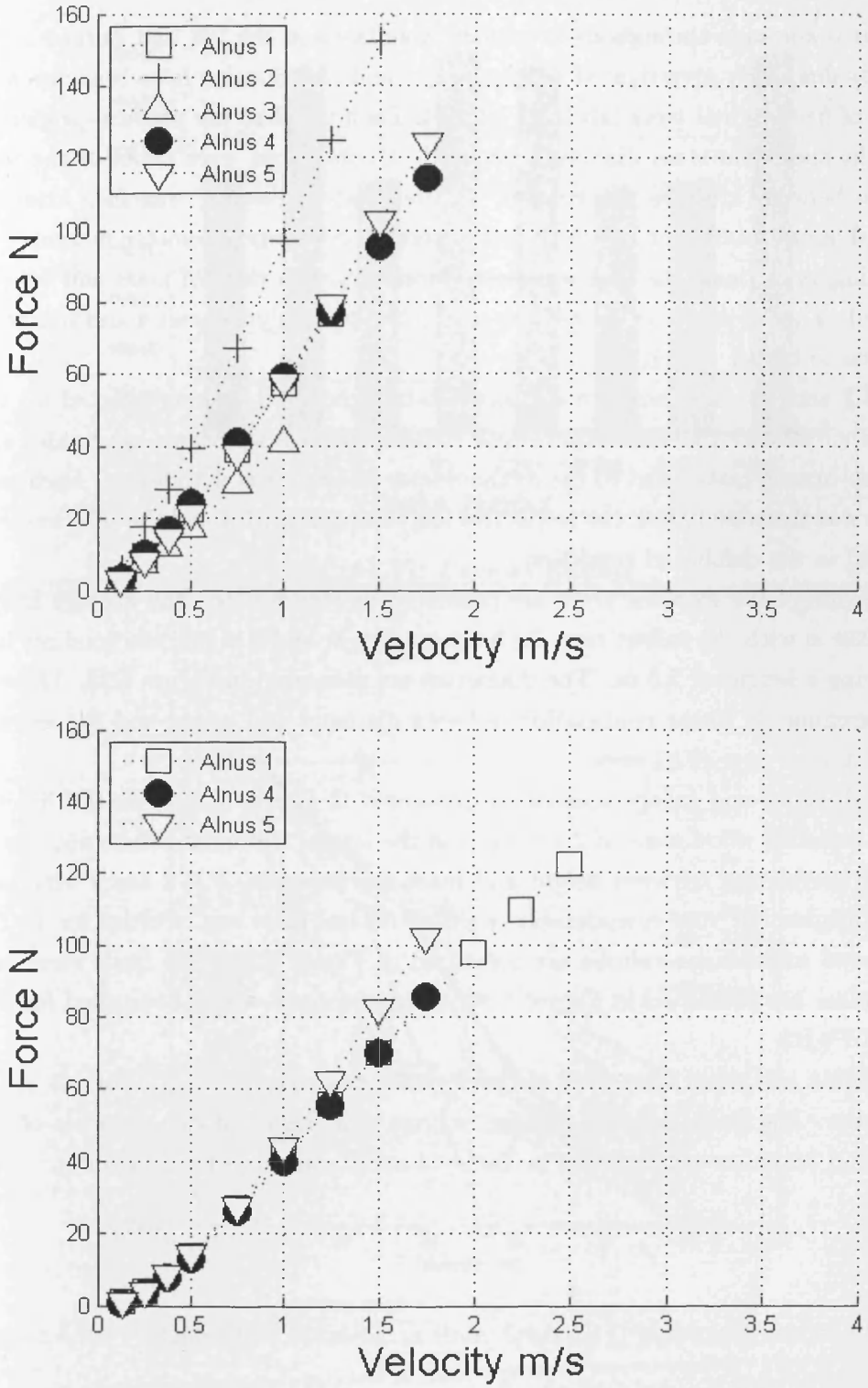

Figure 5.26: *Alnus* Force versus Velocity for full-scale trees (a) foliated trees, (b) defoliated trees

5.4.4 *Populus* Drag Force Data

Populus is common throughout floodplain woodlands in the UK and Europe.
The *Populus* study investigated tree type, size and contribution from branches with a total of five original trees labeled P1 to P4. Each tree had the physical properties of height and main stem diameter recorded. Photographs were taken of the tree, and the bending stiffness determined. While foliated, the tree was then attached to the dynanometer, and the drag force exerted on the dynanometer measured at increasing velocities. The tree was then defoliated, with the leaf mass and volume recorded. The defoliated tree was then reattached to the dynanometer and re-tested, this time to higher velocities.
Trees P2 and P4 each had two distinct sub-branches and so were selected for the sub-branch study. After the initial testing with leaves, the trees were subdivided and each sub-branch reattached to the dynanometer and retested with leaves. Each sub-branch was then defoliated, the respective leaf masses recorded and the sub-branches re-tested in the defoliated condition.
The heights of the *Populus* trees are presented in Figure 5.27. The average height was 3.238 m with the tallest tree $P4$ having a height of 3.9 m and the smallest tree $P3$ having a height of 2.6 m. The diameters are presented in Figure 5.28. There is an approximately linear relationship between diameter and height and the average basal diameter was 32.54 mm.
The fresh wood and foliage masses are presented in Figure 5.29. Tree $P4$ has the largest recorded wood mass of 2.416 kg, and the largest leaf mass. There appears to be little correlation between height and mass, for example, $P2B2$ and $P4B1$ have similar heights but vary considerably in mass. No leaf mass was recorded for 1. The fresh wood and foliage volume are presented in Figure 5.30. The fresh wood and leaf volume are presented in Figure 5.30. Foliage volume was not recorded for $P1$, $P4$ and $P4B2$.
The heights and stem diameters of the *Populus* trees are listed in Table 43 in the Appendix. The fresh and dry masses, volume and fresh and dry densities of the leaves and branches are recorded in Table 44 and Table 45 in the Appendix.

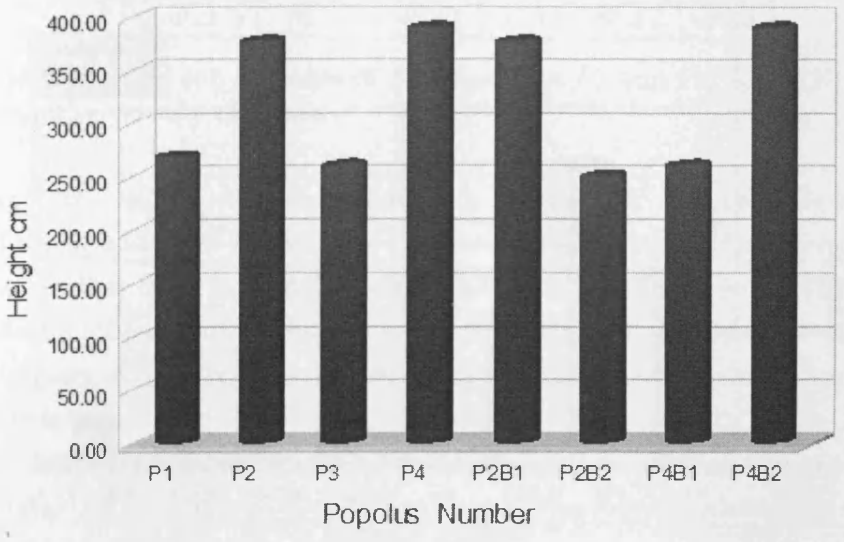

Figure 5.27: *Populus* Heights

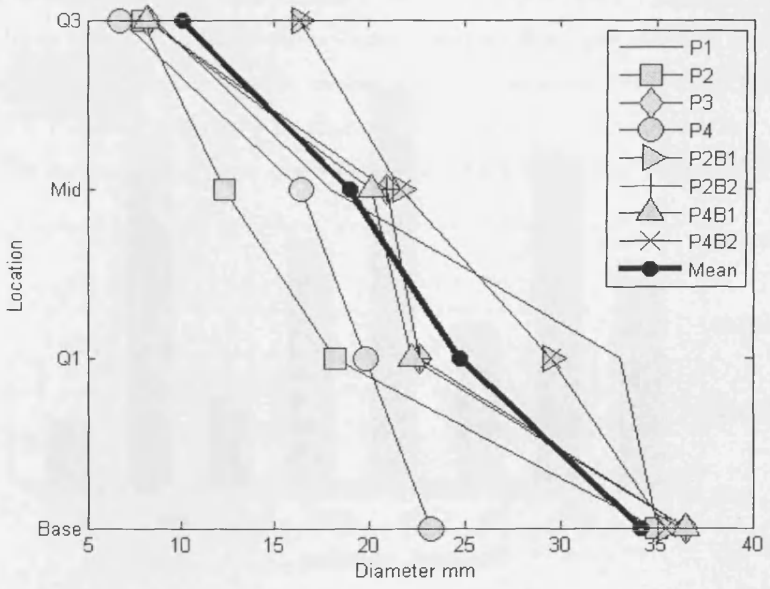

Figure 5.28: *Populus* Stem Diameter at Base, Quartile 1, Mid and Quartile 3 heights

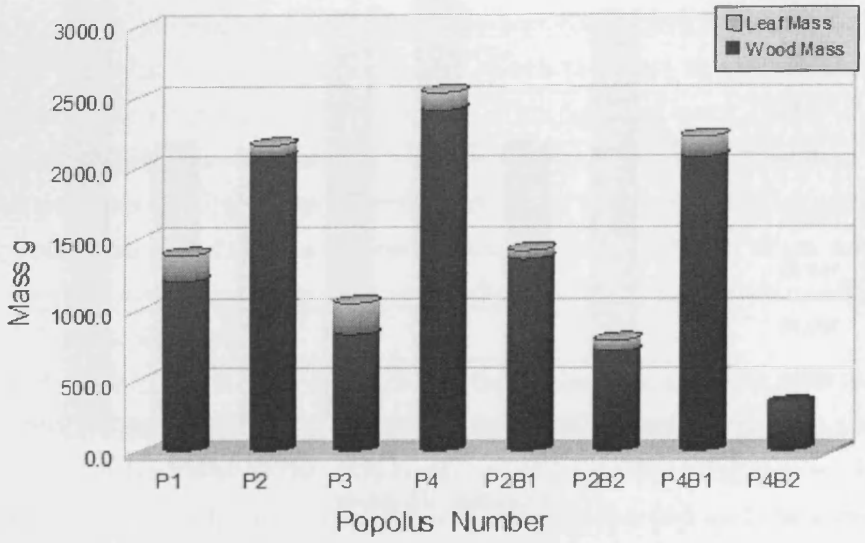

Figure 5.29: *Populus* Wood and Leaf Mass

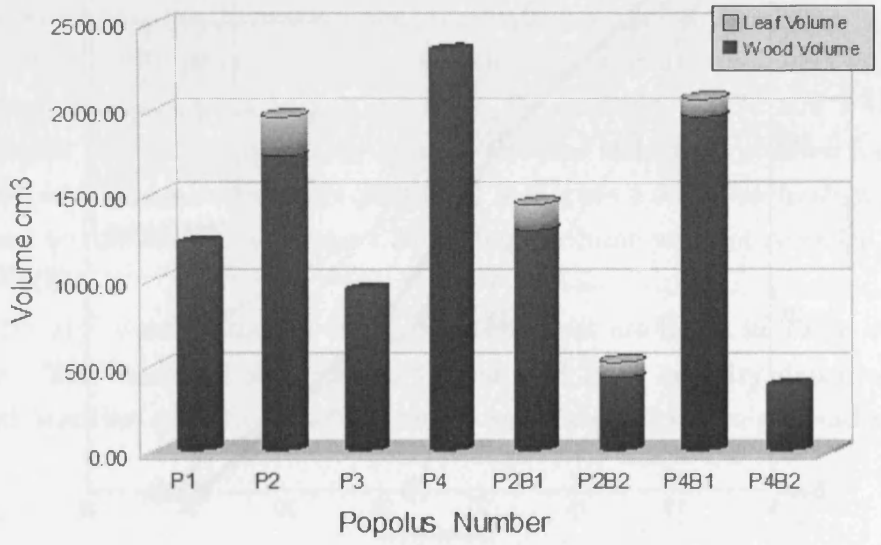

Figure 5.30: *Populus* Wood and Leaf Volume

Tree	Whole	B1	B2	$\sum B$	%
Populus 2	75.71	56.65	21.73	78.38	3.53
Populus 4	86.55	48.81	33.11	81.92	-5.35

Table 5.7: Whole and sub-branches of *Populus* trees $P2$ and $P4$, force (N) measured at a streamwise velocity of 1 m/s

The drag force - velocity data is presented in Figure 5.31. The two largest trees in terms of height and mass $P2$ and $P4$, produce the largest force for a given velocity, while the smallest trees in terms of height and mass $P3$, $P2B2$ and $P4B2$, produce the smallest force for a given velocity. At low velocities, force appears to vary linearly with the square of velocity, while at high velocities, the force appears to vary linearly with velocity.

Trees $P2$ and $P4$ were divided into two sub-branches. Comparisons can be made for the data. At a velocity of 1 m/s, the streamwise force measured for the whole tree and the sub branches are shown in Table 5.7.

The combined force of the sub-branches $P2B1$ and $P4B2$ is larger than the force from the whole $P2$ tree. Conversley, the combined force of the sub-branches $P4B1$ and $P4B2$ is smaller than the force from the whole P. The error margin for the *Populus* sub-branches is greater than that for the *Salix*. This could be due to the differences in stiffness and morphology between *Salix* and *Populus*. Images in the Appendix from the side camera show that *Populus* does not deflect as much as *Salix*, even though the trees have similar diameters and masses. This could mean that the branches in a *Populus* act more as distinct individual elements, rather than melding together. For examples of this, see Figures 47 and 66 in the Appendix.

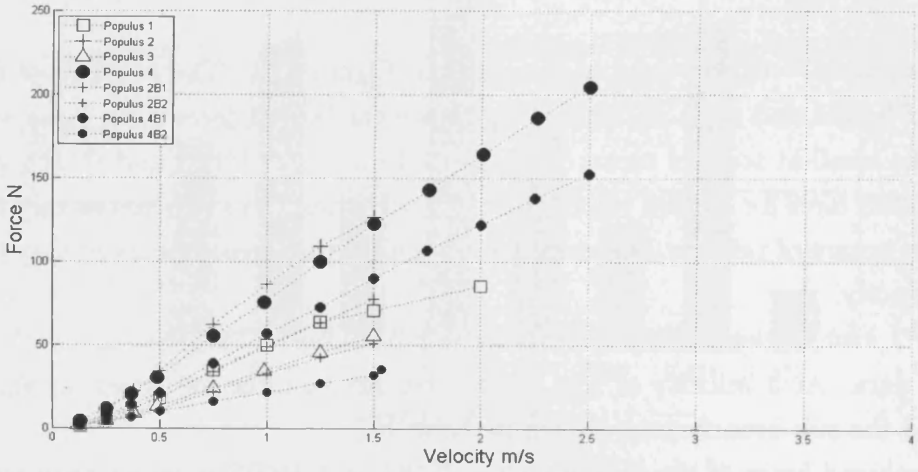

(a)

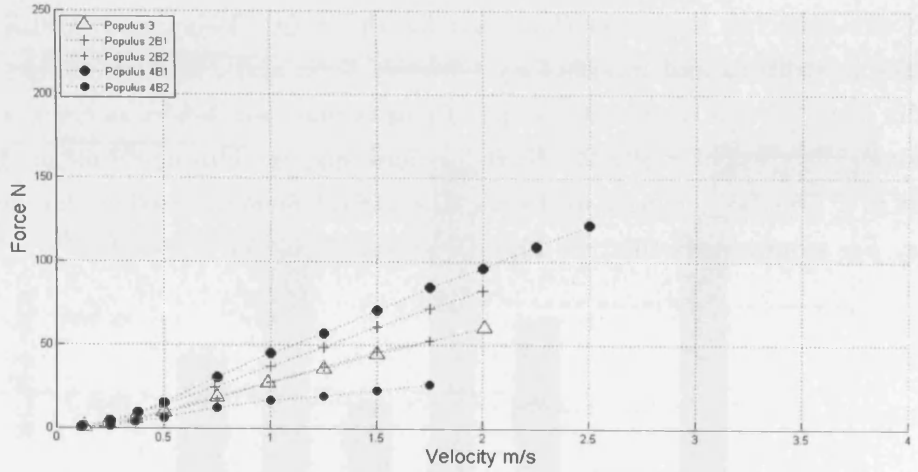

(b)

Figure 5.31: *Alnus* Force versus Velocity for full-scale trees (a) foliated trees, (b) defoliated trees

5.5 Tree Canopy Compression

5.5.1 Tree Height Reduction

Weissteiner (2009) collated results from the video footage to record the plant height reduction at different velocities and forces. An example of this is shown in Figure 5.32 for $S4$ for both the foliated and defoliated condition. It can be seen that as the velocity increases, there is an increasing streamlining of the tree. From 0 m/s to 0.125 m/s, there is not much deformation in the tree, although some branches with leaves are seen to incline. At a velocity of 0.375 m/s there is a substantial reconfiguration of the branches, and until 1.00 m/s, this reconfiguration results in a further streamlining of the branches and a consequent compaction of the foliage mass. Equivalent images from other trees are shown in the Appendix.

Comparing the foliated and defoliated conditions, it is clear that there is a greater degree of streamlining for each branch when it is foliated, although there does not appear to be a greater inclination on the main stem. Much further research in analysis of the photographs could be carried out to investigate the deformation of the branches and main stem with and without foliage.

Selected results are presented in Figures 5.33 (a) and (b) from Weissteiner (2009). It can be seen that as velocity and force increase, the rate reduction in plant height reduces. At lower velocities and forces, the rate of reduction in plant height is almost linear. At higher velocities/ forces, the rate of reduction begins to reach an apparently asymptotic level. The reduction in plant height is directly related to the reduction in projected area (A_p).

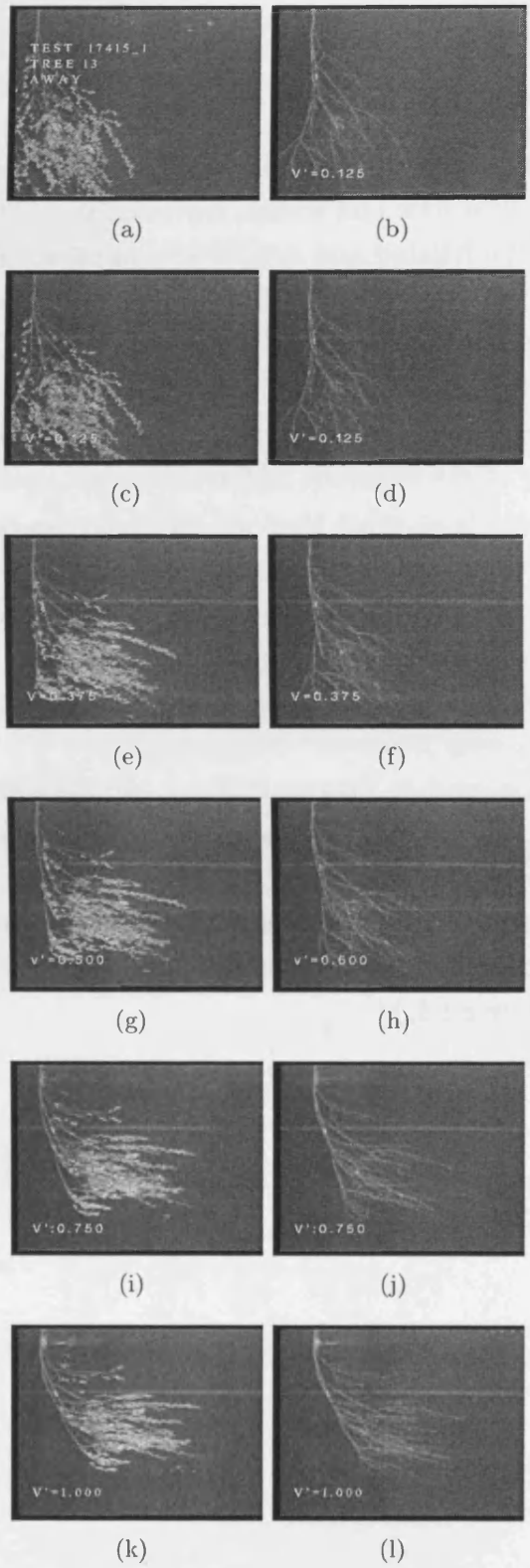

Figure 5.32: Images from foliated (left) and defoliated (right) *Salix* 4 from 0 m/s to 1 m/s

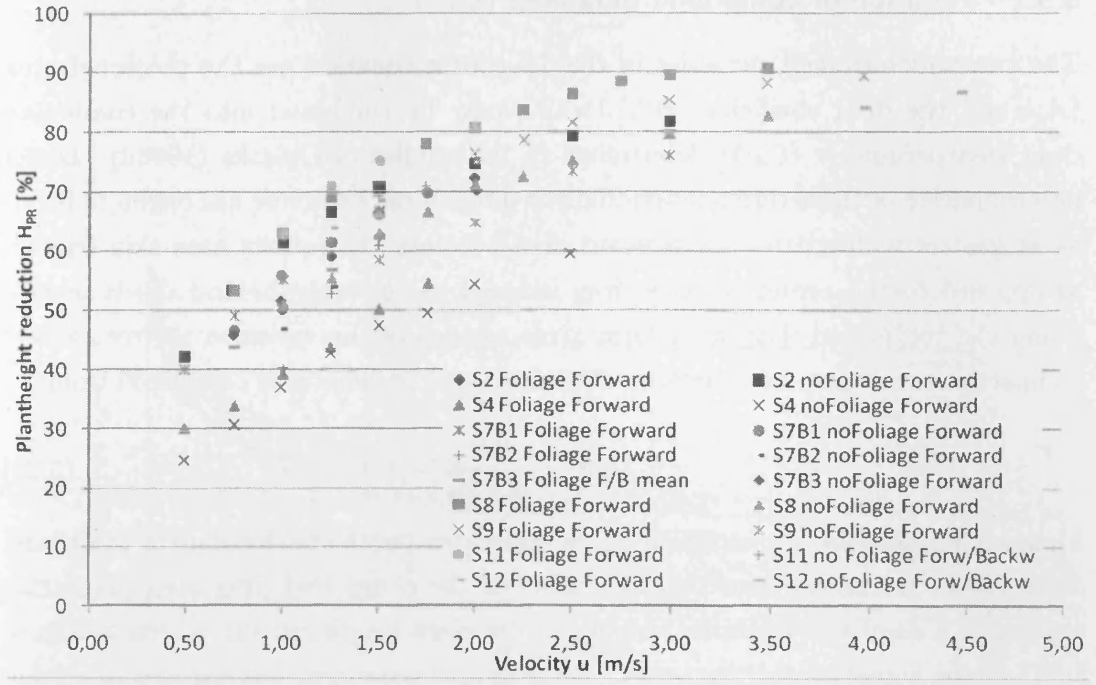

(a)

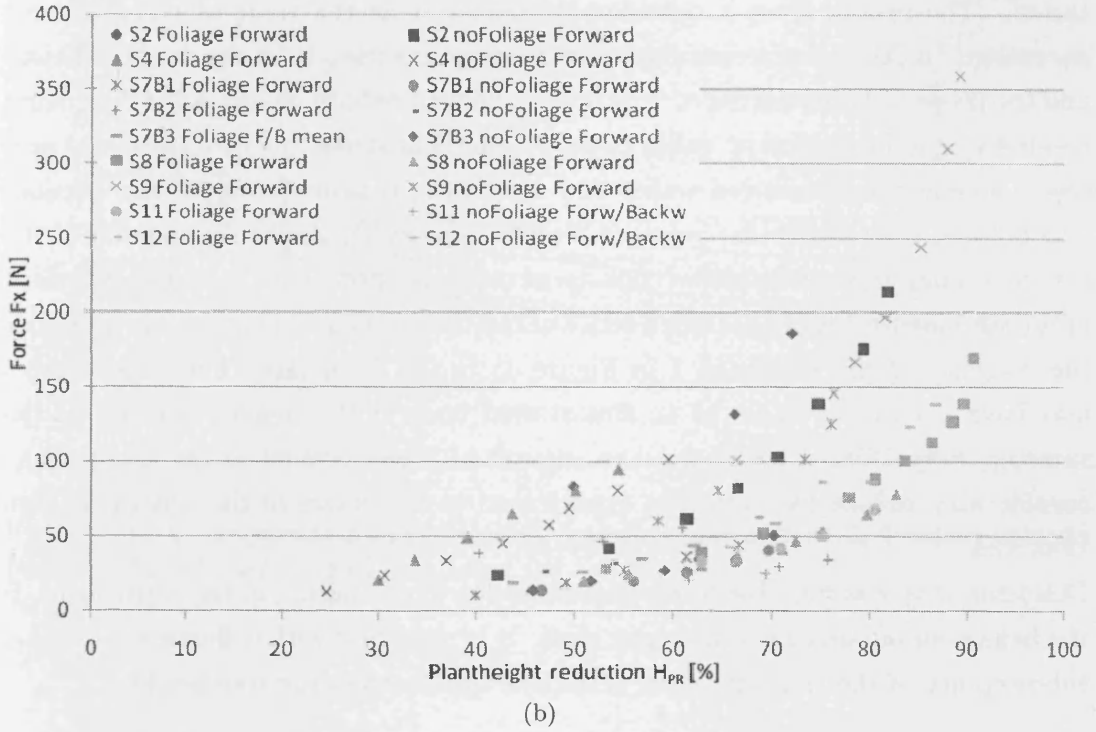

(b)

Figure 5.33: *Salix* plant height reduction versus (a) velocity (m/s) and (b) force (N). Figures from Weissteiner (2009)

5.5.2 Variation of compound drag area (C_dA)

The two undetermined variables in the drag force equation are the projected area (A_p) and the drag coefficient (C_d), which may be combined into the compound drag area parameter (C_dA) determined in the studies of Oplatka (1998*a*). Direct determination of these terms individually is difficult once the tree has begun to bend, as at greater inclinations the relevant area becomes the surface area skin friction as opposed to the projected area drag induced by the wake behind the branches. Using the compound drag area term gives an idea of the variation in tree canopy compaction while the trees deform. The drag area parameter is calculated from:

$$C_dA = \frac{2F}{\rho U^(2)_0} \tag{5.25}$$

Figure 5.34 presents the variation in the drag area parameter for nine of the tested *Salix* trees. It can be seen that the value of the compound drag area parameter reduces in a similar asymptotic manner to the plant height reduction seen in Figure 5.33. At the highest velocities tested, the drag area parameter has reduced to a value several magnitudes smaller than the original value obtained at the lowest velocities tested. The results show a considerable reduction in the value of the drag area parameter. As the trees streamline at increasing velocities, both the drag coefficient and the projected area decrease. The drag coefficient reduces as instead of drag being created by the formation of wakes behind cylindrical stems, the inclined stems may create smaller, form-induced wakes and more drag is instead due to skin friction, which has a drag coefficient value of a much smaller value. As compaction of the canopy occurs, the tree could be considered more as a porous body that is elongated in the streamwise direction, than a series of individual cylinders and leaves. Consider the images of *Salix* 6 Branch 1 in Figure 45 in the Appendix. The foliated trees may have a tendency to act as an almost bluff body at the higher velocities. In the summer, fully foliated condition, the amount of leaves present in the canopy may considerably reduce the velocities experienced in the centre of the canopy at high velocities.

One issue that was not able to be addressed due to the nature of the experiment, is the behaviour of partially submerged trees. It is clear that with deflection occurring, submergence of the tree will occur at depths smaller than the tree height.

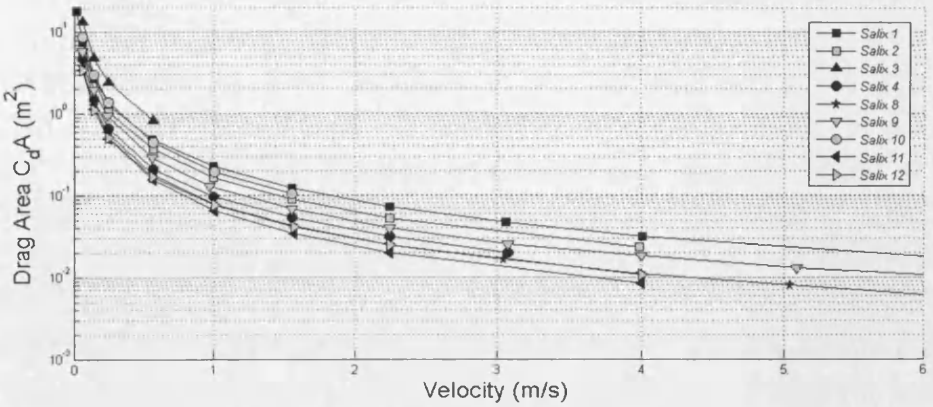

(a)

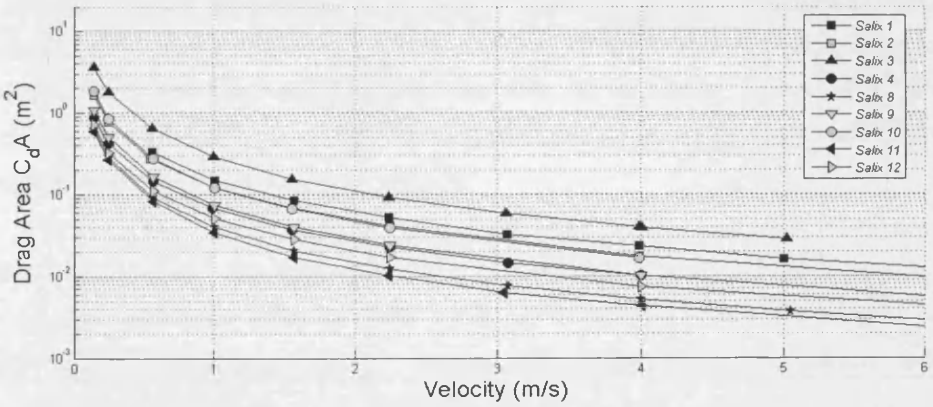

(b)

Figure 5.34: *Salix* variation in compound drag area parameter C_dA versus velocity (m/s) in the foliated (a) and defoliated (b) conditions

5.6 Functional Relationships between Tree Physical Characteristics and Force Exerted

5.6.1 Zones of Hydraulic Influence

The trees were subjected to uniform velocities up to 6 m/s. The high resolution of recorded force and velocity data, in addition to the underwater images taken from the sideview central submerged camera, provide a clear picture of the nature of the deformation of the tree from low to high velocities. With the present data set, two clear zones of deformation can be defined in the trees tested. The data from tree *Salix* 4 in Figure 5.35 has been selected to illustrate this zonal division. The first zone, Zone A, is the initial deformative zone. Here, there is a non-linear relationship between velocity and streamwise drag force. It is proposed that the deflection in this zone is minimal, with the streamwise force from the water transmitted principally through a shearing action within the main stem. This can be confirmed through inspection of Figure 5.32, showing the deformation of $S4$ at velocities between 0.125 m/s and 1.0 m/s in the foliated and defoliated conditions.

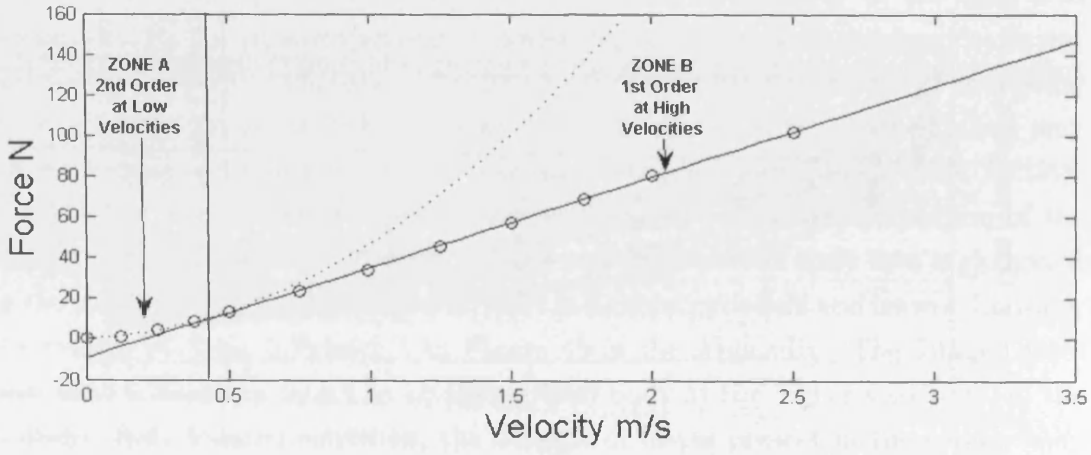

Figure 5.35: Salix 4. Variation of drag force (N) with velocity (m/s) Data points are represented by circles. A proposed trend line representing the relationship of Zone A is shown by the dotted line. A proposed trend line representing the relationship of Zone B is shown by a continuous line. Zone A and B are separated by U_{AB} at approximately U = 0.470 m/s. The Zone B trend line meets the y-axis at a force value of F_I

As the velocity increases, the tree makes the transition into Zone B, where most trees exhibit an apparent linear relationship between velocity and force. This is due to the tree experiencing both bending and shearing action in response to the increased force. The exception is tree *Salix* 9, which displays a second order relationship characteristic of Zone A for the majority of velocities tested. The reason for *Salix* 9 to display such different behaviour is yet to be ascertained, *Salix* 9 is a tree of average main stem size, stiffness, mass and volume.

The linear trend in Zone B continues until the tree experiences a point of maximum bend and enters a third Zone, named Zone C. At this point, the rate of increase of force with velocity decreases, and for most trees tested, the relationship is no longer linear. Many of the trees tested did not enter Zone C, with the linear relationship continuing to the highest velocity tested, however, it is hypothesised that all trees, if tested to high enough velocities, will reach Zone C. Inspection of the image of $S1$ at a velocity of 2.5 m/s in Figure 39 shows that the tree is almost fully streamlined.

Consider a defoliated tree. At low velocities with negligible deformation, the tree can be likened to a series of cylinders perpendicular to the streamwise flow direction. The drag coefficient (C_d) is related principally to the shape of the projected area (A_p). At the highest velocities, the tree may be considerably streamlined and likened to a series of parallel cylinders. In this case, the drag coefficient is a function both of the projected area (A_p) and also the skin friction from the surface area(A_s). Thus is it extremely difficult to separate the individual terms with C_dA, as all are as yet unknown functions of streamwise velocity.

It is proposed that the observed threshold velocity (U_{AB}) is a function of the threshold stiffness of the tree, perhaps related to the wood fibre elasticity. This value of elasticity may have evolved as a result of the mean inundation velocity or highest windspeed experienced. Thus in Zone A, there is a gradual transition from rigid body behaviour to a flexing body behaviour. Above a certain velocity (proposed as the zonal transition velocity), the tree is deforming at a rate which maintains a constant force variation with velocity. The location of the threshold velocity was determined by applying linear regression initially to the full dataset, then progressively removing the lowest velocity points until the coefficient of multiple determination (R^2) attained a value of greater than 0.99. A power relationship was then fitted to the low velocity data previously removed and the lowest two or three velocity data points of the linear regression. The threshold was determined at the intersection point of the fitted curve and line. The mean threshold velocity values for the foliated and defoliated *Salix*, *Alnus* and *Populus* trees are given in Table 5.8.

Tree	Foliated U_{AB}	Defoliated U_{AB}
Test	m/s	m/s
Salix	0.353	0.331
Alnus	0.648	0.648
Alnus	0.472	0.534

Table 5.8: Whole and sub-branches of *Populus* trees $P2$ and $P4$, force (N) measured at a streamwise velocity of 1 m/s

The mean value of al six results given in 0.498 m/s. The value of the threshold for the individual foliated and defoliated trees are given in Table 46 in the Appendix. It can be seen from the spread of values in the tables in the Appendix that there is poor consistency. IT was expected to see a difference in the threshold velocity for the defoliated and foliated trees. A higher resolution of data or an improved method of data fitting may provide more meaningful values.

As mentioned previously in Chapter 2 and in Section 5.1, the hydrodynamic drag force behaviour of flexible trees has been observed as a linear relationship (Fathi-Maghadam & Kouwen (1997), Oplatka (1998*a*), Freeman et al. (2000)). The drag force data collected in the present study is of a higher resolution than previous studies and perhaps due to this, the second order relationship at low velocities has only seldomly been commented on, although it has been seen in the studies into small trees of Armanini et al. (2005). From Figure 5.35, it is clear that assuming a linear relationship through the origin over the entire range of velocities will inevitably lead to an overprediction in the drag force at lower velocities. The different behaviour in each Zone leads to the requirement to define the drag force - velocity relationship within each zone separately and to define the point of transition between Zones A and B, U_{AB}. The linear relationship in Zone B is also defined by the y-intercept 'stiffness force', denoted F_I. It is proposed that the stiffness force (F_I) is a term related to the rigidity of the tree.

5.6.2 Functional Relationships in Zone B ($U > U_{AB}$)

Trees have a complex and random growth pattern. This growth pattern is however, governed by auxins in the tree and influenced by autogenic factors such as stresses imposed on the tree during growth, and affected by allogenic environmental factors such as climate and planting density. Studies have shown that branches of a tree display similar branching patterns and branch order diameter ratios to the whole tree (McMahon 1975, Kane & Smiley 2006). This implies that a single measurement

of a particular characteristic of the tree may lead to drag characteristics, including force exerted, for the tree in the unleaved condition.
As the R^2 value of the regression line is maintained above $R^2 > 0.99$ in Zone B for all datasets, the linear relationship can be assumed to be valid, and thus there are two relevant coefficients to consider, the linear coefficient and the y-intercept. For velocities greater than U_{AB} (Zone B), and to make use of the observed linear relationship, in the interests of inter- and intra-species comparison, the linear coefficient may be extracted as the compound drag area parameter ($C_dA.U_0$) can be reduced to Equation 5.34:

$$F_x = (C_dA.U_0)\frac{1}{2}\rho U_0 + F_I \tag{5.26}$$

Where F_x is the streamwise force, ρ is the fluid density, $C_dA.U_0$ is the drag area parameter with units m^3/s, U_0 is the streamwise velocity and F_I is the stiffness force, equivalent to the y-intercept of the the Zone B linear relationship.
In the following section, the functional relationships between the drag area parameter ($C_dA.U_0$) and physical characteristics of the trees within Zone B are explored. Within Zone B, the aim is to obtain the drag area parameter ($C_dA.U_0$) and the intercept force (F_I) correlation with parameters that are easily measurable in the field.
The value of F_I, may relate to the resistance to deformation, or stiffness, of the plant. The stiffer the main stem of the tree, the higher the transition point U_{AB} i.e. the velocity at which the tree begins to absorb the oncoming hydraulic force by bending rather than shearing.

5.6.2.1 Drag area parameter $C_dA.U_0$ for Defoliated Trees within Zone B

Since it is the linear coefficient, the drag area parameter ($C_dA.U_0$) is a measure of the physical form and flexibility of the defoliated tree and can be computed from the gradient of the force - velocity relationship for each tree. The drag area parameter remains a constant value at all velocities within Zone B, therefore each tree will have a single value of $C_dA.U_0$ within Zone B. Through comparison with the various physical characteristics obtained from the woody parts of the trees, the characteristics that are best correlated with $C_dA.U_0$ can be identified. $C_dA.U_0$ has been obtained for each tree from Equation 5.28.

$$C_dA.U_0 = \frac{2\Delta F_x}{\rho \Delta U_0} \tag{5.27}$$

Where $C_dA.U_0$ is the defoliated drag area parameter with units m^2, ΔF_x is the change in streamwise force F_x over Zone B for the defoliated specimen, ρ is the fluid density and ΔU_0 is the change in streamwise velocity over Zone B for the defoliated specimen.

Figure 5.36 presents the calculated drag area parameter $C_dA.U_0$ values for the defoliated condition within Zone B. The data presented in Figure 5.37 correlate the dimensional parameters of the woody parts of the tree against the computed drag area parameter $C_dA.U_0$. The dimensional parameters are the Height h, and the diameter at the base d_{Q0}, 1st quartile height d_{Q1}, mid-height d_{Q2} and the 3rd quartile d_{Q3} height. The plots include only the data from trees in the unleaved condition, to avoid bias introduced by the drag contribution of the leaves. Since $C_dA.U_0$ is a term containing the projected area A_p, it is assumed that there will be a positive correlation between parameters that increase with the size of the tree and the value of $C_dA.U_0$. The sample size is too limited to form a definitive conclusion, however, it is clear that overall, correlation with height is poorer that that for any of the diameter measurements (see Figure 5.37). It should be noted that for *Populus*, the correlation with height is positive and linear, whereas for the *Salix* and *Alnus* trees, there is no obvious positive correlation. Regarding correlation with the four diameter measurements, the *Populus* data has the strongest linear correlation at the first quartile diameter d_{Q1} and the mid-height diameter d_{Q2}.

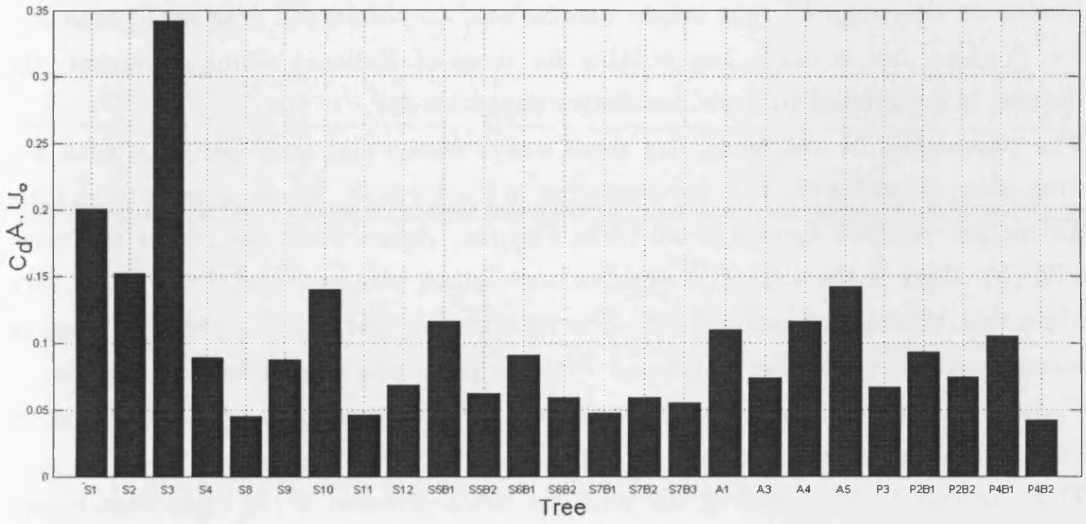

Figure 5.36: drag area parameter $C_dA.U_0$ for trees tested in defoliated condition within Zone B ($U \geq U_{AB}$)

In the field, the characteristic diameter to be taken is usually defined as the diameter of the largest stem at 'chest-height'. For these, smaller and multi-stemmed trees, the equivalent location of chest-height will lie between d_{Q1} and d_{Q2}. Inter-species differences can be determined between *Salix*, *Alnus* and *Populus* specimen. For example, consider the data within Figure 5.37 (b) presenting $C_dA.U_0$ against the first quartile diameter d_{Q1}. Considering the spread of available data, for trees of diameter $d = 20$ mm, *Populus* has the lowest associated drag area parameter $C_dA.U_0$, with *Alnus* the next highest, and the average from the *Salix* trees giving the highest drag area parameter $C_dA.U_0$ for the diameter. This order is also reflected in Figures 5.37 (c) and (d). This suggests that between three species of tree with similar diameters, *Salix* provides the highest resistance, *Alnus*, the next highest, and *Populus* the lowest. It also suggests that height can be used to obtain the drag area parameter for *Populus*, but is much less reliable for trees of *Salix* or *Alnus*. However, the dataset is too limited to draw conclusive dependencies.

The parameters of wet mass, dry mass and volume, and their variation with the drag area parameter $C_dA.U_0$ are presented in Figure 5.38. There appears to be little distinction between species in all three Figures. Apart from one outlier in Figure 5.38 (b), there is the expected positive correlation with recorded Fresh Mass, Dry Mass and Volume. *Alnus* appears provides the highest $C_dA.U_0$ per unit mass or volume, with the data for *Salix* and *Populus* providing similar rates of increase in $C_dA.U_0$ with increasing unit mass or volume. For reference, the average fresh wood density was calculated as shown in Figure 5.39.

This suggests that measuring the physical characteristics of the main stem is less reliable than determining the mass or volume of the trees. Since many floodplain woodland species display multi-stem growth patterns, the dominant trunk diameter will not provide enough information about the resistive characteristics of the tree as a whole. In the field, a non destructive method that could be undertaken to determine the mass or volume, is to use photographic methods, or measure the diameters of all stems that intersect the levels at the base, 1st quartile, mid-height and 3rd quartile, in a similar method undertaken in Chapter 3.

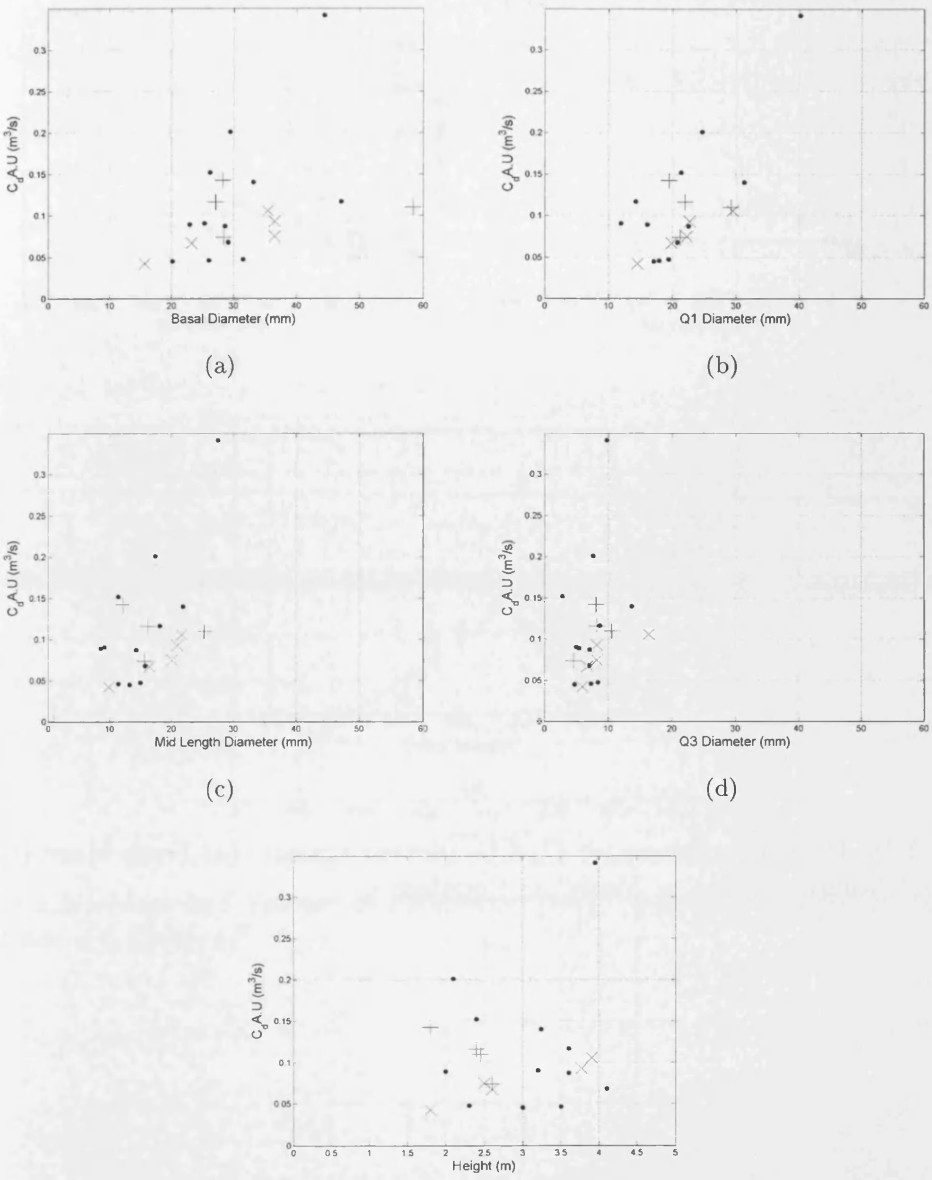

Figure 5.37: Drag area parameter $C_dA.U_0$ plotted against: (a) Basal diameter (d_{Q0}); (b) 1st quartile diameter (d_{Q1}); (c) mid-height diameter (d_{Q2}); (d) 3rd quartile diameter (d_{Q3}); (e) Height (h). Salix: •; Alnus: +; Populus: x

5.6.2.2 Drag area parameter $C_dA.U_0$: variation with wood mass and volume

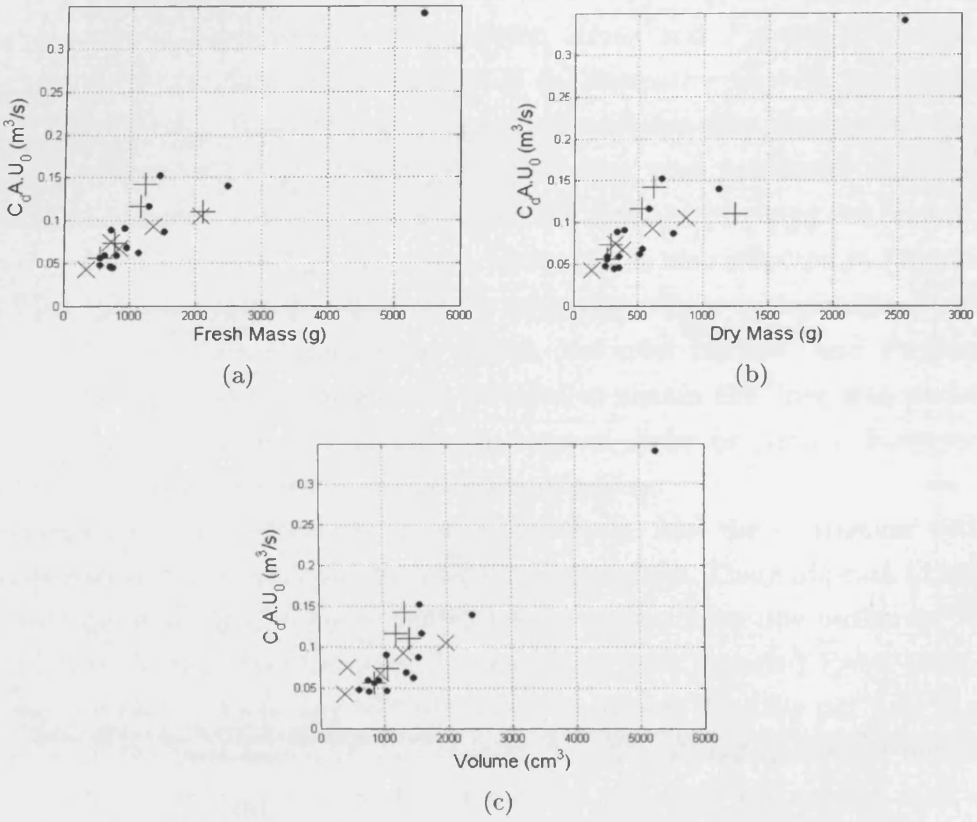

Figure 5.38: Drag area parameter $C_dA.U_0$ plotted against: (a) Fresh Mass; (b) Dry Mass, (c) Volume. Salix: •; Alnus: +; Populus: x

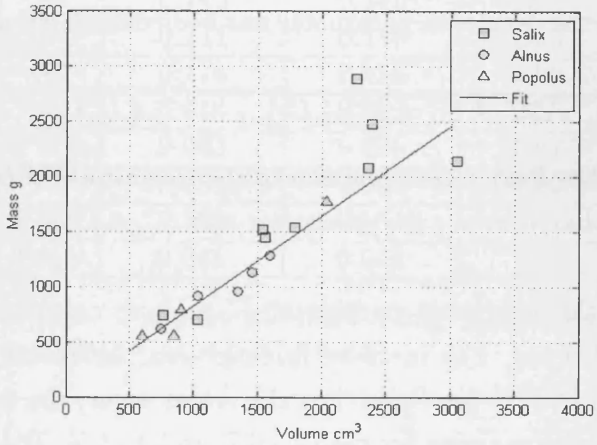

Figure 5.39: Mass and Volume of Prototype Trees. Density evaluated from linear regression is 0.82 kg/m^3

5.6.2.3 *Leaf Contribution to $C_dA.U_0$ within Zone B*

One of the contributions to the uncertainty of determining the hydraulic roughness of vegetation is the contribution of leaves. The foliage of a tree or shrub will vary with tree age, spacing, season, soil nutrient level, altitude and latitude. The drag contribution of leaves has been recorded as 3 to 4 times that of the unleaved condition (Freeman et al. 2000, Wilson et al. 2003). As mentioned previously, the study was carried out in March and April 2008. The trees tested therefore have leaves in the spring stage of growth. The drag area coefficient for the foliated trees is computed using the following:

$$C_dA.U_0 = \frac{2\Delta F_x}{\rho \Delta U_0} \tag{5.28}$$

The contribution to the drag area parameter has been calculated using the following.

$$\Delta C_dA.U_0 = (C_dA.U_0)_{wf} - (C_dA.U_0)_{df} \tag{5.29}$$

Where $\Delta C_dA.U_0$ is the foliage contribution to the magnitude of the drag coefficient, $(C_dA.U_0)_{wf}$ is the foliated drag area parameter and $(C_dA.U_0)_{df}$ is the defoliated drag area parameter.

Table 5.9 presents the drag area parameter $C_dA.U_0$ as calculated for the foliated and defoliated conditions. The increase in drag area parameter ($\Delta C_dA.U_0$) varies between 15.6 % and 56.6 % for *Salix*. For the *Alnus* trees, the increase ($\Delta C_dA.U_0$) due to foliage contribution varies between 13.6 % and 24.4 %. For the *Populus* trees, the increase ($\Delta C_dA.U_0$) due to foliage contribution varies between 9 % and 21.5 %. Bearing in mind the Spring conditions and the leaves are new growth, allowing for the uncertainty due to the small sample, it appears that the leaf contribution from *Salix* and *Alnus* at this time of year is greater than that of *Populus*.

Figure 5.46 presents the actual leaf contribution to $C_dA.U_0$, measured against the recorded physical properties of the foliage including fresh mass, dry mass and volume. The mass/ volume fractions of the foliage, with respect to the whole tree, are also compared with the previously computed percentage foliage contribution to the drag area parameter $\Delta C_dA.U_0$. The fresh mass fraction of the leaves is computed according to the following form:

$$m_{foliage,f} = \frac{M_{foliage,f}}{M_{wood,f} + M_{foliage,f}} \tag{5.30}$$

Where $m_{foliage,f}$ is the fresh mass fraction of the leaves, $M_{foliage,f}$ is the fresh mass

Test	$(C_dA.U_0)_{wf}$	$(C_dA.U_0)_{df}$	$\Delta C_dA.U_0$
S1	0.282	0.2011	28.8
S2	0.202	0.152	24.7
S4	0.118	0.089	24.4
S6B1	0.118	0.091	23.0
S6B2	0.070	0.059	15.8
S7B1	0.065	0.048	26.4
S7B2	0.080	0.059	26.1
S7B3	0.066	0.056	15.6
S8	0.100	0.045	54.8
S9	0.201	0.087	56.6
S10	0.225	0.140	37.8
S11	0.070	0.046	33.7
S12	0.094	0.068	27.3
A1	0.145	0.110	24.4
A4	0.144	0.116	18.5
A5	0.174	0.150	13.6
P2B1	0.118	0.093	21.5
P2B2	0.083	0.075	10.4
P3	0.084	0.067	19.9
P4B1	0.133	0.106	20.9
P4B2	0.045	0.042	9.0

Table 5.9: *Salix, Alnus, Populus* Modified Drag Area Coefficient for foliated ($(C_dA.U_0)_{wf}$) and defoliated ($(C_dA.U_0)_{df}$) trees

of the foliage in kg and $M_{wood,f}$ is the fresh mass of the wood in kg. Equation 5.30 is also applied to the dry foliage mass ($M_{foliage,d}$) and the fresh foliage volume ($V_{foliage,d}$) to obtain the foliage dry mass fraction ($m_{foliage,d}$) and the foliage fresh volume fraction ($v_{foliage,f}$).

Overall, there is less correlation linking the leaf mass or volume to percentage drag contribution. Figures 5.40 (a) and (b) present the fresh mass data against the drag area parameter ($C_dA.U_0$) and the foliage drag area parameter fraction ($\Delta C_dA.U_0$) respectively. Both figures show a slight linear trend, as the fresh mass increases, so too does the actual and fractional contribution to the drag area parameter. There appears to be a stronger relationship for the lower masses in Figure 5.40 (a).

Figures 5.40 (c) and (d) present the dry mass data against the drag area parameter ($C_dA.U_0$) and the foliage drag area parameter fraction ($\Delta C_dA.U_0$) respectively. The results are highly scattered, although Figure 5.40 (c) again shows a stronger correlation at low masses.

Figures 5.40 (e) and (f) present the fresh volume data against the drag area parameter ($C_d A.U_0$) and the foliage drag area parameter fraction ($\Delta C_d A.U_0$) respectively. There appears to be better correlation and fewer outliers with the foliage volume in Figure 5.40 (e) than foliage volume fraction in Figure 5.40 (f). Although there are indications of a correlation between foliage mass/ volume (and the mass/ fraction) and the contribution to the drag area parameter from the foliage, the sample number is too small and the trees too diverse in structure to provide definitive evidence of a physical link.

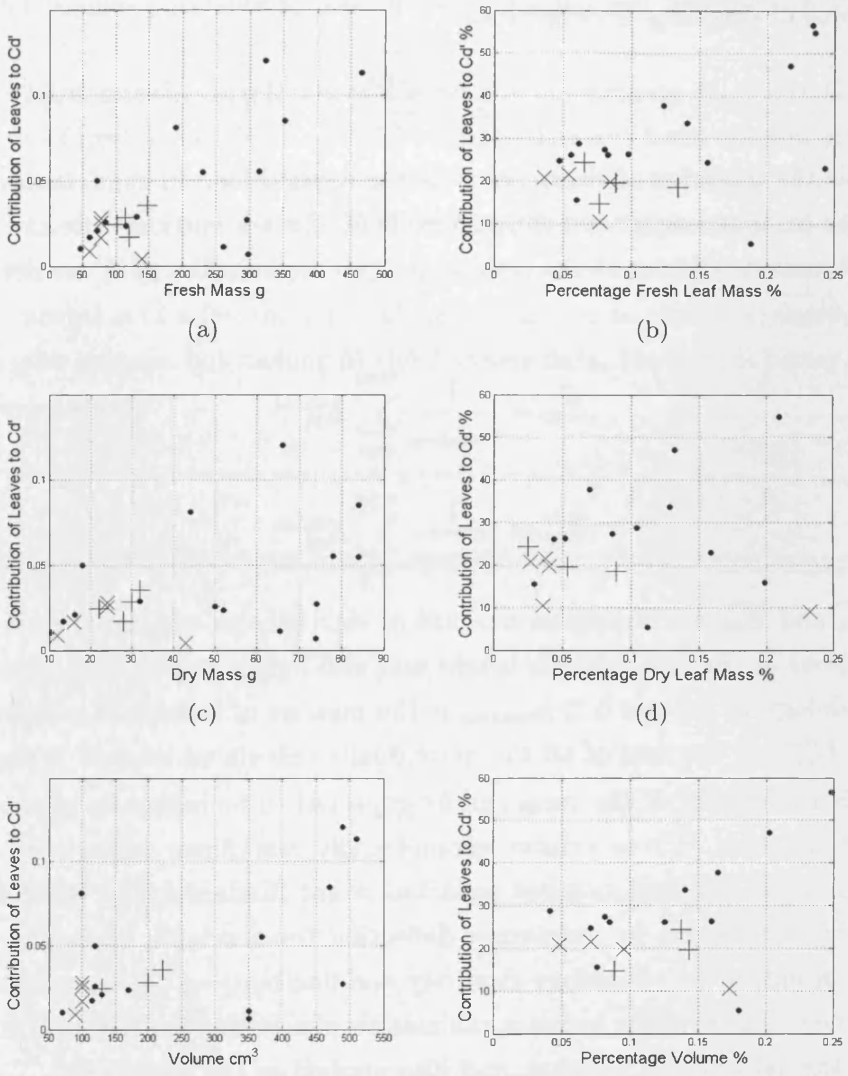

Figure 5.40: Drag area parameter $C_d A.U_0$ against: (a) fresh foliage mass; (c) dry foliage mass; and (e) fresh foliage volume. Foliage drag area parameter fraction $\Delta C_d A$ against: (b) fresh foliage mass fraction $m_{foliage,f}$; (d) dry foliage mass fraction $m_{foliage,d}$; (f) fresh foliage volume fraction ($v_{foliage,f}$). Salix: •; Alnus: +; Populus: x

5.6.2.4 *Functional Relationships with Stiffness*

Modulii of Elasticity $E_{25\%}$ and $E_{50\%}$

The modulus of elasticity is defined as:

$$E = \frac{PL^3}{3\delta I} \tag{5.31}$$

Where E is the modulus of elasticity, P is the applied load in N, L is the distance between the anchored point and the applied load, δ is the vertical deflection and I is the second moment of area of the tree stem. Two mean values of E are determined, $\overline{E_{25\%}}$ and $\overline{E_{50\%}}$:

$$\overline{E_{25}} = \frac{1}{n_{masses}} \sum_{min}^{max} E_{25}^{mass} \tag{5.32}$$

$$\overline{E_{50}} = \frac{1}{n_{masses}} \sum_{min}^{max} E_{50}^{mass} \tag{5.33}$$

Where $\overline{E_{25}}$ and $\overline{E_{50}}$ are the mean modulii of elasticity as calculated from weights and deflections at the first quartile height and mid-height respectively, according to the methodology in Section 5.2, n_{masses} is the number of individual masses applied and $\sum_{min}^{max} E_{50}^{mass}$ is the sum of all the individually calculated modulii of elasticity.

Physical characteristics of the trees can be expected to be indicative of the relative stiffness of the tree. Trees exhibit geometrically non linear behaviour, and the application of the bending moment equation is not fundamentally valid, however, it is a useful model and by measuring deflection from weights applied at specific distances, an indication of relative elasticity and flexibility of the trees tested could be determined. The bending moment calculation was carried out twice, with weights applied at the 1st quartile location, and also applied at the mid-point.

Figure 5.41 presents the correlation of the modulii of elasticity E, $E_{25\%}$ and $E_{50\%}$, as determined from Equation 5.31, against dimensional parameters of height and the diameters at base, 1st quartile, mid-height and 3rd quartile. The left hand column presents the average E determined from weights applied at the 1st Quartile $E_{25\%}$. The right hand column data presents the average E determined from weights applied at the mid-height location $E_{50\%}$. It can be seen that in comparing $E_{25\%}$ and $E_{50\%}$, the stiffness determined for the trees is consistantly higher when measured at the mid-height location, when compared to the 1st quartile location. This may

be due to an insufficiently fixed base, as any rotation at the base of the tree would disproportionatly affect E_{25} determined at the 1st quartile.

There does not appear to be much correlation between either $E_{25\%}$ or $E_{50\%}$, and most of the dimensional parameters. Correlation appears best against the 1st quartile diameter.

Figure 5.42 presents the correlation of the modulii of elasticity $E_{25\%}$ and $E_{50\%}$ against parameters of fresh mass, dry mass and volume. The left hand column presents the average E determined from weights applied at the 1st quartile $E_{25\%}$. The right hand column data presents the average E determined from weights applied at the mid-height location $E_{50\%}$. Both fresh mass and dry mass correlate positively with E, with the exception of a few outliers. There appears to be little correlation for *Salix* or *Alnus* with volume, but looking at the *Populus* data, the data is better correlated in the $E_{50\%}$ dataset.

5.6.2.5 $E_{25\%}$ (left) and $E_{50\%}$ (right) against dimensional parameters

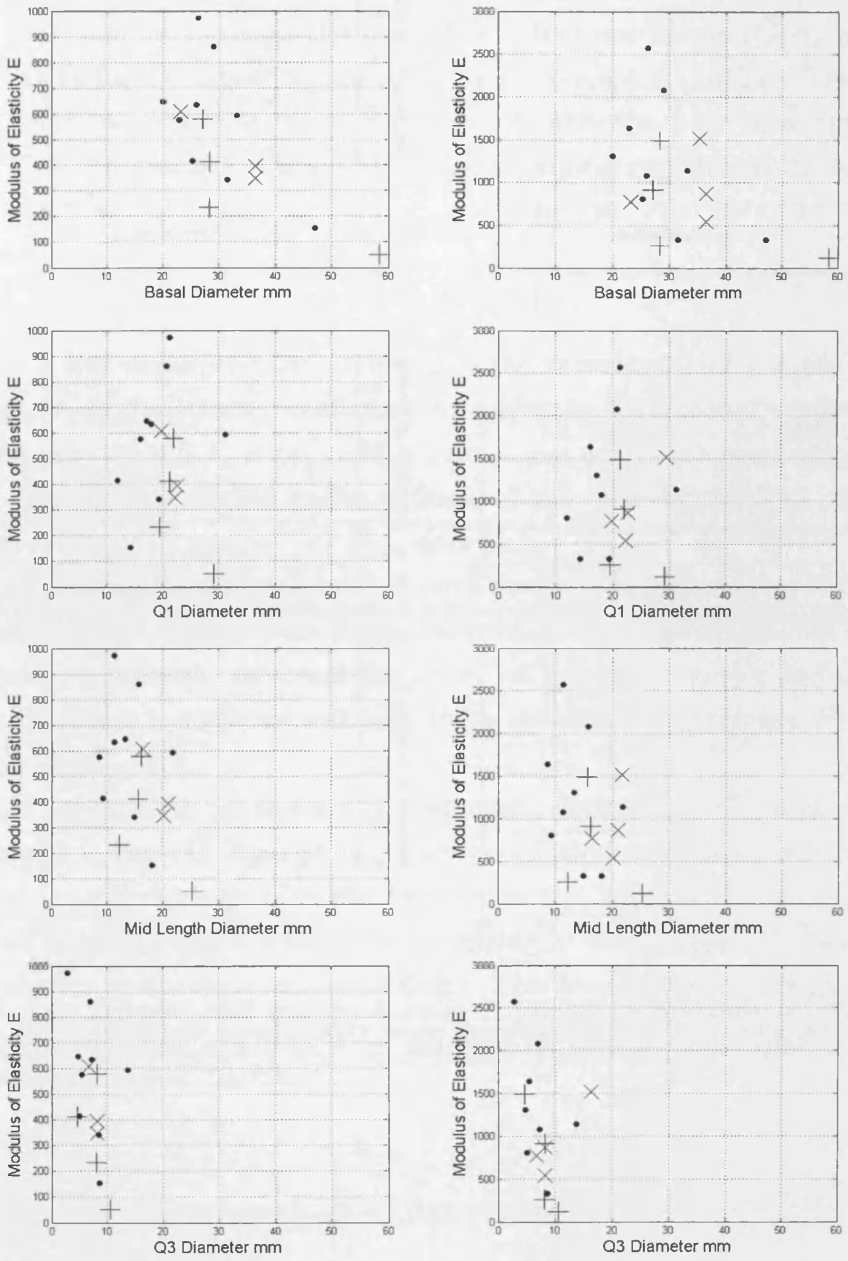

Figure 5.41: Modulus of Elasticity E plotted against Height, Basal Diameter d_{basal}, First Quartile d_{Q1}, Mid-height d_{mid} and Third Quartile d_{Q1}. Salix: •; Alnus: +; Populus: x. Note y-axis scales are different.

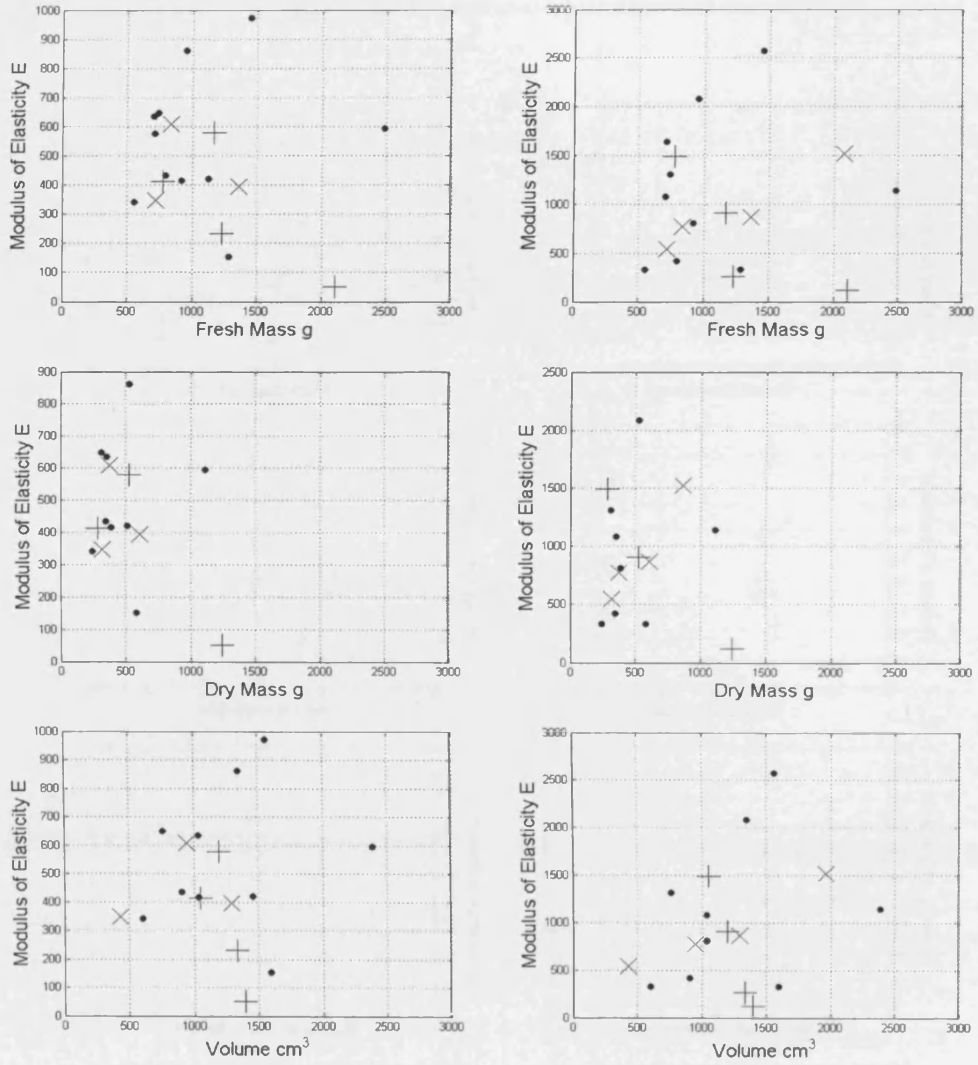

Figure 5.42: Modulus of Elasticity E plotted against Wet Mass(a), Dry Mass(b), Volume (c). Salix: dots; Alnus: +; Populus: x. Note y-axis scales are different.

Zone B Stiffness Intercept F_I

The linear relationship that the trees experience in Zone B in Equation 5.34 requires a linear coefficient (a function of the modified drag coefficient ($C_dA.U_0$), already explored) and a force constant representing the y-intercept of the Zone B relationship regression line (see Figure 5.35). This constant takes the form of a rigidity force constant F_I. The aim is to obtain measurable parameters with which to estimate F_I.

$$F_x = \frac{1}{2}\rho C_d A U_1 U_x + F_I \tag{5.34}$$

Where F_x is the streamwise drag force, ρ is the density, $C_dA.U_0$ is the drag area parameter, U_1 is the velocity coefficient to maintain dimensional similarity, U_x is the stream velocity and F_I is the rigidity force constant. It is hypothesised that the value of F_I is directly related to the stiffness of the tree. Figure 5.43 presents the computed values of F_I against (a) $E_{25\%}$ and $E_{50\%}$

Figure 5.44 presents the correlation of F_I with dimensional parameters of the trees of height and diameter. There is not a good correlation with tree height, but looking at the diameter parameters, the basal diameter, 1st quartile diameter and mid-height diameter all appear to correlate well with F_I, as the diameters increase, F_I decreases, indicting a stiffer plant.

Figure 5.45 presents the parameters of fresh mass, dry mass and volume against F_I, as determined in Zone B. Against, dry mass correlation is minimal, however, better correlation is achieved with both the fresh mass and volume. There is a repeated trend in all three subfigures, with *Salix* appearing to have a lower F_I value to *Alnus* and *Populus* for equivalent mass and volume. This is validated by the photographic evidence, Salix deformed significantly more than the other two species, and therefore possesses a more elastic nature.

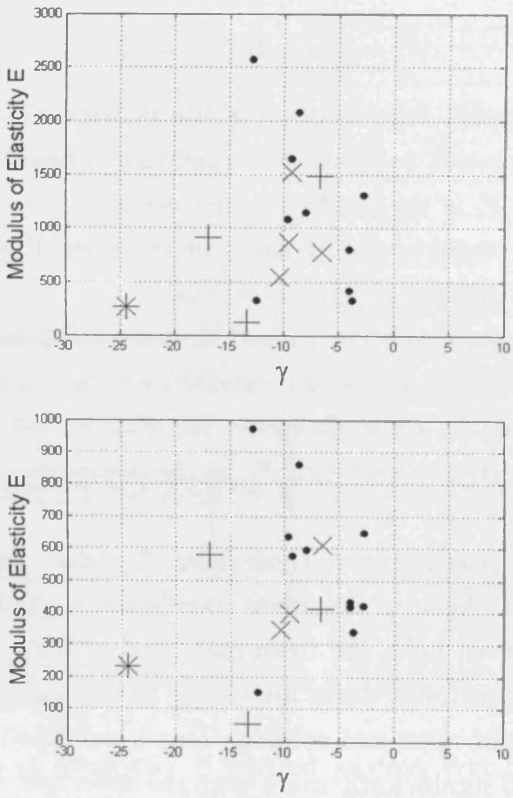

Figure 5.43: F_I variation with modulii of elasticity (a) $E_{25\%}$ and (b) $E_{50\%}$. Salix: dots; Alnus: +; Populus: x

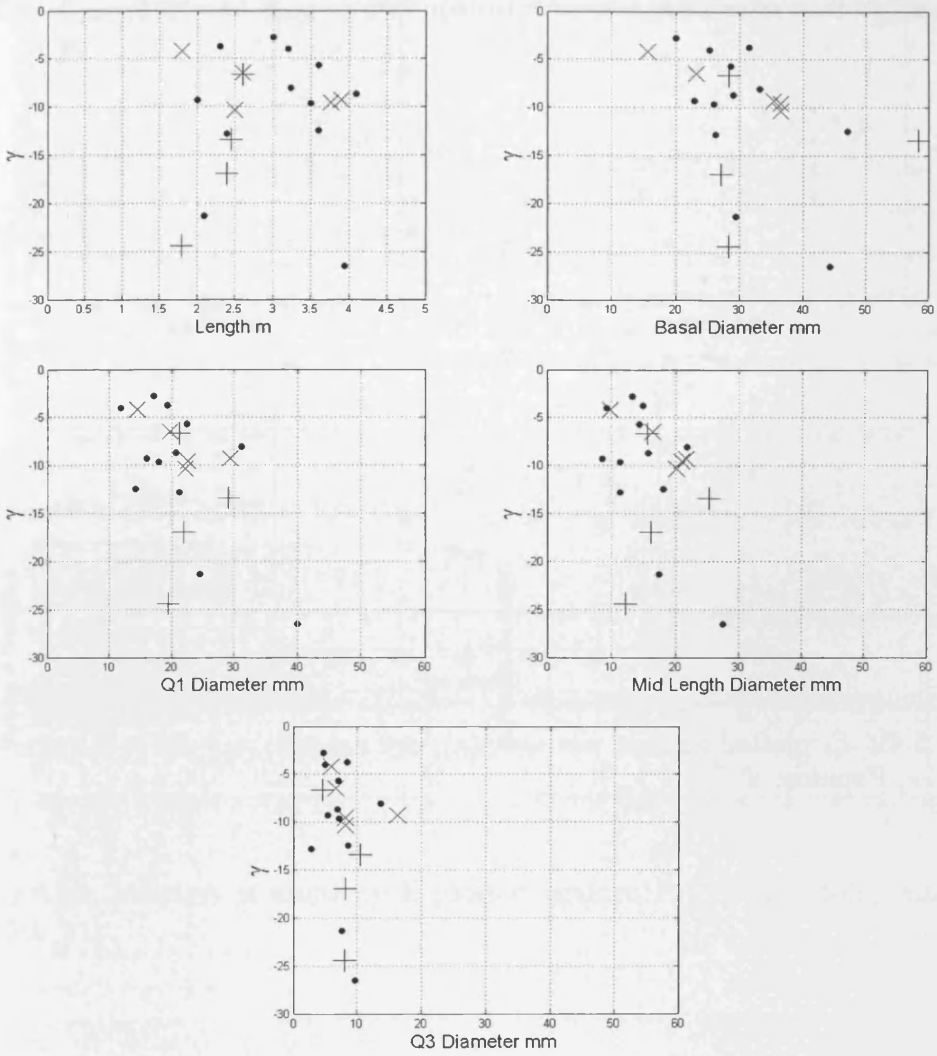

Figure 5.44: F_I plotted against height, basal diameter d_{basal}, first quartile d_{Q1}, mid-height d_{mid} and third quartile d_{Q1}. Salix: dots; Alnus: +; Populus: x

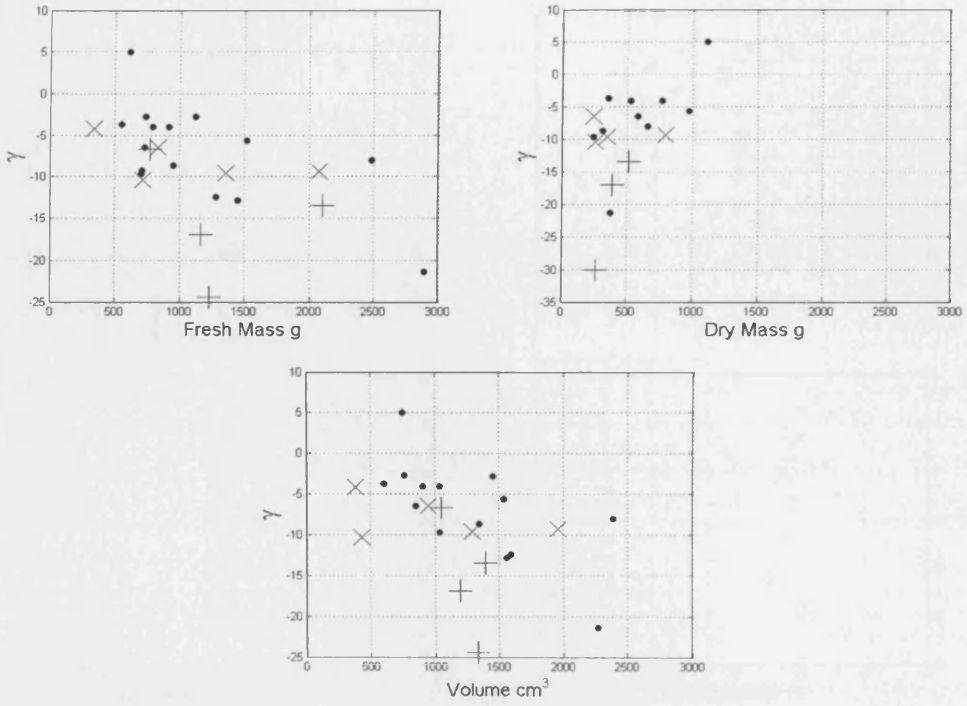

Figure 5.45: F_I plotted against wet mass(a), dry mass(b), volume (c). Salix: dots; Alnus: +; Populus: x

5.6.2.6 $E_{25\%}$ (left) and $E_{50\%}$ (right) against drag area parameter and stiffness force F_I

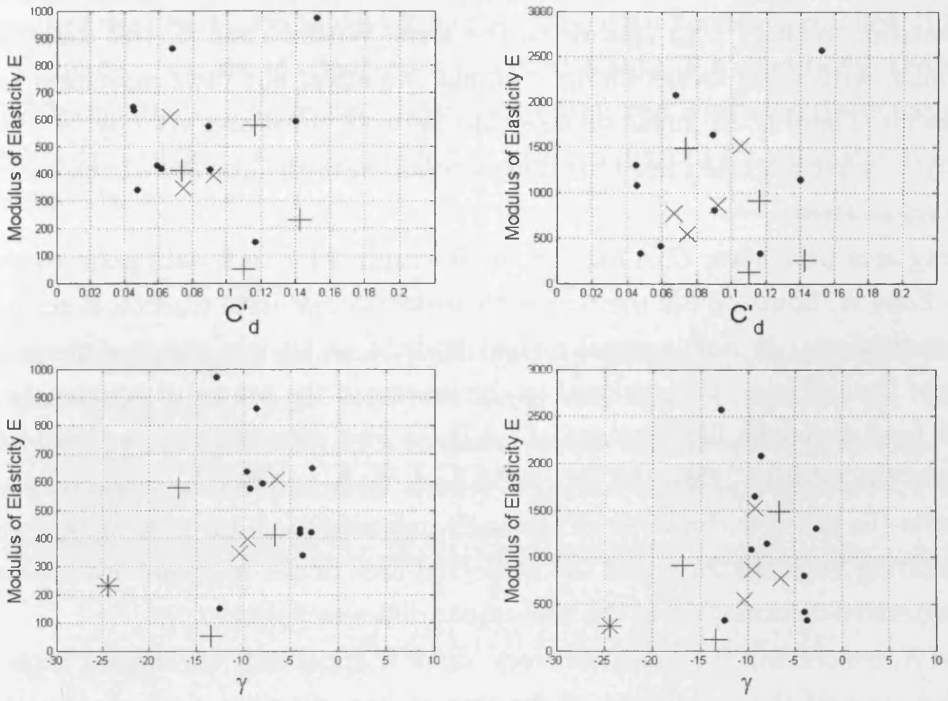

Figure 5.46: Modulus of elasticity E plotted against F_I). Salix: dots; Alnus: +; Populus: x

5.6.3 Functional Relationships in Zone A ($U < U_{AB}$)

5.6.3.1 Variation of drag area parameter $C_dA.U_0$ in Zone A

Zone A covers a range of low velocities from a minimum of U = 0.125 m/s up to the transition velocity U_{AB} specific to the tree. Within Zone A, tree deformation is minimal, with some streamlining of minor branches, but little movement in the main stem. There is no linear relationship between force and velocity in Zone A, contrary to what has often been previously reported in the literature concerning the drag force of trees.

The drag area parameter $C_dA.U_0$, can be determined for each data point measured within Zone A, however the method with which to calculate $C_dA.U_0$ is subject to some uncertainty. In flow around a rigid body, $C_dA.U_0$ is a constant property in turbulent flow regimes, proportional to the inverse of the square of velocity. In flow around (and through) flexing trees, $C_dA.U_0$ is also constant, proportional to the inverse of the velocity. Thus, in both rigid body flow, and flexing tree flow, $C_dA.U_0$ represents the resistive character of the body, relevant to all turbulent flow regimes, incorporating both the form and the projected area of the tree, and accounting for the progressive deformation of the tree under different flows.

In Zone A, concerning the unleaved trees, there is apparently an ongoing transition from flow around the rigid body of the tree at low velocities, to flow through the streamlining tree, for which $C_dA.U_0$ has been previously determined in Zone B. The existence of laminar flow around the smaller branches at the lower velocities is an additional complicating factor. In the force - velocity relationships in Zone A, there is apparently a second order relationship. Therefore, three different derivations of $C_dA.U_0$ for flows within Zone A are explored. The aim is to obtain a value for $C_dA.U_0$ for each tree that is consistent throughout in both Zone A and Zone B flows. The three regimes to be investigated are:

1. $(C_dA)_{ZA1}$: drag area parameter for a rigid body
2. $(C_dA.U_0)_{ZA2}$: transitional drag area parameter for a rigid/ Zone B flexing body
3. $(C_dA.U_0)_{ZA3}$: transitional drag area parameter for a rigid/ flexing body

The first relationship tested is the standard approach for drag force of a rigid body, Equation 5.35, producing a drag area parameter termed $(C_dA)_{A1}$.

$$(C_dA)_{A1} = \frac{2F}{\rho U_0^2} \Longrightarrow U_0 \leq U_{AB} \tag{5.35}$$

As the tree does not significantly deform under the lowest velocities, but with increasing velocities begins to deflect increasingly, until Zone B is reached, it follows that the force - velocity relationship is in between that of a rigid body, and that of a fully flexible body. The second relationship proposed combines the equations for a rigid body, and the linear regression relationship derived for velocities in Zone B, Equation 5.36:

$$F = \frac{1}{2}\rho(C_dAU_0)U_0 + F_I \Longrightarrow V \geq V_{AB} \tag{5.36}$$

This has been applied to the force - velocity data in Zone A, to recalculate the drag area parameter $(C_dA.U_0)_{A2}$. Both the linear and squared elements are weighted linearly by φ (Equation 5.38) in accordance to the velocity relative to U_{AB}. As the velocity approaches the transition velocity U_{AB}, the equation will close towards the value of $(C_dA.U_0)_B$ for the tree within Zone B:

$$(C_dA.U_0)_{A2} = \frac{F - ((1-\varphi)F_I)}{\varphi((\rho U_0^2)/(2)) + (1-\varphi)((\rho U_0 U_B)/2)} \tag{5.37}$$

$$\varphi = \frac{U_{AB} - U}{U_{AB}} \tag{5.38}$$

The term U_B in Equation 5.43 has a value of 1.0 and is inserted to maintain dimensional homogeneity. The third relationship combines the equations for a rigid body and a fully flexing body (assuming no stiffness force intercept F_I) to produce drag area parameter $(C_dA.U_0)_{A3}$. In this situation, the relationship would take the form in Equation 5.43.

$$(C_dA.U_0)_{A3} = \frac{F}{\varphi((\rho V^2)/(2)) + (1-\varphi)((\rho V)/2)} \tag{5.39}$$

The results for the drag area parameters $(C_dA)_{A1}$, $(C_dA.U_0)_{A2}$ and $(C_dA.U_0)_{A3}$ as calculated from data points in Zone A are presented in the following pages.

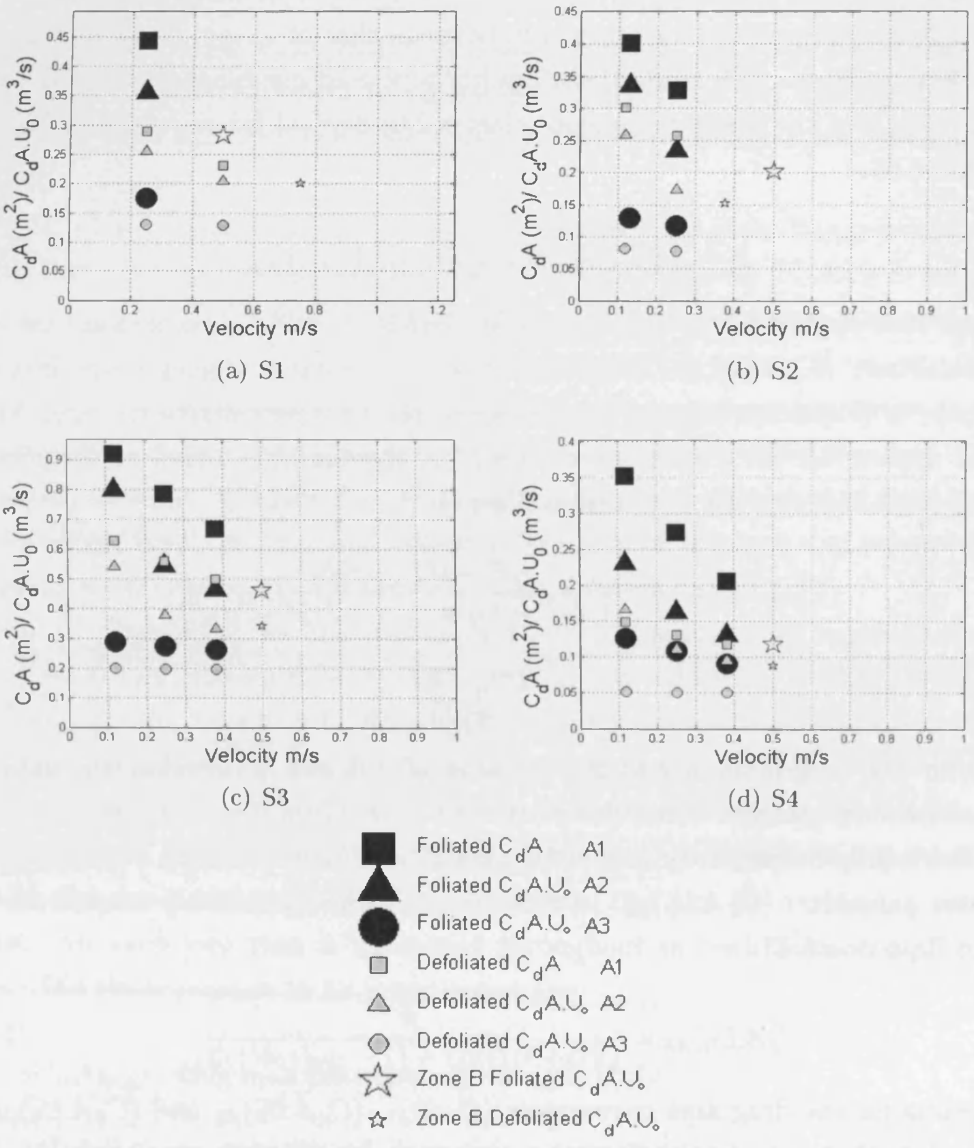

Figure 5.47: Drag area parameters $(C_dA)_{A1}$, $(C_dA.U_0)_{A2}$ and $(C_dA.U_0)_{A3}$ as calculated for *Salix* trees in Zone A

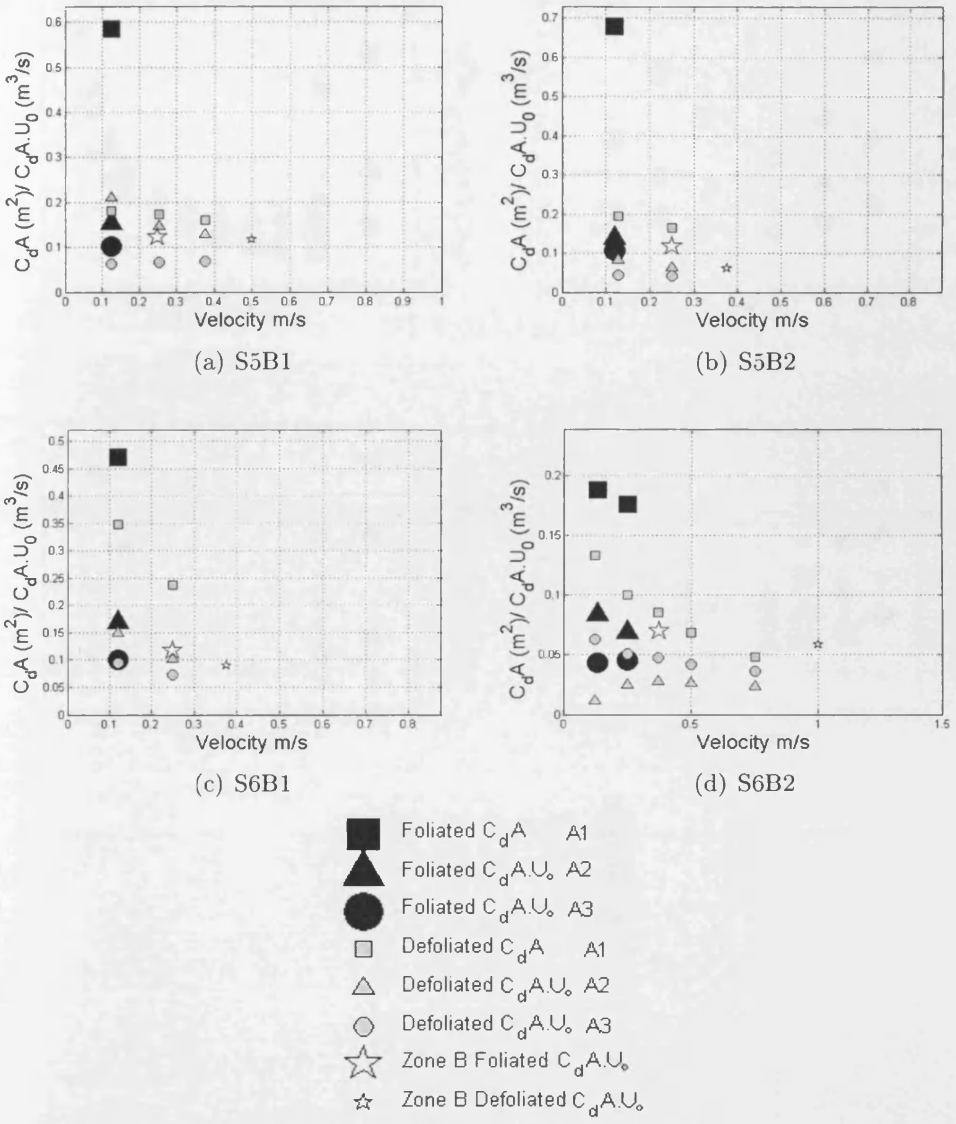

Figure 5.48: Drag area parameters $(C_dA)_{A1}$, $(C_dA.U_0)_{A2}$ and $(C_dA.U_0)_{A3}$ as calculated for *Salix* trees in Zone A

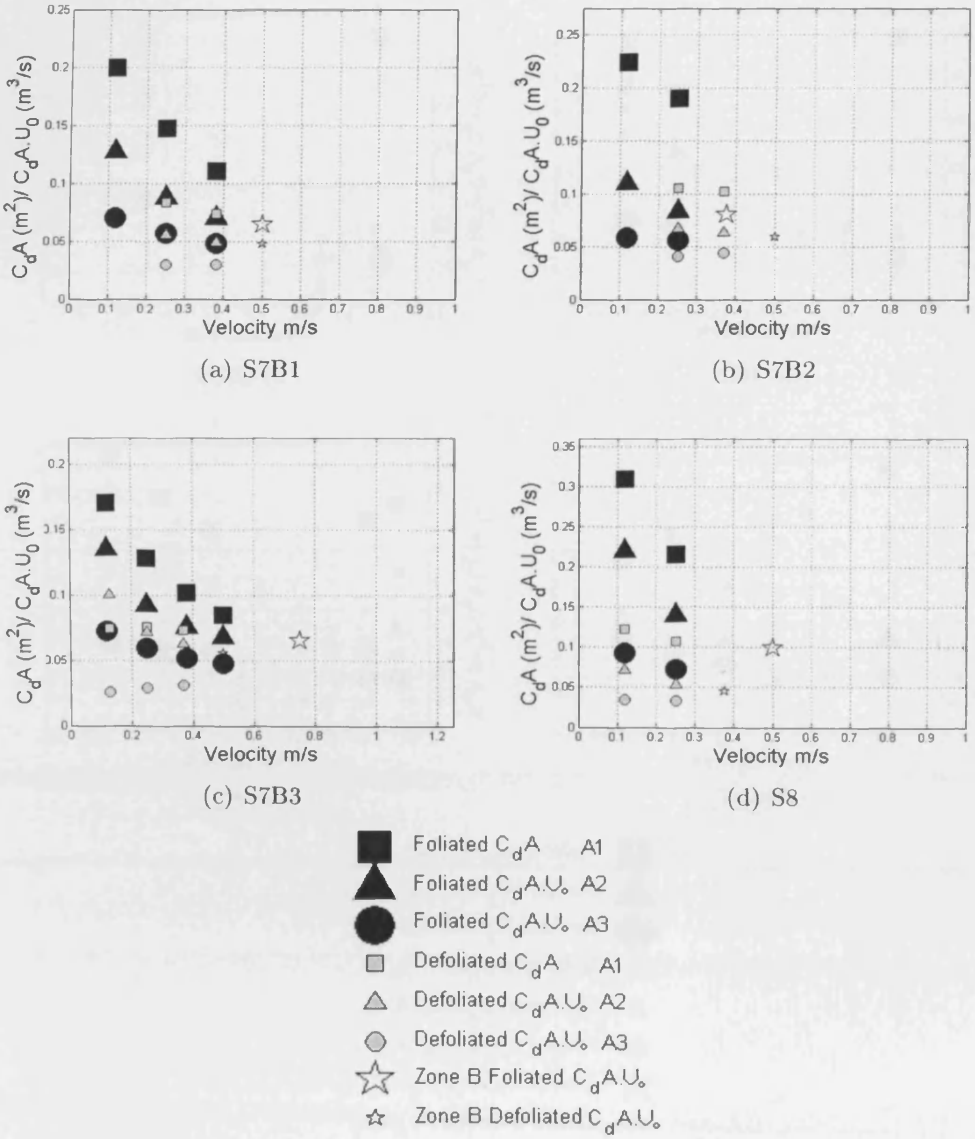

(a) S7B1

(b) S7B2

(c) S7B3

(d) S8

Figure 5.49: Drag area parameters $(C_dA)_{A1}$, $(C_dA.U_0)_{A2}$ and $(C_dA.U_0)_{A3}$ as calculated for *Salix* trees in Zone A

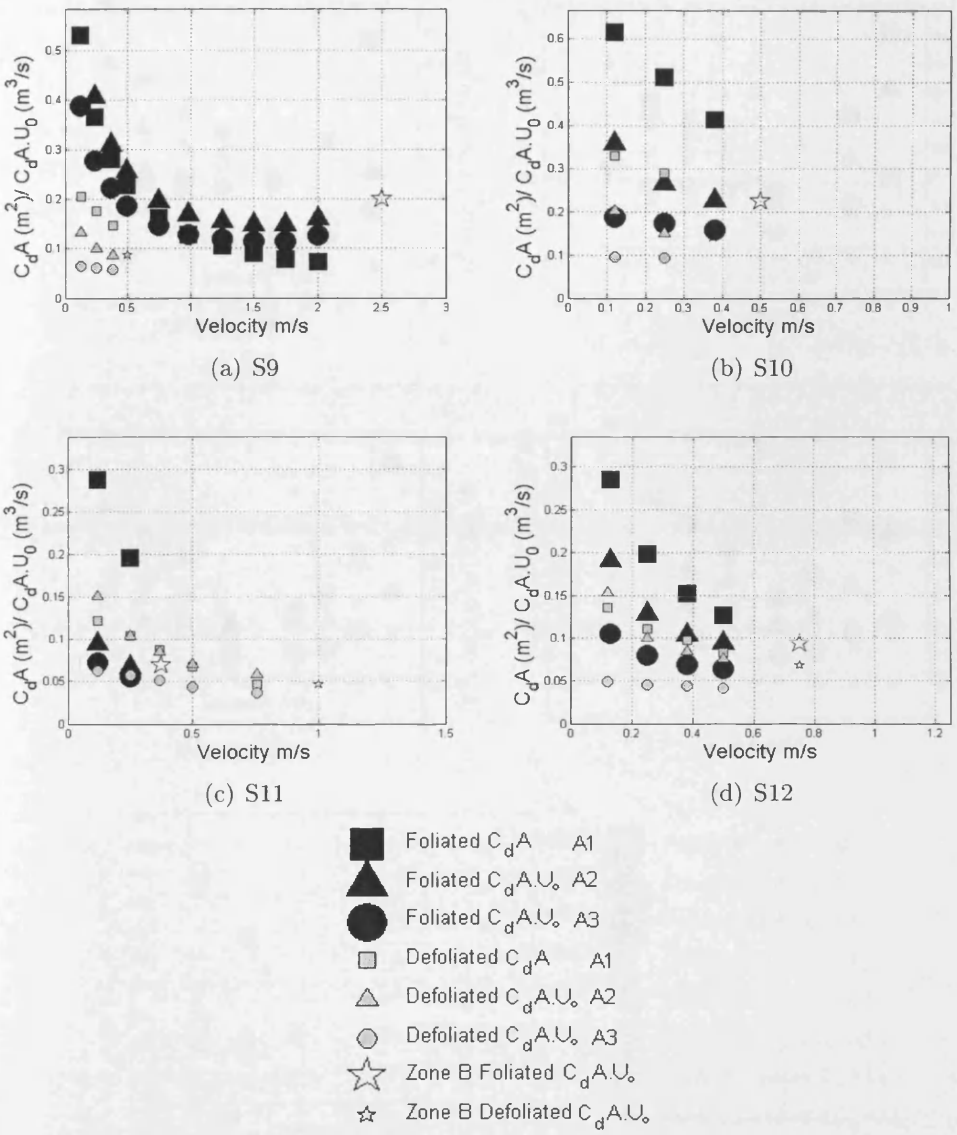

Figure 5.50: Drag area parameters $(C_dA)_{A1}$, $(C_dA.U_0)_{A2}$ and $(C_dA.U_0)_{A3}$ as calculated for *Salix* trees in Zone A

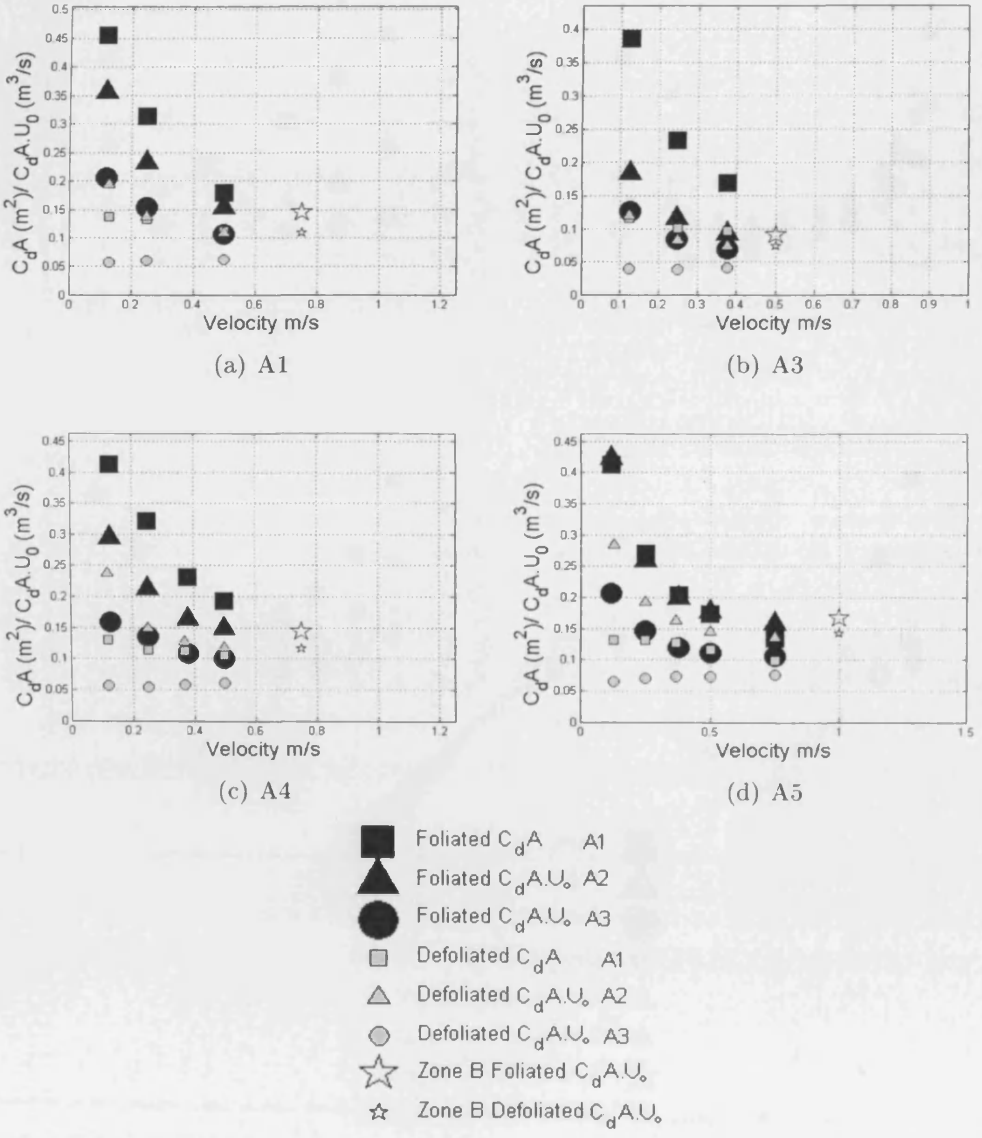

Figure 5.51: Drag area parameters $(C_dA)_{A1}$, $(C_dA.U_0)_{A2}$ and $(C_dA.U_0)_{A3}$ as calculated for *Salix* trees in Zone A

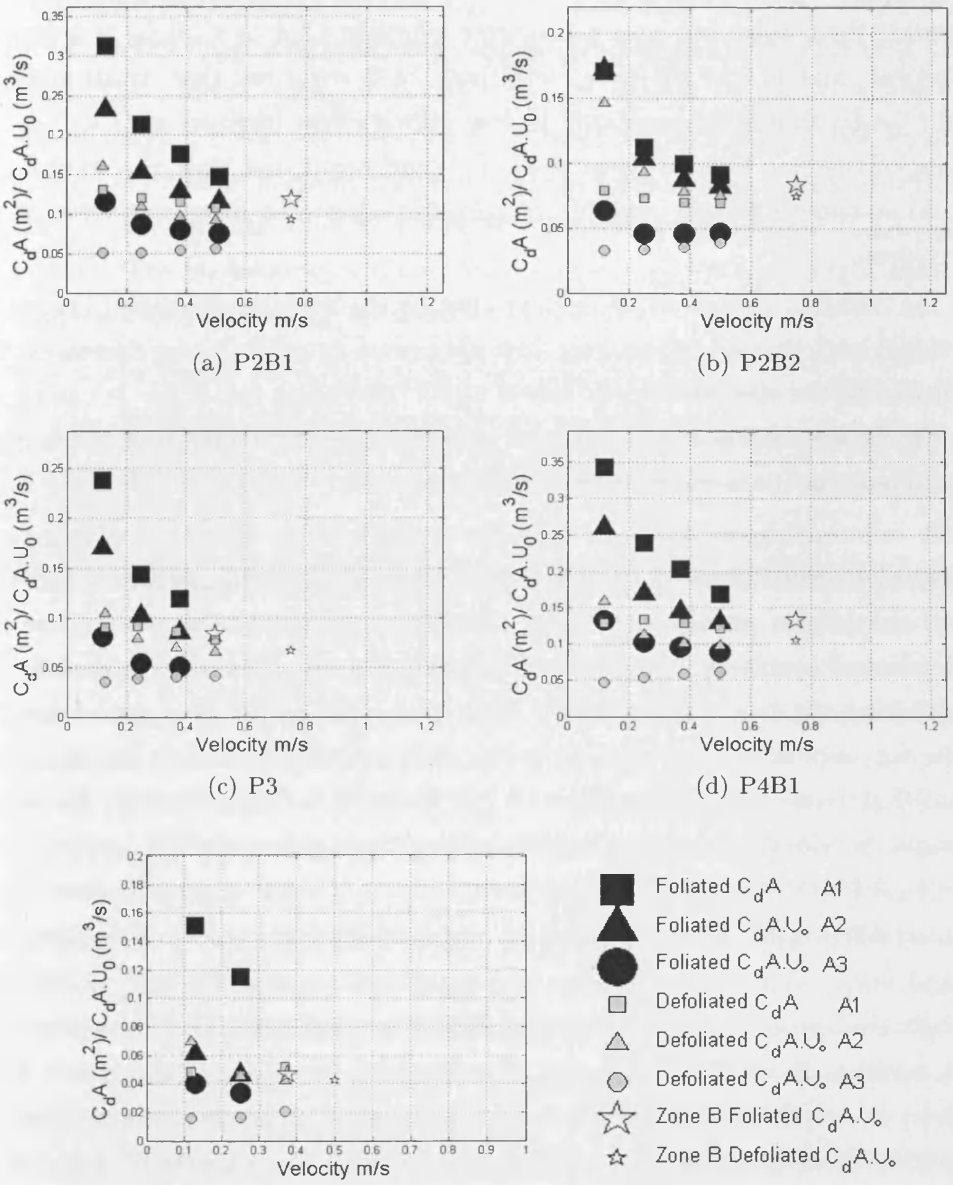

(a) P2B1

(b) P2B2

(c) P3

(d) P4B1

(e) P4B2

Figure 5.52: Drag area parameters $(C_dA)_{A1}$, $(C_dA.U_0)_{A2}$ and $(C_dA.U_0)_{A3}$ as calculated for *Salix* trees in Zone A

Discussion of drag area parameter varients of Zone A $C_dA.U_0$

The three proposed varients of the drag area parameter have been calculated and plotted against the value of $C_dA.U_0$ in Zone B. Since in both rigid body flow and fully flexible flow, the drag area parameter whether C_dA or $C_dA.U_0$ is a property of the object, and not of the flow conditions, it is expected that at all flows, the value of $C_dA.U_0$ should be constant. In low velocity flow (defined as $U < U_{AB}$), the behaviour of the tree falls between that of a rigid body, and that of a fully flexible body, and so three different possible relationships between force and velocity have been explored.

For all the datasets presented, it is clear that as the velocity increases, overall, the proportional contribution to the drag area parameter from the leaves decreases. This could be due to the streamlining of leaves under increasing velocities. It can be seen that in the figures on the previous pages, there is a general trend of decreasing drag area parameter as the velocity increases for both the foliated and defoliated trees.

The first relationship explored is that for a rigid body, where C_dA is inversely proportional to the square of velocity, giving $(C_dA)_{A1}$. Applying this relationship produces the largest variation in drag area parameter for each tree (apart from some defoliated specimens), and the relationship is often linear. It is clear that in approaching the transition velocity U_{AB}, the values of $(C_dA)_{A1}$ and $(C_dA.U_0)_B$ often do not appear to coincide, although due to a lack of resolution of data in the transition zone, the exact nature of this cannot be ascertained for certain. In transitional or velocities that increase or decrease going through U_{AB}, a jump to the value of $C_dA.U_0$ in Zone B is likely to occur.

The second relationship using $(C_dA.U_0)_{A2}$ explored combines the relationship defined for a rigid body, with the linear relationship already derived for each tree in Zone B through the use of a linear weighting factor φ. By it's nature, this variant of $C_dA.U_0$ assumes the validity of using the drag area parameter C_dA at the lowest velocities - i.e. that the tree behaves as a rigid body, but closes towards the value obtained for Zone B $(C_dA.U_0)_B$. As such, a smooth transition will occur as the velocity approaches U_{AB}. However, both the foliated and defoliated condition $(C_dA.U_0)_{A2}$ decrease with increasing velocity, rather than maintaining a constant value. Assuming that $(C_dA.U_0)_{A2}$ is a property of the tree and not the flow regime, it is expected that it should be a constant value. This means either that the assumption of linear transition is not appropriate or alternatively, the theory of a constant $C_dA.U_0$ should be reconsidered, and higher values used at lower velocities.

The third relationship $(C_dA.U_0)_{A3}$ combines the relationship defined for a rigid body with a linear relationship, with no F_I intersect value included. Interestingly, this relationship provides an almost linear value for $(C_dA.U_0)_{A3}$ at all velocities, with some instances increasing or decreasing with increasing velocity. However, in no instance does the drag area parameter appear to correlate well with that obtained in Zone B. The constant value of the drag area parameter obtained, suggests that is possible to assign a single parameter value to flows in both Zone A and Zone B, but a modification must be made to increase it to the level at which Zone B relationship is defined. It is likely the solution is a blend between the varients of $(C_dA.U_0)_{A2}$ and $(C_dA.U_0)_{A3}$. The problem with non-constant value may lie in the treatment of F_I. It is proposed that this is explored in future research.

5.6.4 Linking Branch Projected Area to Zonal drag area parameters

5.6.4.1 Branch Area

The ability to determine the resistive properties of trees from easily measurable physical characteristics, is highly desirable. Of the parameters explored in the Zone B relationship, correlation with volume in Figure 5.38 is positive, however there is still a large degree of uncertainty associated with the data. This is reasonable, as in flow conditions with Stem Reynold's numbers greater that 200, it is the projected area A_p of a tree or object that is linked to the drag area parameter $C_dA.U_0$, rather than the total mass or volume. The measurement of branch projected area cannot be determined directly from the volume calculations. A large branch composed of the same volume as a group of branches with smaller diameters will have a lower projected surface area.

A few of the trees had their entire branch system photographed in quartile heights before being dried. As well as providing a photographic record of the nature of the branches, for example, for species determination or the degree of roughness due to surface pitting, the photographs can be digitally analysed to determine projected area and average diameter. Having obtained the projected area A_p, the drag coefficient C_d can be determined from the drag area parameter $C_dA.U_0$ according to Equation 5.40.

By approximating the defoliated tree to a series of cylinders of projected area A_p determined from the photographs, the drag area parameter $C_dA.U_0$, can be converted to the Drag Coefficient C_d via Equation 5.40.

$$C_d = \frac{C_d A}{A_p} \tag{5.40}$$

Since the projected area determined from the branches will only be valid at very low velocities, the C_d values obtained using this method are valid only in flow conditions where the tree does not flex under the force of the oncoming flow, i.e. within the lowest velocities in Zone A.

In contrast, within Zone B, the product of the drag coefficient C_d and the projected area A_p is the drag area parameter $C_d A.U_0$. As seen in the results, $C_d A.U_0$ remains almost constant throughout Zone B. It follows, that as the projected area A_p is inversely correlated to streamwise velocity, the drag coefficient C_d must increase in order to maintain $C_d A.U_0$ at a constant value.

However, the value of $C_d A.U_0$ that is adopted is subject to some uncertainty due to the transition from a rigid body to a fully flexing body as the velocity increases. If $C_d A.U_0$ is held to be a constant property of the tree at all velocities, then the value of drag area parameter in Zone B $(C_d A.U_0)_B$ can be used with confidence. If however, at low velocities, at the point of initial bending, the drag area parameter varies from that for a fully flexing body, and exists at some transition between a rigid body and fully flexing body, then $(C_d A.U_0)_{A2}$ gives the most improved correlation. To further ascertain the validity of $(C_d A.U_0)_{A2}$, a study into the determination of the drag coefficient C_d using the branch projected area has been carried out.

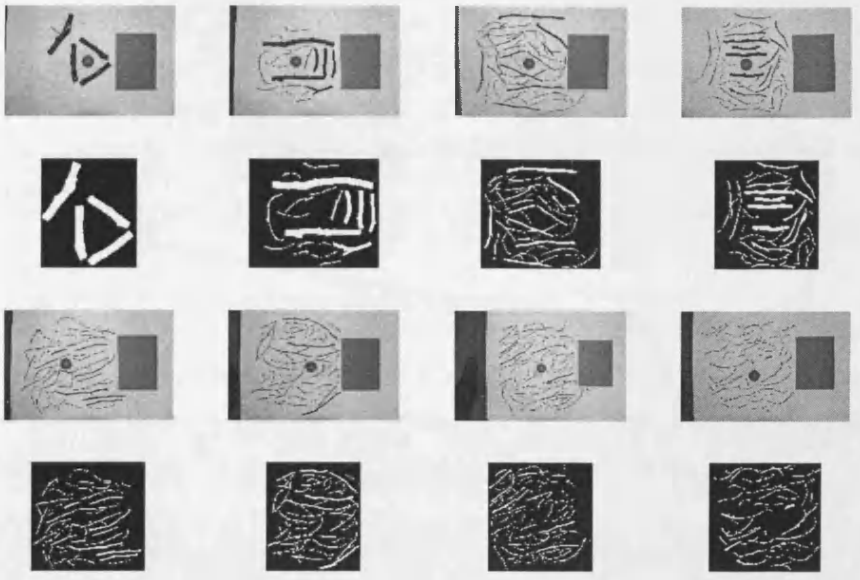

Figure 5.53: *Alnus* 1

Determining Branch Projected Area

Photographs of the branches for trees *Salix*14, *Alnus*1 and *Populus*1 were taken, however, only *A*1 was tested in the unleaved condition. The branches for each tree were grouped into quartiles by the tree height and photographed beside a ball of known diameter and an A4 sheet of paper. The presence of the ball and the paper allowed digital determination of the number of pixels in 1 mm. Each photograph was split into two halves, one with the branches, and one with the A4 paper. The images were converted to binary using an appropriate threshold value determined by eye to check that only the branches were included, and not shadows or particles of dirt. The image with the A4 piece of paper was analysed first for the number of pixels contained in the sheet of A4 paper.

Dividing the pixel number composing the A4 sheet by the known number of mm^2 in an A4 sheet of paper, the number of pixels per mm^2 were determined. The number of pixels in the binary image containing the branches was then counted. Figure 5.53 shows the original photographs above the binary image of the branches only. Dividing the branch pixels by the pixels per mm^2 as determined from the A4 sheet of paper, the area of the branches in mm^2 could be determined.

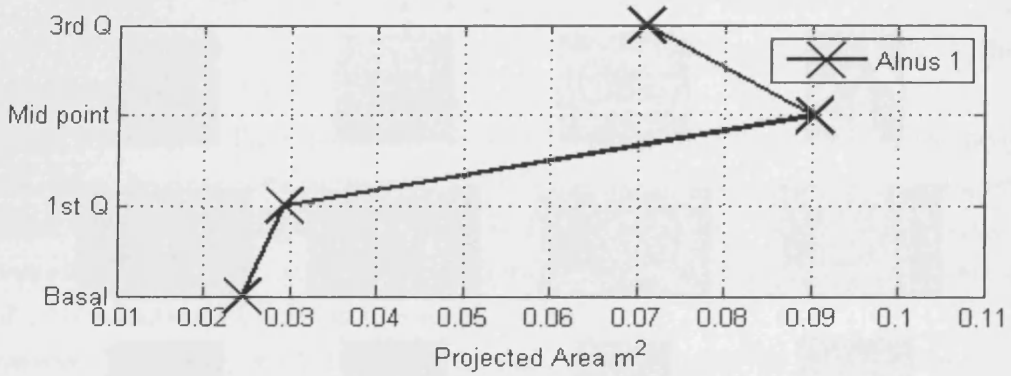

Figure 5.54: *Alnus* 1 Projected Area by section

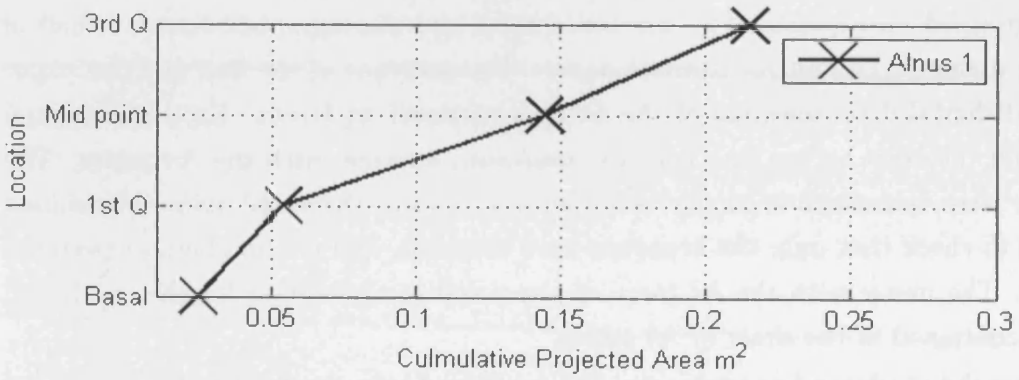

Figure 5.55: *Alnus* 1 Cumulative Projected Area by section

	A1 Ap	A1 Ap Culm
Location	m^2	m^2
Basal	0.024	0.025
Q1	0.029	0.054
Mid point	0.090	0.144
Q3	0.071	0.215

Table 5.10: *Alnus* 1 Projected Area and Cumulative Projected Area by section

Using Projected Area to Obtain Drag Coefficient C_d

The drag area parameter value for *Alnus* 1 is $(C_dA.U_0)_B = 0.195$ at $U = 0.125m/s$ in Zone A and $(C_dA.U_0)_B = 0.110$ at all velocities in Zone B. By applying Equation 5.40, the drag coefficient C_d can be obtained as shown in Table 5.11.

	$C_dA.U_0$	Ap	C_d
$(C_dA.U_0)_{A2}$	0.195	0.215	0.907
$(C_dA.U_0)_B$	0.110	0.215	0.512

Table 5.11: *Alnus* 1 drag area parameter and drag coefficient

The variation between C_d calculated is large. As the defoliated tree is a series of long cylinders, and the value of C_d for a cylinder is of the order $C_d = 1.0$ 1.2, and the C_d calculated from $(C_dA.U_0)_{A2}$ is closer in value at $C_d = 0.907$. This seems to confirm the fact that a tree has different drag area parameter $(C_dA.U_0)$ values in Zone A and Zone B.
Assuming the ratio of projected area to tree volume is consistent for *Alnus* trees, the drag coefficient (C_d) of the other trees of the same species can be assessed. The ratio of projected area (A_p) to volume can be calculated as:

$$Vol = \frac{\pi d}{4} A_p \tag{5.41}$$

$$A_p = dh \tag{5.42}$$

Where Vol is the tree volume, d is the diameter, A_p is the projected area and h is the height. In this calculation, the average diameter of the tree is needed to complete the conversion. Using data from *Alnus* 1, the ratio can be determined as $\frac{\pi d}{4} = 0.008$. Here, an assumption has been made that all the *Alnus* trees are a similar size and have a similar average diameter. This approach is only partially valid, as although by volume, *Alnus* 1 is similar in size to *Alnus* 3, but approximately 25 % larger

than *Alnus* 3 and 4. For greater accuracy, further work can be done in analysing the photographic records to determine the true average diameter.

Tree	$(C_dA.U_0)_{A2}$	$(C_dA.U_0)_B$	A_p	C_dZA	C_dZB
A1	0.195	0.110	0.215	0.907	0.512
A3	0.073	0.121	0.162	0.744	0.452
A4	0.116	0.238	0.184	1.295	0.632
A5	0.142	0.284	0.205	1.385	0.694
			Average	**1.083**	**0.573**

Table 5.12: *Alnus* 3, 4 and 5. Zonal drag area parameter and Drag Coefficient. $(C_dA.U_0)_{A2}$ measured at V = 0.125 m/s. $(C_dA.U_0)_B$ measured from Zone B

Although a limited study involving only 4 trees, and the uncertainty associated with the determination of the projected area, the mean value for C_d for Alnus 1, 2, 3 and 4 is $C_d = 1.083$ which lies approximately between 1.0 and 1.2, the Drag Coefficient value cited for a cylinder in turbulent flow. Due to the physical differences between *Alnus*, *Salix* and *Populus*, this cannot be reasonably extended to the other two trees species.

5.7 Summary of Drag Force Tests on Full Scale Trees

The determination of branch projected area in Section 5.6.4 further validated the assumption that a tree can be modelled as a series of cylinders at low flows. However, as the tree flexes increasingly, the drag coefficient undergoes a transition to the lower value recorded in Zone B. Equation 5.43, shown again here, covers this transition through the use of a weighting factor ϕ.

$$(C_dA.U_0)_{A2} = \frac{F - ((1-\varphi)\gamma)}{\varphi((\rho V^2)/(2)) + (1-\varphi)((\rho V)/2)} \tag{5.43}$$

Further research is needed, especially high resolution data from Drag Force tests on full scale trees, to further validate this assumption.

6

Numerical Modelling of Floodplain Woodland Vegetation

6.1 Computational Fluid Dynamics

6.1.1 Introduction

The numerical modelling of river flows plays an increasingly important role in river management and flood prediction, however, major issues involving adequate grid resolution and vegetation representation remain (Bates et. al. 2005). Aquatic and riparian plants provide an obstruction to the flow, reducing mean flow velocities and turbulent length scales in comparison to non-vegetated regions (Stoesser et al. 2003).

The reduced shear stress within vegetated channels in comparison to non-vegetated channels affects bed shear stress levels and, consequently, changes in vegetation can affect river morphology. Representation of floodplain vegetation within a river model often takes a bulk roughness approach, where the vegetation is represented through the use of a roughness factor such as Manning's n Vionett (2004), friction factor (Beffa & Connell 2001) or a drag coefficient (Mazda et al. 1997).

Determination of roughness coefficients is hampered by a lack of data for floodplain woodland vegetation. In this chapter, data collected in previous chapters will be used to enhance the available dataset on numerical woodland and applied within the two-dimensional finite difference numerical model DIVAST.

6.1.2 Scope of the Chapter

The aim of this Chapter is to calibrate the existing DIVAST FLUME model to represent vegetation more effectively. The flume was modelled numerically with a grid of 6cm x 10.4cm (equivalent to the lateral and longitudinal spacing of the most dense arrangement of vegetation tested), a slope of $S = 0.001$, an upstream flow boundary, and a downstream elevation boundary controlled by a weir equation. The experimental results from Chapter 3 that established stage discharge relationships for single stem and multi-stem model trees were used to calibrate the model with respect to bed and vegetative roughness, as these results represent pseudo-uniform flow conditions over a range of velocities and associated depths. The stage discharge relationship of the dowels and real vegetation is described in chapter 3.5.

6.2 DIVAST - Depth Integrated Velocities and Solute Transport

DIVAST is a two-dimensional, depth-integrated, time-variant model, originally developed for estuarine and coastal modelling. DIVAST simulates two-dimensional distributions of velocity and various water quality parameters within the modelling domain as functions of time, taking into account the hydraulic characteristics governed by bed topography and boundary conditions (Falconer 1977, Lin and Falconer 1997) More recent versions of DIVAST include the representation of vegetation as a cylindrical drag force (Struve et al. 2003) and have also included the blockage effect represented by vegetation (Westwater 2000). DIVAST is particularly appropriate for the current studies as much emphasis has been focused in this code on modelling numerically the flooding and drying processes (Falconer & Chen 1991).

6.2.1 Governing Theory

Shallow water flows cover flow scenarios including estuaries and rivers, and assume the following:

1. predominantly horizontal flow with minimal vertical accelerations

2. minimal stratification effects with a uni-directional velocity component

Incompressible turbulent flow conditions are to be considered. Thus, the forces on the fluid particles within the water body are limited to the fluid weight per unit volume, the frictional force due to bed shear and obstacles in the water column, including vegetation, and surface shear forces due to wind stress. If the datum is set at mean sea level, the hydrostatic pressure distribution can be determined according to the coordinate system in Figure 6.1:

$$p(z) = \rho g(\zeta - z) + p_a \tag{6.1}$$

Where p is the pressure at elevation z, ρ is fluid density,g is gravitational acceleration, ζ is the water surface elevation above mean sea level, d is the bed elevation above the datum, and p_a is the atmospheric pressure, usually assumed to be negligible, in which case, Equation 6.2 reduces to:

$$p(z) = \rho g(\zeta - z) \tag{6.2}$$

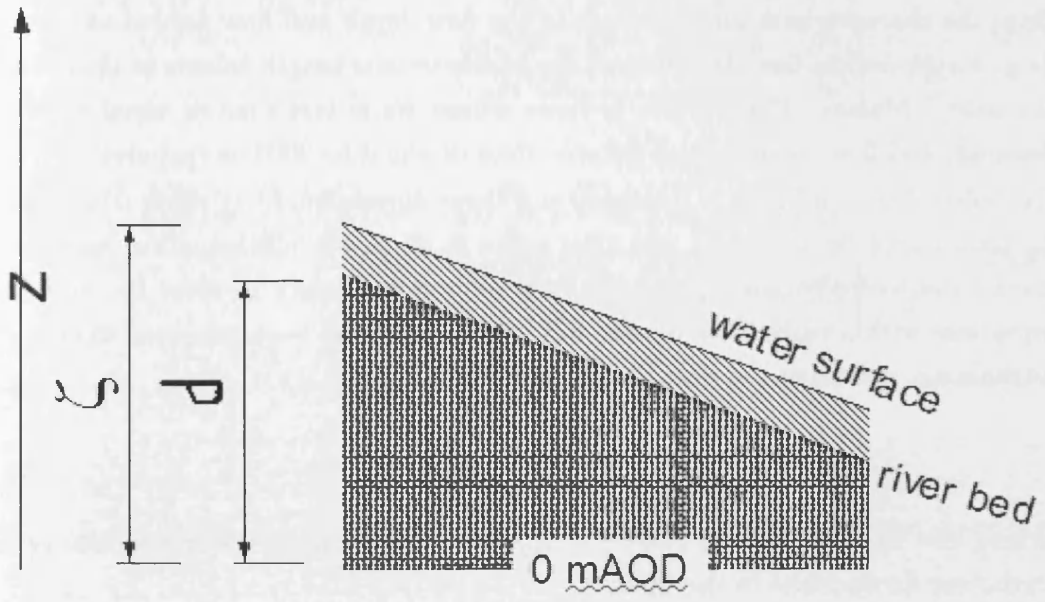

Figure 6.1: Water surface and bed elevation against datum (0 mAOD)

Boundary layer theory describes how the combined nature of the boundary and the state of flow influence the development of the vertical velocity profile (Schlichting 2000). Fluid flow can exist in 3 states, laminar, turbulent and transitional. In laminar flow, viscous forces predominate and frictional forces are negligible, with water particles moving in parallel streamlines. In turbulent flow, the frictional forces are dominant and the viscous forces are relatively weak, promoting irregular motion of the fluid particles. In transitional flow, viscous and frictional forces are of a similar magnitude and the flow moves from the laminar to transitional states.

By relating the inertial forces to the viscous fores, Reynolds defined the *Reynolds number*:

$$\frac{\rho U d}{\mu} = \frac{U d}{\nu} \tag{6.3}$$

Where ρ is the fluid density, U is the velocity, d is the characteristic length, μ is the fluid viscosity and ν is the kinematic viscosity. Reynolds found that two flows were similar when the Reynolds number was equal. The characteristic length relates to the scale of the largest eddies created. In pipe flow, the characteristic length relates to the diameter of the pipe. In wide, open channel, unobstructed flow, the characteristic length relates to the flow depth and flow around an obstacle (e.g. a cylinder) in free stream flow, the characteristic length relates to the cylinder diameter. Massey (1997) refers to flows where Re is less than or equal to 200 as laminar, and flows where Re is greater than or equal to 2000 as turbulent.

Turbulent flow is inherently unsteady and three dimensional. At the smallest scales, turbulent motion is chaotic and thus there is no direct mathematical solution to model the hydrodynamic processes, and so it is necessary to close the governing equations with a turbulence model. Several models have been proposed to close the turbulence, including the Boussinesq eddy viscosity (ϵ):

$$\overline{\tau_{xy}} = \epsilon \frac{\partial \overline{u}}{\partial y} \tag{6.4}$$

where the Reynolds stress relies on the determination of the magnitude of the turbulent fluctuations in the fluid:

$$\overline{\tau_{xy}} = -\rho \overline{u'v'} \tag{6.5}$$

where u' and w' are the turbulent fluctuations in the streamwise and vertical planes. Also in common use is Prandtl's mixing length model (Schlichting 2000).

The governing equations of shallow water flows can now be considered.

6.2.2 Navier-Stokes Equations

Numerical modelling of fluid flows is grounded in the principles of conservation of mass and the conservation of momentum, which together describe the fundamental parameters of pressure and velocity within a fluid body (Hinze, 1975). If the flow is assumed to be incompressible and Newtonian, then the Reynolds-averaged Navier-Stokes equations are the governing relationships to describe the fluid motion. In the depth-integrated form, the equations are:

Conservation of Mass:

$$\frac{\theta \partial \zeta}{\partial t} + \frac{\partial p}{\partial x} + \frac{\partial q}{\partial y} = 0 \tag{6.6}$$

Conservation of Momentum:

$$\begin{aligned} \frac{\partial p}{\partial t} + \frac{\partial}{\partial x}\left(\frac{p^2}{H}\right) + \frac{\partial}{\partial y}\left(\frac{pq}{H}\right) = & -gH\frac{\partial \zeta}{\partial x} + \frac{\rho_a}{\rho}\theta C_w W_x \sqrt{W_x^2 + W_y^2} \\ & - \frac{gp\sqrt{p^2+q^2}}{H^2 C^2} + \epsilon H\left[\frac{\partial^2 p}{\partial x^2} + \frac{\partial^2 p}{\partial y^2}\right] - F_x \end{aligned} \tag{6.7}$$

$$\begin{aligned} \frac{\partial q}{\partial t} + \frac{\partial}{\partial x}\left(\frac{pq}{H}\right) + \frac{\partial}{\partial y}\left(\frac{q^2}{H}\right) = & -gH\frac{\partial \zeta}{\partial y} + \frac{\rho_a}{\rho}\theta C_w W_y \sqrt{W_x^2 + W_y^2} \\ & - \frac{gq\sqrt{p^2+q^2}}{H^2 C^2} + \epsilon H\left[\frac{\partial^2 q}{\partial x^2} + \frac{\partial^2 q}{\partial y^2}\right] - F_y \end{aligned} \tag{6.8}$$

where:

p, q	discharges per unit width in the x and y directions respectively $(m^3/s/m)$
θ	porosity factro, resulting from the blockage of flow area from the plants
U, V	depth average velocity components in the x and y directions respectively (m/s)
β	momentum correction factor for a non-uniform vertical velocity profile
g	gravitational acceleration $(= 9.807\ m/s^2)$
ζ	water surface elevation above (or below) datum (m)
H	total water depth $= \zeta + h$
ρ_a	density of air $(\cong 1.292\ kg/m^3)$
ρ	density of water (kg/m^3)
C	Chezy roughness coefficient $(m^{1/2}/s)$
C_w	air/ fluid resistance coefficient (assumed to be 2.6 x 10^{-3})
W	wind stress
ϵ	depth averaged turbulent eddy viscosity (m^2/s)
F_x	Drag force in the x direction (kgm/s^2)
F_y	Drag force in the y direction (kgm/s^2)

6.3 Representing Vegetation in 2-D models

The bulk roughness approach has been adopted in this numerical study, in which roughness is implicitly represented within the Reynolds-averaged Navier-Stokes equations through the use of an energy absorbing factor such as the Chezy factor or Manning's n for the bed resistance and a drag force for form resistance. DIVAST solves the Navier-Stokes equations using an alternating direction implicit finite difference scheme. The flume domain was represented by a space staggered grid with dimensions $x = 0.060$ m and $y = 0.106$ m in the lateral and longitudinal directions respectively. Velocities and depth values recorded at the centre sides to conserve momentum and scalar variables are located at the grid centre (Falconer 1977).

The momentum equation for the y (streamwise) direction (Equation 6.8) illustrates a limitation in the representation of vegetation within the numerical model. The second term on the L.H.S. of Equation 6.8 is the lateral advective acceleration term and the fifth term on the R.H.S. is the lateral turbulence. In unvegetated flows with no obstacles, these terms are generally relatively small. However, with increasing

vegetation, this term will increase as the flow field becomes less regular and the proportion of lateral flow motion is increased by the movement of fluid around the dowels.

In the one-dimensional method of calculating the energy loss as Manning's n or a drag coefficient (C_d), the system is considered with uniform flow conditions. In uniform flow, the overall force exerted by the vegetation is balanced by the gravitational force of the water body directed streamwise. In this case, the value of the drag coefficient includes wake interaction effects from the pattern of cylinders, so will not be equivalent to the drag coefficient C_d of an isolated cylinder.

This is a vastly simplified steady state derivation, and thus it cannot be directly related to the unsteady solution of the Navier-Stokes equations. The force acts in each plane but neglects to specify effects on lateral advection and turbulence. In the future, further manipulation of the lateral advective and turbulence terms may achieve a better correlation.

6.3.1 Roughness factors

The representation of vegetation in 1-D and 2-D river models has often taken the form of a roughness coefficient such as Manning's n or the Chezy roughness factor Chow (1959), although increasingly the use of drag coefficient terms (the last term in Equations 6.7 and 6.8) are used to represent emergent vegetation, where emergent is defined as vegetation that extends vertically throughout and beyond the water column (Mazda 1995; Wu et. al. 2001), creating a form drag through the wake.

In particular, roughness coefficients of floodplain woodlands are described in the literature with a large degree of uncertainty attached. The Roughness Adviser proposes Manning's n values for floodplains with trees, together with upper and lower limits, listed in Table 2.1.

A review of the literature of vegetated flows may be found in Chapter 2. Experimental work in Chapters 3 and 5 obtained the resistance factors for scaled tree arrays, and single trees respectively. These values give a range of applicable Manning's n values for use in modelling. However, the single value of Manning's n does not account for changes in stream velocity or flow depth, while Manning's n is dependent on both (Ree 1958, Turner & Chanmeesri 1984, Kadlec 1990).

A variety of plants species many be found on a floodplain, those recognised as key species in the National Vegetation Classification tables are listed in Chapter 1 Table 1.3. While some genera such as established *Alnus* and *Populus* are rigid and will not

move under flow conditions (Musleh & Cruise 2006), many plants typically found on floodplains are flexible, and respond dynamically under increasing fluid velocities (Kouwen & Fathi-Maghadam 2000).

Wilson and Shaw (1977) proposed a drag force related term to be included in the Navier-Stokes equations to account for the flow resistance of vegetation. The standard drag coefficient value for a cylinder of $C_d = 1.0$ (Massey 1997) has been used widely to represent the hydraulic resistance of rigid cylindrical vegetation, particularly in the field of the modelling of mangrove vegetation Mazda et al. (1997), Naot et al. (1996). Equation 6.9 presents the drag force equation in one dimension.

$$F_d = \frac{1}{2} C_d N A_p U_0^2 \tag{6.9}$$

where F_d is the drag force exerted on/ by the vegetation, C_d is the drag coefficient (in turbulent flows this relates to the shape of the obstacle), N is the number of trees (or alternatively the number of stems if the trees are multi-stemmed), A_p is the projected area of an individual tree (or stem if the trees are multi-stemmed), and U is the depth-averaged streamwise velocity.

The value of the drag coefficient for mangrove vegetation remains a source of uncertainty. Mazda (1997) analysed field data and found the mangrove vegetation drag coefficient (C_d) value varied between 0.4 and 10. Wu et. al. (2001) incorporated the blockage (porosity) effect of the vegetation in the numerical model DIVAST. Struve et. al. (2003) used flume experiments to obtain drag forces between 0 and 4.5.

Studies into the planting density and consequent sheltering effects have been carried out (Li & Shen 1973, Dunn 1996, Nepf 1999, Musleh & Cruise 2006). Researchers in both the hydrodynamic and aerodynamic fields have directly measured the drag force and drag coefficients of real broad leaf and evergreen floodplain woodland vegetation (Mayhead 1973, Fathi-Maghadam & Kouwen 1997, Oplatka 1998*a*, Kane & Smiley 2006).

According to the original derivation, the 2-D form of the drag coefficient term (C_d) specifically relates to an isolated, rigid and infinite cylinder in a wide flow field, in which the velocity is U_0 (Massey 1997). Various authors have considered modifications to the term, and variants include the bulk drag coefficient ($\overline{C_d}$) indicating the bulk drag of a collection (or array) of plants in a mean-area flow with a corresponding velocity of $\overline{U}$ (Nepf 1999), given by:

$$F_d = \frac{1}{2}\rho \overline{C_d} \mathbf{a} \overline{U}^2 \tag{6.10}$$

where F_d is the drag force exerted, ρ is the fluid density, $\overline{C_d}$ is the bulk drag coefficient, $\mathbf{a}$ is the project plant area per unit volume and $\overline{U}$ is the mean area velocity. The vegetal drag coefficient (C_d') of Wu et al. (1999) accounts for effects of density.

$$F_d = \frac{1}{2}\rho C_d' A_p \overline{U}^2 \tag{6.11}$$

where F_d is the drag force exerted, ρ is the fluid density, C_d' is the vegetal drag coefficient, A_p is the projected area and $\overline{U}$ is the mean area velocity. The modified drag coefficient (C_dA), which incorporates the projected area (A_p) and the drag coefficient (C_d) for a single plant (Oplatka 1998*a*) given by:

$$F_d = \frac{1}{2}\rho C_d A \overline{U}^2 \tag{6.12}$$

where F_d is the drag force exerted, ρ is the fluid density, C_dA is the bulk drag coefficient, and $\overline{U}$ is the mean area velocity. This drag area coefficient term (C_dA) is particularly suited to defining the drag force of flexible vegetation. As a plant deflects under fluid loading, the projected area (A_p) reduces. However, many experimental studies where the direct drag force was measured have shown there is a linear variation between force and velocity, rather than the squared relationship suggested by Equation 6.9 (Mayhead 1973, Fathi-Maghadam & Kouwen 1997, Oplatka 1998 *a*, Kane & Smiley 2006).

In Chapter 5, the drag area coefficient ($C_dA.U_0$) was defined for 22 saplings of the genera *Salix*, *Alnus* and *Populus*. The linear drag force equation for a single plant (6.9) was modified to:

$$F_d = \frac{1}{2}\rho C_d A U_B U_0 + F_\gamma \tag{6.13}$$

where F_d is the drag force exerted, ρ is the fluid density, C_dA is the modified drag coefficient, U_B is the velocity coefficient with units of m/s necessary to maintain dimensional consistency where U_B is equal to 1.0, U_0 is the free stream velocity and F_γ is the stiffness force, representing the force that the tree can absorb through shearing, before deforming and reconfiguring it's shape. Equation 6.13 is valid only when the tree is fully flexing in flows above the transition velocity U_{AB}, possessing a value of approximately $U = 0.5m/s$ for the sapling trees investigated in chapter

5.

Within DIVAST, the presence of vegetation is currently incorporated through inclusion of the drag force term (F_d), the last term in Equations 6.7 and 6.8, and a porosity term (θ) representing the blockage effect of the vegetation in the mass conservation equation.

$$F_x = C_d N d \frac{p\sqrt{p^2+q^2}}{H} \tag{6.14}$$

$$F_y = C_d N d \frac{q\sqrt{p^2+q^2}}{H} \tag{6.15}$$

where F_x and F_y are the drag force exerted in the x- and y-dimensions respectively, C_d is the drag coefficient, N is the number of trees per m^2, d is the average diameter of the trees, p is the discharge per unit width in the x-direction, q is the discharge per unit width in the y-direction and H is the total water depth.

Equations 6.14 and 6.15 can be complemented by a second model adapted to simulate different densities of flexible floodplain woodland vegetation using the modified drag term C_dA from Chapter 5. Where more than one type of vegetation exists in a modelled reach, different areas can be assigned different modified drag coefficients and spacing N and sheltering factors S_θ.

$$F_x = C_d A N \frac{p\sqrt{p^2+q^2}}{H} \tag{6.16}$$

$$F_y = C_d A N \frac{q\sqrt{p^2+q^2}}{H} \tag{6.17}$$

Where F_x and F_y are the drag force exerted in the x- and y-dimensions respectively, C_dA is the modified drag coefficient for a single tree, N is the number of trees per m^2, p is the discharge per unit width in the x-direction, q is the discharge per unit width in the y-direction and H is the total water depth. This numerical scheme is flexible and allows for both rigid and fully flexible submerged trees to be included at different densities, although does not as yet account for the effect of sheltering. As yet there is no scheme to model partially submerged flexible trees, this is a planned improvement to be made to the model in future studies. The proposed scheme for selecting the drag coefficients is determined by the following procedure.

Procedure for determining C_d, d and N for rigid emergent vegetation:

1. In a sample quadrant of the field, determine the mean 1st quartile stem

diameter d, and the mean number of trees and mean number of stems (N) per unit m^2

2. Determine the Solid Volume Fraction (θ), where θ = 1 - $\pi d^2 N/4$

Procedure for determining C_dA and N for flexible submerged vegetation:

1. Either (a) in a sample quadrant of the field, photograph trees to determine the mean projected area and volume in still air, and correlate the volume to C_dA, or (b) obtain the average projected area A_p at the anticipated flood depth H, and assuming C_d = 1.0 for a single stem, obtain C_dA as A_p (For a proof of this method, see Section 5.6.4)

2. Determine the Solid Volume Fraction (θ), where θ = 1 - $\pi d^2 N/4$

Both the methods above assume the trees are in the unleaved condition. An additional factor to consider is the presence of leaves.
The porosity term θ (Wu et. al., 2001) accounts for the reduction in cross-sectional flow area due to vegetation.

$$\theta = 1 - \pi \frac{d^2 N}{4} \tag{6.18}$$

where θ is the porosity term representing effective flow area, d is the vegetation diameter and N is the number of trees per unit sq m.

6.3.2 Modelling Floodplain Woodland Roughness with Manning's n

Floodplain woodlands are variable environments with many species. The uniformity of trees will depend on the purpose of the woodland. If the wood is intended for production, for construction or biomass purposes, planting may be dense, with trees typically every 0.5 m. Where the woodland is not intended for production, trees are generally more sparsely distributed. Depending on whether the land is productive or for ecological and environmental purposes will also affect the roughness.
The drag area parameters (C_dA) of the tree saplings measured in Chapter 5 have been used here to derive an equivalent Manning's n roughness. This approach is modified from the conversion in Fathi-Maghadam & Kouwen (1997).
The drag area parameter (C_dA) can first be expressed as the Darcy-Weisbach friction factor f. Equation 6.19 expresses f in terms of shear stress as follows:

$$f = 8\left(\frac{U_*^2}{U_0^2}\right) \tag{6.19}$$

where U is the free stream mean velocity, and U_* is the shear velocity. The boundary shear stress τ_0 can be related to the drag force exerted on the individual tree, by consideration of a unit area of ground a, giving:

$$\tau_0 = \frac{F_d}{a} = \frac{1}{2a} C_d A N \rho U_0 U_B + \frac{\gamma}{a} \tag{6.20}$$

where τ_0 is the boundary shear stress, F_d is the force exerted by one tree, a is the unit area of ground, C_dA is the drag area parameter encompassing both the drag coefficient C_d and the projected area A_p, N is the number of trees per unit area, ρ is the unit density of fluid, U_0 is the mean free stream velocity, U_B is the velocity parameter and F_γ is the stiffness intercept that relates to the rigidity of the tree. Bed friction is neglected. Both the drag area parameter (C_dA) and the stiffness force (F_γ) are obtained for different trees from the data in Chapter 5. Note that the drag force is proportional to the free-stream streamwise velocity (U_0). This is in contrast to the standard relationship for a rigid body where the drag force (F) is proportional to the square of velocity. Dimensional similarity is maintained through the addition of the velocity factor term (U_B). The data for the *Salix* trees has been used in this example. The properties of the *Salix* specimens are presented in Table 6.1.

Test	**Height m**	**1st Quartile**
S1	2.100	24.68
S2	2.400	21.36
S3	3.950	40.12
S4	2.000	16.06
S5	3.600	14.25
S6	3.200	11.95
S7	2.300	19.40
S8	3.000	17.13
S9	3.600	22.50
S10	3.240	31.27
S11	3.500	17.94
S12	4.100	20.80
Average	**3.170**	**21.63**

Table 6.1: Salix specimen lengths and main stem diameters at 1st Quartile height

The boundary shear stress is directly related to the shear velocity by:

$$\tau_0 = \rho U_*^2 \tag{6.21}$$

where τ_0 is the boundary shear stress, ρ is the fluid density, U_* is the shear velocity. Using Equations 6.19,6.20 and 6.21, f can be obtained in relation to C_dA, given by:

$$f = \frac{\rho C_d A N U_B U_0 + \gamma}{2a} \frac{8}{\rho U_0^2} \tag{6.22}$$

where f is the Darcy-Weisbach friction factor, ρ is the fluid density, C_dA is the drag area parameter, N is the number of trees per sq. m, U_0 is the mean fluid velocity and a is the unit ground area. Through consideration of a control volume of fluid with a unit area of 1 m^2 and balancing momentum under uniform flow conditions, the average boundary shear stress experienced is expressed as:

$$\tau_0 = \rho g R S \tag{6.23}$$

where τ_0 is the boundary shear stress, ρ is the fluid density, g is the gravitational constant, R is the hydraulic radius and S is the bed slope. Conversion to Manning's n is then possible by considering the Chezy equation:

$$C = \frac{R^{1/6}}{n} \tag{6.24}$$

where C is the Chezy coefficient, R is the hydraulic radius and n is Manning's n. Using Equations 6.19,6.21 and 6.23, the Chezy coefficient (C) can be related to the Darcy-Weisbach friction factor f:

$$C = \sqrt{\frac{8g}{f}} \tag{6.25}$$

where C is the Chezy coefficient, g is the gravitational constant and f is the Darcy-Weisbach friction factor. Equation 6.22 can be substituted into Equation 6.26. In a wide shallow flow areas, such as a floodplain, the hydraulic radius (R) can be assumed to be equal to the flow depth (h), therefore n can be related to C_dA using:

$$n = \sqrt{N \left(\frac{4 C_d A U_B}{U_0} + \frac{8 F_\gamma}{\rho V^2} \right) \left(\frac{h^{1/3}}{8g} \right)} \tag{6.26}$$

where n is Manning's n, N is the number of trees per m^2, C_dA is the drag area parameter, U_B is the velocity coefficient with a value of 1.0. U_0 is the mean fluid velocity, F_γ is the stiffness intercept, ρ is the fluid density, and h is the flow depth.

Equation 6.26 is dimensionally inhomogeneous, and must be applied with units of m, kg and s. The formula is only applicable for fluid velocities in Zone B of deformation, above approximately 1 m/s. Below this velocity, the bending behaviour of trees under consideration falls into the Zone A of deformation, where the variation between drag force and velocity is no longer linear. For more detail on the zones of deformation, please refer to Chapter 5. It can be seen that Manning's n is proportional to the flow depth and inversely proportional to velocity. A simplified version of Equation 6.26 can be obtained by excluding the second term in the first bracket. The term $\frac{8F_L}{\rho U_0^2}$ will only become significant for velocities below $U_0 = 1\ m/s$. The simplified version of Equation 6.26 is given as:

$$n = \sqrt{\left(\frac{NC_dAU_By^{1/3}}{2gU_0}\right)} \tag{6.27}$$

Two planting densities are to be considered, broad leaf plantations and biomass plantations. Tables 6.2 and 6.3 presents n values calculated for combinations of depth and velocity, based on the mean foliated drag area parameter of $C_dA = 0.203\ m^{-2}$, calculated from the *Salix* trees in Chaper 5 section 5.6.2.1. The defoliated drag area parameter is obtained using:

$$C_dADefoliated = (1 - LC)FoliatedC_dA \tag{6.28}$$

where LC_{mean} is the mean percentage contribution of leaves to C_dA in Zone B, LC_{mean}=0.26. The defoliated C_dA is therefore C_dA=0.150 m^{-2}. The maximum and minimum values are also presented.

Depth	U = **1** m/s			U = **2** m/s			U = **3** m/s		
y	**LL**	μ	**UL**	**LL**	μ	**UL**	**LL**	μ	**UL**
0.5	0.015	**0.034**	0.054	0.013	**0.250**	0.039	0.011	**0.021**	0.032
1.0	0.017	**0.038**	0.060	0.015	**0.028**	0.043	0.013	**0.023**	0.036
1.5	0.019	**0.040**	0.065	0.016	**0.030**	0.046	0.014	**0.025**	0.038
2.0	0.019	**0.042**	0.068	0.017	**0.032**	0.049	0.014	**0.026**	0.040

Table 6.2: Manning's n values for juvenile *Salix* Broad leaf Plantation, λ = 0.167 m^{-2}. Mean μ, Lower Limit LL, Upper Limit UL

Depth	U = **1** m/s			U = **2** m/s			U = **3** m/s		
y	**LL**	μ	**UL**	**LL**	μ	**UL**	**LL**	μ	**UL**
0.5	0.106	**0.181**	0.274	0.075	**0.128**	0.193	0.062	**0.105**	0.158
1.0	0.120	**0.204**	0.307	0.085	**0.144**	0.217	0.069	**0.118**	0.177
1.5	0.129	**0.218**	0.328	0.090	**0.154**	0.232	0.074	**0.126**	0.190
2.0	0.134	**0.229**	0.345	0.095	**0.162**	0.244	0.077	**0.132**	0.199

Table 6.3: Manning's n values for *Salix* Biomass Plantation, $\lambda = 4\ m^{-2}$. Mean μ, Lower Limit LL, Upper Limit UL

The bottom friction is accounted for separately from the vegetation with the Chezy coefficient C:

$$C = -18 \times 4log10\left(12\frac{k}{H}\right) \tag{6.29}$$

Where C is the Chezy coefficient, k is the roughness length and H is the total water depth. The depth-averaged eddy viscosity ϵ to close the turbulence was calculated during each time step of the simulation according to the following depth-mean formation

$$\epsilon = C_e\frac{H}{C}\sqrt{g\left(\frac{p^2+q^2}{H}\right)} \tag{6.30}$$

Where C_e is assumed to have a value of $C_e = 1.0$, H is the total flow depth, C is the Chezy coefficient, g is the gravitational acceleration, p is the discharge per unit width in the x-direction and q is the discharge per unit width in the y-direction.

6.3.3 Finite Difference and Numerical Representation

Various numerical methods can be applied to solve the governing equations. Bates et. al. (2005) provide descriptions and limitations for each of the three main approaches: finite difference, finite element and finite volume.

DIVAST is a finite difference model, and Falconer (1993) notes that this numerical technique has an advantage in the analysis of free surface and time-dependent flows. Within a finite difference model, the governing equations are replaced by finite difference versions. The domain is discretised into a regular grid, and the model solves the partial difference equations iteratively.

The Alternating Difference Implicit (ADI) scheme drives the numerical solution scheme within DIVAST. This requires each time step to be subdivided into two half-time steps, with each of the two dimensions of the domain applied consecutively within each time step. This creates a more stable numerical process. Thus, on the first half time step, all x-direction variables (velocity and water elevation) are solved implicitly, whilst the y-direction variables are solved explicitly. On the second time step, all y-direction variables are solved implicitly, whilst the x-direction variables are solved explicitly.

With specified boundary conditions, the finite difference equations are able to be solved via Gauss elimination and back substitution (Westwater, 2000).

The variables are based on a space-staggered grid. Water surface elevation is

specified at the grid centre, and depths and velocities are given at the centres of the sides of each grid.

6.4 Methodology of DIVAST Development

6.5 Establishing Flume Code Bed Roughness and Weir Equation

Before the investigation into the effect of single stem against the multi-stem model trees, it was necessary to ensure the numerical code would represent the bed, side walls and boundaries accurately. The data from Experimental Series A (Section 3.5) includes the results for uniform flow relationships in the empty flume, so these stage - discharge data were used for the purposes of boundary roughness and weir calibration.

6.5.1 Bed Roughness Calibration Data

To commence the investigation, the computed Manning's n values were determined by applying the Manning's equation to the results.

Discharge Q l/s	Depth mm	n
11.1	44.6	0.018
17.7	57.0	0.017
21.2	67.3	0.017
29.3	83.9	0.019
45.2	87.3	0.013
56.1	88.8	0.011

Table 6.4: Empty Flume Experimental Results

While the numerical DIVAST FLUME model was designed to replicate the real flume in the hydraulics laboratory at Cardiff University, a true match presents difficulties. The 10 m flume had insufficient length to achieve fully developed flow, and the values in Table 6.4 assume fully developed flow. However, these values provide a guide and a starting point for the investigation.

Selected measured results for the empty flume, plus the results from the fitted power relationship obtained for the results are shown in Table 6.5.

Q l/s	Measured Depth mm	Smoothed Depth mm	n1	n2
11.1	44.6	51.3	0.018	0.019
17.7	57.0	60.4	0.017	0.021
21.2	67.3	65.4	0.017	0.020
29.3	83.9	73.8	0.019	0.017
45.2	87.3	87.0	0.013	0.011
56.1	88.8	94.5	0.011	0.008

Table 6.5: Manning's n from Measured vs. Smoothed Data

6.5.2 Weir Boundary Calibration

Within DIVAST, the weir boundary was treated using the formula suggested by Rehbock:

$$h_1 = \left(\frac{Q}{C_D weir \frac{2}{3} b \sqrt{2g}}\right)^{2/3} \tag{6.31}$$

where h_1 is the depth of flow above the weir, Q is the discharge in m^3/s, $C_D weir$ = Weir Coefficient, b = width of flume and g is the gravitational constant. The weir coefficient was initially calculated using the Rehbock suggested formulation given as:

$$C_D weir = 0.602 + 0.0832 \frac{h_1}{P_1} \tag{6.32}$$

Where $C_D weir$ = Weir Coefficient, b = width of flume, h_1 = depth of flow above weir and P_1 = height of weir. Ackers et. al. (1978) state there are limitations to the use of equations 6.31 and 6.32 and proposes the following constraints:

$$\begin{aligned} 0.03m < \; & h_1 \; < 0.75m \\ b \; & > \; 0.3m \\ P_1 \; & > \; 0.3m \\ \frac{h_1}{P_1} \; & < \; 1.0 \end{aligned}$$

However the conditions found in the empty flume did not fall within the ranges specified. The flow regime was further complicated by the presence of the undulations of the bed. The Rehbock formulation also neglects to take into account

the velocity head. A related weir equation, the I.M.F.T formula (Ackers 1978), was based on data collected in a flume with similar dimensions to the flume used for the scaled array experiments that form part of this study. It also explicitly accounts for the velocity head. According to the I.M.F.T. formula, the weir coefficient is calculated according to the following formula:

$$C_D weir = 0.627 + 0.0180\frac{H_1}{P_1} \tag{6.33}$$

$$H_1 = h_1 + \frac{U^2}{2g} \tag{6.34}$$

where H_1 is the total head, h_1 is the depth of flow above the weir, U is the velocity of flow over the weir and g is the gravitational constant. The criterion for the application of the I.M.F.T. equation follow:

$$H_1 > 0.03\text{m}$$
$$b > 0.2\text{m}$$
$$P_1 > 0.1\text{m}$$
$$\frac{h_1}{P_1} < 2.5$$

The experiments carried out fall within these ranges. Using the settings for stage and discharge for the empty flume and applying equation 6.31, the calculated $C_D weir$ values could be determined. Due to the raised bed, both the flow depth above the raised bed and the true flow depth were used to calculate $C_D weir$ values and are displayed in Table 6.6 alongside $C_D weir$ values calculated from the data.

	Raised	**Raised**	**True**	**True**	
Q m^3/s	$C_D weir$ **R**	$C_D weir$ **I**	$C_D weir$ **R**	$C_D weir$ **I**	$C_D weir$ **D**
11.1	0.737	0.663	0.674	0.646	0.390
17.7	0.736	0.662	0.685	0.649	0.420
21.2	0.765	0.668	0.703	0.653	0.410
29.3	0.786	0.675	0.718	0.657	0.470
45.2	0.820	0.688	0.740	0.665	0.570
56.1	0.834	0.696	0.749	0.670	0.640

Table 6.6: $C_D weir$ calculated from Rehbock (R) and I.M.F.T. (I), both from Raised Bed and True Bed $H1/P1$ ratios, and from measured data (D)

It can be seen that varying the formulation between The Rehbock and the I.M.F.T., and using the raised or true bed depth, then $C_D weir$ lies within the range of 0.65

to 0.834, however no scheme matches the $C_D weir$ values as calculated from (6.31). This discrepancy may be due to the weir becoming drowned, perhaps as a result of streamline disturbance from the step down from the raised bed to the true bed shortly before the weir. Using the linear relationship between $\frac{H_1}{P_1}$ and $C_D weir$, the data collected was used to derive the unique relationship for the data collected for the empty flume. In Figure 6.2, it can be seen that the linear relationship is maintained, and the resulting equation is given below:

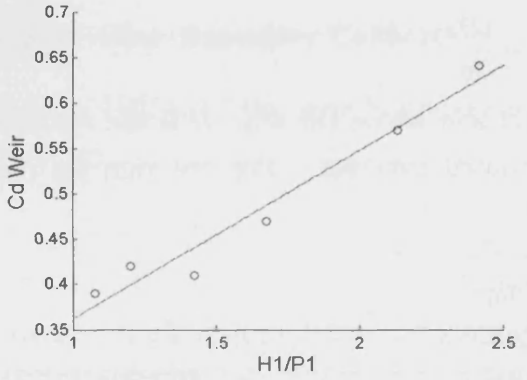

Figure 6.2: Linear Correlation of Measured Data for Empty Flume. Relationship follows $C_D weir$=0.18 + 0.19 x $\frac{H_1}{P_1}$

$$C_D weir = 0.18 + 0.19x\frac{H_1}{P_1} \tag{6.35}$$

To validate this model, the equation was checked with the vegetated flume data. When the vegetated flume model was run using Equation (6.35), the model did not match the measured values from the experimental series, therefore the same approach was adopted as for the empty flume. Optimal values of $C_D weir$ were found and then related to the ratio $\frac{H_1}{P_1}$. However, with the vegetated flume data, there did not appear to be a correlation between $\frac{H_1}{P_1}$ and $C_D weir$. Individual $C_D weir$ values were instead determined for each flow condition.

6.6 Single Stem Modelling

Once calibrated to simulate the depth-discharge relationship of the flume, DIVAST was then employed to model the roughness elements. The dowel model trees were an average diameter of 25.0 mm, with a longitudinal to lateral spacing ratio of 1 : 0.58. The dowels were placed at different staggered densities of 8.818 m^2, 19.841 m^2 and

80.645 m^2. For more details on the experimental conditions please refer to Chapter 3.

DIVAST allows two methods of representing vegetation. Firstly, the compound Manning's n n_c can be determined, including a combination of bed roughness n_b and vegetative roughness n_v after the method in Chow (1959) where $n_b + n_v = n_c$. Secondly, the model includes the drag force effect directly for the cylinders in the form of an explicit drag force. Both methods benefit from the use of porosity to block out the flow area. By calculating both and comparing with the theoretical values obtained in Chapter 3, a comparison of the validity of the respective methods can be derived, both theoretical and numerically.

6.6.1 Modelling vegetation with Manning's n

The Manning's n_c values that produce uniform flow within the DIVAST flume code were compared with the values as calculated from the comparative density experiments in Chapter 3.

Within DIVAST the lower weir coefficient was first checked to obtain the correct downstream level. Manning's n values were then varied to obtain the uniformly deep flow profile obtained from the measured data. The results are shown in Table 6.7.

	Discharge	**Weir**	**Depth**	**Model n_c**	**Measured n_c**	**Error**
DL	0.010	0.047	0.059	0.040	0.032	25
DL	0.020	0.078	0.106	0.050	0.041	22
DL	0.030	0.102	0.142	0.050	0.043	17
DL	0.040	0.119	0.167	0.045	0.041	11
DL	0.050	0.127	0.179	0.038	0.036	5
DM	0.050	0.039	0.037	0.040	0.029	36
DM	0.010	0.060	0.078	0.060	0.046	31
DM	0.020	0.127	0.161	0.100	0.076	32
DM	0.030	0.200	0.244	0.120	0.099	21
DH	0.005	0.071	0.072	0.130	0.089	47
DH	0.010	0.150	0.153	0.200	0.142	41
DH	0.015	0.225	0.233	0.260	0.179	45
DH	0.020	0.300	0.313	0.320	0.207	55

Table 6.7: Model vs Measured Manning's n values

For many 1-D and 2-D depth integrated models it is common to use Manning's n values to represent land use effects. However, it can be seen clearly here that there is a chance of a relatively large degree of error being made should Manning's n values

derived from measured vegetation data be put directly into a numerical model. The reason for this is clear. There is no accounting for the blockage effect - the true flow area will be markedly reduced in the experimental data by the presence of dowels, but there is no equivalent compensatory effect within most widely available numerical models. There is also a higher degree of turbulence within a vegetated water column. As a result, to achieve an equivalent resistance effect, the Manning's n value in the model must be artificially raised. Although this is a scientifically unsatisfying method, it may be the only option where a reasonable estimate of the blockage effect cannot be effectively calculated - within a reach for example, where only water depth and discharge can be monitored.

The second option available is to obtain a Manning's n value based on actual flow area, and run DIVAST with the inclusion of this blockage effect. If the flow area used in the calculation of Manning's n is reduced with respect to blockage, the equivalent Manning's n will be reduced, particularly for higher values of Manning's n. In Figure 6.3, both the bulk Manning's n number n_B and the Manning's n number with porosity factored in n_p are plotted against the Manning's n number as derived from the experiments earlier.

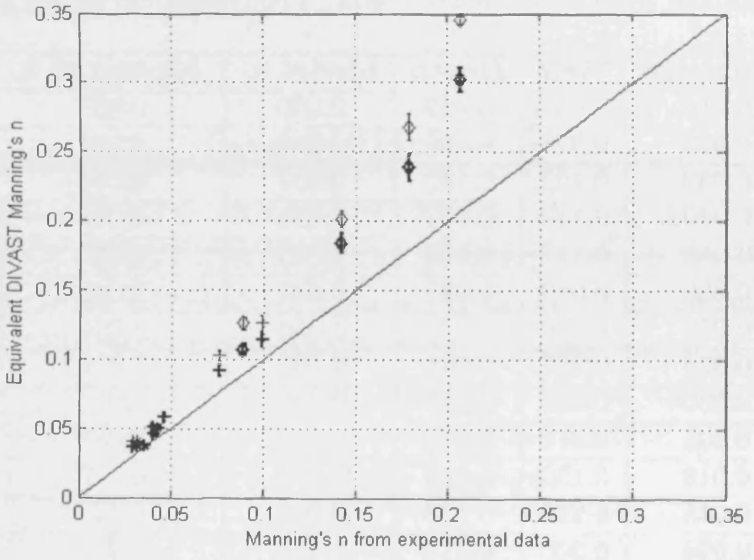

Figure 6.3: Comparison of Measured n vs. DIVAST Manning's n

Full values including upper and lower limits can be found in Table 12 in the appendix. Further agreement could be improved by adjustments to the eddy viscosity value to represent the increased degree of turbulence, as well as the change in slip condition

to better represent the velocity gradient as the flow passes the dowels.

6.6.2 Modelling Vegetation with Cylinder Drag C_d

Representing the vegetation as cylinders, as opposed to an equivalent roughness is more reflective of the physics and includes a definitive link between vegetation and porosity throughout the height of the water column. The cylinder drag force equation is a physically based model to use to represent cylindrical vegetative forms. The bed roughness values derived earlier are used in the model and the modified drag coefficient (C_dA) obtained i.e. the combined effect of the planting density λ and interaction effects due to flow conditions, for comparison with the derived values from the data. A similar approach to the Manning's n review in the previous section has been adopted. The boundary friction is often neglected in such an analysis, as it is assumed that any vegetation will have a markedly bigger impact on the flow structure in comparison with that due to a smooth boundary. The C_d value for a smooth flat plate parallel to the direction of flow is generally assumed to be about 0.001, although this depends on bed roughness. It is likely that the boundary C_d will have a larger value than this due to the inhomogeneity of the bed. To determine this, the boundary C_d was determined from a force balance approach. Table 6.8 shows the C_d values as calculated from the no vegetation flume.

Discharge l/s	Depth mm	Velocity m/s	Re	C_d
0.005	0.021	0.196	4167	0.011
0.010	0.038	0.219	8333	0.015
0.020	0.065	0.257	16667	0.017
0.030	0.083	0.302	25000	0.016
0.040	0.091	0.365	33333	0.012
0.050	0.091	0.459	41667	0.007

Table 6.8: C_{db} with no vegetation, skin friction drag only

Taking the average boundary C_{db} as 0.013, this was then subtracted from the C_{dv} values calculated from the experimental data to give the drag force as it relates to vegetation alone. The bed boundary roughness was represented by a Manning's n value of 0.018, which was obtained from *Chapter 3* investigations into the roughness factors for the case with no vegetation in the flume.

The measured C_{dv} values for each flow condition from the smoothed dataset are shown in Table 6.9, alongside the Model C_{dv} that gave the appropriate level of resistance. This relationship is more clearly depicted by Figure 6.4.

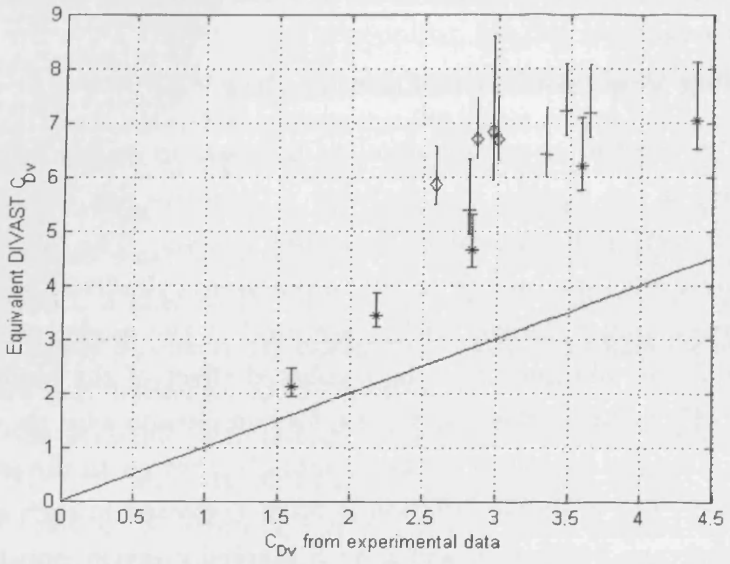

Figure 6.4: Comparison of Measured C_{dv} vs. DIVAST C_{dv}

From the investigation into roughness factors, the magnitude of the limitation of using experimental data directly in models could be confirmed.

Vegetation	Q	weir	h	C_{dv}	Model C_{dv}	Model C_{dv} LL	Model C_{dv} UL
DL	0.010	0.047	0.059	4.38	6.515	5.98	7.05
DL	0.020	0.078	0.106	3.58	5.760	5.32	6.20
DL	0.030	0.102	0.142	2.83	4.325	4.00	4.65
DL	0.040	0.119	0.167	2.18	3.215	3.00	3.43
DL	0.050	0.127	0.179	1.60	1.945	1.77	2.12
DM	0.005	0.039	0.037	2.81	4.925	4.46	5.39
DM	0.010	0.060	0.078	3.34	5.980	5.55	6.41
DM	0.020	0.127	0.161	3.47	6.785	6.35	7.22
DM	0.030	0.200	0.244	3.64	6.725	6.28	7.17
DH	0.005	0.071	0.072	2.58	5.495	5.14	5.85
DH	0.010	0.150	0.153	2.86	6.325	5.95	6.70
DH	0.015	0.225	0.233	2.97	5.935	5.05	6.82
DH	0.020	0.300	0.313	3.01	6.300	5.90	6.70

Table 6.9: Measured C_{dv} versus model C_{dv} using vegetation flume data, LL = Lower Limit, UL = Upper limit

6.7 Modelling Floodplain Woodland at Reach Scale

6.7.1 Introduction

The development and refinement of numerical models of rivers and catchments has brought increasing benefits as the processing power of computers has increased to allow more accurate models to be created. Areas at risk of flooding can be identified, point source and discrete pollutant dispersal and processing can be predicted. The upstream and downstream effects of channel modifications can be assessed in advance and before costly hard engineering structures are constructed.
As computer processing power has increased, then grid sizes have become smaller and the topography and bathymetry have both been represented more accurately in models. However, there remains a large degree of uncertainty attached to the modelling of vegetated flows. The natural environment presents challenges to the numerical modeller. Vegetation characteristics can alter from month to month, and a large range and placement of different species can occur over a small area.
The River Laver lies West of Ripon in North Yorkshire. Figure 6.5 shows the River Laver and its siting relative to the town of Ripon. The river drains an area of 75 km^2. A range of landuse is present, from moorland in the upper reaches, to areas of established floodplain woodland, to arable and pastureland. The town of Ripon is situated at the confluence of the Rivers Laver and Skell. In 2000, Ripon experienced severe flooding, as peaks in storm water levels along both the Laver and the Skell coincided in Ripon.

6.7.2 The Ripon Multi-Objective Project

The Ripon Multi-Objective Project was aimed at investigating the potential for delivering flood risk management through land use and land management changes at a catchment scale, whilst also pursuing resource protection, biodiversity and access opportunities (Posthumus et al. (2006)). The project was initiated in 2004 and funded by DEFRA. The Ripon MOP worked with landowners and local stakeholders to identify changes in landuse that could alleviate flooding. At a stakeholder workshop in March 2006, factors thought to contribute to flooding were identified. Changing climate conditions and land use were identified by most stakeholders as key factors. In the opinion of the participants, the loss of floodplains, and constriction of natural channels was cited as a cause of increasing run-off.
A fundamental part of the Ripon Multi-Objective Project was the promotion of

schemes to promote floodplain woodland through Environmental Stewardship, a scheme by which landowners receive a stipend to create and maintain an area of floodplain woodland on their land. The value of the stipend is linked to the benefit derived from the floodplain woodland (Executive 2002). Benefits cited include:

- Improving timber quality
- Improving woodland biodiversity
- Reducing deer numbers
- Landscape improvement
- Native woodlands
- Developing community involvement
- Developing alternative systems to clear-felling
- Woodland recreation

If alleviation of downstream flooding from restored floodplain woodlands can be realised, as proposed by Anderson et al. (2006), such a benefit may promote the distribution of a higher stipend rate, so encouraging the conversion to floodplain woodland. Possible areas of floodplain land suitable for conversion to floodplain woodland along the River Laver were identified.
Phase 1 of the Ripon Multi-Objective Project was completed in 2007, and Phase 2 commenced shortly after. As yet, there are no plans for floodplain woodland construction due to a lack of landowner consent. More details of the project can be found in Posthumus et al. (2006).

6.7.3 Scope of the Chapter

This Chapter presents the modelling results for 1-D and 2-D models of the River Laver. Topography and boundary conditions for each model are presented. Calibration data were taken from the flood of October 2005, where the River Laver was modelled in its existing condition. Annual Maxima data were obtained from HiFlows UK, and a series of return period floods have been derived. Various floodplain woodland planting locations and densities (based on those selected for the Ripon MOP) were introduced, with a view to ascertaining consequent impacts on the peak and duration of floodwaves.

(a)

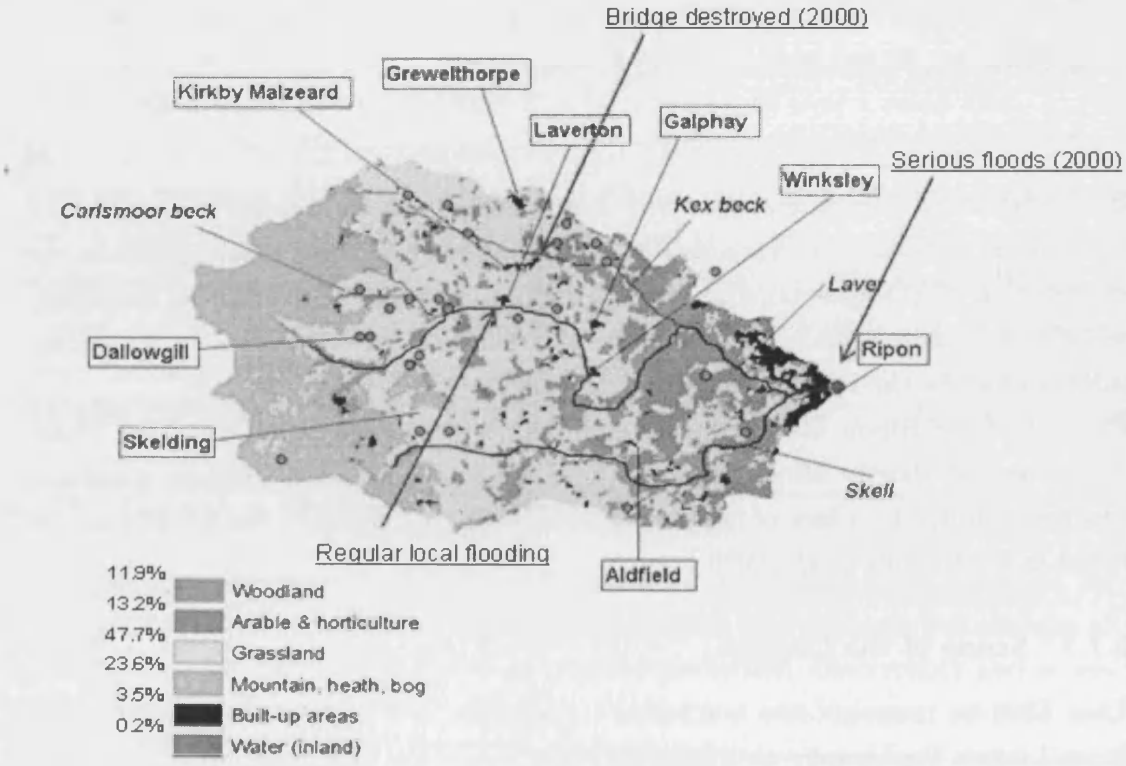

(b)

Figure 6.5: (a)Location Map of Laver, the upland reach covering steep moorland has an average bed slope of 1:50, the middle and lower reach has an average bed slope of between 1:70 and 1:100./ (b)Landuse and flood damage 2000 (Posthumus et al. 2006).

6.7.4 Downstream Rating Curve and Peak Flows

Within the town of Ripon, there is a gauging station on the River Laver, before the confluence with the River Skell. Depths and discharges are monitored daily at this gauging station, providing both a rating curve for the downstream boundary, and a record of annual peak flows dating back to 1978, from which approximation return period floods can be derived. The rating curve plotted from daily flows is presented in Figure 6.6, where the rating equation (black line) is given as:

$$\zeta = 0.141Q^{0.625} + 29.599 \tag{6.36}$$

Where ζ is the stage in mAOD, and Q is the discharge in m^3/s. The rating curve can be used as a boundary condition in the modelling stage.

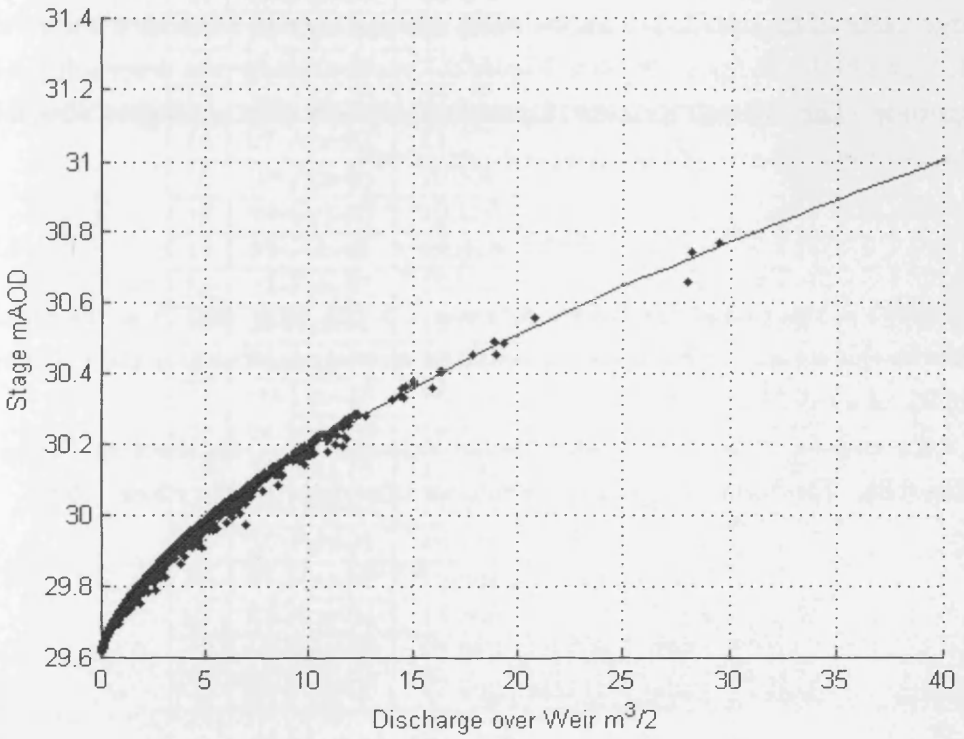

Figure 6.6: Rating Curve at Gauging Station 27059 River Laver at Ripon

The peak flows measured at Ripon are presented in Figure 6.7 for each Water Year (the period running from the beginning of October in the previous year to the end of September in the year of consideration). The QMED Flood was recorded as 22.0

m^3/s (HiFlows UK 2007).

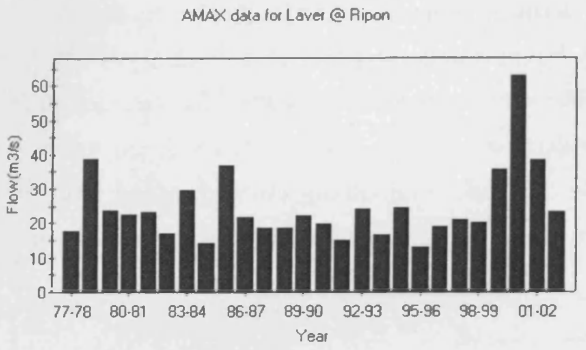

Figure 6.7: Annual Maxima at Gauging Station 27059 River Laver @ Ripon

The T-year flood with peak discharge Q_T can be determined, where Q_T is the peak discharge likely to be equalled or exceeded on average once in a specified period of T years (Shaw 1994). The peak flows in Figure 6.7 were rearranged in descending order of magnitude. The Weibull formula (Equation 6.37) was then applied to obtain the probability of exceedence of the observed peak flows.

$$P(X) = \frac{r}{N+1} \tag{6.37}$$

where $P(Xr)$ is the probability of exceedence, r is the rank, and N is the number of events in the series. Table 6.10 presents the annual maxima and the calculated probability of exceedance $P(Xr)$.
These data can be fitted using the Gumbel extreme value distribution (Type 1) Equation 6.38. The following procedure follows that described in Shaw (1994).

$$F(X) = exp[-e^{-b(X-a)}] \tag{6.38}$$

$$a = \hat{\mu_Q} - \frac{\gamma}{b} \tag{6.39}$$

$$b = \frac{\pi}{\hat{\sigma_Q}\sqrt{60}} \tag{6.40}$$

Where $F(X)$ is the probability of the annual maximum Q $\leq$ X, $F(X) = 1 - P(X)$. a and b are related to the moments of the population, $\hat{\mu_Q}$ is the sample mean, γ is a constant at γ=0.5772, $\hat{\sigma_Q}$ is the sample variance. For the gauging station annual

r	Date	Q m^3/s	y m	$P(X)$	$F(X)$
1	02-Nov-00	62.680	1.858	0.033	0.967
2	28-Dec-78	38.636	1.390	0.067	0.933
3	02-Aug-02	38.452	1.386	0.100	0.900
4	17-Apr-86	36.946	1.353	0.133	0.867
5	04-Jun-00	35.466	1.320	0.167	0.833
6	09-Dec-83	29.677	1.185	0.200	0.800
7	31-Jan-95	24.671	1.059	0.233	0.767
8	15-Sep-93	24.215	1.047	0.267	0.733
9	27-Dec-79	23.537	1.029	0.300	0.700
10	03-Jan-82	23.462	1.027	0.333	0.667
11	30-Dec-02	23.350	1.024	0.367	0.633
12	22-Mar-81	22.609	1.004	0.400	0.600
13	30-Jan-90	22.132	0.991	0.433	0.567
14	07-Apr-87	21.878	0.984	0.467	0.533
15	08-Jan-98	20.836	0.955	0.500	0.500
16	24-Oct-98	20.165	0.936	0.533	0.467
17	23-Feb-91	19.815	0.926	0.567	0.433
18	21-Feb-97	19.055	0.904	0.600	0.400
19	16-Apr-05	19.055	0.904	0.633	0.367
20	10-Aug-04	19.021	0.903	0.667	0.333
21	09-Feb-88	18.714	0.894	0.700	0.300
22	24-Mar-89	18.477	0.887	0.733	0.267
23	28-Jan-78	17.739	0.865	0.767	0.233
24	20-Dec-82	17.014	0.843	0.800	0.200
25	27-Feb-94	16.786	0.836	0.833	0.167
26	31-Mar-92	15.041	0.781	0.867	0.133
27	03-Nov-84	14.365	0.759	0.900	0.100
28	02-Apr-06	13.972	0.746	0.933	0.067
29	02-May-96	12.965	0.712	0.967	0.033

Table 6.10: Flood Frequency Analysis

maxima data for the River Laver, $\hat{\mu_Q} = 23.818\ m^3/s$ and $\hat{\sigma_Q} = 10.300$. The Q_T T-return period flood has been taken directly from the data, and these values are presented in Table 6.10.

6.7.5 Calibration Data: October 2005 Flood

The flood of October 2005 was used to calibrate models for the River Laver. The flood lasted from the 24th until the 29th October. From the rainfall data and the catchment characteristics, a flow - time hydrograph was derived for the upstream boundary. The weir rating curve was used for the downstream boundary. Some inundation on the floodplain occurred during the flood, and so both the channel and floodplain roughness could be checked.

6.8 1-D ISIS Model of the River Laver

6.8.1 Topography Data

The topographic data were taken from 1 m grid LiDAR data collected in 2005. Sections perpendicular to the channel direction were selected from the data at approximately 100 m intervals along the reach, extending to cover both floodplains. The downstream boundary was located along the line of the weir. Due to a high bed gradient in the upper portion of the reach at 1:100, the location of the upstream boundary was selected as a point upstream of Ings Bridge. From Ings Bridge to the downstream weir, the gradient is constant at approximately 1:300. Bathymetric data were added to the model based on the recorded water depth at Galphay Mill on the day of the LiDAR sampling, 9th February 2006, where h=0.184. No other locations within the model boundary had water monitoring data for that date. However, by comparing a date with a similar flow depth on 30th September 2006, where Galphay Mill h=0.180, the depth at Ings Bridge DS was h=0.288, and the depth at Ings Bridge US was h=0.230. From observation at the water level gauging station sites at low flows, the water depths were of the order of 0.200 m, so the values of water depth recorded on 30th September 2006 were assumed to be an appropriate modification to the Lidar data. However, further cross-sectional data are required to improve the model in the future. The bathymetric modification values were added to the lowest points in each cross section, using the value of the nearest measured point.

6.8.2 Boundary Conditions

The upstream boundary for the calibration comes from an FEH generated hydrograph measured from recorded rainfall at the River Laver weir at Ripon. The downstream boundary was the rating curve at the weir location (430131E 471013N).

6.8.3 Calibration of 1D model

The event of October 2005 was used to calibrate the 1D model of the River Laver. Discharge data were obtained from the Gauging Station 27059 i.e. the River Laver at Ripon. The thick black lines in Figures 6.8 to 6.12 presents the recorded stage (m AOD) at two locations, namely, Ings Bridge D/S (426246E 471026N) and Galphay Mill (426770E 471998N). The stage is the recorded stage from pressure transducers at each location. The model was run for the flood duration of 47.5 hrs, beginning at 10:00 am 24th October 2005. The model was run first under the steady conditions to set up the initial conditions, and the model was then run for unsteady conditions using an adaptive time step, with a maximum time step of 5 s and a minimum time step of 1 s.

It was observed for some of the existing floodplain woodland areas that a large amount of dead wood had collected in the river channel. This additional roughness occurred only in wooded areas, with the channel in partially wooded and arable areas clearer of debris. Thus, the model was run again, with different roughnesses in the wooded area compared to the arable areas. The four roughness coefficients are:

- n_{ca} Channel Roughness in arable areas
- n_{fa} Floodplain Roughness in arable areas
- n_{cw} Channel Roughness in woodland areas
- n_{fw} Floodplain Roughness in woodland areas

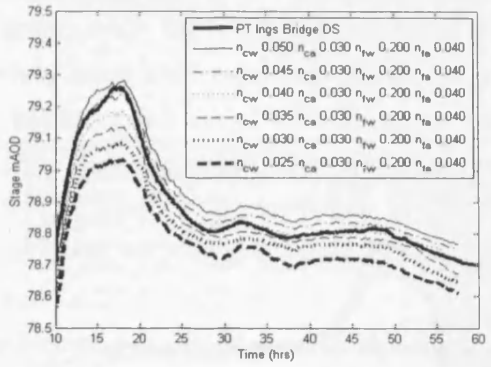

(a) Ings Bridge DS

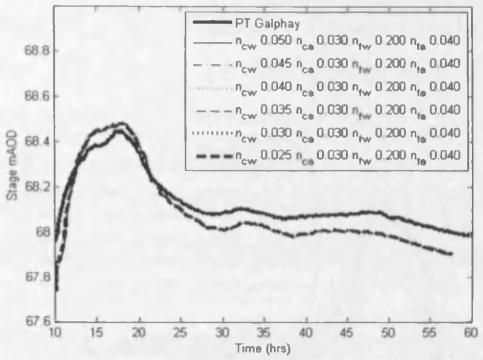

(b) Galphay

Figure 6.8: Calibration1

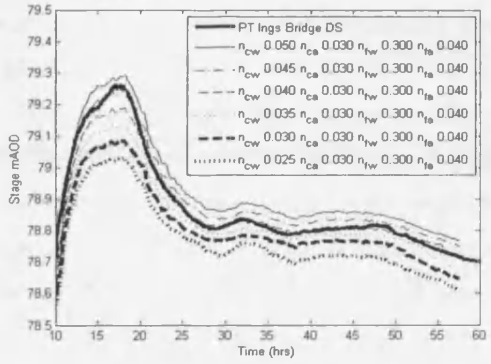

(a) Ings Bridge DS

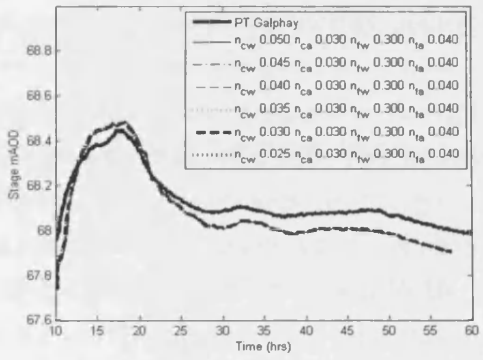

(b) Galphay

Figure 6.9: Calibration2

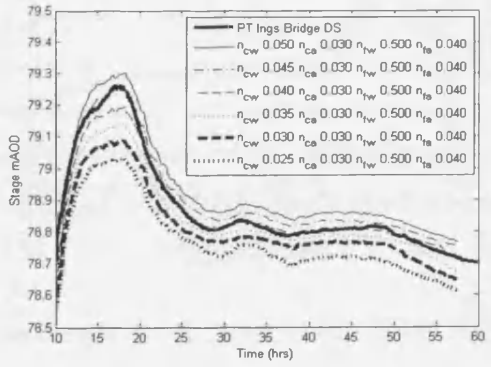

(a) Ings Bridge DS

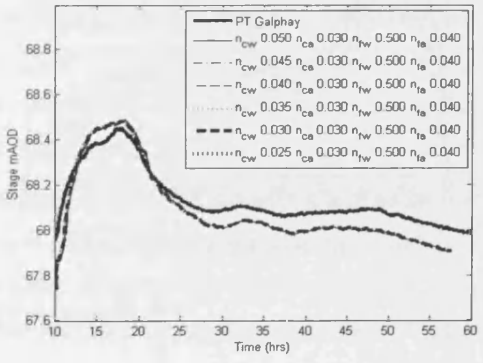

(b) Galphay

Figure 6.10: Calibration3

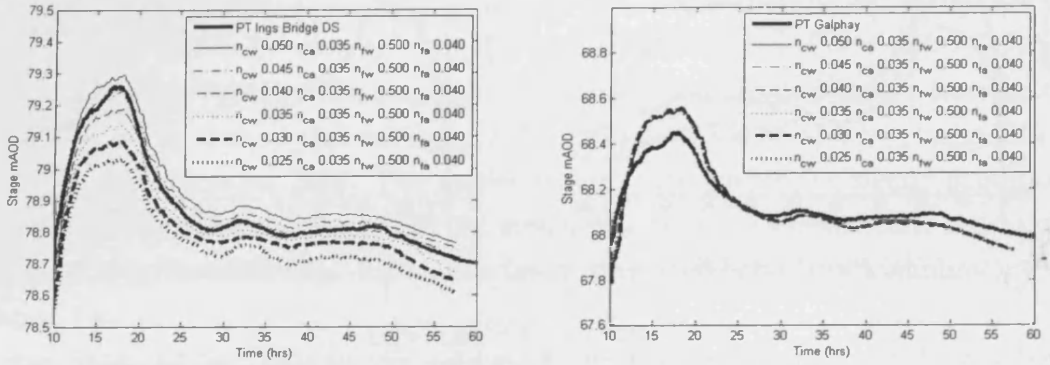

(a) Ings Bridge DS (b) Galphay

Figure 6.11: Calibration4

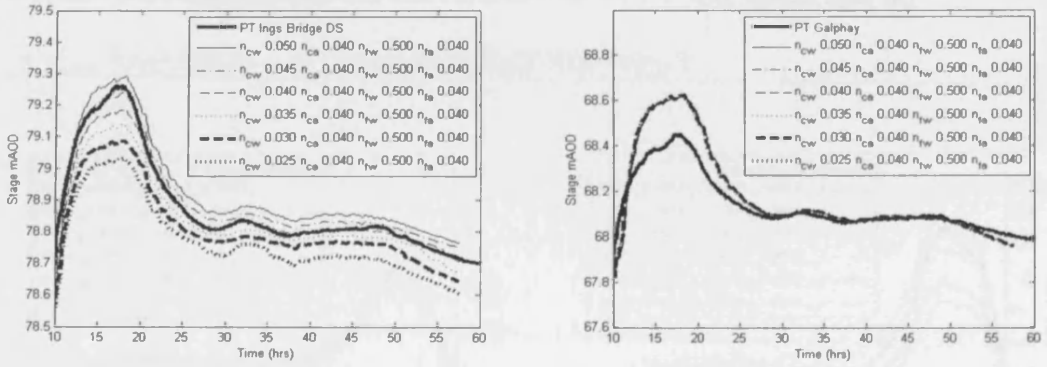

(a) Ings Bridge DS (b) Galphay

Figure 6.12: Calibration5

Results from the calibration exercise are presented in Figures 6.8 to 6.12. For each Figure, only the woodland channel roughness n_{cw} was varied. Other roughness values were kept constant within each Figure. In Figure 6.8 (a), the most closely predicted peak stage was found to occur for a channel Manning's value (n_{cw}) of 0.045. Post-peak, the best prediction was for for a channel Manning's value (n_{cw}) of 0.040. There was no variation at Galphay Mill (6.8 (b)), with all woodland channel roughness variations overpredicting the peak stage, and underpredicting post-peak stage.

In Figure 6.9 (a), the most closely predicted peak stage across the floodplain was found to occur for a channel Manning's value (n_{cw}) of 0.045. The increased floodplain woodland roughness improved slightly on the previous result given in Figure 6.8 (a). Post-peak, the best prediction was for a channel Manning's value (n_{cw}) of 0.040. There was no variation at Galphay Mill (6.9 (b)), with all woodland channel roughness variations overpredicting the peak stage, and underpredicting post-peak stage.

In Figure 6.10 (a), the most closely predicted peak stage across the floodplain was found to occur for a channel Manning's value (n_{cw}) of 0.045, the increased floodplain woodland roughness improved slightly on the previous results given in Figures 6.8(a) and Figure 6.9 (a). Post-peak, the best prediction was for a channel Manning's value (n_{cw}) of 0.040. There was no variation at Galphay Mill (6.10 (b)), with all woodland channel roughness variations overpredicting the peak stage, and underpredicting post-peak stage. There was no discernible influence of increasing floodplain woodland roughness at Galphay Mill, as can be seen in Figures 6.8 (b), 6.9 (b) and 6.9 (c).

In 6.11 (a), the most closely predicted peak stage across the floodplain was found to occur for a channel Manning's value (n_{cw}) of 0.045. Post-peak, the best prediction was for a channel Manning's value (n_{cw}) of 0.040. There was improved post-peak stage prediction at Galphay Mill (6.11 (b)), however, all woodland channel roughness variations continued to overpredict the peak stage.

In 6.12 (a), the most closely predicted peak stage across the floodplain was found to occur for a channel Manning's value (n_{cw}) of 0.045. Post-peak, the best prediction is for a channel Manning's value (n_{cw}) of 0.040. There was good post-peak stage predictions at Galphay Mill (6.12 (b)), however all woodland channel roughness variations continues to overpredict the peak stage.

Following calibration of the River Laver 1D model to the flood of October 2005, four zonal roughnesses were defined for the existing condition, these are presented

Manning's n	Value	Location	Landuse	Left Bank	Right Bank
n_{ca}	0.040	Channel	Arable	47-16	47-16
n_{cw}	0.043	Channel	Woodland	74-48	74-48
n_{fa}	0.040	Floodplain	Arable	63-27	47-27
n_{fw}	0.500	Floodplain	Woodland	74-62/26-16	74-48/26-16

Table 6.11: October 2005 Flood Calibration: Manning's n zonal roughnesses and node numbers for left and right banks

in Table 6.11

Roughness validation was obtained by modelling the flood of 2nd April 2006. The thick black lines in Figures 6.8 to 6.12 present the recorded stage (m AOD) at two locations, namely Ings Bridge D/S (426246E 471026N) and Galphay Mill (426770E 471998N). The stage was the recorded stage from the pressure transducers at each location. The model was run for the flood duration of 57.5 hrs, beginning at 00:00 on 2nd April 2006. The model was again run first under steady state conditions to set up the initial conditions, and then run for unsteady state conditions using an adaptive time step, with a maximum time step of 5 s and a minimum time step of 1 s.

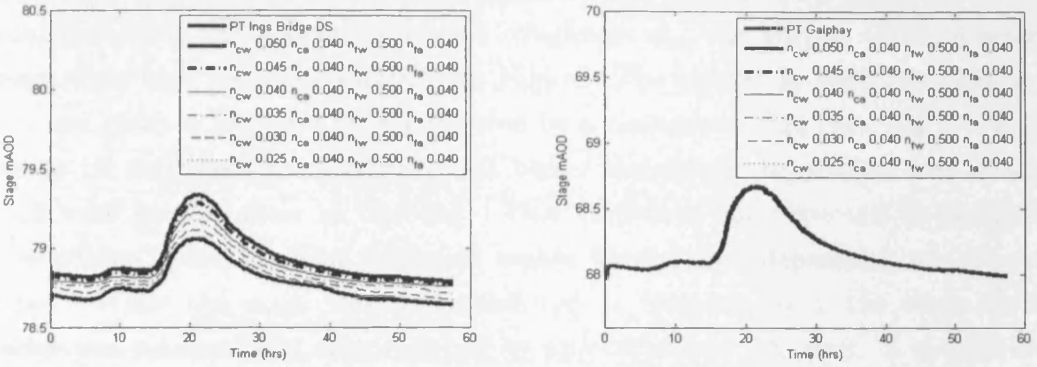

(a) Ings Bridge DS (b) Galphay

Figure 6.13: Validation1

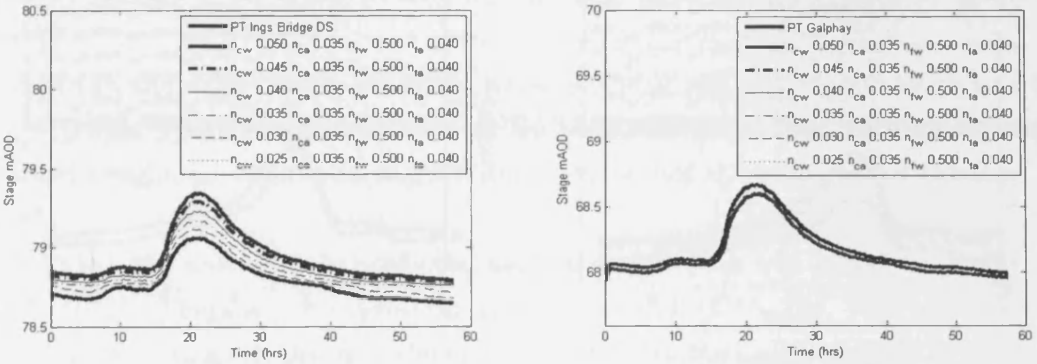

(a) Ings Bridge DS (b) Galphay

Figure 6.14: Validation3

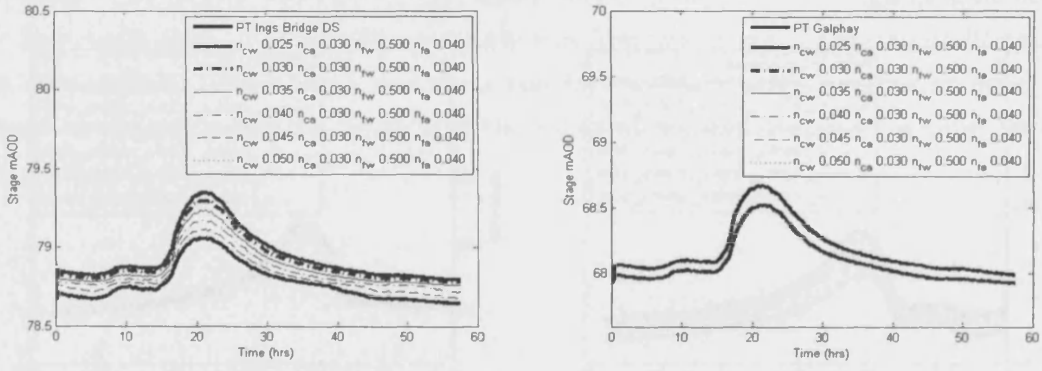

(a) Ings Bridge DS (b) Galphay

Figure 6.15: Validation4

The 1-D model validation results are presented in Figures 6.13 to 6.15. For each simulation, only the woodland channel roughness n_{cw} was varied. Other roughness values were kept constant within each Figure. The closest fit with the calibration data was given in Figure 6.13, represented by a continuous thin line. Some variation was to be expected, as in-stream and bank/ floodplain vegetation conditions in April were sparser than in October. This variation was expected to be greater in woodland areas than on managed arable floodplains, depending on the crops grown. While the stage was well predicted at Galphay Mill, the stage at Ings Bridge was substantially overpredicted by approximately 200 mm. A similar range of roughnesses were investigated for the October 2005 calibration stage and were repeated for the 2004 validation data.

In 6.13 (a), the most closely predicted peak and post-peak was found to occur when $n_{cw} = 0.025$. There was no variation at Galphay Mill (6.13 (b)), with all woodland channel roughness variations predicting the stage at all times of the flood extremely closely.

In 6.14 (a), the most closely predicted peak and post-peak was found to occur when $n_{cw} = 0.025$. There was no variation at Galphay Mill (6.14 (b)), with all woodland channel roughness variations slightly underpredicting the stage at all times of the flood.

In 6.15 (a), the most closely predicted peak and post-peak was found to occur when $n_{cw} = 0.025$. There was no variation at Galphay Mill (6.15 (b)), with all woodland channel roughness variations underpredicting the stage at all times of the flood.

The validation data from the flood of 2nd April 2006 provided a check on the calibration data taken from the flood of October 2005. For both datasets, there was agreement in the roughness of the river channel in arable areas with a value of $n_{ca} = 0.040$. While 0.040 is a high value of Manning's n for a river channel, according to Chow (1959), it is consistent with the presence of dead wood and general sinuosity of the channel. The most appropriate roughness in the woodland area varies from $n_{cw} = 0.043$ in October 2005, to $n_{cw} = 0.025$. This change was thought to be due to seasonal variation of riparian vegetation growth characteristics. The lower value was inconsistent with observed levels of dead wood in the channel, therefore it was thought possible that the pressure transducer at Ings Bridge DS had been moved over the winter months.

Table 6.12 presents the Manning's n results based on both the calibration and validation data. Due to the uncertainty of the woodland channel roughness n_{cw}, the chosen roughness was an average of the October 2005 calibration data giving

Manning's n	Value	Location	Landuse	Left Bank	Right Bank
n_{ca}	0.040	Channel	Arable	47-16	47-16
n_{cw}	0.035	Channel	Woodland	74-48	74-48
n_{fa}	0.040	Floodplain	Arable	63-27	47-27
n_{fw}	0.500	Floodplain	Woodland	74-62/26-16	74-48/26-16

Table 6.12: Post Validation with 2nd April 2006 flood: Manning's n zonal roughnesses

$n_{cw} = 0.045$ with the April 2006 validation data giving $n_{cw}0.025$.

6.9 DIVAST 2-D Model of the River Laver

The 2-D topography of the River Laver is shown in Figure 6.16 (a). The Laver catchment covers an area of 74 km^2 and extends for a distance of 20 km. The river rises in moorland above Ripon, before entering an area of established floodplain woodland, where the reach descends steeply, reaching a maximum slope of 1:70. Mid-reach, arable land and pastures dominate the riparian area, where the bed slope is fairly constant at a bed slope of 1:160, before the Laver enters the town of Ripon. A section measuring 1 km by 2.5 km containing the northernmost meander, was selected for modelling with a square grid size of 5 m. The domain (initially specifying two regions - main channel (light) and floodplain (dark)) was defined in Figure 6.16 (b). The domain required some refining, however it was assumed to be adequate representation during the model development phase.

As mentioned previously, DIVAST was originally developed to model shallow estuarine and coastal waters, typically exhibiting a relatively small bed profile. To date, most hydrodynamic investigations that DIVAST has been applied to conform to this condition, e.g. the River Ribble (cite), the Merbok Estuary (Westwater 2000) etc. In contrast, the modelled section of the River Laver experiences a drop in elevation of the channel thalweg of 20 m over approximately 3.5 km, i.e. a bed slope (S_0) of 1:160.

DIVAST Laver was governed by an upstream time dependent discharge (Q) boundary and a downstream time-dependent water level (h) boundary. In order to for the model to simulate the discharge and velocity profile throughout a water body, it was first necessary to set initial conditions. For a relatively flat water body, such as an estuary, the initial water level across the domain can be set to a single horizontal value, for example, the mean-tide elevation. Setting non-horizontal initial conditions that a shallow and steep reach requires can cause stability problems in the model. Therefore, in order to set up the initial conditions for the DIVAST model of the River Laver, the water level was initially set artificially high, at an elevation that would flood the domain to the upstream boundary. The water level at the downstream boundary was then gradually lowered over time (at a rate of $\Delta 0.2$ m per hour using a half time step of HFΔT = 1 s). The schematic in Figure 6.17 illustrates this process.

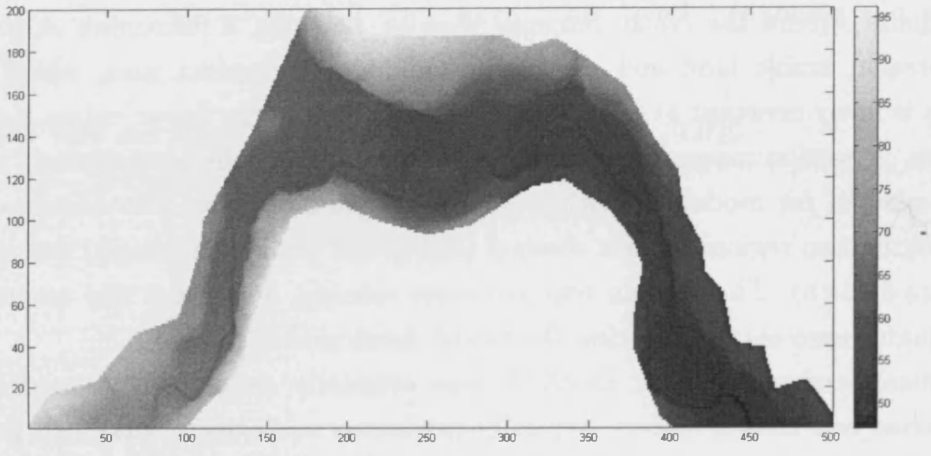

(a)

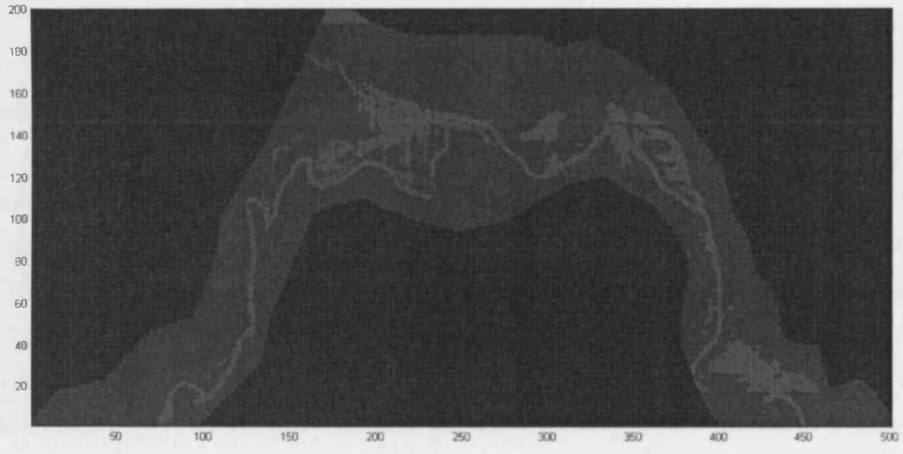

(b)

Figure 6.16: (a) Elevation of River Laver in mAOD. (a) Channel (light colour) and Floodplain (dark colour) domain

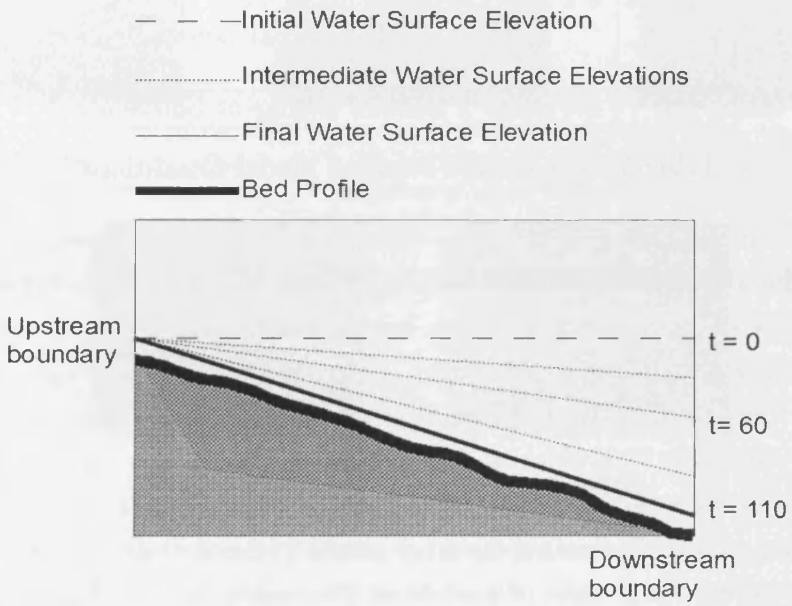

Figure 6.17: Model Water Elevation (ζ) Initial Conditions

6.9.1 Model Results

The DIVAST Laver model was run to obtain initial conditions with a pilot upstream discharge of 3 m/s The model conditions are presented in Table 6.13.

Δx	5 m	Northing grid size spacing
Δy	5 m	Easting grid size spacing
T	110 hrs	Simulation time
$HF\Delta t$	1 s	Half time step
Q	3 m^3/s	Total upstream discharge
ζ_{intial}	71.0 m	Initial water level
ζ_{final}	49.2 m	Final water level
$\Delta\zeta$	0.2 m/hr	Rate of change of water elevation at downstream boundary
Δh	0.2 m/hr	Rate of change at boundary

Table 6.13: LaverD1 Selected Model Conditions

Water elevation plots can be seen in Figure 6.18. It can be seen that as time progresses, the water level does decrease, however, towards the end of the simulation, there was a rise in the water level. This can be seen more clearly by comparing the specified input water elevation boundary with the model output water level at the boundary in Figure 6.19. It can be seen that although the input water boundary data has a linear variation with time, the model output boundary shows an increasing discrepancy over time, and between 90 hrs and 109 hrs, there is a sharp increase in the water level. The complex topography might indicate that certain regions were experiencing supercritical flow, in particular through wide and shallow parts of the reach. Therefore, simulations were carried out with increased discharges of 50, 100 and 200 m^3. None of the alternative discharges affected the output downstream boundary levels (in comparison to the model with Q = 3 m^3/s) until the simulation time reached 109 hrs, and then there was a corresponding rise in water level of 66.0 m for a discharge of 50 m^3/s and 67.5 m for a discharge of 100 m^3/s.

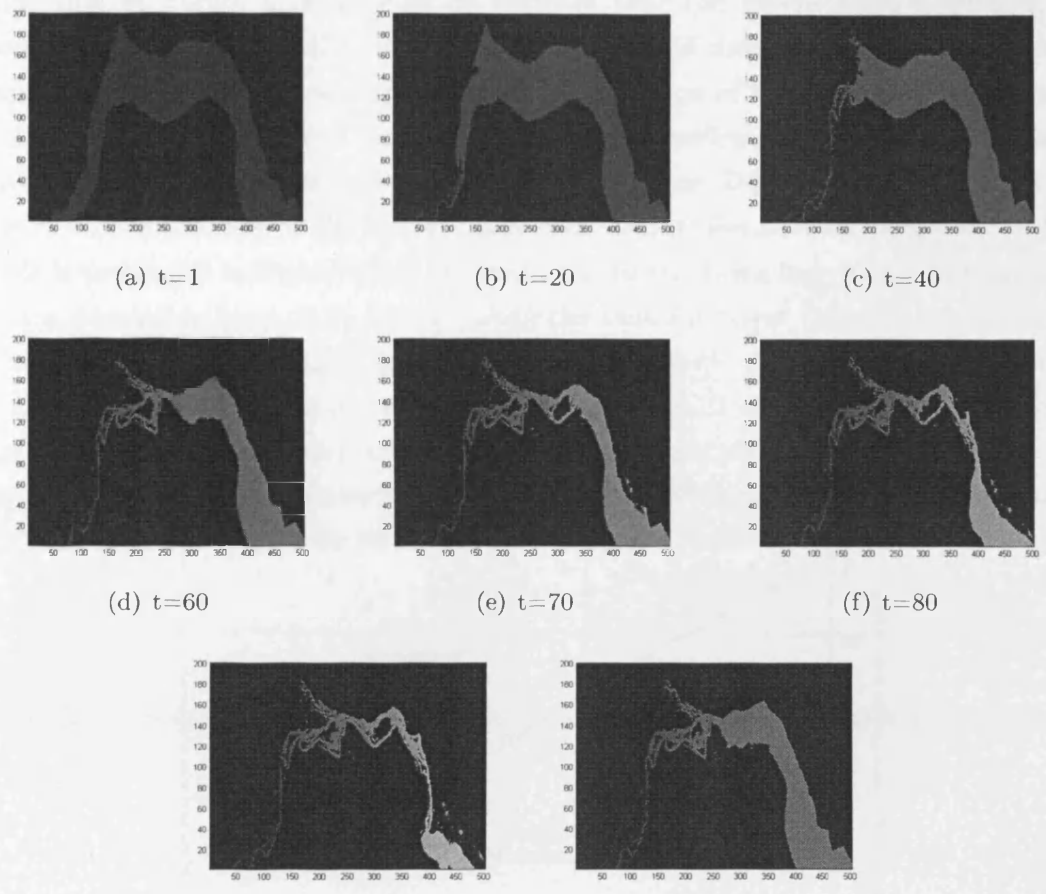

(a) t=1 (b) t=20 (c) t=40

(d) t=60 (e) t=70 (f) t=80

(g) t=90 (h) t=109

Figure 6.18: Water Elevation (ζ) of River Laver between t = 1 hr to t = 109 hr. The darker plots indicate a higher water elevation. Domain is defined by grid cell size where 1 cell = 5 m

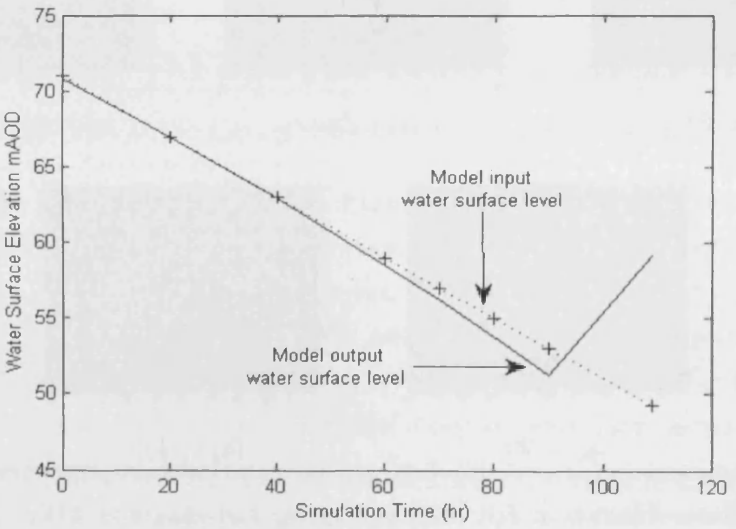

Figure 6.19: Comparison between model input and output downstream water level boundary data

Inspection of Figure 6.18 appears to indicate that the downstream boundary is modelled effectively until the model reaches 40 hours of simulation time. The reason could be related to the topography of the lower portion of the reach. To investigate this possibility, two reduced model domains were developed, Laver Domain 2 and Laver Domain 3. The water elevation results for Laver Domain 2 are presented in Figure 6.20 and a plot of the model input and output downstream boundary water levels is presented in Figure 6.21. A rise in the model boundary water level occurs after a simulation time of 76 hours. Using the reduced Laver Domain 2, variations in the eddy viscosity (ϵ) and flooding and drying depth were altered. The results at the downstream boundary are shown in Figures 6.22 and 6.23. It can be seen that while altering the eddy viscosity and the flooding and drying depth, none of the variations correct the rise in water level. All the simulation results in Figures 6.22 and 6.23 were run with no upstream discharge.

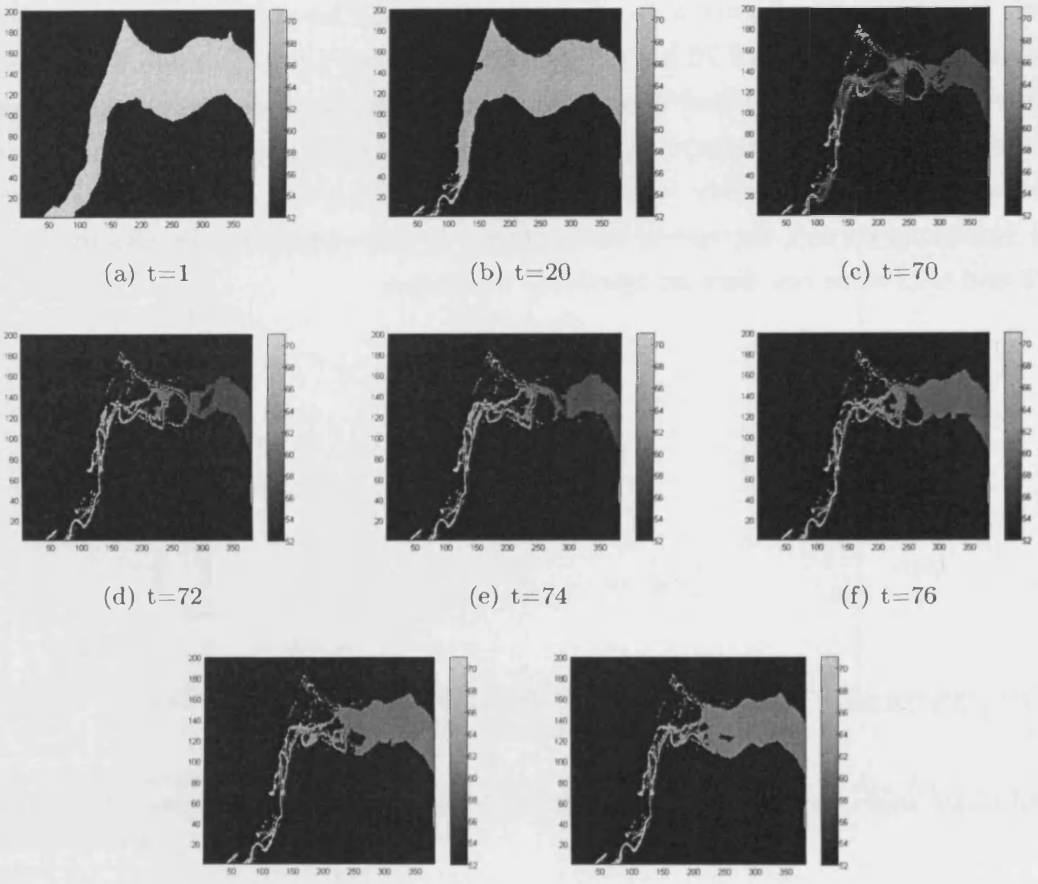

(a) t=1 (b) t=20 (c) t=70

(d) t=72 (e) t=74 (f) t=76

(g) t=78 (h) t=80

Figure 6.20: Water Elevation (ζ) of River Laver D2 between t = 1 hr to t = 80 hr. Lighter plots indicate a higher water elevation. Domain is defined by grid cell size where 1 cell = 5 m

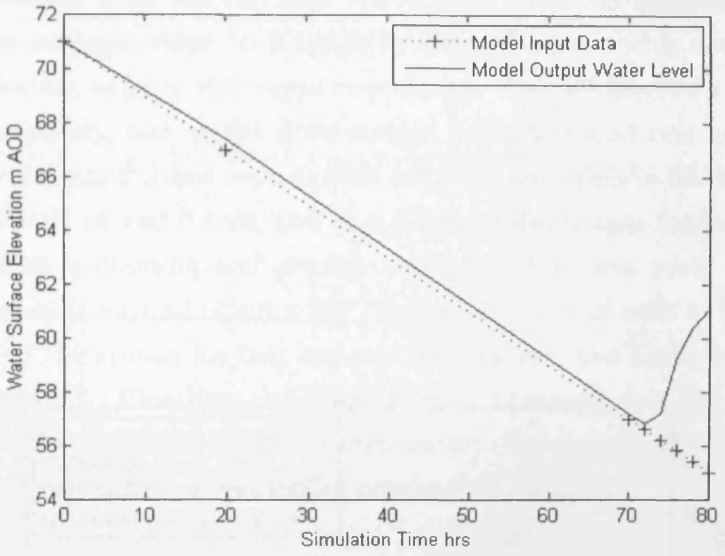

Figure 6.21: Comparison between model input and output downstream water level boundary data for Laver Domain 2

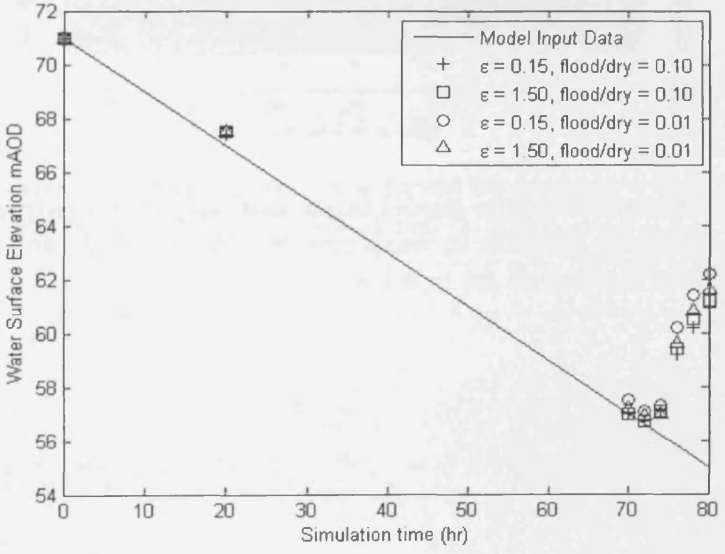

Figure 6.22: Comparison between model input and output downstream water level boundary data for Laver Domain 2, variations in eddy viscosity and min flooding/ drying depth

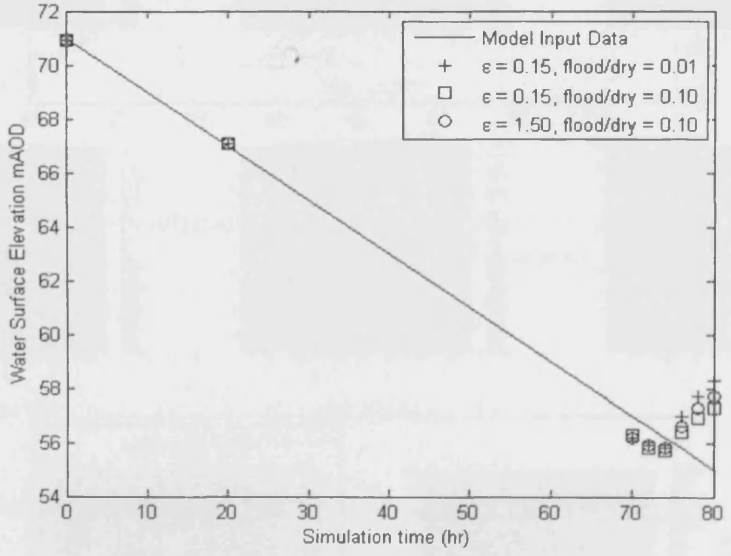

Figure 6.23: Comparison between model input and output downstream water level boundary data for Laver Domain 2, variations in eddy viscosity and min flooding/ drying depth with a timstep of $\Delta t = 0.1\ s$

A second approach to set initial conditions up over the steep and narrow reach is to flood the domain from the top end. To achieve this, the initial water level was converted from a single value to a spatially defined array, with each point in the array corresponding to an x and y grid coordinate. This allowed two different initial water levels to be set, one at the downstream boundary and one at the upstream boundary. Several simulations were carried out with variation in flooding and drying depth between 0.01 m and 0.1 m, and at a range of discharges from 3 m^3/s. It was found that unless a flooding and drying depth of 0.1 m was used, the simulation would not flood cells beyond column J67 (the vertical row of cells at location x = 67 in Figure 6.24). The reason for this was not determined, but is likely due to critical flow being exceeded. Flooding the domain from upstream has the added benefit that cells are only flooded from the watercourse. Several pools of low lying land away from the river were flooded in the previous version.

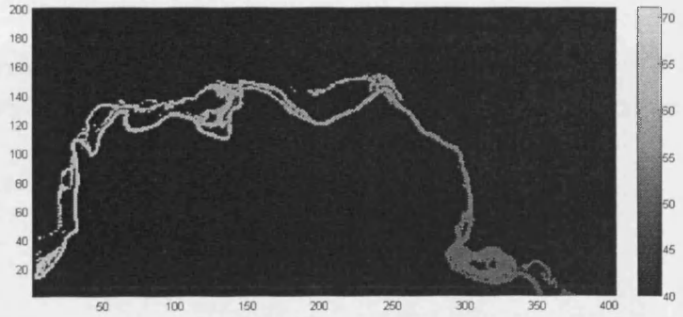

(a) t=1 hr

Figure 6.24: Water Elevation (ζ) of River Laver D2 between t = 1 hr to t = 22 hr. Domain is defined by grid cell size where 1 cell = 5 m

A smaller portion of the reach termed Domain 3 was modelled with success. As there was no field data collection in the modelled domain, the results from the 1-D model were used to create boundary conditions and against which to check results. This approach is clearly extremely limited, however, as an initial investigation, it was assumed to be an appropriate developmental approach to adopt.
The main channel and floodplain boundaries were estimated using a function of the minimum domain depth. This was carried out in two stages. Between cell columns 1 and 125, the minimum channel depth was ascertained within each column and any cells in the same column with a difference in depth of less than 0.75 m were also designated as channel sections. Between cell columns 125 and 255, the minimum channel depth was ascertained within each row, and any cells in the same row with a difference in depth of less than 0.75 m were also designated as channel sections. The domain for this region can be seen in Figure 6.25. A ground-truthing exercise should be carried out to determine the accuracy of this estimate.

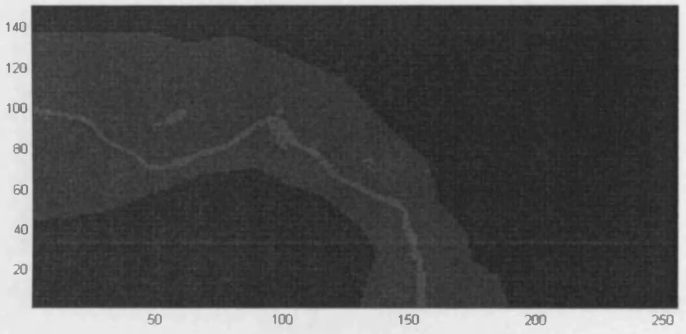

Figure 6.25: Channel and floodplain cell locations. Domain is defined by grid cell size where 1 cell = 5 m

Δx	5 m	Northing grid size spacing
Δy	5 m	Easting grid size spacing
T	90 hrs	Simulation time
$HF\Delta t$	0.1 s	Half time step
Q	13.9 m^3/s	Max upstream discharge
k	5 mm	Roughness Height
Fd	0.1 m	Min flooding and drying depth

Table 6.14: Laver Domain 3 Selected Model Conditions

Two flood scenarios were modelled according to the conditions in Table 6.14. To

1-D ISIS Model	DIVAST Model x	DIVAST Model y
46	55	9
45	81	55
44	72	73
43	61	100
42	82	118
41	95	136
40	100	145
39	118	150
38	131	153

Table 6.15: Equivalent nodes within 1-D and 2-D models

check the viability of the model, the flood of April 2006 (the flood data used in the roughness validation for the 1-D model) was modelled in the 2-D domain, and the water surface elevations were checked against the results of the 1D model. For this model, the downstream boundary rating curve was taken from the 1D model. The following power law equation described the variation of discharge with water elevation with an R^2 value of 0.9999:

$$\zeta = 0.215 \times Q^{0.502} + 51.55 \tag{6.41}$$

where h is the elevation in m AOD and Q is total discharge in m^3/s.
The results from nine nodes within the 1-D model were compared with locations in the 2-D model. Table 6.15 gives the equivalent node locations between the two models. The results from the April 2006 event modelled in the Divast Laver model can be seen in Figure 6.26. It can be seen that along the reach, the prediction of the water elevation is mixed, with a general trend of improved prediction within the lower portion of the reach.

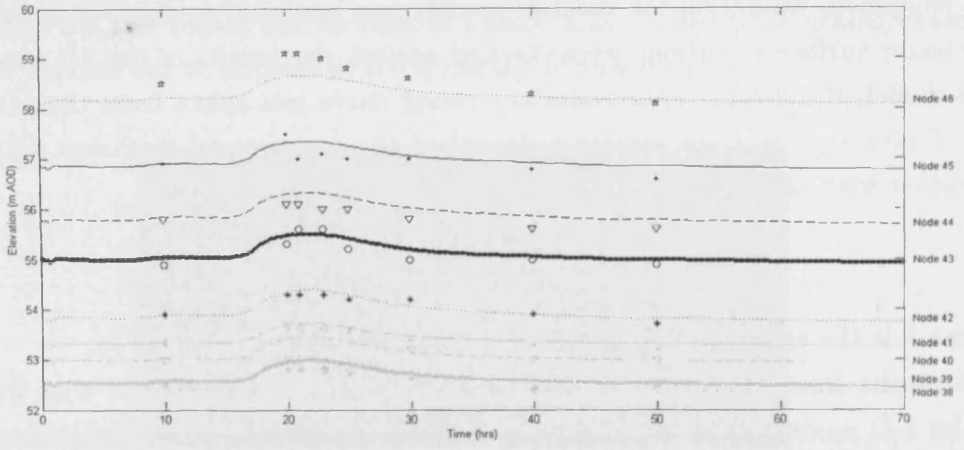

Figure 6.26: April 2006 event modelling. The continuous line represents the 1-D model results for each node, the markers represent the 2-D model results.

6.10 Floodplain Woodland Study

Floodplain woodland may offer an opportunity to delay and diffuse the peak of a flood hydrograph. The extent of this attenuation effect is dependent on physical characteristics of the reach such as slope, floodplain - main channel width ratio, roughness and hydrological characteristics (Anderson et al. 2006). As part of the scoping study Ripon Multi-Objective Project, the River Laver in North Yorkshire was selected to analyse the effect of floodplain woodland on the flooding characteristics of an upland reach.

6.10.0.1 Floodplain Location Options

Proposed planting locations are shown in Figure 6.27. The site at Option 2 was decided as the most appropriate site and this site is the subject of the preliminary study in this research.

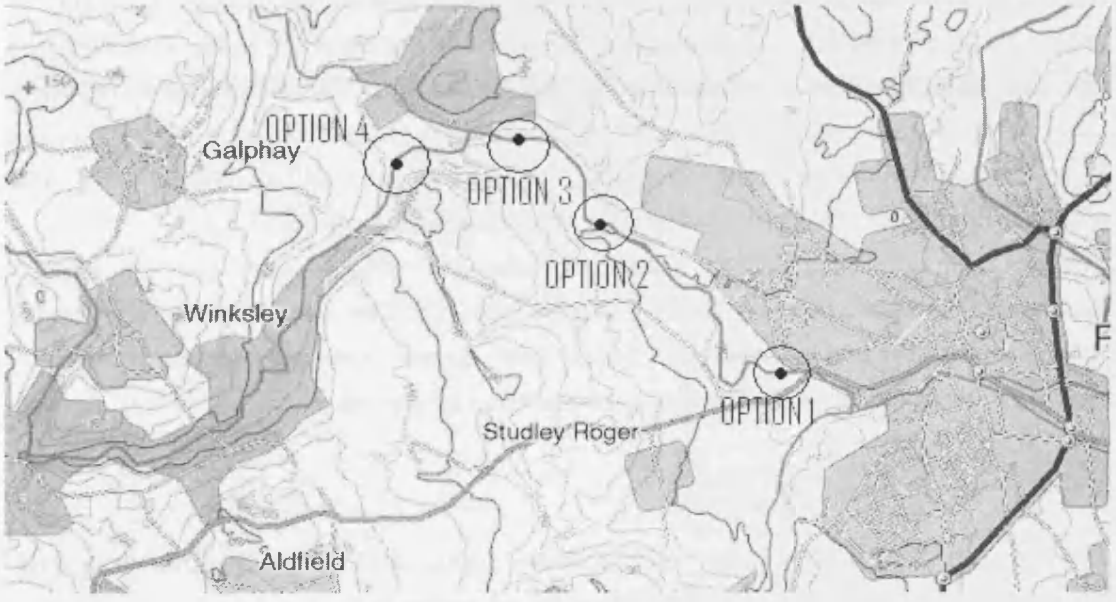

Figure 6.27: Location of Floodplain Woodland Planting Options

Using the results from the DIVAST model as a baseline, a region of 100 floodplain nodes covering the X dimension from node 47 to 56 and the Y dimension from node 86 to 95 was identified. This region approximately corresponds to Planting Site Option 2. This is a particularly interesting option, due to the presence of the low-lying overland flow path that forms a secondary channel during times of high flows (See Figure 6.28, the upper channel on the left bank is the secondary high flow

path). The mean flow depth and the mean magnitude of velocity in this floodplain region were identified using:

$$h_\sigma = \frac{\sum h_{ij}{}_{i,j=1}^{10}}{/} n \tag{6.42}$$

$$UV_\sigma = \frac{\sum \sqrt{U_{ij}^2 + V_{ij}^2}{}_{i,j=1}^{10}}{/} n \tag{6.43}$$

where h_{sigma} is the mean depth in the region, h_{ij} is the depth at node i, j, n is the number of nodes that the operation is carried out over, UV_σ is the mean magnitude of floodplain velocity and U_{ij} and V_{ij} are the vector velocities in the X and Y direction at node i, j.

The mean floodplain velocity at the peak flood height at 23 hrs was determined as 0.413 m/s, and the mean depth was determined at 0.094 m. This is clearly not enough to inundate or significantly deflect any trees, and so the drag area parameter approach developed for fully inundated trees is not appropriate here. However, the upscaled data from the rigid plant array experiments in Chapter 3 can be applied. Inspection of upscaled model results in Figure 3.30 show that at a velocity of 0.4 m/s, the low density (a planting spacing of 2.464 m by 1.440 m) single stem trees with a diameter of 200 mm have a bulk drag coefficient of $\overline{Cd}$ of 4.4.

This planting density is slightly more dense than the recommended planting density for productive woodland (see Table 1.1 in Chapter 1). The medium and high density single stem dowel and multi-stem *Cornus* data do not cover the prototype range of velocities observed, and so are not used here in the model.

6.10.0.2 Preliminary Model Results

The April 2006 high flow event was modelled again with the additional drag from the presence of the trees on the floodplain for all nodes from J = 1 to J = 99. Figures 6.28 and 6.29 present the difference in water elevation (equivalent to the change in depth) between the no vegetation scenario and the vegetated scenario. The values presented are equal to the elevation in the vegetated condition minus the elevation at the equivalent time step in the no vegetation condition:

$$\delta\zeta = \zeta_{vegetated} - \zeta_{unvegetated} \tag{6.44}$$

The peak of the high flow event occurred at 23 hrs. Prior to the peak flow at

21 hrs (Figure 6.28 (a)), and at the time of peak upstream flow (Figure 6.28 (b)) downstream areas experience a reduction in depth due to the added vegetation, and upstream areas experience an increase in depth due to the added vegetation. After the peak flow at 25 hrs (Figure 6.29 (a)) and 30 hrs (Figure 6.29 (b)), there is an increase in depth throughout the channel due to the vegetation. This suggests that the floodpeak has been delayed slightly, although further results are required to confirm this, and whether there is an overall decrease in the peak flood depth throughout the channel

The variation in a portion of the velocity field viewing nodes X 40 to 90 and Y 80 to 120 can be seen in Figure 6.30. It can be seen that there is a greater magnitude of velocity in the no vegetation condition, and that flow is mainly confined to the channel, whereas in the vegetated condition, there is additional flow on the floodplain.

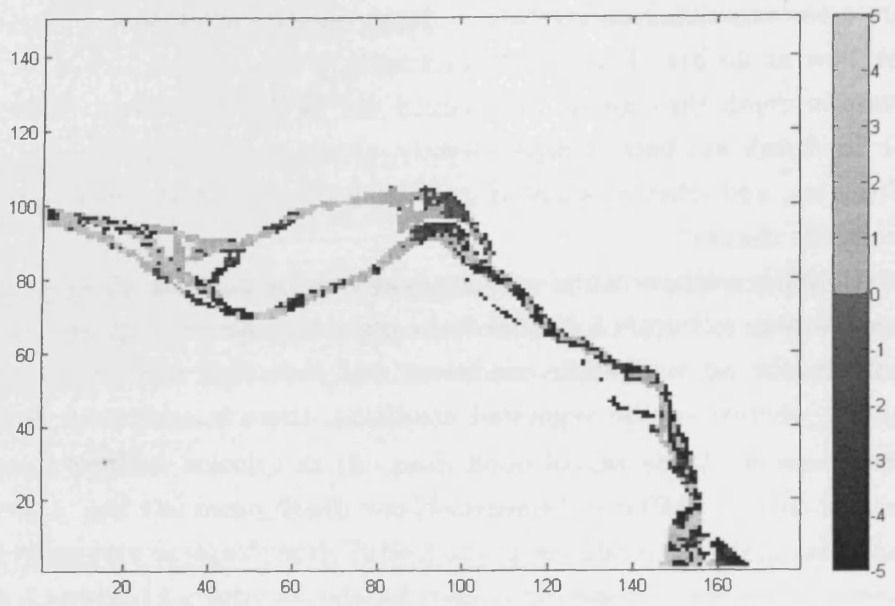

(a) T = 21 hrs

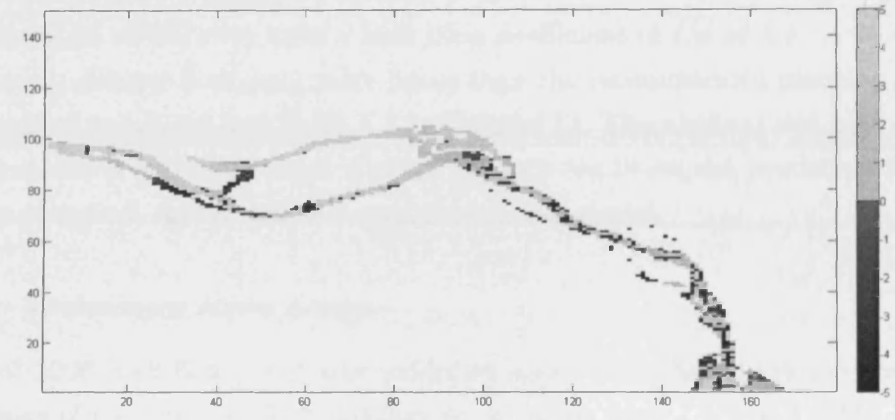

(b) T = 23 hrs

Figure 6.28: Difference in water elevation ($\delta\zeta$) between no vegetation condition (a) and vegetated condition (b). Lighter areas indicate a higher water surface elevation in the vegetated scenario. Darker areas indicate a higher water surface elevation in the no vegetation scenario. Domain is defined by grid cell size where 1 cell = 5 m. ζ units are cm.

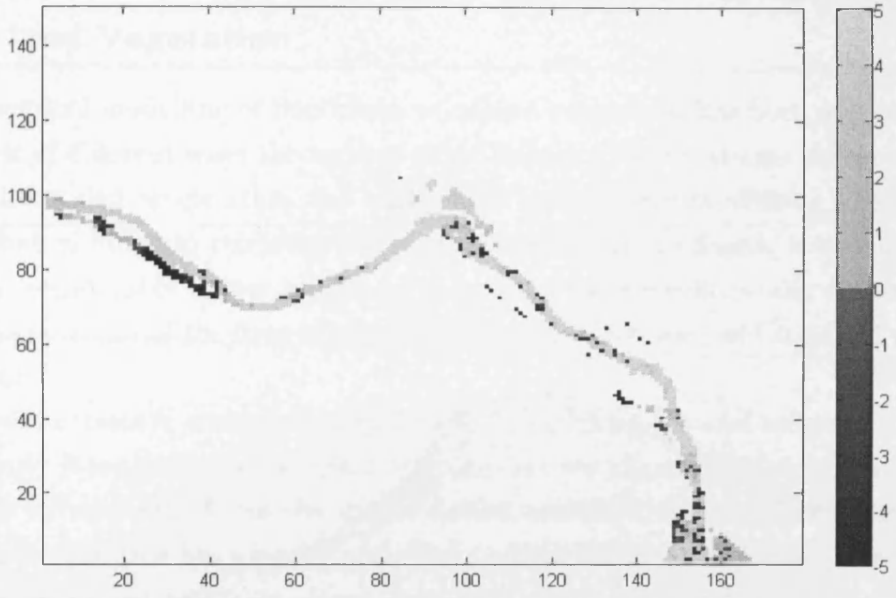

(a) T = 25 hrs

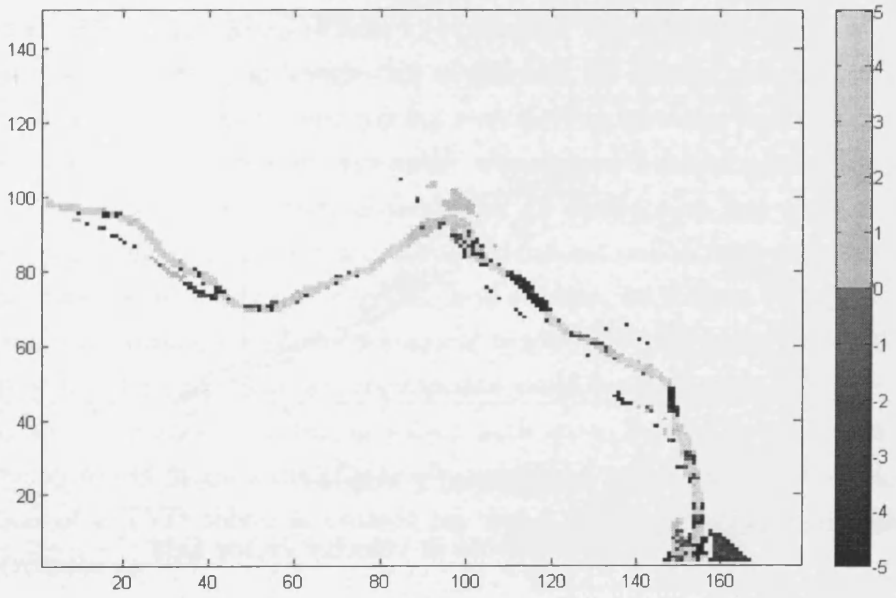

(b) T = 30 hrs

Figure 6.29: Difference in water elevation ($\delta\zeta$) between no vegetation condition (a) and vegetated condition (b). Lighter areas indicate a higher water surface elevation in the vegetated scenario. Darker areas indicate a higher water surface elevation in the no vegetation scenario. Domain is defined by grid cell size where 1 cell = 5 m. ζ units are cm.

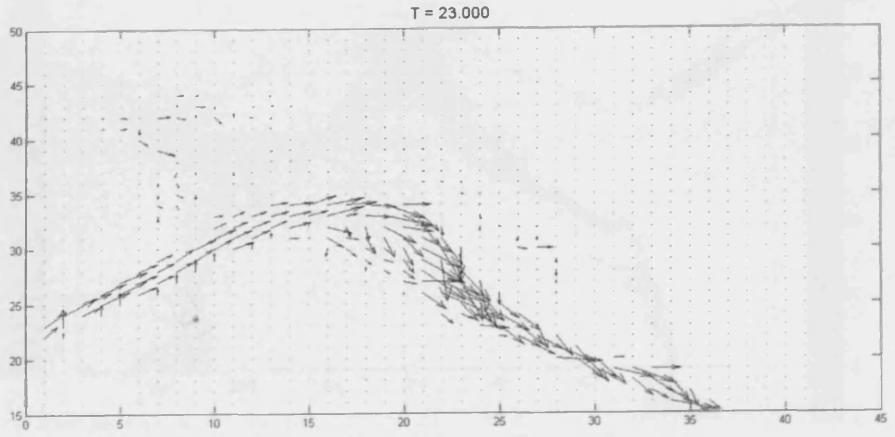

(a) No vegetation T = 23 hrs

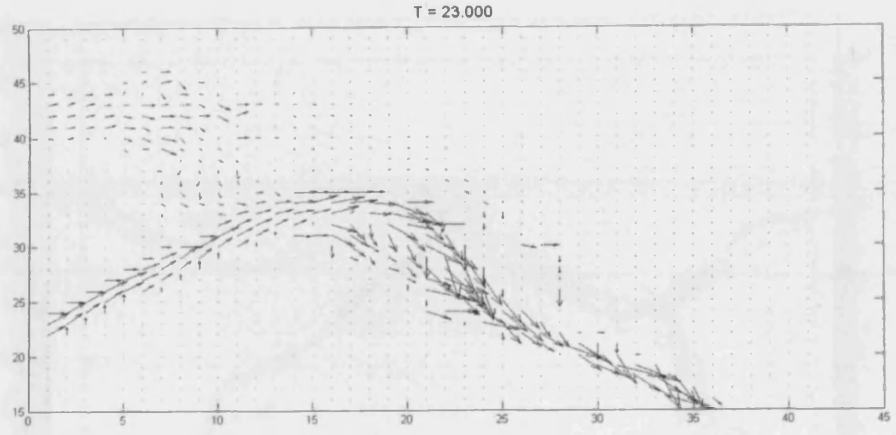

(b) Vegetated T = 23 hrs

Figure 6.30: Variation in velocity vector field

6.11 Summary of Numerical Modelling of Floodplain Woodland Vegetation

The numerical modelling of floodplain woodland vegetation has been approached in a number of different ways throughout this Chapter. The roughness values obtained in the 1:8 scaled single stem and multi-stem arrays were modelled, where it was found that in order to replicate the water elevation in the flume, it was necessary to use a considerably higher roughness value than the experimentally obtained one. The incorporation of the drag-area parameter values obtained in Chapter 5 was also described.

Due to the extensive time necessary for model development and refinement, only a short study into the hydraulic effect of floodplain woodland applied to a river reach has been carried out. From the initial results available, the presence of floodplain woodland vegetation has a significant effect on both depth and velocity. The planting situation modelled is highly dense, but still within the guidelines for a planted woodland, although admittedly the 200 mm tree diameter would probably not exist in a productive woodland.

At the completion of the study, the model of the River Laver was subject to instabilities at the high flows required to simulate the full inundation required for the drag-area parameter, although this is planned for further research. This work is a step towards developing and testing a modelling strategy for modelling dense floodplain woodland at the prototype scale. this chapter has looked at understanding the limitations of using a numerical model for an application site where ther reach is located in teh mid- to upper reach of teh catchment valley, with a gradient higher that those reaches normally modelled in flood studies, with trans-critical flow likely. As a result, the application of the numerical model DIVAST using the ADI method solver may not be the most appropropriate code for this case. There is much potential to use a shock capturing solver such as a Total Variation Diminishing solver, which would include the effects of transitional turbulent flows. Although the application of a TVD solver is outside teh scope of this project, it is planned for future research.

7

Conclusions and Future Research

This research has characterised floodplain woodland hydraulic resistance through full scale and scaled-down experimental investigations. The application of the hydraulic resistance of submerged saplings as a sub-grid roughness within depth-averaged shallow water flow has also been presented. The following points summarise the main research outcomes and suggestions for futher work.

Scaled experiments Experimental investigations into three different densities of single stem dowel and multi-stem *Cornus* model tree arrays, geometrically scaled down by a ratio of 1:8, were carried out in *Chapter 3*. The modelled planting densities were based on woodland planting guidance from the Forestry Commission UK. The dowels and *Cornus* share a similar projected area (A_p) but the dowels possess a larger solid volume fraction (ϕ). As the density increases, the dowels have an increasingly larger resistive effect. Comparisions between the two vegetation types by stem Reynold's number are somewhat hampered, as the much smaller stems of the *Cornus* experience a significantly lower stem Reynold's number. The dowels also experienced surface waves at the higher densities and flow depths, which may explain the negative correlation between flow depth and mean flow field velocity for these model tree arrays. While all the exerimental stem Reynold's numbers are within the

laminar turbulent separation zone, and so the wake-induced resistance of the stems is expected to be of a similar order, it seems that the experiments took place within a transitional zone, as exemplified by the rapid change in the bulk drag coefficient with increasing flow conditions. Future research into model tree arrays with different stem diameters in close proximity would be advised to carry out experiments at a higher bed slope, in order to induce larger and more comparable Reynold's numbers. This would also have the advantage of vastly improving the upscaled results, which are at present limited by the factors mentioned above.

Physical modelling of emergent vegetation arrays under quasi-uniform flow

Roughness values of Manning's n, friction factor f and drag coefficients were determined for different densities of plant. Quasi-uniform flow was established for the model tree arrays investigated in *Chapter 3*. Fully uniform flow was not possible as the flume bed experienced slight undulations and with a length of only 10 m, the flume was not long enough to develop truly uniform flow. However, a constant depth was maintained throughout the measured experimental zone. This constant depth allowed uniformity of flow resistance throughout the vegetation arrays, while a head loss approach would create a spatial variation in flow velocity and Reynold's number. However, adopting uniform flow conditions introduced limitations to the study. The depth of the flume (300 mm) was a limiting factor for the dense planting arrays, as the maximum depth was reached at a relatively low discharge, meaning the total range of flows investigated for the dense arrays is small. The pump capacity of the flume (50 l/s) was a limiting factor for the sparse planting arrays, as the maximum depth that could be attained was relatively small, and consequently the sparse arrays could not be sampled for velocity and turbulence measurements in *Chapter 4*. The adoption of uniform or quasi-uniform conditions should depend on the capacity of the flume. A deeper flume or a larger capacity pump would have enabled comparable stem Reynold's numbers within the different experimental set-ups to be attained. This would facilitate comparison between the different densities and model tree types - something that was not directly possible within this study. Random planting arrays would eliminate the presence of the surface waves that hampered the obtaining of measurements in the dense dowel model tree arrays. An alternative option would be to model the different model trees with different

bed slopes in order to achieve similar flow conditions.

Resistance parameters of vegetation Resistance parameters of Manning's n and the Darcy-Weisbach friction factor f were determined for the results obtained in *Chapter 3*. These roughness coefficients were derived in three variations, by modifying the cross-sectional flow area and wetted perimeter to incorporate the blockage effect of vegetation to varying degrees. The incorporation of the blockage presented by the vegetation reduced the associated roughness factor. The no-blockage derivation termed *Original* produced a wide range of roughness values for the range of flows investigated, while the *Gap* derivation (with the largest blockage factor) produced roughness values spread over a very small range for the same data. This could indicate that the volume occupied by the vegetation, or in the case of the *Gap* derivation, the most constricted cross-sectional area of flow, has a dominant influence on the hydraulic roughness rather than planting density effects on the bulk resistance characteristics. This relationship with volume is further confirmed in the results of *Chapter 5*, where the physical properties of mass and volume of the trees were strongly correlated with the drag force exterted. Further work could include the investigation of vegetation with similar volumes but different projected areas under high enough Reynold's numbers to be compararable.

Hydraulic resistance of single stem and multi-stem model tree arrays While comparison between the single stem (dowel) and multi-stem (*Cornus*) model tree arrays investigated in *Chapter 3* is limited due to surface waves, different ranges of stem Reynold's numbers etc, comparison using the mean area flow variables is possible. At the lowest model tree planting density, the dowels and *Cornus* have almost identical hydraulic resistance. Both are characterised by the highest mean-area velocities investigated of up to approximately 0.25 m/s. Although the solid volume fraction (ϕ) of the *Cornus* is approximately 1/4 of the dowel, the projected area (A_p) of the two is similar. However, at higher model tree planting densities, there is a greater difference between the model tree types. Therefore it could be concluded that within this range of stem Reynold's numbers, at a solid volume fraction (ϕ) of less that 0.455 %, the volume occupied by vegetation is relatively insignificant, while at a solid volume fraction of (ϕ) of 1.023 % and above, the volume occupied by the vegetation plays an increasingly relevant role in the overall hydraulic

resistance. Much further work could be carried out to investigate multi-stemmed and single stem plants. A useful additional experiment to the existing dataset would be to model randomly distributed dowels of the same number and diameter as the individual *Cornus* stems. This would isolate the effect of the multi-stemmed base of the *Cornus*.

Velocity and TKE within single stem and multi-stem model tree arrays Vectrino sampling at 200 Hz was carried out in *Chapter 4*. The sampling encountered a number of problems, including resonance of the acoustic signal off the flume bed that meant sampling at certain heights was not possible, and the need to re-seed the flume water with particulate matter at regular intervals to keep the signal - noise ratio at a reasonable value. The branches of the *Cornus* saplings were orientated to make sure the majority were not in the control volume, however a few remained, and this has resulted in peaks in velocity and turbulence within the control volumes which significantly affect the mean values. There are distinct differences between the dowels and *Cornus* in the spatially averaged velocity and TKE profiles. The dowel arrays present an almost constant variation of velocity and tubulence with depth, while there is a bulge in the lower half of the flow depth of the velocity and turbulent kinetic energy profiles for the *Cornus* arrays. Improved conclusions could be drawn by normalising the results. Another improvement would be carrying out experiments at a similar depth/ stem Reynold's number of flow. Full automation of the system would allow continuous sampling of the flow field, rather than sampling one control volume over several days. This full field sampling approach would be improved through the use of PIV to sample a single plane at once, enabling experiments to be carried out in a much shorter time, although this has the limitation that in a multi-stem environment, the PIV field may be interupted.

Optimised sampling locations within staggered vegetation arrays The comparison methodology adopted in *Chapter 4* uses the spatially averaged mean flow field and the χ^2 distribution test to assess the optimal sampling locations. Three strategies were used, patterns from the literature, transect sampling and random sampling of one and three locations. Certain sampling locations appeared to consistently predict the spatially averaged flow field values accurately, e.g. for streamwise velocity, samples taken at $1/3\ s$ and $2/3\ s$, where s is the mean spacing between the model trees in the transect sampling.

This result was backed up by results from the random sampling. However, not all locations predicted both the mean streamwise velocity and the turbulent kinetic energy equally well, as the best prediction of mean flow field turbulent kinetic energy was at 0.5 s_x, where s_x is the longitudinal spacing between the dowels. Further research will apply the random optimised sampling technique to the original data to analyse all the components of the flow variables including streamwise turbulence, lateral velocity and turbulence and vertical velocity and tubulence. It is then planned to look at the mean associated error in the flow variables against the optimised streamwise velocity.

Characterising physical properites of vegetation Determination of the physical characteristics has intentionally been a central part of this research. In both *Chapter 3* and *Chapter 5*, the plant images were captured photographically, and through digital analysis, the projected area, diameter and volume could be determined. In the bulk resistance derivations of *Chapter 3*, this allowed spatially averaged representation of the vegetation within the derivations for resistance. This is an improvement on many other experimental investigations into vegetation, where the physical characteristics are wither not noted, or limited toa description of the species. Given the wide range of growth forms of any individual species, it is clear that growth characteristics depend on light intensity and duration, plant spacing, and the presence of other plants. Without determining the physical charateristics at the outset of experimentation, any further application of the data is limited, particularly when assessing the drag coefficients of cylindrically stemmed, unleaved plants. In *Chapter 5*, the mass and volume of the trees provided the strongest correlation with the drag area parameter (C_dA), rather than the main stem diameter or height of the trees, and there was not much varience noted between species. There is much scope for further work or analysis of previous data in establishing this volume - drag area parameter link.

Full-scale drag force testing The drag force test carries out on the *Salix*, *Alnus* and *Populus* saplings were carried out by dragging the trees attached to a transducer through a canal in the manner of ?. The experiments are a departure from the field situation in a number of respects. The trees were fully submerged for all experiments and no partially submerged tests were carried out. The base of the trees was mounted in a brass cylinder, and the degree to which this represented a tree in soil was not tested. The experimental

procedure meant that the tree did not experience normal logarithmic boundary layer of shallow water flow. At the basal end of the tree, this will probably have contributed to a larger drag area parameter that the field condition. Further tests would include dragging trees upright through the water, this would enable a range of submergence depths to be considered. Testing groups of trees would be a worthwhile addition to the current study, to see the degree of sheltering depending on streamwise separation distance.

Numerical modelling of vegetation The numerical representation of vegetation is presented in *Chapter 6*. The experiments investigating bulk resistance characteristics of dowel arrays in *Chapter 3* are modelled in DIVAST, a depth-integrated finite difference numerical model. It was found that the conditions in the flume could not replicated within DIVAST unless the numerical model roughness was artificially increased. The inclusion of the drag area parameter and the equivalent Manning's n values based on the *Salix* data collected in Section *Chapter 5* are described. A reach scale model of the River Laver, an area previously designated for floodplain woodland creation, was built, but due to instabilities encountered, the model was not running at the end of this reasearch. Future work will include running the mode with a range of trees, for example, populating the floodplains with the mean drag area parameter value for each of the tested *Salix*, *Alnus* and *Populus* saplings at a range of densities. This will allow determination of the mean area velocity along the reach, and how the presence of trees affects the river hydrodynamics and solute transport.

Bibliography

Ackers, P. (1978), *Weirs and flumes for flow measurement*, John Wiley and Sons.

Anderson, B., Rutherford, I. & Western, A. (2006), 'An analysis of the influence of riparian vegetation on the propagation of flood waves', *Environmental Modelling and Software* **21**, 1290–1296.

Armanini, A., Righetti, M. & Grisenti, P. (2005), 'Direct measurement of vegetation resistance in prototype scale', *Journal of Hydraulic Research* **43**(5), 481–487.

ASCE (2000), *Hydraulic Modelling concepts and practice*, ASCE.

Aylott, M., Casella, E., Tubby, I., Street, N., Smith, P. & Taylor, G. (2008), 'Yield and spatial supply of bioenergy poplar and willow short-rotation coppice in the uk', *New Phytologist* **178**(2), 358 – 370.

Baker, C. J. (1979), 'The laminar horseshoe vortex', *Journal of Fluid Mechanics* **95**, 347 – 367.

Baptist, M., Babovic, V., Uthurburu, J. R., Keijzer, M., Uittenbogaard, R., Mynett, A. & Verwey, A. (2007), 'On inducing equations for vegetation resistance', *Journal of Hydraulic Research* **45**(4), 435 – 450.

Beffa, C. & Connell, R. (2001), 'Two-dimensional flood plain flow. 1: Model description', *Journal of Hydrologic Engineering* **6**, 397–415.

Blevins, R. (1994), *Flow-Induced Vibration*, Kreiger, Malabar, Fla.

Bokaian, A. & Geoola, F. (1984), 'Wake-induced galloping of two interfering circular cylinders', *Journal of Fluid Mechanics* **146**, 383 – 415.

Botaurus-stellaris (2008), 'Groß wasserburg in unterspreewald (2006)', online.

Bradshaw, C., Sodhi, N., Peh, K. & Brook, B. (2007), 'Global evidence that deforestation amplifies flood risk and severity in the developing world', *Global Change Biology* **13**, 2379 - 2395.

Chadwick, A. & Morfett, J. (1999), *Hydraulics in Civil and Environmental Engineering*, EFN Spon.

Chapman, J. & Reiss, M. J. (1999), *Ecology: Principles and Applications*, 2 edn, Cambridge University Press.

Chow, V. T. (1959), *Open Channel Hydraulics*, McGraw-Hill.

Coleman, S., Nikora, V., McLean, S. & Schlicke, E. (2007), 'Spatially averaged turbulent flow over square ribs', *Journal of Engineering Mechanics* **133**(2), 194 - 204.

Copeland, R. (2000), Determination of flow resistance coefficients due to shrubs and woody vegetation, report erdc/chl chetn-viii-3, Technical report, USAE Research and Development Center.

Cousens, J. (1974), *An Introduction to Woodland Ecology*, Oliver and Boyd.

CRC (2003), Weeds of national significance - willow, Technical report, Australian Weed Management.

Defina, A. & Bixio, A. C. (2005), 'Mean flow and turbulence in vegetated open channel flow', *Water Resources Research* **41**(7), 07006 -.

DeJong, J. (2005), Modelling the influence of vegetation on the morphodynamics of the river allier, Master's thesis, Delft TU.

Dong, Z., Gao, S. & Fryrear, D. W. (2001), 'Drag coefficients, roughness length and zero-plane displacement height as disturbed by artificial standing vegetation', *Journal of Arid Environments* **49**, 485 - 505.

Dresner, S., Ekins, P., McGeevor, K. & Tomei, J. (2006), Forests and climate chanc: Global understandins and possible responses, Technical report, Policy Studies Institute.

Dunn (1996), Mean flow and turbulence in a laboratory channel with simulated vegetation, PhD thesis, Dept of Civil Engineering, University of Illinois.

EC (2007), Ec directive 2007/60/ec on the assessment and management of flood risks, Technical report, European Commission.

EnvironmentAgency (2009), Ripon multi objective project phase 2, Technical report, Environment Agency.

Ergun, S. (1952), 'Fluid flow through packed columns', *Chemical Engineering Progress* **48**, 89–94.

Executive, S. (2002), 'Scottish forestry grant schemes', Leaflet.

Fairbanks, J. (1998), Velocity and Turbulence Characteristics in Flows through Rigid Vegetation, PhD thesis, Virginia Polytechnic Institute and State University.

Fairbanks, J. D. & Diplas, P. (1998), Turbulence characteristics of flows through partially and fully submerged vegetation, p. 6.

Falconer, R. (1986), 'A water quality simulation study of natural harbour', *Journal of Waterway, Port, Coastal and Ocean Engineering, ASCE* **112**, 234–259.

Falconer, R. (1993), *An introduction to nearly horizontal flows*, E and F N Spoon Ltd., London, pp. 27–36.

Falconer, R. A. (1977), Mathematical Modelling of Jet-Forced Circulation in Reservois and Harbours, PhD thesis, University of London, London, England.

Falconer, R. A. & Chen, Y. (1991), 'An improved representation of flooding and drying andwind stress effects in a two-dimensional tidal numerical model', *Proceedings Inst. Civil Engineers* **91**, 659–678.

Fathi-Maghadam, M. & Kouwen, N. (1997), 'Nonrigid, nonsubmered, vegetative roughness on floodplains', *Journal of Hydraulic Engineering* **123**(1), 51–57.

Featherstone, A. (2009), 'Common or black alder', Trees for Life website. [online] http://www.treesforlife.or.uk/forest/species/alder.html.

Finnigan, J. (2000), 'Turbulence in plant canopies', *Annual Review of Fluid Mechanics* **32**, 519 – 571.

Fischenich, C. & Dudley, S. (2000), Determining drag coefficients and area for vegetation, report erdc tn-emrrp-sr-08, Technical report, USAE Research and Development Center.

Fleming, G., Frost, L., Huntingdon, S., Knight, D., Law, F. & Rickard, C. (2001), Learning to live with rivers, Technical report, Institution of Civil Engineers.

Foken, T., Thomas, C., Ruppert, J., Luers, J. & Gockede, M. (2004), Turbulent exchange processes in and above tall vegetation, pp. 363 – 366.

ForestResearch (2003), Yield models for energy coppice of poplar and willow (phase 4), Technical report, Forest Research.

Fowler, J., Cohen, L. & Jarvis, P. (1998), *Practical Statistics for Field Biology*, John Wiley and Sons.

Fraser, A. I. (1962), Wind tunnel studies of the forces acting on the crowns of small trees, Technical report, Forest Research U.K.

Freeman, G. E., Rahmeyer, W. J. & Copeland, R. R. (2000), Determination of resistance due to shrubs and woody vegetation, Technical report, US Army Corps of Engineers.

FRMRC (2009), The flood risk management research consortium final report, Technical report, Flood Risk Management Research Consortium.

Fuller, R. J. & Warren, M. S. (1993), *Coppiced Woodlands: Their Management for Wildlife*, 2 edn.

Gibson, C., Lehoucq, F. & Williams, J. (2002), 'Does privatisation protect natural resources? property rights and forests in guatemala', *Social Science Quarterly* **83**(1), 206 – 225.

Goring & Nikora (2002), 'Despiking acoustic doppler velocimeter records', *ASCE Journal of Hydraulic Engineering* **128**, 117 126.

Green, D. W., Winandy, J. E. & Kretschmann, D. E. (2002), Mechanical properties of wood, *in* 'Wood Handbook - Wood as an Engineering Material', U.S. Dept. Agr.

Henshaw, A. & Thorne, C. (2007), Catchment restoration for flood risk and sediment management: Pontbren, mid-wales, *in* 'The River Restoration Centre's 8th Annual Network Cconference'.

HiFlowsUK (2007), 'Flows, river laver at ripon', accessed on HiFlows UK website.

Hinze, J. O. (1975), *Turbulence*, McGraw-Hill, New York.

Horacek, P. (2008), Introduction to tree statics and static assessment. Mendel University of Agriculture and Forestry Brno, Czech Republic.

Hughes, F. (2003), The flooded forest: Guidance for policy makers and river managers in europe on the restoration of floodplain forests, Technical report, FLOBAR2.

IPCC (2007), Climate change 2007:synthesis report, Technical report, IPCC.

James, C. S., Birkhead, A. L., Jordanova, A. A. & O'Sullivan, J. J. (2004), 'Flowresistance of emergent vegetation', *J. Hydraul. Res., IAHR* **42**, 390 – 398.

Jarvela, J. (2002), 'Flow resistance of flexible and stiff vegetation: A flume study with natural plants', *Journal of Hydrology* **269**(1-2), 44 – 54.

Jarvela, J. (2005*a*), 'Effect of submerged flexible vegetation on flow structure and resistance', *Journal of Hydrology* **307**(1-4), 233 – 241.

Jarvela, J. (2005*b*), 'Effect of submerged flexible vegetation on flow structure and resistance', *Journal of Hydrology* **307**(1-4), 233 – 241.

Jarvela, J. & Aberle, J. (2007), ''analysis of manning coefficient for small-depth flows on vegetated beds' by r. garcia diaz', *Hydrological Processes* **21**(16), 2206 – 2208.

Jarvela, J. & Helmio, T. (2004), 'Hydraulic considerations in restoring boreal streams', *Nordic Hydrology* **35**(3), 223 – 235.

Jarvela, J. & Jormola, J. (1998), Restoration of boreal lowland rivers in finland: Problems and approaches with respect to conservation and flood protection, Vol. 1, Memphis, TN, USA, pp. 696 – 701.

Jordanova, A. A., James, C. S. & Birkhead, A. L. (2006), 'Practical estimation of flow resistance through emergent vegetation', *ICE Journal of Water Management* **159**, 173–181.

Kadlec, R. (1990), 'Overland flow in wetlands. vegetation resistance', **116**, 691–706.

Kane, B. & Smiley, T. (2006), 'Drag coefficients and crown area estimation of red maple', *Canadian Journal of Forest Research* **38**(6), 1275 – 1289.

Kang, H. & Choi, S.-U. (2006), 'Turbulence modeling of compound open-channel flows with and without vegetation on the floodplain using the reynolds stress model', *Advances in Water Resources* **29**(11), 1650 – 1664.

Katul, G. G., Mahrt, L., Poggi, D. & Sanz, C. (2004), 'One- and two-equation models for canopy turbulence', *Boundary-Layer Meteorology* **113**(1), 81 – 109.

Kiljn, F., Samuels, P. & Van Os, A. (2008), 'Towards flood risk management in the eu: State of affairs with examples from various european countries', *International Journal of River Basin Management* **6**(4), 307 – 321.

Klebanoff, P. (1955), Charactersitics of turbulence in a boundary layer with zero pressure gradient, Technical report, NACA Technical Notes No.1347, Washington D.C.

Klopstra, D., Barneveld, H., Van Noortwijk, J. & Van Velzen, E. (1997), Analytical model for hydraulic roughness of submerged vegetation, Vol. A, pp. 775 – 780.

Knowe, S. A. & Hibbs, D. E. (1996), 'Stand structure and dynamics of young red alder as affected by planting density', *Forest Ecology and Management* **82**(1-3), 69 – 85.

Kouwen, H., Li, R. M. & Simons, D. B. (1981), 'Flow resistance in vegetated waterways', *Trans. ASAE* **24**, 684 – 698.

Kouwen, N. & Fathi-Maghadam, M. (2000), 'Friction factors for coniferous trees along rivers', *Journal of Hydraulic Engineering* **126**(10), 732–740.

Kouwen, N. & Unny, T. E. (1973), 'Flexible roughness in open channels', *Journal of the Hydraulics Division, ACSE* **99**, 713 – 728.

Leclercq, A. (1997), 'Wood quality of white willow', *Biotechnol. Agron. Soc. Environ* **1**(1), 59 – 64.

Li, R.-M. & Shen, H. W. (1973), 'Effect of tall vegetations on flow and sediment.', **99**(HY5), 793 – 814.

Lin, B. & Falconer, R. (1997), 'Tidal flow and transport modelling using the ultimate quickest scheme', *Journal of Hydraulic Engineering* **123**(4), 303 – 314.

Lindberg, K., Furze, B., Staff, M. & Black, R. (1997), Asia-pacific forestry sector outlook study: Ecotourism and other services derived from forests in the asia-pacific region: Outlook to 2010,working paper no: Apfsos/wp/24, Technical report, Asia-Pacific Forestry Commission.

Lopez, F., Dunn, C. & Garcia, M. (1995), Turbulent open-channel flow through simulated vegetation, Vol. 1, San Antonio, TX, USA, pp. 99 – 103.

Lopez, F. & Garcia, M. (1995), Simulation of suspended sediment transport in vegetated open channel flows with a k-epsilon; turbulence model, Vol. 1, San Antonio, TX, USA, pp. 104 – 108. Vegetation;Averaged mean velocity;Standard deviations;Velocity components;Eddy viscosities;Equilibrium vertical distribution;Suspended sediment transport;Non vegetated channels;.

Lopez, F. & Garcia, M. H. (2001*a*), 'Mean flow and turbulence structure of open-channel flow through non-emergent vegetation', *Journal of Hydraulic Engineering* **127**(5), 392 – 402.

Lopez, F. & Garcia, M. H. (2001*b*), 'Mean flow and turbulence structure of open-channel flow through non-emergent vegetation', *Journal of Hydraulic Engineering* **127**(5), 392 – 402.

Mabberley, D. (1997), *The Plant Book*, 2 edn, Cambridge University Press.

Marshall, J. K. (1970), 'Drag measurements in roughness arrays of varying density and distribution', *Agricultural Meteorology* pp. 269–292.

Massey, B. S. (1997), *Mechanics of Fluids*, 6 edn, Chapman and Hall.

Mattheck, C., Bethge, K., Kappel, R., Mueller, P. & Tesari, I. (2003), 'Failure modes for trees and related criteria', *International Conference 'Wind effects on trees', University of Karlsruhe, Germany* .

Mattheck, C. & Breloer, H. (1995), *The body language of trees*, HMSO, London.

Mayhead, G. J. (1973), 'Some drag coefficients for british forest trees derived from wind tunnel studies', *Agricultural Meteorology* **12**, 123 – 130.

Mazda, Y., Wolansky, E., King, B., Sase, A., Ohtsuka, D. & Magi, M. (1997), 'Drag force due to the vegetation in mangrove swamps', *Mangroves and Salt Marshes* **1**, 193–199.

McBride, M., Hession, W. C., Rizzo, D. M. & Thompson, D. M. (2007), 'The influence of riparian vegetation on near-bank turbulence: A flume experiment', *Earth Surface Processes and Landforms* **32**(13), 2019 – 2037.

McMahon, T. A. (1975), 'The mechanical design of trees', *Scientific American* **233**, 93 – 102.

Musleh, F. A. & Cruise, J. (2006), 'Functional relationships of resistance in wide flood plains with rigid unsubmerged vegetation', *Journal of Hydraulic Engineering* **132**(2), 163 – 171.

Naot, D., Nezu, I. & Nakagawa, H. (1996), 'Hydrodynamic behaviour of partly vegetated open channels', *Journal of Hydraulic Engineering, ASCE* **122**, 625–633.

NationalStatistics (2009), Land use change statistics, Technical report, Office of the Deputy Prime Minister.

Natural England, N. (2008), *Entry Level Stewardship Handbook*, Natural England.

Nehal, L., Yan, Z.-M. & Xia, J.-H. (2005), 'Study of the flow through non-submerged vegetation', *Journal of Hydrodynamics* **17**(4), 498 – 502.

Nepf, H. (1999), 'Drag, turbulence and diffusion in flow through emergent vegetation', *Water Resources Research* **35**(2), 479 – 489.

Nepf, H., Sullivan, J. & Zavistoski, R. (1997), 'A model for diffusion within emergent vegetation', *Limnology and Oceanography* **42**, 1735 – 1745.

Newsholme, C. (1992), *Willows*, 1 edn, Betsford Ltd, London.

Nezu, I. & Onitsuka, K. (2001), 'Turbulent structures in partly vegetated open-channel flows with lda and piv measurements', *Journal of Hydraulic Research/De Recherches Hydrauliques* **39**(6), 629 – 642.

Nikora, V. (2000), 'Comment on 'drag, turbulence, and diffusion in flow through emergent vegetation' by h. m. nepf', *Water Resources Research* **36**(7), 1985 – .

NVC (2004), *(revised 2004), National vegetation classification field guide to woodland*, NVC. 117 pages A5 softback, ISBN 1 86107 554 5.

Oplatka, M. (1998*a*), Stabilität von Weidenverbauungen an Flu/βufern, PhD thesis, Technischen Hochschule Zürich.

Oplatka, M. (1998*b*), Stroemungskraefte auf weiden- versuche im eichkanal der lhg, Technical report, Versuchsanstalt fuer Wasserbau Hydrologie und Glaziologie ETH Zuerich.

Petryk, S. (1969), Drag on cylinders in open channel flow; Ph. D. thesis, Colorado State University, Fort Collins, PhD thesis.

Petryk, S. & Bosmajian, G. I. (1975), 'Analysis of flow through vegetation', **101**(7), 871 – 884.

Poggi, D., Porporato, A., Ridolfi, L., Albertson, J. & Katul, G. (2004), 'The effect of vegetation density on canopy sub-layer turbulence', *Boundary-Layer Meteorology* **111**(3), 565 – 587.

Posthumus, H., Morris, J., Hewett, C., Quinn, P. & Murphy, D. (2006), Laver: Report of stakeholder workshop, Technical report, Laver MOP.

Prochnow, D. (2000), 'Impact of vegetation on the turbulent flow in rivers', *Systems Analysis Modelling Simulation* **38**(3), 495 – 518.

Rahmeyer, W., Werth, D. & Cleere, R. (1995), The study of resistance and stability of vegetation in flood channels, lab report usu-376, Technical report, USAEWES.

Rauch, H. P., Meixner, H., Vollsinger, S. & Florineth, F. (2005), *RIPFOR - The scientific report: Field work and the Wien River*, Universiteat Berlin.

Raupach, M. (1992), 'Drag and drag partition on rough surfaces', *Boundary Layer Meteorology* **60**, 375 – 395.

Raymer, W. (1962), 'Wind resistance of conifers', *NPL Aero Rept* **1008**, 5.

Record, S. (1914), *The mechanical properties of wood, including a discussion of the factors affecting the mechanical properties, and methods of timber testing*, J. Wiley and Sons, Inc.

Ree, W. O. (1958), 'Retardation coefficients for row crops in division terraces', *Trans. Am. Soc. Agric. Eng.* **1**, 78 – 80.

Ree, W. O. & R., C. F. (1977), 'Friction factors for vegetated waterways', *Agric. Eng. USDA ARS-S-151* .

Richter, A. (1973), Current strength on stiff circle cylinders between parallel walls, in german, Master's thesis, Karlsruhe.

Righetti, M. & Armanini, A. (2002), 'Flow resistance in open channel flows with sparsely distributed bushes', *Journal of Hydrology* **269**, 55 – 64.

Roberts, N. (1998), *The Holocene: An Environmental History*, 2 edn, Blackwell.

Rodwell, J. & Patterson, G. (1994), Creating new native woodlands. forestry commission bulletin 112, Technical report, Forestry Commission, Edinburgh.

Rudman, T. (2008), 'Salix infesting river channel', Department of Primary Industries and Water, Tasmania, online.

Sahin, B., Ozturk, N. A. & Akilli, H. (2007), 'Horseshoe vortes system in the vicinity of the vertical cylinder mounted on a flat plate', *Flow Measruement and Instrumentation* **18**, 57 – 68.

Schindler, R. J. (2005), The role of in-stream macrophytes in the modification of three-dimensional turbulence structure, PhD thesis, School of Geography, University of Leeds.

Schlichting, H. (2000), *Boundary Layer Theory*, 8 edn, Springer.

ScottishExecutive (2002), Scottish forestry grant schemes, Technical report, Scottish Executive.

Sengupta, S. & Lee, S. S. (1986), 'Time dependent three dimensional simulation of flows in shallow domains with vegetative obstruction.', *Applied Mathematical Modelling* **10**(1), 2 – 10.

Shaw, E. (2004), *Hydrology*, Cambridge University Press.

Smith, R. J., Hancock, N. H. & Ruffini, J. L. (1990), 'Flood flow through tall vegetation', *Agricultural Water Management* **18**, 317,332.

Somes, N. L., Bishop, W. A. & Wong, T. H. (1999), 'Numerical simulation of wetland hydrodynamics', *Environment International* **25**(6-7), 773 – 779.

Starr, C. (2005), *Woodland Management: A Practical Guide*.

Stern, N. (2005), *The economics of climate change: the Stern review*.

Stoesser, T., Neary, V. & Wilson, C. (2003), 'Modeling vegetated channel flows: challenges and opportunities'.

Stone, B. & Shen, H. (2002), 'Hydraulic resistance of flow in channels with cylindrical roughness', *Journal of Hydraulic Engineering* **128**, 500 – 506.

Struve, J., Falconer, R. A. & Wu, Y. (2003), 'Influence of model mangrove trees on the hydrodynamics in a flume', *Esturine, Coastal and Shelf Science* **58**, 163–171.

Sumer, B., Christiansen, N. & e, F. (1997), 'The horseshoe vortex and vortex shedding around a vertical wall-mounted cylinder exposed to waves', *Journal of Fluid Mechanics* **332**, 41 – 70.

Tanino, Y. & Nepf, H. (2008*a*), 'Laboratory investigation of mean drag in a random array of rigid, emergent cylinders', *Journal of Hydraulic Engineering* **134**, 34–41.

Tanino, Y. & Nepf, H. M. (2008*b*), 'Lateral dispersion in random cylinder arrays at high reynold's number', *Journal of Fluid Mechanics* **600**, 339 – 371.

Tansley, A. G. (1949), *The British Isles and their Vegetation*, 2 edn.

Temple, D. M. (1987), '"closure 'velocity distribution coefficients for grass-lined channels' by darren temple"', *J. Hydraul. Div., ASCE* **113**, 1224 – 1226.

Thompson, G. T. & Robertson, J. A. (1976), 'A theory of flow resistance for vegetation channels', *Trans. Am. Soc. Agric. Eng.* **19**, 288 – 293.

Trust, W. (2004), Great triley wood management plan 2003 to 2008, Technical report, Woodland Trust.

Tsujimoto, T. & Kitamura, T. (1998*a*), Model for flow over flexible vegetation-covered bed, Vol. 1, pp. 556 – 561.

Tsujimoto, T. & Kitamura, T. (1998*b*), Model for flow over flexible vegetation-covered bed, Vol. 2, pp. 1380 – 1385.

Turner, A. K. & Chanmeesri, N. (1984), 'Shallow flow of water through non-submerged vegetation', *Agricultural Water Management* **8**, 375 – 385.

Turner, A. K., Langford, K. J., Myo, W. & Clift, T. R. (1978), 'Discharge-depth equation for shallow flow', *Proc. ASCE* **104**, 95 – 110.

UN (2006), United nations forum on forests. report on the sixth session, Technical report, United Nations.

UN (2008), Millennium development goals indicators database series: terrestrial areas protected, Technical report, UN.

UN (2009), State of the world's forests 2009, Technical report, Food and Agriculture Organization of the United Nations.

USDA (1947), Handbook of channel design for soil and water conservation, Technical report, United States Department of Agriculture, Soil Conservation Service.

Velasco, D., Bateman, A., Redondo, J. M. & Demedina, V. (2003), 'An open channel flow experimental and theoretical study of resistance and turbulent characterization over flexible vegetated linings', *Flow, Turbulence and Combustion* **70**(1-4), 69 – 88.

Vionnet, C., Tassi, P. & Martin Vide, J. (2004), 'Estimates of flow resistance and eddy viscosity coefficients for 2d modelling on vegetated floodplains', *Hydrological Processes* **18**(15), 2907 – 2926.

Vogel (1994), *Life in moving fluids*, 2nd edn, Princeton University Press.

Vogel, S. (1989), 'Drag and reconfiguration of broad leaves in high winds', *Journal of Experimental Botany* **40**, 941–948.

Wales, E. A. (2009), Flooding in wales, Technical report, Environment Agency.

Weissteiner, C. (2009), Biomechanical behaviour of plants under hydraulic load, Technical report, University of Natural Resources and Applied Life Sciences, Vienna.

Westwater (2000), Simulated Flows in Mangrove Canopies, PhD thesis, Cardiff School of Engineering, Cardiff University.

White, F. M. (1991), *Viscous fluid flow*, 2 edn, McGraw-Hill, New York.

Wilson, C. (2007), 'Flow resistance models for flexible submerged vegetation', *Journal of Hydrology* **342**, 213 222.

Wilson, C., Hoyt, J. & Schnauder, I. (2008), 'Impact of foliage on the drag force of vegetation in aquatic flows', *Journal of Hydrologic Engineering* **134**, 885 891.

Wilson, C., Schnauder, I., Mas, J. & Hoyt, J. (2005), Measuring the drag force of vegetation, *in* 'IAHR 31st Conference Congress, Spet 11-16, Korea', p. 93530.

Wilson, C., Yagci, O., Rauch, H. P. & Stoesser, T. (2003), Numerical modelling of vegetation flow interaction: the wienfluss test case, *in* 'EGS-AGU-EUG Joint Assembly, 06.-11.04.2003, Nice, France', pp. 383–390.

Wilson, C. et al. (2003), 'Open channel flow through different forms of submerged flexible vegetation', *Journal of Hydraulic Engineering* **129**(11), 847 – 853.

Wilson, N. R. & Shaw, R. H. (1977), 'A higher order closure model for canopy flow', *Journal of Applied Meteorology* **16**, 1198–1205.

Wu, F., Sgen, H. W. & Chou, Y. (1999), 'Variation of roughness coefficients for unsubmerged and submerged vegetation', *Journal of Hydraulic Engineering* (9).

Yang, K.-J., Liu, X.-N., Cao, S.-Y. & Zhang, Z.-X. (2005), 'Turbulence characteristics of overbank flow in compound river channel with vegetated floodplain', *Shuili Xuebao/Journal of Hydraulic Engineering* **36**(10), 1263 – 1268.

ZHANG, J.-t. & SU, X.-h. (2008), 'Numerical model for flow motion with vegetation', *Journal of Hydrodynamics* **20**(2), 172 – 178.

List of Figures

List of Tables

.1 Stage Discharge Data

Weir Height mm	Discharge l/s	Flow Depth mm
30	11.05396825	44.63203824
37	17.70643275	55.79403934
36	17.63967505	56.98999278
38	17.89444444	63.95703824
35	21.97490347	66.54979392
35	21.15996272	67.26840187
38	20.7531746	72.87181096
38	29.31944444	83.85249278
38	45.22348516	87.26840187
37	56.14516153	88.77408369

Table 1: Empty Flume Measured Data

Weir Height mm	Discharge l/s	Flow Depth mm
33.0000	5.3500	34.4914
34.0000	5.6250	36.6489
35.0000	6.1667	37.2139
50.0000	11.6333	63.9639
60.0000	15.9619	78.5964
82.0000	22.3722	118.8264
106.0000	23.6778	145.7939
108.0000	33.1663	159.9589
122.0000	49.1432	175.8214
128.0000	56.2596	182.3514

Table 2: Dowel Low Density Measured Data

Weir Height mm	Discharge l/s	Flow Depth mm
39.0000	5.3000	40.0576
40.0000	6.0000	43.0889
42.0000	6.0950	44.8364
60.0000	10.5278	74.0514
98.0000	14.4444	117.7794
127.0000	19.4942	158.5564
175.0000	22.2500	219.1889
200.0000	30.6778	249.7389

Table 3: Medium Density Dowel Measured Data

Weir Height mm	Discharge l/s	Flow Depth mm
58.0000	3.6100	55.1164
78.0000	5.5650	79.1089
70.0000	5.9200	73.8114
125.0000	10.9164	136.5889
150.0000	9.9333	160.6889
165.0000	10.4043	176.8639
180.0000	12.8800	195.7014
235.0000	15.2593	250.3139

Table 4: High Density Dowel Measured Data

Weir Height mm	Discharge l/s	Flow Depth mm
30.0000	4.7700	27.9833
34.0000	6.2375	33.6741
59.0000	13.8194	71.2207
62.0000	17.4984	88.1730
75.0000	21.9860	117.2889
80.0000	19.0740	104.9622
90.0000	29.3901	138.9511
106.0000	52.1875	160.7431
107.0000	39.7942	159.8183
108.0000	59.3001	163.7520

Table 5: Low Density Cornus Sanguinea Measured Data

Weir Height mm	Discharge l/s	Flow Depth mm
55.0000	10.8211	65.7564
81.0000	17.1242	112.7100
109.0000	21.7939	147.3484
150.0000	41.3333	201.7014
150.0000	27.8500	202.5514
150.0000	55.3500	203.0014

Table 6: Medium Density Cornus Sanguinea Measured Data

Weir Height mm	Discharge l/s	Flow Depth mm
50.0000	6.2000	55.5764
100.0000	11.2333	113.9639
165.0000	17.0547	189.7064
219.0000	21.2049	257.0314
250.0000	27.9778	295.5264

Table 7: High Density Cornus Sanguinea Measured Data

Type	5	10	20	30 D	40	50
Empty	21.285	38.128	64.972	82.692	91.288	90.760
Dowel Low	30.315	58.645	106.452	142.457	166.660	179.061
Dowel Med	36.676	78.041	159.771	249.501	290.231	408.961
Dowel High	72.456	152.656	313.056	473.456	633.856	794.256
Cornus Low	28.789	57.335	104.468	138.323	158.900	166.199
Cornus Med	35.269	75.266	139.856	183.906	207.416	210.386
Cornus High	51.306	107.556	220.056	332.556	445.056	557.556

Table 8: Fitted Values

Density	Q	h	n	RE	C_D
Low	0.010	0.059	0.032	3547	4.401
Low	0.020	0.106	0.041	3920	3.603
Low	0.030	0.142	0.043	4407	2.851
Low	0.040	0.167	0.041	5023	2.195
Low	0.050	0.179	0.036	5844	1.621
Medium	0.005	0.037	0.029	2941	2.810
Medium	0.010	0.078	0.050	2699	3.342
Medium	0.020	0.161	0.076	2648	3.473
Medium	0.030	0.244	0.096	2588	3.635
High	0.005	0.072	0.089	1499	2.579
High	0.010	0.153	0.142	1423	2.863
High	0.015	0.233	0.179	1398	2.965
High	0.020	0.313	0.207	1388	3.011

Table 9: Dowel Manning's n and C_D with Dowel Reynold's number RE_d

Density	Q	h	n	RE	C_D
Low	0.020	0.104	0.040	2237	6.219
Low	0.030	0.138	0.041	2534	4.846
Low	0.040	0.159	0.048	2941	3.597
Low	0.050	0.166	0.032	3515	2.518
Medium	0.010	0.075	0.047	1555	5.766
Medium	0.020	0.140	0.062	1673	4.977
Medium	0.030	0.184	0.063	1909	3.825
Medium	0.040	0.207	0.057	2257	2.737
Medium	0.050	0.210	0.046	2781	1.802
High	0.005	0.051	0.051	1151	2.539
High	0.010	0.108	0.083	1098	2.790
High	0.020	0.220	0.124	1073	2.920
High	0.030	0.333	0.150	1065	2.964

Table 10: Cornus Manning's n and C_D with Dowel Reynold's number RE_d

Type	**Q** m^3/s	y_m mm	U_m m/s	Re_{dm}	y_p **mm**	U_p m/s	Re_{dp}	Fr
Dowel Low	0.010	0.059	0.142	3547	0.295	0.317	39658	0.287
Dowel Low	0.020	0.107	0.157	3920	0.534	0.351	43830	0.317
Dowel Low	0.030	0.142	0.176	4407	0.712	0.394	49275	0.356
Dowel Low	0.040	0.167	0.201	5023	0.833	0.449	56159	0.406
Dowel Low	0.050	0.179	0.234	5843	0.895	0.523	65337	0.472
Dowel Medium	0.005	0.038	0.118	2941	0.190	0.263	32884	0.238
Dowel Medium	0.010	0.078	0.108	2698	0.390	0.241	30170	0.218
Dowel Medium	0.020	0.159	0.106	2647	0.795	0.237	29601	0.214
Dowel Medium	0.030	0.244	0.104	2587	1.220	0.231	28934	0.209
Dowel Medium	0.040	0.326	0.103	2582	1.630	0.231	28874	0.209
Dowel High	0.005	0.072	0.060	1498	0.362	0.134	16757	0.121
Dowel High	0.010	0.153	0.057	1422	0.763	0.127	15908	0.115
Dowel High	0.015	0.233	0.056	1398	1.165	0.125	15634	0.113
Dowel High	0.020	0.313	0.056	1387	1.565	0.124	15515	0.112
Cornus Low	0.020	0.104	0.160	2396	0.522	0.357	26791	0.417
Cornus Low	0.030	0.138	0.181	2714	0.692	0.405	30351	0.472
Cornus Low	0.040	0.159	0.210	3150	0.795	0.470	35228	0.548
Cornus Low	0.050	0.166	0.251	3765	0.831	0.561	42101	0.655
Cornus Medium	0.010	0.075	0.111	1665	0.376	0.248	18624	0.290
Cornus Medium	0.020	0.140	0.120	1793	0.699	0.267	20046	0.312
Cornus Medium	0.030	0.184	0.136	2045	0.920	0.305	22867	0.356
Cornus Medium	0.040	0.207	0.161	2417	1.037	0.360	27034	0.420
Cornus Medium	0.050	0.210	0.199	2979	1.052	0.444	33315	0.518
Cornus High	0.005	0.051	0.082	1233	0.257	0.184	13788	0.214
Cornus High	0.010	0.108	0.078	1176	0.538	0.175	13154	0.205
Cornus High	0.020	0.220	0.077	1150	1.100	0.171	12858	0.200
Cornus High	0.030	0.333	0.076	1141	1.663	0.170	12763	0.198

Table 11: Model and Prototype depth, velocity and RE_d

V	Q l/s	Weir mm	Depth mm	$n_c data$	$n_c L$	$n_c U$	n_{cp}	$nc_{cp}L$	$n_{cp}U$	n_{cp}
DL	0.010	0.047	0.059	0.032	0.039	0.041	0.040	0.036	0.038	0.037
DL	0.020	0.078	0.106	0.041	0.049	0.052	0.051	0.049	0.052	0.051
DL	0.030	0.102	0.142	0.043	0.048	0.051	0.050	0.048	0.051	0.050
DL	0.040	0.119	0.167	0.041	0.044	0.047	0.046	0.044	0.047	0.046
DL	0.050	0.127	0.179	0.036	0.036	0.038	0.037	0.036	0.038	0.037
DM	0.005	0.039	0.037	0.029	0.038	0.041	0.040	0.034	0.037	0.036
DM	0.010	0.060	0.078	0.046	0.056	0.060	0.058	0.055	0.061	0.058
DM	0.020	0.127	0.161	0.076	0.099	0.106	0.103	0.088	0.096	0.092
DM	0.030	0.200	0.244	0.099	0.120	0.132	0.126	0.109	0.118	0.114
DH	0.005	0.071	0.072	0.089	0.121	0.130	0.126	0.103	0.111	0.107
DH	0.010	0.150	0.153	0.142	0.195	0.207	0.201	0.177	0.191	0.184
DH	0.015	0.225	0.233	0.179	0.258	0.278	0.268	0.229	0.248	0.239
DH	0.020	0.300	0.313	0.207	0.342	0.348	0.345	0.293	0.311	0.302

Table 12: Measured and Modelled Manning's n values with and without Porosity

.2 Chapter 4 tables

.2.1 Sampling from literature

Exp	S1	S1	S2	S2	S3	S3	S4	S4
Exp	σ err	χ^2	σ err	χ^2	σ err	χ^2	σ err	χ^2
D2b	-21.0732	2.6828	-12.4736	0.9393	-4.0792	0.1644	1.9185	0.0500
D2c	-19.3454	5.7439	-9.7198	1.4688	-4.9629	0.4071	1.5452	0.0494
D3b	-19.1837	2.0467	-14.1468	1.1285	-7.6732	0.3284	0.1478	0.0449
D3c	-7.2575	1.1372	-8.3851	0.2672	-9.8102	0.3698	2.4303	0.0738

Table 13: Mean and χ^2 values for sampled streamwise velocities from Dowel Experiments

Exp	S1	S1	S1	S1	S2	S2	S2	S2
	$\sigma\ err_l$	$\sigma\ err_g$	$\chi^2 l$	$\chi^2 g$	$\sigma\ err_l$	$\sigma\ err_g$	$\chi^2 l$	$\chi^2 g$
V2b	-0.4543	9.4101	0.6735	2.8224	-0.5218	9.3360	0.0789	1.6964
V2c	-3.5242	-7.0617	1.8946	4.6574	-2.6413	-6.2111	0.4145	2.6191
V2d	-1.0399	-8.6919	1.3267	4.3647	-6.3422	-13.5842	1.5404	4.9545
V2e	-2.0075	-0.5477	1.2021	5.1418	1.7880	3.3043	0.6810	3.4387
V2f	6.7420	6.1703	1.1779	1.2466	2.2052	1.6578	0.1513	0.2264
V2g	0.3358	0.8732	0.3732	0.6724	-5.7376	-5.2328	0.8087	0.4487
V3b	-7.1422	0.9654	0.8531	0.1650	-3.4097	5.0238	0.1954	0.4897
V3c	-14.5884	-19.0876	3.2639	5.5525	-2.3705	-7.5132	0.1070	0.8438
V3d	-11.5367	-12.6820	1.8981	2.5455	-6.7959	-8.0026	0.9430	1.5335
V3e	-12.4369	-14.3361	2.2288	3.6585	-5.4613	-7.5118	0.5486	1.6405
V3f	-0.3317	-2.5949	0.2481	0.1387	2.2790	-0.0435	0.0557	0.0860
V3g	-9.6356	-7.5837	1.2810	1.0431	-2.2073	0.0133	0.1368	0.2137

Table 14: Mean and χ^2 values for sampled streamwise velocities from Cornus Experiments for Sampling Patterns S1 and S2, measured against the local sampling volume values (l) and the combined global values g

Exp	S3	S3	S3	S3	S4	S4	S4	S4
	$\sigma\ err_l$	$\sigma\ err_g$	$\chi^2 l$	$\chi^2 g$	$\sigma\ err_l$	$\sigma\ err_g$	$\chi^2 l$	$\chi^2 g$
V2b	-0.5091	9.3499	0.0586	1.7644	6.8778	17.4688	0.7837	4.8463
V2c	-0.4377	-4.0883	0.0637	1.7753	4.9596	1.1111	0.3570	1.5920
V2d	1.1718	-6.6512	0.0678	2.2015	0.6267	-7.1541	0.0722	2.7869
V2e	0.4009	1.8965	0.1660	4.8238	2.4959	4.0227	0.2352	3.5885
V2f	3.2703	2.7173	0.1196	0.1442	-0.2918	-0.8258	0.1877	0.1901
V2g	1.3330	1.8757	0.2064	0.2949	0.4383	0.9763	0.0863	0.0385
V3b	0.5476	9.3266	0.0262	1.4763	1.1735	10.0072	0.0690	1.7190
V3c	0.1874	-5.0901	0.0474	0.4380	5.1226	-0.4149	0.4523	0.1578
V3d	0.9228	-0.3838	0.0429	0.2911	2.9285	1.5958	0.1881	0.4383
V3e	1.5460	-0.6564	0.0618	0.7332	0.1988	-1.9744	0.0914	0.9979
V3f	-1.4703	-3.7076	0.1106	0.1386	4.9071	2.5250	0.3049	0.1901
V3g	2.2593	4.5813	0.0739	0.3780	5.1131	7.4999	0.2942	0.6616

Table 15: Mean and χ^2 values for sampled streamwise velocities from Cornus Experiments for Sampling Patterns S3 and S4, measured against the local sampling volume values (l) and the combined global values g

Exp	S1	S1	S1	S1	S2	S2	S2	S2
	$\sigma\ err_l$	$\sigma\ err_g$	$\chi^2 l$	$\chi^2 g$	$\sigma\ err_l$	$\sigma\ err_g$	$\chi^2 l$	$\chi^2 g$
V2b	45.2343	30.9806	40.6587	31.6300	2.6915	-7.3870	4.7408	4.3224
V2c	-4.9204	-18.5948	2.3061	4.8501	0.3633	-14.0710	1.4528	4.0341
V2d	5.5418	8.5386	6.6009	17.3185	18.8936	22.2695	8.2901	19.7275
V2e	2.8551	24.8218	16.2155	23.4566	28.1522	55.5216	16.8630	73.0886
V2f	1.8759	1.2801	1.9101	6.1897	-11.1478	-11.6675	1.4082	2.9198
V2g	-8.4647	-7.9294	1.8002	4.6764	-6.1714	-5.6227	0.9220	1.4864
V3b	45.5391	18.0939	9.8558	3.7776	22.5442	-0.5647	2.2136	1.7832
V3c	6.8808	-1.8155	1.1227	1.6756	14.0155	4.7387	1.2138	0.8499
V3d	-8.0510	-6.2258	1.1777	1.1657	10.1126	12.2983	2.1296	3.6327
V3e	-9.1545	13.5651	11.9031	5.4750	60.5999	-100.7644	80.7161	259.6159
V3f	2.1448	1.7033	0.4398	1.0193	-0.9732	-1.4012	0.3632	1.3167
V3g	-0.3429	0.0879	1.7568	1.5047	-0.2029	0.2285	1.8738	1.2412

Table 16: Mean and χ^2 values for sampled turbulent kinetic energy from Cornus Experiments for Sampling Patterns S1 and S2, measured against the local sampling volume values (l) and the combined global values (g)

Exp	S3	S3	S3	S3	S4	S4	S4	S4
	$\sigma\ err_l$	$\sigma\ err_g$	$\chi^2 l$	$\chi^2 g$	$\sigma\ err_l$	$\sigma\ err_g$	$\chi^2 l$	$\chi^2 g$
V2b	3.2731	-6.8624	3.7482	4.3001	18.9065	7.2367	5.8150	3.8593
V2c	10.4890	-5.4016	1.4818	5.2698	-7.1892	-20.5373	0.8807	4.5731
V2d	0.6445	3.5022	0.6980	5.6419	-1.8053	0.9829	0.8792	4.4038
V2e	8.2119	31.3227	8.7104	11.1273	-12.2425	6.4999	2.9361	4.6577
V2f	-2.6557	-3.2250	0.2492	3.1061	22.5693	21.8525	4.4917	8.4623
V2g	-23.7422	-23.2963	4.7157	6.5220	17.7339	18.4225	13.3607	5.3157
V3b	-3.2881	-21.5256	0.0757	3.0578	-8.8644	-26.0503	0.6049	3.9915
V3c	-9.4844	-16.8491	0.6119	2.0389	7.2244	-1.4999	2.2948	1.8913
V3d	-10.4414	-8.6636	0.5618	1.7900	11.9838	14.2067	2.3700	3.7496
V3e	-23.7218	-4.6454	8.1932	1.5766	16.6168	45.7815	9.6364	57.0136
V3f	-3.7199	-4.1361	0.3956	0.2557	7.3521	6.8880	1.5667	0.8751
V3g	-7.3865	-6.9861	0.3832	0.6835	2.0274	2.4684	0.5672	1.5523

Table 17: Mean and χ^2 values for sampled turbulent kinetic energy from Cornus Experiments for Sampling Patterns S3 and S4, measured against the local sampling volume values (l) and the combined global values (g)

.2.2 Transect sampling tables

Exp	Tx1	Tx2	Tx3	Tx4	Tx5	Tx6	Tx7	Tx8	Tx9	Tx10	Tx11
D2b	8.49	7.55	-3.74	-3.78	-4.72	-4.07	-3.26	-2.07	-1.21	1.58	5.25
D2c	8.39	10.28	-5.46	-5.06	-3.28	-4.96	-3.83	-3.49	-3.49	3.50	7.41
D3b	13.04	15.98	-4.52	-5.57	-6.44	-7.67	-7.10	-6.25	-6.43	2.49	12.49
D3c	20.16	15.43	-6.74	-6.40	-7.45	-9.81	-9.38	-9.47	-8.67	4.32	18.03

Table 18: Mean errors for sampled streamwise velocity U from Dowel Experiments for Transect samples Tx 1-11

Exp	Ty1	Ty2	Ty3	Ty4	Ty5	Ty6	Ty7
D2b	-11.85	-3.61	12.82	15.73	13.79	-6.41	-34.95
D2c	-11.35	-2.47	13.59	17.56	12.08	-15.29	-30.31
D3b	-8.60	-1.93	5.60	16.89	17.86	-10.92	-37.64
D3c	5.50	1.71	11.77	15.79	3.14	-28.28	-29.35

Table 19: Mean values for sampled streamwise velocity U from Dowel Experiments for Transect Samples Ty 1-11

Exp	Tx1	Tx2	Tx3	Tx4	Tx5	Tx6	Tx7	Tx8	Tx9	Tx10	Tx11
V2b	12.98	-1.50	0.47	-0.24	-0.95	-0.50	-0.64	-2.74	-0.96	-2.08	-3.79
V2c	-1.21	-3.03	0.07	-0.31	-0.42	-0.43	-0.70	-0.19	1.48	1.45	3.32
V2d	5.09	-3.27	-2.51	0.13	0.59	1.17	0.12	-3.33	-1.32	1.42	1.90
V2e	-0.58	-2.72	0.75	-3.07	0.46	0.40	0.85	0.74	1.69	-0.01	1.49
V2f	-14.30	-6.10	-0.51	1.26	1.05	3.27	4.51	3.85	4.05	3.55	-0.65
V2g	1.50	1.73	0.14	-0.21	-0.00	1.33	1.30	-2.59	-1.62	-1.37	-0.21
V3b	-1.02	-1.93	-0.63	-0.04	0.38	0.54	0.58	0.33	0.42	0.45	0.91
V3c	-7.75	-2.75	-2.04	-1.47	0.63	0.18	0.63	3.51	3.09	2.72	3.24
V3d	-2.86	-0.35	-0.24	-1.94	2.86	0.92	1.12	1.23	1.33	1.42	-3.48
V3e	-0.44	0.55	1.22	1.53	1.65	1.54	1.03	-2.36	0.22	-2.12	-2.84
V3f	-3.06	-1.73	-1.53	-0.01	0.43	-1.47	6.11	1.19	2.38	2.43	-4.74
V3g	-8.54	-1.66	2.14	1.43	2.58	2.25	2.63	2.13	2.16	1.65	-6.79

Table 20: Mean values for sampled streamwise velocity U from Cornus Experiments for Transect Samples Tx 1-11

Exp	Ty1	Ty2	Ty3	Ty4	Ty5	Ty6	Ty7
V2b	4.50	-0.85	-0.44	2.88	-0.27	-3.31	-2.50
V2c	7.48	7.70	8.93	8.93	-2.01	-6.65	-24.38
V2d	1.05	-0.42	3.05	4.75	8.22	4.11	-20.78
V2e	-6.06	-6.32	-7.06	3.41	5.90	6.85	3.28
V2f	11.90	10.17	5.76	2.92	-5.18	-10.58	-14.99
V2g	-0.06	0.97	2.69	4.65	5.19	0.79	-14.24
V3b	-9.00	4.68	8.98	8.44	3.26	-4.49	-11.87
V3c	-19.23	-13.11	4.31	19.81	13.19	4.88	-9.80
V3d	-1.88	6.22	15.44	14.07	2.26	-5.36	-30.76
V3e	-24.81	3.96	9.75	10.78	3.98	-0.16	-3.51
V3f	-1.19	4.97	6.58	13.92	1.10	-10.53	-14.85
V3g	-8.12	1.68	10.80	14.83	9.34	-5.67	-22.86

Table 21: Mean values for sampled streamwise velocity U from Cornus Experiments for Transect Samples Ty 1-7

Exp	Tx1	Tx2	Tx3	Tx4	Tx5	Tx6	Tx7	Tx8	Tx9	Tx10	Tx11
D2b	0.97	0.38	0.08	0.09	0.30	0.16	0.07	0.05	0.21	0.24	0.35
D2c	1.08	1.64	0.49	0.41	0.17	0.40	0.23	0.19	0.20	0.19	0.88
D3b	0.98	1.46	0.13	0.19	0.24	0.32	0.29	0.23	0.28	0.05	0.90
D3c	1.51	0.89	0.17	0.16	0.24	0.36	0.31	0.39	0.27	0.14	1.23

Table 22: χ^2 values for sampled streamwise velocity U from Dowel Experiments for Transect Samples Tx 1-11

Exp	Ty1	Ty2	Ty3	Ty4	Ty5	Ty6	Ty7
D2b	0.87	0.08	1.12	1.49	1.16	0.53	7.41
D2c	1.98	0.10	2.83	4.76	2.24	3.60	14.07
D3b	0.42	0.10	0.21	1.62	1.83	0.74	7.82
D3c	0.81	0.09	0.62	1.11	0.09	2.89	3.15

Table 23: χ^2 values for sampled streamwise velocity U from Dowel Experiments for Transect Samples Ty 1-7

Exp	Tx1	Tx2	Tx3	Tx4	Tx5	Tx6	Tx7	Tx8	Tx9	Tx10	Tx11
V2b	2.84	0.68	0.45	0.05	0.05	0.05	0.13	0.26	0.07	0.13	0.52
V2c	0.77	0.40	0.05	0.07	0.11	0.06	0.04	0.02	0.05	0.05	0.16
V2d	0.42	0.20	0.11	0.03	0.07	0.06	0.01	0.30	0.09	0.06	0.09
V2e	0.46	0.70	0.28	0.51	0.21	0.16	0.13	0.08	0.15	0.14	0.23
V2f	2.19	0.54	0.07	0.06	0.08	0.11	0.30	0.22	0.20	0.15	0.50
V2g	0.12	0.10	0.09	0.10	0.35	0.20	0.10	0.46	0.24	0.42	0.55
V3b	0.30	0.26	0.01	0.01	0.01	0.02	0.02	0.02	0.02	0.02	0.06
V3c	1.37	0.33	0.08	0.04	0.03	0.04	0.05	0.20	0.19	0.15	0.28
V3d	0.41	0.05	0.18	0.60	0.13	0.04	0.04	0.04	0.04	0.04	1.51
V3e	0.18	0.06	0.06	0.07	0.05	0.06	0.05	1.07	0.12	0.50	0.44
V3f	0.71	0.17	0.16	0.02	0.01	0.11	0.41	0.05	0.13	0.15	0.40
V3g	1.15	0.17	0.06	0.11	0.08	0.07	0.10	0.07	0.07	0.05	1.27

Table 24: χ^2 values for sampled streamwise velocity U from Cornus Experiments for Transect Samples Tx 1-11

Exp	Ty1	Ty2	Ty3	Ty4	Ty5	Ty6	Ty7
V2b	2.67	0.39	1.38	1.61	0.46	0.55	0.69
V2c	2.28	0.99	1.27	1.81	1.40	1.06	9.39
V2d	0.47	0.28	0.28	0.61	1.59	0.44	8.41
V2e	2.51	3.20	2.74	2.34	4.07	2.30	1.07
V2f	2.98	1.73	0.61	1.20	2.55	1.18	2.80
V2g	0.51	0.76	0.27	0.41	0.39	0.50	2.07
V3b	1.96	0.43	1.33	1.23	0.23	0.32	2.34
V3c	5.30	2.54	0.39	5.49	2.45	1.23	2.60
V3d	0.29	0.62	3.66	3.06	0.40	0.83	14.16
V3e	9.32	0.52	1.46	1.90	1.05	0.31	1.62
V3f	0.60	0.81	0.67	2.03	0.24	1.23	4.98
V3g	1.24	0.30	1.28	2.54	1.86	1.55	6.46

Table 25: χ^2 values for sampled streamwise velocity U from Cornus Experiments for Transect Samples Ty 1-7

Exp	Tx1	Tx2	Tx3	Tx4	Tx5	Tx6	Tx7	Tx8	Tx9	Tx10	Tx
D2b	-7.67	-14.26	30.04	13.26	9.52	1.53	3.65	-4.85	-7.53	-9.21	-14.
D2c	-18.70	-21.75	32.88	21.10	12.31	5.75	-0.52	-6.28	-9.94	-4.98	-9.8
D3b	-4.27	-6.95	33.41	18.64	-5.90	-19.74	-23.29	-15.72	3.87	15.53	4.4
D3c	-1.83	-1.99	26.89	-0.85	-22.22	-23.49	-19.72	-2.71	15.29	15.77	14.8

Table 26: Mean values for sampled TKE from Dowel Experiments for Transect Samples Tx 1-11

Exp	Ty1	Ty2	Ty3	Ty4	Ty5	Ty6	Ty7
D2b	-5.42	-7.13	-22.23	-32.01	-25.21	31.78	88.03
D2c	-5.90	-9.70	-28.75	-37.59	-16.71	53.93	75.48
D3b	-25.35	-28.69	-22.87	-16.63	3.50	44.41	51.69
D3c	-23.19	-28.62	-27.71	-10.21	15.79	37.35	35.55

Table 27: Mean values for sampled TKE from Dowel Experiments for Transect Samples Ty 1-7

Exp	Tx1	Tx2	Tx3	Tx4	Tx5	Tx6	Tx7	Tx8	Tx9	Tx10	Tx11
V2b	28.14	3.30	1.19	2.62	2.01	3.27	-10.39	2.00	-19.51	-10.37	-2.27
V2c	-8.67	-5.62	22.95	23.37	18.30	10.48	6.37	-5.04	-15.12	-22.57	-24.44
V2d	-1.89	25.66	25.92	15.91	12.88	0.64	-11.63	-8.30	-16.94	-23.24	-19.01
V2e	-39.52	-7.71	26.55	70.81	11.00	8.21	2.41	-11.24	-18.28	-20.93	-21.30
V2f	-5.60	24.57	26.51	4.87	10.10	-2.65	-17.76	-4.96	-0.84	-23.80	-10.43
V2g	78.28	18.16	4.83	-6.19	-16.01	-23.74	-25.83	-31.96	-8.78	-18.40	29.65
V3b	-14.27	21.26	24.63	5.76	0.40	-3.28	-4.73	-2.68	-6.90	-8.58	-11.60
V3c	7.70	43.77	30.29	11.76	-9.00	-9.48	-13.58	-18.35	-16.53	-19.07	-7.51
V3d	10.91	38.88	34.85	25.46	2.30	-10.44	-14.67	-18.68	-22.60	-23.61	-22.40
V3e	-9.40	-1.77	-8.41	-17.28	-22.11	-23.72	-27.13	104.57	21.13	-16.48	0.63
V3f	12.79	46.07	28.32	9.21	0.39	-3.71	-5.01	-18.03	-21.24	-24.53	-24.24
V3g	9.07	37.89	29.23	19.99	0.32	-7.38	-11.10	-15.15	-18.92	-20.58	-23.36

Table 28: Mean values for sampled TKE from Cornus Experiments for Transect Samples Tx 1-11

Exp	Ty1	Ty2	Ty3	Ty4	Ty5	Ty6	Ty7
D2b	83.72	24.32	19.70	-33.14	-31.06	-33.55	-29.99
D2c	-37.76	-32.85	-34.45	-33.25	32.11	67.43	38.78
D2d	-1.21	-5.00	-21.76	-26.35	-19.57	3.77	70.14
D2e	35.70	45.85	26.28	12.61	-29.42	-42.63	-48.38
D2f	-34.47	-39.52	-19.67	-0.27	53.29	18.70	21.95
D2g	-6.07	-3.51	-18.04	2.18	-19.46	6.28	38.64
D3b	94.96	-15.51	-37.64	-26.42	-12.56	0.56	-3.37
D3c	-2.23	-28.96	-40.29	-24.25	10.49	-5.16	90.41
D3d	-7.61	-13.60	-24.52	-12.72	8.28	17.05	33.14
D3e	69.69	-27.30	-38.23	-39.65	22.64	-6.86	19.71
D3f	-13.72	-7.05	-24.00	-27.47	3.95	13.74	54.56
D3g	-14.03	-15.22	-37.76	-35.81	15.46	25.99	61.37

Table 29: Mean values for sampled TKE from Cornus Experiments for Transect Samples Ty 1-7

Exp	Tx1	Tx2	Tx3	Tx4	Tx5	Tx6	Tx7	Tx8	Tx9	Tx10	Tx11
D2b	1.75	2.23	6.42	1.30	0.96	0.14	0.21	0.21	0.50	0.61	1.44
D2c	9.31	12.47	28.59	11.73	4.04	1.03	0.11	1.13	2.60	0.84	2.73
D3b	0.33	0.98	12.15	3.97	0.65	4.50	5.90	2.86	0.55	2.90	0.32
D3c	0.05	0.17	6.56	0.29	4.236	4.81	3.34	0.14	2.16	2.18	2.05

Table 30: χ^2 values for sampled TKE from Cornus Experiments for Transect Samples Tx 1-11

Exp	Ty1	Ty2	Ty3	Ty4	Ty5	Ty6	Ty7
D2b	0.22	0.40	4.38	8.28	5.07	8.68	60.38
D2c	1.27	2.56	21.76	37.07	7.53	76.77	149.63
D3b	6.90	8.87	5.61	3.02	0.25	21.20	28.67
D3c	5.53	7.03	6.55	1.35	2.23	11.68	10.93

Table 31: χ^2 values for sampled TKE from Dowel Experiments for Transect Samples Ty 1-7

Exp	Tx1	Tx2	Tx3	Tx4	Tx5	Tx6	Tx7	Tx8	Tx9	Tx10	Tx11
V2b	12.11	4.27	2.71	3.49	3.85	3.74	1.60	3.85	2.43	2.59	2.94
V2c	3.95	3.57	4.77	5.08	3.08	1.48	0.75	0.35	1.48	2.82	3.72
V2d	4.87	8.13	4.88	2.04	3.07	0.69	1.10	2.30	2.23	3.63	3.49
V2e	14.48	12.90	10.10	39.61	10.07	8.71	1.10	1.77	2.86	4.05	4.44
V2f	7.85	13.77	5.71	0.32	0.85	0.24	2.44	1.99	3.86	4.22	3.45
V2g	95.85	5.66	0.72	0.67	3.14	4.71	5.61	7.50	3.64	8.33	31.71
V3b	0.98	5.43	3.54	0.58	0.20	0.07	0.20	0.88	0.61	0.74	0.72
V3c	2.53	10.99	4.95	0.99	0.59	0.61	0.98	1.87	1.51	1.90	2.80
V3d	7.31	8.80	8.43	6.03	0.17	0.56	1.20	1.93	2.77	3.13	4.01
V3e	7.00	8.43	7.78	7.09	7.76	8.19	9.02	320.52	24.52	6.86	12.77
V3f	1.81	14.74	4.54	0.55	0.12	0.39	0.25	1.87	2.50	3.26	3.31
V3g	9.60	11.97	6.08	5.58	0.07	0.38	0.81	1.42	2.14	2.66	3.46

Table 32: χ^2 values for sampled TKE from Cornus Experiments for Transect Samples Tx 1-11

Exp	Ty1	Ty2	Ty3	Ty4	Ty5	Ty6	Ty7
V2b	48.99	11.03	12.71	10.65	9.76	9.48	6.21
V2c	8.46	8.04	9.22	11.88	19.29	32.24	18.74
V2d	6.26	3.83	6.19	6.51	5.55	3.97	53.14
V2e	27.34	21.84	16.57	18.93	17.93	16.73	20.83
V2f	12.11	16.59	19.50	2.58	33.04	7.53	11.36
V2g	1.86	3.31	6.31	16.32	2.95	15.40	16.71
V3b	37.93	3.87	6.06	3.12	0.92	1.00	1.14
V3c	0.61	4.92	8.06	4.74	3.11	2.56	42.87
V3d	1.68	2.19	5.15	7.96	10.92	10.18	15.14
V3e	40.88	8.72	13.28	14.40	21.45	5.80	7.47
V3f	2.63	0.87	3.89	4.53	2.87	1.82	40.54
V3g	1.26	1.37	8.75	7.88	20.84	8.72	40.68

Table 33: χ^2 values for TKE from Cornus Experiments for Transect Samples Ty 1-7

.2.3 Optimised Sampling

Dowel Array	**x**	**y**	**Vx**σ_{err}	**TKE**σ_{err}	$U\ {\chi_{err}}^2$	**TKE**${\chi_{err}}^2$
1	3	6	0.093886	45.337	0.088803	16.808
1	6	2	-0.324	-10.468	0.027315	1.0313
1	5	2	-1.2469	-4.8681	0.056337	0.69858
1	4	2	-1.8667	-5.8139	0.040274	1.1523
1	4	6	-2.1247	54.719	0.058263	21.852
2	4	2	1.1931	-3.8441	0.031476	1.2202
2	3	2	1.4299	-8.7776	0.084071	2.8429
2	1	2	-1.6045	4.1464	0.15422	1.016
2	2	2	1.6163	-4.572	0.11365	0.86466
2	5	2	2.5771	-5.888	0.15698	2.0653
3	8	3	-0.0883	-31.429	0.37361	10.764
3	5	1	0.1347	-46.156	0.17324	23.483
3	4	1	-0.2672	-35.707	0.024489	13.914
3	9	3	0.41784	-16.081	0.54092	3.8091
3	7	3	0.85795	-39.94	0.17873	17.162
4	3	5	0.0193	45.253	0.24823	18.28
4	8	3	0.4757	-34.955	0.31424	10.631
4	7	4	0.55622	-14.329	0.42332	3.143
4	6	2	0.57926	-51.9	0.043047	22.416
4	9	2	-1.19	11.348	0.862	14.366

Table 34: Dowel Arrays mean and χ^2 values for U and TKE

Cornus Array	x	y	Vxσ_{err}	TKEσ_{err}	U ${\chi_{err}}^2$	TKE${\chi_{err}}^2$
1	3	5	0.075736	-26.056	0.68325	10.843
1	6	2	-0.20866	36.31	0.37181	23.424
1	5	5	0.25086	-31.103	0.71605	9.0799
1	7	5	0.26627	-39.547	0.34282	10.64
1	10	2	-0.35059	6.1324	0.68753	1.6519
2	4	5	0.25485	39.344	1.4978	52.973
2	3	6	-1.797	78.338	1.467	78.562
2	3	5	3.1797	40.835	1.1488	52.066
2	1	2	3.3558	-24.162	1.3809	6.5489
2	5	6	-4.9248	92.691	1.3361	87.132
3	1	1	0.071479	8.2494	3.4293	67.79
3	5	3	-0.076213	-10.336	0.65065	17.183
3	4	3	-0.15171	1.673	0.56521	20.757
3	10	1	0.32117	-5.4031	0.6744	5.7139
3	9	6	0.43362	-9.1729	0.33144	4.9162
4	10	1	0.52371	18.114	1.4056	30.919
4	3	4	0.60502	38.619	7.4413	118.91
4	8	1	-0.68	8.5839	1.5037	20.303
4	3	3	-1.0702	110.54	8.2069	160.75
4	2	2	1.2109	-7.1148	6.0505	22.867
5	10	6	-0.39432	-28.4548	0.41189	18.228
5	1	4	0.493	176.8510	2.2989	357.43
5	8	5	0.57951	-15.6694	2.6478	110.14
5	9	5	0.67145	-17	2.5713	84.429
5	9	6	-1.8194	18.736	0.31382	22.741
6	1	3	-0.0467	-20.1981	2.1691	3.6037
6	1	4	0.2087	-7.3136	0.1875	1.5713
6	5	6	0.5272	-1.6224	0.4137	3.9567
6	4	6	0.6298	-1.2760	0.5716	3.5668
6	3	2	0.7332	-12.9635	1.2244	4.4774
7	9	2	2.2807	7.5325	0.52877	17.252
7	8	2	2.2974	16.671	0.47805	34.673
7	10	2	2.6104	3.5532	0.5158	11.106
7	8	5	2.868	-11.828	0.16578	0.86333
7	6	5	2.8968	-13.313	0.20164	0.97889

Table 35: Cornus Arrays mean and χ^2 values for U and TKE

Cornus Array	**x**	**y**	**Vx**σ_{err}	**TKE**σ_{err}	$U\ {\chi_{err}}^2$	**TKE**${\chi_{err}}^2$
8	8	7	-0.020762	4.204	0.56307	9.4995
8	4	3	-2.4657	-44.467	0.18966	9.4848
8	5	3	-2.5825	-45.041	0.21165	9.8838
8	7	3	-2.5928	-50.096	0.19241	11.897
8	3	3	-2.61	-44.787	0.26636	9.7195
9	3	1	-0.066217	7.2488	0.18879	2.1867
9	4	1	0.18102	-1.1409	0.13992	1.2507
9	10	1	-0.26355	-22.69	0.61912	3.551
9	9	5	1.1261	-14.756	0.29964	2.7428
9	6	1	1.1504	-9.5558	0.15862	1.8054
10	7	7	0.38438	-28.599	0.20018	8.4351
10	5	6	0.4451	-17.53	0.17878	8.0732
10	3	6	-0.53316	-12.37	0.24497	6.8341
10	2	6	-0.79736	-12.173	0.73309	7.9252
10	8	6	0.80581	-30.359	0.48575	9.2926
11	3	2	-0.029477	-8.9646	0.45278	1.8458
11	6	5	-0.16354	-10.129	0.19161	2.2696
11	5	5	0.23465	-1.6639	0.24495	2.2865
11	2	6	0.26832	55.528	0.058476	25.877
11	2	5	0.58839	65.628	0.63631	57.822
12	10	2	1.183	-26.072	0.061554	3.8893
12	4	6	-1.3481	41.028	0.80151	28.276
12	4	5	1.7183	102.22	6.71	349.32
12	5	6	-1.7378	30.863	0.67875	14.556
12	7	1	-1.7776	-19.61	0.096809	2.0956

Table 36: Cornus Arrays mean and χ^2 values for U and TKE

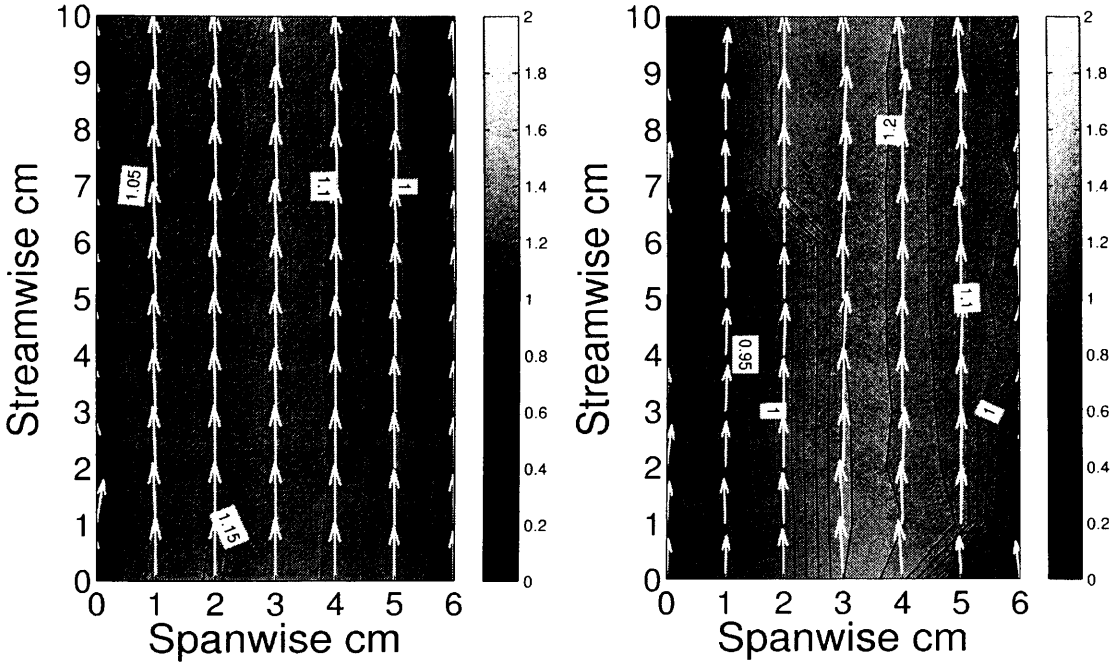

(a) *Cornus*, N=19.8 m^{-2}, high depth

(b) *Cornus*, N=19.8 m^{-2}, high depth

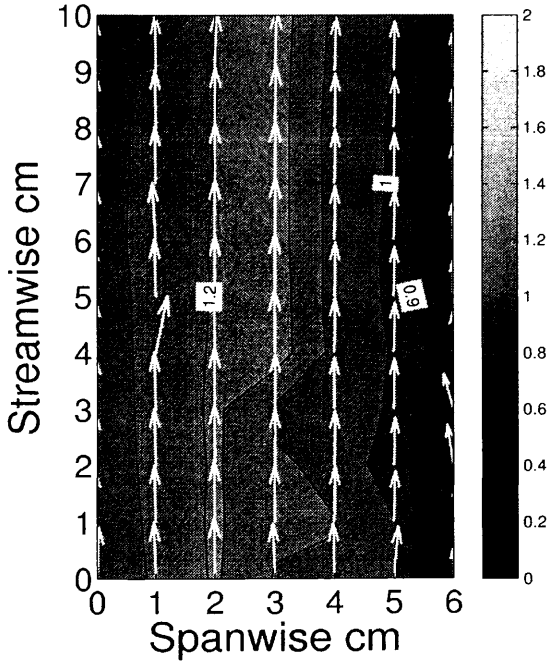

(c) *Cornus*, N=19.8 m^{-2}, high depth

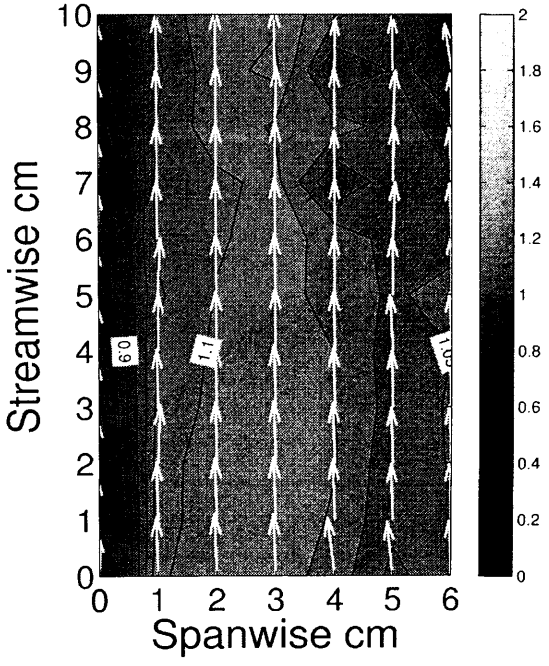

(d) *Cornus*, N=19.8 m^{-2}, high depth

Figure 1: Normalised depth-averaged streamwise velocity U in cm/s in medium density, high depth *Cornus* array

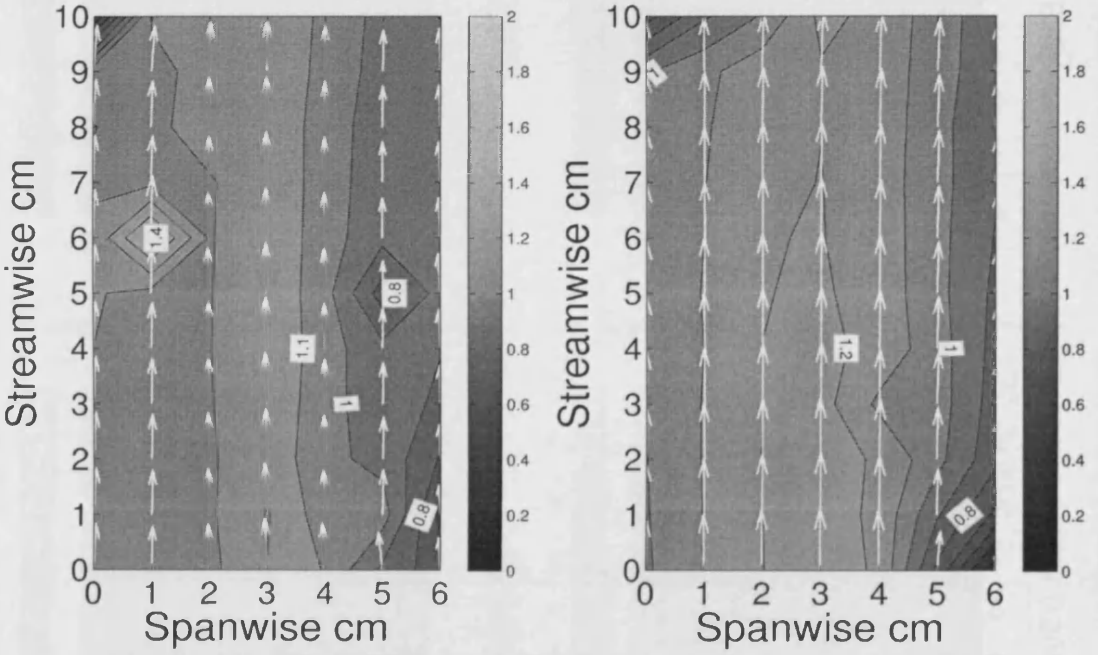

(a) *Cornus*, N=19.8 m^{-2}, low depth

(b) *Cornus*, N=19.8 m^{-2}, low depth

Figure 2: Normalised depth-averaged streamwise velocity U in cm/s in medium density, low flow depth *Cornus* Arrays

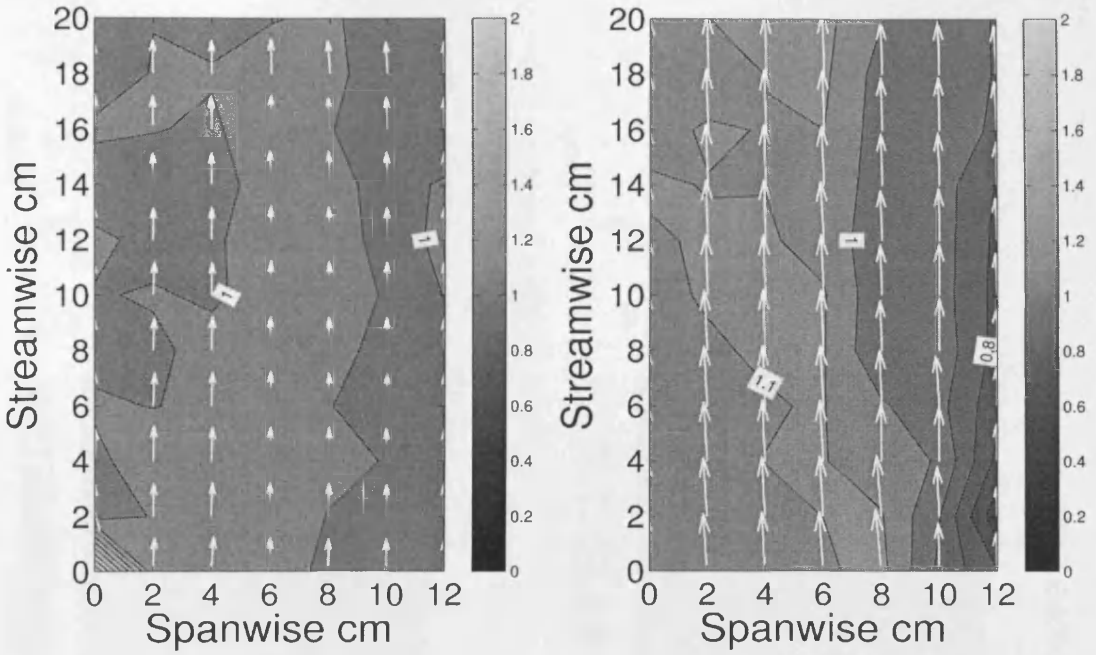

(a) *Cornus*, N=80.6 m^{-2}, high depth

(b) *Cornus*, N=80.6 m^{-2}, high depth

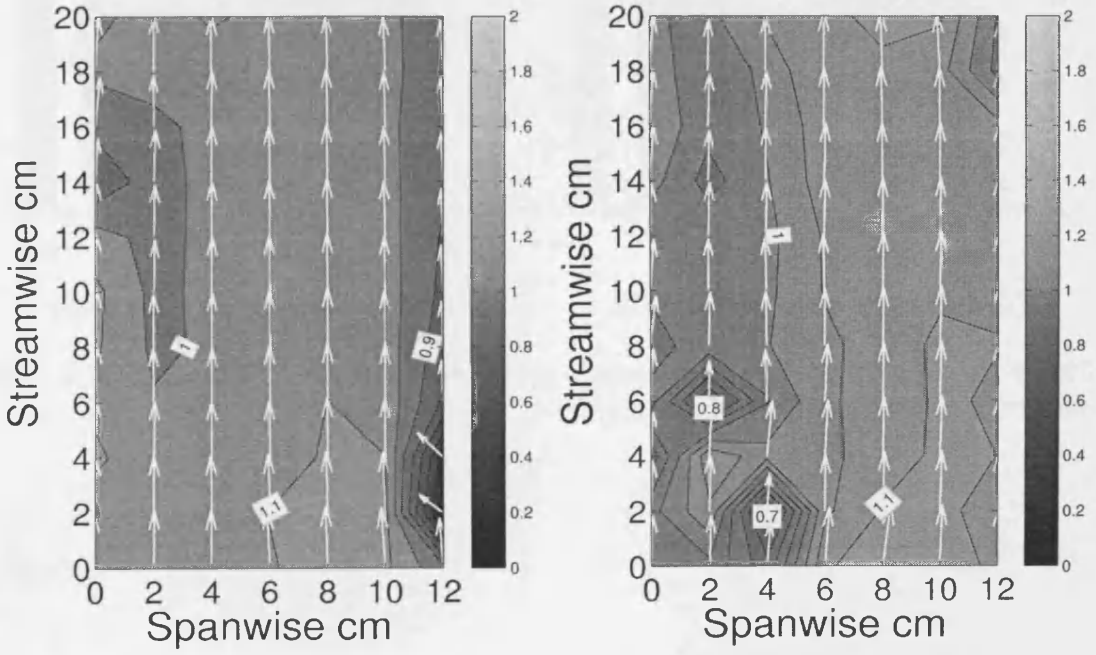

(c) *Cornus*, N=80.6 m^{-2}, high depth

(d) *Cornus*, N=80.6 m^{-2}, high depth

Figure 3: Normalised depth-averaged streamwise velocity U in cm/s in high density, high flow depth *Cornus* Arrays

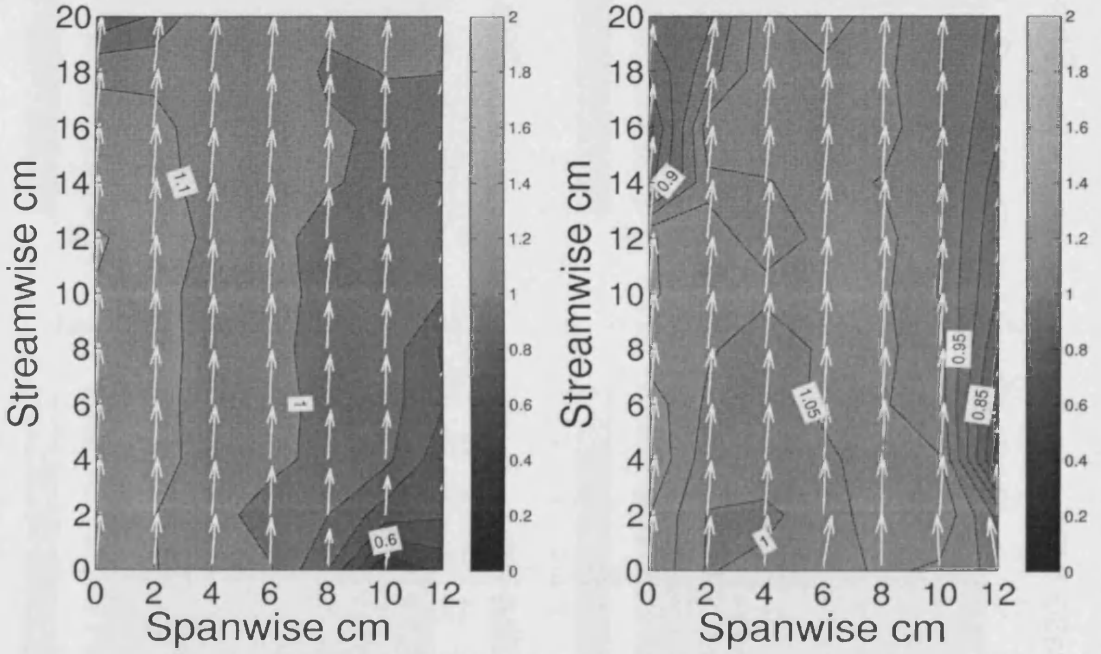

(a) *Cornus*, N=80.6 m^{-2}, low depth

(b) *Cornus*, N=80.6 m^{-2}, low depth

Figure 4: Normalised depth-averaged streamwise velocity (U) in cm/s in high density, low flow depth *Cornus* Arrays

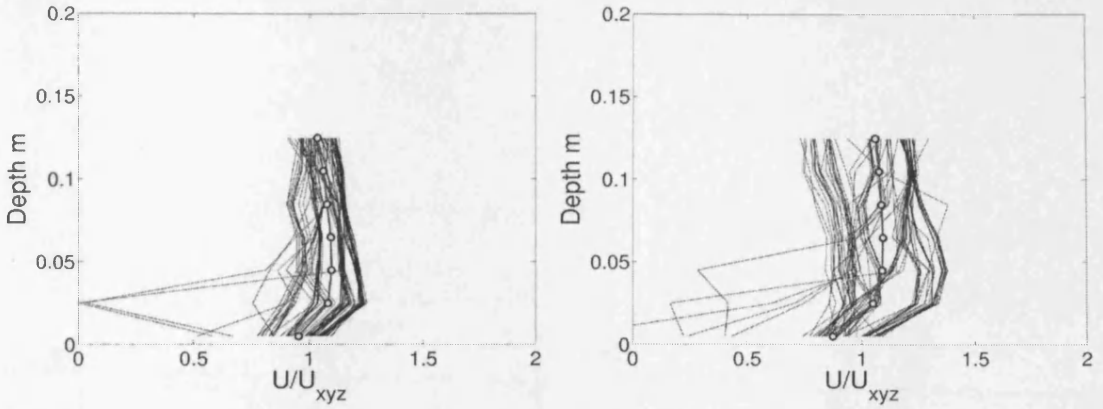

(a) *Cornus*, N=19.8 m^{-2}, high depth

(b) *Cornus*, N=19.8 m^{-2}, high depth

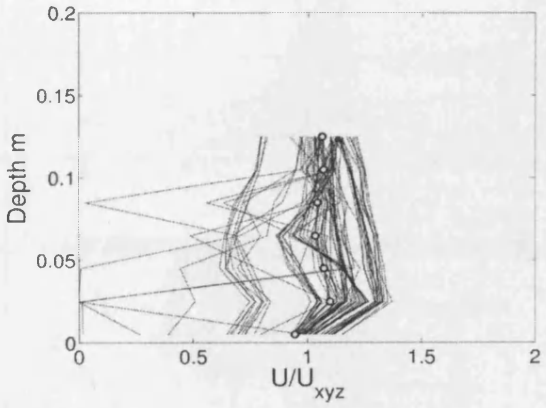

(c) *Cornus*, N=19.8 m^{-2}, high depth

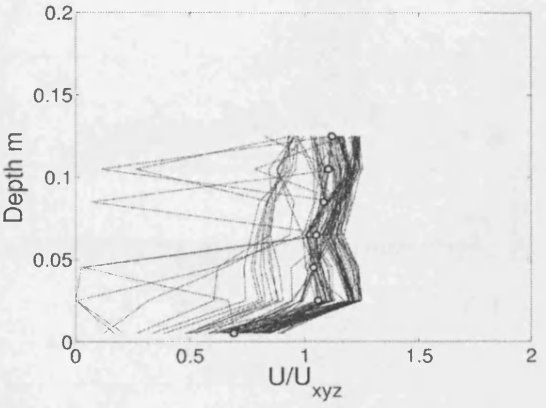

(d) *Cornus*, N=19.8 m^{-2}, high depth

Figure 5: Normalised vertical profiles of streamwise velocity (U) in cm/s in medium density, high depth *Cornus* Arrays

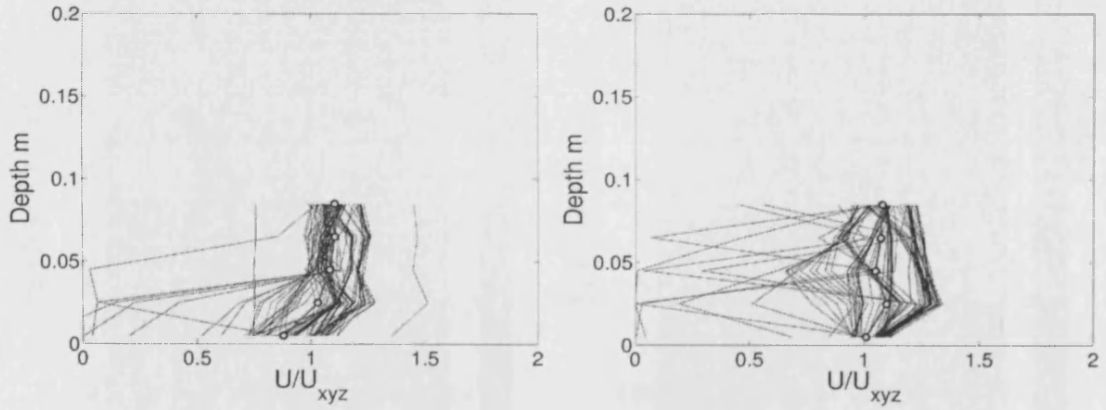

(a) *Cornus*, N=19.8 m^{-2}, low depth

(b) *Cornus*, N=19.8 m^{-2}, low depth

Figure 6: Normalised vertical profiles of streamwise velocity (U) in cm/s in medium density, low depth *Cornus* Arrays

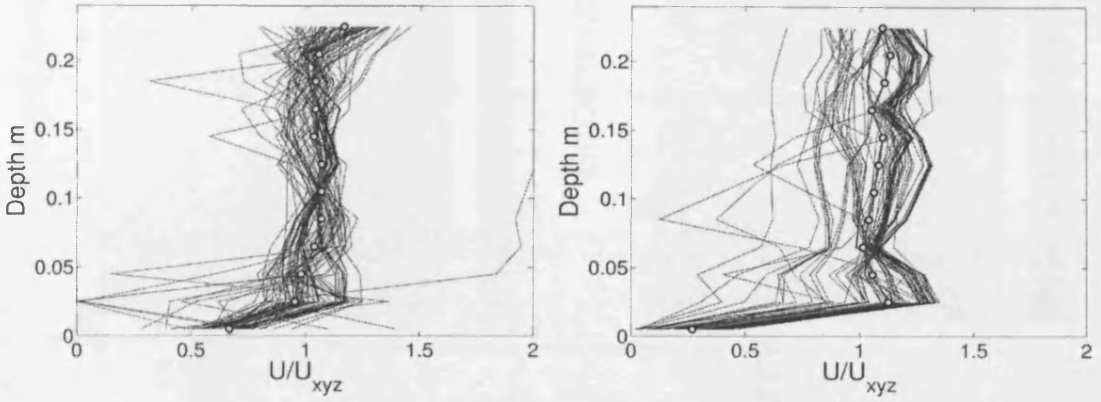

(a) *Cornus*, N=80.6 m^{-2}, high depth

(b) *Cornus*, N=80.6 m^{-2}, high depth

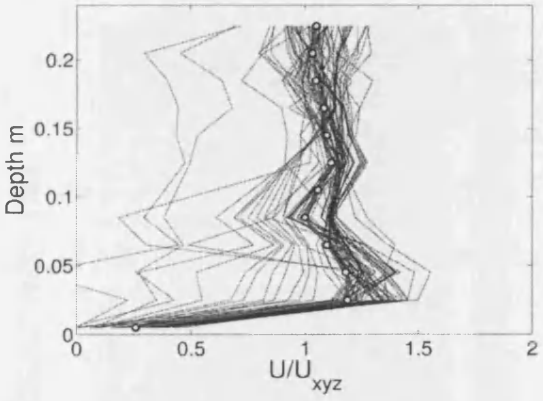

(c) *Cornus*, N=80.6 m^{-2}, high depth

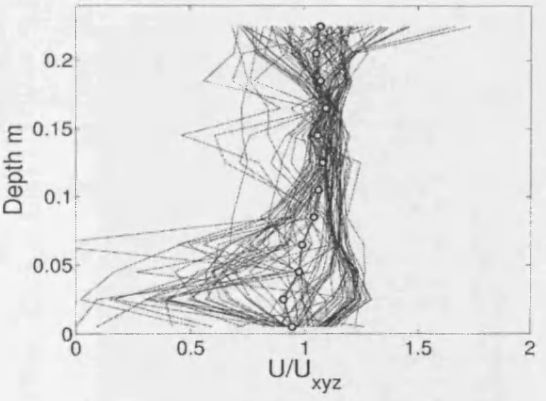

(d) *Cornus*, N=80.6 m^{-2}, high depth

Figure 7: Normalised vertical profiles of streamwise velocity (U) in cm/s in high density, high depth *Cornus* Arrays

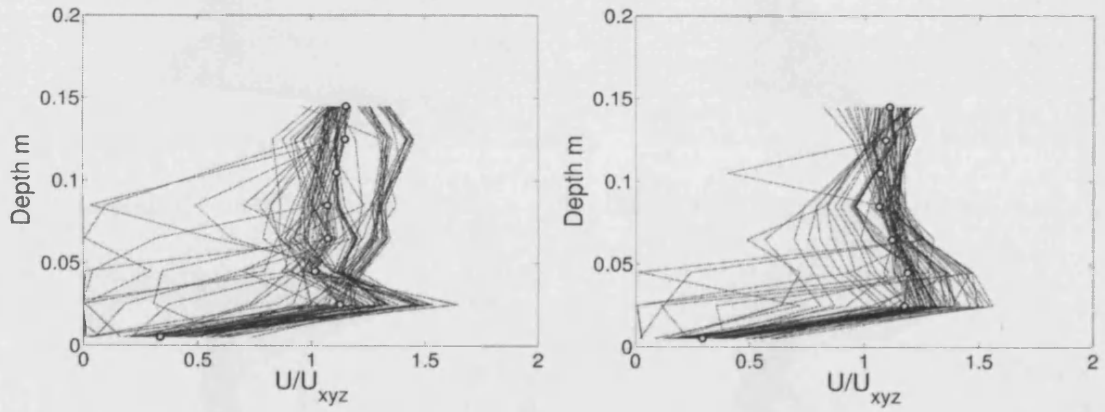

(a) *Cornus*, N=80.6 m^{-2}, low depth

(b) *Cornus*, N=80.6 m^{-2}, low depth

Figure 8: Normalised vertical profiles of streamwise velocity (U) in cm/s in high density, low depth *Cornus* Arrays

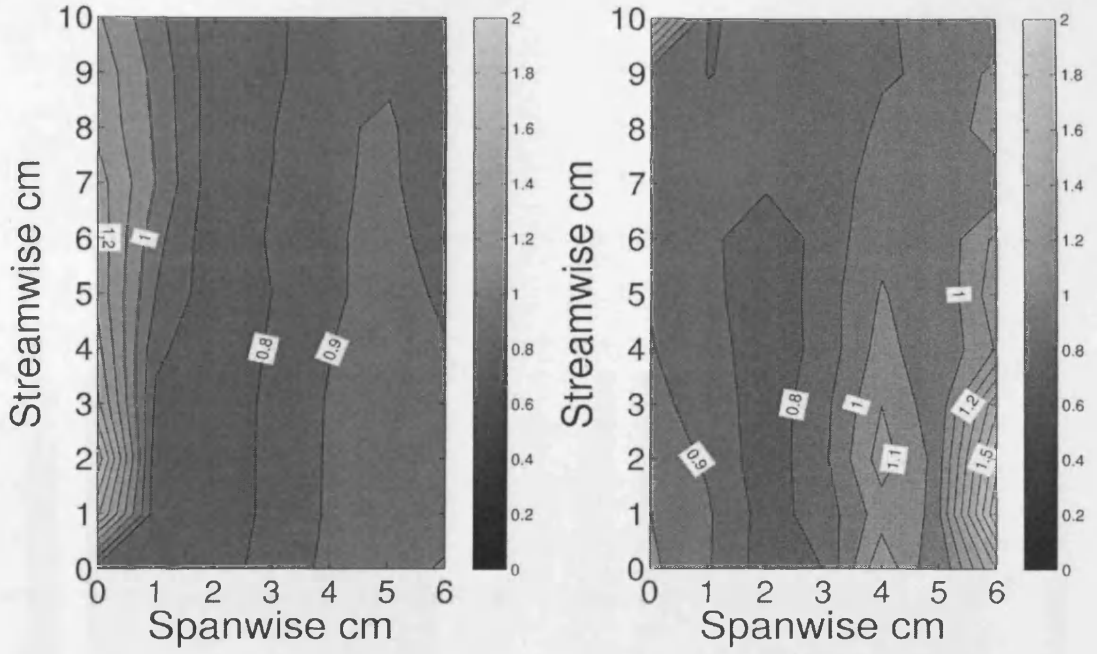

(a) *Cornus*, N=19.8 m^{-2}, high depth

(b) *Cornus*, N=19.8 m^{-2}, high depth

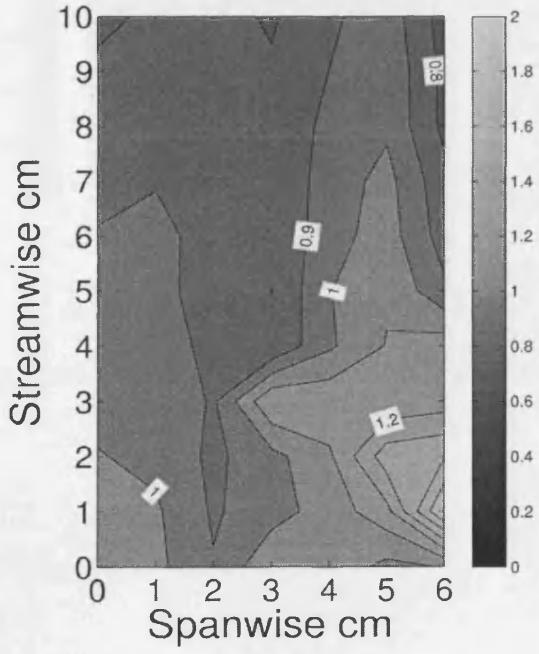

(c) *Cornus*, N=19.8 m^{-2}, high depth

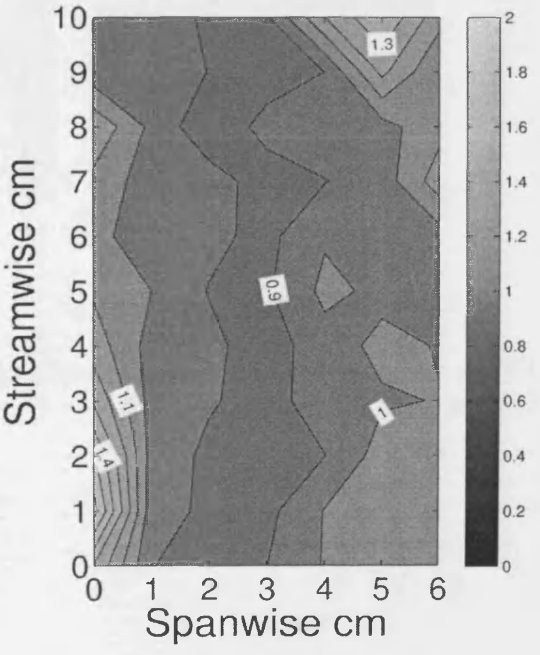

(d) *Cornus*, N=19.8 m^{-2}, high depth

Figure 9: Normalised depth-averaged streamwise turbulence u' in medium density, high depth *Cornus* array

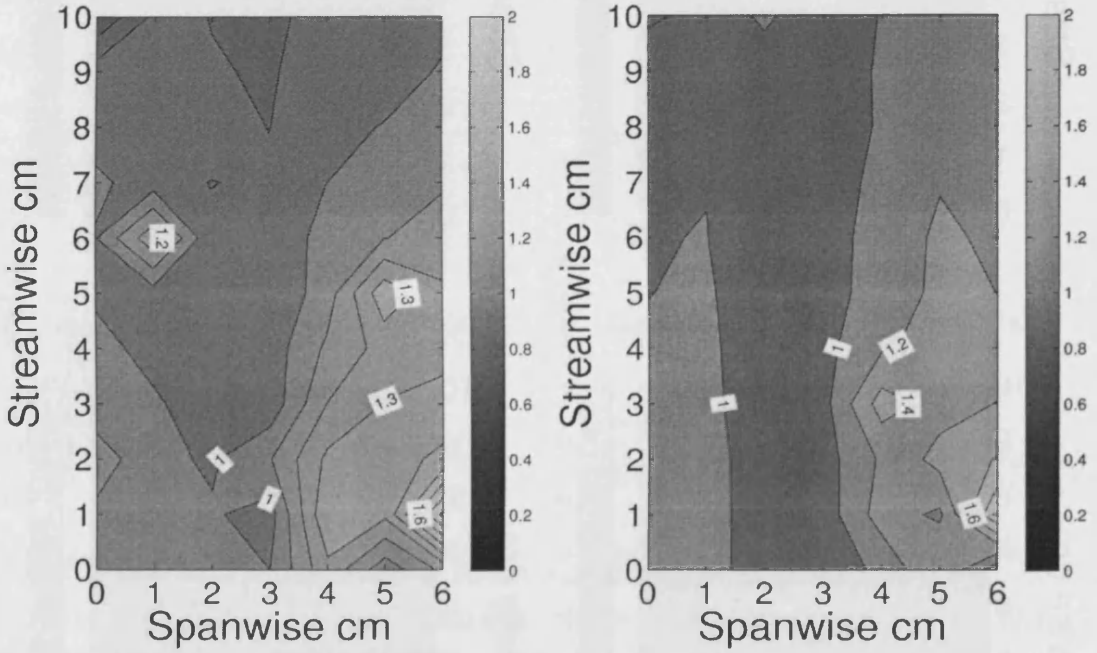

(a) *Cornus*, N=19.8 m^{-2}, low depth

(b) *Cornus*, N=19.8 m^{-2}, low depth

Figure 10: Normalised depth-averaged streamwise turbulence u' in medium density, low depth *Cornus* array

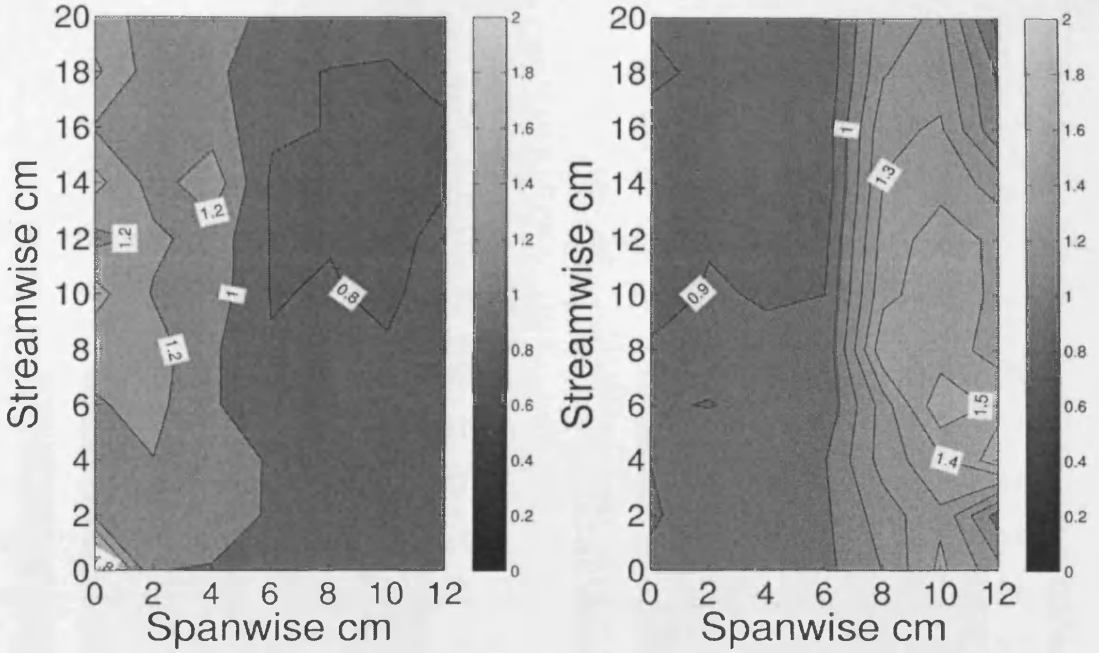

(a) *Cornus*, N=80.6 m^{-2}, high depth

(b) *Cornus*, N=80.6 m^{-2}, high depth

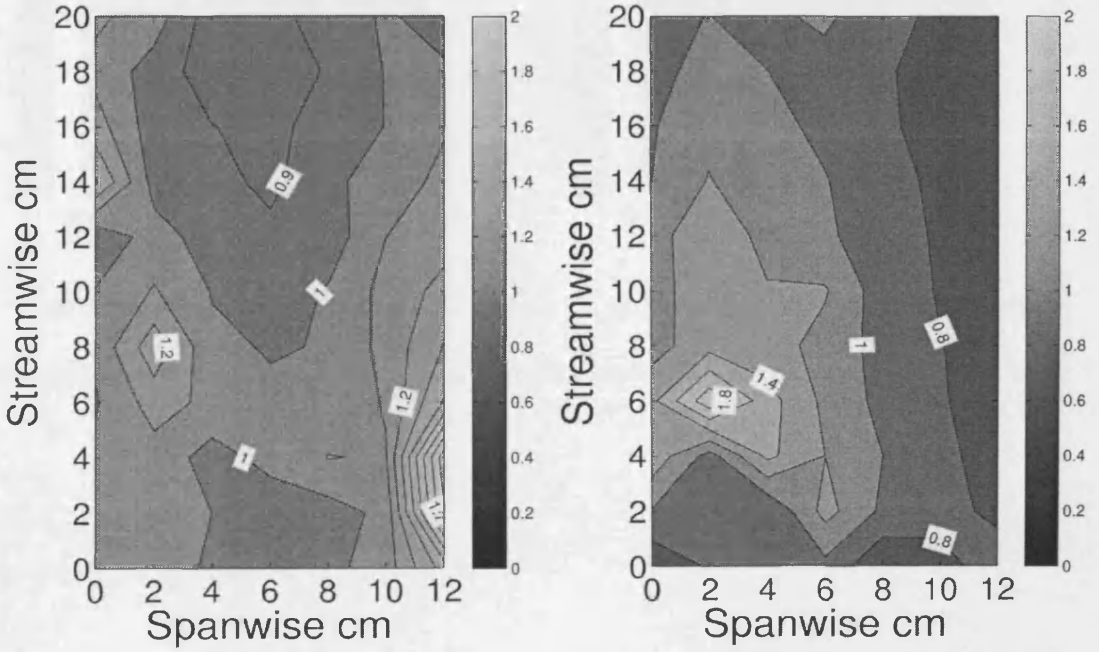

(c) *Cornus*, N=80.6 m^{-2}, high depth

(d) *Cornus*, N=80.6 m^{-2}, high depth

Figure 11: Normalised depth-averaged streamwise turbulence u' in high density, high depth *Cornus* array

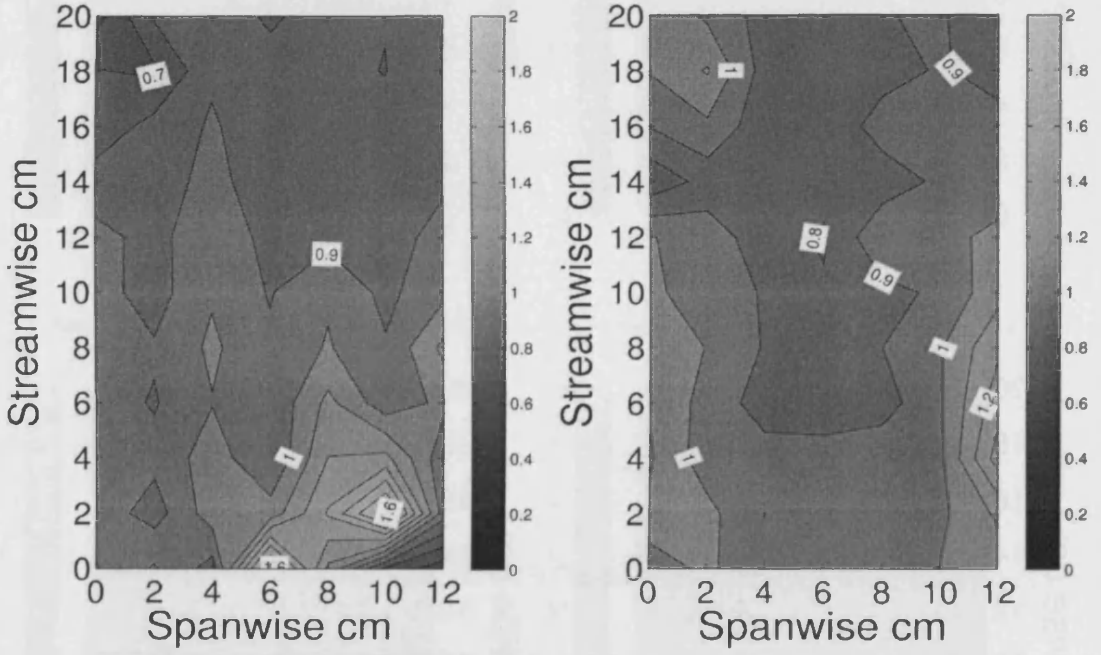

(a) *Cornus*, N=80.6 m^{-2}, low depth

(b) *Cornus*, N=80.6 m^{-2}, low depth

Figure 12: Normalised depth-averaged streamwise turbulence u' in high density, low depth *Cornus* array

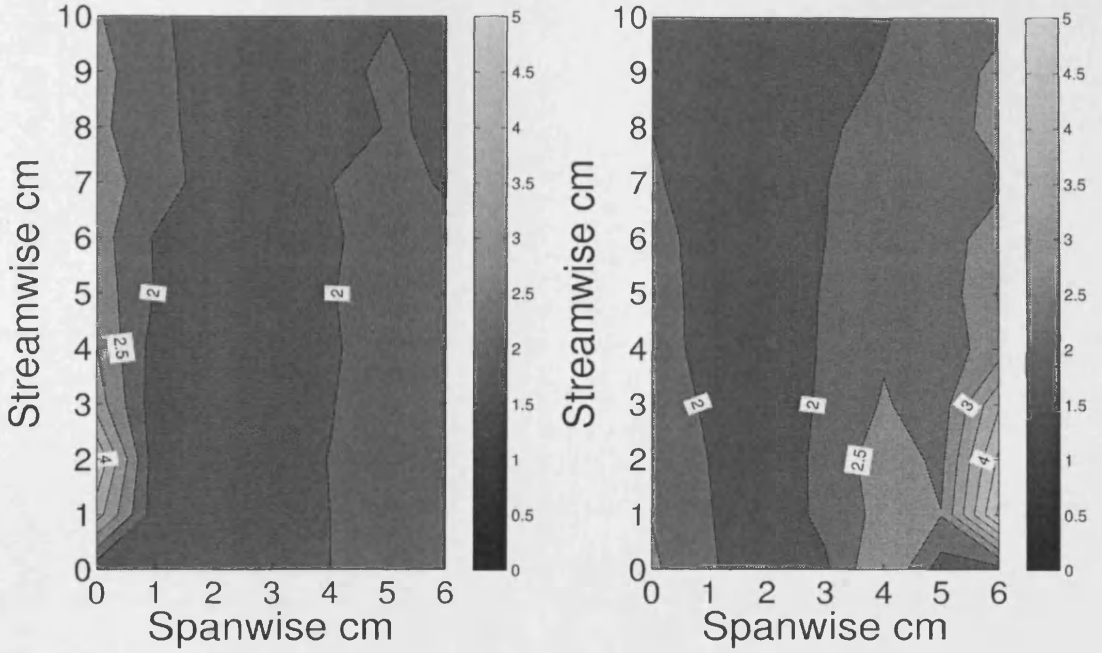

(a) *Cornus*, N=19.8 m^{-2}, high depth

(b) *Cornus*, N=19.8 m^{-2}, high depth

(c) *Cornus*, N=19.8 m^{-2}, high depth

(d) *Cornus*, N=19.8 m^{-2}, high depth

Figure 13: Normalised depth-averaged cross-streamwise turbulence v' in medium density, high depth *Cornus* array

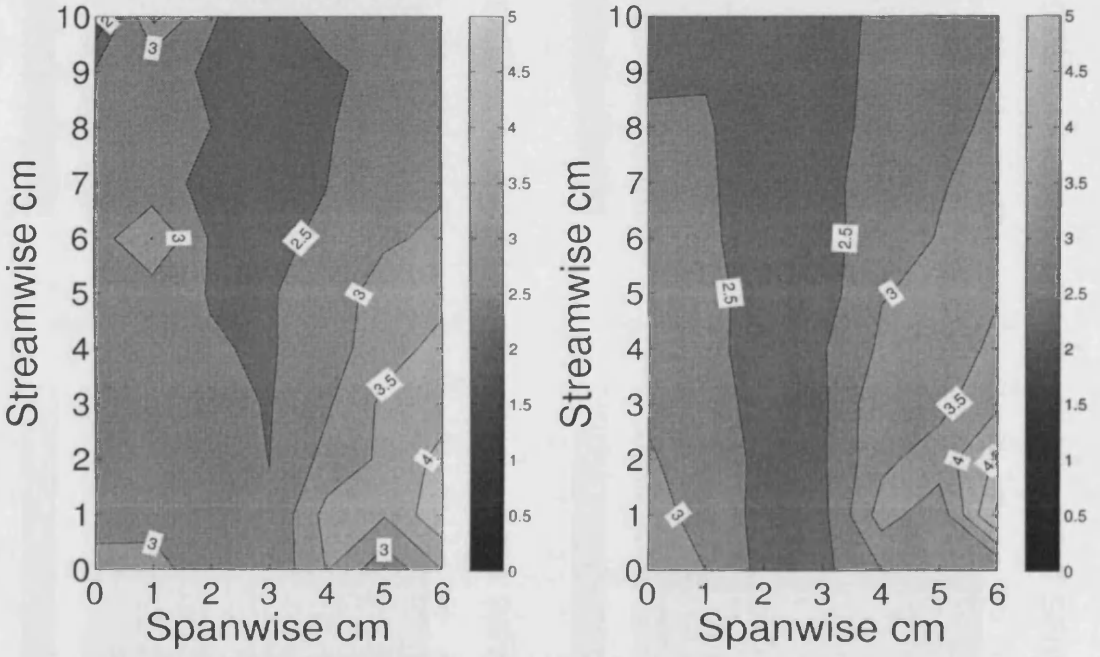

(a) *Cornus*, N=19.8 m^{-2}, low depth

(b) *Cornus*, N=19.8 m^{-2}, low depth

Figure 14: Normalised depth-averaged cross-streamwise turbulence v' in medium density, low depth *Cornus* array

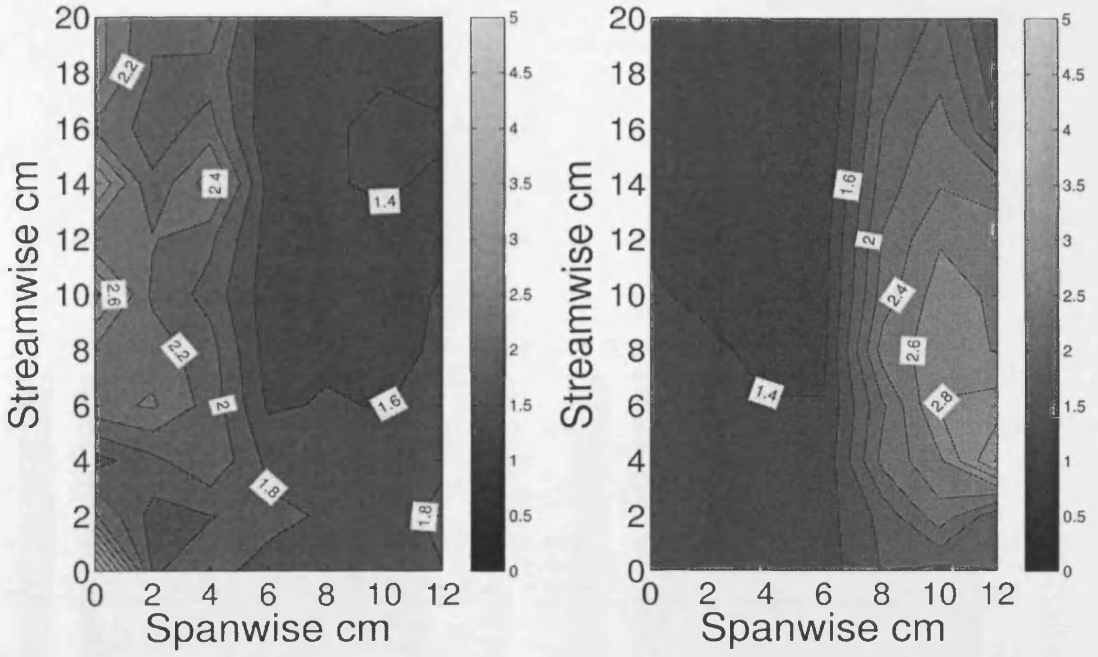

(a) *Cornus*, N=80.6 m^{-2}, high depth

(b) *Cornus*, N=80.6 m^{-2}, high depth

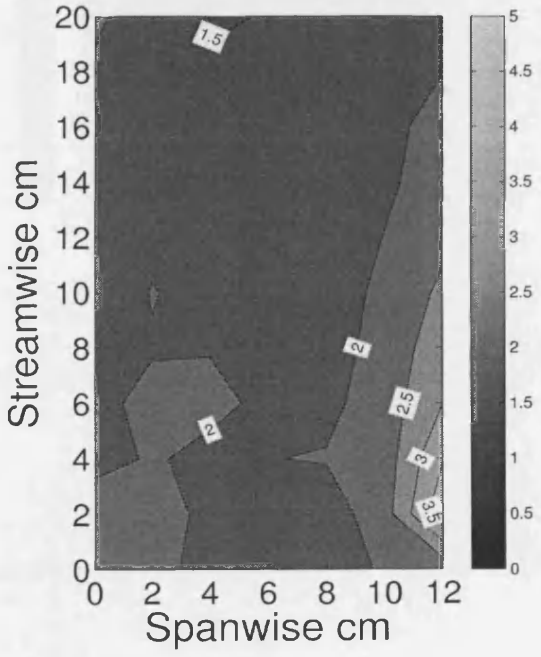

(c) *Cornus*, N=80.6 m^{-2}, high depth

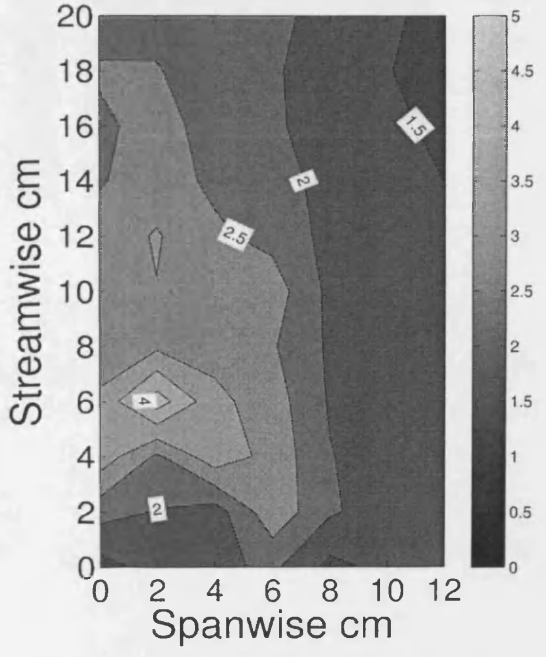

(d) *Cornus*, N=80.6 m^{-2}, high depth

Figure 15: Normalised depth-averaged cross-streamwise turbulence v' in high density,high depth *Cornus* array

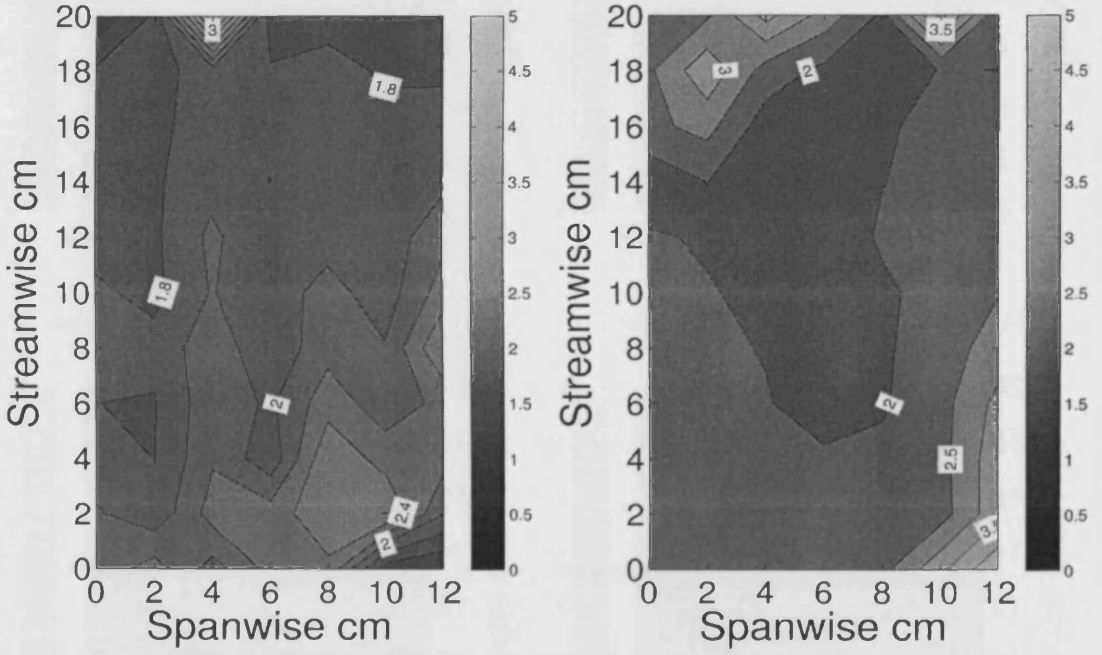

(a) *Cornus*, N=80.6 m^{-2}, low depth

(b) *Cornus*, N=80.6 m^{-2}, low depth

Figure 16: Normalised depth-averaged cross-streamwise turbulence v' in high density, low depth *Cornus* array

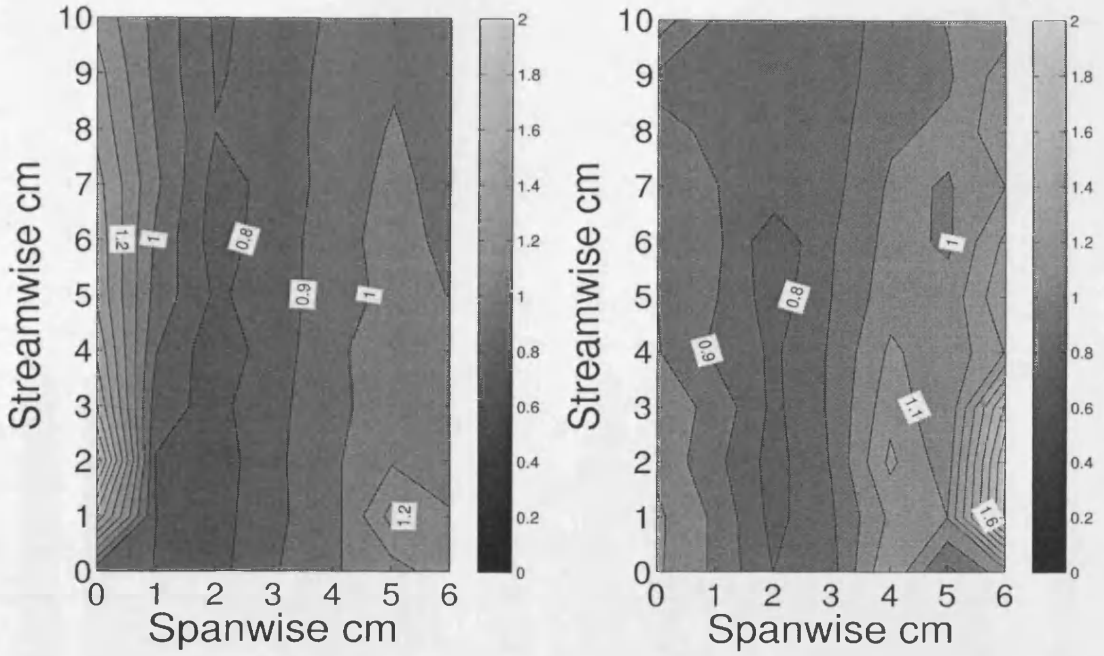

(a) *Cornus* CV1, N=19.8 m^{-2}, high depth (b) *Cornus* CV2, N=19.8 m^{-2}, high depth

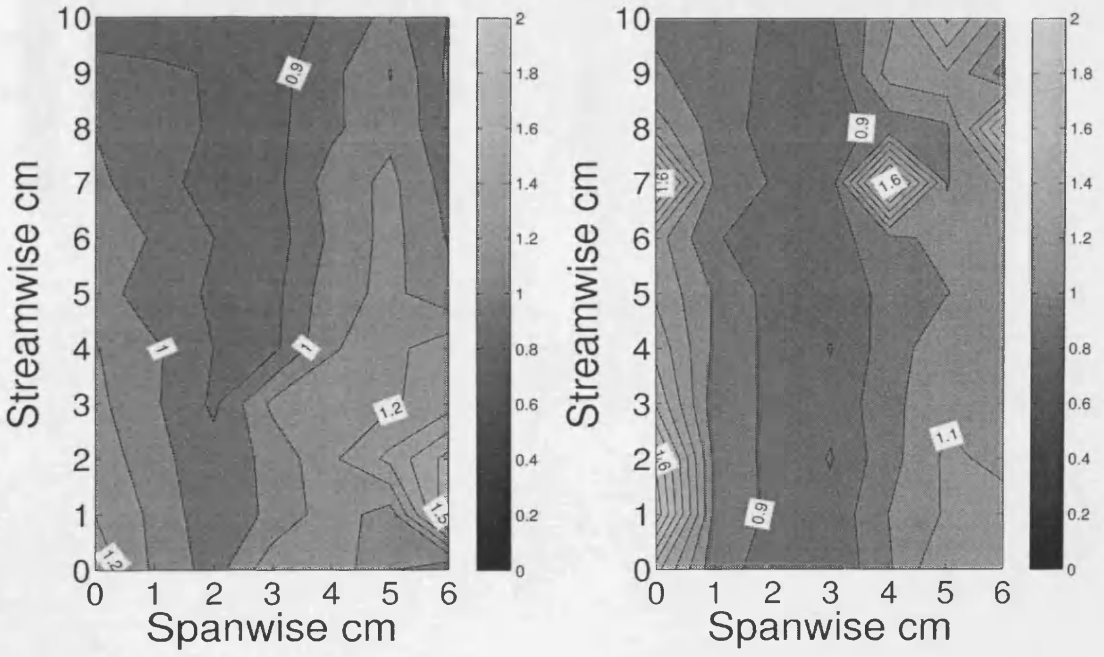

(c) *Cornus* CV3, N=19.8 m^{-2}, high depth (d) *Cornus* CV4, N=19.8 m^{-2}, high depth

Figure 17: Normalised depth-averaged vertical turbulence w' in medium density, high depth *Cornus* array

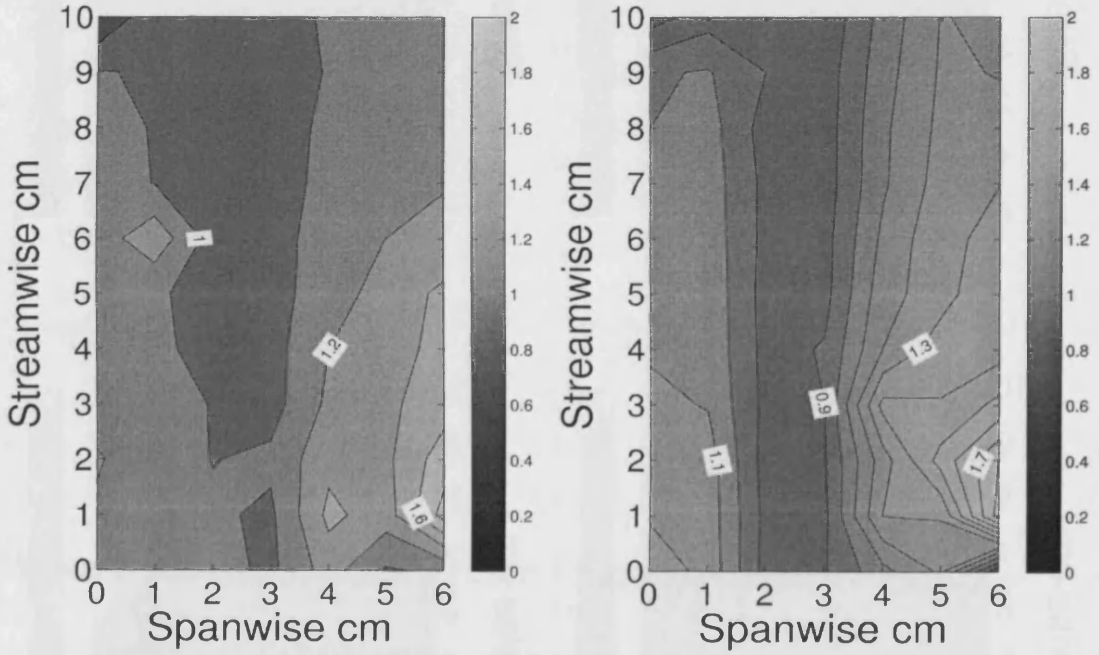

(a) *Cornus* CV2, N=19.8 m^{-2}, low depth (b) *Cornus* CV3, N=19.8 m^{-2}, low depth

Figure 18: Normalised depth-averaged vertical turbulence w' in medium density, low depth *Cornus* array

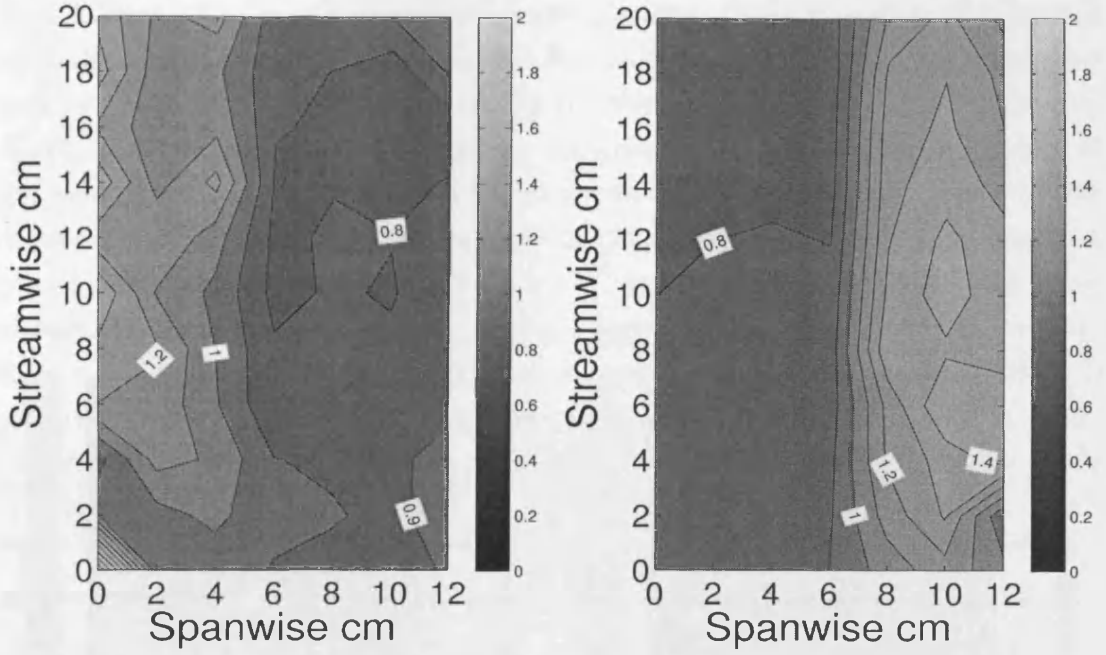

(a) *Cornus* CV1, N=80.6 m^{-2}, high depth

(b) *Cornus* CV2, N=80.6 m^{-2}, high depth

(c) *Cornus* CV3, N=80.6 m^{-2}, high depth

(d) *Cornus* CV4, N=80.6 m^{-2}, high depth

Figure 19: Normalised depth-averaged vertical turbulence w' in high density, high depth *Cornus* array

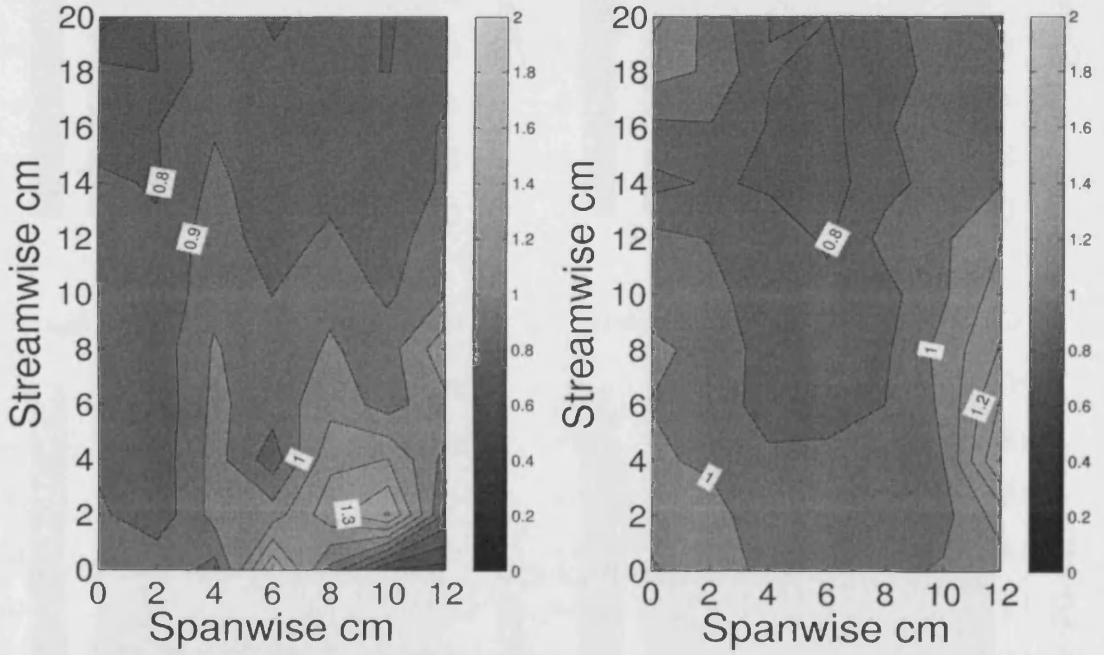

(a) *Cornus* CV2, N=80.6 m^{-2}, low depth

(b) *Cornus* CV3, N=80.6 m^{-2}, low depth

Figure 20: Normalised depth-averaged vertical turbulence w' in high density, low depth *Cornus* array

The vertically sampled profiles in Figures 5 to 24 give another picture of the flow field. Looking first at the streamwise velocity profiles, again it is clear that there is a smaller spatial variation thoughout the flow field. However, the vertically sampled profiles show distinct differences between the flow characteristics of the single stem dowels and the multi-stemmed cornus. sanguinea saplings. There are points of low velocity at seemingly random locations throughout the depth. These points occur around the location of the saplings and are a result of the probe having been placed immediately downstream of a stem. These points also coincide with areas of high TKE values. Many of the plan averaged velocity profiles for the saplings show a peak near the base of the water column. This would suggest that flow is preferentially diverted below the biomass center of the plant, where flow is relatively unobstructed. This behaviour would perhaps cause scour near the bed in a sandy or silty environment.

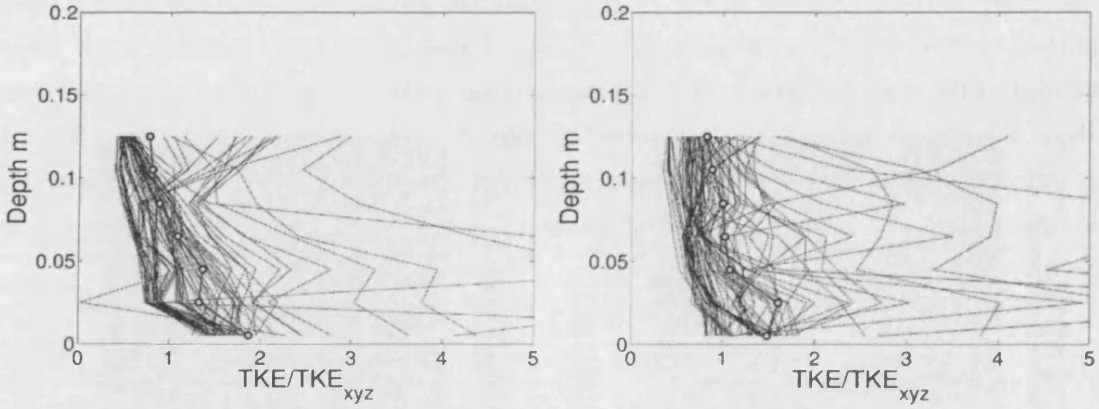

(a) *Cornus* CV1, N=19.8 m^{-2}, high depth

(b) *Cornus* CV2, N=19.8 m^{-2}, high depth

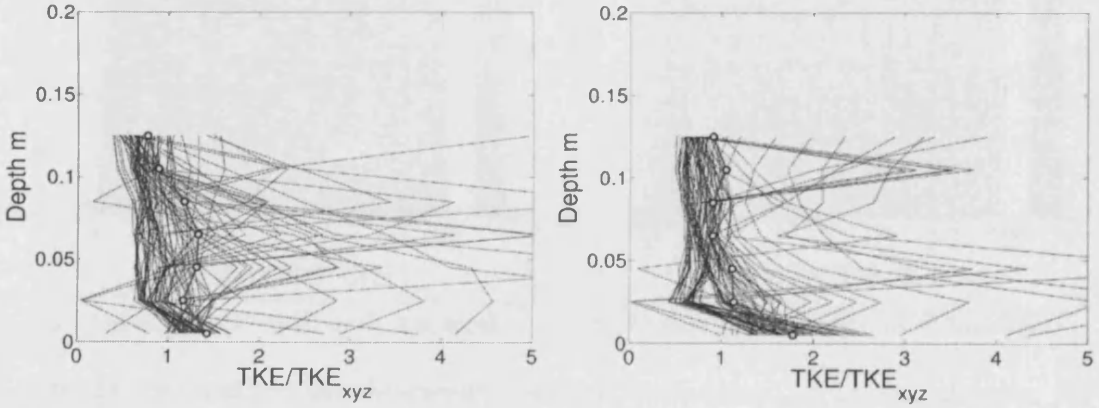

(c) *Cornus* CV3, N=19.8 m^{-2}, high depth

(d) *Cornus* CV4, N=19.8 m^{-2}, high depth

Figure 21: Normalised vertical profile turbulent kinetic energy TKE in medium density, high depth *Cornus* array

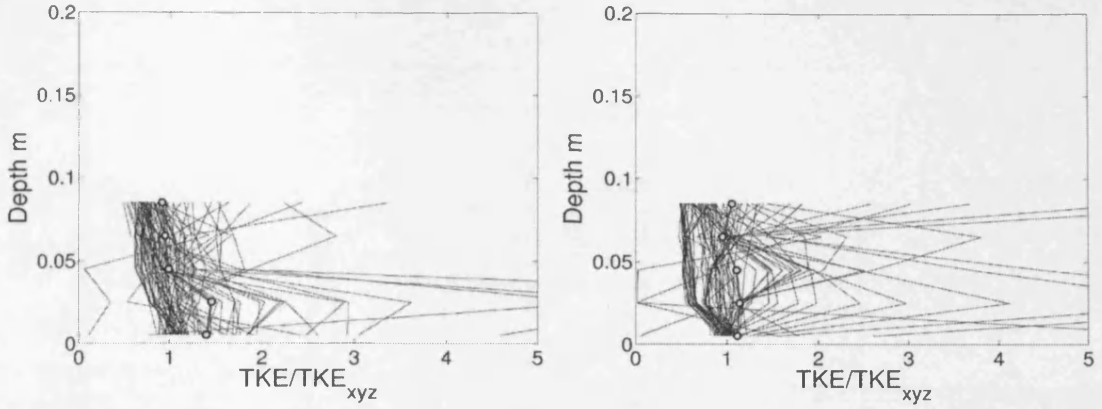

(a) *Cornus* CV2, N=19.8 m^{-2}, low depth (b) *Cornus* CV3, N=19.8 m^{-2}, low depth

Figure 22: Normalised vertical profile turbulent kinetic energy TKE in medium density, low depth *Cornus* array

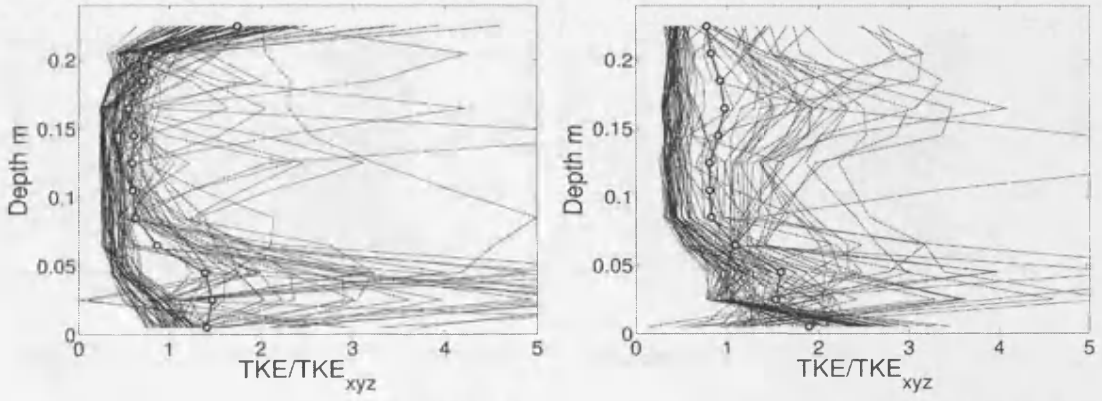

(a) *Cornus* CV1, N=80.6 m^{-2}, high depth (b) *Cornus* CV2, N=80.6 m^{-2}, high depth

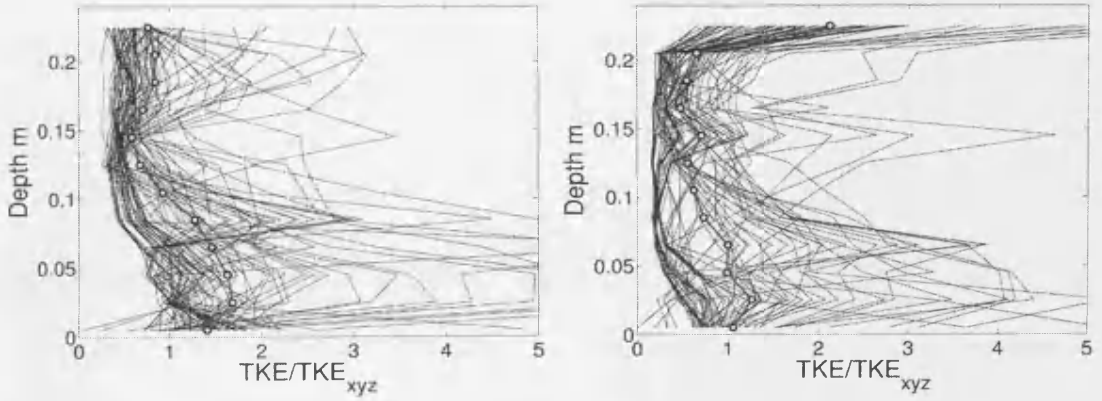

(c) *Cornus* CV3, N=80.6 m^{-2}, high depth (d) *Cornus* CV4, N=80.6 m^{-2}, high depth

Figure 23: Normalised vertical profile turbulent kinetic energy TKE in high density, high depth *Cornus* array

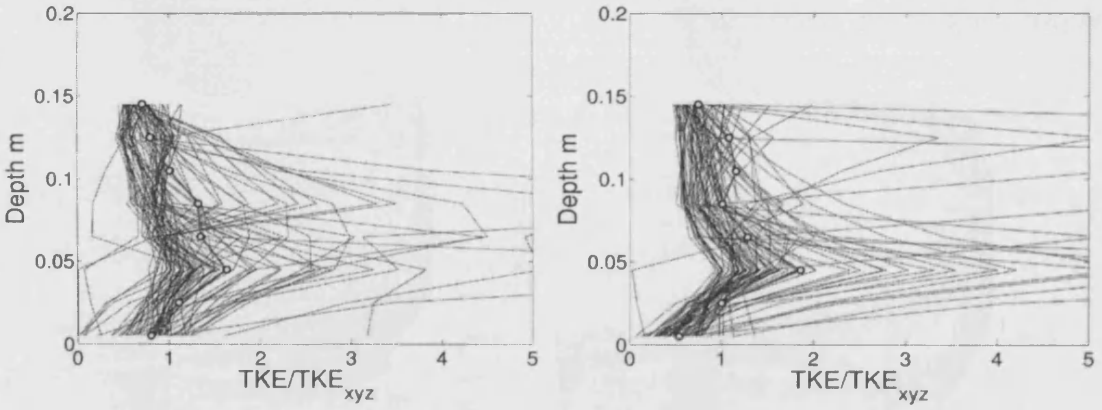

(a) *Cornus* CV2, N=19.8 m^{-2}, high depth (b) *Cornus* CV3, N=19.8 m^{-2}, high depth

Figure 24: Normalised vertical profile turbulent kinetic energy TKE in medium density, low depth *Cornus* array

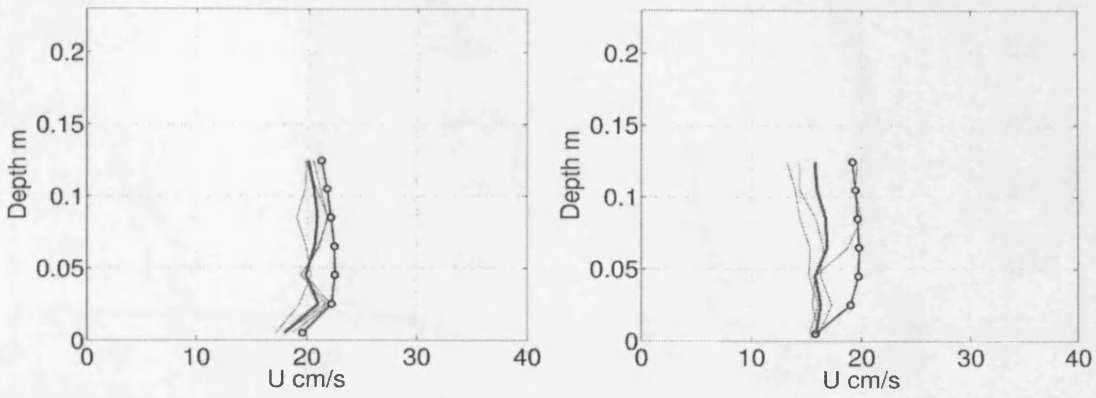

(a) *Cornus* CV1, N=19.8 m^{-2}, high depth

(b) *Cornus* CV2, N=19.8 m^{-2}, high depth

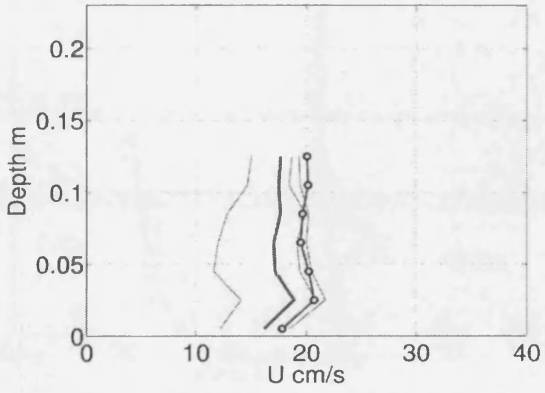

(c) *Cornus* CV3, N=19.8 m^{-2}, high depth

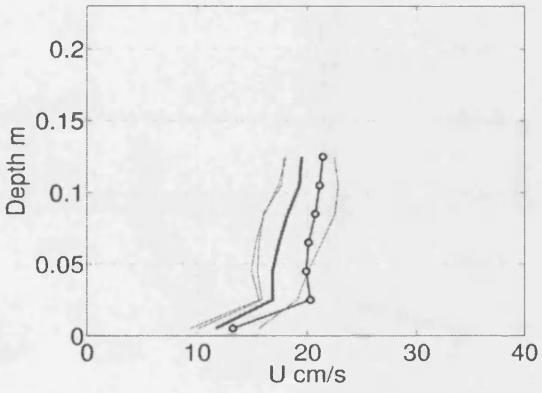

(d) *Cornus* CV4, N=19.8 m^{-2}, high depth

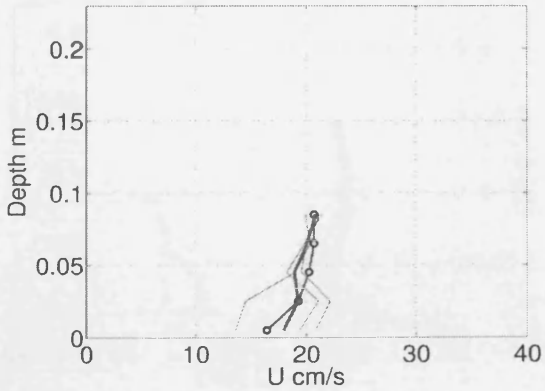

(e) *Cornus* CV2, N=19.8 m^{-2}, low depth

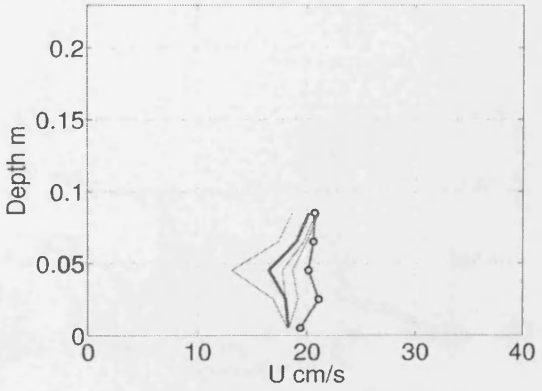

(f) *Cornus* CV3, N=19.8 m^{-2}, low depth

Figure 25: Sampled streamwise velocity U using Sampling Pattern 1 in Cornus Medium Density Arrays. (a) V2b, (b) V2c, (c) V2d, (d) V2e, (e) V2f and (f) V2g

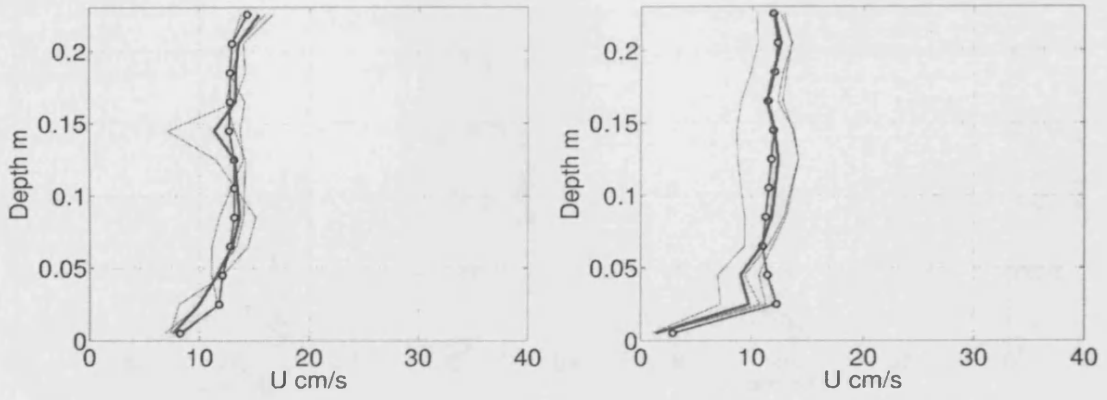

(a) *Cornus* CV1, N=80.6 m^{-2}, high depth

(b) *Cornus* CV2, N=80.6 m^{-2}, high depth

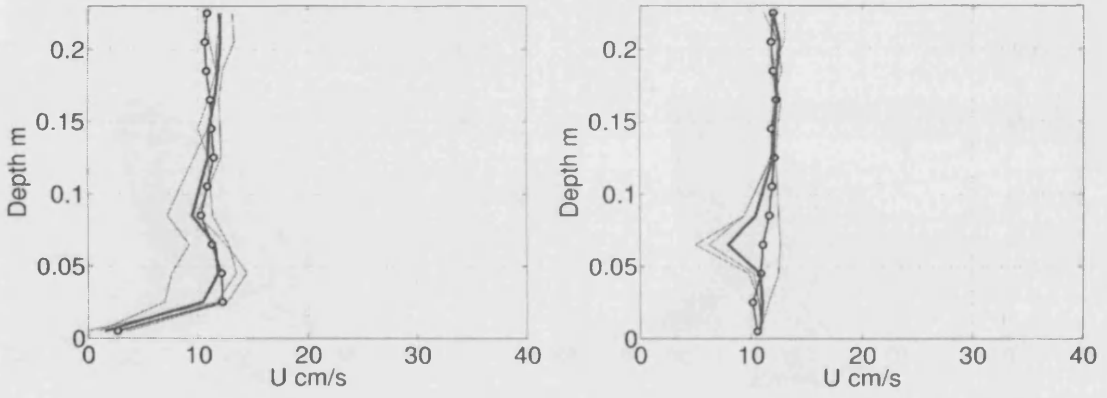

(c) *Cornus* CV3, N=80.6 m^{-2}, high depth

(d) *Cornus* CV4, N=80.6 m^{-2}, high depth

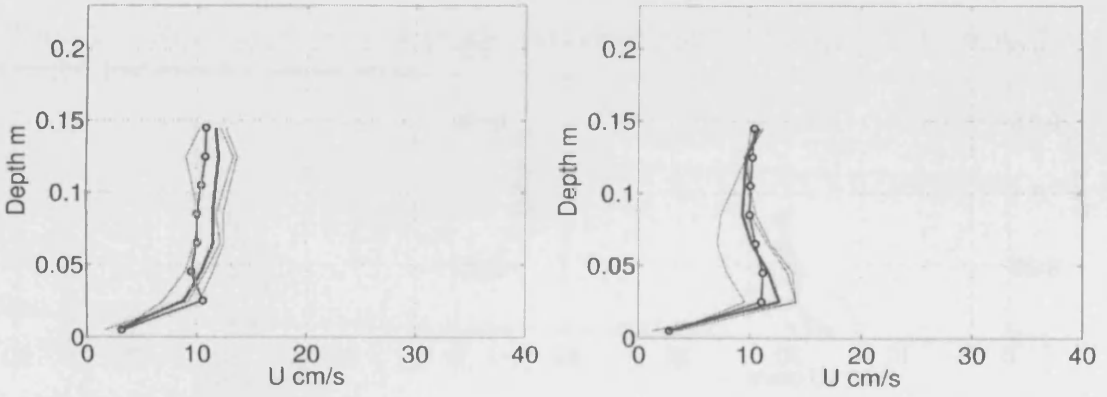

(e) *Cornus* CV2, N=80.6 m^{-2}, low depth

(f) *Cornus* CV3, N=80.6 m^{-2}, low depth

Figure 26: Sampled streamwise velocity U using Sampling Pattern 1 in Cornus High Density Arrays. (a) V3b, (b) V3c, (c) V3d, (d) V3e, (e) V3f and (f) V3g

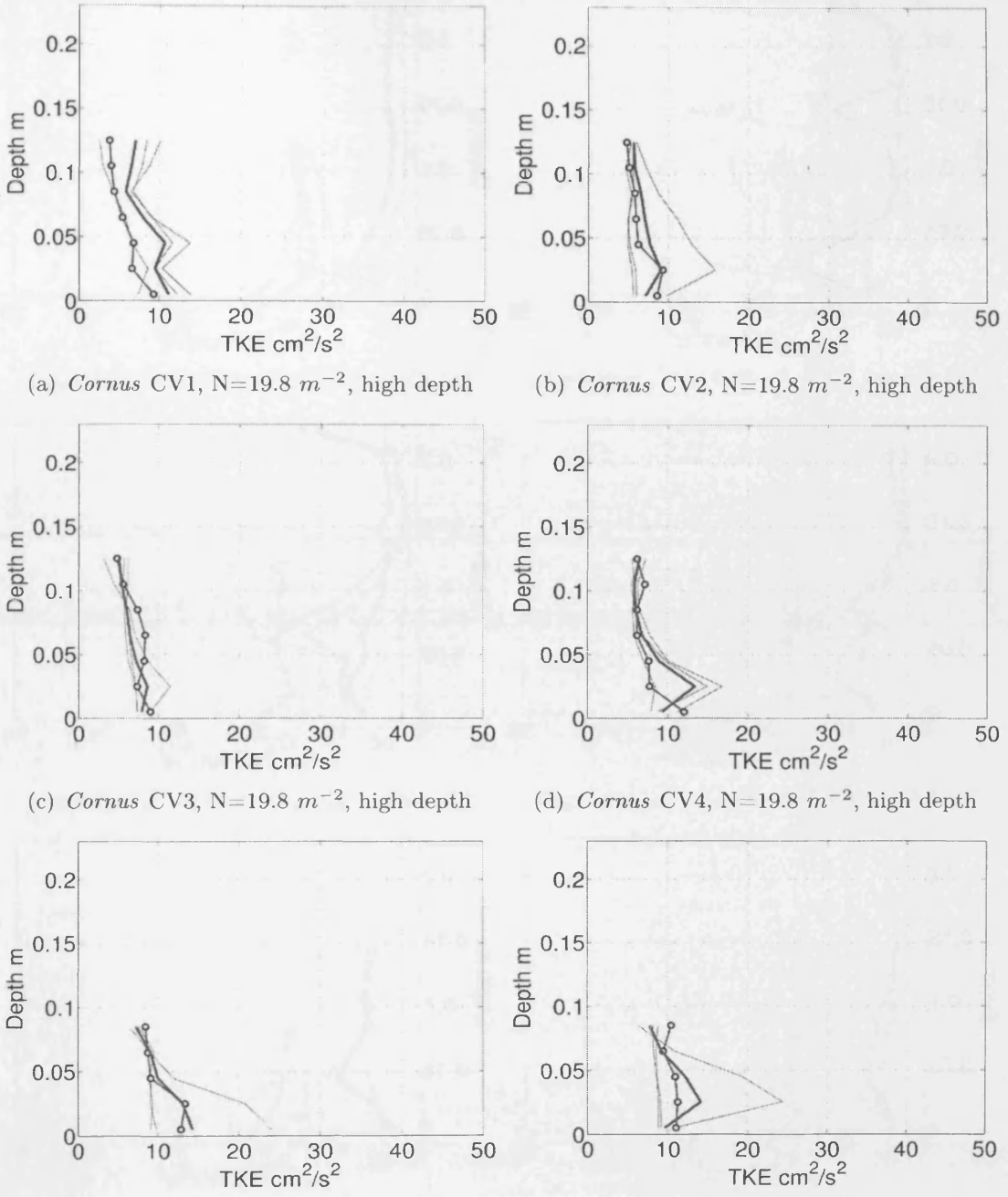

(a) *Cornus* CV1, N=19.8 m^{-2}, high depth

(b) *Cornus* CV2, N=19.8 m^{-2}, high depth

(c) *Cornus* CV3, N=19.8 m^{-2}, high depth

(d) *Cornus* CV4, N=19.8 m^{-2}, high depth

(e) *Cornus* CV2, N=19.8 m^{-2}, low depth

(f) *Cornus* CV3, N=19.8 m^{-2}, low depth

Figure 27: Sampled Turbulent Kinetic Energy using Sampling Pattern 1 in Cornus Medium Density arrays. Top row L to R: Sampling Volumes B, C, D and E at $Re = 1373$. Bottom row L to R: Sampling Volumes C and D at $Re = 1409$

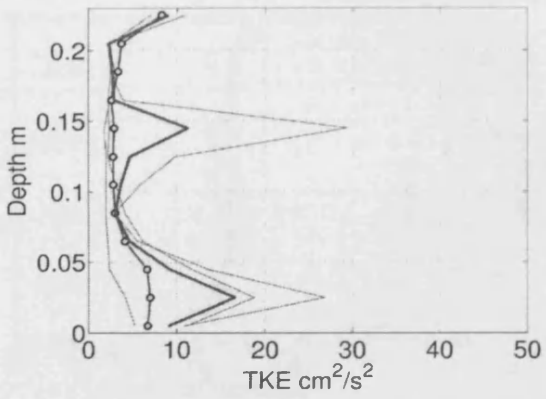

(a) *Cornus* CV1, N=80.6 m^{-2}, high depth

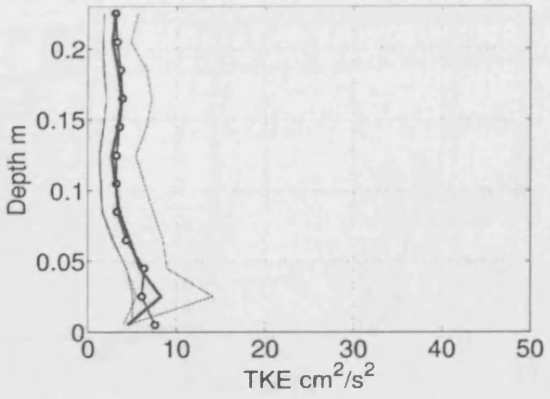

(b) *Cornus* CV2, N=80.6 m^{-2}, high depth

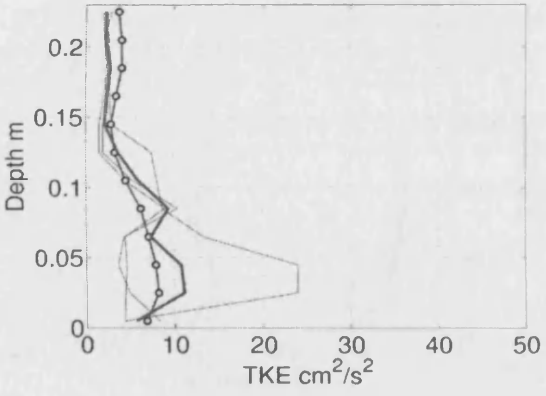

(c) *Cornus* CV3, N=80.6 m^{-2}, high depth

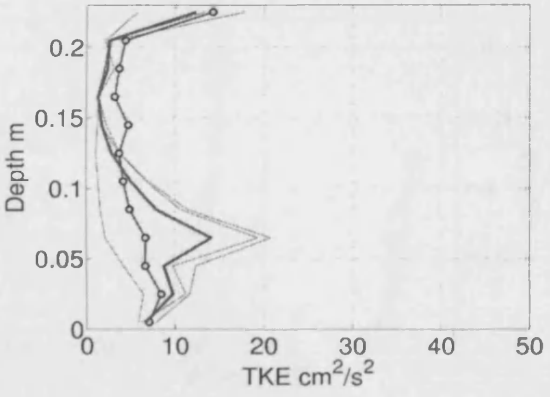

(d) *Cornus* CV4, N=80.6 m^{-2}, high depth

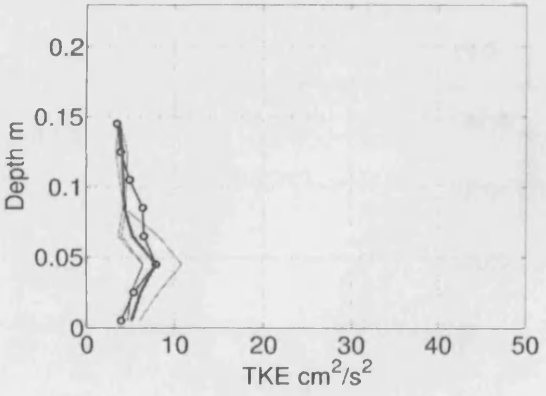

(e) *Cornus* CV2, N=80.6 m^{-2}, low depth

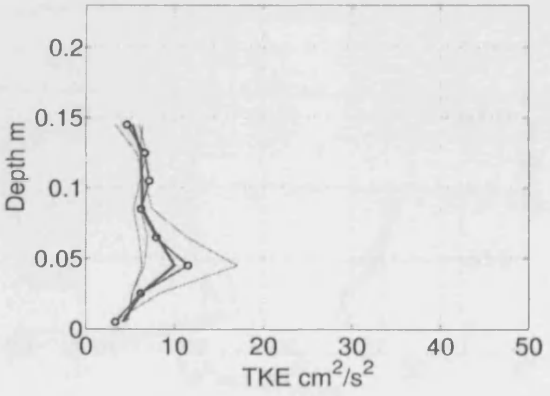

(f) *Cornus* CV3, N=80.6 m^{-2}, low depth

Figure 28: Sampled Turbulent Kinetic Energy using Sampling Pattern 1 in Cornus High Density arrays. Top row L to R: Sampling Volumes B, C, D and E at $Re = 742$. Bottom row L to R: Sampling Volumes C and D at $Re = 778$

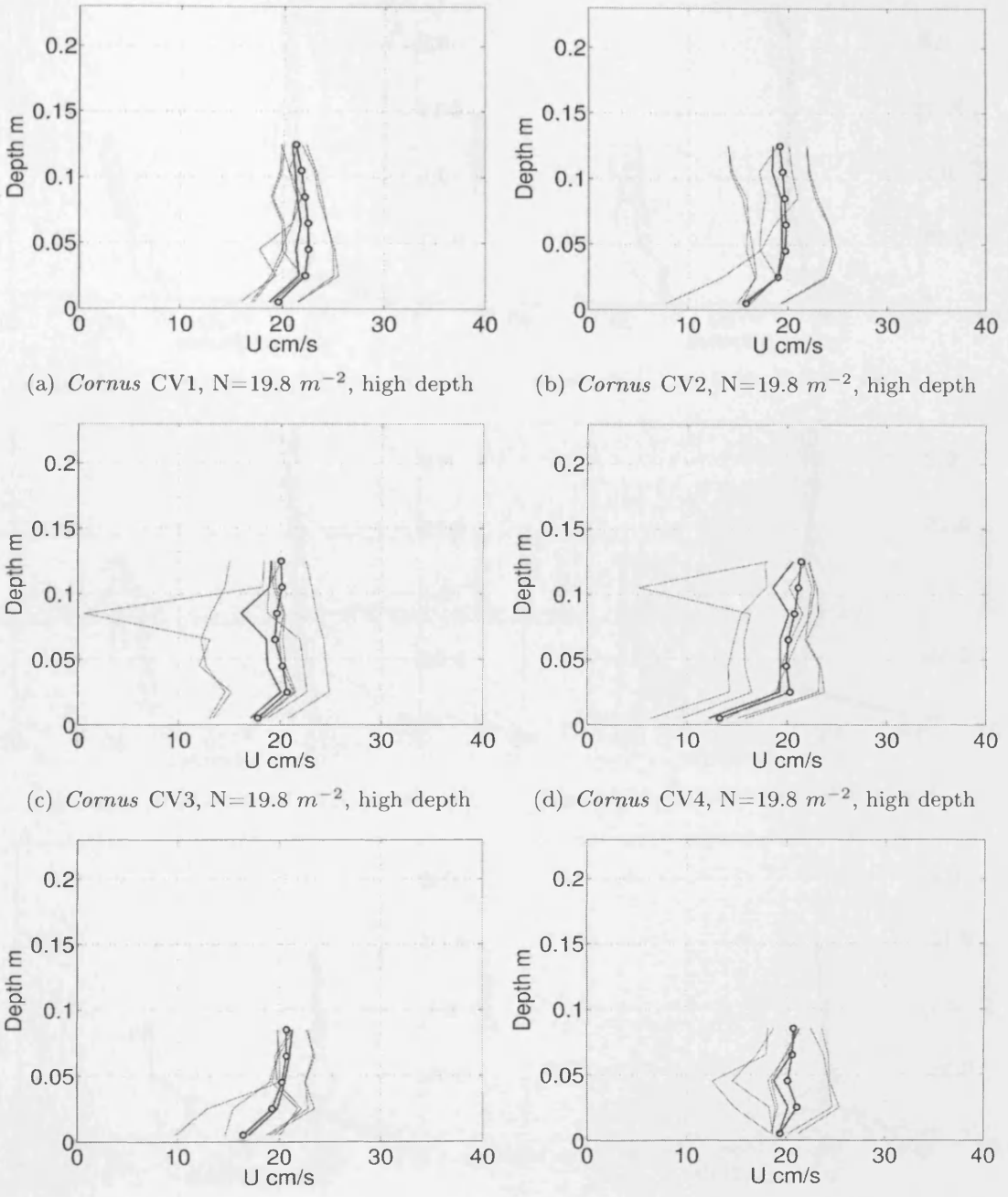

(a) *Cornus* CV1, N=19.8 m^{-2}, high depth

(b) *Cornus* CV2, N=19.8 m^{-2}, high depth

(c) *Cornus* CV3, N=19.8 m^{-2}, high depth

(d) *Cornus* CV4, N=19.8 m^{-2}, high depth

(e) *Cornus* CV2, N=19.8 m^{-2}, low depth

(f) *Cornus* CV3, N=19.8 m^{-2}, low depth

Figure 29: Sampled Streamwise Velocity U using Sampling Pattern B in Cornus Medium Density arrays. Top row L to R: Sampling Volumes B, C, D and E at $Re = 1373$. Bottom row L to R: Sampling Volumes C and D at $Re = 1409$

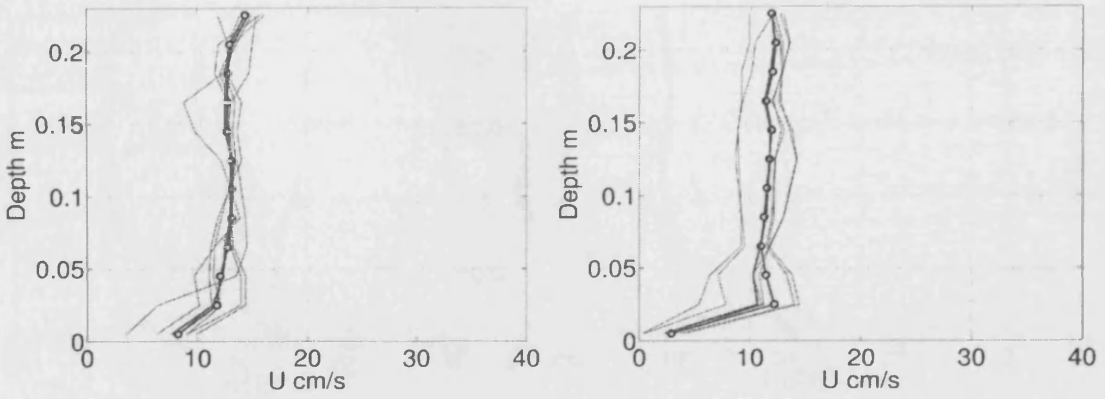

(a) *Cornus* CV1, N=80.6 m^{-2}, high depth

(b) *Cornus* CV2, N=80.6 m^{-2}, high depth

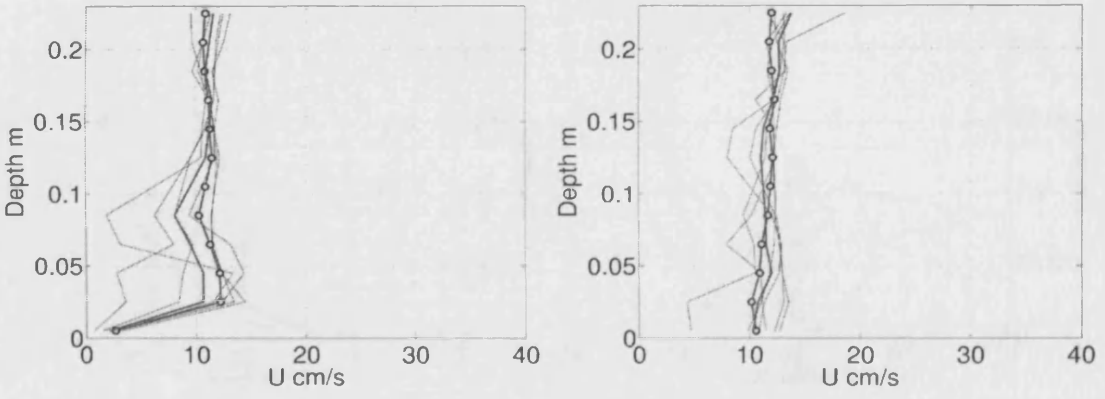

(c) *Cornus* CV3, N=80.6 m^{-2}, high depth

(d) *Cornus* CV4, N=80.6 m^{-2}, high depth

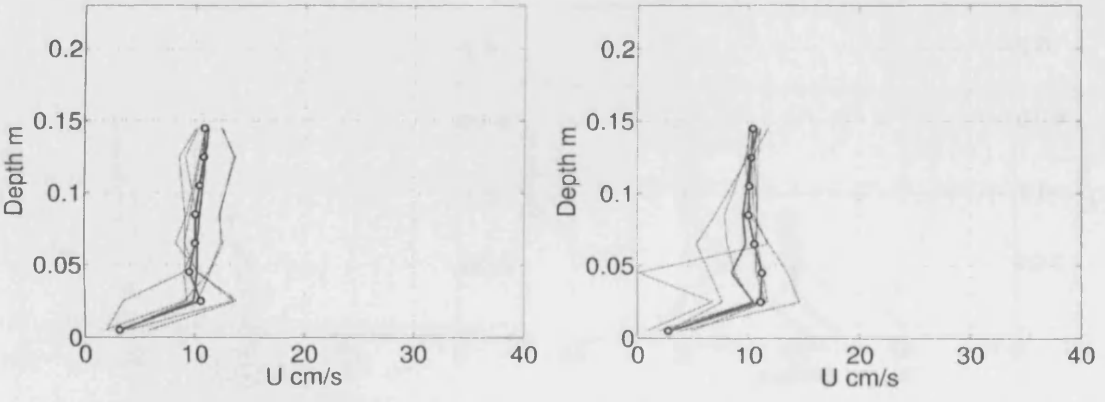

(e) *Cornus* CV2, N=80.6 m^{-2}, low depth

(f) *Cornus* CV3, N=80.6 m^{-2}, low depth

Figure 30: Sampled Streamwise Velocity U using Sampling Pattern B in Cornus High Density arrays. Top row L to R: Sampling Volumes B, C, D and E at $Re = 742$. Bottom row L to R: Sampling Volumes C and D at $Re = 778$

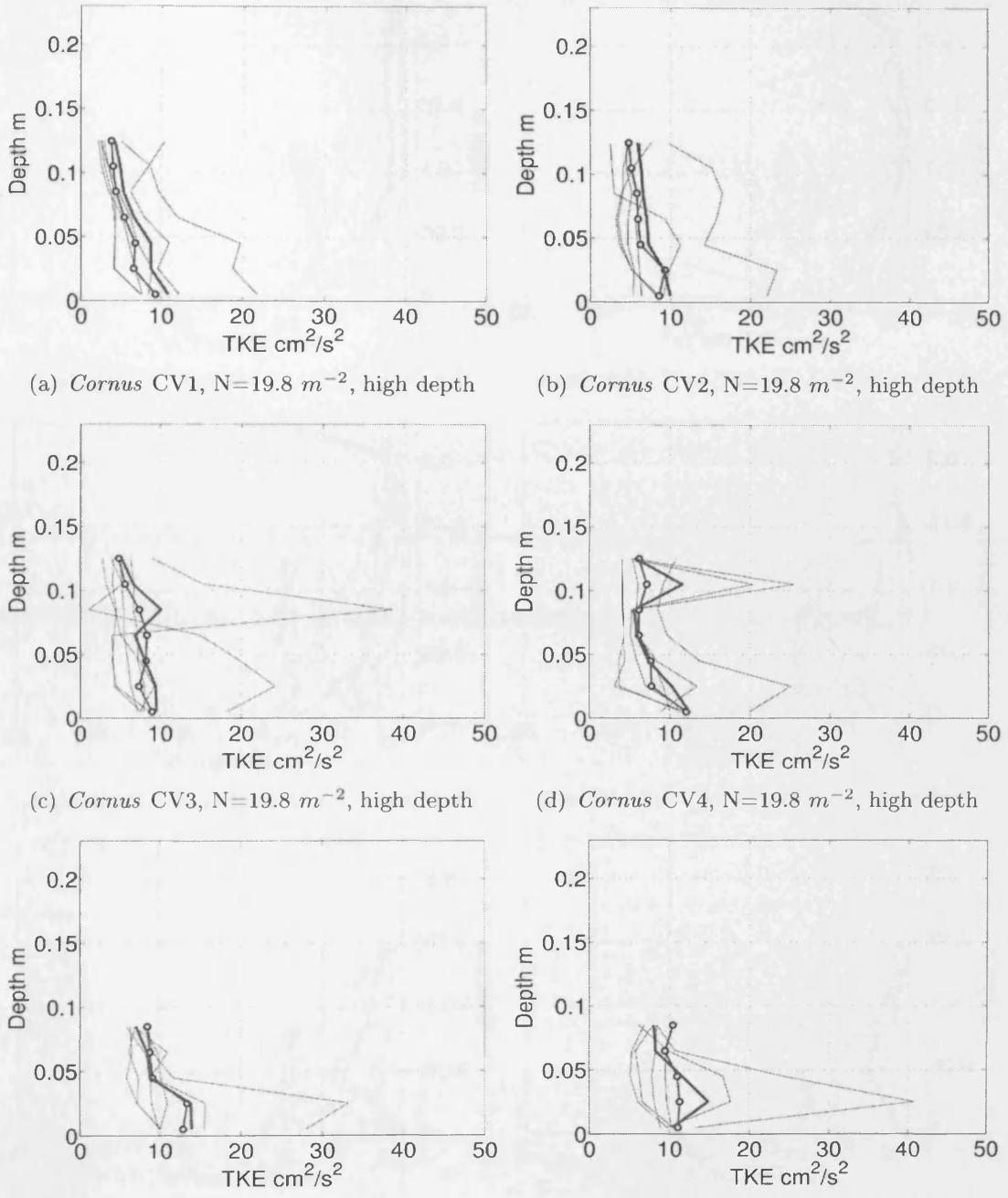

(a) *Cornus* CV1, N=19.8 m^{-2}, high depth

(b) *Cornus* CV2, N=19.8 m^{-2}, high depth

(c) *Cornus* CV3, N=19.8 m^{-2}, high depth

(d) *Cornus* CV4, N=19.8 m^{-2}, high depth

(e) *Cornus* CV2, N=19.8 m^{-2}, low depth

(f) *Cornus* CV3, N=19.8 m^{-2}, low depth

Figure 31: Sampled Turbulent Kinetic Energy using Sampling Pattern 2 in Cornus Medium Density arrays. Top row L to R: Sampling Volumes B, C, D and E at $Re = 1373$. Bottom row L to R: Sampling Volumes C and D at $Re = 1409$

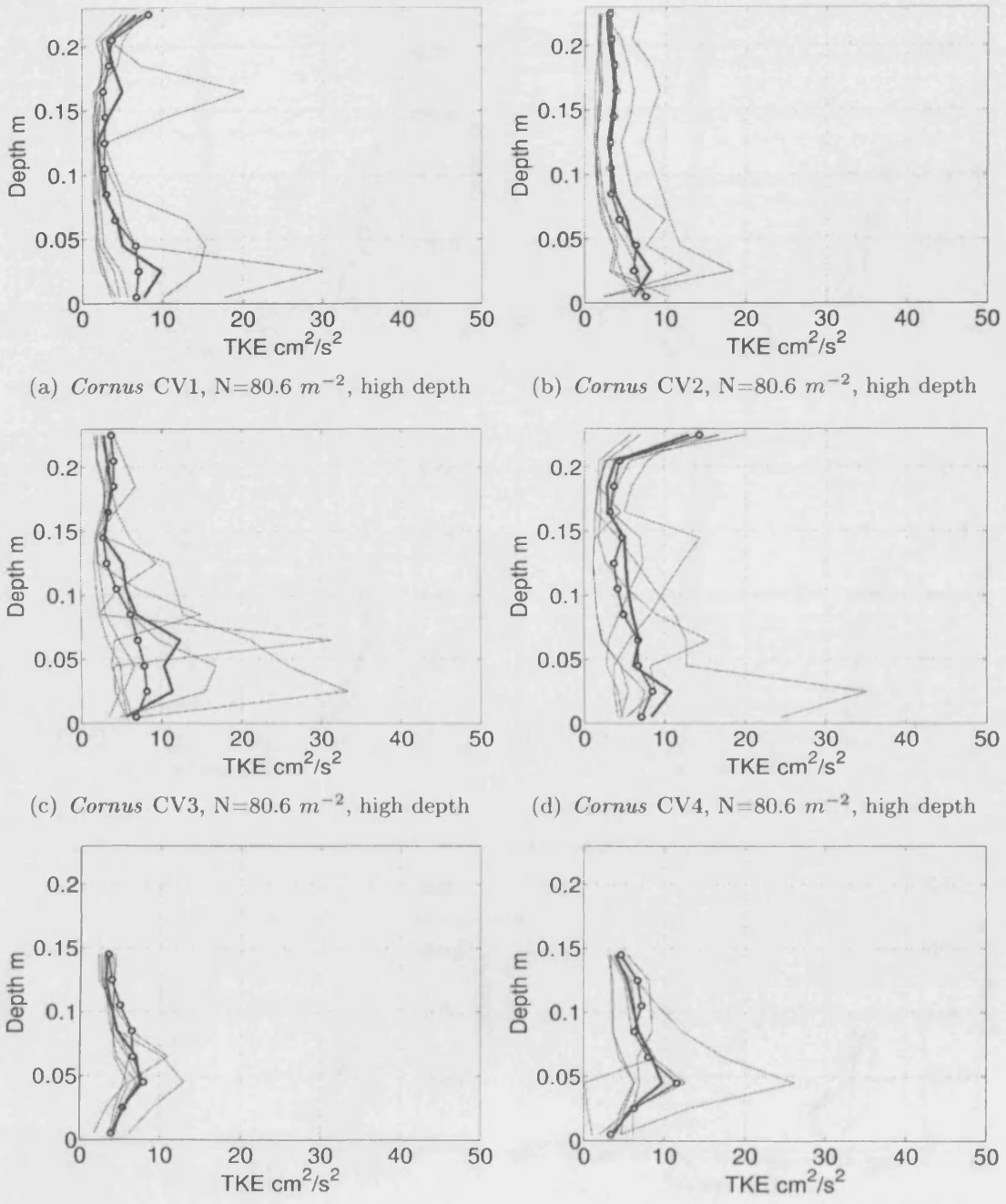

(a) *Cornus* CV1, N=80.6 m^{-2}, high depth

(b) *Cornus* CV2, N=80.6 m^{-2}, high depth

(c) *Cornus* CV3, N=80.6 m^{-2}, high depth

(d) *Cornus* CV4, N=80.6 m^{-2}, high depth

(e) *Cornus* CV2, N=80.6 m^{-2}, low depth

(f) *Cornus* CV3, N=80.6 m^{-2}, low depth

Figure 32: Sampled Turbulent Kinetic Energy using Sampling Pattern 2 in Cornus High Density arrays. Top row L to R: Sampling Volumes B, C, D and E at $Re = 742$. Bottom row L to R: Sampling Volumes C and D at $Re = 778$

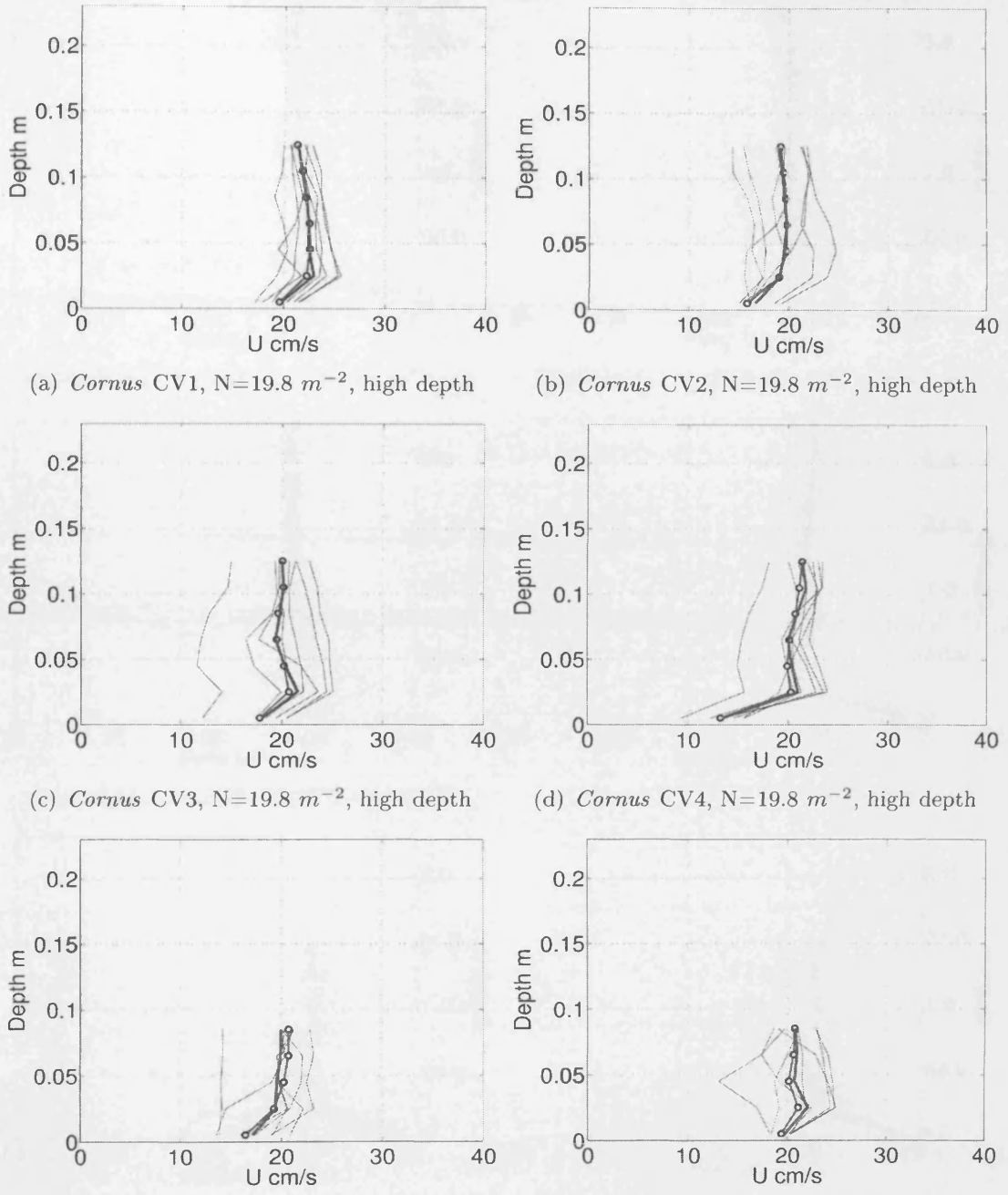

(a) *Cornus* CV1, N=19.8 m^{-2}, high depth

(b) *Cornus* CV2, N=19.8 m^{-2}, high depth

(c) *Cornus* CV3, N=19.8 m^{-2}, high depth

(d) *Cornus* CV4, N=19.8 m^{-2}, high depth

(e) *Cornus* CV2, N=19.8 m^{-2}, low depth

(f) *Cornus* CV3, N=19.8 m^{-2}, low depth

Figure 33: Sampled streamwise velocity U using Sampling Pattern 3 in Cornus Medium Density arrays. Top row L to R: Sampling Volumes B, C, D and E at $Re = 1373$. Bottom row L to R: Sampling Volumes C and D at $Re = 1409$

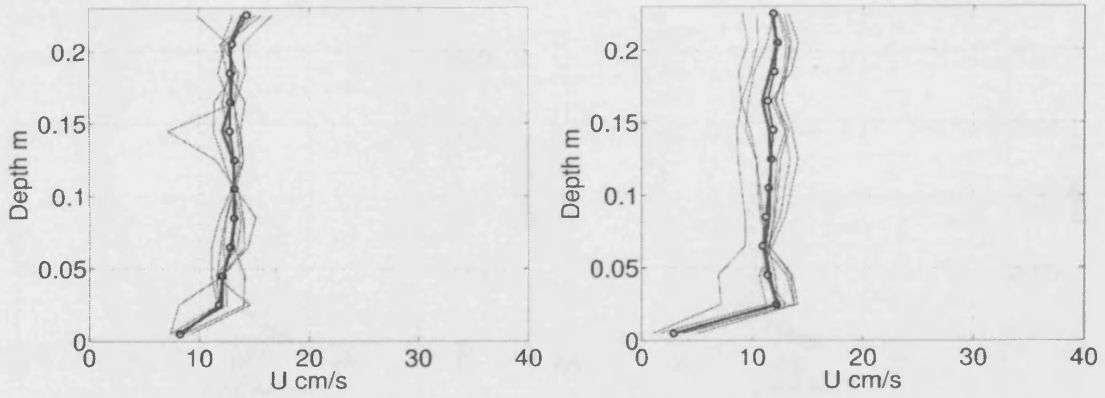

(a) *Cornus* CV1, N=80.6 m^{-2}, high depth

(b) *Cornus* CV2, N=80.6 m^{-2}, high depth

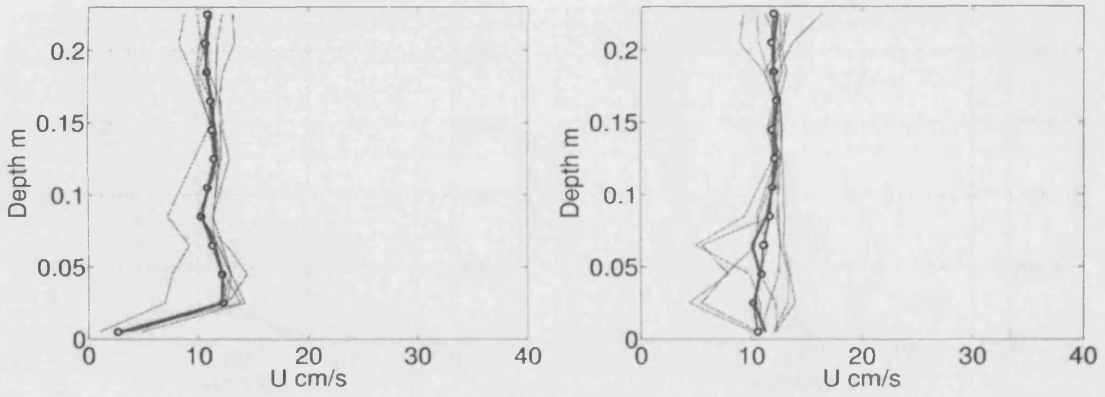

(c) *Cornus* CV3, N=80.6 m^{-2}, high depth

(d) *Cornus* CV4, N=80.6 m^{-2}, high depth

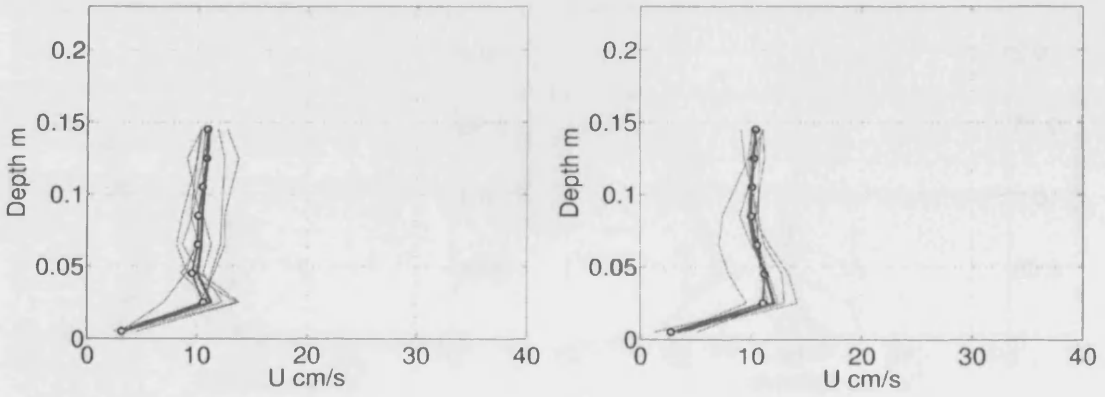

(e) *Cornus* CV2, N=80.6 m^{-2}, low depth

(f) *Cornus* CV3, N=80.6 m^{-2}, low depth

Figure 34: Sampled streamwise velocity U using Sampling Pattern 3 in Cornus High Density arrays. Top row L to R: Sampling Volumes B, C, D and E at $Re = 742$. Bottom row L to R: Sampling Volumes C and D at $Re = 778$

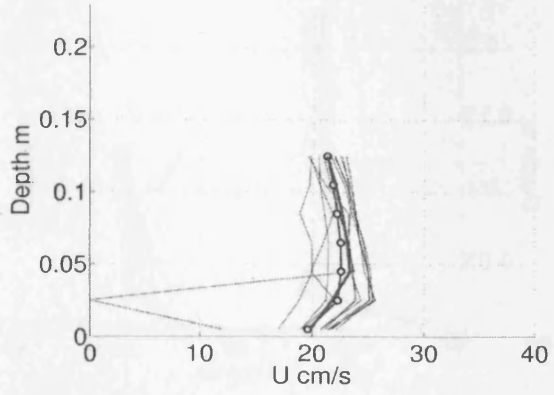

(a) *Cornus* CV1, N=19.8 m^{-2}, high depth

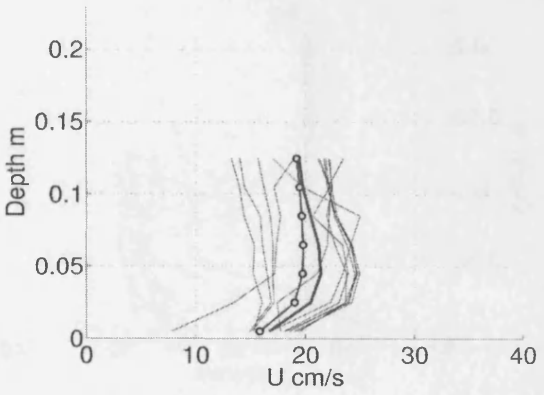

(b) *Cornus* CV2, N=19.8 m^{-2}, high depth

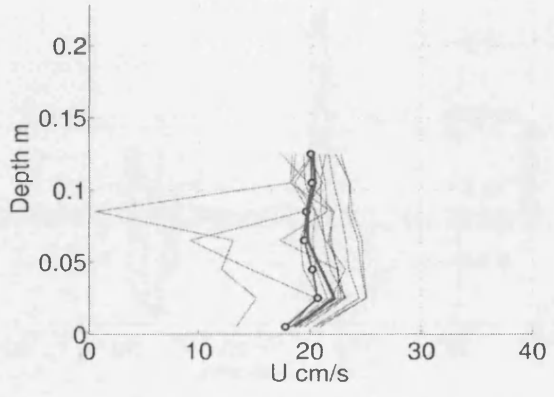

(c) *Cornus* CV3, N=19.8 m^{-2}, high depth

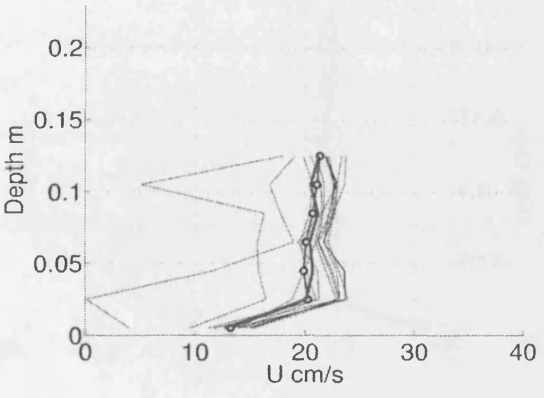

(d) *Cornus* CV4, N=19.8 m^{-2}, high depth

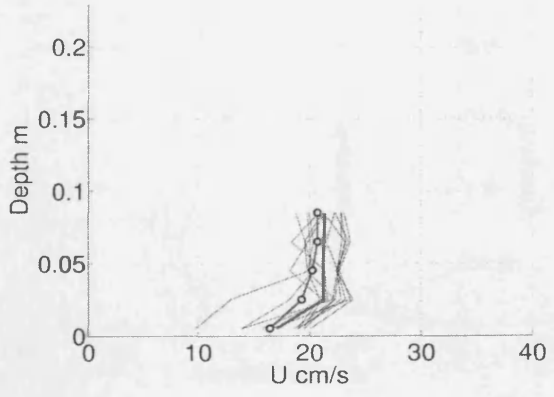

(e) *Cornus* CV2, N=19.8 m^{-2}, low depth

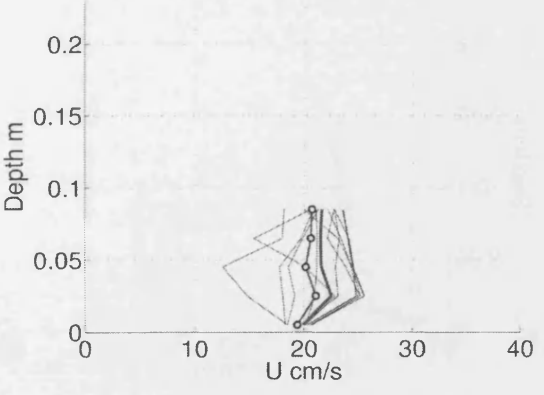

(f) *Cornus* CV3, N=19.8 m^{-2}, low depth

Figure 35: Sampled streamwise velocity U using Sampling Pattern 4 in Cornus Medium Density arrays. Top row L to R: Sampling Volumes B, C, D and E at $Re = 1373$. Bottom row L to R: Sampling Volumes C and D at $Re = 1409$

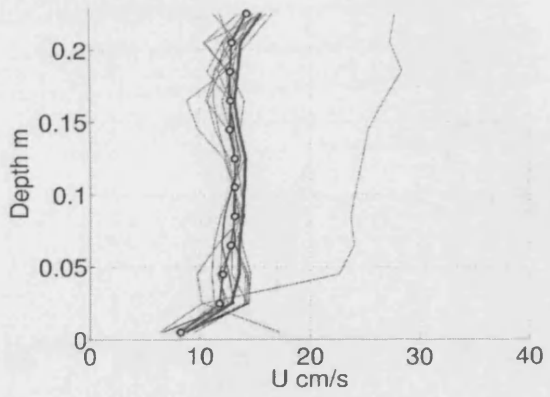

(a) *Cornus* CV1, N=80.6 m^{-2}, high depth

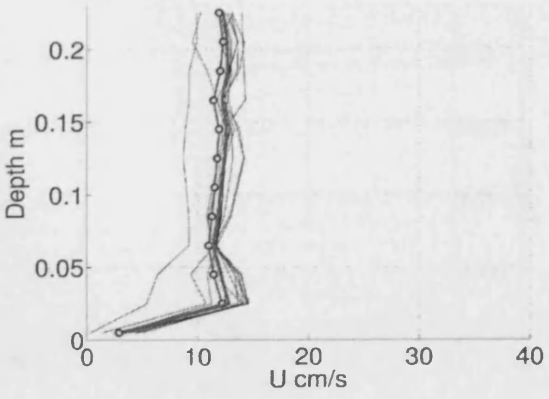

(b) *Cornus* CV2, N=80.6 m^{-2}, high depth

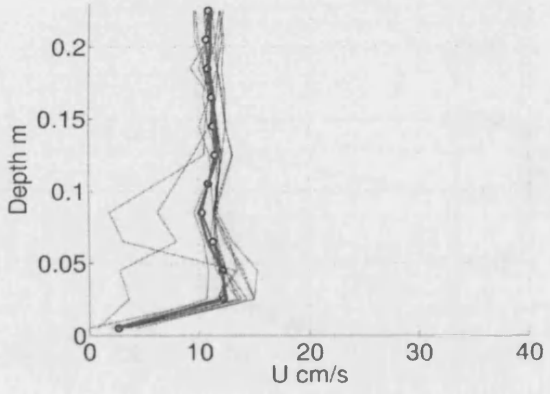

(c) *Cornus* CV3, N=80.6 m^{-2}, high depth

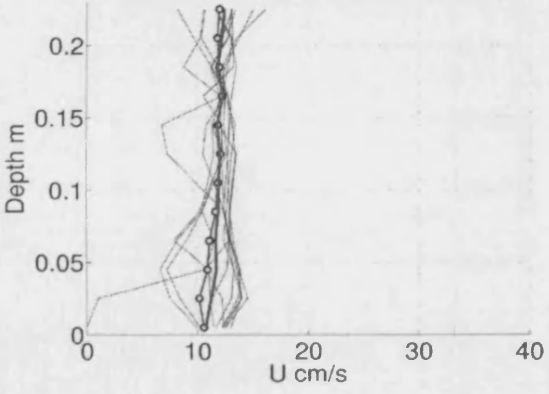

(d) *Cornus* CV4, N=80.6 m^{-2}, high depth

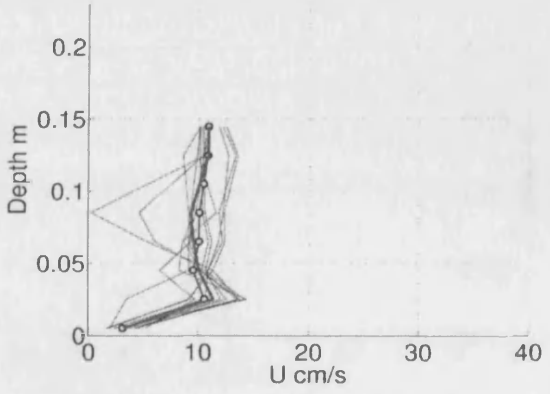

(e) *Cornus* CV2, N=80.6 m^{-2}, low depth

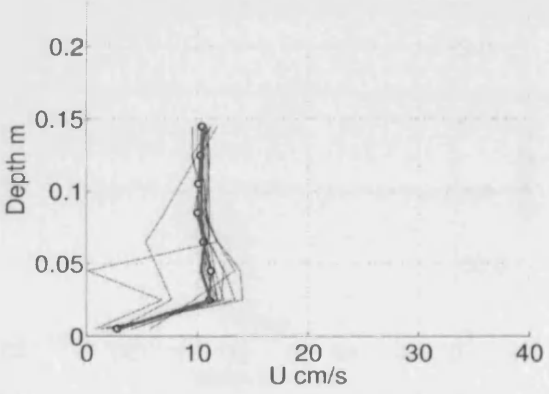

(f) *Cornus* CV3, N=80.6 m^{-2}, low depth

Figure 36: Sampled streamwise velocity U using Sampling Pattern 4 in Cornus High Density arrays. Top row L to R: Sampling Volumes B, C, D and E at $Re = 742$. Bottom row L to R: Sampling Volumes C and D at $Re = 778$

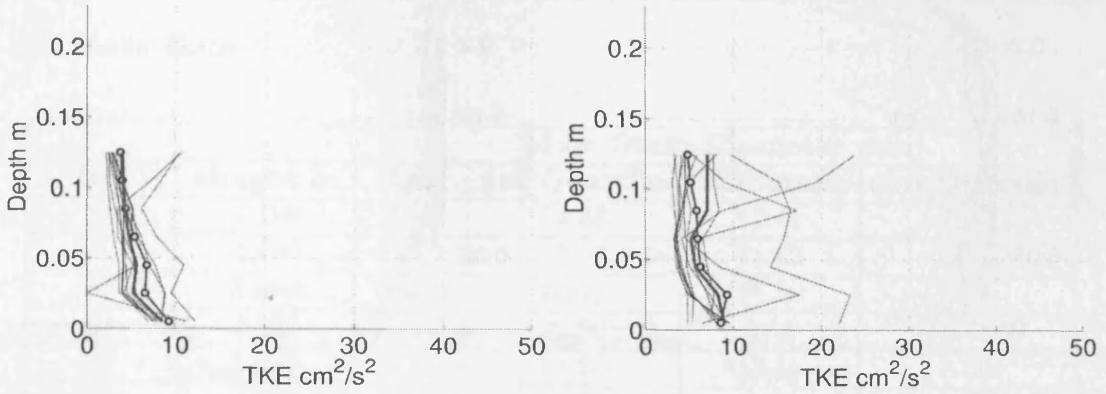

(a) *Cornus* CV1, N=19.8 m^{-2}, high depth

(b) *Cornus* CV2, N=19.8 m^{-2}, high depth

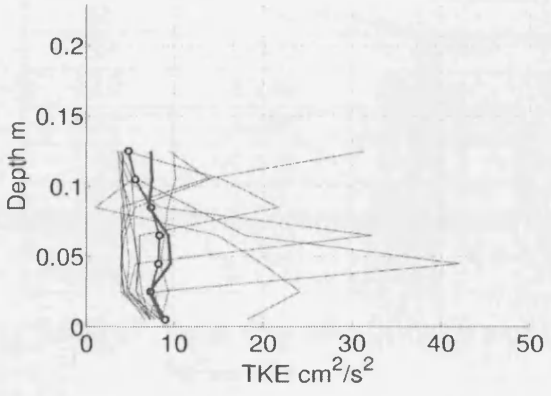

(c) *Cornus* CV3, N=19.8 m^{-2}, high depth

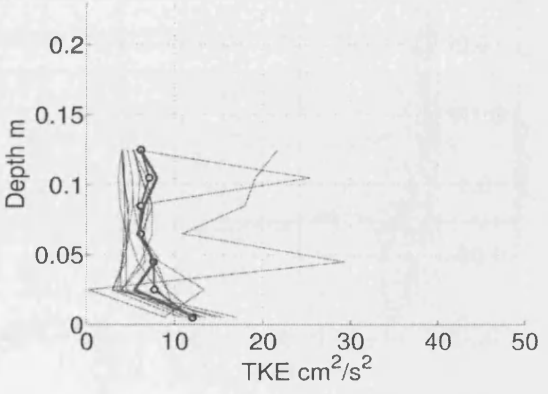

(d) *Cornus* CV4, N=19.8 m^{-2}, high depth

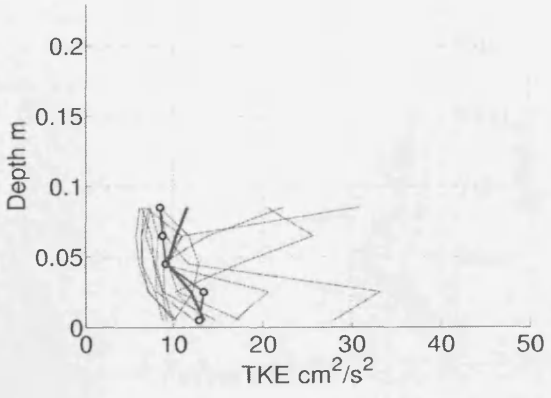

(e) *Cornus* CV2, N=19.8 m^{-2}, low depth

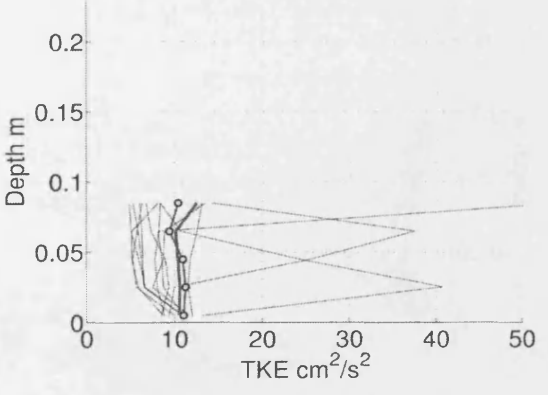

(f) *Cornus* CV3, N=19.8 m^{-2}, low depth

Figure 37: Sampled Turbulent Kinetic Energy using Sampling Pattern 4 in Cornus Medium Density arrays. Top row L to R: Sampling Volumes B, C, D and E at $Re = 1373$. Bottom row L to R: Sampling Volumes C and D at $Re = 1409$

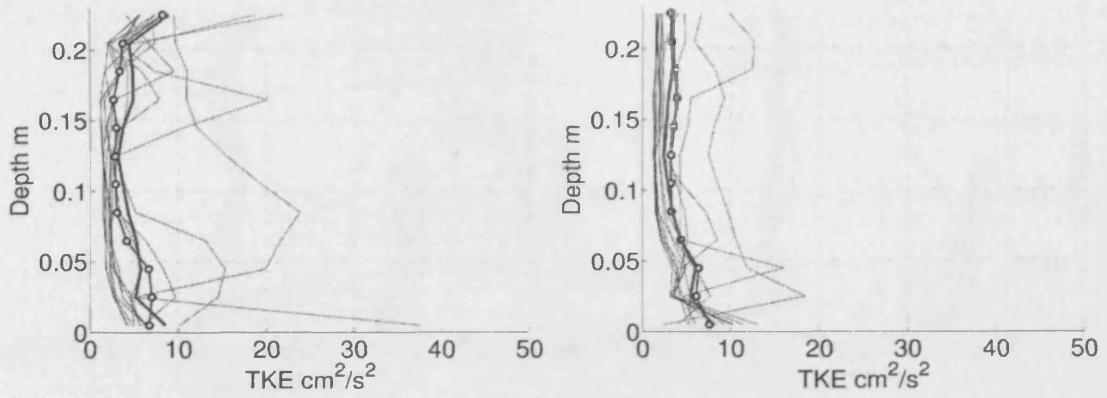

(a) *Cornus* CV1, N=80.6 m^{-2}, high depth

(b) *Cornus* CV2, N=80.6 m^{-2}, high depth

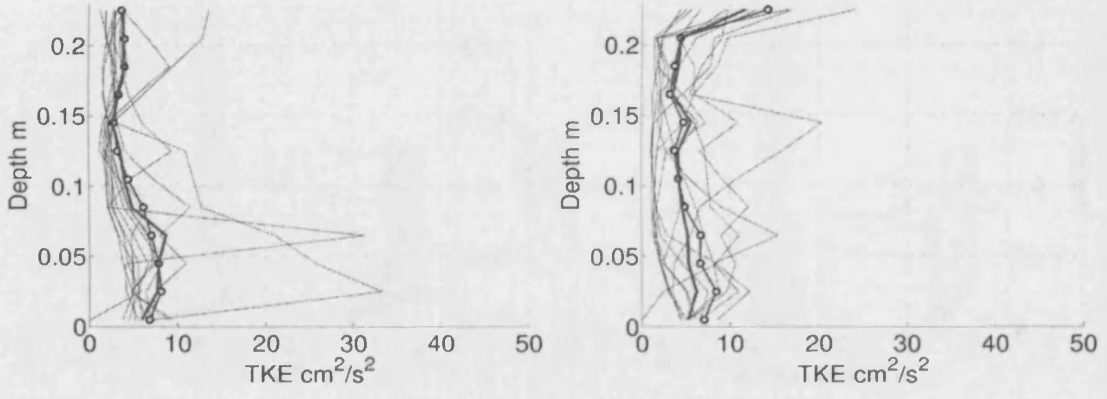

(c) *Cornus* CV3, N=80.6 m^{-2}, high depth

(d) *Cornus* CV4, N=80.6 m^{-2}, high depth

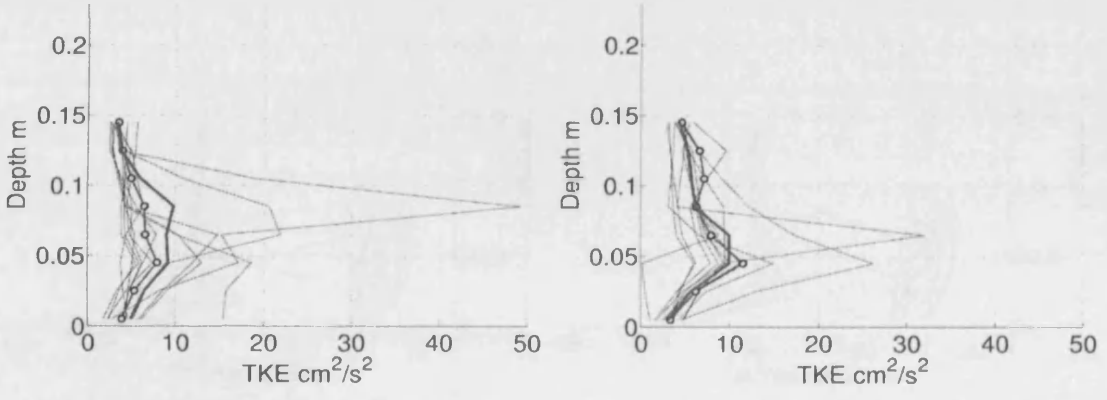

(e) *Cornus* CV2, N=80.6 m^{-2}, low depth

(f) *Cornus* CV3, N=80.6 m^{-2}, low depth

Figure 38: Sampled Turbulent Kinetic Energy using Sampling Pattern 4 in Cornus High Density arrays. Top row L to R: Sampling Volumes B, C, D and E at $Re = 742$. Bottom row L to R: Sampling Volumes C and D at $Re = 778$

.3 Chapter 5

.3.1 Salix Data

		Main Stem Diameter mm			
Test	**Height m**	**Base**	**1st Quartile**	**Mid-stem**	**3rd Quartile**
S1	2.100	29.42	24.68	17.41	7.66
S2	2.400	26.21	21.36	11.42	2.79
S3	3.950	44.40	40.12	27.50	9.75
S4	2.000	22.90	16.06	8.62	5.43
S5	3.600	47.07	14.25	18.15	8.66
S6	3.200	25.31	11.95	9.27	4.99
S7	2.300	31.46	19.40	14.99	8.42
S8	3.000	20.13	17.13	13.27	4.74
S9	3.600	28.60	22.50	14.37	7.10
S10	3.240	33.12	31.27	21.90	13.72
S11	3.500	25.98	17.94	11.42	7.29
S12	4.100	29.08	20.80	15.78	7.01
S13	3.600	38.18	22.14	15.46	9.44
S14	3.750	30.07	23.20	16.40	7.90
Average	**3.170**	**30.85**	**21.63**	**15.43**	**7.49**

Table 37: Salix specimen lengths and main stem diameters at quartile height

	Wet Mass	Dry Mass	Volume	Wet Density	Dry Density
Test	**kg**	**kg**	cm^3	kg/m^3	kg/m^3
S1	2892	378	2271	1273.4	166.4
S2	1450	NaN	1561	928.9	NaN
S3	5450	NaN	5250	1038.1	NaN
S4	714	NaN	NaN	NaN	NaN
S5	2416	973	3051	791.9	318.9
S5B1	1286	583	1594	806.7	365.7
S5B2	1130	512	1457	775.5	351.4
S6	1538	655	1788	300.8	366.3
S6B1	920	392	1039	885.4	377.2
S6B2	618	263	749	825.1	351.1
S7	2070	856	2359	877.4	362.8
S7B1	554	244	604	917.2	403.9
S7B2	796	351	907	877.6	386.9
S7B3	720	262	848	849.0	308.9
S8	744	316	765	972.5	413.0
S9	1524	770	1540	989.6	500.0
S10	2486	1115	2388	1041.0	466.9
S11	706	353	1039	679.4	339.7
S12	954	529	1346	708.7	393.0
S14	1780	796	2039	873.9	390.3

Table 38: *Salix* Wood Wet and Dry Total Mass, Volume and Wet and Dry Density

	Wet Mass	Dry Mass	Volume	Wet Density	Dry Density
Test	**kg**	**kg**	cm^3	kg/m^3	kg/m^3
S1	190.0	44.0	NaN	NaN	NaN
S2	72.0	18.0	120.0	600.0	150.0
S3	324.0	66.0	490.0	661.2	134.7
S4	132.0	32.0	NaN	NaN	NaN
S5B1	298.0	74.0	350.0	851.4	211.4
S5B2	314.0	NaN	370.0	848.6	NaN
S6B1	296.0	74.0	490.0	604.1	151.0
S6B2	262.0	65.5	350.0	748.6	187.1
S7B1	60.0	NaN	115.0	521.7	NaN
S7B2	72.0	NaN	130.0	553.8	NaN
S7B3	47.0	NaN	70.0	671.4	NaN
S8	230.0	84.0	NaN	NaN	NaN
S9	466.0	NaN	510.0	913.7	NaN
S10	352.0	84.0	470.0	748.9	178.7
S11	116.0	52.0	170.0	682.4	305.9
S12	84.0	50.0	120.0	700.0	416.7
Mean	*207.2*	*58.5*	*288.8*	*700.5*	*216.9*

Table 39: *Salix* Leaf Wet and Dry Total Mass, Volume and Wet and Dry Density

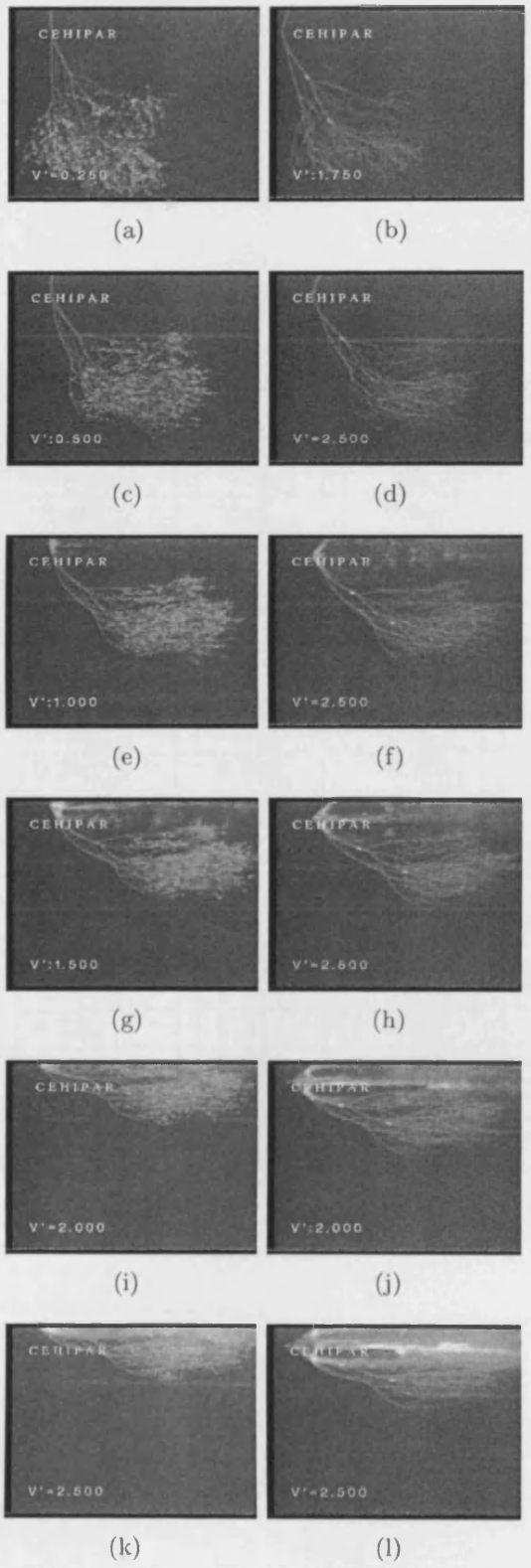
CEHIPAR
V*=0.250
(a)
CEHIPAR
V*:1.750
(b)
CEHIPAR
V*:0.500
(c)
CEHIPAR
V*=2.500
(d)
CEHIPAR
V*:1.000
(e)
CEHIPAR
V*=2.500
(f)
CEHIPAR
V*:1.500
(g)
CEHIPAR
V*=2.500
(h)
CEHIPAR
V*=2.000
(i)
CEHIPAR
V*:2.000
(j)
CEHIPAR
V*=2.500
(k)
CEHIPAR
V*=2.500
(l)

Figure 39: S1

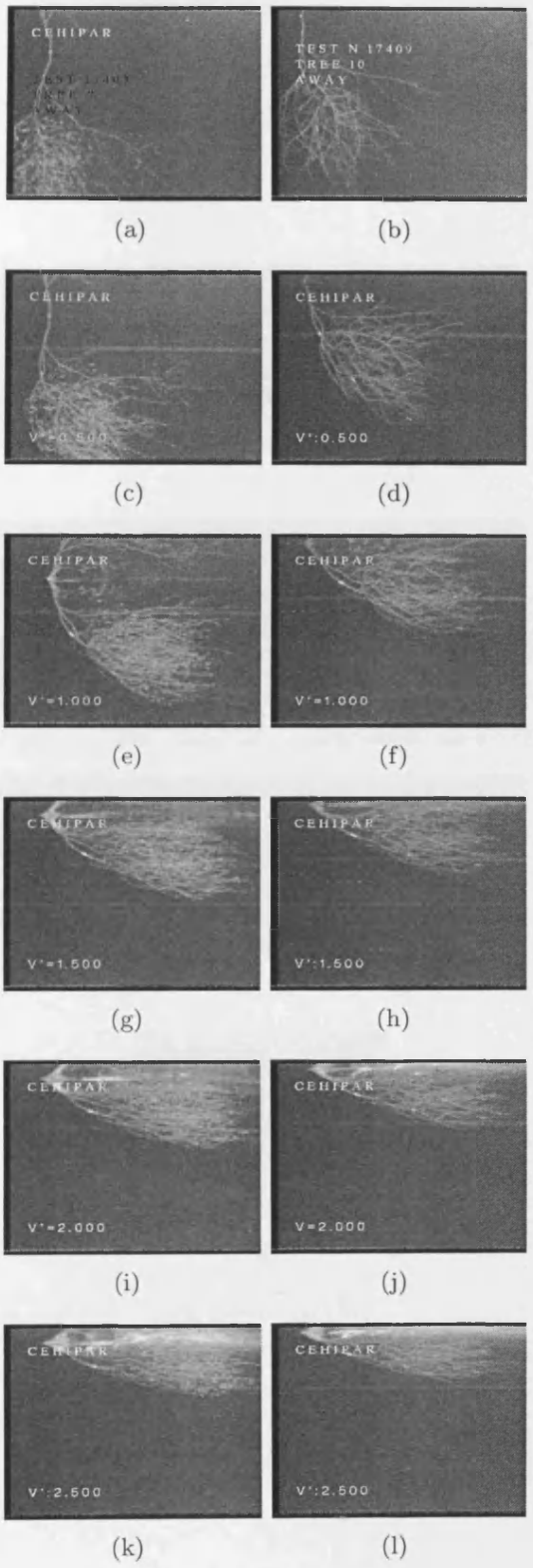

(a) (b)

(c) (d)

(e) (f)

(g) (h)

(i) (j)

(k) (l)

Figure 40: S2

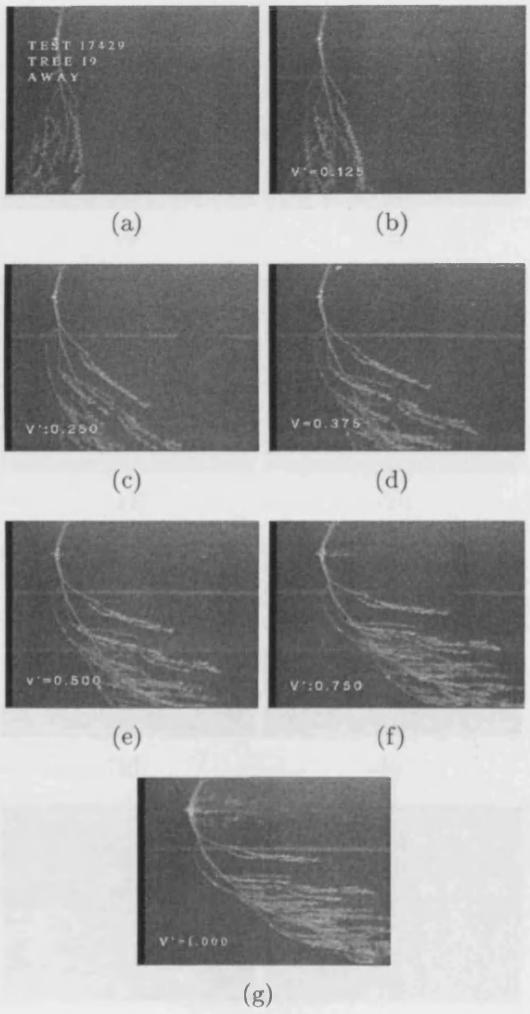

(a) (b) (c) (d) (e) (f) (g)

Figure 41: S5

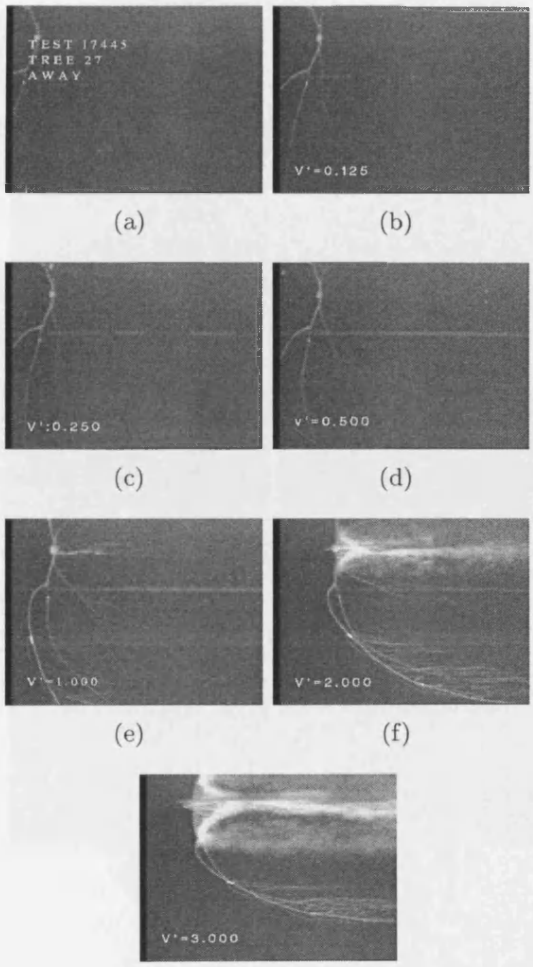

(a) (b) (c) (d) (e) (f) (g)

Figure 42: S5B1

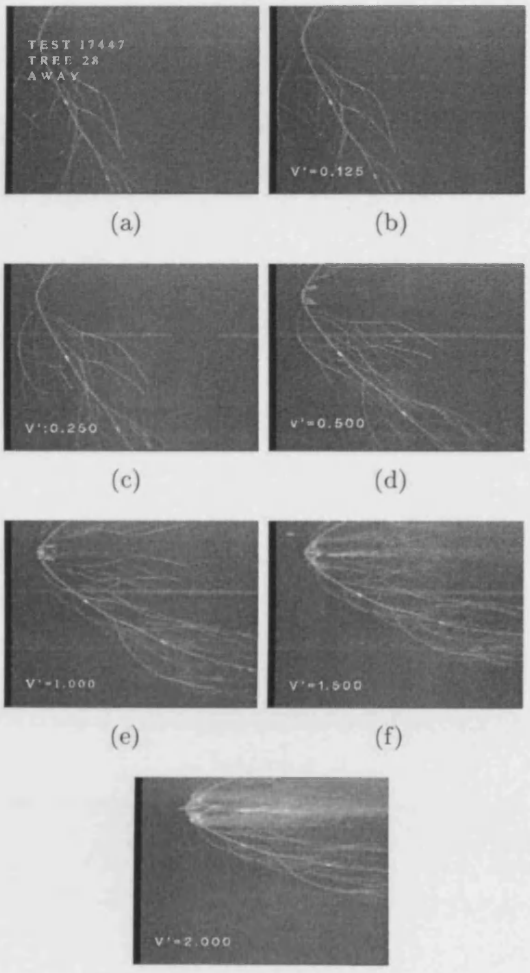

(a) (b) (c) (d) (e) (f) (g)

Figure 43: S5B2

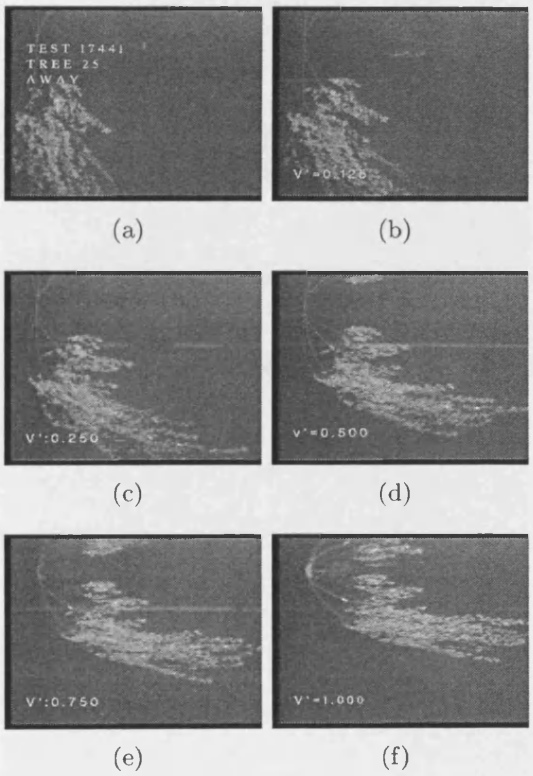
TEST 17441
TREE 25
AWAY
V':0.125
(a)
(b)
V':0.250
V':0.500
(c)
(d)
V':0.750
V':1.000
(e)
(f)

Figure 44: S6

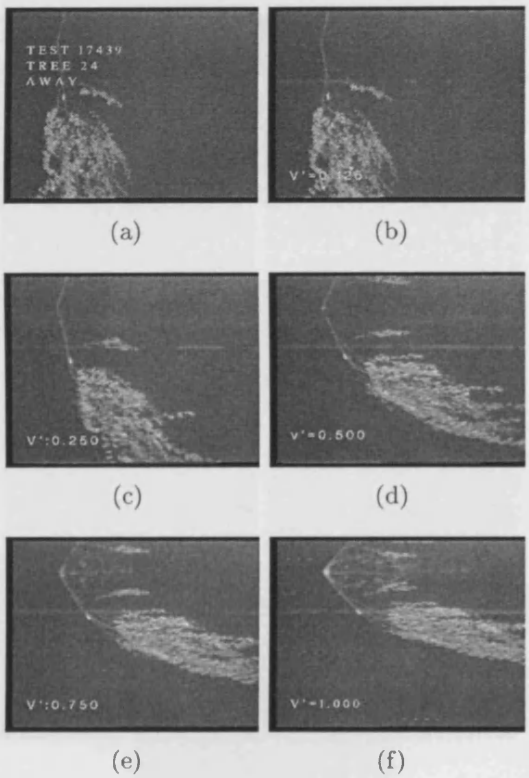

(a) (b) (c) (d) (e) (f)

Figure 45: S6B1

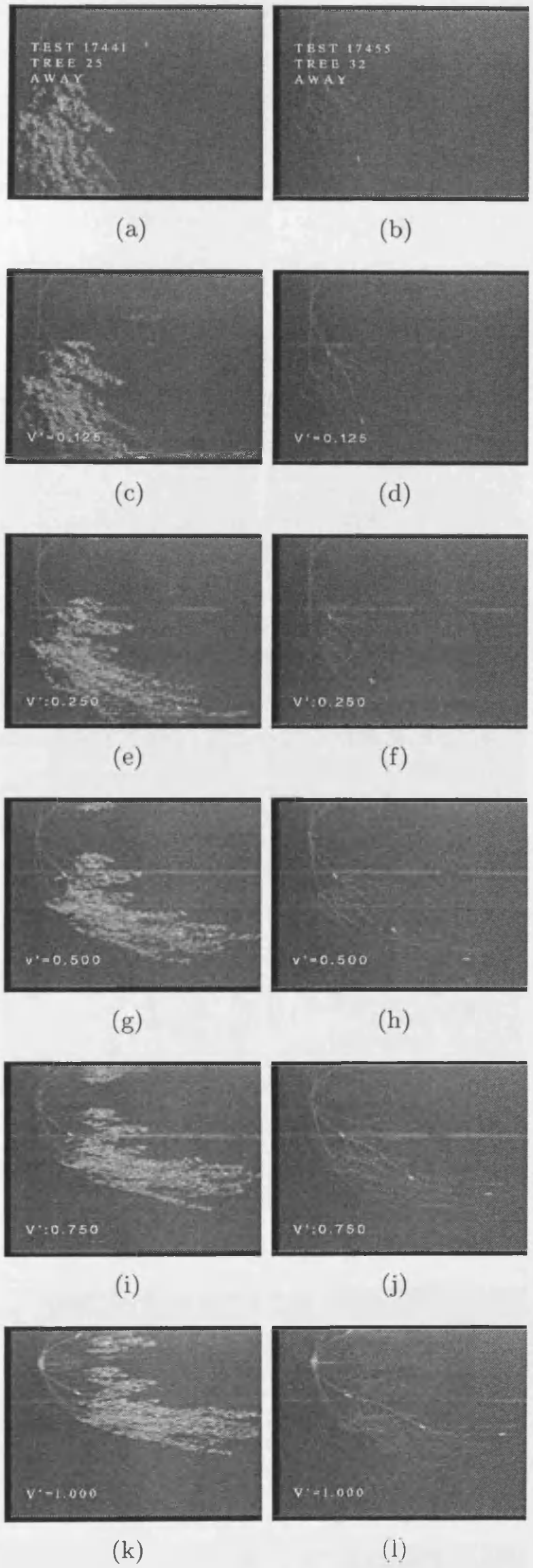

(a) (b) (c) (d) (e) (f) (g) (h) (i) (j) (k) (l)

Figure 46: S6B2

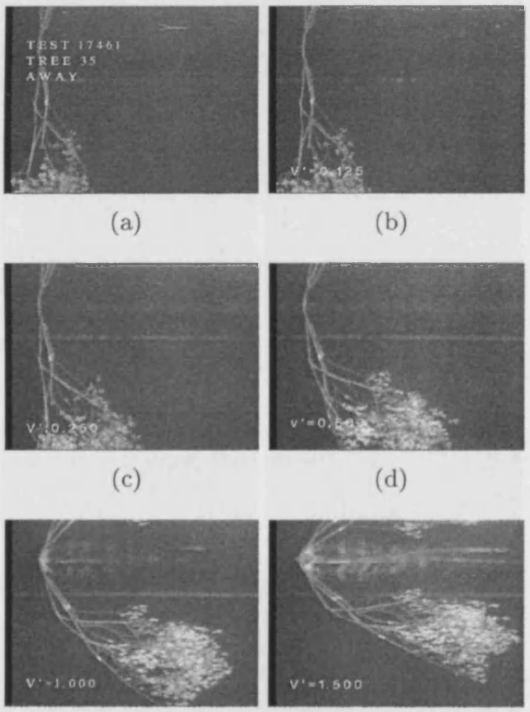

(a) (b)

(c) (d)

(e) (f)

Figure 47: S7

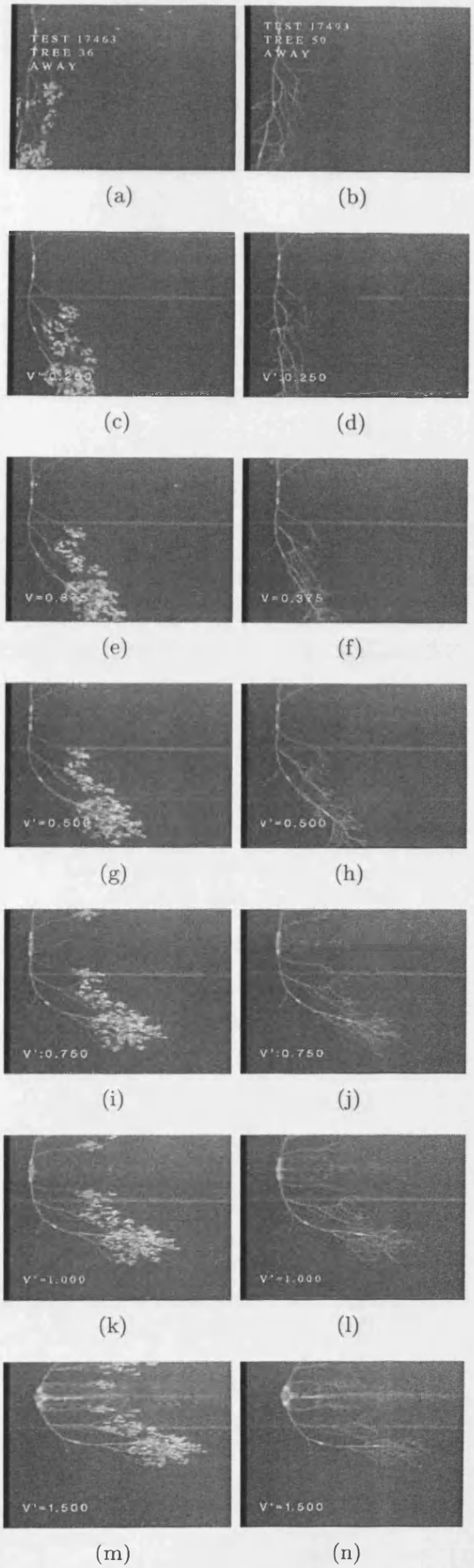

(a) (b)

(c) (d)

(e) (f)

(g) (h)

(i) (j)

(k) (l)

(m) (n)

Figure 48: S7B1

(a)

(b)

(c)

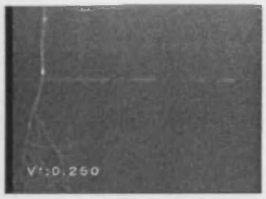

(d)

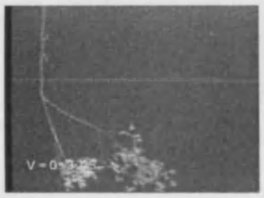

(e)

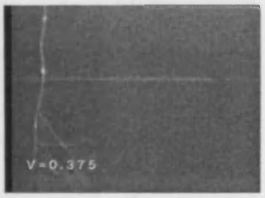

(f)

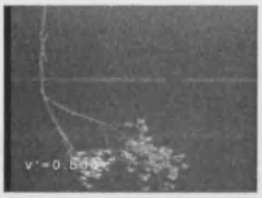

(g)

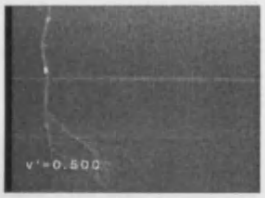

(h)

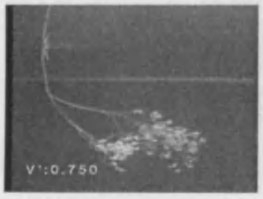

(i)

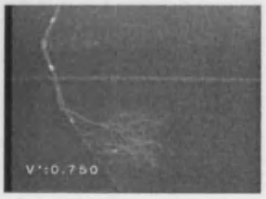

(j)

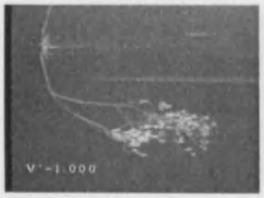

(k)

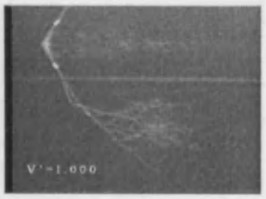

(l)

Figure 49: S7B2

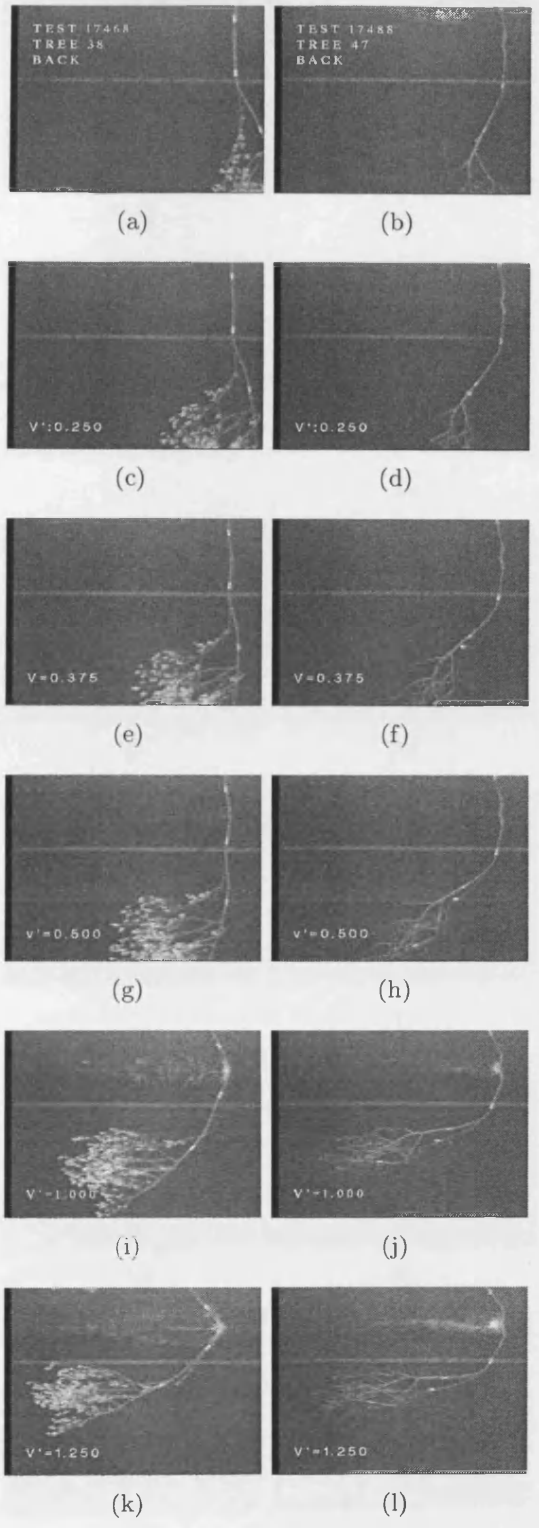

(a) (b)

(c) (d)

(e) (f)

(g) (h)

(i) (j)

(k) (l)

Figure 50: S7B2

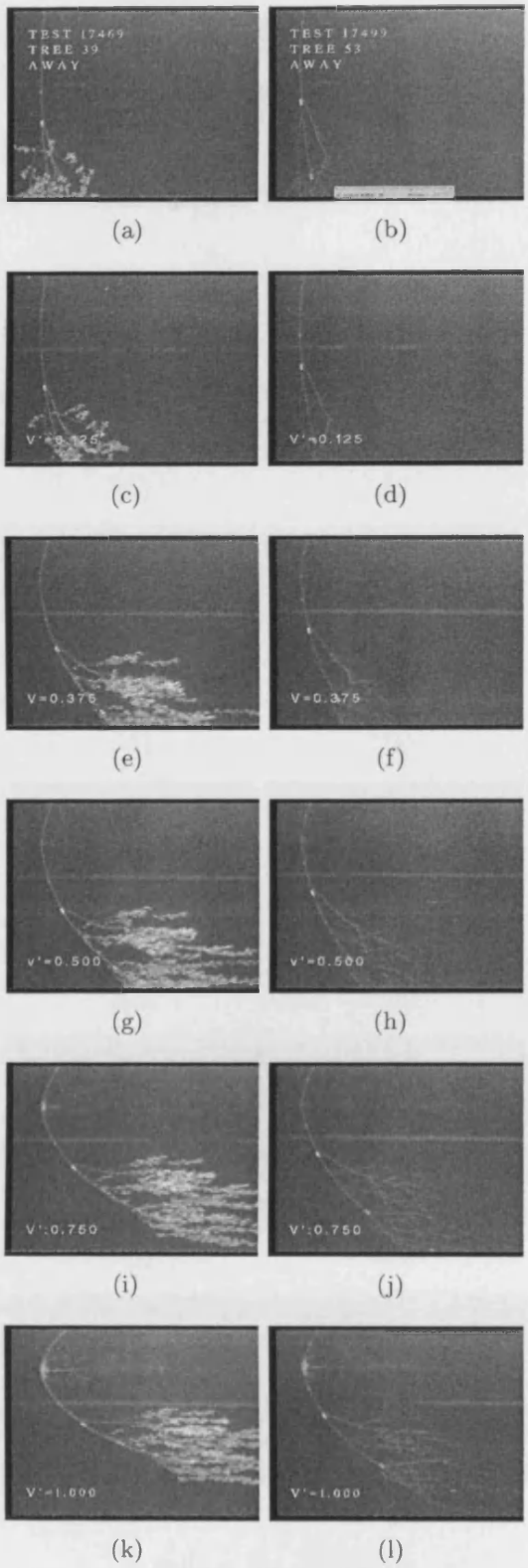

(a) (b)

(c) (d)

(e) (f)

(g) (h)

(i) (j)

(k) (l)

Figure 51: S8

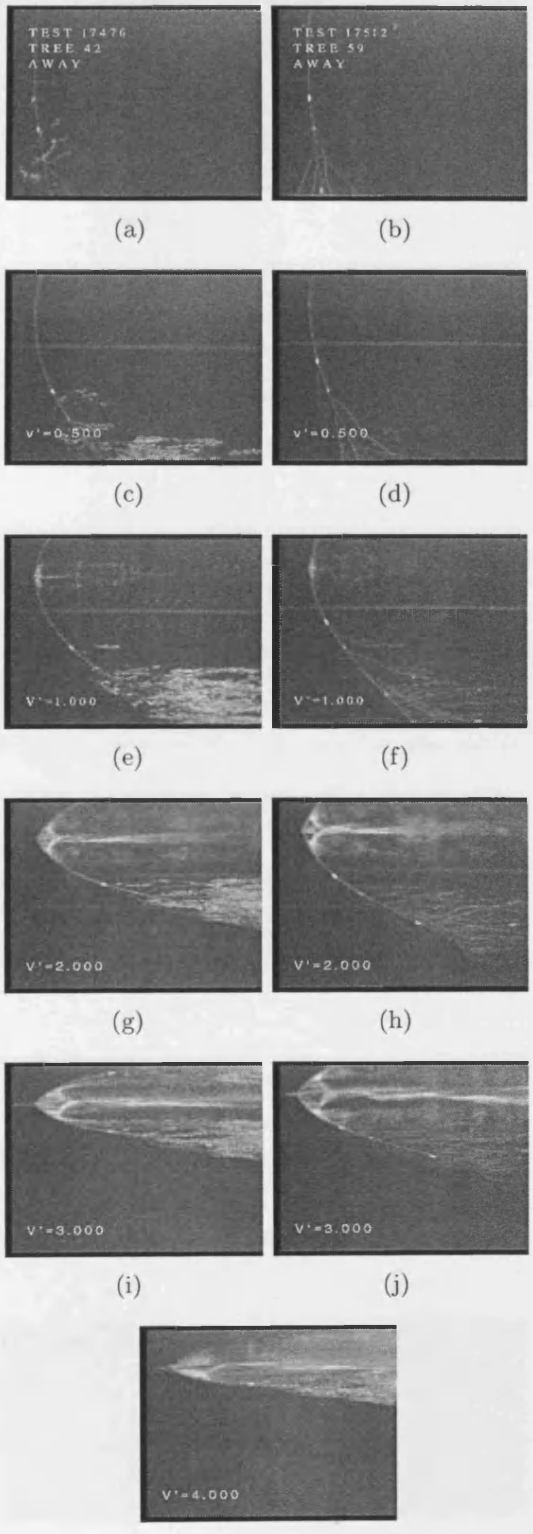

(a) (b) (c) (d) (e) (f) (g) (h) (i) (j) (k)

Figure 52: S9

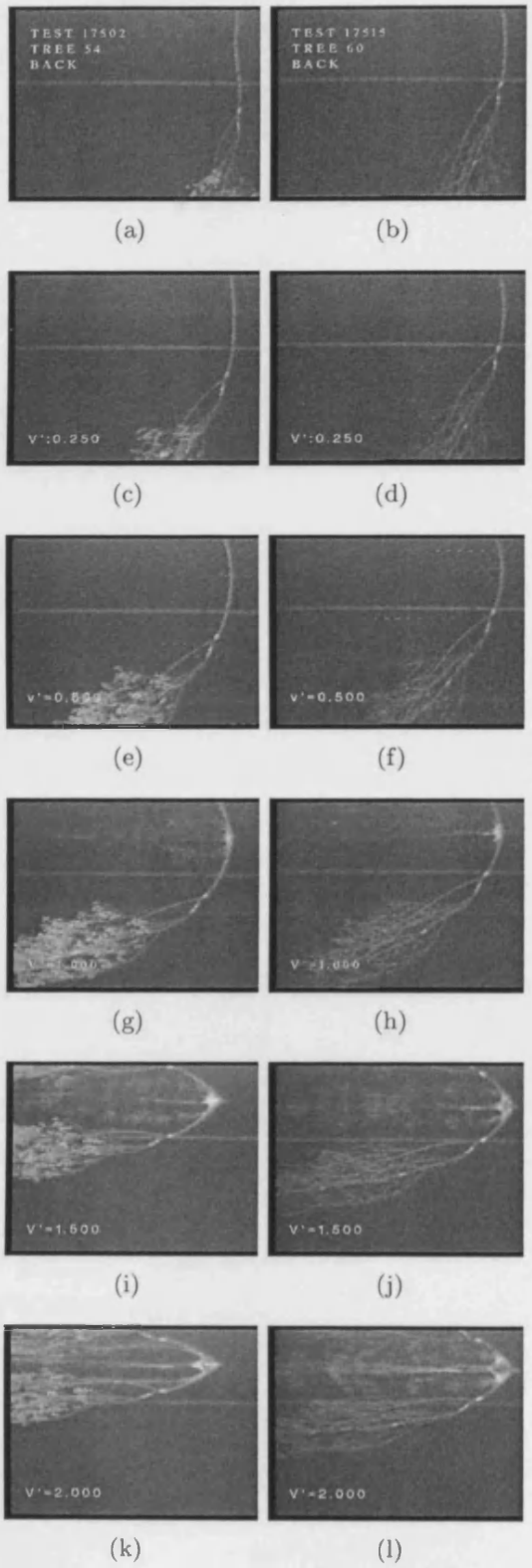

Figure 53: S10

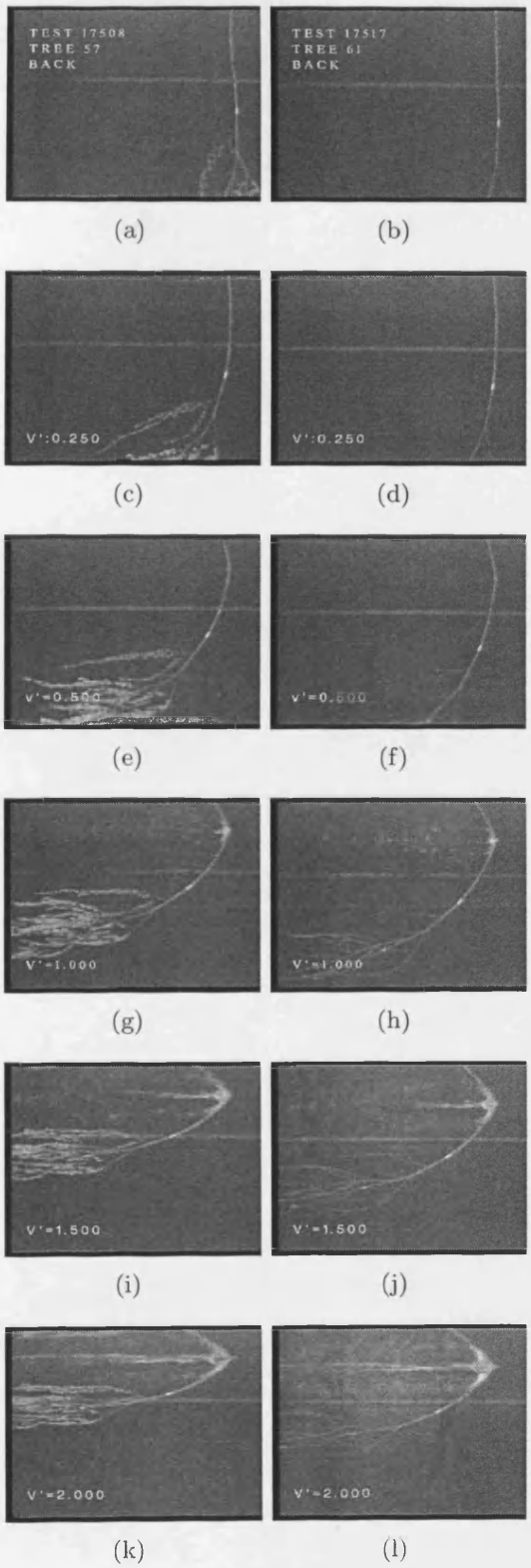

(a) (b)

(c) (d)

(e) (f)

(g) (h)

(i) (j)

(k) (l)

Figure 54: S11

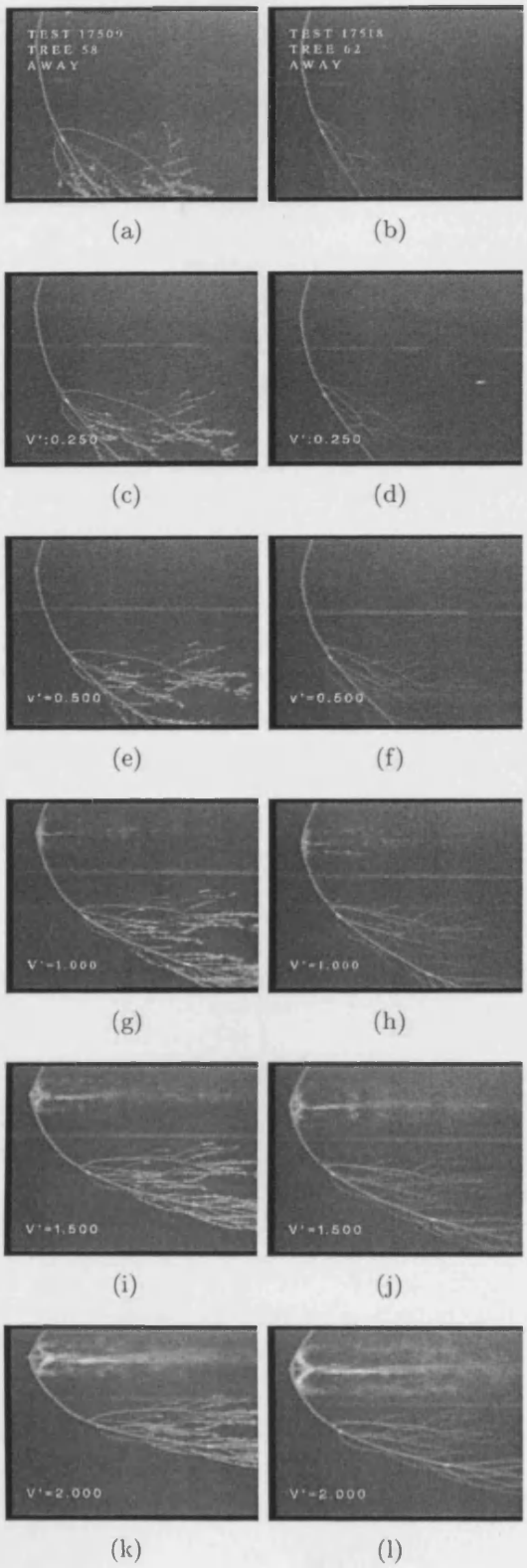

(a) (b)

(c) (d)

(e) (f)

(g) (h)

(i) (j)

(k) (l)

Figure 55: S12

.3.2 Alnus Data

Test	Height m	Main Stem Diameter mm			
Test	Height m	Base	1st Quartile	Mid-stem	3rd Quartile
A1	2.450	58.41	29.24	25.31	10.52
A2	3.600	35.02	33.16	17.98	8.58
A3	2.600	28.38	21.26	15.67	4.63
A4	2.400	27.08	21.99	16.23	8.20
A5	1.800	28.29	19.52	12.20	8.06
Average	2.570	35.44	25.03	17.99	7.99

Table 40: *Alnus* specimen lengths and main stem diameters at quartile height

Test	Wet Mass	Dry Mass	Volume	Wet Density	Dry Density
Test	kg	kg	cm^3	kg/m^3	kg/m^3
A1	2110	NaN	1394	1513.6	NaN
A2	2772	1289	2866	967.2	449.7
A3	NaN	NaN	NaN	NaN	NaN
A3NB	NaN	NaN	NaN	NaN	NaN
A1NB50	268	90	395	678.4	227.8
A4	1168	529	1194	978.2	443.0
A5	1228	NaN	1331	922.6	NaN

Table 41: *Alnus* Wood Wet and Dry Total Mass, Volume and Wet and Dry Density

Test	Wet Mass	Dry Mass	Volume	Wet Density	Dry Density
Test	kg	kg	cm^3	kg/m^3	kg/m^3
A1	148.0	32.0	222.0	666.7	144.1
A2	220.0	48.0	290.0	758.6	165.5
A4	144.0	30.0	200.0	720.0	150.0
A5	102.0	22.0	130.0	784.6	169.2
Mean	*153.5*	*33.0*	*210.5*	*732.5*	*157.2*

Table 42: *Alnus* LeafWet and Dry Total Mass, Volume and Wet and Dry Density

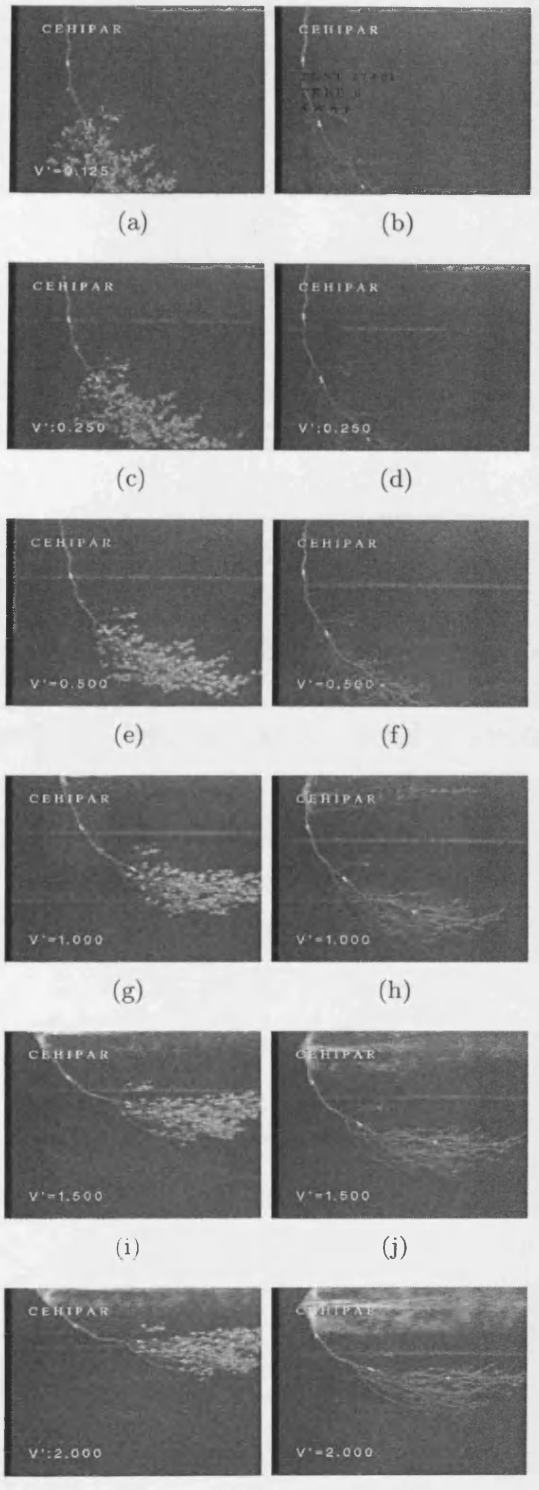
CEHIPAR
V'=0.125
(a)
CEHIPAR
(b)
CEHIPAR
V':0.250
(c)
CEHIPAR
V':0.250
(d)
CEHIPAR
V'=0.500
(e)
CEHIPAR
V'=0.500
(f)
CEHIPAR
V'=1.000
(g)
CEHIPAR
V'=1.000
(h)
CEHIPAR
V'=1.500
(i)
CEHIPAR
V'=1.500
(j)
CEHIPAR
V':2.000
(k)
V'=2.000
(l)

Figure 56: A1

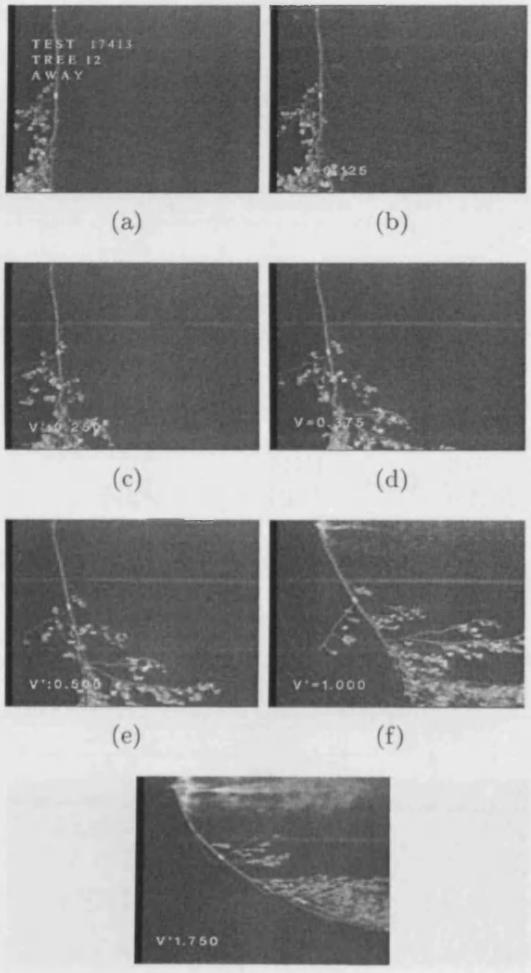

(a) (b) (c) (d) (e) (f) (g)

Figure 57: A2

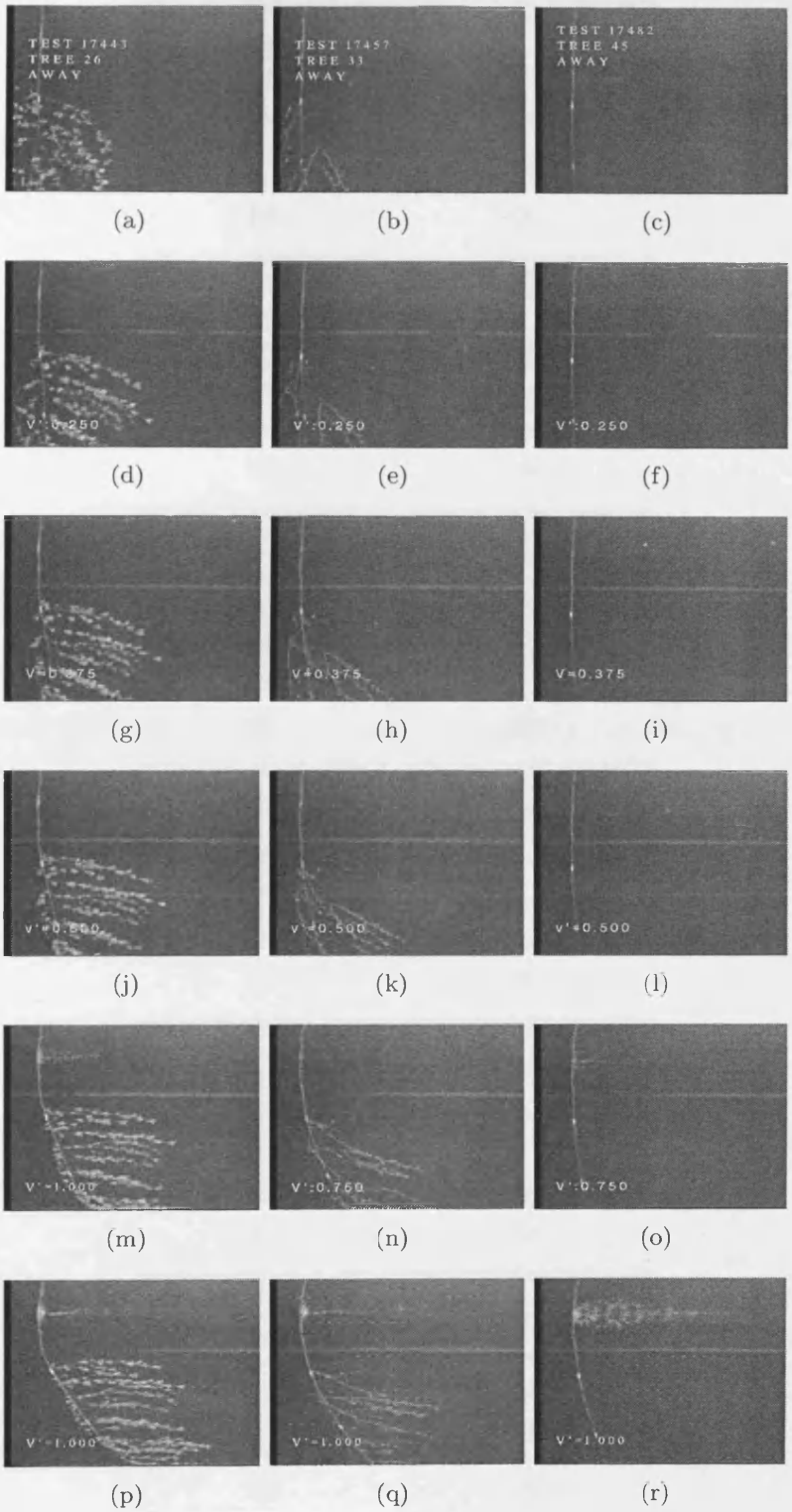

(a) (b) (c)

(d) (e) (f)

(g) (h) (i)

(j) (k) (l)

(m) (n) (o)

(p) (q) (r)

Figure 58: A3

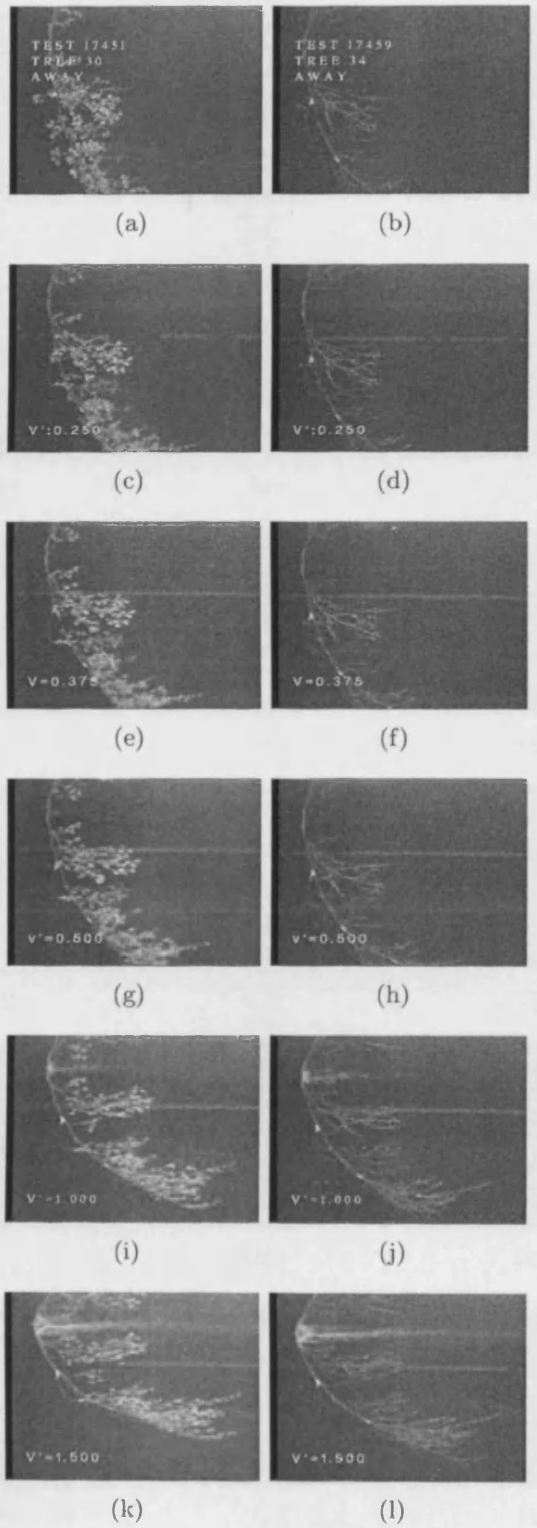

(a) (b) (c) (d) (e) (f) (g) (h) (i) (j) (k) (l)

Figure 59: A4

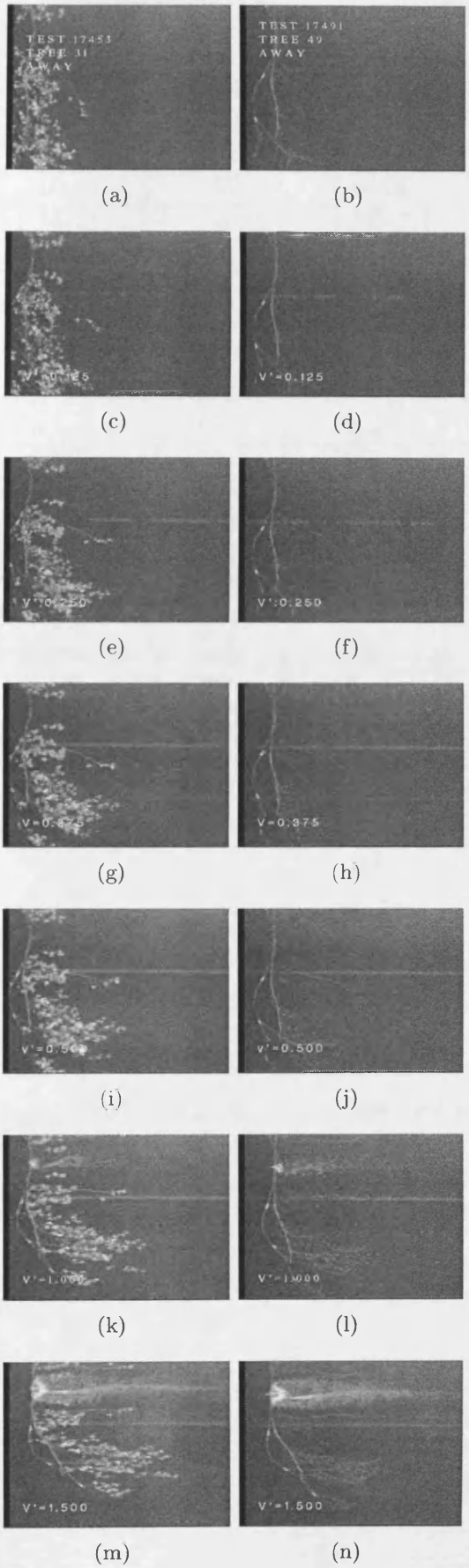

(a) (b)

(c) (d)

(e) (f)

(g) (h)

(i) (j)

(k) (l)

(m) (n)

Figure 60: A5

.3.3 Populus data

Test	Height m	Main Stem Diameter mm			
Test	Height m	Base	1st Quartile	Mid-stem	3rd Quartile
P1	2.680	34.97	18.20	12.38	7.95
P2	3.770	36.50	22.70	21.00	8.24
P3	2.600	23.23	19.85	16.44	6.73
P4	3.900	35.44	29.48	21.68	16.37

Table 43: *Popolus* specimen lengths and main stem diameters at quartile height

Test	Wet Mass	Dry Mass	Volume	Wet Density	Dry Density
Test	kg	kg	cm^3	kg/m^3	kg/m^3
P1	1210	560	1218	993.4	459.7
P2	2082	933	NaN	NaN	NaN
P2B1	1364	611	NaN	NaN	NaN
P2B2	718	317	417	1721.8	760.1
P3	840	378	945	888.8	400.0
P4	2416	1009	2344	1030.7	430.4
P4B1	2076	867	1964	1057.0	41.4
P4B2	340	142	380	894.7	373.6

Table 44: *Popolus* Wood Wet and Dry Total Mass, Volume and Wet and Dry Density

Test	Wet Mass	Dry Mass	Volume	Wet Density	Dry Density
Test	kg	kg	cm^3	kg/m^3	kg/m^3
P2B1	122.0	24.1	150.0	813.3	160.7
P2B2	60.0	11.9	90.0	666.7	132.2
P3	78.0	16.0	100.0	780.0	160.0
P4B1	78.0	24.0	100.0	780.0	240.0
P4B2	140.0	43.1	NaN	NaN	NaN
Mean	*95.6*	*23.8*	*110.0*	*760.0*	*173.22*

Table 45: *Popolus* Leaf Wet and Dry Total Mass, Volume and Wet and Dry Density

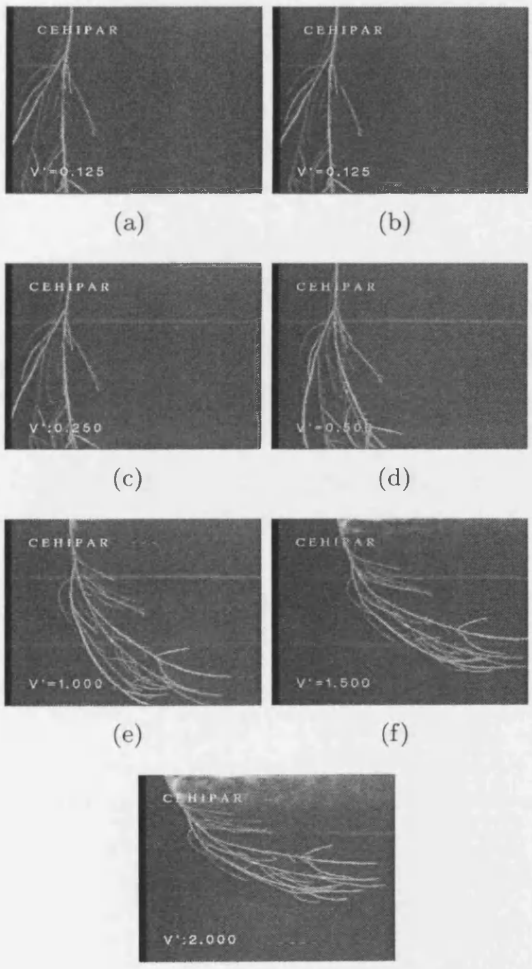
CEHIPAR
V*=0.125
(a)
CEHIPAR
V*=0.125
(b)
CEHIPAR
V*=0.250
(c)
CEHIPAR
(d)
CEHIPAR
V*=1.000
(e)
CEHIPAR
V*=1.500
(f)
CEHIPAR
V*=2.000
(g)

Figure 61: P1

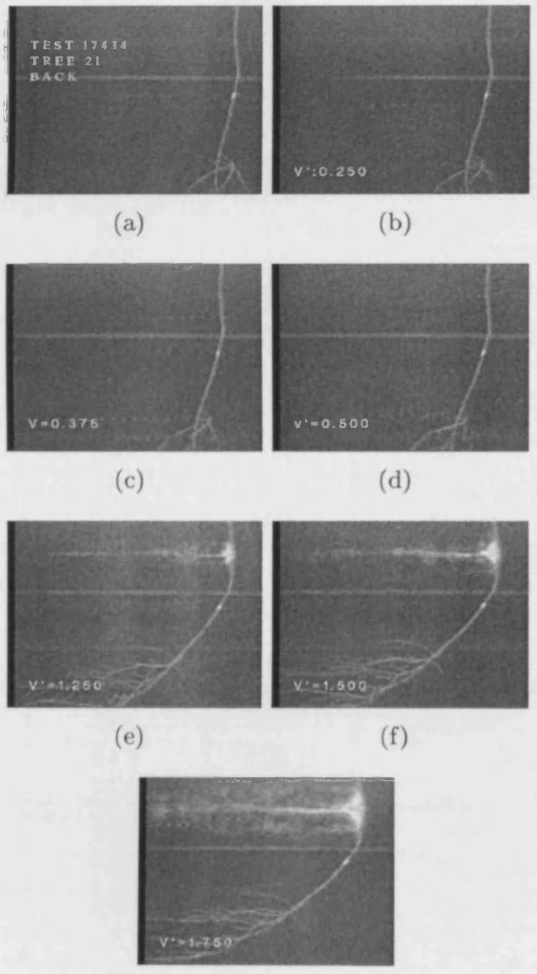

(a) (b) (c) (d) (e) (f) (g)

Figure 62: P2B1

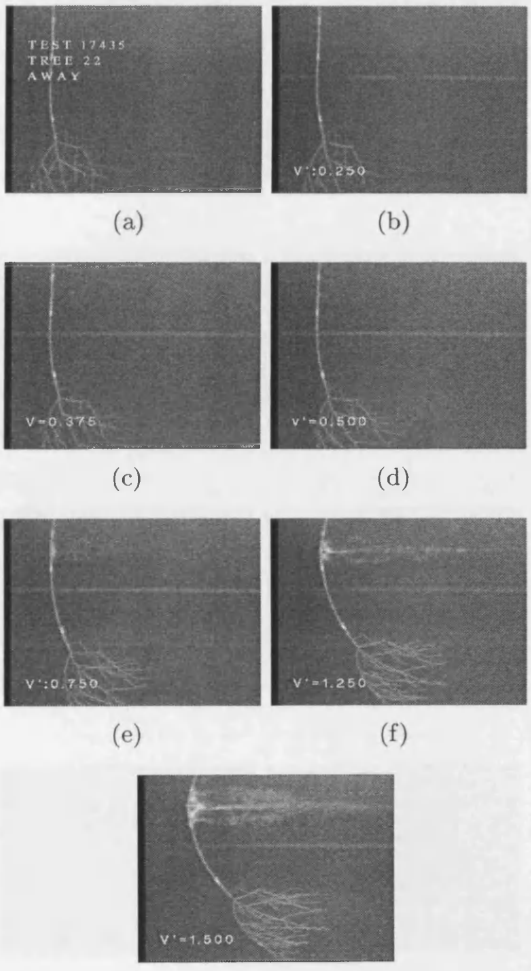

(a) (b) (c) (d) (e) (f) (g)

Figure 63: P2B1

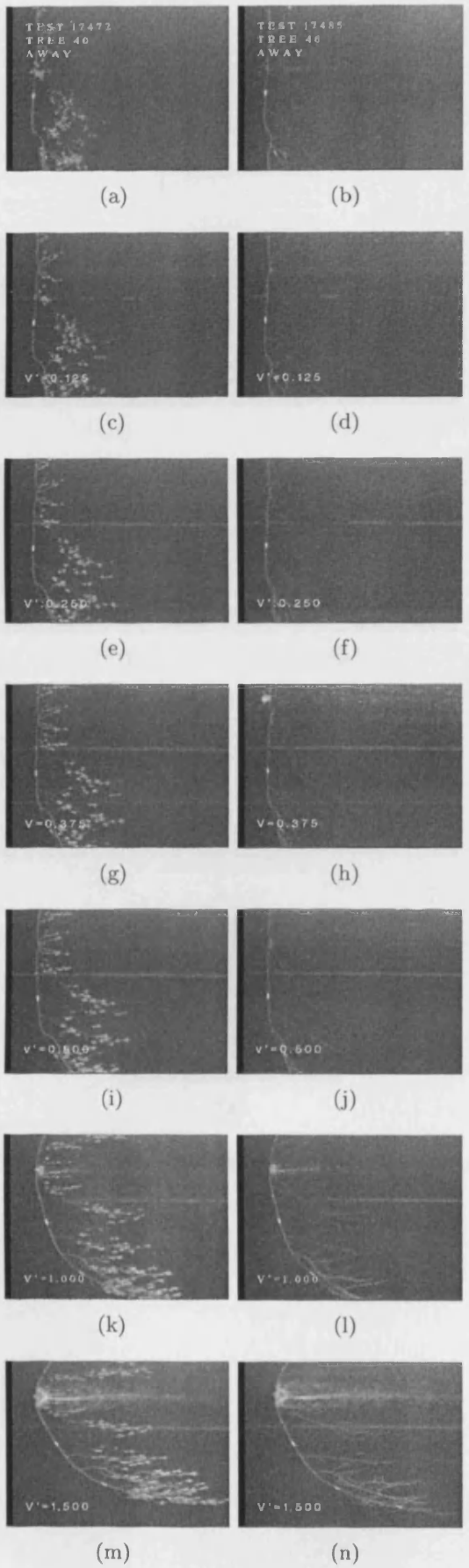
TEST 17472
TREE 46
AWAY
TEST 17485
TREE 46
AWAY
V'=0.125
V'=0.125
V'=0.250
V'=0.250
V=0.375
V=0.375
v'=0.600
v'=0.600
V'=1.000
V'=1.000
V'=1.500
V'=1.500
(a)
(b)
(c)
(d)
(e)
(f)
(g)
(h)
(i)
(j)
(k)
(l)
(m)
(n)

Figure 64: P3

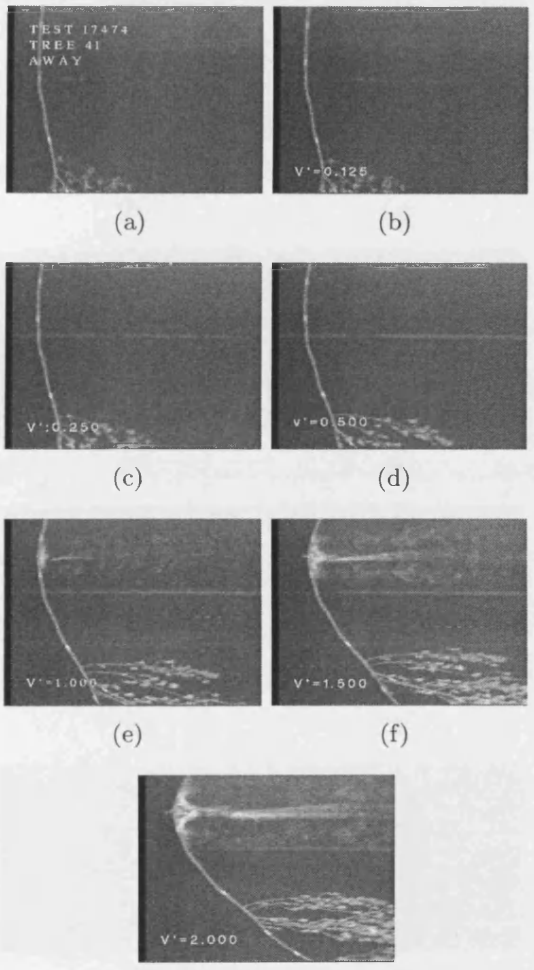

(a) (b) (c) (d) (e) (f) (g)

Figure 65: P4

(a) (b)

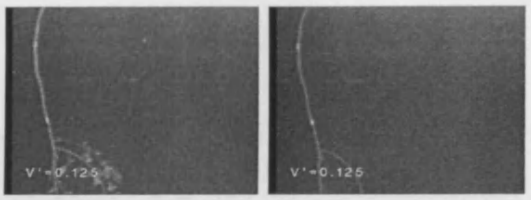

(c) (d)

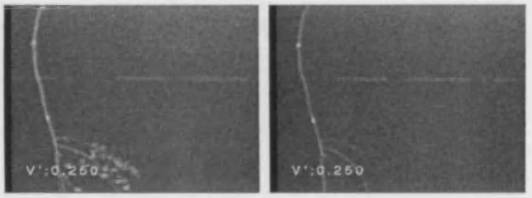

(e) (f)

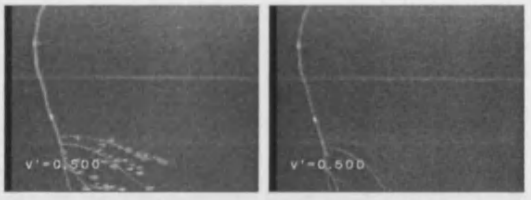

(g) (h)

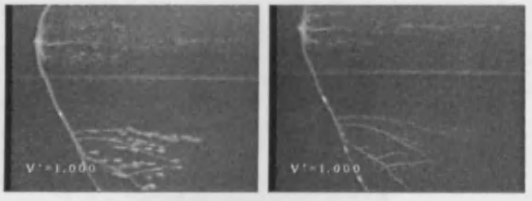

(i) (j)

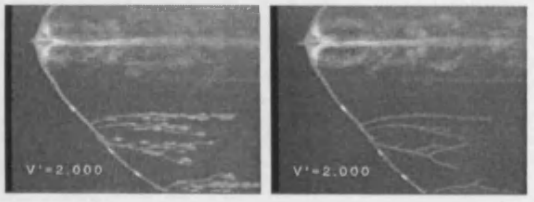

(k) (l)

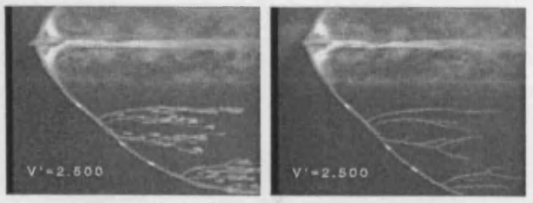

(m) (n)

Figure 66: P4B1

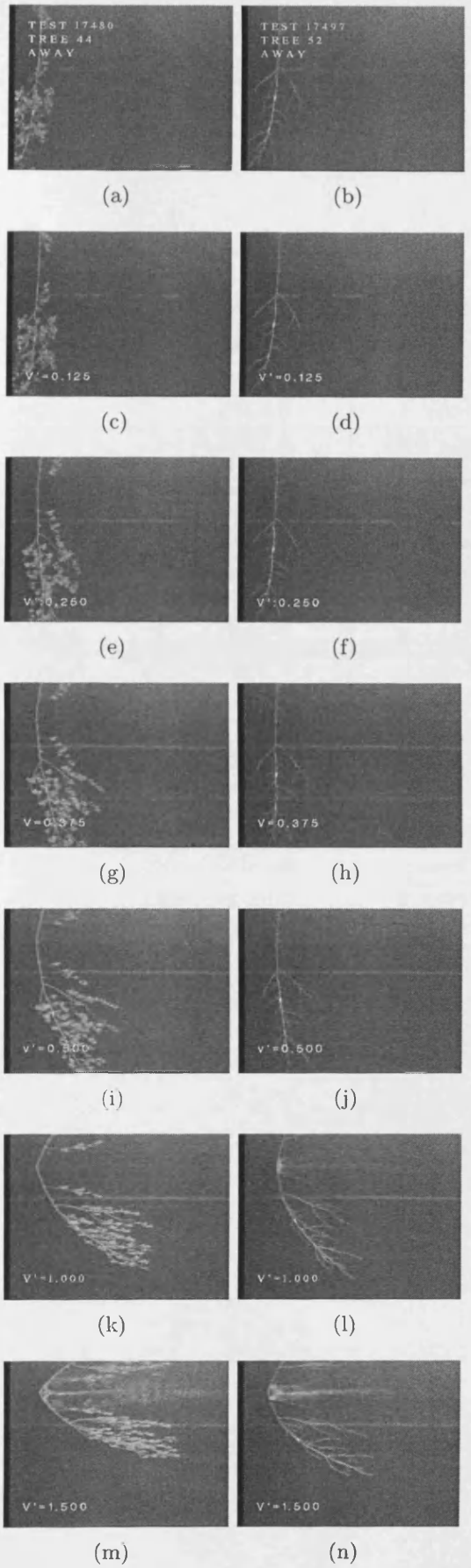

Figure 67: P4B2

Tree	**Foliated U_{AB}**	**Defoliated U_{AB}**
Test	**m/s**	**m/s**
Salix 1	0.4883	0.6247
Salix 2	0.4184	0.3266
Salix 3	0.3980	0.4038
Salix 4	0.4915	0.4698
Salix 5B1	0.1646	0.2580
Salix 5B2	0.2373	0.3300
Salix 6B1	0.2595	0.7792
Salix 6B2	0.4778	0.4223
Salix 7B1	0.3123	0.4777
Salix 7B2	0.6481	0.4646
Salix 8	0.3782	0.3380
Salix 9	2.3881	0.3914
Salix 10	0.3834	0.3548
Salix 11	0.2959	0.9133
Salix 12	0.5076	0.5015
Salix 14	0.1845	0.2580
Alnus 1	0.7278	0.6309
Alnus 3	0.4304	0.4462
Alnus 4	0.5446	0.6730
Alnus 5	0.8890	0.8399
Populus 3	0.4523	0.5508
Populus 2B1	0.5113	0.5563
Populus 2B2	0.5242	0.6297
Populus 4B1	0.5584	0.5090
Populus 4B2	0.3120	0.4197

Table 46: Threshold velocity values for *Salix*, *Alnus* and *Populus*